ISSN 2301-1092 • ISSN (en línea) 2301-1106

MEMORIA

INVESTIGACIONES EN INGENIERÍA

Nº 28

FACULTAD DE INGENIERÍA

UM
UNIVERSIDAD DE MONTEVIDEO

MEMORIA

Investigaciones en Ingeniería

ISSN 2301-1092 • ISSN (en línea) 2301-1106

Núm. 28 (2025)

Sumario

Págs.

Editorial – Innovación Técnica y Multidisciplinariedad en la Ingeniería Contemporánea.

Rafael Sotelo **1-2**

Polymer Pathways: A sustainable approach to plastic waste disposition

Vías de polímeros: un enfoque sostenible para la eliminación de residuos plásticos

E. A. Jafri, I. Asif, B. Fatima, M. F. Aamir **3-19**

Enhanced Mobility Aid for the Visually Impaired: An Ultrasonic Sensor and Arduino-Based Smart Walking Stick

Ayuda de movilidad mejorada para personas con discapacidad visual: un sensor ultrasónico y un bastón inteligente basado en Arduino

S. Memon, M. M. Aamir, S. Ur Rehman, H. Mustafa, M. Shakir Sheikh **20-31**

Design and Development of IoT-based Harvesting Robo-Vec

Diseño y desarrollo de Robo-Vec de recolección basado en IoT

S. Ur Rehman, Y. Abdul Wahab **32-44**

Post Weld Quenching Impact on Microstructure and Mechanical Properties (Tensile, Impact, Hardness) of High-Strength Low-Alloy Steel

Impacto del temple posterior a la soldadura en la microestructura y las propiedades mecánicas del acero de baja aleación y alta resistencia

A. Shazad, M. Uzair **45-57**

Mechanical Characterization of Post weld quenched Al 6082-T6 TIG welded Joints

Caracterización mecánica de uniones soldadas TIG de Al 6082-T6 templadas después de la soldadura

A. Shazad, M. Uzair, J. Jadoon, S. Khan Marwat **58-70**

Interacción Suelo-Estructura de una edificación con losa de cimentación con los modelos estáticos de Winkler y Pasternak

Soil-Structure interaction of a building with a foundation slab with the static models of Winkler and Pasternak

J. Contreras, G. Villarreal **71-84**

Design of a vehicular emergency intercom system using electronic circuits and sensors

Diseño de un sistema de intercomunicación de emergencia vehicular utilizando circuitos electrónicos y sensores

H. Santillán, C. López, K. García, D. Cárdenas **85-109**

Explorando las Profundidades: Reconstrucción de Cuevas y detección de Murciélagos mediante Imágenes Infrarrojas

Exploring the Depths: Cave Reconstruction and Bat Detection Using Infrared Imaging

I. Cruz Rangel, J. A. Arroyo Romero, I. Barcenas Reyes, J. B. Hurtado Ramos, F. J. Ornelas-Rodriguez, A. Ramirez Pedraza, J. J. González-Barbosa **110-125**

Interacción suelo-estructura de una edificación con losa de cimentación por los modelos dinámicos de Barkan y Savinov, Norma Rusa SNIP 2.02.05-87 y Gazetas y Mylonakis

Soil-structure interaction of a building with a foundation slab with the dynamic models of Barkan and Savinov, Russian Standard SNIP 2.02.05-87 and Gazetas and Mylonakis

J. Contreras, G. Villarreal **126-153**

An IoT-Based Autonomous Waiter Robot

Un robot camarero autónomo basado en IoT

S. Ur Rehman **154-167**

Two-Dimensional Numerical Analysis on the Double Shear Specimens of Timber-Concrete Composite Structures: Effects of Screw Dimensions and Timber Density

Análisis Numérico Bidimensional de Especímenes de Doble Corte en Estructuras Compuestas de Madera y Concreto: Efectos de las Dimensiones del Tornillo y la Densidad de la Madera

L. Jun En, M. A. Mohd Snin, S. N. Fatimah Ghazali, N. A. Fatihah Mokhtar, M. Ikmal Zainal, R. Suryavarman **168-182**

Eficiencia de la lombriz roja californiana en la biorremediación de suelos contaminados con hidrocarburos

Efficiency of the Californian red earthworm in the bioremediation of soils contaminated with hydrocarbons

S. Baldeon Coronado, K. Baltazar Torres, J. P. Ríos Bartra **183-192**

Application of Six Sigma Methodology for Enhancement of Soft Plastic Extrusion Process

Aplicación de la Metodología Seis Sigma para la mejora del proceso de extrusión de plásticos blandos

M. M. Uz Zaman Siddiqui, A. Tabassum **193-221**

Parametric Optimization of Electric Discharge Machining for AISI 1045 Steel: A Comprehensive Study

Optimización paramétrica del mecanizado por electroerosión para acero AISI 1045: un estudio exhaustivo

M. M. Uz Zaman Siddiqui, S. Amir Iqbal, A. Zulqarnain, A. Tabassum **222-268**

Direct Air Carbon Capture Using Metal-Organic Frameworks: Techno-Economic Performance of Temperature Vacuum Swing Adsorption Systems

Captura directa de carbono en el aire mediante estructuras metalorgánicas: Rendimiento técnico-económico de sistemas de adsorción por oscilación de temperatura y vacío

H. Ali, D. Uddin, A. A. Naqvi, U. Naeem, N. Akhtar, S. Shams, A. Karim **269-286**

On-Time Delivery Improvement in an Injection Molding Process Applying a Problem-Solving Approach Based on Lean-Sigma and the MSA Effect

Mejora del índice de Entregas a Tiempo en un Proceso de Moldeo por Inyección de Plástico Utilizando un Enfoque Orientado a la Solución de Problemas Basado en Lean-Sigma y el Efecto del Sistema de Medición

O. Celis-Gracia, J. L. García-Alcaraz, F. Hermosillo-Villalobos **287-302**

Evaluación de los factores de riesgos psicosociales y la incidencia en el desempeño laboral de los trabajadores de la Municipalidad Distrital de Yuracyacu

Evaluation of psychosocial risk factors and their impact on the work performance of the workers of the District Municipality of Yuracyacu

A. J. García Castillo, E. N. Meza Pérez, B. T. Padilla Macedo **303-310**

Evolución de la Metrología Eléctrica en Uruguay Parte I: Desde sus inicios hasta la primera mitad del siglo XX

Evolution of electrical metrology in Uruguay Part I: Beginnings up to the first half of the 20th century

D. Slomovitz **311-329**

Lista de Autores – Memoria Investigaciones en Ingeniería 330-332

Lista de Revisores – Memoria Investigaciones en Ingeniería 333

Editorial – Innovación Técnica y Multidisciplinariedad en la Ingeniería Contemporánea.

Nos complace presentar una nueva edición de Memoria Investigaciones en Ingeniería, en la que continuamos nuestro compromiso con la difusión de trabajos científicos y técnicos que reflejan la constante evolución de la ingeniería y su capacidad para responder a desafíos de gran relevancia para la sociedad. Esta entrega destaca por su marcada diversidad temática y por la riqueza de enfoques que combinan sostenibilidad, automatización, tecnologías emergentes e ingeniería estructural avanzada.

Abrimos esta edición con un enfoque en sostenibilidad medioambiental, mediante el artículo Polymer Pathways, que propone alternativas innovadoras para la disposición de residuos plásticos, abordando uno de los problemas más críticos de la actualidad con soluciones basadas en ingeniería verde.

La inclusión de tecnologías accesibles para mejorar la calidad de vida está representada por el desarrollo de un bastón inteligente para personas con discapacidad visual. Este dispositivo, basado en sensores ultrasónicos y Arduino, ejemplifica cómo la ingeniería puede democratizar la asistencia tecnológica.

El avance de la robótica aplicada al sector agrícola se plasma en el diseño de Robo-Vec, un sistema autónomo IoT orientado a la cosecha eficiente. Este trabajo evidencia el impacto de la automatización inteligente en la agricultura sostenible.

La caracterización mecánica y microestructural continúa siendo un pilar de nuestra revista. Dos investigaciones abordan los efectos del enfriamiento post-soldadura en aceros de alta resistencia y en aleaciones de aluminio, revelando cómo las condiciones de tratamiento térmico influyen en propiedades críticas como la tenacidad, la dureza y la resistencia.

En el ámbito de la ingeniería civil y estructural, se presentan comparaciones entre modelos de interacción suelo-estructura estáticos y dinámicos (Winkler, Pasternak, Barkan, Savinov, SNIP y Gazetas), aplicados a losas de cimentación. Estos trabajos fortalecen el análisis de comportamiento estructural ante distintas condiciones geotécnicas.

La seguridad en el transporte motiva el diseño de un sistema de intercomunicación vehicular basado en sensores electrónicos, una propuesta que puede integrarse en entornos urbanos inteligentes para una mejor respuesta en situaciones de emergencia.

Desde el ámbito de la exploración subterránea, destacamos un artículo que emplea imágenes infrarrojas para la reconstrucción de cuevas y la detección de murciélagos, integrando visión artificial en aplicaciones ecológicas y geoespaciales.

La robótica de servicios también tiene cabida con un desarrollo de camarero autónomo basado en IoT, orientado a entornos de hospitalidad. Esta solución demuestra cómo la ingeniería puede optimizar la atención al cliente en el sector servicios.

El análisis numérico de uniones compuestas madera-hormigón mediante doble corte aporta nueva evidencia sobre el impacto de variables geométricas y materiales en la resistencia estructural, fortaleciendo las bases para el diseño eficiente en sistemas híbridos.

En el campo de la remediación ambiental, se investiga la eficiencia de la lombriz roja californiana en la limpieza de suelos contaminados por hidrocarburos, destacando un enfoque biotecnológico para la recuperación ecológica.

La mejora de procesos industriales se aborda desde diferentes ángulos: mediante la aplicación de Six Sigma en extrusión de plásticos blandos, la optimización paramétrica del mecanizado por descarga eléctrica en acero AISI 1045, y el uso de metodologías Lean-Sigma para mejorar la puntualidad en procesos de moldeo por inyección.

https://doi.org/10.36561/ING.28.1
ISSN 2301-1092 • ISSN (en línea) 2301-1106

En el ámbito energético y ambiental, se presenta un análisis tecnoeconómico sobre captura directa de carbono en aire usando sistemas de adsorción tipo TVSA basados en estructuras metal-orgánicas, una solución clave en la lucha contra el cambio climático.

Desde la gestión organizacional, se incluye un estudio de riesgos psicosociales y su efecto en el rendimiento laboral en una entidad pública, ampliando la visión de la ingeniería hacia el bienestar de las personas en el entorno de trabajo.

Finalmente, se ofrece una revisión histórica de la evolución de la metrología eléctrica en Uruguay, aportando una perspectiva única sobre la consolidación de estándares y tecnologías a lo largo del siglo XX.

Agradecemos a todos los autores por sus valiosas contribuciones, a los revisores por su rigurosidad y compromiso, y a nuestros lectores por seguir apoyando la divulgación científica de calidad. Les invitamos a explorar cada uno de estos trabajos y a sumarse activamente a las futuras convocatorias de nuestra revista.

Dr. Ing. Rafael Sotelo
Editor en Jefe
Facultad de Ingeniería
Universidad de Montevideo

https://doi.org/10.36561/ING.28.1
ISSN 2301-1092 • ISSN (en línea) 2301-1106

Polymer Pathways: A sustainable approach to plastic waste disposition

Vías de polímeros: un enfoque sostenible para la eliminación de residuos plásticos

Caminhos dos polímeros: uma abordagem sustentável para a disposição de resíduos plásticos

Ifrah Asif[1(*)], Eylia Abbas Jafri[2], Bushra Fatima[3], Mehak Fatima Aamir[4]

Recibido: 28/07/2024 Aceptado: 28/10/2024

Summary. - Pakistan is a land filled with natural resources, but gradually due to depletion of these, the country aims to benefit use from different materials that can serve the intended purpose with the minimal cost. Our country annually generates 3.3 million tons of plastic waste. The plastic waste disposal is one of the most threatening challenges to all major metropolitan areas around the world. If not sorted out immediately, it might degrade in the environment for many years. This study proposes the use of waste PET bottles in road construction. The main objective is to analyse and compare the properties of plastic-mixed bitumen roads over non-plastic mixed bitumen roads. Shredded plastic bottles were mixed with bitumen in different ratios (0%, 6%, 8% and 10%) to enhance the stability and durability of roads. Different tests like Marshall stability, penetration, ductility, and softening tests were performed in the laboratory. The results showed that bitumen with 8% plastic has a low flow value. Also, the plastic modifier to bitumen increases the density of the mixture which improves the structural performance of the asphalt pavement. There is an increase in the softening point which illustrates that plastic modified bitumen roads can withstand hot weather more effectively than traditional bitumen roads This addition of plastic in bitumen will be a boon for Pakistan's road industry.

Keywords: Polyethylene terephthalate (PET), asphalt, binder, Marshall stability, waste plastics, aggregates, bitumen, optimum binder content.

(*) Corresponding author.

[1] Lecturer, Department of Mechanical Engineering, NEDUET (Pakistan), ifrahasif@neduet.edu.pk,
ORCID iD: https://orcid.org/0000-0001-7551-2199

[2] Lecturer, Department of Mechanical Engineering, PNEC-NUST (Pakistan), eylia@pnec.nust.edu.pk,
ORCID iD: https://orcid.org/0009-0009-0859-4134

[3] Lecturer, Department of Mechanical Engineering, NEDUET (Pakistan), bushrafatima@neduet.edu.pk,
ORCID iD: https://orcid.org/0009-0008-8586-249X

[4] Student, Department of Mechanical Engineering, NEDUET (Pakistan), fatima4500257@cloud.neduet.edu.pk,
ORCID iD: https://orcid.org/0009-0005-8161-7444

Memoria Investigaciones en Ingeniería, núm. 28 (2025). pp. 3-19
https://doi.org/10.36561/ING.28.2
ISSN 2301-1092 • ISSN (en línea) 2301-1106 – Universidad de Montevideo, Uruguay

Resumen. - *Pakistán es un país repleto de recursos naturales, pero debido a su agotamiento gradual, el país busca aprovechar el uso de diferentes materiales que puedan cumplir su propósito con un costo mínimo. Nuestro país genera anualmente 3,3 millones de toneladas de residuos plásticos. La eliminación de estos residuos es uno de los desafíos más importantes para las principales áreas metropolitanas del mundo. Si no se gestiona de inmediato, podría degradarse en el medio ambiente durante muchos años. Este estudio propone el uso de botellas de PET desechadas en la construcción de carreteras. El objetivo principal es analizar y comparar las propiedades de las carreteras con asfalto mezclado con plástico frente a las de asfalto mezclado sin plástico. Se mezclaron botellas de plástico trituradas con asfalto en diferentes proporciones (0 %, 6 %, 8 % y 10 %) para mejorar la estabilidad y durabilidad de las carreteras. Se realizaron diversas pruebas de laboratorio, como pruebas de estabilidad Marshall, penetración, ductilidad y ablandamiento. Los resultados mostraron que el asfalto con un 8 % de plástico tiene un bajo índice de fluidez. Además, el modificador plástico del asfalto aumenta la densidad de la mezcla, lo que mejora el rendimiento estructural del pavimento asfáltico. Hay un aumento en el punto de ablandamiento que ilustra que las carreteras de betún modificado con plástico pueden soportar el clima cálido de manera más efectiva que las carreteras de betún tradicionales. Esta adición de plástico al betún será una bendición para la industria vial de Pakistán.*

Palabras clave: *Tereftalato de polietileno (PET), asfalto, aglutinante, estabilidad Marshall, residuos plásticos, áridos, betún, contenido óptimo de aglutinante.*

Resumo**. -** *O Paquistão é um país repleto de recursos naturais, mas, devido ao esgotamento gradual desses recursos, o país busca se beneficiar do uso de diferentes materiais que possam atender aos propósitos pretendidos com o mínimo custo. Nosso país gera anualmente 3,3 milhões de toneladas de resíduos plásticos. O descarte de resíduos plásticos é um dos desafios mais ameaçadores para todas as principais áreas metropolitanas do mundo. Se não forem tratados imediatamente, podem se degradar no meio ambiente por muitos anos. Este estudo propõe o uso de garrafas PET na construção de estradas. O objetivo principal é analisar e comparar as propriedades de estradas com mistura de plástico e asfalto em comparação com estradas com mistura de asfalto sem plástico. Garrafas plásticas trituradas foram misturadas com asfalto em diferentes proporções (0%, 6%, 8% e 10%) para aumentar a estabilidade e a durabilidade das estradas. Diferentes testes, como estabilidade Marshall, penetração, ductilidade e amolecimento, foram realizados em laboratório. Os resultados mostraram que o asfalto com 8% de plástico apresenta baixo valor de fluidez. Além disso, o modificador plástico no asfalto aumenta a densidade da mistura, o que melhora o desempenho estrutural do pavimento asfáltico. Há um aumento no ponto de amolecimento, o que ilustra que estradas de asfalto modificado com plástico podem suportar climas quentes de forma mais eficaz do que estradas de asfalto tradicionais. Essa adição de plástico ao asfalto será uma bênção para a indústria rodoviária do Paquistão.*

Palavras-chave: *Tereftalato de polietileno (PET), asfalto, ligante, estabilidade Marshall, resíduos plásticos, agregados, betume, teor ideal de ligante.*

1. Introduction. - In research, it has been found that plastic waste can sustain on earth surface for about 4500 years without being changed or decomposed [1]. Plastic is a vital substance, and it is present everywhere in various forms, from synthetic fishing nets to single-use items like water bottle and trash bags. Currently, 400 million tonnes of plastic waste produces every year, and it is observed that plastics are not biodegradable and are unaltered under the surface of earth for about a period of 4500 years. The manufacturing of plastics has grown exponentially since 1950, rising from 2 metric tonnes in 1950 to 322 metric tonnes in 2015. Global manufacturing reached an astounding 8.3 metric billion annually as of 2017. Around 36 metric million tons of plastic waste is generated in the United States every year [2]. It is approximated that by 2050 a billion metric tons of plastics is consumed and present in landfills. The plastic is a threat to biosphere. Why? The answer to this statement lies in the properties of plastic itself. Plastics are very much flexible, handy, cheap, lightweight and durable so once they have been used, they can't easily be disposed even they take centuries to be decomposed completely [3].

Landfilling is a conventional approach to deal with plastic waste but due to lack of space for landfills, it was no longer a justified solution. An alternative to landfilling is incineration of plastic waste but it was also an ineffective solution due to the release of noxious fumes which are unhealthy to the environment [2]. The best and productive solution for the disposal of waste plastic is to reuse it. In this way the need for the production of plastic reduces and it will circulate around the surroundings, hence reduces the health risks. Steps have been taken to reuse plastic waste in different sectors including clothing accessories, transportation and construction [4]. Researchers found that plastic- bitumen mixed pavements are more flexible than the ordinary asphalt pavements. When water gathers over the asphalt pavements, it penetrates and create depressions known as potholes decreasing the strength and the life of roads and bridges. On the contrary, plastic increases the strength and durability of roads when it is added to the bituminous mix. It also increases the slip resistance and lowers the cost of the construction [1].

Plastic is a flexible synthetic polymer that can be heated and moulded into different shapes. It is cheap, strong, formable, lightweight and corrosion resistant. On the basis of physical properties, it is classified as thermoplastic or thermosetting plastic. Thermoset plastics are formed by the process of irreversible polymerization. They do not soften upon heating once they have moulded. Examples of widely used thermosets are vulcanized rubber, polyurethane foams and phenolic resins. On the contrary, thermoplastics undergo multiple heating and cooling cycles and becoming soft and hard during these cycles. Atoms and molecules in thermoplastics consist of long and short carbon chains that work independently. This structure makes these materials non-biodegradable due to their resistance to degradation or hydrolytic cleaving of chemical bonds. A common example of thermoplastics is polyethylene terephthalate (PET) in clothing fibers and in packaging of beverages and foods [5], [6], [7].

PET or Polyethylene terephthalate is the most used and recyclable plastic in the world. It is used to package 70% of carbonated soft drinks, fruit juices and bottled water. It is flexible, colorless and translucent polymer. It has a good tensile strength and chemical resistance. In South Asia only, the consumption of PET by the six largest countries is to almost double from 886,000 tons in 2018 to 1.52 million tons in 2030 [8]. Due to its good creep resistance and low moisture absorption, it is suitable to be used in asphalt pavement [9], [10]. The plastics can reduce thermal susceptibility to bitumen, such as rutting in warm temperatures and fatigue cracking in cold temperature [8]. Plastic waste can be added to the bitumen either by wet or dry process. The dry process is considered to be simple and economical while the wet process involves a higher investment and machinery. Hence, it is not commonly used [11]. In the wet process, plastic waste is made into powder form and then add to the hot bitumen before the aggregates are mixed. The temperature range for this method is preferably 155ºC to 165ºC. On the contrary, dry process involves the shredding of waste plastic. These plastics are coated over pre-heated aggregates. The bitumen is heated to 160ºC and get mixed with plastic coated aggregates [12], [13]. A study reported a marked improvement in various parameters such as Marshall stability and tensile strength for the outputs of dry process in comparison to that of wet process [11].

The use of plastic-modified bitumen in roads construction is indeed a great idea which has been adopted by many countries in order to solve the problem of plastic waste disposal and to increase the lifetime of their roads. The United Kingdom government had invested £23 million into plastic roads technologies. A Ghana based plastic recycling company produced pavement blocks from waste plastic that have been approved by Ghana's Ministry of Science and

Technology and have been used to construct a road in Accra. Moreover, Netherlands have also built a 30-meter cycle path in the Zwolle municipality [14], [15]. India was also one of the biggest promoters of PET modified roads. Many other countries including China and Ethiopia have been working under this idea to enhance their roads quality [16]. The authorities in Pakistan also took initiatives to build plastic modified roads across the country. Pakistan's first plastic road under the "World Without Waste" program was completed in December 2021 at F-Park and Ataturk Avenue, Islamabad, using almost 8 tons of polyethylene terephthalate recycled plastics. Over 2.5 tons of discarded lubricant bottles were recycled for the construction of 730 feet long and 60 feet wide road on which a multinational firm is located in Karachi. The discarded lubricant's plastic bottles were incorporated in the construction of the asphalt road using the dry process method, reducing plastic waste [17]. More projects regarding plastic modified bitumen roads are under operation in the province of Sindh and Punjab [18].

The increasing use of plastic and its disposal has become a worldwide issue which needs to be resolved by taking some effective measures. This study shows a comparative analysis between plastic modified bitumen and non-plastic bitumen roads. It highlights the mechanical properties and usefulness of PET modified roads and listed all the results that have been obtained from the experiments performed. It focused on the need of a sustainable action that makes the true use of plastic wastes instead of their elimination. For the present study, we use waste PET bottles as a plastic modifier. Around 100 bottles were crushed to a size of 2-4mm in a crusher machine and then1 sieved thorough 4.5mm sieve.

2. Methodology. - The optimized bituminous mix's binder content was optimized using the Marshall mix design. In addition, the same procedure was used to optimize three other plastic types. The amount of bitumen needed in the bituminous mix to produce fully coated aggregates, sealed air gaps, and increased durability is known as the optimal binder content. The Marshall Testing Machine was used to conduct this test. The specimens with 2.5%, 3%, 3.5%, 3.9%, 4.6%, 5.5%, and 7% asphalt by weight of aggregates, were made using standards ASTM D1559-89 and AASHTOO standard, T245-82.

Approximately 1200 grams of aggregates are heated to 160-185℃. The first trial involves heating bitumen to 130-150℃ and adding 2.5% bitumen by weight to the aggregates. The heated aggregates and bitumen were completely mixed at a temperature of 150–160℃. The mixture is then placed in a prepared mold and crushed using a rammer with 75 blows on both sides at a temperature of 130-150℃. The produced mixture is then placed into the Marshall Testing Machine. The Design Criteria or the Marshall Method Table I were used to determine the optimal binder content for heavy traffic surface and base mixes.

Marshall Method Mix Criteria	Surface and Base Mix					
	Light Traffic		Medium Traffic		Heavy Traffic	
	Minimum	Maximum	Minimum	Maximum	Minimum	Maximum
Compaction, no. of blows at each end of the specimen	35		50		75	
Stability, (lb.)	500	-	750	-	1500	-
Flow (0.01 inch)	8	20	8	18	8	16
Percentage of air voids	3	5	3	5	3	5
Percentage of voids in mineral aggregate (VMA) for 3/4″size	14	-	14	-	14	14

Table I. - Design Criteria of the Marshall Method.

After determination of optimal binder content of bitumen, a mixture consisting solely of virgin bitumen as well as PET was prepared. Different percentages of plastic were chosen and analyzed for each modified mix. Two different processes i.e. wet process and dry process can be used. However dry process was used as it is more economical and does not require any extra effort to preheat the plastic. To begin, an asphalt sample core with 4% plastic content was to be made. This process involves the heating of aggregates having 12.5mm dimensions at 170ºC. About 100 waste PET bottles were crushed to a size of 2-4mm size in a crusher machine and then sieved thorough 4.5mm sieve. These aggregates are then coated by hot shredded plastic. Grade 60/70 bitumen which confirms to the ASTM standards is then mixed with plastic coated aggregates. A digital scale is used to measure the sample weights, and an industrial grade mixer is used to uniformly mix the contents.

The following procedure is applied on the sample.
a. Heating the sample in a special apparatus to obtain a cylindrical shape as per the standards.
b. Then the sample is left in the oven for 4 hours.
c. The asphalt molds are then air cooled at room temperature.
All The above steps are repeated with varying content of plastic by weight of bitumen (0%, 6%, 8% and 10%).

As shown in Figure I, each sample was labelled according to its plastic content, and each has a diameter of 100mm and a height of 64mm as per AASHTO standards.

Once the samples cool, the bitumen quality tests were to be applied. At first, the Marshall Stability Test was to be performed. This test estimates the maximum load that a bitumen sample can bear under standard testing temperature of 60ºC. It was performed by Marshall Testing Machine Figure IV. Along with the MS, density, stability and flow determination, stability and penetration, ductility and softening of the cores were checked in Figure V.

The density of the specimen can be determined by weighing it in air and clean water at room temperature and the difference between the two gives the density value called Density Determination. Another test value that can be measured from Marshal Stability tester is the Stability and Flow determination. The flow value is the vertical deformation when the maximum load is applied to the specimen.

After stability, the penetration, ductility and softening of the sample cores were to be checked. This test determines the consistency of bitumen materials by measuring the depth (in units of one tenth of mm) to which a standard needle will penetrate under specific condition of load, duration and temperature. The weight of the standard needle assembly is 100 gm. The needle penetrates in the sample for a duration of 5 seconds at 25ºC and is used for the purpose of grading. The softer the bitumen the greater will be the penetration. ASTM Standard D5-86 and AASHTO standard T49-68. The penetration sample is shown in the Figure I.

Figure I. Penetration Sample.

Another major factor is Ductility; expressed as a distance in centimeters to which a standard briquette of bitumen can be stretched before the thread breaks. This test helps to determine the asphalt's flexibility and its resistance to cracking in cold weather conditions, as shown in Figure II.

Figure II. Ductility Sample.

Softening point is the temperature at which the sample attains a particular degree of softening under specified conditions. The apparatus used for this test is known as ring and ball apparatus. It was conducted to assess the temperature susceptibility and suitability of asphalt mixtures in specific climates and weather conditions, especially in hot weather. Figure III.

Figure III. Softening Point Sample.

Figure IV. Marshall Tester.

Figure V. Sample Core.

3. Results and Discussions. - The laboratory results for both virgin mix and modified plastic specimen, as well as the impact of plastic are discussed below in Table 2.

% of bitumen by wt. of mix	Unit wt. (pcf.)	% Air voids	Flow in 1/100 inch	Stability, Lbs.	% VMA
2.5	137.5	15.2	6	1000	20
3	142	10	7	2350	16.7
3.5	145.5	7.6	8	2700	15.6
3.9	147.5	5.5	11	2750	14.9
4.6	148	3.7	16.5	2000	15.3
5.5	147.5	2.8	30	1250	16.1
7	146	2	44	400	17.6

Table II. Experimental Results for Optimum Binder Content.

According to the Marshal mix design, the trial findings for optimum binder content are determined where the best value of stability occurs, and the air voids are within acceptable limits (usually between 3% and 8%). The graph shows that when the binder content increases, air voids decrease. These details better compaction and performance however values below 3% can restrict the expansion of asphalt binder during temperature fluctuations, causing potential cracking and instability [19]. There is an increase in the stability value with the percentage of bitumen up to 3.9% where it peaks at 2750 lbs. Although there is an increase at flow value with the increase in binder, reaching a maximum at 4.6, but the stability begins to decline. Also, the minimum % VMA is at 3.9% bitumen content but within the acceptable range. On comparison with the stability and flow values; it is concluded the optimum bitumen binder content is 3.9%. This is also consistent with [20]. The results of tests performed to find optimum bitumen content are listed in Table II.

When plastic is added, the mixture's viscosity decreases, and its Marshall Stability value rises until it reaches its ideal content. However, the increased friction between the mixture's various particles causes the MS value to drop after the optimal content. The use of different kinds of plastic, varying volumes of bitumen, and a variable mixing technique are the causes of the variation in the ideal percentages that has been noticed as shown in Figure VI.

Figure VII shows the effect on flow value with varying percentage of plastic in asphalt mixture. As seen, flow value decreases while adding plastic to the bitumen. Plastic increases the viscosity and stiffness of the bitumen, and the mixture become less susceptible to deformation, especially under high temperature conditions. As shown, bitumen with 8% plastic has a low flow value. This decrease in flow value indicates greater resistance to rutting, which is a common problem in asphalt pavements. Further, as shown in Figure VIII, density increases with plastic content up to 8% and

thereafter decreases. Thus, the addition of plastic modifiers to bitumen increases the density of the bitumen mixture which improves the structural performance of the asphalt pavement. Similarly, the stability of the mixture increases with plastic content up to a certain value i.e. 8% and thereafter decreases as shown in Figure IX. According to the data, there exists an ideal range for the binder content that maintains acceptable flow values while optimizing stability. Hence, the optimum plastic content was found to be 8%.

All the reading taken from the penetration test are listed in Table II. Each sample was tested thrice to get the average penetration value. Figure X; illustrates the effect of plastic concentration on penetration. The penetration depth decreases as the amount of plastic increases up to 8% and thereafter increases. This explains that the asphalt mix has the greater stiffness, durability and resistance to rutting at 8% plastic content. The results of ductility test are listed in Table III. The distance the specimen stretched before breaking was measured and recorded as its ductility value.

As shown in Figure XI, ductility increases with plastic content up to 8% and decreases afterwards. This means that the bitumen modified with 8% plastic have greatest elongation or elasticity before it fails. The results of softening test are listed in table 4. In this test, when either of the two balls touched the base of the cylinder, the temperature was measured and recorded as the softening point of the given bitumen sample.

It is shown in Figure X that the softening point increases with plastic content up to 8% and thereafter decreases. This increase in the softening point illustrates that plastic modified bitumen roads can withstand hot weather more effectively than traditional bitumen roads.

According to the data, there exists an ideal range for the binder content that maintains acceptable flow values while optimizing stability [21].

Figure XII highlights the superiority of plastic-mixed bitumen sample over non-plastic bitumen sample. It is less susceptible to softening in hot weather, hence, reducing the risk of rutting and pothole formation. It remains flexible at lower temperatures, reducing the risk of cracking and deformation. It enhances bitumen's resistance to wear and tear, resulting in more durable roads. Furthermore, reusing plastic waste contributes in a sustainable environment and reduces the maintenance time and cost. Therefore, in order to enhance asphalt's overall qualities, this amount of plastic modification is advised. It is significant to remember that using modified asphalt in construction might result in pavement structures that are more resilient and long-lasting.

Specimen	Optimum binder %		Marshall Stability (lbs)	Flow value in 1/100 inch	Density (PCF)
	bitumen %	plastic %			
1	100	0	1926.84	22	2.23
2	96	4	2647.75	21	2.25
3	94	6	3105.21	24	2.25
4	92	8	3430.39	23	2.26
5	90	10	2438.31	26.5	2.19

Table III. Experimental Results.

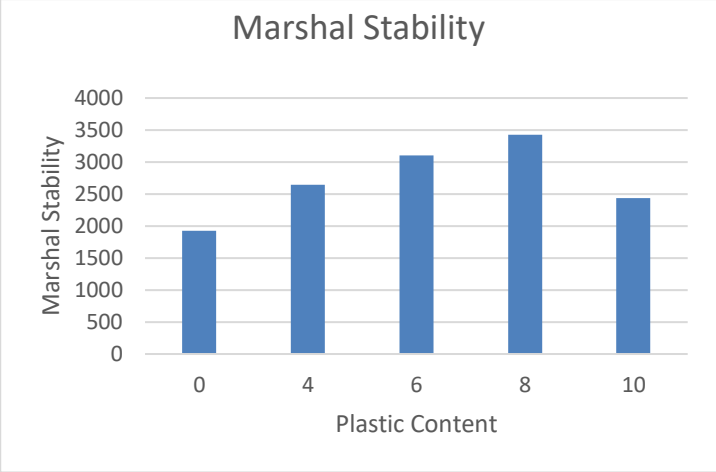

Figure VI. Experimental Results of Marshal Stability.

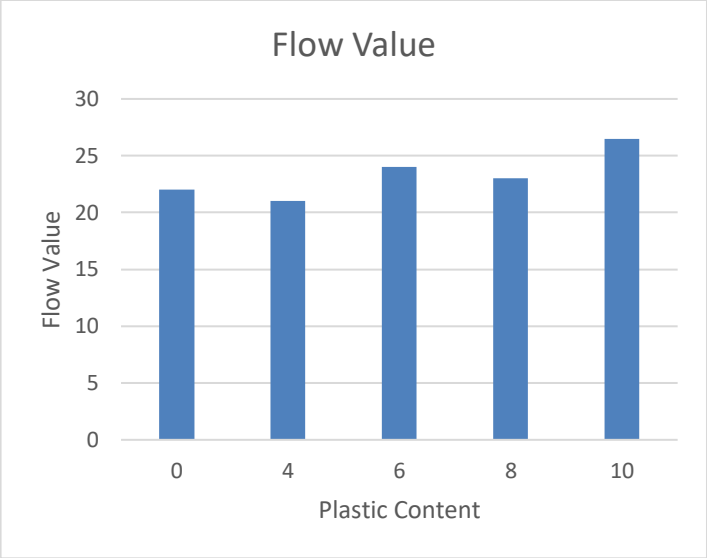

Figure VII. Experimental Results of Flow Value.

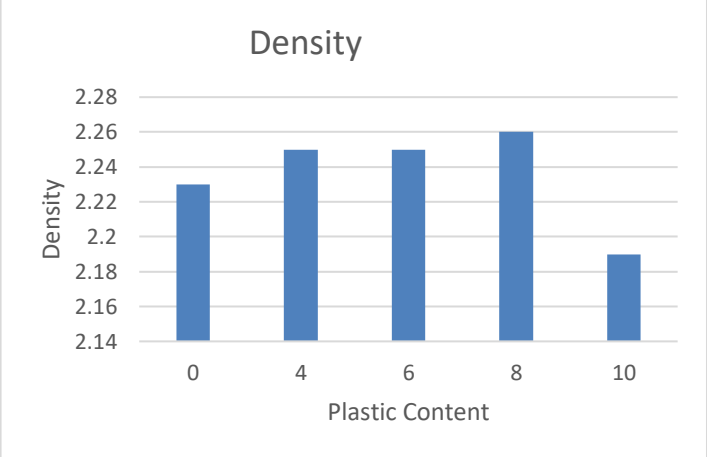

Figure VIII. Experimental Results for Density.

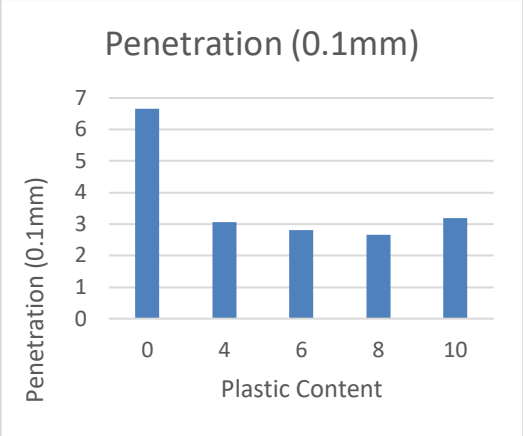

Figure IX. Experimental Results of Penetration.

Specimen	Plastic %	Ductility (cm)
1	0	108
2	4	110
3	6	112
4	8	115
5	10	110

Table IV. Experimental Results of Ductility.

Specimen	Plastic %	Softening point (°C)		
		Ball 1	Ball 2	Average
1	0	45	46	45.5
2	4	60	61	60.5
3	6	62	61	61.5
4	8	62	63	62.5
5	10	60	61	60.5

Table V. Experimental Results of Softening.

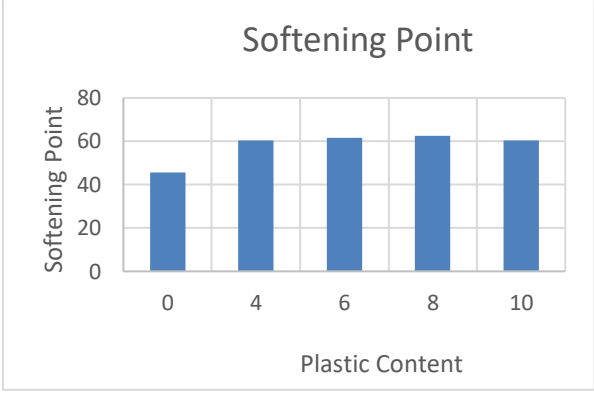

Figure X. Experimental Results for Softening Point.

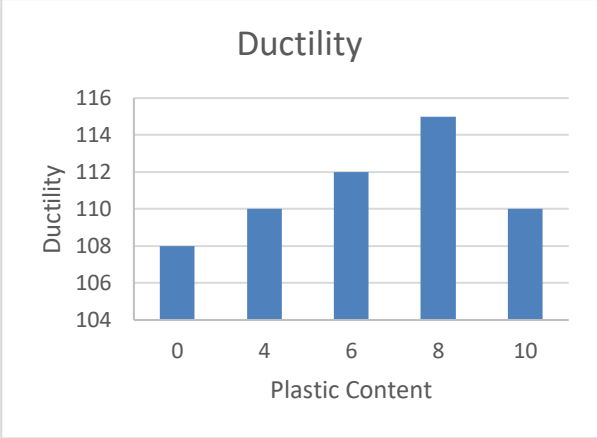

Figure XI. Experimental Results for Ductility.

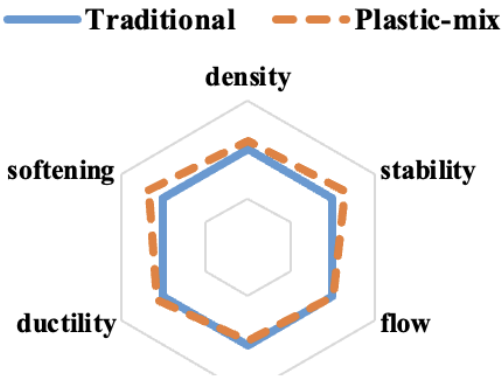

Figure XII. Performance indicators of Traditional vs Plastic Bitumen-modified.

3.1. Statistical Analysis. - A correlation analysis was performed amongst the Plastic content and various properties like Ductility, Marshal Stability, Penetration and Softening Point. The results are discussed below:

1. There is a moderately positive association between ductility and plastic content, indicating that ductility tends to rise in tandem with plastic content. This relationship may not be consistent across samples, though, as it is not statistically significant ($p > 0.05$).
2. The moderate positive correlation between Plastic content and Marshal Stability indicates that higher plastic content is associated with higher Marshal Stability values, but this rise in Marshal Stability is only valid till 8% of plastic content, however it reduces at 10% plastic content.
3. According to a strong negative association, penetration drops as plastic content rises, meaning that more plastic materials are less permeable.

		Ductility	Marshal Stability	Penetration	Softening Point
Plastic	**Pearson Correlation**	0.589	0.576	-0.796	0.817
	P-VALUE	0.296	0.31	0.107	0.091
	n	5	5	5	5

Table VI. Experimental Results of Statistical Analysis.

4. Economic Analysis of Plastic Bitumen Road for Pakistan.

4.1 Pakistan's Bitumen Import Cost. - Approximately, Pakistan imported bitumen of about $ 3 million in the year of 2023, increasing cost of bitumen per year shown in Figure X. Roads made from plastic waste give an opportunity to reduce the amount of bitumen use for the road construction and eventually reduce the import cost of bitumen annually. The details of 2023 bitumen import cost approx. in USD $ 45,814.70K and the total tonnage was about 207240 metric ton from the world [22]. By using plastic waste in roads, we can approx. reduce 10% cost of bitumen import and will be able to build more sustainable and eco-friendly roads network.

4.1.1 Cost Estimation of Plastic Waste Processing. - Use of plastic waste for road construction, in the bituminous mixture is 6% to 8% of weight of bitumen. Cost of waste plastic shreds in kilogram is between Rs.85/kg to Rs.90/Kg [23].

S.NO	PARTICULARS	APPROX RATE (Rs./kg)
1	Waste plastic	1
2	Collection of plastic	2
3	Transportation	2
4	Cleaning and shredding	2
5	Labor charges	3
6	Machinery charges (electricity and maintenance)	2
	Total	**Rs. 12 / kg**

Table VII. Per kilogram waste plastic processing cost.

4.2 Cost Estimation and Comparison of Conventional Roads and Plastic Roads

4.2.1 Material Costing. - For the cost comparison initially take the standard of construction of 1-kilometre road of and width of 3.7 m [23].

• Bitumen cost per kg is Rs.119 per kg.
• Surface area of road which will be covered by bitumen is given as Road surface area = Road length x width of road = 1000 meters x 3.7 meters = 3700m2.
• Gravels chips cost = Rs.12,000 to Rs 13,000 per 1 brass (2.83 m3)
• The volume of bitumen required for all types of roads surface is 0.98 kg to 1.10 kg per m2 [22].

4.2.2 Pure Bitumen Seal Coated Roads Cost Estimation. -Now for the comparison analysis first evaluate the estimated cost required for the construction and seal coating of aggregate with pure bitumen. We have taken the standard of 1 kilometer road of width 3.7 meters [20].

• Total volume of bitumen required for road coating Bitumen = (road surface area) x (bitumen required per m2)
= 3700 m2x 1 kg/m2 = 3700 kg
• Gravel chips volume required for road.
• Gravel volume = (road surface area) x (Gravel chips layer thickness) = 3700 m2x 0.005m (5mm) = 18.5 m3
• Pure bitumen cost for road coating.
• Total Bitumen cost = (total bitumen volume) x (cost of bitumen per kg) = 3700 kg x Rs.119 /kg = Rs. 440,300/ km
• Total cost of gravels or aggregate is given as
Total Gravel cost = (total volume of Gravels) x (rate of Gravel)
= 18.5m3 x (13,000 / 2.83 m3) {1 brass = 2.83}
= 18.5 x 4,593
= Rs.84,970 / km

• Total cost of the pure bitumen coated road is estimated as
Total cost of bitumen road = (total cost of bitumen) + (total cost Gravel)
= Rs.440,300 + Rs. 84,970
= Rs.525,270 (approx.).

4.2.3 Costing Evaluation Result. - Hence the total cost for the construction of 1 km and width of 3.7 m road is approximately estimated as Rs.525, 270. It should be considered that it is estimated cost of the material that is required for the construction of roads it does not include the cost of labor, machinery and traveling.

4.2.4 Modified Plastic Bituminous Mixture Road Cost Estimation. - The use of plastic shredded waste in bituminous mixture of road is 6% to 8% of weight of bitumen. For cost estimation again consider the construction of road of 1 kilometer having width of 3.7 meters.
• Cost of shredded plastic waste is Rs 85. /kg to Rs.90/kg
• Total volume required of waste shredded plastic for aggregate coating is Total shredded plastic volume = (total bitumen volume) x (% of plastic) = (3700 kg) x (8%) = 296 kg

• Total cost of shredded plastic required for road is
Total shredded plastic cost = (total plastic volume) x (rate per kg)
= 296 kg x RS.90/kg = Rs.26, 640 /km.

• Total cost of bituminous mixture with shredded plastic can be estimated as.
Total cost of mixture = (cost of bitumen after plastic addition) + (Shredded plastic cost)
= [(3700 kg – 296 kg) x119] + Rs.26,640 = Rs. 431,716/km

• Total cost of plastic road can be estimated as.
Total cost of plastic road = (plastic/bitumen mixture cost) + (Gravel cost)
= Rs.431,716 + Rs 84,970. = Rs. 516,686 / km

4.3 Costing Evaluation Result. - Hence the cost estimation for plastic road is calculated as Rs. 516,686 /km. It does not include the labor, machinery and travelling cost. We have taken the standard of 1-kilometer road having a width of 3.7 meters. The reduction is cost with plastic shredded particulate in the bituminous mixture can be approximately calculate as 4% to 6% as compared to pure bitumen road construction.

4.3.1 Bitumen Cost Reduction. - The cost of bitumen is also reduced by using plastic in the road mixture as plastic replaces the amount of bitumen uses for affective coating of the aggregate, the reduction in cost can be calculated as.
• Bitumen cost (conventional road) = 3700 kg x Rs.119/kg = Rs. 440,300/kg
• Modified Plastic bitumen cost = [(3700 kg – 296 kg) x 119] = Rs. 405,076
• Cost reduction = Rs.440,300 – Rs.405,076 = Rs.35,224/ km

Hence a cost reduction of Rs.35, 224 is saved in bitumen mixture by using shredded plastic as an additive in the bituminous mixture for road construction shown

4.3.2 Overall Road Construction Cost Analysis. - From the above calculation we have derived some of the major cost reduction by using shredded plastic waste in the bituminous mixture. The reduction in cost for construction of road per kilometer can be calculated as:

• Cost reduction = (cost of pure bitumen road) – (cost of modified plastic bitumen)
= Rs. 525,270-516,686
= Rs. 8,584 /km

The findings of this study show that using waste plastic in road construction can be a smart and eco-friendly solution for Pakistan. By mixing shredded plastic into bitumen, it can reduce the number of traditional materials needed, which helps lower costs and makes roads stronger and more durable. This approach not only helps tackle the serious issue of plastic waste in the environment but also supports the building of better roads that can withstand wear and tear. As Pakistan adopts these innovative practices, it opens the door to a cleaner future where waste is reused effectively. Overall, this method can lead to significant savings and contribute to a healthier planet for everyone.

5. Future Recommendations. -

a. Further studies should investigate the potential leaching of harmful chemicals from plastic additives into soil and waterways. As some plastics can release toxic substances when heated, understanding these risks is crucial for ensuring the safety of road construction practices.

b. Many studies so far have been conducted using several other forms of plastics like PET, LDPE and HDPE. Further material like Polypropylene (PP) or Polystyrene (PS) to assess their suitability in the asphalt mix.

c. Further research can incorporate detailed analysis on microstructure of plastic-bitumen sample. This was not conducted in this study due to limitations of resources.

d. Further studies with bigger sample sizes may offer more conclusive insights into this relationship, as the correlation approaches significance but falls short of traditional standards.

6. Conclusions. - This research explored the use of waste PET bottles in asphalt mixtures, highlighting the environmental and economic benefits of incorporating plastic into road construction. Following conclusions could be interpreted from the results.

a. In our study, we created five sample cores with varying plastic content: 0%, 4%, 6%, 8%, and 10%. The results showed that asphalt with 8% plastic content by weight of Optimum Binder Content (OBC) exhibited the highest Marshall Stability, with values of 3430.29 lbs.

b. Also the value of ductility and softening point at 8% plastic content is maximum. This increase in the softening point illustrates that plastic modified bitumen roads can withstand hot weather more effectively than traditional bitumen roads

c. Additionally, using plastic in bitumen not only improves road performance but also leads to substantial cost savings. For instance, roads made with plastic-modified bitumen can reduce overall construction costs by approximately 4% to 6% compared to traditional methods. This innovative approach not only helps manage plastic waste effectively but also supports the development of stronger, more resilient road networks.

d. By adding waste plastic to asphalt, we can significantly reduce the amount of plastic that ends up in landfills and oceans, promoting more sustainable practices.

References

[1] A. H. Mir, 'Use of Plastic Waste in Pavement Construction: An Example of Creative Waste management'.

[2] O. Alabi, K. Ologbonjaye, O. Awosolu, and O. Alalade, 'Public and Environmental Health Effects of Plastic Wastes Disposal: A Review', J. Toxicol. Risk Assess., vol. 5, Apr. 2019, doi: 10.23937/2572-4061.1510021.

[3] A. Babafemi, B. Šavija, S. Paul, and V. Anggraini, 'Engineering Properties of Concrete with Waste Recycled Plastic: A Review', Sustainability, vol. 10, no. 11, p. 3875, Oct. 2018, doi: 10.3390/su10113875.

[4] V. Sahajwalla and V. Gaikwad, 'The present and future of e-waste plastics recycling', Curr. Opin. Green Sustain. Chem., vol. 13, pp. 102–107, Oct. 2018, doi: 10.1016/j.cogsc.2018.06.006.

[5] M. Kazemi, S. Faisal Kabir, and E. H. Fini, 'State of the art in recycling waste thermoplastics and thermosets and their applications in construction', Resour. Conserv. Recycl., vol. 174, p. 105776, Nov. 2021, doi: 10.1016/j.resconrec.2021.105776.

[6] X.-Q. Xu, S. Liao, and Y. Wang, 'Recycling of Thermosetting Plastics', in Recent Developments in Plastic Recycling, J. Parameswaranpillai, S. Mavinkere Rangappa, A. Gulihonnehalli Rajkumar, and S. Siengchin, Eds., in Composites Science and Technology. , Singapore: Springer, 2021, pp. 95–119. doi: 10.1007/978-981-16-3627-1_5.

[7] M. E. Grigore, 'Methods of Recycling, Properties and Applications of Recycled Thermoplastic Polymers', Recycling, vol. 2, no. 4, Art. no. 4, Dec. 2017, doi: 10.3390/recycling2040024.

[8] S. Nizamuddin, M. Jamal, R. Gravina, and F. Giustozzi, 'Recycled plastic as bitumen modifier: The role of recycled linear low-density polyethylene in the modification of physical, chemical and rheological properties of bitumen', J. Clean. Prod., vol. 266, p. 121988, Sep. 2020, doi: 10.1016/j.jclepro.2020.121988.

[9] F. Welle, 'The fats about PET (update 2018)', 2018.

[10] R. Nisticò, 'Polyethylene terephthalate (PET) in the packaging industry', Polym. Test., vol. 90, p. 106707, Oct. 2020, doi: 10.1016/j.polymertesting.2020.106707.

[11] B. Mishra and M. K. Gupta, 'Use of plastic waste in bituminous mixes by wet and dry methods', Proc. Inst. Civ. Eng. - Munic. Eng., vol. 173, no. 2, pp. 87–97, Jun. 2020, doi: 10.1680/jmuen.18.00014.

[12] A. K. Sahu and R. K. Singh, 'Application of Waste Plastic Materials in Road Construction', 2016.

[13] P. N. A. Asare, F. A. Kuranchie, and E. A. Ofosu, 'Evaluation of incorporating plastic wastes into asphalt materials for road construction in Ghana', Cogent Environ. Sci., vol. 5, no. 1, p. 1576373, Jan. 2019, doi: 10.1080/23311843.2019.1576373.

[14] M. Sasidharan, M. E. Torbaghan, and M. Burrow, 'Using Waste Plastics in Road Construction', May 2019, Accessed: Sep. 05, 2023. [Online]. Available: https://opendocs.ids.ac.uk/opendocs/handle/20.500.12413/14596

[15] A. Biswas, A. Goel, and S. Potnis, 'Performance comparison of waste plastic modified versus conventional bituminous roads in Pune city: A case study', Case Stud. Constr. Mater., vol. 13, p. e00411, Dec. 2020, doi: 10.1016/j.cscm.2020.e00411.

[16] A. Biswas and S. Potnis, 'Plastic Bituminous Roads: A Sustainable Technology–For Better Handling Distresses', Eur. J. Eng. Technol. Res., vol. 7, no. 1, pp. 63–69, 2022.

[17] ‘https://www.shell.com.pk/media/news-and-media-releases-2023/recycled-plastic-shell-pakistan-builds-road-in-karachi.html’.

[18] S. B. Abd Karim et al., ‘Plastic Roads in Asia: Current Implementations and Should It Be Considered?’, Materials, vol. 16, no. 16, Art. no. 16, Jan. 2023, doi: 10.3390/ma16165515.

[19] A. M. Zaltuom, ‘A Review Study of The Effect of Air Voids on Asphalt Pavement Life’, in Proceedings of First Conference for Engineering Sciences and Technology: Vol. 2, AIJR Publisher, Nov. 2018, pp. 618–625. doi: 10.21467/proceedings.4.29.

[20] M. M. Shah, J. Yousaf, U. Khalid, H. Li, J.-J. Yee, and S. A. Z. Naqvi, ‘Plastic roads: asphalt mix design and performance’, Discov. Appl. Sci., vol. 6, no. 4, p. 195, Apr. 2024, doi: 10.1007/s42452-024-05772-x.

[21] ‘Standard Test Method for Marshall Stability and Flow of Asphalt Mixtures’. [Online]. Available: https://www.astm.org/d6927-15.html

[22] ‘https://trendeconomy.com/data/h2/Pakistan/2714,"’.

[23] ‘“Petroleum Corporation limited, Pakistan”.’

Author contribution:

1. Conception and design of the study
2. Data acquisition
3. Data analysis
4. Discussion of the results
5. Writing of the manuscript
6. Approval of the last version of the manuscript

EAJ has contributed to: 1, 2, 3, 4, 5 and 6.

IA has contributed to: 1, 2, 3, 4, 5 and 6.

BF has contributed to: 1, 2, 3, 4, 5 and 6.

MFA has contributed to: 1, 2, 3, 4, 5 and 6.

Acceptance Note: This article was approved by the journal editors Dr. Rafael Sotelo and Mag. Ing. Fernando A. Hernández Gobertti.

Enhanced Mobility Aid for the Visually Impaired: An Ultrasonic Sensor and Arduino-Based Smart Walking Stick

Ayuda de movilidad mejorada para personas con discapacidad visual: un sensor ultrasónico y un bastón inteligente basado en Arduino

Auxílio de mobilidade aprimorado para deficientes visuais: um sensor ultrassônico e uma bengala inteligente baseada em Arduino

Shahzor Memon[1(*)], Mirza Muhammad Aamir[2], Sadiq Ur Rehman[3], Halar Mustafa[4], Muhammad Shakir Sheikh[5]

Recibido: 08/08/2024 Aceptado: 29/10/2024

Summary. - This study introduces a smart walking stick for the blind and visually impaired that uses ultrasonic sensors with Arduino and Raspberry Pi. The World Health Organization estimates that 37 million people worldwide are blind. People who are blind or visually impaired frequently rely on assistance from outside sources, which may come in the form of humans, dogs that have been trained, or specialized technological gadgets that play the role of decision-making support systems. We were then inspired to create a smart walking stick in order to get around these restrictions. In order to achieve this, we fitted the stick with ultrasonic sensors at strategic locations that activated the buzzer sound while giving the user information about the surroundings. Our proposal was for a low-cost, lightweight device that uses a microcontroller to interpret signals and emit beeps to notify the visually impaired individual of any obstacles, water, or dark places. The system consists of obstacle and moisture detection sensors that receive, process, and send signals to the alarm system, which then warns the user to take action. The system was conceived and programmed in C, tested for accuracy, and checked by a visually challenged individual. Our technology can identify obstructions within around 2 meters of the user.

Keywords: Ultrasonic sensor, Arduino ATmega328 Microcontroller, Mobility aid, Visually Impaired Person, Alarm system

(*) Corresponding author.

[1] M.E. Assistant Professor, FEST, Hamdard University (Pakistan), Shahzor.memon@hamdard.edu.pk, ORCID iD: https://orcid.org/0009-0008-8867-7070

[2] M.E. Assistant Executive Engineer, Pakistan Water & Power Development Authority (Pakistan), engr.aamir2@gmail.com, ORCID iD: https://orcid.org/0009-0009-5304-1950

[3] Ph.D., Assistant Professor, FEST, Hamdard University (Pakistan), sadiq.rehman@hamdard.edu.pk, ORCID iD: https://orcid.org/0000-0002-6308-450X

[4] M.E, Lecturer, FEST, Hamdard University (Pakistan), halar.mustafa@hamdard.edu.pk, ORCID iD: https://orcid.org/0000-0002-7021-5010

[5] Lecturer, Szabist University (Pakistan), muhammad.shakir@szabist.edu.pk, ORCID iD: https://orcid.org/0009-0005-5902-6461

Resumen. - *Este estudio presenta un bastón inteligente para personas ciegas o con problemas de visión que utiliza sensores ultrasónicos con Arduino y Raspberry Pi. La Organización Mundial de la Salud estima que 37 millones de personas en todo el mundo son ciegas. Las personas ciegas o con problemas de visión a menudo dependen de la ayuda de fuentes externas, que pueden venir en forma de humanos, perros que han sido entrenados o dispositivos tecnológicos especializados que desempeñan el papel de sistemas de apoyo a la toma de decisiones. Entonces nos inspiramos para crear un bastón inteligente para superar estas restricciones. Para lograrlo, equipamos el bastón con sensores ultrasónicos en lugares estratégicos que activaban el sonido del timbre mientras brindaban al usuario información sobre los alrededores. Nuestra propuesta era un dispositivo liviano y de bajo costo que utiliza un microcontrolador para interpretar señales y emitir pitidos para notificar a la persona con problemas de visión sobre cualquier obstáculo, agua o lugares oscuros. El sistema consta de sensores de detección de obstáculos y humedad que reciben, procesan y envían señales al sistema de alarma, que luego advierte al usuario para que tome medidas. El sistema fue concebido y programado en C, se probó su precisión y fue revisado por una persona con discapacidad visual. Nuestra tecnología puede identificar obstrucciones a unos 2 metros del usuario.*

Palabras clave: *Sensor ultrasónico, Microcontrolador Arduino ATmega328, Ayuda a la movilidad, Persona con discapacidad visual, Sistema de alarmas*

Resumo. ***-*** *Este estudo apresenta uma bengala inteligente para cegos e com deficiência visual que utiliza sensores ultrassónicos com Arduino e Raspberry Pi. A Organização Mundial de Saúde estima que 37 milhões de pessoas em todo o mundo são cegas. As pessoas cegas ou com deficiência visual dependem frequentemente da assistência de fontes externas, que pode surgir sob a forma de seres humanos, cães treinados ou dispositivos tecnológicos especializados que desempenham o papel de sistemas de apoio à tomada de decisões. Fomos então inspirados a criar uma bengala inteligente para contornar estas restrições. Para tal, equipámos o stick com sensores ultrassónicos em locais estratégicos que ativavam o som da campainha e davam ao utilizador informações sobre o meio envolvente. A nossa proposta foi um dispositivo leve e de baixo custo que utiliza um microcontrolador para interpretar sinais e emitir sinais sonoros para avisar o deficiente visual de qualquer obstáculo, água ou local escuro. O sistema é constituído por sensores de deteção de obstáculos e humidade que recebem, processam e enviam sinais para o sistema de alarme, que avisa o utilizador para agir. O sistema foi concebido e programado em C, testado quanto à sua precisão e verificado por um deficiente visual. A nossa tecnologia pode identificar obstruções a cerca de 2 metros do utilizador.*

Palavras-chave: *Sensor ultrassónico, microcontrolador Arduino ATmega328, ajuda à mobilidade, pessoa com deficiência visual, Sistema de alarme*

1. Introduction. - Vision is the most vital part of human physiology as 83% of information humans get from the environment is via sight. According to a report by the WHO (World Health Organization) estimates that in the world about 1% of the human population is visually impaired. There are over 2.2 billion individuals with a vision impairment of some description across the globe among them about 10% are fully blind (or moderate to severe) distance vision impairment and 90% (about 63 million people) with low vision. In 2015, a survey was conducted by the Royal National Institute of Blind People (RNIB) (Wilson, 2015) including approximately 500 visually impaired persons for whom a collision with an obstacle over three months was reported.

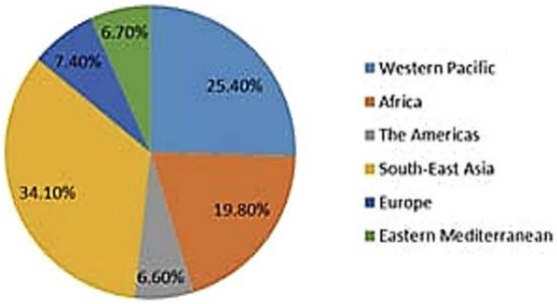

Figure I: A Pie Chart Showing Blind People Across the World.

The most traditional and oldest mobility aids for individuals with vision impairments are the walking cane (sometimes referred to as a white cane or stick) and guide dogs. The most significant flaws of these aids are the required skills and training phase, the range of motion, and the limited information supplied. The rapid growth of current technology, both in hardware and software, has created the opportunity to deliver intelligent navigation capabilities. Recently, various Electronic Travel Aids (ETA) have been designed and developed to assist the blind in navigating independently and safely. Furthermore, the most expensive technical options for assisting blind people in navigating freely have only recently been introduced. While these systems are suitable for outdoor navigation due to the need for line-of-sight access to satellites, they still require additional components to improve resolution and proximity detection in order to prevent blind people from colliding with other objects and thus endangering their lives. In contrast to other technologies, many blind guide systems use ultrasound because it is resistant to surrounding noise. Another reason why ultrasonic technology is widely used is that it is relatively inexpensive. Additionally, ultrasound emitters and detectors are tiny enough to be transported without the need for complicated electronics. In the related research [16], The project developed a low-cost mobility aid using ultrasonic sensors for obstacle detection, providing alerts through LEDs, buzzers, and vibrating motors. It effectively detects objects within 2 to 50 cm, enhancing mobility for visually impaired individuals. The research article [17] presents a voice-based navigation system utilizing ultrasonic sensors for obstacle detection, enhancing mobility for visually impaired individuals. This system integrates real-time voice assistance, ensuring safer travel by alerting users to obstacles and slippery surfaces. In [18] the research presents a mobility stick utilizing ultrasonic sensors and haptic motors to assist visually impaired individuals. This system enhances navigation by providing haptic feedback, while also monitoring movement and potential falls, integrating data through the Internet of Things. In research [19], The Smart Cane is used that incorporates an ultrasonic sensor for obstacle detection, enhancing mobility for visually impaired individuals. This feature alerts users to nearby obstacles, significantly improving their safety and independence while navigating their environment.

It is difficult for blind people to move or live without help. So, blind people generally use a white cane to guide them during moving. Although it can be helpful, it doesn't guarantee saving blind people from risks. These conventional ways can be used for low-level obstacle detection only.

The goal of this study is to develop a theoretical model and a system idea for providing a smart electronic aid to blind individuals. In comparison to traditional navigation systems, blind aid systems can be equipped with depth measurement circuitry, which is useful for sensing the depth when dealing with stairs, and a recorded message is played to notify the obstacle alert. These various units are described in order to create a "smart stick" concept.

2. Motivation. - The proposed system offers a range of features designed to enhance usability, safety, and accessibility for visually impaired users. First, the system integrates lightweight components into the stick, making it highly user-

friendly and easy to carry. It provides a fast response to nearby obstacles within a range of up to 2 meters, thanks to the inclusion of ultrasonic sensors. Training for this product is minimal and cost-effective, as it only requires a simple description of the stick's components and their usage positions, unlike the extensive training required for other assistive devices.

For seamless communication, the stick transmits information to the user via earphones. Instead of relying on vague sounds that may cause confusion or social discomfort, the earphones deliver clear, spoken warning messages, helping alert the user without drawing undue attention. Additionally, to improve the independence and ease of use for blind individuals, the stick includes a clap sensor that assists in locating it if misplaced, providing added convenience.

The ultrasonic sensor is crucial for detecting obstacles, pits, and staircases, and it plays a vital role in generating spoken warnings whenever an obstacle is detected. This feature enables the user to alter their path in time to avoid hazards. A water sensor is also included to detect water on the floor, offering timely alerts to help the user avoid potential slips. Moreover, a fire sensor enhances safety by alerting the user to the presence of fire, while a light sensor increases nighttime visibility. This sensor helps notify others in the vicinity of the blind person’s presence, encouraging them to make way and allowing the user to walk with ease.

The designed smart stick detects obstacles and can recognize and speak aloud the upward and downward stairs or puddles as shown in Figure 2.

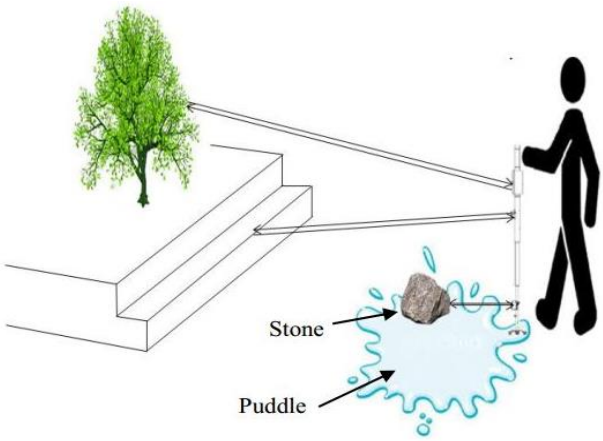

Figure II: Smart stick detects the obstacles in front of a blind person.

3. Experimental Setup and Procedure. - Different sensors are interfaced with Raspberry Pi and after the process, it gives feedback to blind persons by using multi-recorded warning messages if any hurdle is detected within the set range. Figure III Shows the Complete Block Diagram of the Project.

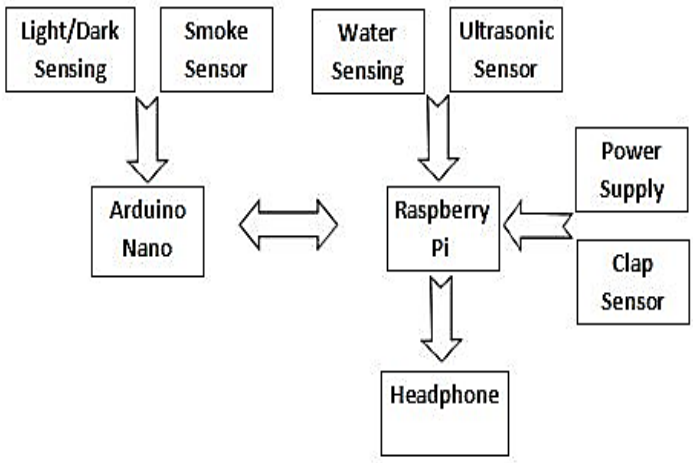

Figure III. System Block Diagram

4. Details of Component. -

4.1 Power Supply. - A power supply is an electrical device that supplies electric power to an electrical load. The primary function of a power supply is to convert electric current from a source to the correct voltage, current, and frequency to power the load.

The basic electrical specification of a power supply suitable for a Raspberry Pi is that it supplies a regulated 5V DC (direct current) and can supply a current of up to 700mA. It must have a micro USB plug on the end of the lead.

4.2 Ultrasonic Sensor HC – SR04. -

Specifications

Power Supply: 5V DC
Operating Current: 15mA
Measuring Range: 2 cm to 400 cm (0.78 inches to 157 inches)
Resolution: 0.3 cm
Measuring Angle: ~15 degrees
Ultrasonic Frequency: 40 kHz
Accuracy: ± 3mm

The HC-SR04 sensor uses sonar to measure the distance to an object. It sends out a high-frequency sound wave and measures the time the echo returns after bouncing off an object. Figure IV Shows the Different angles for staircase detection. The distance can be calculated using the following expression:

$$\text{Distance} = \frac{\text{Time} \times \text{Speed of Sound}}{2}$$

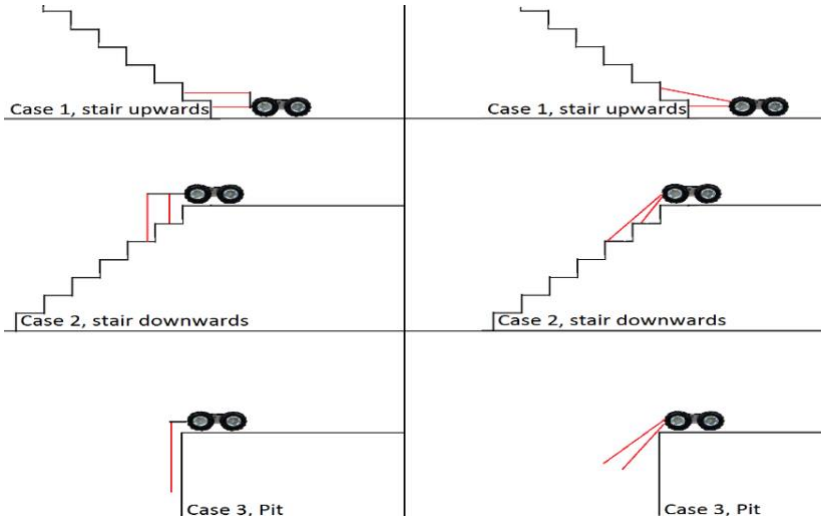

Figure IV. An ultrasonic sensor used for obstacle detection and staircase detection.

4.3 Smoke Sensor (MQ-2). - The MQ-2 smoke sensor is a popular gas sensor for detecting smoke, LPG, butane, methane, alcohol, hydrogen, and other combustible gases. It's commonly used in gas leak detection systems in homes, industries, offices, and simple air quality monitoring applications.

The MQ-2 sensor uses a small heating element to detect gases. When gases like LPG, smoke, or methane are present, the sensor's resistance changes, causing a voltage drop that can be measured. The sensor's analog output can be read directly or converted to a digital signal using an analog-to-digital converter (ADC). The smoke sensor has a built-in potentiometer that allows you to adjust the sensor's digital output (D0) threshold. This threshold sets the value above which the digital pin will output a HIGH signal.

The output can be an analog signal (A0) that can be read with an analog input or a digital output (D0) that can be read with a digital input.

We will wire the MQ-2 to an Arduino so that the Arduino can read the amount of voltage output by the sensor and sound a buzzer if the sensor outputs a voltage above a certain threshold.

Specifications
Operating Voltage: 5V DC
Power Consumption: Less than 150 mA
Detection Range: 300-10,000 ppm (parts per million)
Output: Analog and digital (threshold adjustable)
Preheat Time: About 20 seconds (for stable output)

4.4 Water Sensing on Floor (HW-482). - A water sensor is used to detect the presence of water and provide an alert in time for path change to avoid slipping. A typical design is a small cable or device that lies flat on a floor and depends on the electrical conductivity of water to decrease the resistance across two contacts.
HW-482, which consists of exposed metal traces or probes on a PCB. these probes are fitted at the bottom of the stick to sense obstacles like water pits, when water contacts these traces, it bridges the gap between them, allowing current to flow and creating a signal that can be read by a microcontroller. This module typically has both analog and digital output options:
Analog Output (AO): Provides a variable voltage corresponding to the amount of water detected.
Digital Output (DO): Provides a simple HIGH or LOW signal when water is detected, with a threshold adjustable via a potentiometer.

Specifications:
Operating Voltage: 3.3V - 5V DC
Output Type:
Digital Output (DO): High/Low signal, adjustable via onboard potentiometer.
Analog Output (AO): Analog voltage signal that varies based on water presence and coverage on the sensor probes.
Current Consumption: Typically, around 20 mA

4.5 Light/Dark Sensing (LDR). - A light sensor is useful at night or dark. When there is darkness, it aware the people in the surrounding area that a blind person is walking and allows space so that the blind person can walk easily.
Light-dependent resistors, LDRs, or photoresistors are generally used in circuits where it is necessary to detect the existence or the level of light. They can be expressed by a variety of names from a light-dependent resistor, LDR, photoresistor, photocell, or photoconductor. Even though other devices such as photodiodes or phototransistors can also be used, LDRs or photoresistors are particularly appropriate electronic components to use. They give large changes in resistance to changes in light level.
Considering their low cost, ease of manufacture, and ease of use LDRs have been used in a variety of different applications.

Specifications:
Operating Voltage: 3.3V - 5V DC
Output Type:
Digital Output (DO): HIGH/LOW output, with an adjustable threshold via a potentiometer.
Analog Output (AO): Variable voltage that corresponds to the light intensity.
Current Consumption: Typically, around 20 mA
Sensitivity Adjustment: Onboard potentiometer for setting threshold levels for digital output

5. Experimental Results and Discussion. - Hardware consists of Raspberry Pi, Arduino Nano, and other components like ultrasonic sensor, smoke sensor, clap sensor, LDR sensor, and water sensor. Hardware connections can be seen below in the figures. In this project ultrasonic sensor is used for obstacle and staircase detection and smoke sensor is used to detect fire and clap sensor is used for stick finding and LDR sensor is used to detect lightness/darkness, and a

water sensor is used to detect the water on floor. Figure V demonstrates the complete experimental setup of a blind person stick.

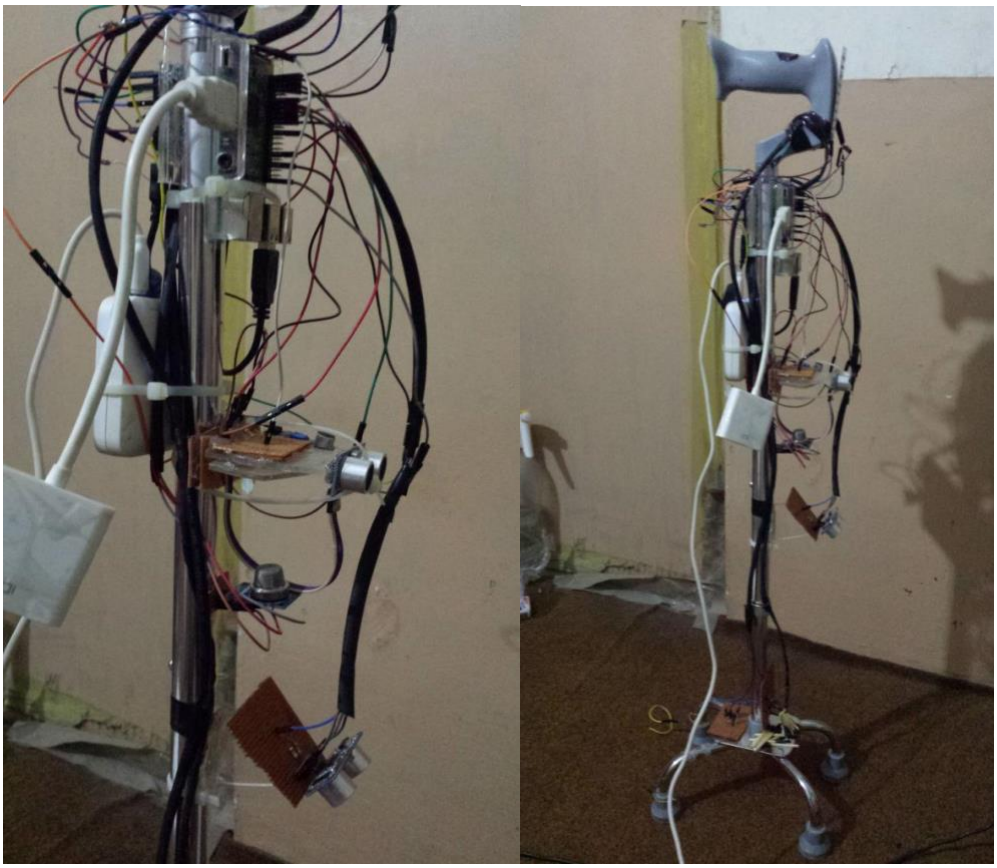

Figure V. Experimental Setup.

The ultrasonic sensor has four output formats: pulse width output, analog voltage output, and serial digital output. The pulse width (PW) representation of the range provides information on the distance between the sensor tip and the obstruction. As a result, the distance value can be estimated with a scale factor of 147uS per inch. The sensor readings fluctuate depending on the topography, in our example, the floor or rising or descending staircases, as seen in Figure VI.

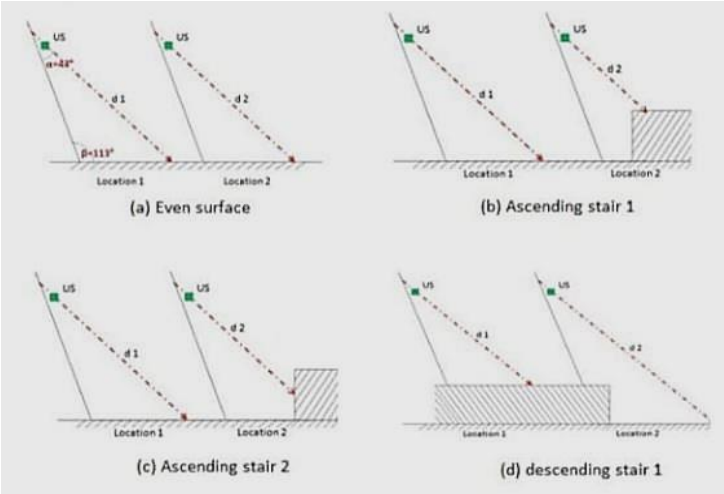

Figure VI. Ultrasonic Sensor Results.

Figure VII depicts three curves that illustrate the distances between the sensor and the nearest obstacle in three walking situations:

The top left curve depicts the distance values obtained while the user walks on a floor with no change in floor state. Because of the wide angle of incidence with the floor, the output of the ultrasonic sensor fluctuates as the user walks. As a result, it is incapable of providing accurate measurements. The bottom curve depicts the values of distance as the user walks on a floor, and the cane detects rising steps.

The top right curve depicts the values of distance when the user approaches falling steps on an even surface.
Logically, when the cane obtains descending (or ascending) steps, the distance values must become larger (or lower) than those acquired with a floor. However, the curves in Figure VII do not appear to show that the sensor readings alter in accordance with floor states. Indeed, vibrations occur during cane movement, causing some mistakes in the ultrasonic output signal.

To separate the three cases experimental data identification rules of the floor, ascending and descending states are developed in the following section.

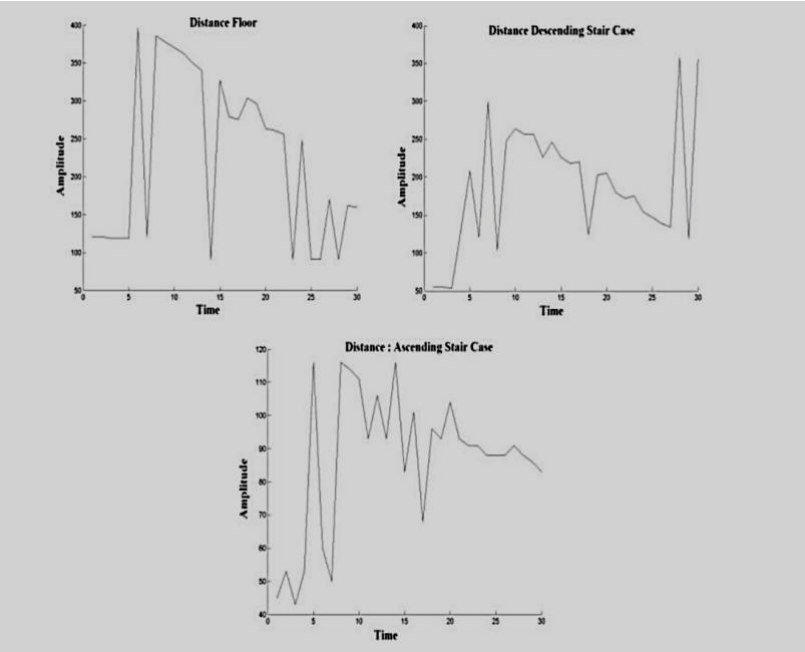

Figure VII. Range sensor raw data – even surface (top left), ascending stairs (bottom) and descending stairs (top right)

To process these three signals effectively and extract useful information for detecting floor surfaces, ascending stairs, and descending stairs, we can apply several signal-processing techniques to distinguish between the three cases.
The raw ultrasonic sensor data shown in each plot is noisy due to variations in the angle of incidence, especially for the flat surface case (top left plot). To reduce noise and improve readability, apply smoothing techniques such as: Moving Average filter, Low-pass filtering to remove high-frequency noise that doesn't contribute to identifying floor state changes and Exponential Smoothing.

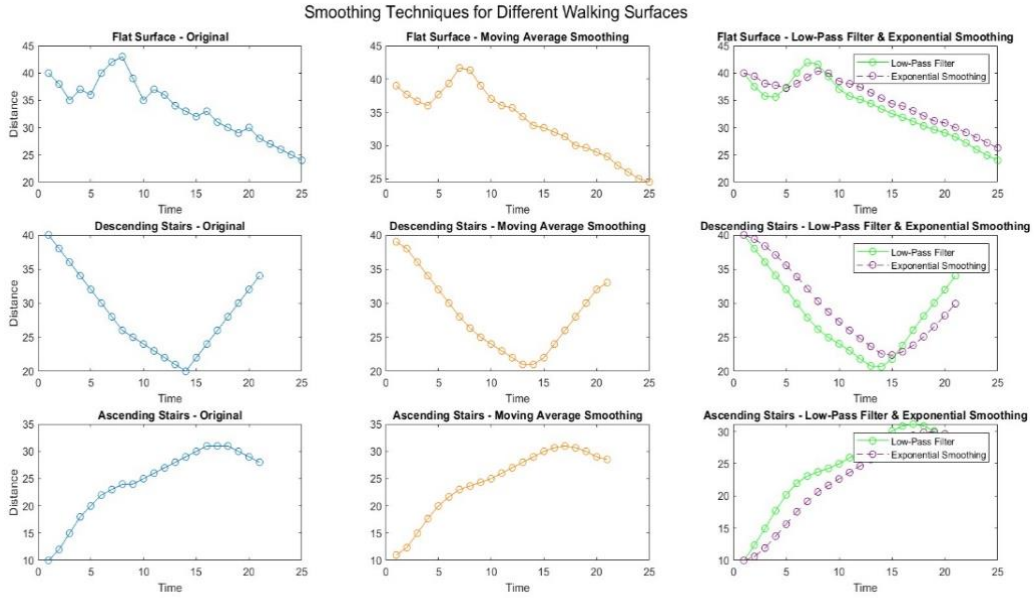

Figure VIII. Smoothing technique results in enhancing the readability of ultrasonic signals for flat surfaces, ascending stairs, and descending stairs.

After smoothing, extract key features to differentiate between flat surfaces, ascending stairs, and descending stairs. These features can include Mean and Standard Deviation as given in Table I:

Flat Surface	Moving Average: Mean = 33.59	Std Dev = 5.13
Flat Surface	Low-Pass Filter: Mean = 33.59,	Std Dev = 5.24
Flat Surface	Exponential Smoothing: Mean = 34.88,	Std Dev = 4.40
Descending Stairs	Moving Average: Mean = 28.30	Std Dev = 5.60
Descending Stairs	Low-Pass Filter: Mean = 28.33	Std Dev = 5.81
Descending Stairs -	Exponential Smoothing: Mean = 29.45	Std Dev = 5.86
Ascending Stairs	Moving Average: Mean = 24.45	Std Dev = 6.14
Ascending Stairs	Low-Pass Filter: Mean = 24.44	Std Dev = 6.26
Ascending Stairs	Exponential Smoothing: Mean = 22.30	Std Dev = 6.79

Table I: Mean and standard deviation for three cases.

The mean and standard deviation values extracted from each smoothed dataset provide insight into the overall trend and variability of the signals for different types of surfaces.

The floor flat surface Mean values around 33-35 show that the signal is relatively high. This is expected, as flat surfaces usually have a steady level without significant upward or downward trends. In the Descending Stairs case the mean is lower at around 28-29. This reflects the downward trend in the signal due to descending steps, which bring the values lower on average. The mean for the ascending stairs case is even lower, around 22-24, especially in the exponential smoothing case. This indicates an upward trend that starts lower but gradually increases, consistent with going upstairs.

The standard deviation reflects the spread or variability of the signal values. A higher standard deviation indicates more fluctuations, while a lower standard deviation suggests a more stable, consistent signal. In the flat Surface case, the standard deviation is generally lower (around 4.4 to 5.3), indicating that flat surfaces are more consistent and less variable, with fewer abrupt changes. while in the descending stairs case, The standard deviation is slightly higher (around 5.6 to 5.9), showing increased variability as the signal moves downward with each step. However, in the ascending stairs, the standard deviation is the highest (around 6.1 to 6.8), suggesting greater variability, likely due to the upward movement that tends to vary more in amplitude compared to descending stairs or flat surfaces.

Finally, Pattern Recognition with Thresholding to identify distinct surface types: Set a threshold range for standard deviation values. If the distance variations fall within this range with no clear upward or downward trend, classify the surface as a flat floor if it identifies a consistent downward trend in the distance values. Apply a threshold on the gradient (negative values) to trigger an ascending stair detection. and a sudden increase in the distance values after a period of stability, indicating a possible stair edge. A positive gradient exceeding a certain threshold can signal the start of a descending stair. The following table 02 shows the classification results after applying thresholding on the data set for the three cases.

Mean	Standard Deviation	Classified as
33.59	5.13	Flat Surface
28.30	5.60	Descending Stairs
24.45	6.14	Ascending Stairs

Table II: Classification Results using Extracted Features.

6. Conclusion. - Blind and visually impaired people require assistance to engage with their surroundings with greater security. As a result, a multi-sensor system that analyzes floor surfaces for the presence of stairs, obstacles, fire, darkness, and water was created.

In this research, we offer a unique electronic instrument with two ultrasonic sensors designed to assist the visually impaired. Only one ultrasonic sensor is utilized to detect and identify three different floor states: even floor, ascending staircase, and descending staircase. To this goal, we devised a method for detecting floor states. Such performances are challenging because no prior techniques have proposed detecting stairs.

The experimental results demonstrate that mean and standard deviation values extracted from smoothed signals are powerful features for differentiating between flat surfaces, ascending stairs, and descending stairs. By implementing a threshold-based pattern recognition system using these features, one can achieve accurate and efficient surface-type classification. The findings provide a foundation for developing real-time applications in health, fitness, and navigation. Future work can explore refining thresholds, incorporating additional features, and testing in dynamic environments to enhance the robustness and versatility of this approach.

Future research in surface classification holds significant potential for enhancing navigation, mobility assistance, and health monitoring. By leveraging advanced sensors, machine learning, and augmented reality, these systems can provide more accurate, adaptable, and user-friendly solutions. Such advancements could lead to more personalized, real-time assistance for various applications, ultimately improving safety, engagement, and independence for diverse user groups.

References

[1] M. S. Nowak and J. Smigielski, “The Prevalence and Causes of Visual Impairment and Blindness among Older Adults in the City of Lodz, Poland.” Medicine, vol 94, number 5, pp. e505, February 2015 doi:10.1097/MD.0000000000000505

[2] G. Gayathri, M. Vishnupriya, R. Nandhini and M. Banupriya “Smart Walking Stick for Visually Impaired.” International Journal of Engineering and Computer Science, vol. 3, number 3, pp. 4057-4061, 2014.

[3] R. Radhika, P.G. Pai, S. Rakshitha and R. Srinath “Implementation of Smart Stick for Obstacle Detection and Navigation.” International Journal of Latest Research in Engineering and Technology, vol. 2, number 5, pp. 45-50, 2016.

[4] M.H. Mahmud, R. Saha and S. Islam “Smart Walking Stick – An Electronic Approach to Assist Visually Disabled Persons.” International Journal of Scientific and Engineering Research, vol. 4, number 10, pp. 111-114, 2013.

[5] A. Jose, G. George, M.R. Nair, M. J. Shilpa and M. B. Mathai “Voice Enabled Smart Walking Stick for Visually Impaired.” International Journal of Advanced Research in Electrical, Electronics and Instrumentation Engineering, vol. 5, pp. 80-85, 2016.

[6] R. Sheth, S. Rajandekar, S. Laddha and R. Chaudhari “Smart White Cane – An Elegant and Economic Walking Aid.” American Journal of Engineering Research. Vol. 3, number 10, pp. 84-89, 2014.

[7] C.S. Kher, Y.A. Dabhade, S.K Kadam., S.D. Dhamdhere and A.V. Deshpande “An Intelligent Walking Stick for the Blind.” International Journal of Engineering Research and General Science, vol. 3, number 1, pp. 1057-1062, 2015.

[8] B.G. Roopashree, B.S. Patil and B.R. Shruthi “Smart Electronic Stick for Visually Impaired.” International Journal of Innovative Research in Science, Engineering and Technology, vol. 4, number 7, pp. 6389-6395, 2015.

[9] O. O. Olakanmi, “A Multidimensional Walking Aid for Visually Impaired Using Ultrasonic Sensors Network with Voice Guidance", International Journal of Intelligent Systems and Applications (IJISA), vol. 6, number 8, pp. 53-59, 2014. DOI: 10.5815/ijisa.2014.08.06

[10] E. J. Chukwunazo and G. M. Onengiye “Design and Implementation of Microcontroller Based Mobility Aid for Visually Impaired People.” International Journal of Science and Research. Vol. 5, issue 6, pp. 680-686, 2015. Available at http://dx.doi.org/10.21275/v5i6.NOV164233.

[11] G. Prasanthi and P. Tejaswitha “Sensor Assisted Stick for the Blind People.” Transactions on Engineering and Sciences, vol. 3, number 1, pp. 12-16, 2015.

[12] Shahid Karim, Muhammad Shakir, Ali Sheikh, Shahzor Memon, Halar Mustafa, Vishal Kumar “A Novel Eye-Tracking Device Designed with a Head Gesture Control Modul” Big Data fusion and Intelligent Information Integration, October 2021

[13] Muhammad Shakir, Shahid Karim, Muhammad Imran Saeed, Halar Mustafa, Shahzor Memon, S. Abbad Kazmi “IOT Based Real-time clinical healthcare system for aging and unprivileged areas” Int. J. Computational vision and robotics, January 2022

[14] Wasiq Khan, Abir Hussain, Bilal Muhammad Khan, Keeley Crockett, “Outdoor mobility aid for people with visual impairment: Obstacle detection and responsive framework for the scene perception during the outdoor mobility of people with visual impairment”, Expert Systems with Applications, Volume 228, 2023, 120464, ISSN 0957-4174, https://doi.org/10.1016/j.eswa.2023.120464.

[15] Cardona Mesa AA, Vasquez Salazar RD. “Mobility aids for visually impaired persons: Journals reviewed. Wearable Technology” 2021; 2(1): 73–81.

[16] Ricardo Yauri, Kevin Alvarez, Junior Cotaquispe, Jordy Ynquilla, Oscar Llerena “Guidance device for visually impaired people based on ultrasonic signals and open hardware” International Journal of Reconfigurable and Embedded Systems (IJRES)Vol. 13, No. 3, November 2024, pp. 520~527 ISSN: 2089-4864, DOI: 10.11591/ijres.v13.i3.pp520-527.

[17] Arshad, Khan., Gerard, Deepak. (2024). Voice-Based Navigation System for Visually Impaired Using Ultrasonic and Moisture Sensor via Bluetooth and GPS Tracker. Deleted Journal, 2(1):20-28. doi: 10.48001/jocevd.2024.2120-28.

[18] J, S, Raghul., Durga, Devi, K., M., Sreya., S, Maithreye. (2024). Mobility Stick with Haptic Feedback for People with Vision Impairments. 1-6. doi: 10.1109/iconscept61884.2024.10627855.

[19] A, Harini., C, Buvana., M, Harshini., S., Keerthana., Dr.Ramkumar, prabhu., S., K., UmaMaheswaran. (2024). Iot Based Smart Assistant Cane For The Visually Impaired. doi: 10.1109/ic3iot60841.2024.10550222.

Author contribution:

1. Conception and design of the study
2. Data acquisition
3. Data analysis
4. Discussion of the results
5. Writing of the manuscript
6. Approval of the last version of the manuscript

SM has contributed to: 1, 2, 3, 4, 5 and 6.

MMA has contributed to: 1, 2, 3, 4, 5 and 6.

SUR has contributed to: 1, 2, 3, 4, 5 and 6.

HM has contributed to: 1, 2, 3, 4, 5 and 6.

MSS has contributed to: 1, 2, 3, 4, 5 and 6.

Acceptance Note: This article was approved by the journal editors Dr. Rafael Sotelo and Mag. Ing. Fernando A. Hernández Gobertti.

Design and Development of IoT-based Harvesting Robo-Vec

Diseño y desarrollo de Robo-Vec de recolección basado en IoT

Projeto e desenvolvimento de colheita Robo-Vec baseada em IoT

Sadiq Ur Rehman[1(*)], Yasmin Abdul Wahab[2]

Recibido: 13/08/2024 Aceptado: 30/10/2024

Summary. - This article presents "Harvesting Robo-Vec" an IoT-based autonomous harvesting robot designed to enhance agricultural efficiency and precision. Integrating IoT technology with traditional methods, the robot automates tasks and offers real-time monitoring and control. It navigates crop fields autonomously, detects ripe produce using advanced sensing and imaging technologies, and performs precise harvesting maneuvers. Harvesting Robo-Vec features an IoT communication module for seamless connectivity with a centralized control system, enabling remote management of multiple robots. The paper outlines the robot's architecture, including its mechanical structure, sensors, control algorithms, and communication infrastructure, along with safety, power management, and robustness considerations. Iterative design, prototyping, and testing refined the robot's performance. Experimental results show that Harvesting Robo-Vec improves efficiency, reduces labor costs, and enhances productivity compared to manual methods. This study underscores the potential of IoT-based robots in agriculture, contributing to precision farming and autonomous robotics research.

Keywords: IoT, Harvesting Robot, Computer Vision, Agriculture, Automation.

[1] Ph.D., Assistant Professor, FEST, Hamdard University (Pakistan), sadiq.rehman@hamdard.edu.pk,
ORCID iD: https://orcid.org/0000-0002-6308-450X

[2] Ph.D., Assistant Professor, NANOCAT, Universiti Malaya (Malaysia), yasminaw@um.edu.my,
ORCID iD: https://orcid.org/0000-0002-1681-2201

Resumen. - *Este artículo presenta "Harvesting Robo-Vec", un robot de recolección autónomo basado en IoT diseñado para mejorar la eficiencia y precisión agrícola. Al integrar la tecnología IoT con métodos tradicionales, el robot automatiza tareas y ofrece monitoreo y control en tiempo real. Navega por los campos de cultivo de forma autónoma, detecta productos maduros utilizando tecnologías avanzadas de detección e imágenes y realiza maniobras de cosecha precisas. Harvesting Robo-Vec cuenta con un módulo de comunicación IoT para una conectividad perfecta con un sistema de control centralizado, lo que permite la gestión remota de múltiples robots. El documento describe la arquitectura del robot, incluida su estructura mecánica, sensores, algoritmos de control e infraestructura de comunicación, junto con consideraciones de seguridad, gestión de energía y robustez. El diseño iterativo, la creación de prototipos y las pruebas refinaron el rendimiento del robot. Los resultados experimentales muestran que Harvesting Robo-Vec mejora la eficiencia, reduce los costos de mano de obra y mejora la productividad en comparación con los métodos manuales. Este estudio subraya el potencial de los robots basados en IoT en la agricultura, contribuyendo a la investigación en agricultura de precisión y robótica autónoma.*

Palabras clave: *IoT, Robot cosechador, Visión por computadora, Agricultura, Automatización.*

Resumo. ***-*** *Este artigo apresenta o "Harvesting Robo-Vec", um robô de colheita autônomo baseado em IoT projetado para aumentar a eficiência e a precisão agrícola. Integrando a tecnologia IoT com métodos tradicionais, o robô automatiza tarefas e oferece monitoramento e controle em tempo real. Ele navega pelos campos de cultivo de forma autônoma, detecta produtos maduros usando tecnologias avançadas de detecção e imagem e realiza manobras de colheita precisas. O Harvesting Robo-Vec apresenta um módulo de comunicação IoT para conectividade perfeita com um sistema de controle centralizado, permitindo o gerenciamento remoto de vários robôs. O artigo descreve a arquitetura do robô, incluindo sua estrutura mecânica, sensores, algoritmos de controle e infraestrutura de comunicação, juntamente com considerações de segurança, gerenciamento de energia e robustez. O design iterativo, a prototipagem e os testes refinaram o desempenho do robô. Os resultados experimentais mostram que a colheita Robo-Vec melhora a eficiência, reduz os custos de mão-de-obra e aumenta a produtividade em comparação com os métodos manuais. Este estudo ressalta o potencial dos robôs baseados em IoT na agricultura, contribuindo para a agricultura de precisão e a pesquisa em robótica autônoma.*

Palavras-chave: *IoT, Robô de colheita, Visão computacional, Agricultura, Automação.*

1. Introduction. - Agriculture uses traditional manual harvesting methods that are labor-intensive, time-consuming, and prone to human error. These methods find it difficult to meet the expanding demands of a globalizing population [1-2]. In addition, the problem is exacerbated by the dire consequences resulting from a shortage of personnel in numerous sectors. Creative solutions that may automate and optimize the harvesting process are therefore desperately needed to boost output, reduce costs, and improve crop quality [3].

The work on Internet of Things (IoT) [4-5] based smart agriculture monitoring systems in [6] offers a noteworthy breakthrough by employing multiple algorithms to identify, measure, and evaluate vegetable development. Integrating computer vision techniques and machine learning [7], these systems achieve over 90% accuracy, particularly focusing on tomato cultivation. The development of autonomous smart agriculture robots, such as the Agri-Bot in [8], further revolutionizes farming by performing labor-intensive tasks like planting, plowing, fertilizing, and harvesting, leveraging Arduino UNOs and NodeMCUs for seamless automation. In [9], intelligent tomato-picking robots demonstrate considerable improvements in agricultural efficiency, employing precise grasping mechanisms, enhanced color segmentation, and advanced vision positioning to achieve an 83.9% success rate. Similarly, mechanical harvesting robots for fresh-eating tomatoes in [10], equipped with stereo visual units, end-effectors, and rail-based carriers, achieve an 83% success rate, significantly enhancing productivity and reducing labor costs.

Apple harvesting robots [11], featuring geometrically optimized manipulators, pneumatic grippers, and vision-based recognition systems, further illustrate the potential of robotic technology in agriculture, successfully harvesting apples with a 77% success rate. The integration of IoT and wireless sensors [12] in smart agriculture marks a transformative shift from statistical to quantitative methods [13], exploring the potential of UAVs [14], precision farming, and wireless sensors while discussing the benefits and challenges these technologies present. In [15] the design of greenhouse tomato-picking robot chassis showcases advancements in precise positioning and cruising capabilities through kinematic models [16], simulations, and physical testing, ultimately increasing the efficiency of greenhouse harvesting. These studies highlight the advancements in IoT-based agriculture monitoring systems and robotic harvesting technologies, underscoring their potential to revolutionize modern farming practices. Considering the research gaps, we aim to create an innovative solution for the agricultural sector by developing an autonomous harvesting robot named "Harvesting Robo-Vec" that leverages IoT technology. The objectives of the proposed system include:

- Develop a robust and efficient design for the harvesting robot, equipped with necessary sensors, actuators, and control systems to perform autonomous operations in the field.
- Incorporate IoT modules to enable real-time monitoring, data collection, and communication with a centralized control system.
- Make accurate harvesting decisions with minimal crop losses by effective detection and recognition of ripe fruits and vegetables using computer vision algorithms and proximity sensors.

Through this initiative, we seek to revolutionize the agriculture sector with a cost-effective, scalable solution, leading to increased output, reduced dependence on labor-intensive farming practices, and strides toward precision farming.

2. Proposed system model.- The Harvesting Robo-Vec is an innovative harvesting robot that automates the process of picking tomatoes. It integrates multiple hardware and software (See Figure I) components to make the field more efficient and accurate.

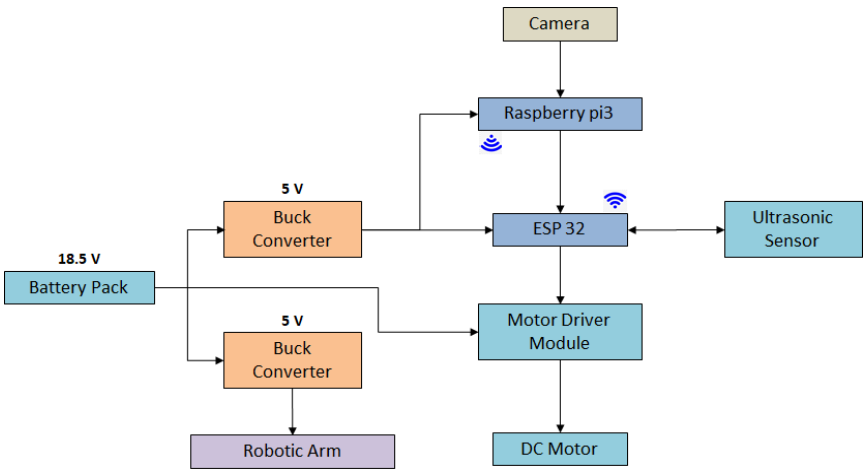

Figure I. System Block Diagram

2.1 Hardware Components

2.1.1 Microcontrollers. - The ESP32 microcontroller [17] is a low-power microcontroller, both Wi-Fi and Bluetooth capable. It is responsible for the communication line between different sensors and the robotic arm. It manages to aggregate data retrieval, and actuation as a whole well. The main processing unit is the Raspberry Pi Model 3B+ [18], which works in conjunction with the ESP32. This mini-computer has a complete Linux OS and handles complicated functionalities like image processing and computer vision algorithms

2.1.2 Sensors. - Sensors in use provide the data about the environment to the system. The Pi Camera [19] takes high-resolution images, and video of the crops, which is vital for processing visual information to identify ripe tomatoes. Ultrasonic sensors [20] send out sound waves and measure the distance to nearby obstacles using the time-of-flight of the received echo. Additionally, proximity sensors mounted on the robotic arm ensure that the distance to the tomatoes is accurately gauged for effective harvesting.

2.1.3 Actuators. - The robotic arm is powered by high-torque servomotors, which enable precise control over its movements, such as rotating and gripping. Motor driver modules interface with the microcontroller and servomotors, allowing for control over speed and direction.

2.1.4 Power Management. - The robot's operations are sustained by a battery management system (BMS) that monitors and regulates the rechargeable batteries, ensuring they are charged safely and used efficiently. Buck converters help manage voltage levels for different components, maintaining a stable power supply. Table I. presents the battery configuration for the Harvesting Robo-Vec.

Parameter	Value
Number of Cells	5
Nominal Voltage per Cell	3.7 V
Total Voltage	18.5 V
Estimated Total Current	6.35 A
Operational Duration	4 hours
Battery Capacity	25.4 Ah
Total Energy Capacity	469.9 Wh

Table I. Battery configuration

Additionally, Table II presents an analysis of energy consumption along with suggested improvements and Figure II is regarding the hardware used in the proposed model.

Energy Consumption Factor	Current Issues	Expected Amperes (A)	Suggested Improvements
Microcontrollers	High power draw from ESP32 and Raspberry Pi.	ESP32: 0.15 A Raspberry Pi: 1.2 A	Optimize algorithms for energy efficiency. Consider edge computing to reduce Raspberry Pi load.
Sensors	Continuous operation leads to increased power usage.	Pi Camera: 0.5 A Ultrasonic Sensors: 0.1 A each Proximity Sensors: 0.1 A each	Implement smart sensor activation (on-demand use). Utilize low-power modes during inactivity.
Actuators	High energy consumption for servomotors.	2 A (per motor, typically)	Use variable torque control based on task needs. Explore energy recovery systems (e.g., regenerative braking).

Table II. Energy consumption of Harvesting Robo-Vec

Figure II. Hardware used in the proposed model

2.2. Software Components

2.2.1 Operating System. - The Raspberry Pi operates on a Linux-based system, which provides a robust platform for running applications and managing resources.

2.2.2 Programming Languages. - The software is developed using Python for applications running on the Raspberry Pi, particularly for image processing tasks. The ESP32 microcontroller is programmed using C/C++, which is ideal for handling low-level control and real-time sensor data processing.

2.2.3 Image Processing. - OpenCV [21] is a critical library used for computer vision tasks. It aids in tasks such as color detection and image filtering, allowing the robot to identify ripe tomatoes based on their color and shape. The system transforms images to the HSV color space for better color differentiation.

2.2.4 Control Algorithms. - The gripping and harvesting algorithm modulates the final gripping strength and positioning given to feedback from the proximity sensors. This guarantees that tomatoes are taken carefully to protect them from damage during harvesting. Using the ultrasonic sensors as input, the obstacle avoidance algorithm makes sure the robot does not bump into obstacles while moving. Dijkstra's algorithm [22] calculates obstacles and determines the optimal path to get through the crop field.

2.2.5 Communication Protocols. - The communication between Raspberry Pi and ESP32 is based on RESTFull API [23] that allows command executing and data transmitting. This provides connectivity for remote control of the robot and ensures seamless communication between all components

In Figure III, the flowchart shows the entire process of the proposed system.

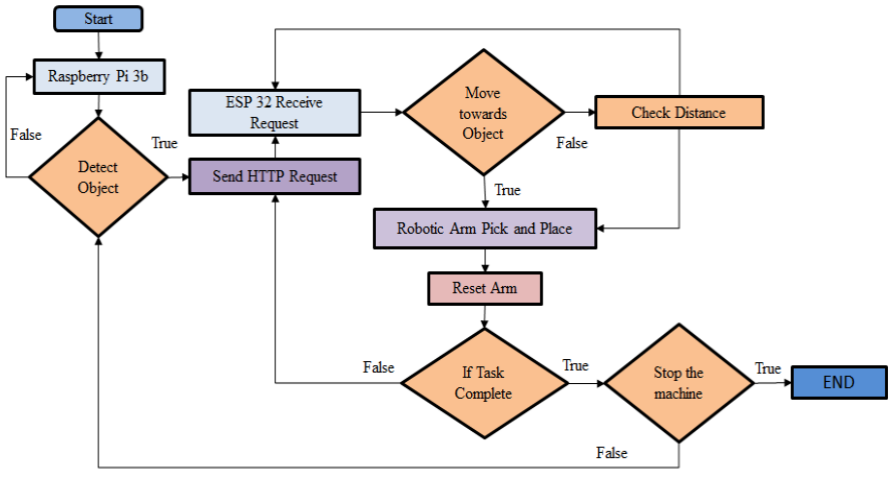

Figure III. Process flowchart.

3. Testing Procedures and Experimental Setup.- Since the testing procedure and setup will be vital for assessing the performance and functionality of Harvesting Robo Vec. The testing methods evaluate the performance parameters of Harvesting Robo Vec in tomato identification and detection. The experimental frame for testing the performance of the robot was established by simulating real agricultural environments incorporating a variety of factors. In the tomato plantation, the cultivated areas consisting of plants were organized to replicate the arrangement and density of plants in various fields, enabling a determination of robot efficiency to detect ripe tomatoes while navigating through diverse arrangements. To ensure the efficient maneuvering of the robot, different obstetrical were designed to test the real farming challenges which include soil types, and terrain variations. Moreover, the testing was performed concerning various illuminations, considering the different times of the day and weather (e.g. sunny and cloudy) conditions. Finally, the testing included levels for different soil types (e.g., clay, sandy, and loamy). This enabled us to compare the collective effects of these factors on the robot's ability to harvest in terms of stability, traction, and efficiency.

Different testing scenarios were created to assess distinct operations of Harvesting Robo Vec with different situations and are highlighted in Table III.

Condition	Description	Soil Type	Crop Variety	Lighting Condition	Obstacle Configuration
Test 1	Standard Row Planting	Loamy	Ripe Tomatoes	Clear, Midday	Few Rocks
Test 2	Cluster Planting with Intermixed Weeds	Sandy	Ripe Tomatoes	Overcast	Wooden Fences
Test 3	Row Planting with Uneven Growth	Clay	Ripe Tomatoes	Clear, Early Morning	Tall Grass
Test 4	Standard Row Planting with Different Tomato Varieties	Loamy	Cherry Tomatoes	Clear, Late Afternoon	Few Rocks
Test 5	Mixed Crop Field (Tomatoes with Other Vegetables)	Sandy	Mixed Crops	Rainy	Bushes

Table III. Experimental Conditions and Setup

Key metrics analyzed included detection accuracy, which measures the percentage of correctly identified tomatoes, providing insights into the reliability of the detection algorithms. Harvesting efficiency was also assessed, quantified by the number of tomatoes harvested per minute, offering a clear indicator of the robot's productivity.

All sensor data, camera data, and performance logs were used to analyze how well the robot performed in the agricultural environment. The use of detection accuracy, which explains the percentage of correctly identified tomatoes, provides information about the reliability of the detection algorithms and thus, it will be one of the key metrics analyzed in this work. We also evaluated harvesting efficiency (i.e., the number of harvested tomatoes per minute), providing a direct measure of the productivity of the robot. Moreover, the time spent performing the harvesting task was also recorded to assess the overall efficiency. Finally, the damage rate was measured as the percentage of damaged tomatoes during harvesting, which is crucial for understanding the impact of the robot's operations on crop quality as can be seen in Table IV.

Test Condition	Detection Accuracy (%)	Harvesting Efficiency (Tomatoes/Min)	Time Taken (Min)	Damage Rate (%)
Test 1	92	10	15	5
Test 2	85	8	20	10
Test 3	78	6	25	15
Test 4	90	9	18	6
Test 5	80	7	22	12

Table IV. Performance Metrics under Different Conditions

For this purpose, a comparative analysis between the proposed Harvesting Robo Vec and traditional manual harvesting methods was carried out as shown in Table V which demonstrates the effectiveness and efficiency of the proposed Harvesting Robo Vec over the traditional manual tomato harvesting method.

Method	Average Detection Accuracy (%)	Average Harvesting Efficiency (Tomatoes/Min)	Average Time Taken (Min)	Average Damage Rate (%)
Manual Harvesting	90	8	15	6
Robo Vec Harvesting	92	10	12	4

Table V. Comparison of Harvesting Methods

4. Results and Analysis. - In the results and analysis of Harvesting Robo-Vec, a more complex analysis of objectives was performed on the robot's live-operating performance against multiple metrics.

4.1 Tomato Detection Accuracy. - In regard to tomato detection accuracy results, the confusion matrix [24] (see Table. VI), summarizes the performance of the algorithm in terms of true positive (TP), true negative (TN), false positive (FP), and false negative (FN) detections. The confusion matrix shows the classification results and is used to assess the accuracy of the tomato detection algorithm.

Predicted	Actual Tomato	Actual Not Tomato
Tomato	True Positive (TP)	False Positive (FP)
Not Tomato	False Negative (FN)	True Negative (TN)

Table VI. Confusion Matrix Key Term

To obtain the essential parameters, we used the following formulae:

$$\text{Accuracy: } (TP + TN) / (TP + TN + FP + FN) \quad \text{Eq (1)}$$

$$\text{Precision: } TP / (TP + FP) \quad \text{Eq (2)}$$

$$\text{Recall: } TP / (TP + FN) \quad \text{Eq (3)}$$

By using data of TP = 120, TN = 700, FP = 150, and FN = 10, an accuracy of 83.67%, precision of 44.44%, and recall of 92.31% was obtained. The result for the tomato detection with other objects placed and with only tomato(s) can be seen in Figure IV.

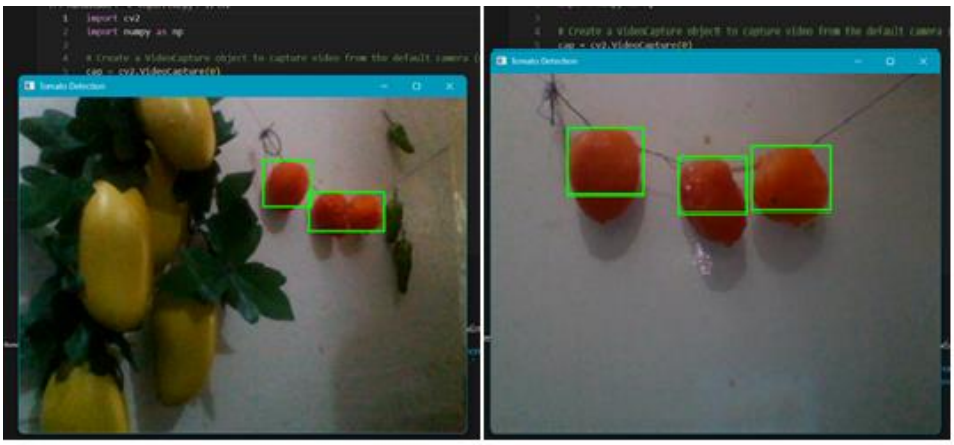

Figure IV. Tomato detection.

4.2 Obstacle Avoidance Performance. - In terms of obstacle avoidance, the robot successfully navigated around 95% of obstacles, with only 2 near misses and 3 collisions out of 100 encounters. This high success rate highlights the effectiveness of the obstacle detection and avoidance systems, though further fine-tuning could enhance performance.

4.3 Robotic Arm Manipulation Efficiency. - The robotic arm's manipulation efficiency was impressive, achieving a 90% success rate in gripping attempts and an 85% success rate in harvesting tomatoes. These metrics underscore the arm's reliability and effectiveness, with potential for further optimization in control algorithms and gripper design to

improve precision and reduce damage to the product. Figure V represents the gripping and dropping of tomato from the robotic arm at the predefined location.

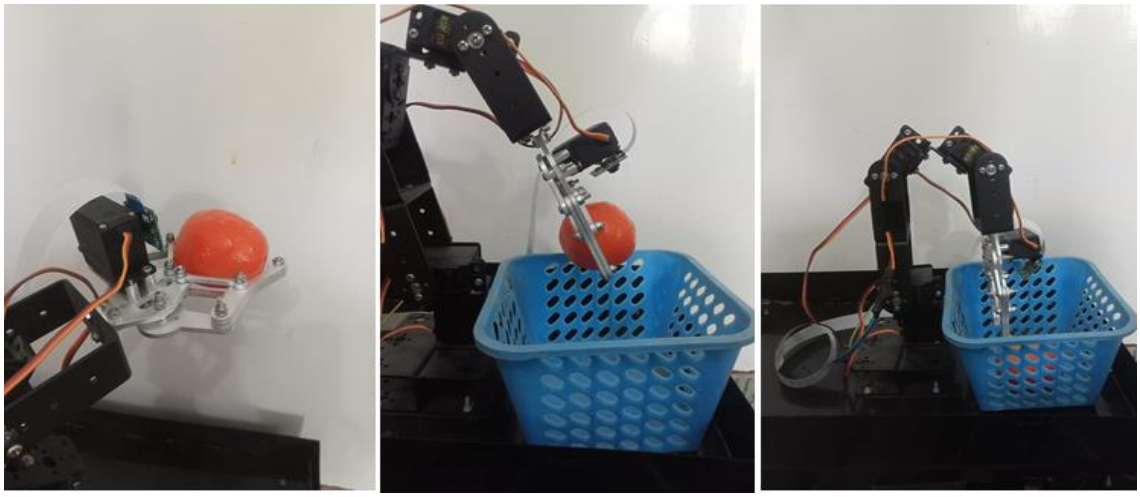

Figure V. Robotic Arm Manipulation.

The chassis of the vehicle, its charging port, and the resting position of the robotic arm placed in the final product can be seen in Figure VI.

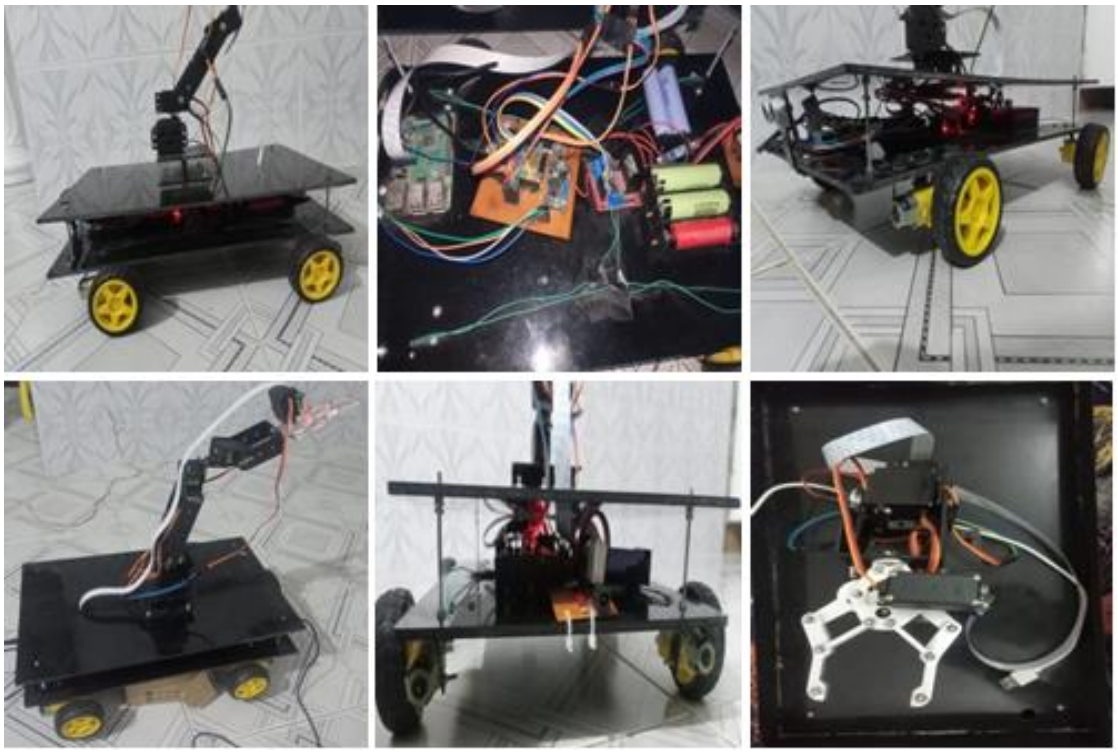

Figure VI. Robotic Arm Manipulation.

4.4 User Interface. - The prototype is controlled remotely using an Android application named "Harvesting Robot" (see Figure VII). To operate it, the Android phone connects to the access point of the ESP-32 module named "Harvesting Robot".

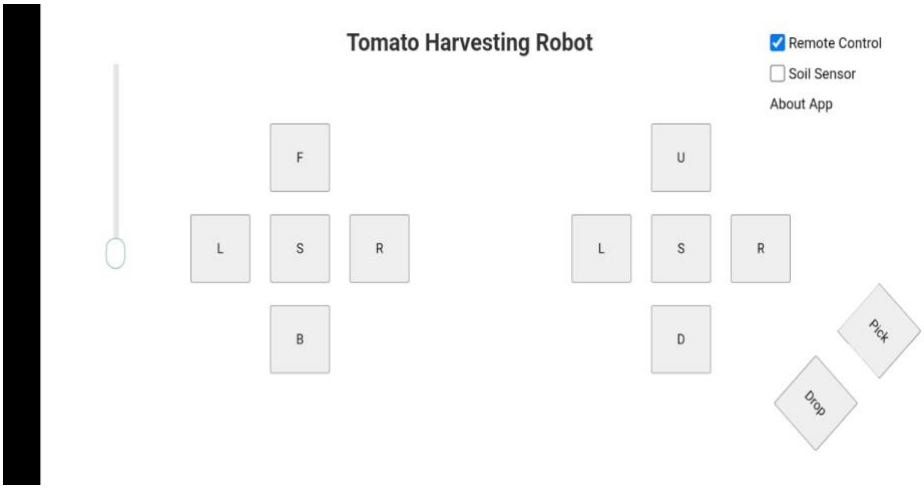

Figure VII. Remote Control of Robo-Vec.

The User Interface for controlling and monitoring the Harvesting Robo-Vec is designed as an intuitive Android application, enabling remote operation of the robot. Key features include straightforward control options that allow users to remotely direct the robot's movements and harvesting actions. The app provides manual control capabilities, as well as options for pausing and resuming operations as needed. Additionally, users can adjust specific parameters, such as speed and harvesting sensitivity, to tailor the robot's performance to various field conditions or crop types. The total cost analysis of IoT-based Harvesting Robo-Vec is presented in Table VII.

Component	Cost Estimate (Pkr)
Development and Prototyping	15,000
Microcontrollers (ESP32, Raspberry Pi)	37,500
Sensors (camera, ultrasonic, proximity)	2,600
Actuators (servomotors)	5,000
Battery (Li-ion system)	750
Chassis and Frame	5,000
Software Development	5,000
Contingencies	6,000
Total Initial Investment	**76,850**

Table VII. Cost analysis of IoT-based Harvesting Robo-Vec

5. Limitations and Failure Modes. - While the Harvesting Robo-Vec indeed works autonomously and can be a useful tool in agricultural scenarios, it does have its limitations and possible problems that could arise with its operations. We, therefore, explore these hurdles and propose solutions.

5.1 Obstacle Proximity Challenges. - The robot may have a problem identifying obstacles that are too close, which can cause collisions, or the robot to unexpectedly stop. This can be compensated for by adding additional sensors and moving their position

5.2 Detection Errors in Tomato Identification. - Tomato harvesting depends on precise detection with no leading fault. Such reliability can also be achieved using advanced image processing and methods of machine learning.

5.3 Energy Consumption and Limited Battery Life. - Prolonged operation can lead to quick battery depletion, especially under heavy workloads. Implementing energy-saving modes and optimizing operational paths can help extend battery life.

5.4 Mechanical Wear and Tear. - If the robot has run for some time there can be wear in the robotic components that can affect the performance. This problem can be minimized by making use of durable materials and also by following regular maintenance schedules.

6. Ethical and Social Implications. - Harvesting Robo-Vec will raise real ethical and social considerations that need to be addressed.

6.1 Impact on Jobs. - Automation will improve efficiency and help reduce service costs; It will also decrease the traditional demand for farm workers. Conversely, this tech can also generate employment in terms of maintaining, operating, and managing the robot systems, which can assist workers with the transition into new positions.

6.2 Environmental Considerations. - The Robo-Vec is designed to be energy-efficient, helping to lessen its environmental impact through smart power management and low-energy components. Future models might even use renewable energy sources, such as solar panels, to further decrease reliance on traditional power, supporting more sustainable farming practices.

6.3 Workers Safety. - Proximity sensors and emergency stop buttons are also added to Robo-Vec to ensure the safety of human workers around it. They even have sensors that are sensitive enough to detect anybody walking by, ultimately stopping the robot from doing its task to avoid an accident

With the continuous expansion of agricultural robotics, it is necessary to consider these ethical and social dimensions to ensure these advancements benefit society and the environment.

7. Conclusion and Future Work. - The proposed system model successfully achieved its goals and made significant advancements in automated tomato harvesting. The meticulous design and integration of the robotic system's components resulted in an effective and reliable outcome. The implementation of a Raspberry Pi-based color recognition algorithm enabled accurate tomato detection, while the integration of the ESP32 microcontroller facilitated seamless movement control, obstacle detection, and robotic arm manipulation. The findings indicate that the IoT-based Harvesting Robo-Vec has the potential to revolutionize tomato harvesting by reducing manual labor, increasing productivity, and ensuring consistent results through the successful integration of hardware, software algorithms, and IoT capabilities. Future work could enhance the tomato detection system's accuracy and robustness using machine learning techniques or advanced image processing algorithms and improve control through real-time data analytics and remote monitoring via IoT connectivity. Future iterations might also incorporate renewable energy sources, such as solar power, to enhance the system's sustainability and operational efficiency.

References

[1] Rehman, S.U., Zaidi, A.A., Wahab, Y.A., Arafat, M.Y. and Hatta, S.F.W.M., "Advanced Solar-Powered Seed Sowing Machine with Precision Seeding and Smart Control Features". *IEEE Regional Symposium on Micro and Nanoelectronics (RSM)* pp. 134-137. IEEE. August 2022. https://doi.org/10.1109/RSM59033.2023.10326842

[2] Haider, W. and Rehman, A., "Knowledge-based Soil Classification Towards Relevant Crop Production". *Int. J. Adv. Comput. Sci. Appl*., 10(12), pp.488-501. 2019. https://doi.org/10.14569/IJACSA.2019.0101266

[3] Haider, W., Rehman, A.U., Durrani, N.M. and Rehman, S.U., "A generic approach for wheat disease classification and verification using expert opinion for knowledge-based decisions". *IEEE Access*, 9, pp.31104-31129, 2021. https://doi.org/ 10.1109/ACCESS.2021.3058582

[4] Aqeel-ur-Rehman, S.U.R., Khan, I.U., Moiz, M. and Hasan, S., "Security and privacy issues in IoT". *International Journal of Communication Networks and Information Security (IJCNIS),* 8(3), pp.147-157. 2016.

[5] Rehman, S.U., Mustafa, H., Shaikh, M.A. and Memon, S., "Towards Sustainable Energy Storage: A Low-Cost IoT Solution for Real-time Monitoring of Lead-Acid Battery Health". *Memoria Investigaciones en Ingeniería*, (26), pp.202-212, 2024. https://doi.org/10.36561/ING.26.12

[6] Siddiquee, K.N.E.A., Islam, M.S., Singh, N., Gunjan, V.K., Yong, W.H., Huda, M.N. and Naik, D.B., "Development of Algorithms for an IoT-Based Smart Agriculture Monitoring System". *Wireless Communications and Mobile Computing*, 2022(1), p.7372053. 2022.

[7] Attri, Ishana, Lalit Kumar Awasthi, and Teek Parval Sharma. "Machine learning in agriculture: a review of crop management applications." Multimedia Tools and Applications 83, no. 5 (2024): 12875-12915. https://doi.org/10.1155/2022/7372053

[8] Rai, H.M., Gupta, D., Mishra, S. and Sharma, H., "Agri-Bot: IoT Based Unmanned Smart Vehicle for Multiple Agriculture Operation". *International Conference on Simulation, Automation & Smart Manufacturing (SASM)*, pp. 1-6. IEEE. August 2021. https://doi.org/10.1109/SASM51857.2021.9841182

[9] Feng, Q., Wang, X., Wang, G. and Li, Z., "Design and test of tomatoes harvesting robot". *IEEE international conference on information and automation,* pp. 949-952. IEEE. August 2015. https://doi.org/10.1109/ICInfA.2015.7279423

[10] Feng, Q., Zou, W., Fan, P., Zhang, C. and Wang, X., "Design and test of robotic harvesting system for cherry tomato". *International Journal of Agricultural and Biological Engineering*, 11(1), pp.96-100, 2018. https://doi.org/10.25165/j.ijabe.20181101.2853

[11] De-An, Z., Jidong, L., Wei, J., Ying, Z. and Yu, C., "Design and control of an apple harvesting robot". *Biosystems engineering*, 110(2), pp.112-122, 2011. https://doi.org/10.1016/j.biosystemseng.2011.07.005

[12] Rehman, A.U., Rehman, S.U. and Raheem, H., "Sinkhole attacks in wireless sensor networks: A survey". *Wireless Personal Communications*, 106, pp.2291-2313, 2019. https://doi.org/10.1007/s11277-018-6040-7

[13] Ayaz, M., Ammad-Uddin, M., Sharif, Z., Mansour, A. and Aggoune, E.H.M., "Internet-of-Things (IoT)-based smart agriculture: Toward making the fields talk". *IEEE access*, 7, pp.129551-129583, 2019. https://doi.org/10.1109/ACCESS.2019.2932609

[14] Pandey, G.K., Gurjar, D.S., Yadav, S., Jiang, Y. and Yuen, C. "UAV-Assisted Communications With RF Energy

Harvesting: A Comprehensive Survey". *IEEE Communications Surveys & Tutorials*, 2024. https://doi.org/10.1109/COMST.2024.3425597

[15] Su, L., Liu, R., Liu, K., Li, K., Liu, L. and Shi, Y., "Greenhouse tomato picking robot chassis". *Agriculture*, 13(3), p.532, 2023. https://doi.org/10.3390/agriculture13030532

[16] Russo, M., Zhang, D., Liu, X.J. and Xie, Z., "A review of parallel kinematic machine tools: Design, modeling, and applications". *International Journal of Machine Tools and Manufacture*, p.104118, 2024. https://doi.org/10.1016/j.ijmachtools.2024.104118

[17] El-Khozondar, H.J., Mtair, S.Y., Qoffa, K.O., Qasem, O.I., Munyarawi, A.H., Nassar, Y.F., Bayoumi, E.H. and Abd El, A.A.E.B., "A smart energy monitoring system using ESP32 microcontroller." *e-Prime-Advances in Electrical Engineering, Electronics and Energy*, 9, p.100666, 2024. https://doi.org/10.1016/j.prime.2024.100666

[18] Shakir, M., Karim, S., Memon, S., Rehman, S.U. and Mustafa, H., "An improvement in IoT-based smart trash management system using Raspberry Pi". *International Journal of Computational Vision and Robotics*, 14(2), pp.191-201, 2024. https://doi.org/10.1504/IJCVR.2024.136997

[19] Groffen, J. and Hoskin, C.J., "A portable Raspberry Pi-based camera set-up to record behaviours of frogs and other small animals under artificial or natural shelters in remote locations". *Ecology and Evolution*, 14(3), p.e10877, 2024. https://doi.org/10.1002/ece3.10877

[20] Khaleel, H.Z., Ahmed, A.K., Al-Obaidi, A.S.M., Luckyardi, S., Al Husaeni, D.F., Mahmod, R.A. and Humaidi, A.J., "Measurement enhancement of ultrasonic sensor using pelican optimization algorithm for robotic application". *Indonesian Journal of Science and Technology*, 9(1), pp.145-162, 2024. https://doi.org/10.17509/ijost.v9i1.64843

[21] Zhang, Y. and Xu, D., "Design of an intelligent medication delivery robot based on CNN and OpenCV". *Ninth International Symposium on Sensors, Mechatronics, and Automation System (ISSMAS 2023)*, vol. 12981, pp. 1451-1458. SPIE, March, 2024. https://doi.org/10.1117/12.3014833

[22] Maristany de las Casas, P., Kraus, L., Sedeño-Noda, A. and Borndörfer, R., "Targeted multiobjective Dijkstra algorithm". Networks, 82(3), pp.277-298, 2023. https://doi.org/10.1002/net.22174

[23] Ehsan, A., Abuhaliqa, M.A.M., Catal, C. and Mishra, D., "RESTful API testing methodologies: Rationale, challenges, and solution directions". Applied *Sciences,* 12(9), p.4369, 2022. https://doi.org/10.3390/app12094369

[24] Amperawan, A., Andika, D., Anisah, M., Rasyad, S. and Handayani, P., "Confusion Matrix Using Yolo V3-Tiny on Quadruped Robot Based Raspberry PI 3B", *7th FIRST 2023 International Conference on Global Innovations (FIRST-ESCSI 2023),*(pp. 549-562. Atlantis Press, February, 2024. https://doi.org/10.2991/978-94-6463-386-3_56

Author contribution:

1. Conception and design of the study
2. Data acquisition
3. Data analysis
4. Discussion of the results
5. Writing of the manuscript
6. Approval of the last version of the manuscript

SUR has contributed to: 1, 2, 3, 4, 5 and 6.

TAW has contributed to: 1, 2, 3, 4, 5 and 6.

Acceptance Note: This article was approved by the journal editors Dr. Rafael Sotelo and Mag. Ing. Fernando A. Hernández Gobertti.

Post Weld Quenching Impact on Microstructure and Mechanical Properties (Tensile, Impact, Hardness) of High Strength Low Alloy Steel

Impacto del temple posterior a la soldadura en la microestructura y las propiedades mecánicas del acero de baja aleación y alta resistencia

Impacto da têmpera pós-soldagem na microestrutura e nas propriedades mecânicas de aços de alta resistência e baixa liga

Atif Shazad[1(*)], Muhammad Uzair[2]

Recibido: 27/09/2024 Aceptado: 26/01/2025

Summary. - Shielded Metal Arc Welding (SMAW) is the most widely used welding technique in engineering industries. Compared to other arc welding techniques like TIG, SMAW is less heat-concentrating. However, welding thick jobs using SMAW can result in serious issues such as structural distortion due to non-uniform input heat distribution. High thermal stresses and distortions can degrade mechanical properties, similar to high input heat. Fast heat removal may prevent such defects, and different quenching media like sand, water, and oil were used to investigate variations in mechanical properties. High-strength low-alloy steel was selected due to its good weldability and easy availability, which makes it suitable for many industrial applications, such as in the space and defense industries. The tensile testing results showed that oil quenching was superior to other quenching techniques because oil-cooled joints had the highest tensile strength and ductility. However, water-cooled joints showed the highest yield strength, but oil-quenched joints had the highest welding efficiency. The hardness of water-cooled joints in the heat-affected zone and weld zone was greater due to rapid cooling in water. The impact energy of oil-cooled joints in the heat-affected zone was superior to that of other joints. Overall, the mechanical properties of oil-cooled joints were superior and showed better geometric configuration, such as minimal distortions.

Keywords: Tensile strength; hardness; Impact strength; SMAW; High strength low alloy steel; quenching media.

[1] Research Scholar, NEDUET (Pakistan), atifshahzad2717@gmail.com, ORCID iD: https://orcid.org/0000-0002-3277-7901

[2] Associate Professor, NEDUET (Pakistan), uzair@neduet.edu.pk, ORCID iD: https://orcid.org/0000-0002-2033-6244

Memoria Investigaciones en Ingeniería, núm. 28 (2025). pp. 45-57
https://doi.org/10.36561/ING.28.5
ISSN 2301-1092 • ISSN (en línea) 2301-1106 – Universidad de Montevideo, Uruguay

Resumen. - *La soldadura por arco metálico protegido (SMAW) es la técnica de soldadura más utilizada en las industrias de ingeniería. En comparación con otras técnicas de soldadura por arco como TIG, SMAW concentra menos calor. Sin embargo, soldar trabajos gruesos utilizando SMAW puede provocar problemas graves, como distorsión estructural debido a una distribución no uniforme del calor de entrada. Las altas tensiones y distorsiones térmicas pueden degradar las propiedades mecánicas, de forma similar al calor de entrada elevado. La eliminación rápida del calor puede prevenir tales defectos, y se utilizaron diferentes medios de enfriamiento como arena, agua y aceite para investigar las variaciones en las propiedades mecánicas. Se seleccionó acero de alta resistencia y baja aleación debido a su buena soldabilidad y fácil disponibilidad, lo que lo hace adecuado para muchas aplicaciones industriales, como en las industrias espacial y de defensa. Los resultados de las pruebas de tracción mostraron que el enfriamiento con aceite fue superior a otras técnicas de enfriamiento porque las juntas enfriadas por aceite tenían la mayor resistencia a la tracción y ductilidad. Sin embargo, las uniones enfriadas por agua mostraron el límite elástico más alto, pero las uniones enfriadas con aceite tuvieron la mayor eficiencia de soldadura. La dureza de las uniones enfriadas por agua en la zona afectada por el calor y en la zona de soldadura fue mayor debido al rápido enfriamiento en agua. La energía de impacto de las juntas enfriadas por aceite en la zona afectada por el calor fue superior a la de otras juntas. En general, las propiedades mecánicas de las juntas enfriadas por aceite fueron superiores y mostraron una mejor configuración geométrica, como distorsiones mínimas.*

Palabras clave: *Resistencia a la tracción; dureza; Fuerza de impacto; SMAW; Acero de baja aleación de alta resistencia; medios de enfriamiento.*

Resumo**. -** *A soldagem por arco metálico blindado (SMAW) é a técnica de soldagem mais amplamente utilizada nas indústrias de engenharia. Em comparação com outras técnicas de soldagem a arco, como TIG, o SMAW concentra menos calor. No entanto, a soldagem de trabalhos espessos usando SMAW pode resultar em problemas sérios, como distorção estrutural devido à distribuição não uniforme do calor de entrada. Altas tensões e distorções térmicas podem degradar as propriedades mecânicas, semelhante à alta entrada de calor. A rápida remoção de calor pode prevenir tais defeitos, e diferentes meios de têmpera como areia, água e óleo foram usados para investigar variações nas propriedades mecânicas. O aço de alta resistência e baixa liga foi selecionado devido à sua boa soldabilidade e fácil disponibilidade, o que o torna adequado para muitas aplicações industriais, como nas indústrias espacial e de defesa. Os resultados dos testes de tração mostraram que a têmpera em óleo foi superior a outras técnicas de têmpera porque as juntas resfriadas a óleo apresentaram maior resistência à tração e ductilidade. No entanto, as juntas resfriadas a água apresentaram o maior limite de escoamento, mas as juntas temperadas a óleo tiveram a maior eficiência de soldagem. A dureza das juntas resfriadas a água na zona afetada pelo calor e na zona de solda foi maior devido ao rápido resfriamento em água. A energia de impacto das juntas resfriadas a óleo na zona afetada pelo calor foi superior à das outras juntas. No geral, as propriedades mecânicas das juntas resfriadas a óleo foram superiores e apresentaram melhor configuração geométrica, como distorções mínimas.*

Palavras-chave: *Resistência à tracção; dureza; Resistência ao impacto; SMAW; Aço de baixa liga de alta resistência; meios de extinção.*

1. Introduction. - Shielded Metal Arc Welding (SMAW) is widely used in various industries due to its affordability and availability. It has a higher power density than gas fusion welding, but lower than Tungsten Inert Gas (TIG) welding. However, extensive distortions can occur during SMAW due to the low concentration of flame. Skilled welders can be easily sourced locally. High Strength Low Alloy Steel, known for its durability and strength, is utilized in upper atmosphere research, power production, and defense industries [1,2]. High Strength Low Alloy Steel is widely used in various industries due to its exceptional strength to weight ratio, enhanced toughness, ductility, and weldability. However, welding joints of low alloy high strength steel can experience a degradation of strength in the joined material. Welded joints exhibit reduced hardness and impact strength, and their ductility is also mitigated. These changes in mechanical properties are caused by the high heat input during welding, which results in alterations to both the microstructure and macrostructure of the welded samples [3,4].

Srinivasan et al. conducted a research study and revealed that the impact of heat on the mechanical properties of TIG welded joints made from High Strength Low Alloy (HSLA) steel. The study found that the strength of the welded joints decreased to 55% of the strength of the base material due to the welding process [5,6]. To address this issue, the samples were subjected to heat treatment, which resulted in an increase in strength. However, while other mechanical properties such as hardness were improved, the ductility of the welded samples was found to be lower than that of the base metal [7,8]. Sapthagiri et al. conducted a study on the impact of filler wire variation on the mechanical properties of welded joints made from low alloy high strength steel. The study found that using copper-coated filler wire resulted in an improvement in both yield strength and percent elongation [9].

Arc welding is more likely to produce defects such as angular and linear distortions compared to advanced techniques like laser and electron beam welding. Rami et al. investigated the impact of different welding clamps used in gas metal arc welding on the mechanical properties of the welded joints. The study found that using a heat treatment clamping technique resulted in achieving welding efficiency of over 80% [10]. Srivastava et al. conducted a study on the penetration depth of filler material in welding. The findings showed that changes in input heat and welding speed had a negative impact on the penetration depth, which, in turn, affected the joint efficiency [11].

Li et al. studied the effect of changes in welding input heat on the mechanical properties of low carbon steel and found that different microstructural phases were generated due to aberrations in cooling rate [12]. Eroglu et al. investigated the microstructural variations in High Strength Low Alloy Steel caused by changes in input heat energy. They observed that the hardness property in the weld region and heat-affected zone was reduced due to increased input heat. While martensite was produced as a result of lower heat input, hardness property decreased beyond a certain point with further increase in heat input [13]. Bijaya et al. conducted a study comparing the mechanical properties of mild steel joints that were welded using GMAW and SMAW methods. The rapid cooling rate after welding resulted in the development of bainite and martensite structures, which led to an increase in the hardness and tensile strength of the joints. However, the impact strength was found to have been reduced [14]. Ruming et al. investigated the enhancement of mechanical properties of welding joints through the addition of Cerium. The results revealed an improvement in toughness attributed to the surplus of crack-free energy. Additionally, the tensile strength of low alloy steel was enhanced due to the refined grain structure, resulting in a noticeable increase in welding efficiency upon the addition of Ce [15].

Narwadkar et al. conducted a study on the production of angular distortions in different types of welded joints. The results indicated that the bevel groove joint was more susceptible to angular distortions than single and double V groove joints, which were found to have lower angular distortions [16]. In another study, Adamczuk et al. investigated the correlation between the number of welds passes and angular distortion. It was found that there was a direct relationship between the number of passes and the angular distortions, with a greater shrinkage power resulting from the welding of thicker plates due to the direct effect of increasing the amount of weld metal on angular distortions [17]. Wei et al. studied the impact of distortions on the performance of welding joints and revealed that distortions have a direct effect on joint strength and dimensional accuracy [18]. Despite significant advancements in arc welding technology, distortion induced by welding remains one of the most noticeable challenges in the production industry for ensuring higher weld efficiency. Anis et al. investigated the impact of weld thickness and position on the residual stress generated during welding due to the contraction and expansion of the welding joint [19,20]. Residual stresses generated during welding hindered the joint efficiency increment, hence M Islam et al. performed a research work to evaluate joint mechanical properties after different post welding treatments. Pre-bending and pre-heating are some techniques utilized to control distortions [21,22].

2. Research Objective and Novelty. - The degradation of strength caused by high heat input during welding is a primary factor contributing to joint failure under load. Uneven thermal distribution across the joint amplifies the effects of residual stresses and increases the size of the Heat Affected Zone (HAZ). This study aims to improve the mechanical

properties of welded joints. Achieving this goal is challenging due to the fact that high input heat during welding can reduce the strength, ductility, hardness, and toughness of the welded structure by as much as 50% compared to the base metal. The density of input energy, or the concentration of heat, is a critical factor influencing the performance of welded joints. TIG welding is known for its high concentration of heat, whereas SMAW distributes the heat over a wider area, ultimately diminishing the mechanical and microstructural properties. Therefore, this study focuses on quenching the welded joints immediately after welding in various media to explore the impact on mechanical properties. Distortions that arise in welded structures are a major cause of strength degradation. Uneven temperature distribution across the welded joint causes distortions, ultimately weakening the structure. Consequently, enhancing the mechanical properties is vital to ensuring the reliability of welded joints. Ductility is especially important in large structures like pressure vessels. In this study, the quenching and cooling of welded joints immediately after welding are investigated to assess their impact on the mechanical properties of welded structures.

3. Experimental Methodology. - Quenching media were selected from local market due to easy availability. Normally welded joints are cooled in Air. Hence, to make direct comparative study welded joints after welding were cooled in Air, Water, Sand and old hydraulic oil (used) etc. Following experiments were performed after cooling in different media,

a. Tensile Testing
b. Impact testing
c. Hardness Testing
d. Microstructural characterization

High Strength Low Alloy Steel plate of 8mm thick was selected as base material and its chemical composition performed by spectroscopy and mechanical properties of base material was evaluated by using Universal Testing Machine (UTM) Tinius Olsen H150KV in material and metallurgy lab. Chemical composition of HSLA plate is represented in Table I and mechanical properties are represented in Table II.

Element	C	Si	Mn	Mo	V	Cr	S	P	Fe
Maximum	0.18	0.22	0.98	1.12	0.27	1.25	0.018	0.017	Remaining

Table I: Spectroscopy results of High Strength Low Alloy Steel

Material	Yield stress (MPa)	Ultimate strength (MPa)	Elongation %	Hardness (HV)
High Strength Low Alloy Steel	545	705	13	200

Table II: Tensile Strength and Hardness of Base metal (annealed state)

3x welded joints were tested in each testing category. Hardness testing and impact testing were performed to investigate effects of variations in cooling media. Hardness of base metal was checked by using Ernst hardness tester. Charpy Impact test was performed on machine of 300J capacity. Welding rod E-7018 was used for welding purpose, welding current of around 150Amp and welding speed of 200mm/min were used as welding parameters. Impact testing samples were prepared as per ASTM E23-18 standard. Charpy impact testing setup was utilized to evaluate toughness of welded joints. All quenching media were at standard atmospheric values of temperature and pressure before quenching.

4. Results and Discussions. -

4.1 Microstructural characterization. - The microstructural study was conducted to assess the impact of different quenching media on grain boundaries and grain sizes, which ultimately affect the mechanical properties. As shown in Figures Ia and Ib, the air-cooled samples primarily consisted of a ferrite phase. The slow cooling rate due to natural convection in air resulted in coarse ferrite grain boundaries and a minimal presence of pearlite, which was enveloped

by a ferrite matrix. In contrast, Figures Ic and Id reveal finer grain boundaries due to rapid cooling in water. The spacing between lamellae of pearlite and ferrite was reduced as represented in Figure Id. This decrease is associated with enhanced strength but reduced ductility due to the rise in hardness.

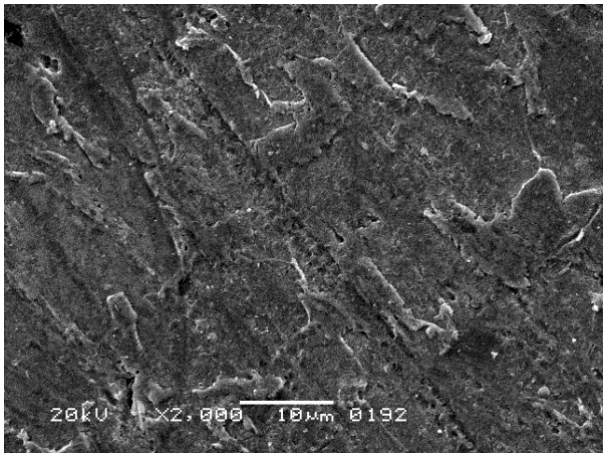

(a)

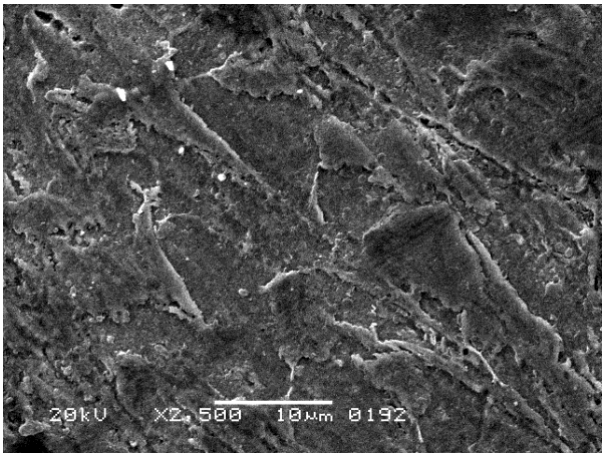

(b)

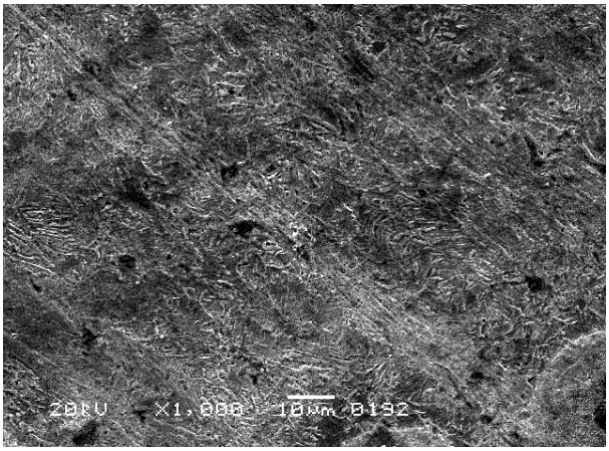

(c)

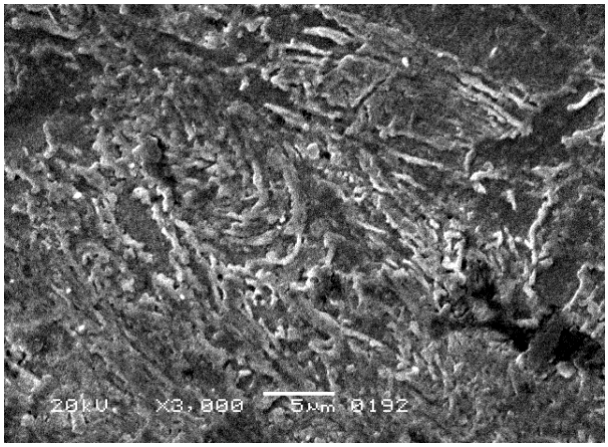

(d)

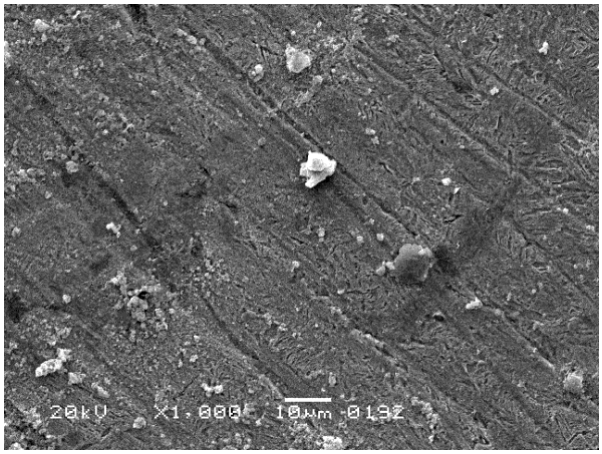

(e)

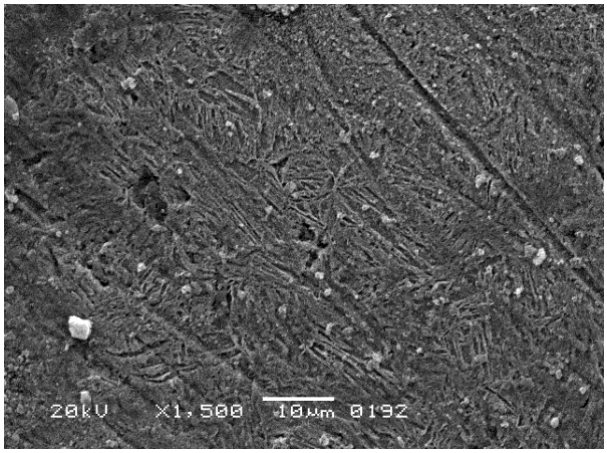

(f)

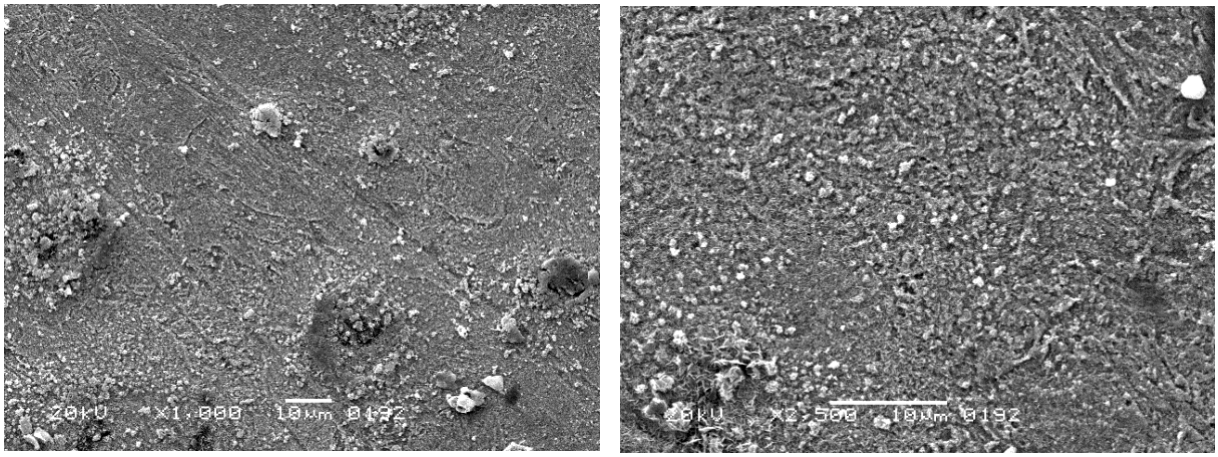

(g) (h)

Figure I: Microstructural Graphs (a) Air-cooled Samples (b) Water-cooled samples (c) Sand- cooled samples (d) Oil-cooled samples.

Sand cooling was relatively ineffective due to its slow cooling rate, attributed to the poor thermal conductivity of sand. As shown in Figures Ie and 1f, the microstructure exhibited coarse grain boundaries of ferrite and pearlite. Consequently, the mechanical properties are expected to be similar to those of air-cooled samples. In contrast, high-resolution micrographs of oil-cooled samples revealed a fine network of ferrite and pearlite, contributing to enhanced strength and hardness. The moderate cooling rate in oil facilitated precipitate diffusion along grain boundaries, as illustrated in Figures Ig and 1h, which could impede dislocation movement. Additionally, the grain boundaries in oil-cooled samples were larger compared to those in water-cooled samples, suggesting a potential improvement in ductility due to the balanced cooling effect of oil.

4.2 Hardness testing. - Welding reduces hardness of steel joint and base metal because high input heat deteriorates microstructure. Hardness of steel after welding mitigated to almost 60% of base metal hardness. Enhancement in hardness of welded joints was observed due to immediate quenching in water and oil. Water quenching significantly ameliorated hardness because of development of very fine and compact ferrite and pearlite lamellae in welding regions and heat affected regions. Results of comparison of WZ hardness are showed in Figure II, hardness 222HV was observed in WZ of water-cooled joints as compared to 140HV hardness of air-cooled joints. Air and sand cooled joints showed similar range of hardness because of slow cooling processes. Oil cooling represented significant enhancement as compared to normal air cooling after welding. Oil-cooled joints hardness was greater than air and sand cooled joint, however less than water-cooled joints because oil cooling are not as rapid as water cooling due high viscosity of oil.

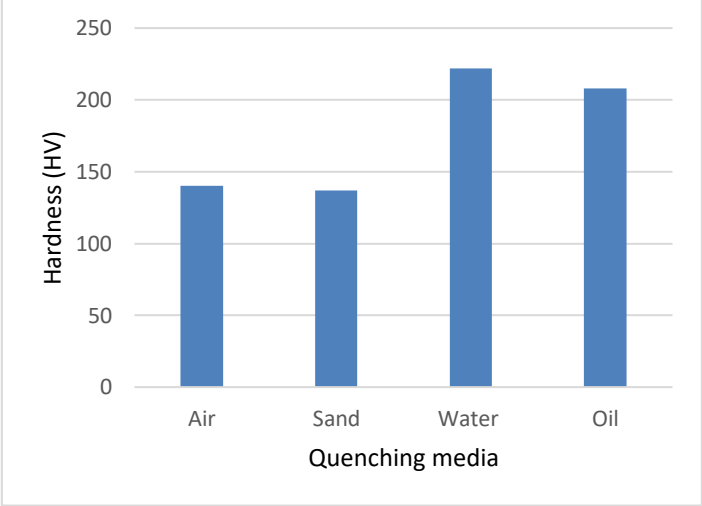

Figure II: WZ Hardness.

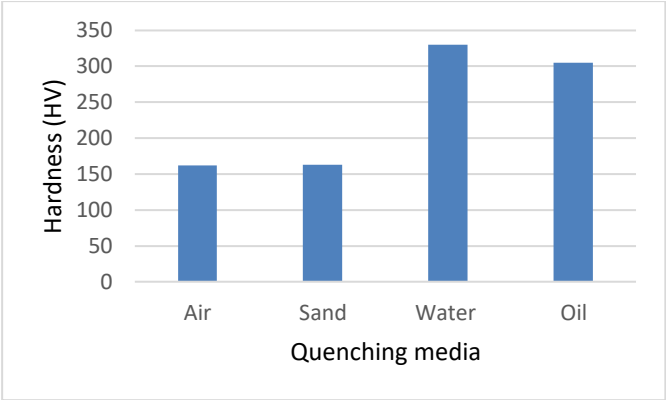

Figure III: HAZ Hardness.

Comparison of HAZ hardness between welded joints quenched in different media are represented in Figure III. Water cooling showed maximum hardness than others, 330HV hardness was attained after water cooling of welded joints. Fine grains development due to rapid cooling in HAZ because low concentrated heat input, dislocation motion was restrained, and internal stresses induced which causes brittleness. Oil cooling is a slow cooling process as compared to water cooling due to high viscosity of oil. 305HV hardness was observed in HAZ after oil cooling of welded joints and ultimately results in low internal stresses. Air and sand cooling, both are very slow cooling processes and imparted similar effects on welded joints with minimum variations. Welded joints are normally air cooled hence degradation of hardness from 200HV to 162HV in HAZ were observed. Enhancement in hardness was observed after quenching of welded structures in water and oil.

4.3 Tensile Testing. - Mechanical behavior of welding joints were investigated under tensile loading. Ultimate tensile strength (UTS), Yield strength (YS) and % elongation was evaluated to investigate the direct impact of cooling in different media on welding joints. Comparative study had been performed to appraise difference in strength properties of welded joints. Samples from welded joints were tested as per ASTM standard and samples after testing are represented in Figure IV.

Figure IV: Tensile Testing Samples.

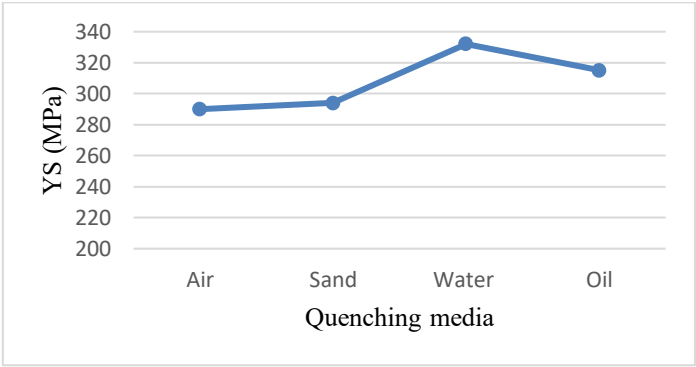

Figure V: Yield Strength Comparison.

Results represented in Figure V manifest comparison of YS of welded joints, water cooled joints exhibited maximum yield strength of 332MPa. Water cooled joints were brittle in nature because rapid cooling promotes internal stresses in WZ and HAZ. Moreover, due to fine grain boundaries in WZ and HAZ areas enhanced yield strength and ultimately promoted brittleness. Oil cooling was comparatively slow process than water cooling but fast than air and sand cooling. Little internal stresses produced during oil cooling because of slow cooling in oil. Hence, higher yield strength was attained due to good heat sinking of oil and ultimately improved microstructure. Air and sand cooled joints didn't reveal any remarkable difference between strength properties because both are slow cooled processes.

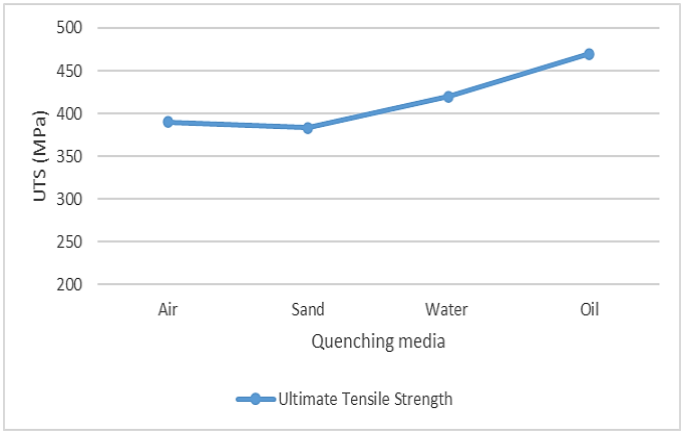

Figure VI: Ultimate Tensile Strength Comparison

Results represented in Figure VI delineate comparison of UTS of welding structures. It is normally observed that UTS dropped to 50% due to impact of high heat input, however oil cooled joints showed higher strength of 470MPa as compared to air cooled joints of 390MPa. Water cooled joints UTS was ameliorated as compared to air and sand cooled joints but not as significant as oil cooled joints. he cooling rate of water is higher than that of oil, making it more effective in rapidly reducing temperature. However, this higher cooling rate also induces internal stresses and increases brittleness due to the formation of harder phases. In the case of the welded samples, the 8mm thickness acted as a heat sink, affecting the overall cooling behaviour. However, in thicker sections, microstructural variations may not be as pronounced due to uneven heat dissipation, leading to less uniform phase transformation across the sample.
Difference between core and surface microstructure which leads to some ductility due to austenite and ferrite. Already used hydraulic oil has moderate viscosity which provides greater cooling rate than critical cooling rate. Vapor blanket stage was not established because of moderate viscosity, hence higher UTS was achieved in oil cooling. It is conspicuous from results represented in Figure VII that ductility of HSLA degraded from 13% elongation (base metal) to 7.2% elongation (air-cooled joints). High input heat mitigated ductility by deteriorating materials microstructure. Water cooling was detrimental to ductility because rapid cooling constrained dislocation motion and developed internal stresses. Oil cooling enhanced ductility by increasing % elongation from 7.2% to 9% for oil cooled joints.

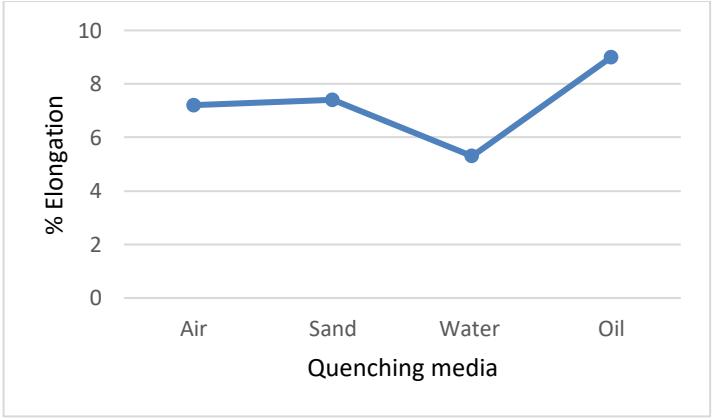

Figure VII: Percent Elongation Comparison

Oil cooling is comparatively slower than water cooling due to higher viscosity of oil. Air and sand cooled joints are not much distinguished in % elongation because both are slow cooling techniques. Statistical data analysis was conducted to assess the variations in mechanical properties, with the results presented in Table III. The analysis revealed the largest range in Ultimate Tensile Strength and Hardness, which can be directly linked to the influence of cooling rate. Statistical analysis plays a crucial role in identifying and quantifying the relationships between different variables, ensuring that the observed trends are reliable and representative.

		Mean	Median	Standard Deviation	Range
UTS		415.75	405	34.27	87
YS		307.7	304.5	16.9	42
% Elongation		7.225	7.3	1.4	3.7
Hardness	**WZ**	176.75	174	38.64	85
	HAZ	240	234	78	168
Impact Energy	**WZ**	48.25	50.5	6.98	18
	HAZ	94.125	95.75	14.6	41

Table III: Statistical Analysis

4.4 Welding Efficiency. - Welding efficiency of normal air-cooled joints is 50-55 %, tensile strength degrades after welding due to input heat. SMAW is a widely used technique, but joints are less efficient than TIG welding joints.

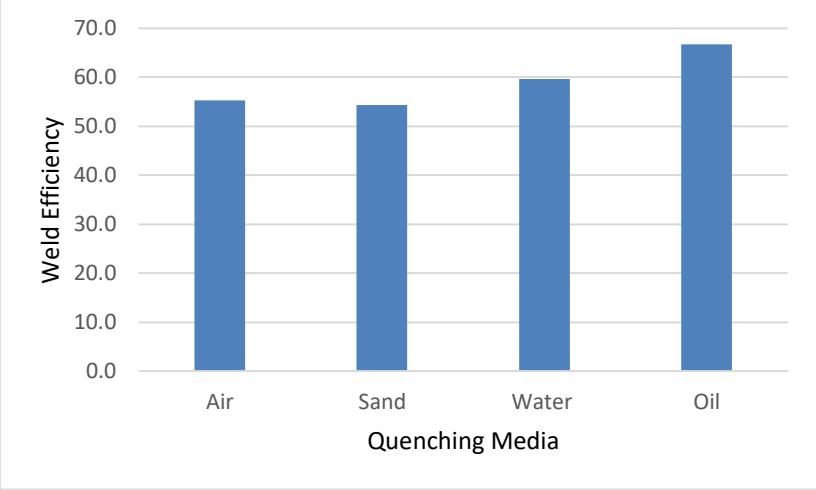

Figure VIII: Welding Efficiency Comparison

Input heat concentration is low, hence wider HAZ resulted which ultimately diminishes mechanical properties of joints. Thicker joints behave like heat sink, hence localized improvements in strength after welding was observed in normal air and sand cooled joints. Rapid cooling of welding joints in water reduced the width of HAZ and hinder the dislocation movements. Efficiency of welded joints quenched in water was less than efficiency of oil quenched welded joints as represented in Figure VIII. Severe internal stresses developed during water cooling was responsible of low UTS due to brittle behavior of joints. Almost 12% of UTS was enhanced due to oil cooling of welding joints. Improvements in

weld efficiency of oil quenched weld joints were due to moderate viscosity of used hydraulic oil because no vapor blanket developed in moderately viscous oil. Air and sand cooled weld joints were equally efficient because slow cooling resulted in both processes.

4.5 Impact Testing. - Impact testing was performed to appraise toughness of welded joints after quenching in different media. Charpy impact tester was utilized, and sample was prepared having V notch of 2mm depth. Toughness property pertinent to ductility because high ductile materials have good toughness. Behavior of welding joints under sudden impact loading was evaluated and difference between toughness of WZ and HAZ is represented in Figure IX. Reduction in impact energy of WZ and HAZ of Normal air-cooled joints revealed degradation in toughness, welding mitigated impact energy from 200J of base metal to 55J in WZ of joint. Rapid cooling in water and oil produced severe effects on toughness in weld zone of joints by reducing impact energy. Rapid cooling in water promotes brittleness due to internal stresses at crystallographic planes, hence impact energy of water-cooled joints was minimum as compared to other joints. Remarkable improvements in Impact energy of oil cooled was observed as value of impact energy in HAZ was increased by 18J than air cooled joints. Moderate cooling rate in oil was attained due to moderate viscosity and responsible for fine grain boundaries. Brittle behavior of joints was negligible due to minimum internal stresses.

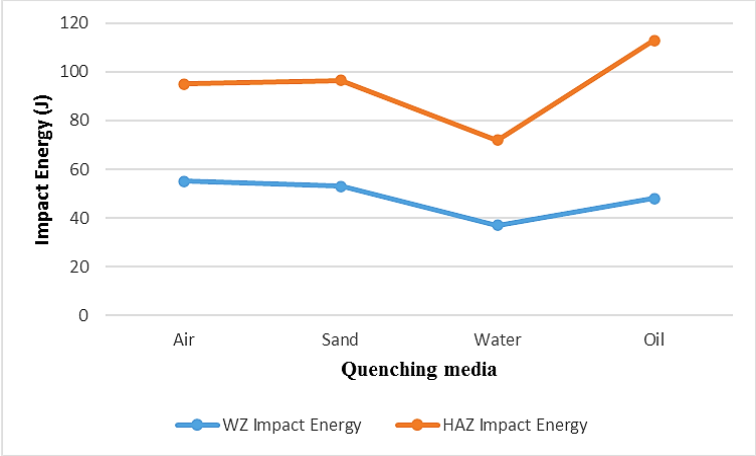

Figure IX: Impact Energy Comparison

5. Conclusion. - Considerable improvements were observed due to immediate quenching after welding of HSLA steel. Results of tensile testing revealed that maximum tensile strength was achieved due to oil quenching. Moreover, greater ductility was observed in form of enhanced % elongation after oil quenching. Water quenching degraded % elongation due to rapid cooling. Yield strength of water-cooled joints was greater because of narrow HAZ and constrained dislocation movement. Generation of internal stresses at crystallographic planes due to fast cooling promoted brittleness, hence UTS of water-cooled joints were less than oil cooled joints. Appreciable enhancement in welding efficiency was observed due to oil quenching. Oil quenched joints were 11% more efficient than normal air-cooled joints. Maximum hardness of 330HV was reported due to water quenching in HAZ and 222HV in WZ. Significant increase in impact energy was observed after oil quenching, water quenching mitigated toughness because impact energy of water-cooled joints was very low as compared to others. Overall performance of oil cooled joints under different mechanical loadings was noteworthy, hence oil quenching after welding would be performed for better mechanical properties of joints.

6. Future Recommendation. - To gain a deeper understanding of the long-term performance and durability of welded joints, it is recommended to incorporate fatigue testing into future studies. Creep testing under high temperature and constant load should be included in future research. Creep resistance is essential for welded joints in high-temperature environments, such as pressure vessels and steam pipes. While various quenching media have been evaluated in this study, it is suggested to explore additional or alternative cooling methods, such as cryogenic cooling or the use of hybrid quenching techniques.

References

[1] R.S.Parmar, “Welding engineering and technology”, Published by Khanna Publishers, Delhi, 2005.

[2] Sindo Kou, “Welding metallurgy” second edition, Wiley interscience publication, 2003.

[3] A. Shazad, J. Jadoon, M. Uzair and M. Akhtar, "Effect of composition and microstructure on the rusting of MS Rebars and ultimately their impact on mechanical behavior," Transactions of the Canadian Society for Mechanical Engineering, 2022.

[4] L. Srinivasan, T. Deepan Bharathi Kannan, and P. Sathiya, “Effect of heat input, heat treatment on microstructure and mechanical properties of GTA welded aerospace material 15CDV6”, Journal of materials research, Apr 2017. https://doi.org/10.1557/jmr.2017.70

[5] A. Shazad and M. Uzair, "Effect of quenching medium on the strength and hardness of 15CDV6 steel welded joints produced by argon arc welding," Metallurgy and Heat Treatment of Metals, vol. 11, pp. 45-45, 2024.

[6] A. Shazad, M. Uzair, and M. Tufail, "Influence of multiple post-weld repairs on mechanical and microstructural properties of butt weld joint utilized in structural members," International Journal of Precision Engineering and Manufacturing, pp. 1-8, 2024.

[7] P. N. Kumar, Y. Bhaskar, P. Mastanaiah, and C. V. S. Murthy, "Study on dissimilar metals welding of 15CDV6 and SAE 4130 steels by inter pulse gas tungsten arc welding," Procedia Materials Science, vol. 5, pp. 2382-2391, 2014.

[8] M. C. Sekhar, D. S. Rao, and D. Ramesh, "Welding development in ESR modified 15CDV6 material," International Journal of Mechanical Engineering and Robotic Research, vol. 3, pp. 499-504, 2014

[9] S Sapthagiri, K Jayathirtha Rao, K Ashok Reddy & C Sharada Prabhakar, “Comparison of Mechanical Properties on 15CDV6 Steel Plates by TIG- Welding with and without copper coated filler wires” International Journal of Advanced Research Foundation, www.ijarf.com, Volume 2, Issue 5, May 2015.

[10] Rami Rafea Abdul-Ameer , Saad Hameed Al-Shafaie, Abdul sameea Jasim Jilabi, “ Controlling distortion in gas metal arc high strength low alloy steel welds” Materials Today: Proceedings, June 2021, https://doi.org/10.1016/j.matpr.2021.06.010.

[11] Srivastava S, Garg RK. “Process parameter optimization of gas metal arc welding on IS: 2062 mild steel using response surface methodology” Journal of Manufacturing Process, 2017;25:296–305. https://doi.org/10.1016/j.jmapro.2016.12.016.

[12] Li C, Wang Y, Han T, et al. “Microstructure and toughness of coarse grain heat-affected zone of domestic X70 pipeline steel during inservice welding” Journal of Material Science, 2011;46(3):727–733. https://doi.org/10.1007/s10853-010-4803-y.

[13] Eroglu M, Aksoy M. “Effect of initial grain size on microstructure and toughness of intercritical heat-affected zone of a low carbon steel” Material Science Engineering A. 2000;286(2):289–297. https://doi.org/10.1016/s0921-5093(00)00801-7.

[14] Bijaya Kumar Khamari, Soumya Sobhan Dash, Swapan Kumar Karak, Bibhuti Bhusan Biswal, “Effect of welding parameters on mechanical and microstructural properties of GMAW and SMAW mild steel joints”, iron making and steel making, Sep 2020.

[15] Ruming Geng, Jing Li, Chengbin Shi , Jianguo Zhi, Bin Lu, “Effect of Ce on microstructures, carbides and mechanical properties in simulated coarse-grained heat-affected zone of 800-MPa high-strength low-alloy steel”, Materials Science and Engineering:A, Apr 2022,

[16] A. Narwadkar, and S. Bhosle, “Optimization of MIG welding parameters to control the angular distortion in Fe410WA steel”. Journal of Materials Manufacturing Processes. 2016. vol. 31. Pp. 2158-2164, doi:0.1080/10426914.2015.1127939.

[17] P. Adamczuk, I.G. Machado, J.A. Mazzaferro, “Methodology for predicting the angular distortion in multi-pass butt-joint welding”, Journal of Materials Processing and Technology. 240 (2017) 305–313, https://doi.org/10.1016/j.jmatprotec.2016.10.006.

[18] Wei Liang, Dean Deng, “Investigating the influence of external restraint on welding distortion in thin plate welded structures by means of numerical simulation technology”, Journal of Physics. Conference. Ser. 1063 (2018) 012082, https://doi.org/10.1088/1742-6596/1063/1/012082

[19] A. Shazad, M. Astif, M. Uzair, A. A. Zaidi, “Evaluation of preheating impact on weld residual stresses in AH-36 steel using Finite Element Analysis,” Memoria Investigaciones en Ingenieria 26 (2024) 225–243

[20] M. Anis, W. Winarto, “Effect of plate thickness and weld position on distortion and residual stress of welded structural steel”, Material. Sci. Forum 689 (2011)296–301 https://doi.org/10.4028/www.scientific.net/msf.689.296

[21] M. Islam, A. Buijk, M. Rais-Rohani, K. Motoyama, “Simulation-based numerical optimization of arc welding process for reduced distortion in welded structures”, Finite Element in Analysis and Design. 84 (2014.vol,) 54–64 https://doi.org/10.1016/j.finel.2014.02.003

[22] A. Shazad, M. Uzair, T. Jamil, N. Muhammad, "A Comparative Study on the Joint Hardness and Tensile Properties of Dissimilar Aluminum Alloy using Tungsten Inert Gas (TIG) Welding," in 4th Int. Conf. Key Enabling Technol. (KEYTECH 2024), Atlantis Press, pp. 173-178, Dec. 2024.

Author contribution:

1. Conception and design of the study
2. Data acquisition
3. Data analysis
4. Discussion of the results
5. Writing of the manuscript
6. Approval of the last version of the manuscript

AS has contributed to: 1, 2, 3, 4, 5 and 6.

MU has contributed to: 1, 2, 3, 4, 5 and 6.

Acceptance Note: This article was approved by the journal editors Dr. Rafael Sotelo and Mag. Ing. Fernando A. Hernández Gobertti.

Mechanical Characterization of Post weld quenched Al 6082-T6 TIG welded Joints

Caracterización mecánica de uniones soldadas TIG Al 6082-T6 templadas después de la soldadura

Caracterização mecânica de juntas soldadas TIG Al 6082-T6 pós-soldagem temperada

Atif Shazad[1], Muhammad Uzair[2(*)], Junaid Jadoon[3], Muhammad Saleem Khan[4]

Recibido: 27/09/2024 Aceptado: 26/01/2025

Summary. - This research aims to enhance the efficiency of weld joints through a cost-effective methodology. Aluminium 6082-T6 is the chosen material due to its frequent use in applications that require intermediate strength with low weight. Welding operations typically lead to a weakening of material strength by up to 50% due to the high input heat. Therefore, the focus of this study is to improve the strength by employing quenching techniques with different media, such as sand, water, and hydraulic oil. A comparative analysis of the mechanical properties is performed based on the quenching of weld joints using these various media. Additionally, microstructure examination is conducted to facilitate this comparative study. The mechanical properties investigated include hardness, tensile strength, yield strength, and toughness, with the goal of understanding the impact of different quenching media. The research reveals that water-cooled joints exhibit higher yield strength, while oil-cooled joints demonstrate superior tensile strength compared to other joints. Furthermore, the ductility of oil-cooled joints is notably higher, as measured by % elongation. Water cooling leads to noteworthy hardness in both the Weld Zone (WZ) and Heat-Affected Zone (HAZ) due to rapid cooling. In contrast, the hardness of oil-cooled joints is not significantly different from that of water-cooled welded joints. Regarding toughness, oil-cooled joints show greater impact energy in the HAZ compared to those quenched with water, sand, and air. However, in the WZ, air-cooled joints exhibit superior impact energy, which directly indicates better toughness properties. Therefore, oil-cooled joints display higher toughness in the HAZ, while air-cooled joints are tougher in the WZ. Overall, the mechanical properties of oil-cooled joints are significantly enhanced, leading to an improved weld efficiency from 55% to 72%.

Keywords: TIG welding; mechanical properties; Al 6082-T6; quenching media.

[1] PhD Scholar, Department of Mechanical Engineering, NEDUET (Pakistan), atifshahzad2717@gmail.com, ORCID iD: https://orcid.org/0000-0002-3277-7901

[2] Associate Professor, Department of Mechanical Engineering, NEDUET (Pakistan), uzair@neduet.edu.pk, ORCID iD: https://orcid.org/0000-0002-2033-6244

[3] Student, Department of Mechanical Engineering, PIEAS (Pakistan), junaidjadoon2012@gmail.com, ORCID iD: https://orcid.org/0000-0002-3277-7901

[4] Student, Department of Metallurgy and Materials Engineering, University of Engineering and Technology (Pakistan), saleemkhan.uet@gmail.com, ORCID iD: https://orcid.org/0000-0002-3277-7901

Resumen. - *Esta investigación busca mejorar la eficiencia de las uniones soldadas mediante una metodología rentable. El aluminio 6082-T6 es el material elegido debido a su uso frecuente en aplicaciones que requieren resistencia intermedia con bajo peso. Las operaciones de soldadura suelen provocar una reducción de la resistencia del material de hasta un 50 % debido al elevado calor de entrada. Por lo tanto, este estudio se centra en mejorar la resistencia mediante técnicas de temple con diferentes medios, como arena, agua y aceite hidráulico. Se realiza un análisis comparativo de las propiedades mecánicas basado en el temple de las uniones soldadas con estos diversos medios. Además, se realiza un examen de la microestructura para facilitar este estudio comparativo. Las propiedades mecánicas investigadas incluyen dureza, resistencia a la tracción, límite elástico y tenacidad, con el objetivo de comprender el impacto de los diferentes medios de temple. La investigación revela que las uniones refrigeradas por agua presentan un mayor límite elástico, mientras que las refrigeradas por aceite demuestran una resistencia a la tracción superior en comparación con otras uniones. Además, la ductilidad de las uniones refrigeradas por aceite es notablemente mayor, medida mediante el porcentaje de elongación. El enfriamiento por agua produce una dureza notable tanto en la zona de soldadura (ZS) como en la zona afectada por el calor (ZAC) debido al rápido enfriamiento. Por el contrario, la dureza de las uniones enfriadas con aceite no es significativamente diferente de la de las uniones soldadas enfriadas con agua. Con respecto a la tenacidad, las uniones enfriadas con aceite muestran una mayor energía de impacto en la ZAC en comparación con las templadas con agua, arena y aire. Sin embargo, en la ZS, las uniones enfriadas con aire exhiben una energía de impacto superior, lo que indica directamente mejores propiedades de tenacidad. Por lo tanto, las uniones enfriadas con aceite muestran una mayor tenacidad en la ZAC, mientras que las uniones enfriadas con aire son más tenaces en la ZS. En general, las propiedades mecánicas de las uniones enfriadas con aceite mejoran significativamente, lo que lleva a una mejora en la eficiencia de la soldadura del 55% al 72%.*

Palabras clave: *Soldadura TIG; propiedades mecánicas; Al 6082-T6; medios de enfriamiento.*

Resumo *. -* *Esta pesquisa visa aumentar a eficiência de juntas soldadas por meio de uma metodologia econômica. O alumínio 6082-T6 é o material escolhido devido ao seu uso frequente em aplicações que exigem resistência intermediária com baixo peso. As operações de soldagem normalmente levam a um enfraquecimento da resistência do material em até 50% devido ao alto calor de entrada. Portanto, o foco deste estudo é melhorar a resistência empregando técnicas de têmpera com diferentes meios, como areia, água e óleo hidráulico. Uma análise comparativa das propriedades mecânicas é realizada com base na têmpera de juntas soldadas usando esses vários meios. Além disso, o exame da microestrutura é realizado para facilitar este estudo comparativo. As propriedades mecânicas investigadas incluem dureza, resistência à tração, resistência ao escoamento e tenacidade, com o objetivo de compreender o impacto de diferentes meios de têmpera. A pesquisa revela que juntas resfriadas a água apresentam maior resistência ao escoamento, enquanto juntas resfriadas a óleo demonstram resistência à tração superior em comparação com outras juntas. Além disso, a ductilidade das juntas resfriadas a óleo é notavelmente maior, medida pela % de alongamento. O resfriamento a água resulta em dureza notável tanto na Zona de Solda (ZS) quanto na Zona Afetada pelo Calor (ZAC) devido ao resfriamento rápido. Em contraste, a dureza das juntas resfriadas a óleo não é significativamente diferente daquela das juntas soldadas resfriadas a água. Em relação à tenacidade, as juntas resfriadas a óleo apresentam maior energia de impacto na ZAC em comparação àquelas temperadas com água, areia e ar. No entanto, na ZC, as juntas resfriadas a ar exibem energia de impacto superior, o que indica diretamente melhores propriedades de tenacidade. Portanto, as juntas resfriadas a óleo apresentam maior tenacidade na ZAC, enquanto as juntas resfriadas a ar são mais tenazes na ZC. No geral, as propriedades mecânicas das juntas resfriadas a óleo são significativamente aprimoradas, levando a uma eficiência de soldagem aprimorada de 55% para 72%.*

Palavras-chave: *Soldagem TIG; propriedades mecânicas; Al 6082-T6; meios de têmpera.*

1. Introduction. - Aluminium alloys are widely used in numerous applications due to their excellent strength-to-weight ratio. Among these alloys, Al 6082 is noted for its significant strength combined with a low weight. Additionally, this alloy exhibits remarkable resistance to rust and possesses good reusability properties [1]. Its application is especially prevalent in the automobile industry, where it is used in the manufacturing of suspension components. Al 6082 is primarily composed of Aluminium (Al), Magnesium (Mg), and Silicon (Si). To further enhance its mechanical properties such as tensile and yield strength, impact strength, and grain boundary size, Al 6082 undergoes heat treatment [2]. A hot forging process is commonly utilized by many industries to produce intricate parts in a single operation. However, this process results in a highly deformed microstructure with significant thermal and mechanical stresses. As a consequence, post-forging heat treatment is often employed to alleviate such defects [3][4].

Joining Al 6082 through welding helps to reduce residual mechanical and thermal stresses to some extent. However, a major drawback of welding is the reduction in joint strength. After welding, the tensile strength and hardness can be reduced by up to 50%, necessitating post-weld heat treatments to enhance joint strength. Unfortunately, these post-weld heat treatments can be expensive [5]. Forging is considered a cost-effective and efficient method for manufacturing small-sized parts; however, for large-sized parts, forging becomes cumbersome and expensive [6]. As a result, welding is commonly employed to join different parts and create giant structures. The choice of welding parameters is known to significantly impact the performance of welded joints, with the type of welding technique playing a crucial role [7]. Tungsten Inert Gas (TIG) welding is preferred in applications requiring concentrated heat, while Shielded Metal Arc Welding (SMAW) is not suitable for such tasks due to its wider heat-affected zone (HAZ) compared to TIG welding [8].

TIG welded joints of Al 6082 have been found to exhibit superior strength compared to Metal Inert Gas (MIG) welded joints. This improvement in strength is attributed to the presence of equally sized grain boundaries after TIG welding, resulting in a very fine spacing between adjacent grains [9]. Furthermore, the hardness of the joints has been shown to be influenced by the speed of the tungsten electrode, with higher speeds contributing to the softening of the joint area. The impact of subzero temperature conditions has been observed to strongly affect the mechanical properties of Al 6082, and thick plate coalescence using arc welding has led to the occurrence of various defects such as cracks and pores [10]. These findings highlight the importance of selecting appropriate welding techniques and parameters to ensure the desired mechanical properties and structural integrity in welded joints, especially when dealing with large-sized structures.

A parametric study to evaluate key influencing factors in TIG welding of Aluminium alloys is considered very essential. An increment in welding current has been found to negatively affect the tensile strength and hardness of the welded joints. However, optimal results have been achieved with a welding current of 150A and a welding speed of 200 mm/min, leading to improved tensile strength and hardness properties [11]. The heat treatment of Al 6082-T6 alloy has produced a serious effect on hardness. Artificial aging at 175°C has significantly enhanced the hardness, whereas performing solution heat treatment before age hardening has led to a degradation in hardness. The development of the Mg2Si phase during artificial aging has increased the brittleness of Al 6082, consequently contributing to its increased hardness [12].

Exploration of input heat influence on the precipitation hardening of Al 6082 during TIG welding has affirmed that the concentrated arc generated during TIG welding allows for directed heat flow to the fusion areas, quickly achieving the desired fusion temperature. Additionally, TIG welding is considered a welding technique with minimal defects, especially when compared to other fusion techniques. The distortions resulting from temperature distribution on welded joints are known to be more severe in other fusion techniques than in TIG welding [13][14]. Severe residual stresses due to non-uniform thermal loading are known to negatively impact the corrosion behaviour of aluminium alloys. The elevated temperatures experienced during welding induce thermal stresses, leading to stress corrosion cracking, precipitation, and subsequent pitting corrosion. These factors ultimately compromise the strength of welded joints [15]. Moreover, the anodic and cathodic behaviour of aluminium alloy precipitates influence the corrosion phenomenon. The research has demonstrated that magnesium dissolution exhibits an anodic behavior and contributes to the enhanced occurrence of pitting corrosion [16].

1.1 Research Motivation. - The strength and hardness of Al 6082-T6 significantly deteriorate due to the high heat input generated during the welding process. A comprehensive literature review reveals that this degradation primarily results from substantial microstructural alterations induced by welding. Given the high thermal conductivity of aluminium, heat is rapidly conducted, leading to an expanded HAZ and subsequent microstructural disruptions, which frequently contribute to joint failure. Moreover, the ductility of welded joints is considerably reduced due to microstructural distortion and reinforcement through the incorporation of additional filler metal. This study explores

the potential enhancement of the mechanical properties of Al 6082-T6 weld joints through post-weld quenching using various cooling media following TIG welding. The HAZ width in samples cooled under ambient air conditions is relatively larger due to the slower heat dissipation, which negatively impacts tensile strength, impact resistance, and hardness. Minimizing the HAZ width is crucial for improving the mechanical performance of welded joints. Therefore, rapid dissipation of post-welding heat is essential to mitigate mechanical property degradation. This investigation evaluates the effect of different cooling media on the mechanical behaviour of Al 6082-T6, recognizing that each cooling medium exhibits distinct heat transfer characteristics, leading to variations in the resulting mechanical properties of the weld joints.

2. Experimental Methodology. - TIG welding technique was utilized in this study for welding of Al 6082-T6 alloy of 8mm thickness, different quenching media were used immediately after welding process to alter mechanical properties and welding efficiency. Following parameters were studied:

a. Microstructural examination
b. Tensile testing
c. Hardness testing
d. Impact testing

To investigate variations in strength and ductility, the researchers conducted tensile testing. Tensile samples were prepared according to the ASTM E8M-16a standard, and a H150KV tensile testing machine (UTM) was employed for this research. The hardness of the samples was evaluated using an Ernst Vickers Hardness Tester. Four different quenching media air, sand, water, and hydraulic oil (Shell Morlina S2 BL 10) were selected for the purpose of cooling. To assess toughness after the cooling process of welded samples, Charpy V-notch impact testing was performed following the ASTM E23-18 standard for sample preparation. Microstructural examination of properly prepared metallurgical specimens/weldments was conducted using an Optical Metallurgical Microscope. The chemical composition of the material was determined using an optical emission spectrometer, and the weight percentages of constituent elements are presented in Table I. For comparison with the welded samples, the mechanical properties of the base material were tabulated in Table II. Based on a comprehensive review of the literature, suitable welding parameters were selected to achieve high-quality welded joints.

Element	Mg	Si	Mn	Cu	Cr	Zn	Ti	Fe	Al
Percentage	1	.7	.95	.13	.26	.21	.12	.48	Balance

Table I: Chemical composition of Al 6082-T6

Base material specimens were cut from 8 mm thick plate and tensile specimens were prepared as per ASTM E8M-16a standard.

Base metal	Yield strength (YS)	Tensile strength (UTS)	% Elongation	Hardness Vicker (HV)
Al 6082-T6	250MPa	300MPa	10%	90

Table II: Base material mechanical properties

For TIG welding, the welding parameters chosen were an electrode traveling speed of 200 mm/min and a current of 180 A. The welding process utilized a Precision TIG AC type machine, and a 3.2mm diameter filler wire AA4043 was selected. To prevent any interference with the mechanical properties, the dwell time after welding was kept to a minimum.

3. Results and Discussion. -

3.1 Microstructure Study. - Microstructural study was performed to evaluate the impact of different cooling media on HAZ of welding joints of Al 6082 T6. The microstructural examination presented in Figure I illustrates distinct grain boundaries within the HAZ. Coarse grain boundaries were observed in both Figure I(a) and Figure I(b),

contributing to improved elongation percentage and ductility but reduced strength. Conversely, Figure I(c) and Figure I(d) depict fine grain boundaries resulting from the rapid cooling process involving water and oil. Notably, oil cooling leads to the formation of elongated grains, as evident in Figure I(d). In comparison, joints cooled with air and sand exhibit higher levels of porosity when compared to those cooled with water and oil. The presence of pores creates points of stress concentration, ultimately causing a degradation in the mechanical strength of the joints. Microstructural analysis of oil cooled joints reveals the presence of fine and equiaxed grains due to the moderate viscosity of the oil, which facilitates quick and uniform heat dissipation without the formation of a vapor shield.

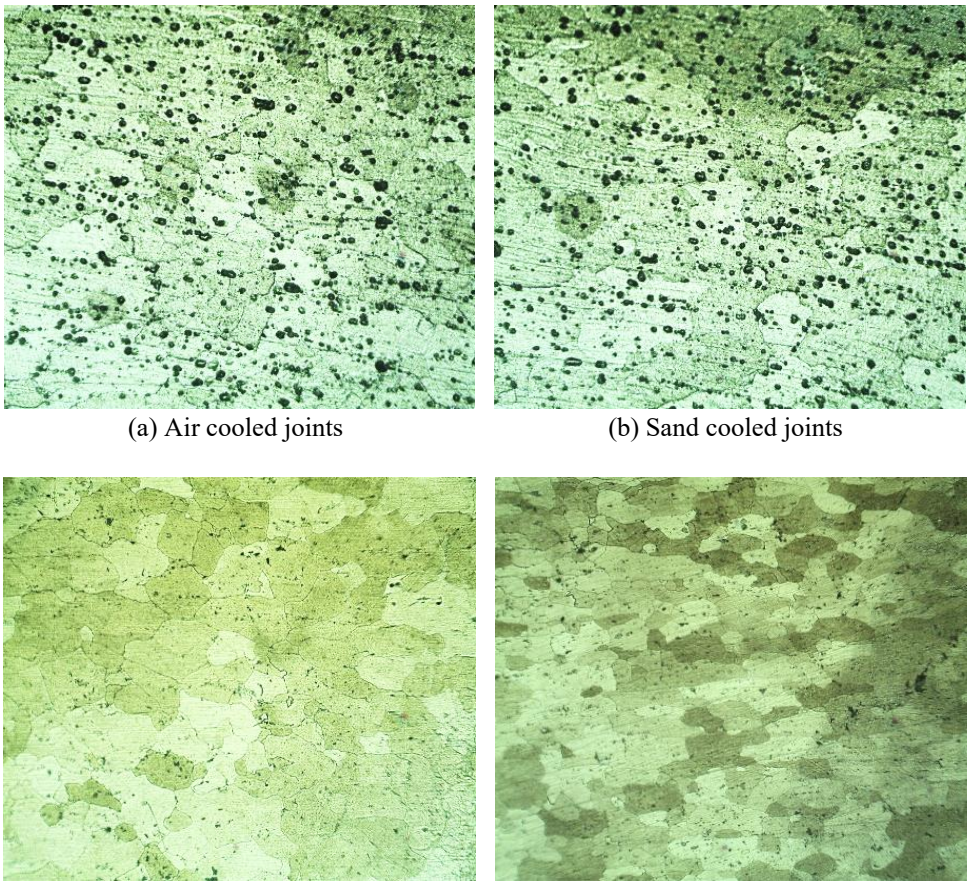

(a) Air cooled joints (b) Sand cooled joints

(c) Water cooled joints (d) Hydraulic-oil cooled joints

Figure I: Microstructure of HAZ of Air, Sand, Water & Hydraulic-oil cooled joints.

Water-cooled joints exhibit fine yet irregular grains due to their rapid but non-uniform cooling process. The black spots observed in the HAZ of air-cooled and sand-cooled samples likely result from the formation of secondary phases, such as Mg_2Si precipitates or other intermetallic compounds, during cooling. The slower cooling rates in air and sand facilitated the diffusion of precipitates along coarse grain boundaries. These precipitates appear darker under optical microscopy due to their distinct optical properties compared to the aluminium matrix. In contrast, rapid cooling in water and oil quenching leaves less time for precipitate formation and growth. Instead, the rapid cooling rate traps solute atoms within the aluminium matrix, inhibiting the development of distinct precipitates. Consequently, black spots are smaller or less noticeable in these samples. Additionally, slower cooling rates may encourage the segregation of elements like Mg or Si at grain boundaries. Rapid cooling, on the other hand, promotes fine grain boundaries, enhancing mechanical strength while reducing the ductility of welded joints. The formation of precipitates restricts dislocation motion under loading, leading to increased strength. Rapid cooling seizes these precipitates along fine grain boundaries, potentially contributing to strength enhancement. This precipitation effect is counteracted by the presence of pores and coarse grain boundaries, meaning slow cooling may not significantly improve strength and hardness.

3.2 Tensile Testing Results. - The strength (both tensile and yield) of welded joints decreased by approximately 50% as a result of the weld heat input effects [5]. Figure II represents the outcomes of the comparison between the yield strength (YS) of welded joints that were quenched or cooled using different cooling methods. For each cooling

treatment, three samples were chosen, and the comparison was based on the average values. The water-quenched welded samples exhibited a higher YS compared to the samples cooled in air, sand, and oil. This improvement in YS was achieved because the rapid cooling in water led to the formation of fine grain boundaries.

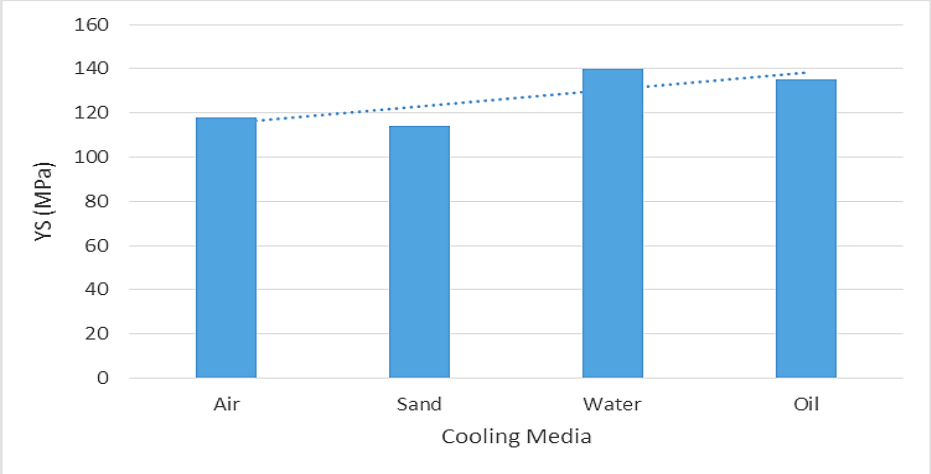

Figure II: Quenching effect on yield strength.

The YS of the oil-quenched welded samples was similar to that of the water-quenched samples due to the higher convectional coefficients facilitating temperature distribution. Additionally, low distortions were observed after oil quenching. The YS of the air and sand-cooled samples were approximately equal since both cases involved slower cooling. Several distortions were observed after water quenching due to its very rapid cooling process. The findings presented in Figure IV illustrate a comparison of the ultimate tensile strength (UTS) among welded joints that were cooled using different quenching media. It was observed that the oil-cooled welded joints displayed higher strength compared to joints cooled in other media. The strength characteristics of the oil-cooled joints were particularly distinctive, showing an improvement of 54MPa compared to the normally air-cooled welded joints. The tensile strength of the oil-cooled joints also exhibited a notable difference of approximately 26MPa when compared to the water-cooled joints. Additionally, Figure III presents the results indicating the ductile behavior of the welded joints cooled in various media. Base metal ductility reduced from 10% elongation to 6% for normal air-cooled welded joints. Oil cooled samples showed 7% elongation, highest amongst other media; thus, oil cooling imparted maximum ductility after welding due to uniform diffusion of precipitates along grains and moderate cooling.

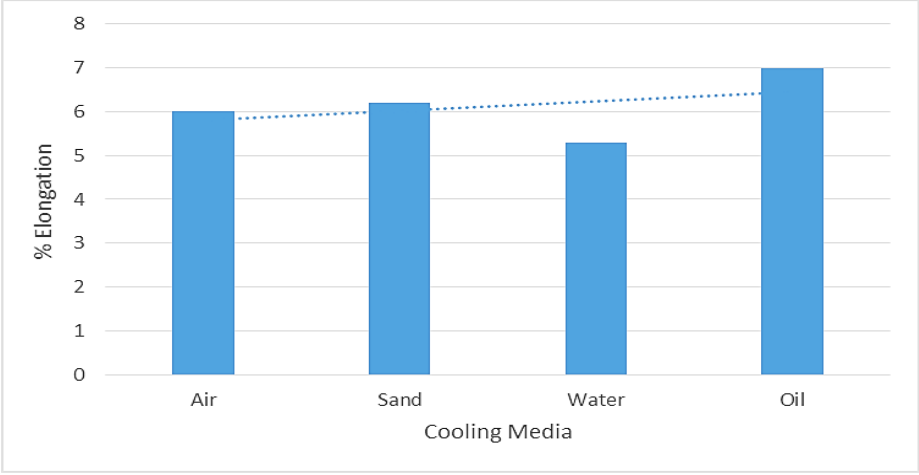

Figure III: Quenching effect on percent elongation.

Fine grain boundaries generally enhance the endurance limit, leading to improved fatigue strength. Rapid cooling methods such as water and oil cooling can further increase fatigue resistance by maximizing dislocation hindrance. In contrast, coarse grain boundaries formed through slower cooling methods like air and sand cooling may reduce fatigue strength due to lower resistance to dislocation movement. Additionally, slow cooling can result in gas porosity, which creates stress concentrations and further diminishes endurance properties.

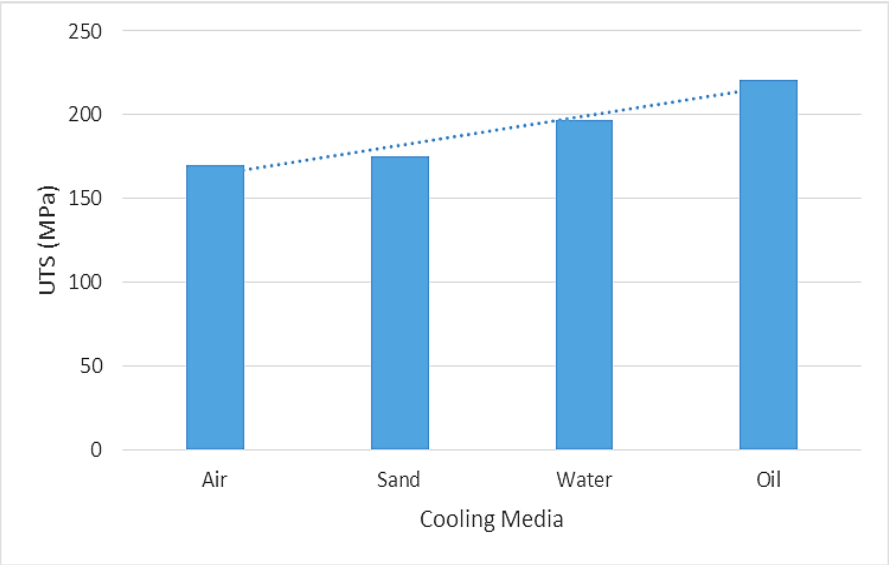

Figure IV: Quenching effect on ultimate tensile strength.

3.3 Welding Efficiency. - The results presented in Figure V demonstrate an enhancement in welding efficiency when utilizing different quenching media for the welded joints compared to normal air-cooled joints. Among the quenching methods, oil-quenched joints exhibited the highest weld efficiency of 72.5%.

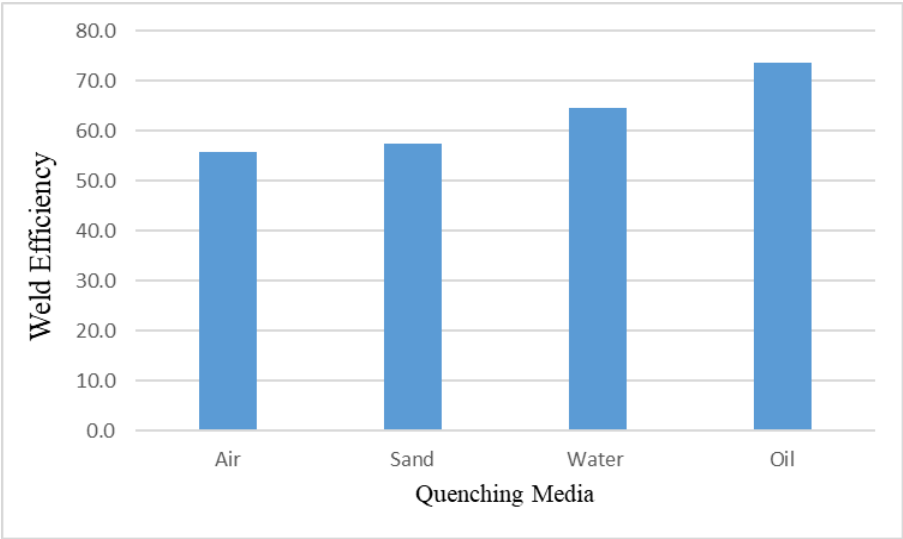

Figure V: Welding Efficiency.

This improvement can be attributed to the development of fine grain boundaries, which occurred due to the higher cooling rate provided by oil quenching compared to air and sand. Additionally, the width of the HAZ was reduced, resulting in improved mechanical properties, as a narrower HAZ is associated with better performance. In both the HAZ and WZ, the coarsening of precipitation size was not significant due to the rapid cooling process, leading to smaller and finer precipitates. Consequently, the oil-quenched joints exhibited higher strength compared to the other methods. On the other hand, water-quenched joints showed strength improvements of up to 64.6%. However, their strength was lower than that of oil-cooled joints due to the extremely rapid cooling in water. Although the water-quenched joints displayed lower tensile strength due to the generation of internal stresses, their yield strength was higher than that of the oil-quenched joints. This can be attributed to the presence of fine grain boundaries and the hindrance of dislocations caused by the rapid water cooling.

3.4 Hardness Testing. - The hardness testing results presented in Figure VI illustrate a comparison among the WZ of

welded joints that were subjected to quenching in various media. Among the different quenching methods employed, the welded joints quenched in water displayed the highest hardness in the WZ. This can be attributed to the segregation of fine grain boundaries and the formation of narrow precipitates, which were more pronounced in comparison to the other quenched joints. The utilization of oil cooling resulted in an enhancement of hardness, increasing it from 56HV (for joints cooled in normal air) to 68HV.

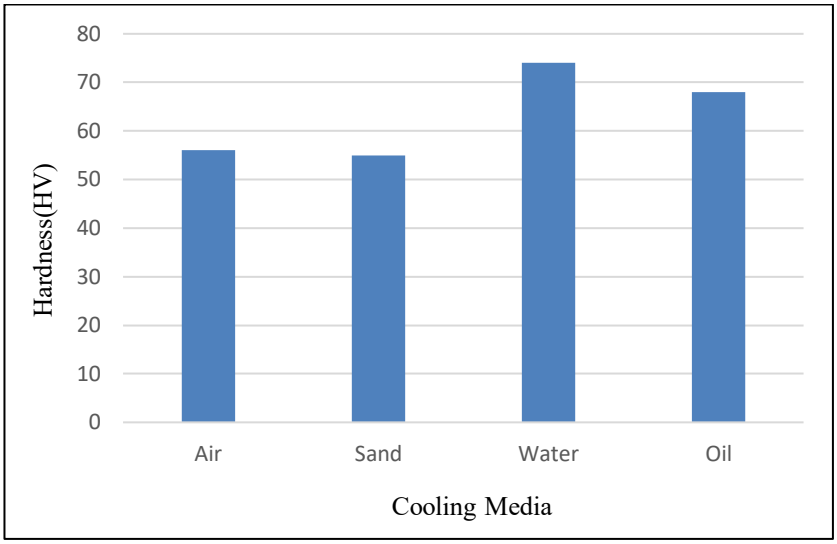

Figure VI: Quenching effect on WZ hardness.

Notably, sand cooling did not yield any significant changes in the welded joints, as the results were similar to those of the air-cooled joints. The input heat effected the width of both the WZ and the HAZ, leading to a decrease in hardness for joints that were slowly cooled (via air and sand) from 90HV to approximately 55HV. The results presented in Figure VII demonstrate a comparison of the hardness in the HAZ of different welding joints after quenching. The HAZ hardness of joints quenched in water was found to be the highest among the various joints, primarily due to the rapid cooling process. The oil-cooled joints exhibited a similar level of hardness in the HAZ, closely following the water-cooled joints. The increased hardness observed in the water and oil-cooled joints can be attributed to the extremely narrow width of the HAZ and the presence of fine precipitates. The rapid cooling employed in these methods restricts the movement of dislocations, leading to the generation of stresses across the crystallographic planes. However, it should be noted that the fast cooling of welded joints in water can result in brittleness, which further increases the hardness and can have a detrimental effect on the tensile strength of the joints.

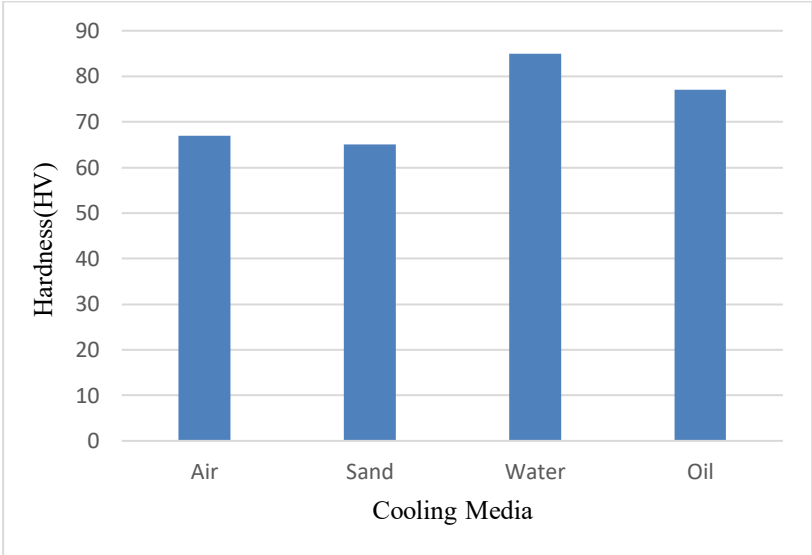

Figure VII: Quenching effect on HAZ Hardness.

3.5 Impact Testing. - The impact absorbed energy (measured in Joules) of the WZ in different media after quenching

is presented in Figure VIII. The amount of impact energy absorbed during testing directly reflects the toughness of the welded joints, as toughness is directly proportional to impact energy. It was observed that the water-cooled welded joints exhibited brittleness. On the other hand, slow cooling in air and sand resulted in generally good toughness due to their favorable ductile nature. The slow cooling process minimizes the generation of internal stresses. However, it should be noted that the microstructure of the sand and air-cooled samples showed signs of porosity. In comparison, the air and sand-cooled welded joints displayed higher impact energy in the WZ compared to the water-cooled joints. In contrast, the WZ of oil-cooled joints exhibited enhanced toughness compared to the other joints. This improvement can be attributed to the fact that the viscosity of the oil allowed for the uniform distribution of input heat throughout the entire area around the WZ, effectively reducing porosity. The moderate cooling provided by the oil, which has higher viscosity than other media, contributed to an overall improvement in impact resistance. Abrupt temperature changes due to fast cooling in water resulted in severe internal stresses and restricted dislocation movement eventually causing the welded joints to become brittle.

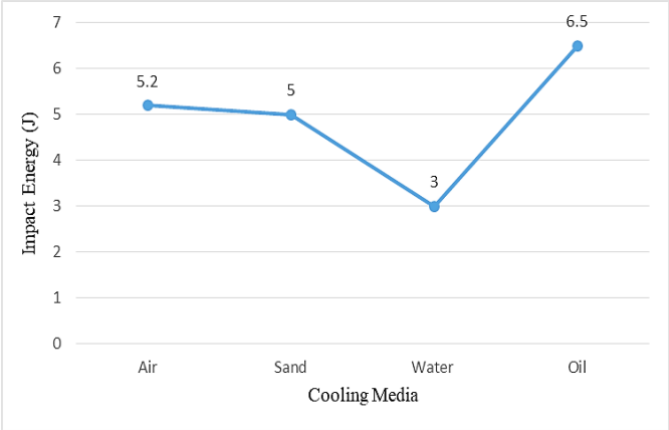

Figure VIII: Quenching effect on WZ Impact Energy

The impact energy of the HAZ in welded joints, quenched using different media, is depicted in Figure IX. Among the various quenching methods, the oil-cooled joints displayed the highest impact energy, measuring 25.5 Joules. This superior performance can be attributed to the uniform distribution of input heat achieved through the moderate viscosity of the oil. Although oil cooling is a faster process compared to air and sand cooling, water cooling is even faster than oil cooling. As a result, the water-cooled joints exhibited a lower impact energy due to the rapid cooling process, which restricts dislocation motion owing to the extremely narrow HAZ. On the other hand, air and sand-cooled joints experienced uneven heat distribution, which facilitated dislocation motion and led to a wider HAZ. Consequently, these joints demonstrated lower impact energy. However, when the welded joints were oil-cooled, they exhibited mild effects and demonstrated enhanced impact energy. This suggests that the oil cooling method had positive effects on the joints. It is important to note that the quenching media used in the experiments were assumed to be at standard temperature. All the experiments were conducted within a carefully controlled laboratory environment, without any heating or cooling of the quenching media being performed.

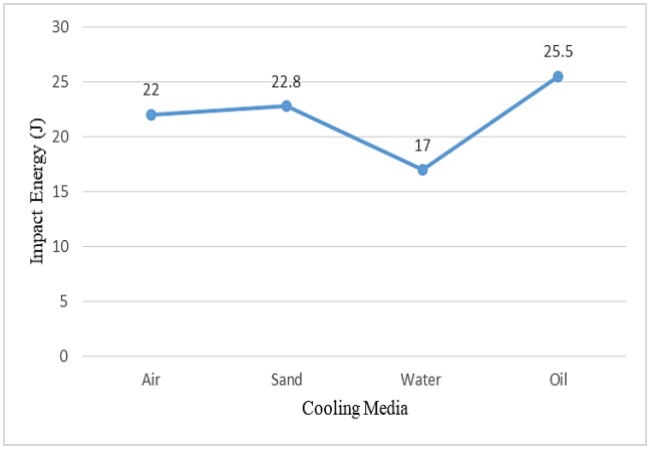

Figure IX: Quenching effect on HAZ Impact Energy.

Table III presents the statistical analysis of the data, highlighting that the ultimate tensile strength exhibited the highest standard deviation. This variability can be attributed to rapid cooling, as UTS increased significantly due to post-weld quenching. Furthermore, the UTS data demonstrated the largest range of 48, reinforcing the correlation between enhanced UTS and swift cooling in comparison to air and sand cooling methods. Similarly, the hardness of the HAZ showed a notable improvement, likely due to refined grain boundaries and precipitate formation. A range of 20 was observed in hardness values, indicating a substantial variation in response to different cooling conditions.

		Mean	Median	Standard Deviation	Range
UTS		189.2	184.5	19.7	48
YS		126.75	126	10.52	25
% Elongation		6.13	6	0.61	1.7
Hardness	**WZ**	63.25	62	8.04	19
	HAZ	73.5	71	9.13	20
Impact Energy	**WZ**	4.9	5.1	1.4	3.5
	HAZ	21.8	22.4	3.53	8.5

Table III: Statistical Analysis of data.

4. Conclusion. - The utilization of different media for quenching weld joints leads to improved mechanical properties due to rapid heat dissipation from the joint area, key improvements are listed below:

- The strength of welded joints is compromised by normal air cooling, resulting in a decrease of up to 50%. Among the various quenching media, water-cooled joints exhibited the highest YS of 140 MPa.
- Oil cooling enhanced the UTS of joints cooled in air from 170 MPa to 221 MPa. Likewise, oil-cooled joints demonstrated the highest percentage of elongation, indicating superior ductility.
- Oil quenching resulted in the maximum weld efficiency of 72.5%, surpassing the 55.7% efficiency of normally air-cooled joints. The notable weld efficiency achieved in oil-cooled joints can be attributed to the moderate viscosity of hydraulic oil.
- The water-cooled joints exhibited higher hardness in the WZ and HAZ compared to other joints. The increased hardness is attributed to residual internal stresses at crystallographic planes.
- The impact energy of water-cooled welded joints decreased to 3 Joules in the WZ, while the impact energy of oil-cooled joints surpassed other joints. In the HAZ, the impact energy of oil-cooled joints was distinct and the highest among all joints due to the narrow width of the HAZ, fine grain boundaries, and fine precipitates.
- Overall, oil-quenched welded joints demonstrated superior performance compared to other welded joints.

5. Future Recommendation. - This study conducted microstructural analysis and mechanical characterization, including tensile, hardness, and impact testing, on quenched welded joints. The scope of mechanical evaluation can be further expanded by incorporating fatigue and creep analysis. Additionally, post-weld heat treatment can be employed to assess the performance of the welded joints. Processes such as solution heat treatment and artificial aging have the potential to induce significant microstructural modifications and alter the mechanical properties of the material.

References

[1] Baskutis, S., Bendikiene, R., & Ciuplys, A. (2019). Effect of weld parameters on mechanical properties and tensile behavior of tungsten inert gas welded AW6082-T6 aluminum alloy. Journal of Mechanical Science and Technology, 33(2), 765–772.

[2] Kaba, L., Djeghlal, M. E., Ouallam, S., & Kahla, S. (2021). Dissimilar welding of aluminum alloys 2024 T3 and 7075 T6 by TIG process with double tungsten electrodes. International Journal of Advanced Manufacturing Technology, 118, 937–948.

[3] Kumar, A., & Sundarrajan, S. (2009). Effect of welding parameters on mechanical properties and optimization of pulsed TIG welding of Al-Mg-Si alloy. International Journal of Advanced Manufacturing Technology, 42(1-2), 118–125.

[4] Kumar, K., Kumar, C. S., Masanta, M., & Pradhan, S. (2022). A review on TIG welding technology variants and its effect on weld geometry. Materials Today: Proceedings, 50, 999-1004.

[5] Li, J.-f., Zheng, Z.-q., Na, J., & Tan, C.-y. (2005). Localized corrosion mechanism of 2XXX series Al alloy containing S(Al2CuMg) and (Al2Cu) precipitates in 4.0% NaCl solution at pH 6.1. Journal of Materials Chemistry and Physics, 91, 325−329.

[6] Miao, W. F., & Laughlin, D. E. (1999). Precipitation hardening in aluminum alloy 6022. Elsevier Science, 40(7), 873–878.

[7] Murali, N., & Li, X. (2021). TIG welding of dissimilar high-strength aluminum alloys 6061 and 7075 with nano-treated filler wires. In L. Perander (Ed.), The Minerals, Metals & Materials Series. Springer.

[8] Muzamil, M., Wu, J., Samiuddin, M., Majeed, A., Siddiqui, S. U., & Mudassir, M. (2020). Macro-mechanical behavior of unique surface welded joints (AA5083) utilizing tungsten inert gas welding against single-stage homogenization annealing. Revista de Metalurgia, 56(3), e173.

[9] Prabhukhot, A. R., & Prasad, K. (2015). Effect of heat treatment on hardness of 6082-T6 aluminum alloy. International Journal of Scientific & Engineering Research, 6.

[10] Rajkumar, T., Prabakara, M. P., Arunkumar, G., & Antony, A. G. (2020). Study on the feasibility in welding of low carbon steel and austenitic stainless steel joint using CO2 laser welding process and analysis of its metallurgical and mechanical properties. Wu Tan Hua Tan Ji Suan Ji Shu, 106(5), 471–476.

[11] Rajkumar, T., Raja, K., Lingadurai, K., Vetrivel, S. D., & Antony, A. G. (2020). Interfacial microstructure analysis of AA2024 welded joints by friction stir welding. Journal of New Materials for Electrochemical Systems, 23(2), 123–132.

[12] Reboul, M. C., & Baroux, B. (2011). Metallurgical aspects of corrosion resistance of aluminum alloys. Journal of Materials and Corrosion, 62, 215−233.

[13] Shazad, A., Astif, M., Uzair, M., & Zaidi, A. A. (2024). Evaluation of preheating impact on weld residual stresses in AH-36 steel using Finite Element Analysis. Memoria Investigaciones en Ingeniería, (26), 225-243.

[14] Shazad, A., Jadoon, J., Uzair, M., & Akhtar, M. (2022). Effect of composition and microstructure on the rusting of MS Rebars and ultimately their impact on mechanical behavior. Transactions of the Canadian Society for Mechanical Engineering.

[15] Shazad, A., Uzair, M., Jamil, T., & Muhammad, N. (2024, December). A Comparative Study on the Joint Hardness and tensile properties of Dissimilar Aluminum Alloy using Tungsten Inert Gas (TIG) Welding. In 4th International Conference on Key Enabling Technologies (KEYTECH 2024) (pp. 173-178). Atlantis Press.

[16] Shazad, A., Uzair, M., & Tufail, M. (2024). Influence of multiple post-weld repairs on mechanical and microstructural properties of butt weld joint utilized in structural members. International Journal of Precision Engineering and Manufacturing, 1, 1–8.

[17] Sathish, T., Armalingam, S., Mohanavel, V., et al. (2021). Weldability investigation and optimization of process variables for TIG-welded aluminum alloy. Advances in Materials Science and Engineering.

[18] Tan, C. F., & Said, M. R. (2009). Effect of hardness test on precipitation hardening aluminum alloy 6061-T6. Science Journal, 36(3), 276–286.

[19] Zhu, J., Jiang, W., Li, G., Guan, F., Yu, Y., & Fan, Z. (2020). Microstructure and mechanical properties of SiCnp/Al6082 aluminum matrix composites prepared by squeeze casting combined with stir casting. Journal of Materials Processing Technology, 283, 116699.

Author contribution:

1. Conception and design of the study
2. Data acquisition
3. Data analysis
4. Discussion of the results
5. Writing of the manuscript
6. Approval of the last version of the manuscript

AS has contributed to: 1, 2, 3, 4, 5 and 6.

MU has contributed to: 1, 2, 3, 4, 5 and 6.

JJ has contributed to: 1, 2, 3, 4, 5 and 6.

SKM has contributed to: 1, 2, 3, 4, 5 and 6.

Acceptance Note: This article was approved by the journal editors Dr. Rafael Sotelo and Mag. Ing. Fernando A. Hernández Gobertti.

Interacción Suelo-Estructura de una edificación con losa de cimentación con los modelos estáticos de Winkler y Pasternak

Soil-Structure interaction of a building with a foundation slab with the static models of Winkler and Pasternak

Interação solo-estrutura de uma edificação com laje de fundação com os modelos estáticos de Winkler e Pasternak

Juan Contreras [1], Genner Villarreal Castro[2,(*)]

Recibido: 30/09/2024 Aceptado: 26/01/2025

Resumen. - Winkler y Pasternak establecieron que la interacción suelo estructura entre la base de una estructura y el suelo de cimentación, se puede idealizar como un conjunto de resortes de rigidez que se desplazan como resultado de la carga aplicada sobre su superficie (Ubani, 2022). El aporte de los modelos estáticos es la incorporación de las propiedades dinámicas del suelo mediante modelos de comportamiento elástico lineal del suelo, facilitando los procedimientos de cálculo en función a las propiedades mecánicas obtenidas del estrato del suelo de fundación. Mediante la incorporación de los coeficientes estáticos obtenidos con las propiedades elásticas del suelo, en un modelo estructural es posible verificar si puede existir alguna variación en el comportamiento estructural del modelo (Villarreal, 2017). En este aspecto la investigación surgió con el objetivo de determinar si esas variaciones pueden ser significativas afectando el comportamiento estructural de la edificación que tiene como fundación una losa de cimentación. Se consideró para ello las propiedades del suelo obtenidas de un estudio de mecánica de suelos (EMS), mediante el cual se determinó que el suelo se categoriza como S3, con un módulo de elasticidad E_s=1150 tonf/m^2, coeficiente Poisson υ=0.30 y altura del estrato en la zona de estudio. La zona sísmica se determinó como una zona de aceleración con 0.25g. Los resultados se obtuvieron de la comparación del modelo con diseño sismorresistente que considera como parte de sus parámetros que el suelo de la cimentación es indeformable, y los modelos con los coeficientes de ISE de Winkler y Pasternak. Mediante los resultados se llegó a concluir que existe un incremento significativo en los esfuerzos cortantes en el nivel que se encuentra en contacto directo con la losa de cimentación, mientras que la variación en el periodo fundamental y la deformación lateral de la edificación no fue significativa, considerando en parte que la estructura es altamente rígida por su sistema estructural de muros a corte.

Palabras clave: Interacción suelo estructura, modelos estáticos de Winkler y Pasternak, coeficientes de rigidez del suelo.

(*) Autor de correspondencia

[1] Doctor en Ingeniería, Universidad Nacional del Santa (Perú), juanalbertocontrerasmoreto1207@gmail.com, ORCID iD: https://orcid.org/0000-0003-2048-130X

[2] Doctor en Ingeniería, Universidad de San Martín de Porres (Perú), gvillarrealc@usmp.pe, ORCID iD: https://orcid.org/0000-0003-1768-646X

https://doi.org/10.36561/ING.28.7
ISSN 2301-1092 • ISSN (en línea) 2301-1106 – Universidad de Montevideo, Uruguay

Summary. - *Winkler and Pasternak established that the soil-structure interaction between the base of a structure and the foundation soil can be idealized as a set of stiffness springs that move as a result of the load applied to its surface (Ubani, 2022). The contribution of static models is the incorporation of the dynamic properties of the soil through linear elastic soil behavior models, facilitating the calculation procedures based on the mechanical properties obtained from the foundation soil stratum. By incorporating the static coefficients obtained with the elastic properties of the soil, in a structural model it is possible to verify if there may be any variation in the structural behavior of the model (Villarreal, 2017). In this aspect, the research arose with the objective of determining if these variations can be significant in affecting the structural behavior of the building that has a foundation slab as a foundation. For this purpose, the soil properties obtained from a soil mechanics study (SMS) were considered, through which it was determined that the soil is categorized as S3, with an elasticity modulus E_s=1150 ton/m2, Poisson coefficient υ=0.30 and height of the stratum in the study area. The seismic zone was determined as an acceleration zone with 0.25g. The results were obtained from the comparison of the model with earthquake-resistant design that considers as part of its parameters that the foundation soil is non-deformable, and the models with the SSI coefficients of Winkler and Pasternak. Through the results, it was concluded that there is a significant increase in the shear stresses at the level that is in direct contact with the foundation slab, while the variation in the fundamental period and the lateral deformation of the building was not significant, considering in part that the structure is highly rigid due to its structural system of shear walls.*

Keywords: *Soil-structure interaction, static Winkler and Pasternak soil models, soil stiffness coefficients*

Resumo ***-*** *Winkler e Pasternak estabeleceram que a interação solo-estrutura entre a base de uma estrutura e o solo de fundação pode ser idealizada como um conjunto de molas de rigidez que se movem em decorrência da carga aplicada em sua superfície (Ubani, 2022). A contribuição dos modelos estáticos é a incorporação das propriedades dinâmicas do solo por meio de modelos de comportamento elástico linear do solo, facilitando os procedimentos de cálculo com base nas propriedades mecânicas obtidas do estrato do solo de fundação. Ao incorporar os coeficientes estáticos obtidos com as propriedades elásticas do solo, em um modelo estrutural é possível verificar se pode haver alguma variação no comportamento estrutural do modelo (Villarreal, 2017). Nesse aspecto, a pesquisa surgiu com o objetivo de determinar se essas variações podem ser significativas em afetar o comportamento estrutural da edificação que possui uma laje de fundação como fundação. Para tanto, foram consideradas as propriedades do solo obtidas a partir de um estudo de mecânica dos solos (MSS), por meio do qual foi determinado que o solo é categorizado como S3, com módulo de elasticidade E_s=1150 ton/m2, coeficiente de Poisson υ=0,30 e altura do estrato na área de estudo. A zona sísmica foi determinada como uma zona de aceleração com 0,25g. Os resultados foram obtidos a partir da comparação do modelo com projeto resistente a terremotos que considera como parte de seus parâmetros que o solo de fundação é não deformável, e os modelos com os coeficientes SSI de Winkler e Pasternak. Por meio dos resultados, concluiu-se que há um aumento significativo nas tensões de cisalhamento no nível que está em contato direto com a laje de fundação, enquanto a variação no período fundamental e na deformação lateral da edificação não foi significativa, considerando em parte que a estrutura é altamente rígida devido ao seu sistema estrutural de paredes de cisalhamento.*

Palavras-chave: *Interação solo-estrutura, modelos estáticos de solo de Winkler e Pasternak, coeficientes de rigidez do solo.*

1. Introducción. - Los modelos estáticos de interacción suelo estructura de Winkler (1867) y Pasternak (1954) integran la rigidez del suelo en el análisis dinámico de las estructuras, mediante coeficientes estáticos, calculados con parámetros geotécnicos obtenidos para los estratos del suelo que soportarán las cargas propias de la cimentación y de las cargas que se transmiten de la superestructura. En la actualidad, la utilización de coeficientes de tipo estáticos para el análisis estructural se realiza mediante el módulo de balasto, no siendo obligatorio su uso según la normativa vigente y quedando a criterio del ingeniero estructural. Bajo estas condiciones los estudios para determinar la influencia de los modelos de interacción suelo-estructura en las edificaciones son escazas y limitadas, aun mas considerando las diversas condiciones sísmicas de un país con alta sismicidad como Perú. En este aspecto, el estudio se realizó en la región de Cajamarca, al norte del Perú, en la provincia de Jaén, utilizando una edificación en muros estructurales y losa de cimentación. La costa peruana y las regiones adyacentes han experimentado sismos significativos, como el ocurrido el 31 de mayo de 1970 en Chimbote, que fue afectada por un sismo de magnitud 7.8 en la escala de Richter, lo que demuestra la importancia y la necesidad de considerar todos los parámetros posibles en el análisis sísmico y el diseño de las estructuras, siendo por ello los modelos de interacción suelo-estructura estáticos, modelos ideales que incorporan la rigidez del suelo en el análisis estructural.

La zona considerada en la investigación presenta una geología que se puede considerar única, debido a que la región se encuentra en una zona de transición entre la Cordillera de los Andes y la llanura amazónica, lo que resulta en zonas con la presencia de fallas geológicas y depósitos sedimentarios. Estas condiciones contribuyen a la complejidad del comportamiento sísmico de las estructuras en este tipo de suelo, suelos blandos, con depósitos fluvioaluviales compactados de baja rigidez.

1.1. Objetivos de la investigación. - Los modelos estáticos de interacción suelo estructura de Winkler y Pasternak de acuerdo a los estudios teóricos de diversos autores, sugieren que la utilización de estos coeficientes estáticos como una representación de las propiedades del suelo pueden afectar al comportamiento estructural de la edificación [1]. En ese aspecto la investigación surge con el objetivo principal de determinar si la influencia de los modelos estáticos de Winkler y Pasternak en el comportamiento estructural de una edificación con muros estructurales y una losa de cimentación es significativa.

Como objetivos secundarios se propuso determinar si la ISE estática en los modelos de Winkler y Pasternak, pueden afectar al periodo fundamental de vibración de la estructura, a las derivas y los esfuerzos cortantes, aspectos fundamentales del comportamiento estructural de una edificación.

1.2 Implicaciones y limitaciones de la investigación. - Villareal, Cerna, & Espinoza (2021) [2] en un estudio realizado en una estructura con plateas de cimentación señalan que los modelos de ISE pueden modificar el comportamiento estructural de las edificaciones, aseverando que se puede realizar un análisis y un diseño de mayor precisión. Asimismo, Bao & Liu (2019) [3] confirman que los modelos ISE afectan a las propiedades inherentes de una estructura como la frecuencia de vibración de la estructura, es decir el periodo puede variar como consecuencia del amortiguamiento y rigidez proporcionados por las cimentaciones al interactuar con el suelo.

En este aspecto, el estudio implica determinar si esa influencia de los modelos estáticos de ISE, pueden modificar el periodo de la estructura, las derivas (deformaciones laterales) y los esfuerzos internos, principalmente en el nivel adyacente que, según el estudio realizado por Fernández, Fernández & Cobelo (2022) [4] provoca que las fuerzas interiores se redistribuyan en los elementos estructurales y la cimentación.

Respecto a las limitaciones de la investigación, el estudio se enmarcó dentro de un análisis convencional por espectros, un análisis modal espectral que tiene como función principal determinar los periodos por modos de vibración, las fuerzas cortantes máximas probables y deformación lateral de entrepiso, otorgando la respuesta total por combinación cuadrática completa (CQC) que están basados en análisis estadísticos que determinan un valor máximo factible. En lo concerniente al suelo, el estudio de suelo determinó que la cimentación descansa en un solo estrato, debido a que la losa de cimentación se define como una cimentación superficial.

1.3 Fuerzas sísmicas para el análisis modal. - El análisis sísmico de la estructura se realizó con fuerzas sísmicas de pseudoaceleración, mediante el procedimiento de análisis modal espectral. La zona de peligro sísmico esta categorizada como Z2 con un coeficiente de 0.25g. De acuerdo el estudio de Mecánica de suelos (EMS) el suelo de acuerdo a la velocidad promedio de las ondas de corte ($\overline{V_s}$) y el promedio ponderado del ensayo estándar de penetración ($\overline{N}_{60}$) se clasifica como un suelo tipo S3. Por tanto, los parámetros establecidos para el sitio (S,T_P,T_L) considerados para una zona de riesgo sísmico Z2 son: Factor de suelo $S_3 = 1.40$, periodo corto del estrato $T_p(s) = 1.0$, periodo largo del estrato $T_L(\mathrm{s}) = 1.6$

El factor de uso de la estructura es $U = 1.0$ (E030, 2018), en lo correspondiente a la configuración estructural de la edificación, se determinó previamente en un análisis de absorción de cortantes por elementos estructurales, que los muros estructurales absorben las fuerzas sísmicas por encima del 70%, por tanto, se categoriza como una edificación con un sistema estructural por muros estructurales, con un factor de reducción de $R = 6.0$ (E030, 2018).

El cálculo del coeficiente símico $C = 2.5$ se determinó mediante la norma (E030, 2018), que señala que para todos los casos donde el periodo de la estructura tiene un periodo fundamental menor al periodo corto del estrato del suelo $T < T_P \rightarrow C = 2.5$.

En la *Tabla I* se aprecia la altura de la edificación y los coeficientes usados para el espectro:

Parámetros	Factor
Altura de edificación h_n	18.60 m
Coeficiente Ct (sistema muros)	60.00
Periodo estático de la edificación T	0.31
T_P (S)	1.00
T_L (S)	1.60
$T < T_P$	Cumple condición
C	2.50

Tabla I.- Parámetros normativos

Con esos datos se procedió a calcular la seudoaceleración elástica y no elástica, así como el espectro reducido por R, con la ecuación de pseudoaceleración de la norma (E030, 2018). Al reemplazar los parámetros de la tabla en la ecuación de pseudoaceleración para el espectro elástico se obtuvo:

$$S_a = \frac{ZUCS}{R} = \frac{0.25 * 1 * 2.5 * 1.4}{6} = 0.145833g$$

Para realizar el análisis modal espectral de la estructura, se procedió a cargar el espectro elástico $S_a = 0.145833g$. Este espectro genera las derivas elásticas, por lo cual se procedió a realizar una combinación de cargas utilizando el factor $0.75R = 0.75(6) = 4.5$ para obtener los resultados con el espectro de pseudoaceleración $S_a = 0.65625\ g$.

$$S_a = \ 0.145833g * 0.75(6) = \ 0.65625\ g$$

2. Estado del Arte. - Los modelos estáticos de ISE de Winkler (1867) y Pasternak (1954) permiten obtener coeficientes que representan la rigidez variable de los suelos elásticos, que pueden reemplazar la idealización de las estructuras como modelos empotrados. Mediante estos modelos ISE, el análisis puede presentar mayor precisión en la respuesta estructural, por lo cual su importancia radica fundamentalmente en mostrar resultados más reales. El principio básico de los modelos estáticos en la determinación del modelo ISE es la discretización de la rigidez del suelo mediante resortes de rigidez que se van a definir como el coeficiente de Balasto, el modelo propuesto por Winkler (1867) y Pasternak (1954) proponen la utilización de resortes equivalentes colocados en la base de la cimentación en una simulación bidimensional, que a continuación se detallan.

2.1 Modelo de Winkler (1867). - El modelo de Winkler propone la representación bidimensional del suelo mediante resortes de rigidez, que se definen o conocen como el módulo de subrasante (C_1) que se pueden determinar de forma experimental o analítica [5]. El módulo de subrasante (C_1) considera básicamente la incorporación del coeficiente en la dirección de reacción del suelo a la cimentación, es decir en forma vertical.

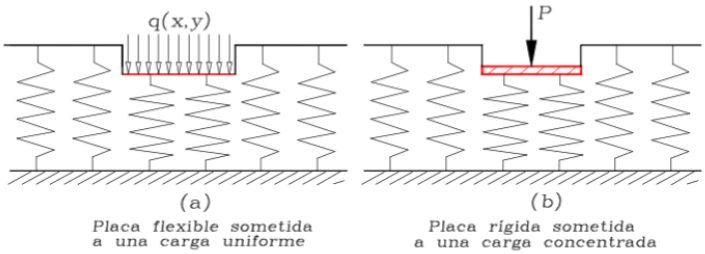

Figura I.- Modelo de Winkler (Aristizabal, 1987)

La teoría de Winkler propuso que existe una relación directamente proporcional entre cualquier punto de apoyo del suelo y la presión resultante de las cargas q y el desplazamiento generado ω (asentamiento del suelo bajo las cargas), lo cual da lugar a una relación de tipo matemática que se aprecia a continuación:

$$q(x,y) = K\ \omega\ (x,y)$$

Donde, los resortes tienen una rigidez K y se consideran como el módulo de balasto único que representa al terreno y que también se puede considerar como constante. Según el modelo propuesto en la *Figura I*, el coeficiente de balasto es constante en cada punto y actúa de forma independiente en cada punto, así se considere una losa flexible (*Figura Ia*) o una losa con rigidez infinita (*Figura Ib*). Esta condición en el modelo de Winkler genera una deficiencia en la condición real del suelo, puesto que considera que los suelos adyacentes a la cimentación no sufren ningún grado de deformación (Santana, 2020) [6], al considerar hipotéticamente que cuentan con rigideces independientes.

El cálculo del módulo de balasto puede definirse en función al número de estratos para uno y dos estratos, cuyas ecuaciones de Winkler se describen a continuación.

- Para un estrato

$$C_1 = \frac{E_1}{h_1(1-2v_1^2)} \qquad (1)$$

- Para dos estratos

$$C_1 = \frac{1}{\frac{h_1}{E_1}(1-2v_1^2)+\frac{h_2}{E_2}(1-2v_2^2)} \qquad (2)$$

Donde:

E_1, E_1 : Módulos de elasticidad del suelo de los estratos 1 y 2
v_1, v_2 : Módulos de la relación de Poisson del suelo de los estratos 1 y 2
h_1, h_2 : Espesor de los estratos 1 y 2

2.2 Modelo de Pasternak (1954). - El modelo de Pasternak propone la representación bidimensional del suelo mediante dos coeficientes de rigidez, el primero el módulo de subrasante propuesto por Winkler en la dirección vertical o a compresión, y el segundo que describe la rigidez de los empujes laterales del suelo en la cimentación (Villarreal et al, 2021) [7].

En el modelo de Pasternak se trata de superar la condición de discontinuidad del modelo de Winkler, proponiendo para ello una capa de corte como se aprecia en la *Figura II* [8] que permitiría de acuerdo al autor considerar la interacción entre los resortes adyacentes, mediante dos constantes elásticas independientes.

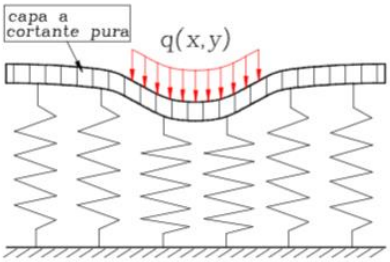

Figura II.- Modelo de Pasternak [8]

El cálculo del módulo de balasto puede definirse en función al número de estratos para uno y dos estratos, tal como se indica a continuación.

- Para un estrato

$$C_1 = \frac{E_1}{h_1(1-2v_1^2)} \qquad (3)$$

$$C_2 = \frac{E_1 * h_1}{6(1-v_1)} \qquad (4)$$

- Para dos estratos

$$C_1 = \frac{1}{\frac{h_1}{E_1}(1-2v_1^2)+\frac{h_2}{E_2}(1-2v_2^2)} \qquad (5)$$

$$C_2 = \frac{1}{6(1-\varepsilon_2)}\left[\frac{E_1 * h_1}{6(1-v_1)}(3+3\varepsilon_2+{\varepsilon_2}^2)+\frac{E_2 * h_2}{(1-v_2)}\right] \qquad (6)$$

Donde:

E_1, E_1 : Módulos de elasticidad del suelo de los estratos 1 y 2
v_1, v_2 : Módulos de la relación de Poisson del suelo de los estratos 1 y 2
h_1, h_2 : Espesor de los estratos 1 y 2

3. Modelado de la estructura. - La estructura inicialmente se procedió a modelar con el empotramiento en la base, considerando para ello las propiedades del concreto, metrados de cargas, sistema estructural, entre otras condiciones.

3.1. Propiedades de la estructura para el modelamiento. - El modelo estructural con las propiedades de los materiales utilizados para el concreto y acero de la estructura se muestran en la *Tabla II*:

Elementos	Propiedades
Concreto en vigas, columnas, losas	f'c=210 kgf/cm^2
Losa de cimentación e=0.40	f'c=210 kgf/cm^2
Acero (resistencia)	f'y=4200 kgf/cm^2
Módulo de elasticidad Ec	Ec= 2188.20 kgf/mm^2
Coeficiente de Poisson del concreto	υ= 0.20
Metro cúbico de concreto (Peso)	γ_{CA}=2.4 tonf/m^3

Tabla II.- Propiedades de Resistencia del concreto

El módulo de elasticidad se determinó con la siguiente ecuación de la norma ACI 318:

$$E_c = 15100\sqrt{f'c}$$

Al ingresar la resistencia del concreto usado en todos los elementos estructurales, se obtuvo el módulo de elasticidad del concreto ingresado al software:

$$E_o = 151\sqrt{210}\ \frac{kgf}{mm^2} = 2188.20\ kgf/mm^2$$

El modelo estructural es una estructura con pórticos y muros estructurales, losas aligeradas en los niveles superiores y una losa de cimentación de e=0.40 m. Para determinar las derivas de entrepiso en el centro de masa se utilizaron diafragmas rígidos para los elementos horizontales.

3.2. Cargas propias e impuestas en la estructura. - En lo concerniente a las cargas se utilizaron las cargas promedio de la norma E.020.

Nivel	Concepto	Carga (tonf/m2)
Semisótano al 5to piso	Tabique	0.140
	Acabado	0.100
	Ladrillo techo	0.090
	Cielo raso	0.050
	Total	0.380
Azotea	Ladrillo techo	0.090
	Cielo raso	0.050
	Total	0.140

Tabla III.- Cargas permanentes de la edificación

En la *Tabla III* se muestran las cargas gravitacionales impuestas (sin función estructural) en el modelo estructural. En la *Tabla IV* se muestran las cargas gravitacionales vivas (por uso de la edificación) en el modelo estructural.

Nivel	Uso (Servicio)	Carga (tonf/m2)
Semisótano	Estacionamiento	0.25
Nivel 1	Vivienda	0.200
Nivel 2	Vivienda	0.200
Nivel 3	Vivienda	0.200
Nivel 4	Vivienda	0.200
Nivel 5	Vivienda	0.200
Azotea	Azotea	0.100

Tabla IV.- Cargas vivas de la edificación

De las tablas elaborados, se procedió a ingresar al modelo en el software ETABS las cargas permanentes (CM) y las cargas vivas (CV) como se muestra el resumen en la *Tabla V*.

Cargas a asignar el ETABS		
Tipo	**Niveles**	**Total (Tonf/m2)**
Carga Permanente	Semisótano	0.380
	1° - 5°	0.380
	Azotea	0.140
Carga Viva	Semisótano	0.250
	1° - 5°	0.200
	Azotea	0.100

Tabla V.- Metrados de cargas en el modelo

El peso sísmico de la edificación se determinó mediante la combinación de cargas definidas en la norma E.030:

$$P_s = 100\%\ CM + 25\%\ CV$$

El modelo estructural se puede apreciar en la *Figura III*. La estructura tiene una planta típica en todos sus niveles.

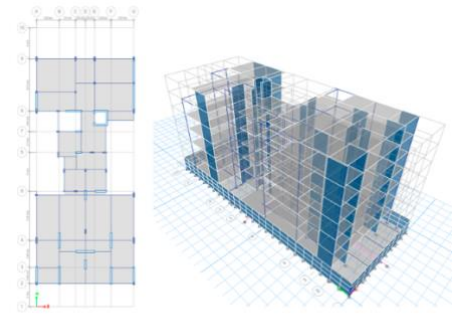

Figura III.- Modelo estructural en planta (a) y vista 3D (b)

En las *Figura IV* en a), b) y c) se aprecian los modos de vibración de la estructura. El primer modo de vibración (a) es en la dirección XX del modelo, el segundo modo de vibración (b) es en la dirección YY del modelo y el tercer modo de vibración de la estructura es torsional como se puede observar en (c).

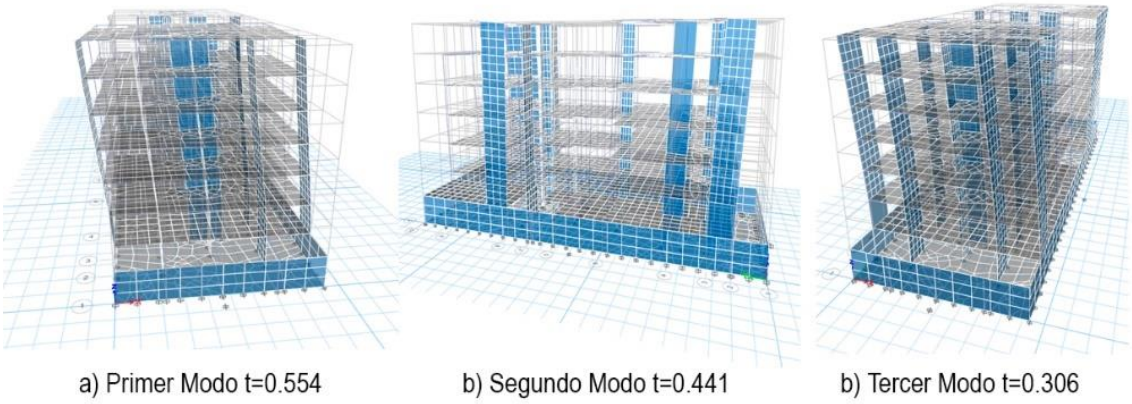

Figura IV.- Modos de vibración de la estructura

La estructura con el análisis convencional cuenta con empotramiento en la cimentación (restricción en los 6 grados de libertad).

4. Modelos estáticos con los coeficientes estáticos. - Para el análisis de la estructura considerando los modelos estáticos de Interacción Suelo Estructura de Winkler y Pasternak, se procedió a modelar la estructura considerando las propiedades de los materiales como la resistencia del concreto a compresión y la fluencia del acero. Se consideró las propiedades del suelo obtenidas del estudio de Mecánica de Suelos, que clasifica el suelo de cimentación como un suelo flexible S3 con un sólo estrato, con un material blando y una granulometría conformada por arena media a fina.

4.1. Propiedades del modelo estático de Winkler. - Se procedió a calcular el coeficiente estático de Winkler (coeficiente de rigidez), que se denomina como coeficiente vertical de balasto C_1 usado a compresión. Para ello se utilizó los parámetros obtenidos en el estudio de Mecánica de Suelos (EMS), considerando además que el suelo se encuentra dentro de los suelos clasificado en la norma (E030, 2018) como blando y que se aprecian a continuación:

- Clasificación del suelo : S3 – Suelo blando (EMS)
- Velocidad de onda : V_S = 165 m/s (Norma E.030)
- Módulo de elasticidad del suelo : E_S= 1150 ton/m^2
- Coeficiente de Poisson del suelo : υ_1 = 0.30
- Altura de estrato : h_1 = 1.00 m

En la ecuación de Winkler (*Eq.1*), se procedió a determinar el módulo de balasto ingresando el módulo de elasticidad del suelo (E_S= 1150 ton/m^2), el coeficiente de Poisson del suelo (υ_1 = 0.30) y la altura del estrato (h_1 = 1.00 m), obteniendo el módulo de balasto C_1 , como se aprecia a continuación:

$$C_1 = \frac{1150\ ton/m^2}{1.00\ m * (1 - 2(0.30)^2)} = 1402\ tonf/m^3$$

El coeficiente estático de Winkler fue incorporado en el modelo mediante el comando *Area spring,* para ello se procedió a discretizar la losa de cimentación. Después de generar el coeficiente C_1, se seleccionó áreas discretizadas, y se procedió a asignar el coeficiente estático a la losa de cimentación del como se aprecia en la *Figura V*:

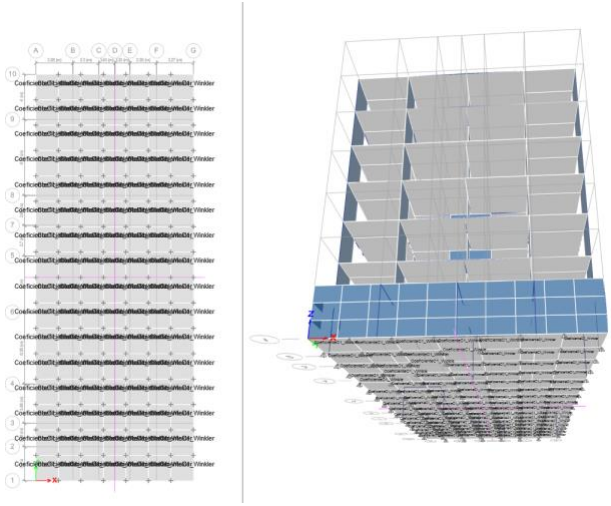

Figura V.- Modelo con los coeficientes estáticos de Winkler

4.2. Coeficientes de interacción suelo estructura estática de Pasternak. - Los coeficientes de rigidez vertical C_1 de Winkler y Pasternak, se determinan mediante la misma ecuación para calcular el coeficiente vertical de balasto C_1 para suelos que tienen un solo estrato. Sin embargo, el modelo de Pasternak considera un coeficiente lateral C_2 (*Eq.4*). Al reemplazar los valores del suelo obtenidas mediante el EMS, como el módulo de elasticidad, el coeficiente de Poisson y la altura del estrato se obtuvo el coeficiente de balasto C_2 como se aprecia a continuación:

$$C_2 = \frac{1150\,\frac{tonf}{m^2} * 1.00m}{6(1-0.30)} = 273.81\ tonf/m$$

El coeficiente vertical C_1 fue el utilizado para Winkler:

$$C_1 = 1402\ tonf/m^3$$

Para incorporar los coeficientes estáticos calculados mediante las ecuaciones de Pasternak, se procedió a discretizar la losa de cimentación. Luego mediante el comando *Area springs* se incorporó los coeficientes de balasto en la dirección vertical C_1 tal como se hizo con Winkler. Mientras que el coeficente lateral C_2 de Pasternak se ingresó mediante el comando *Spring Properties/Point Springs/* incorporando las propiedades en las direcciones horizontales de la losa de cimentación (traslacional en X e Y). El modelo con la incorporación de los coeficientes estáticos de Pasternak se puede apreciar en la *Figura VI.*

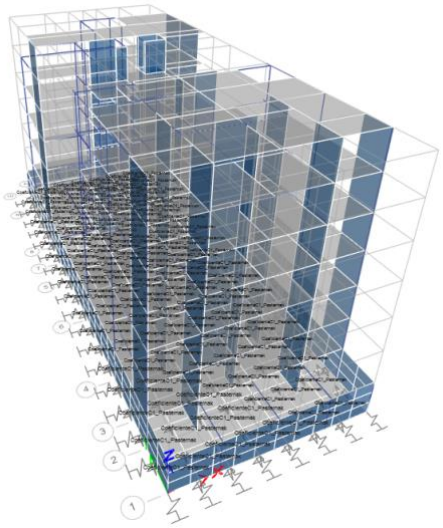

Figura VI.- Modelo con los coeficientes estáticos de Pasternak

5. Resultados del análisis de los modelos con los coeficientes estáticos. - El análisis de resultados se encuentra en función a los objetivos específicos, que consideran la variación del periodo para los primeros casos modales de traslación y rotación, el análisis de la deriva de entrepiso y comparación entre el análisis convencional y usando los modelos ISE estáticos, y la comparación de los esfuerzos cortantes.

5.1. Periodo fundamental con el modelo de Winkler y Pasternak. - Al incorporar los coeficientes estáticos de Winkler y Pasternak al modelo estructural se llegó a determinar que existe una variación en el periodo fundamental de la edificación poco significativa. En la *Tabla VI* se puede observar que el periodo fundamental se incrementó en un máximo de 2.46% para el modelo de Winkler y en 2.29% para el modelo de Pasternak. La utilización de los coeficientes estáticos de Interacción Suelo Estructura (ISE) influyeron mínimamente en los modos de vibración de la estructura.

Modo	Modelo Convencional	Winkler	Pasternak	% de Variación Winkler % Δ	% de Variación Pasternak % Δ
Modal	1	0.568	0.567	2.46%	2.29%
Modal	2	0.448	0.448	1.56%	1.56%
Modal	3	0.313	0.311	2.24%	1.61%

Tabla VI. - Porcentajes de variación de los periodos

En la *Figura VII* se aprecia que mediante la incorporación de los coeficientes de rigidez al análisis para el tipo de suelo y estrato definido en el estudio geotécnico y de mecánica de suelos, se obtuvo que el incremento del periodo fundamental no fue muy significativo.

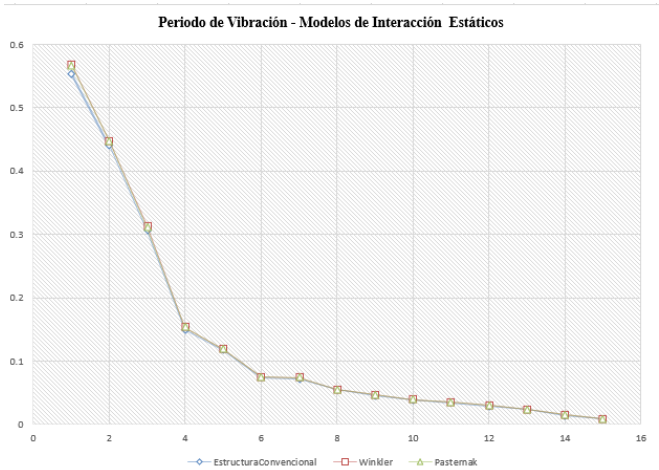

Figura VII. - Periodos obtenidos con los coeficientes estáticos de Winkler y Pasternak

5.2. Deriva de entrepiso del modelo estructural. - Respecto a la deformación lateral de la estructura, en la *Tabla VII* se muestran las derivas de entrepiso de la estructura en ambas direcciones, con la base empotrada y con la incorporación de los coeficientes estáticos de Winkler y Pasternak.

	Dirección - XX			Dirección - YY		
Nivel	Modelo Empotrado	Winkler	Pasternak	Modelo Empotrado	Winkler	Pasternak
Azotea	0.0042	0.0044	0.0044	0.0017	0.0017	0.0017
Story5	0.0044	0.0047	0.0047	0.0017	0.0018	0.0018
Story4	0.0040	0.0042	0.0042	0.0019	0.0020	0.0020
Story3	0.0043	0.0045	0.0045	0.0019	0.0019	0.0019
Story2	0.0040	0.0043	0.0043	0.0016	0.0017	0.0017
Story1	0.0030	0.0033	0.0034	0.0010	0.0011	0.0011
Semisótano	0.0008	0.0012	0.0012	0.0001	0.0001	0.0001

Tabla VII.- Derivas en la dirección XX y YY

En la *Tabla VIII* se muestran los porcentajes de variación de la deformación lateral de la estructura con los coeficientes de Winkler y Pasternak, se llegó a determinar que existe un incremento de las derivas al utilizar los coeficientes estáticos de Winkler y Pasternak. La variacion es significativa en el nivel que se encuentra en contacto con la losa de cimentacion, el nivel definido como semisótano, en vista que la deformación lateral se incrementó en 40.03% con Winkler y 40.69% con Pasternak en la dirección XX de la estructura. En la dirección YY de la estructura, que presenta mucha mayor rigidez que en la direccion XX, el porcentaje de incremento en la deriva en el nivel del semisótano llegó hasta el 26.70% con Winkler y 21.72% con Pasternak. En el primer piso y pisos intermedios la deriva se incrementó en un maximo de 10.24% para ambos modelos estáticos.

	Dirección - XX			Dirección - YY		
Nivel	Modelo Empotrado	Winkler % Δ	Pasternak % Δ	Modelo Empotrado	Winkler % Δ	Pasternak % Δ
Azotea	0.0042	5.26%	5.12%	0.0017	3.43%	2.61%
Story5	0.0044	5.36%	5.25%	0.0017	3.27%	2.46%
Story4	0.0040	5.21%	5.21%	0.0019	3.01%	2.32%
Story3	0.0043	5.53%	5.54%	0.0019	3.06%	2.38%
Story2	0.0040	6.61%	6.63%	0.0016	3.53%	2.72%
Story1	0.0030	10.18%	10.24%	0.0010	5.16%	4.00%
Semisótano	0.0008	40.03%	40.69%	0.0001	26.70%	21.72%

Tabla VIII.- Porcentajes de variación de las derivas en los modelos

5.3. Esfuerzos cortantes en el modelo estructural. - Al evaluar los resultados de las cortantes en el modelo estructural empotrado y los modelos con los coeficientes de Winkler y Pasternak, se obtuvo una variación poco significativa en los entrepisos. En la *Tabla IX* se muestran los resultados de los esfuerzos cortantes de entrepiso de la estructura en ambas direcciones, con base empotrada y con la incorporación de los coeficientes estáticos de Winkler y Pasternak.

	Modelo Empotrado		Winkler		Pasternak	
	Vx (Tonf)	Vy (Tonf)	Vx (Tonf)	Vy (Tonf)	Vx (Tonf)	Vy (Tonf)
Azotea	46.17	47.37	46.77	47.48	46.80	47.39
Story5	109.65	115.74	111.55	115.94	111.65	115.72
Story4	163.87	169.81	166.84	170.15	167.02	169.77
Story3	205.44	209.49	209.53	210.04	209.78	209.51
Story2	234.93	236.94	240.18	237.80	240.48	237.18
Story1	252.28	251.70	258.78	252.99	259.10	252.31
Semisótano	260.95	260.36	268.76	261.41	269.12	260.76

Tabla IX.- Fuerzas cortantes de entrepiso

En la *Tabla X* se aprecia que la cortante se incrementó en un 3.13% como máximo en la dirección XX para el modelo con los coeficientes de Winkler y se incrementó en 3.13% como máximo en la dirección XX para el modelo con los coeficientes de Pasternak, en el nivel del semisotano que se encuentra en contacto con la losa de cimentacion.

Los porcentajes fueron disminuyendo con cada entrepiso, por tanto se determinó que el esfuerzo cortante varía principalmente en el nivel que se encuentra en el primer nivel, el nivel que se encuentra en contacto directo con la losa de cimentacion.

	Modelo Empotrado		Winkler		Pasternak	
	Vx (Tonf)	Vy (Tonf)	Vx % Δ	Vy % Δ	Vx % Δ	Vy % Δ
Azotea	46.17	47.37	1.30%	0.23%	1.36%	0.05%
Story5	109.65	115.74	1.73%	0.17%	1.82%	0.02%
Story4	163.87	169.81	1.81%	0.20%	1.92%	0.03%
Story3	205.44	209.49	1.99%	0.26%	2.11%	0.01%
Story2	234.93	236.94	2.23%	0.36%	2.36%	0.10%
Story1	252.28	251.70	2.58%	0.51%	2.70%	0.24%
Semisótano	260.95	260.36	3.00%	0.40%	3.13%	0.15%

Tabla X.- Porcentajes de variación de fuerzas cortantes de entrepiso

6. Conclusiones y recomendaciones

- Mediante el análisis de la estructura con la base empotrada y la estructura con los modelos de Interacción Suelo Estructura estáticos de Winkler y Pasternak, se llegó a determinar que los coeficientes de rigidez pueden influir significativamente en el comportamiento estructural de la edificación, pues se apreció un incremento significativo de las derivas de entrepiso específicamente con mayor incidencia en los primeros niveles de la edificación, por ende, se puede concluir que los modelos estáticos de ISE pueden influir y condicionar directamente el diseño estructural de una edificación. Al respecto Barnaure & Manoli (2019) [9] señalan respecto a las estructuras de concreto armado, que la ISE puede a veces dar lugar a un comportamiento sísmico desfavorable, siendo algunos de los efectos desfavorables aquellos relacionados con el incremento de los desplazamientos absolutos o de las derivas de piso, como resultado estos efectos pueden dar lugar a un riesgo de golpeteo entre edificios adyacentes, a un aumento de las fuerzas o de las exigencias de ductilidad. Por tanto, se puede concluir que el uso de los coeficientes estáticos de Winkler y Pasternak pueden ser usados para obtener un mayor nivel de exactitud en el análisis y diseño estructural de edificaciones mediante un análisis modal espectral.

- Se llega a concluir que la variación del periodo fundamental de la estructura no fue significativa, considerando que la variación entre el modelo convencional y los modelos con los coeficientes ISE de Winkler y Pasternak se encuentran por debajo del 5% de variación. Se debe considerar que el resultado está condicionado al sistema estructural de la edificación que fue propuesta con muros a corte, no siendo el resultado aplicable a la tipología de estructuras de menor rigidez como las edificaciones en pórticos.

- Se llega a concluir que la variación en las derivas de entrepiso es significativa, específicamente en el nivel que se encuentra en contacto con la losa de cimentación y que transmite las cargas al suelo. Se determinó que esta variación es del 40% en la dirección XX de la estructura, dirección que presenta menor rigidez. Mientras que en la dirección YY el máximo incremento de las derivas fue del 26%. Mediante estos resultados se puede aseverar que los modelos estáticos de Winkler y Pasternak tienen influencias significativas en las deformaciones laterales de una edificación de concreto con losa de cimentación.

- Se llega a concluir que la variación en los esfuerzos cortantes no fue significativa, en vista que los porcentajes de variación se encuentran por debajo del 5% al comparar la estructura con la cimentación empotrada y las estructuras con los modelos ISE de Winkler y Pasternak.

- Tras haber realizado el estudio comparativo de una estructura empotrada con los modelos estáticos de ISE de Winkler y Pasternak es recomendable incorporar el uso de los coeficientes de rigidez de ambos modelos en la norma peruana E030, en vista que se comprobó que existe una influencia significativa en las deformaciones laterales que afectan independientemente al periodo de vibración de la estructura y la distribución de cortantes de entrepiso.

Es recomendable realizar estudios en estructuras aporticadas, que, de acuerdo al resultado encontrado en el comportamiento estructural, pueden ser más afectadas por las derivas de entrepiso, aspecto que podría colocar a la estructura en mayor riesgo de sufrir deformaciones inelásticas, por tanto, mediante la utilización de estos modelos estáticos se proporciona una mayor exigencia y precisión en el análisis y diseño estructural.

Referencias

[1] Aristizábal-Ochoa J. D.*, "Estructuras de Vigas Sobre Suelos Elásticos de Rigidez Variable".* 1987. Universidad Nacional, Medellín, Colombia.

[2] Bao, T. & Liu, Z. *Evaluation of Winkler Model and Pasternak Model for Dinamyc Soil- Structure Interaction Analysis of Structures partially Embedded in Soils*. 2019, Michigan Technological University. USA.

[3] Barnaure M. y Manoli D., *Unfavourable seismic behaviour of reinforced concrete structures due to soil structure interaction*, 2019. Technical University of Civil Engineering, Bucharest, Romania.

[4] Fernández, Fernández & Cobelo, W. *Influencia de la interacción suelo-estructura estática en edificios de 100 metros de altura.* 2022. *Artículo de Investigación.* Ingeniería y Desarrollo, vol. 41, núm. 2, pp. 213-232, 2023. https://doi.org/10.14482/inde.41.02.201.456

[5] MVCS (Ministerio de Vivienda, Construcción y Saneamiento). *Norma E030. Diseño Sismorresistente*. Lima - Perú.

[6] MVCS (Ministerio de Vivienda, Construcción y Saneamiento). *Norma E060. Concreto Armado*. Lima - Perú.

[7] Santana, A. *Modelo Winkler para el Análisis de la Respuesta Dinámica de Estructuras Enterradas*. 2010. Universidad de Las Palmas de Gran Canaria.

[8] Obinna, U. *Modelling of Soil- Structure Interaction*. 2022, Structville Integrated Services Limited. USA. https://structville.com/2022/03/modelling-of-soil-structure-interaction.html#google_vignette

[9] Oz I, Senel S.M., Palanci M. y Kalkan A., *Effect of Soil-Structure Interaction on the Seismic Response of Existing Low and Mid-Rise RC Buildings*, 2020. MDPI, Applied Sciences.

[10] Villarreal, G. *Interacción Sísmica Suelo-Estructura en Edificaciones con Plateas de cimentación*. 2017, Primera edición. Lima, Perú.

[11] Villarreal, G. Cerna, M. & Espinoza, C. S*eismic Interaction of Soil-Structure in Buildings with Limited Ductility Walls on Foundation Plates*. Revista internacional de Ingeniería de Estructuras. 2021. Vol. 26, 1, p 153-178.

Nota contribución de los autores:

1. Concepción y diseño del estudio
2. Adquisición de datos
3. Análisis de datos
4. Discusión de los resultados
5. Redacción del manuscrito
6. Aprobación de la versión final del manuscrito

JC ha contribuido en: 1, 2, 3, 4, 5 y 6.
GVC ha contribuido en: 1, 2, 3, 4, 5 y 6.

Nota de aceptación: Este artículo fue aprobado por los editores de la revista Dr. Rafael Sotelo y Mag. Ing. Fernando A. Hernández Gobertti.

Design of a vehicular emergency intercom system using electronic circuits and sensors

Diseño de un sistema de intercomunicación de emergencia vehicular utilizando circuitos electrónicos y sensores

Projeto de um sistema de intercomunicação de emergência veicular utilizando circuitos eletrônicos e sensores

Holger Santillán[1(*)], Carolina López [2], Kiara García[3], David Cárdenas[4]

Recibido: 04/10/2024 Aceptado: 26/01/2025

Summary. - This study presents the design of a vehicular emergency intercom system aimed at improving motorcyclist safety through the integration of electronic circuits and sensors. The system employs an Arduino UNO R3 microcontroller, GSM SIM900L modules, and ultrasonic and proximity sensors. It is programmed in C++ to detect falls and automatically trigger alerts with high efficiency.

Falls can be detected with 95% accuracy within a range of 2 to 100 cm, with an average response time of 1.2 seconds, making it suitable for emergencies. The system's ability to send alerts quickly enhances user safety in critical situations occurring at distances between 101 and 150 cm. However, limitations in the detection range were identified, particularly at minimum distances between 0.02 cm and 1.96 cm and maximum distances between 151.36 cm and 177.72 cm, which fall outside the operational range. This suggests the need for future adjustments. This project offers an innovative, efficient, and easy-to-implement solution for improving road safety, featuring high sensitivity to optimize emergency response.

Keywords: Vehicle intercom; Traffic emergency; Collision prevention; Vehicle safety.

(*) Corresponding author.

[1] Master's Degree in Telecommunications. Salesian Polytechnic University, Telecommunications Systems Research Group – GISTEL, hsantillan@ups.edu.ec ORCID iD: https://orcid.org/0000-0003-4803-7016

[2] Telecommunications Engineer. Salesian Polytechnic University, Telecommunications Systems Research Group - GISTEL, clopezg3@est.ups.edu.ec, ORCID iD: https://orcid.org/0009-0001-0173-5637

[3] Telecommunications Engineer. Salesian Polytechnic University, Telecommunications Systems Research Group - GISTEL, kgarciag6@est.ups.edu.ec, ORCID iD: https://orcid.org/0009-0001-5404-1436

[4] Master's degree in communication technologies and systems. Salesian Polytechnic University, Telecommunications Systems Research Group - GISTEL, dcardenasv@ups.edu.ec, ORCID iD: https://orcid.org/0000-0003-4241-9929

Resumen. - *En el presente trabajo se ha diseñado un sistema de intercomunicadores de emergencia vehiculares, enfocado a mejorar la seguridad de los motociclistas mediante la integración de circuitos electrónicos y sensores. Se utiliza un microcontrolador Arduino UNO R3, módulos SIM900L GSM y sensores ultrasónicos y de proximidad, el sistema está programado en C++ para detectar caídas y activar alertas automáticas con alta eficiencia.*
Las caídas se pueden detectar con un 95% de precisión y en un rango de 2 a 100 cm, con un tiempo de respuesta promedio de 1,2 segundos, lo que lo hace adecuado para emergencias. También se destacó la capacidad del sistema para enviar alertas rápidamente, lo que aumenta la seguridad del usuario en situaciones críticas que van desde los 101 hasta los 150 cm. Sin embargo, se identificaron limitaciones en el rango de detección, especialmente a distancias mínimas que oscilan entre 0,02 cm y 1,96 cm, y distancias máximas que oscilan entre 151,36 cm y 177,72 cm, mediciones que están fuera del rango de operación, lo que sugiere la necesidad de realizar más ajustes en el futuro. Este proyecto ofrece una solución innovadora, eficiente y fácil de implementar para mejorar la seguridad vial, con un alto grado de sensibilidad para optimizar la respuesta a emergencias.
Palabras clave: *Intercomunicador de vehículos; Emergencia de tráfico; Prevención de colisiones; Seguridad del vehículo.*

Resumo. ***-*** *Neste trabalho, foi projetado um sistema de intercomunicação de emergência veicular, com foco na melhoria da segurança de motociclistas por meio da integração de circuitos eletrônicos e sensores. Utilizando um microcontrolador Arduino UNO R3, módulos GSM SIM900L e sensores ultrassônicos e de proximidade, o sistema é programado em C++ para detectar quedas e disparar alertas automáticas com alta eficiência.*
As quedas podem ser detectadas com 95% de precisão e em um alcance de 2 a 100 cm, com tempo médio de resposta de 1,2 segundos, tornando-o adequado para emergências. A capacidade do sistema de enviar alertas rapidamente também foi destacada, aumentando a segurança do usuário em situações críticas que variam de 101 a 150 cm. No entanto, foram identificadas limitações no alcance de detecção, principalmente em distâncias mínimas que variam de 0,02 cm a 1,96 cm e máximas que variam de 151,36 cm a 177,72 cm, medidas que estão fora da faixa de operação, sugerindo a necessidade de mais ajustes no futuro. Este projeto oferece uma solução inovadora, eficiente e fácil de implementar para melhorar a segurança nas estradas, com alto grau de sensibilidade para otimizar a resposta a emergências.
Palavras-chave: *Intercomunicador veicular; Emergência de trânsito; Prevenção de colisões; Segurança veicular.*

1. Introduction. - Technological progress has revolutionized emergency management, making communication an essential factor in improving response in critical situations, such as traffic accidents. Road safety regulations, promoted by organizations such as the World Health Organization (WHO) and the United Nations (UN), highlight the importance of having efficient communication systems that reduce response times in emergencies. These regulations underline the need to incorporate advanced technologies into vehicular communication devices, thus ensuring their effectiveness and reliability in difficult circumstances, which contributes significantly to road safety and the protection of lives. [1].

The highway via la Costa in Guayaquil, Ecuador, faces a recurring problem of traffic violations that complicate the rapid response to accidents, affecting the effectiveness of emergency teams. To address this situation, it is proposed to integrate advanced electronic circuitry and sensor systems into emergency communication on this road to improve the transmission of vital data during critical incidents. This study justifies the need to innovate in intercom systems to improve coordination and response to emergencies, contributing to the field of telecommunications engineering with a solution adapted to local needs. [2].

This project has the potential to revolutionize road safety through an innovative system of emergency intercoms for motorcycle helmets. Equipped with advanced technology, the system accurately detects falls and collisions using proximity sensors and ultrasound. In the event of detecting a collision, the system automatically makes a call and sends a message to an emergency contact, while, for accident prevention, it sends notifications to the driver to avoid collisions. Experimental tests will be carried out at the Centenario Campus of the Salesian Polytechnic University of Guayaquil, using an Arduino UNO R3 and a GSM SIM900L module to simulate accident scenarios. [3], [4].

This approach seeks to optimize response times in critical cases, improve the reliability and adaptability of the system in various environments, and increase road safety. The system's ability to operate at specific distances and its speed of response ensure efficient communication, significantly reducing risk and providing drivers with a reliable tool to protect their well-being on the road, thus setting a new safety standard and contributing to accident prevention, saving lives and reducing property damage. [3], [4].

The experimental methodology to design a risk prevention circuit for motorcycle helmets through the integration of advanced detection and warning technologies is based on the use of the Arduino UNO R3 Board, GSM SIM900L Modules, and proximity sensors. Initially, individual tests of each component will be carried out to ensure its functionality, followed by its integration into a prototype using a Protoboard board and suitable connections. [5], [6].

C++ programming will develop algorithms that respond to data in real time, triggering alerts through a buzzer and LEDs. In addition, an exhaustive review of the literature will be carried out to identify the most effective technologies, which will guide the design of C++ software that manages the communication between sensors and the GSM module SIM900L. Detailed simulations will assess the detection capability and accuracy in generating alerts, ensuring that the system responds efficiently to emergencies, with key parameters such as response speed measured and compared to predetermined criteria. [7].

1.1 Related Jobs. - The Arduino Uno R3 board, which has been used to teach electronics and programming, demonstrates the ability of this microcontroller to simplify the learning of complex concepts. It was taken as a reference because it mentions the use of each pin that was used and thus able to connect it to the circuit, where each pin of the board has an interface to make it work. [8].

To program the Arduino software, you will take coding examples found in the articles and load them onto the board. The Arduino stands out for its versatility, used in both vehicle safety projects and education. The ease of use and extensive support community make it ideal for both beginners and advanced projects. [9].

The Arduino is also used, as in the article, to integrate voice recognition technologies into vehicular communication systems, demonstrating its versatility in critical communication applications. In this article, it is used for sensor management and emergency communication, which focuses on data transmission to improve the interaction between emergency vehicles [10], [11].

The GSM SIM900 module is one of the elements that stand out in the prototype because its function is to send and receive SMS messages, make calls, and connect to the internet through a network next to the Arduino.

This article [12] Uses the GSM SIM900L module to send real-time alerts to homeowners when an intrusion or suspicious activity is detected in the home. The system is based on IoT technology and uses a network of sensors to

monitor the environment of the house. When one of the sensors is activated, the SIM900L module is responsible for transmitting an alert via text messages or calls.

The GSM SIM900L module is essential for applications that require remote communication. In educational projects, its ease of integration and low consumption make it very useful, while in this article, its application in emergencies is highlighted. And remote communication systems. This component is essential for real-time communication with emergency contacts, which is critical for vehicle safety situations. [13], [14].

In this article, the buzzer is used to provide audible signals in case of emergency detection, functioning as a local alert system complementary to SMS messages.
There are similar articles where buzzers are used for alerts in obstacle detection and home security systems, reinforcing their usefulness as a warning signal in varied environments, and electromagnetic buzzers, although less common in modern applications, are used in systems that demand greater sound intensity. [15].

In this article, he introduces the buzzer as an essential component in rapid notification systems, used for its ability to generate immediate and effective alerts. Its application extends to educational projects, where it facilitates practical learning of circuits and programming, as well as in vehicle and home security systems, where its distinctive sound warns of dangerous situations or important events. This has helped us to know how the circuit works so that it can work. [16].

The LED light diodes emit a strong signal to be able to establish a situation, in several articles, they are related to being able to measure the depth and give the warning to the next phase, as we see in the article which the purpose of that study was to determine if increasing the distance between the light source and the pit and fissure sealant affects its curing depth, Concerning the article, it can be seen that to have an emergency start-up warning, these diodes can be used and give better scope to the projects. [17].

In the article, the ultrasonic sensor is used in obstacle detection systems for robots and in security alarms. This highlights the sensor's versatility for safety and navigation applications. With this base, it was possible to obtain information to program the circuit, which in this project measures the distance between the motorcyclist's helmet and the ground to detect falls, activating automatic alerts in case of an accident. [18], [19].

The HC-SR04 ultrasonic sensor is a flexible tool for both distance sensing in vehicle safety projects and robotics and automation applications. Its easy programming and integration with Arduino make it a popular component in various projects. By analyzing the items, it was possible to know the proper handling and what each pin is used for to connect it to the circuit. [20].

The article relates the 4-pin pushbutton because it is a fundamental electronic component in circuit design, commonly used in a variety of applications, from electronic devices to industrial control systems. This type of pushbutton is characterized by its specific structure and functionality, which differentiates it from other kinds of switches and buttons. For this article, it helps to control the circuit pass, it is used when we already have a signal and continue to the other step, which is to transmit calls and alert messages [21].

Both jumpers and resistors are essential elements in the design and testing of electronic circuits. Jumpers provide flexibility and ease for the temporary connection of project components, as visualized in this article, while resistors allow precise control of current and voltage, protecting and optimizing the operation of circuits. Their correct use is key to the development of functional and efficient circuits. [22].

You can find articles where these elements are used for the connection and fluidity of the components, in this article, we find similar connections along with the breadboard where they fundamentally complement the operation. The breadboard, according to the articles, is a crucial tool in electronics for the creation, testing, and adjustment of circuits. Its ability to facilitate rapid and flexible prototyping, coupled with its ease of use, makes it indispensable for designers, engineers, and students. [23], [24].

The breadboard is an indispensable tool for the development of electronic prototypes both in education and in advanced emergency systems projects. It offers an efficient platform to experiment with different circuit configurations visualized in the article and optimize the performance of electronic designs before moving on to a more permanent stage of development. [25].

Python is crucial in the design and management of modern electronic circuits due to its ease of use. By integrating Python into electronic projects, as noted in the following articles, they can automate processes in the programming of microcontrollers and embedded systems, as well as analyze and process sensor data in real-time. Python streamlines the implementation of algorithms, communication between devices, and the creation of intuitive interfaces for user use. [26], [27].

2. Materials and methods. - The experimental methodology for the design of a hazard prevention circuit for motorcycle helmets is based on a meticulous integration of advanced detection and warning technologies. Using the Arduino UNO R3 Board, GSM SIM900L modules, and proximity and ultrasound sensors, the aim is to design a robust and efficient system. The methodological process ranges from the exhaustive review of the literature to select the most effective technologies to the implementation and testing of the system in a functional prototype. Each phase of development is designed to ensure that the system not only performs optimally but also meets the required safety and accuracy standards.

Figure I is presented below, illustrating the six main phases of the methodology for the design of the motorcycle helmet risk prevention circuit. The detailed explanation of each phase follows below to understand their role in the overall process:

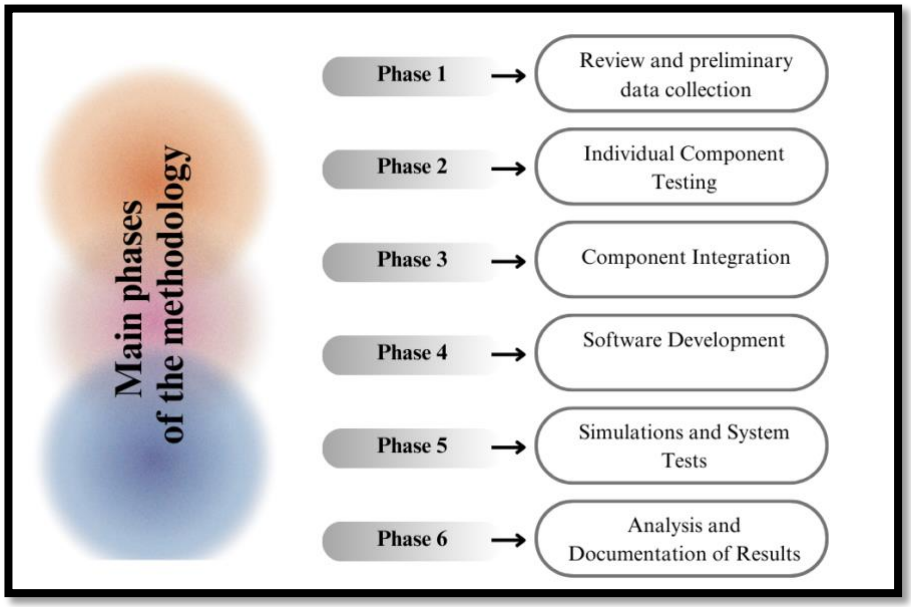

Figure I. Main phases of the methodology.

1. **Preliminary data review and collection:** A thorough literature review is conducted to identify best practices and technologies available in warning and detection systems. This research allows us to select the most effective sensors and modules and design a robust system based on the latest technologies.
2. **Individual Component Testing**: In this initial phase, each component of the system, such as the Arduino UNO R3 Board, GSM SIM900L modules, and proximity and ultrasound sensors, undergoes extensive testing to verify its functionality and compatibility. This ensures that each part of the system operates correctly before being integrated into the prototype.
3. **Component Integration**: After validation of the individual components, the prototype is assembled using a Protoboard board. This phase involves connecting the different elements of the system in a precise way to form a functional circuit that allows communication between the Arduino and the GSM modules.
4. **Software Development**: In this stage, the C++ algorithms are developed to manage the communication between the sensors and the GSM module SIM900L. Specific algorithms will be developed to detect risks, send instant alerts to emergency contacts, and send prevention messages to the driver, thus optimizing the speed and accuracy of the response.
5. **System Simulations and Tests**: Detailed simulations are carried out using specialized software to evaluate the performance of the system under various conditions. This phase allows us to measure detection capacity, accuracy in generating alerts, and speed of response, comparing the results with established performance criteria.

6. **Analysis and Documentation of Results**: The results will be analyzed to measure the detectability and accuracy of the alerts, comparing this data to predetermined performance criteria. The findings will be documented and analyzed to validate the effectiveness of the system in preventing risks and improving road safety.

2.1 Flowchart. - Figure II shows the process of running a prototype designed to notify emergencies and prevent collisions over a specific distance range. It is divided into two main parts based on distance range:

- **Range from 2 to 100 cm (Collision):** If the system detects a collision within this range, a call is made, and a warning message is sent to the emergency contact configured in the programming, alerting to an accident.

- **Range of 101 to 150 cm (Collision Avoidance):** If a potential collision is detected within this range, a caution message is sent to the driver's contact to prevent an accident.

The flow highlights the importance of set distance ranges and the automatic actions the system takes based on detection, prioritizing safety in both prevention and response to potential collisions.

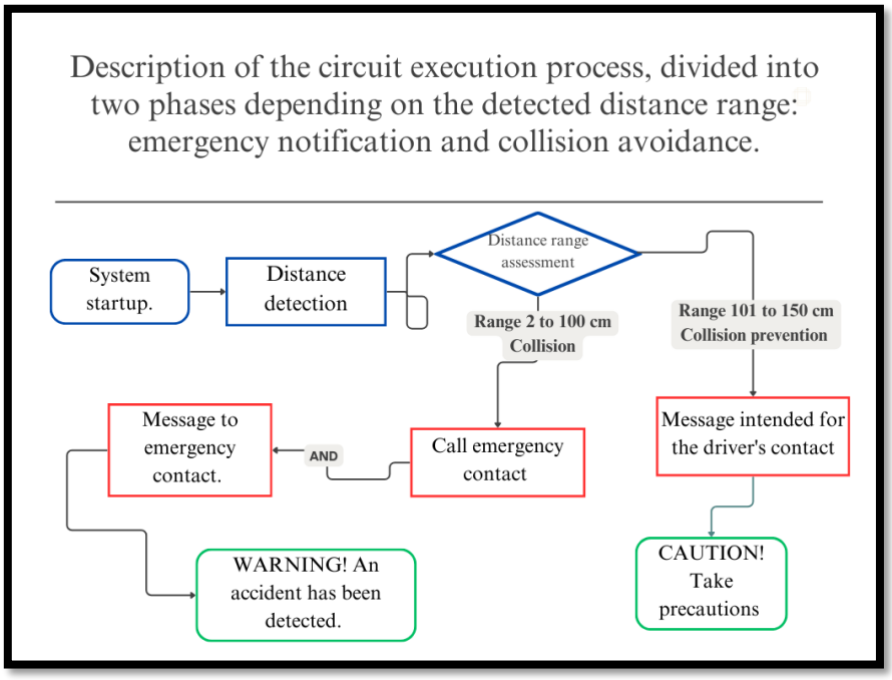

Figure II. Flow chart of the prototype execution process.

2.2 Circuit Schematic. - To develop this project, an Arduino R3 board will be used, which will allow programming and controlling several electronic components, as can be seen in Figure III. Among the materials to be used are a GSM SIM900 board for mobile communication, a laptop to program and monitor the system, an operating chip, an LED sensor, a 5V HC-SR04 4-pin ultrasonic sensor, a 4-pin pushbutton, a buzzer module, resistors, and a Protoboard board to make the necessary connections.

1. Arduino Uno R3 Board
2. GSM SIM900 Board
3. Laptop
4. Operating chip
5. LED Diode Sensor
6. Ultrasonic Sensor 5v HC-SR04 4pin
7. 4-pin push button
8. Modulo buzzer zumbador
9. Resistance
10. Protoboard Board

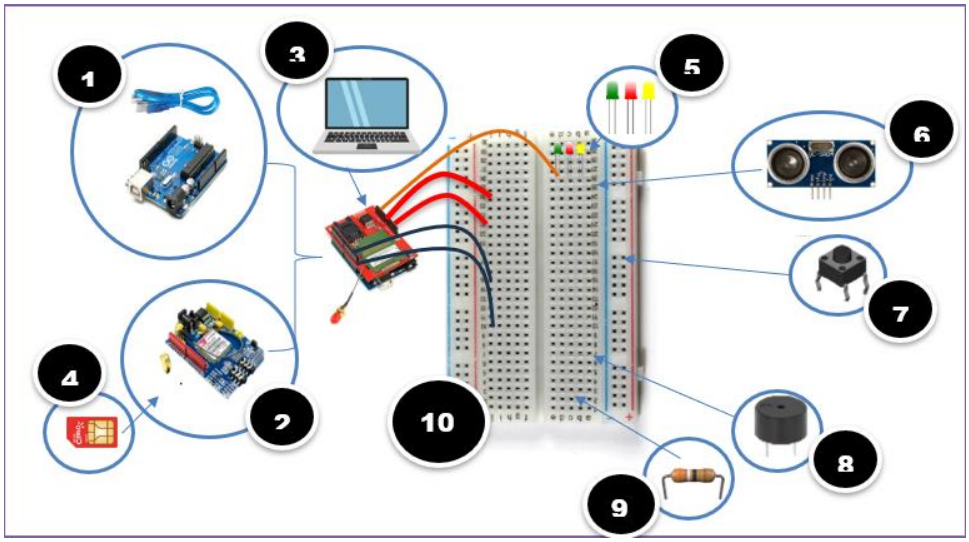

Figure III. Prototype of a design in Protoboard.

2.3 Data analysis methodology. - To start, the pins of the Arduino UNO R3 are related to those of the GSM board SIM900L using a Headers pin, ensuring a correct union between the two. In addition, power was supplied via a power cord to power the device. Once both boards were assembled, they were connected to the computer, and the corresponding programming began. Figure IV shows the plate bonding scheme.

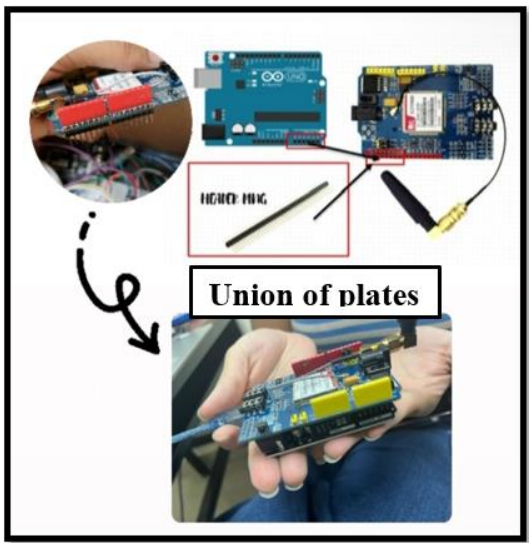

Figure IV. Arduino board and GSM board link scheme.

The stages described below correspond to phases 3 and 4 of the methodology. First, the linked boards, as shown in Figure IV, are connected to the computer, and the appropriate development environment is opened. The necessary code is typed or loaded into the IDE, then compiled and uploaded to the microcontroller. Once the programming has been successfully uploaded, the green LED on the breadboard schematic in Figure III will light up, indicating that the system is operating properly.

Next, manually turn on the GSM SIM 900 module, making sure that it is correctly connected to the microcontroller. After a few seconds, when the GSM module has detected the signal, the red LED will light up, confirming that a signal is available. Then, press the button connected to the microcontroller.

This action will turn on the yellow LED, indicating that the system has detected the activation of the button. At that point, the ultrasonic sensor will begin to detect motion. The microcontroller will process the information from the ultrasonic sensor to take the necessary actions according to the previously uploaded programming. All exposed materials will be placed on the breadboard board, as shown in Figure V.

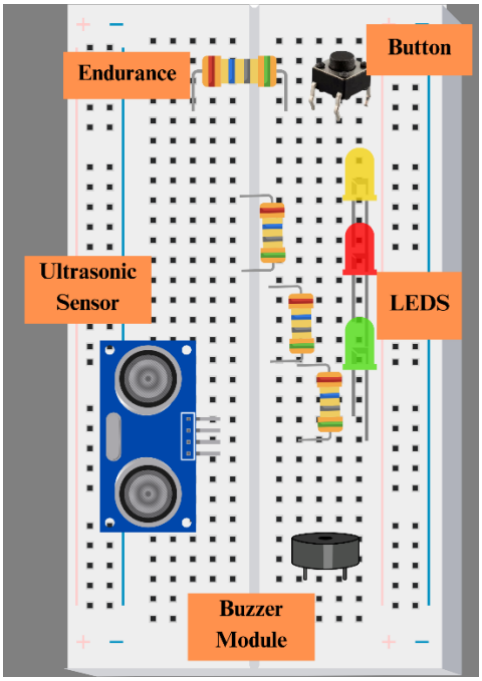

Figure V. Protoboard scheme.

Once the Arduino and GSM boards have been connected, as shown in Figure III, all the sensors, modules, and resistors are integrated into the breadboard. These components are interconnected by breadboard cables (jumpers) to establish a functional and simulation-ready circuit.

The circuit in the breadboard, depicted in Figure V, includes a 5V ultrasonic sensor (HC-SR04, 4-pin), which acts as a means of detecting movements based on the programmed distance. When the set thresholds are exceeded, the system emits a warning sound through the buzzer and sends an SMS or makes a call to the pre-configured number.
Figure VI also shows the complete schematic of the circuit, detailing the connection between the GSM module, the Arduino board, the buzzer, a proximity sensor, a pushbutton, resistors, and LEDs. All these components are connected to a breadboard, powered with 9 volts for the amplifier and 3.3 volts for the sensor and the analog-to-digital converter, ensuring the correct operation of the system.

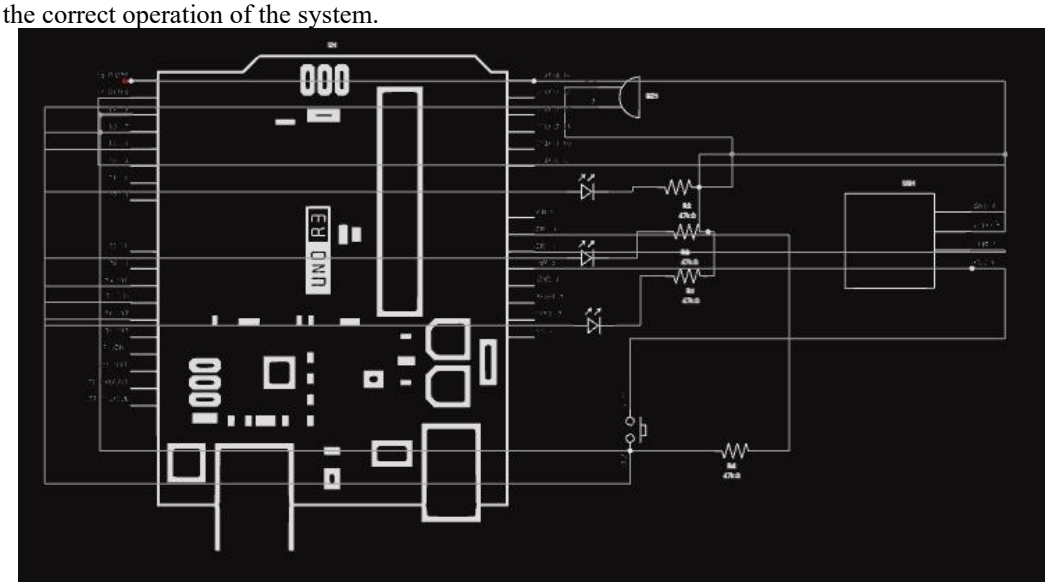

Figure VI. Circuit diagram.

2.4 Schematic simulation methodology of the circuit compiled on an Arduino UNO R3 board. -

2.4.1 Programme implementation. - Figure VII shows the complete signaling process of the GSM module. Initially, the program is entered without a signal, displaying the AT+CREG message, which indicates that the module is looking

for a signal. Once the signal is established, the system transmits a message confirming "alarm fully initiated," and the red LED lights up to indicate that the GSM module has been successfully connected and is ready to go.

Figure VII. Programmed implementation.

Figure VIII illustrates the connection of the GSM SIM900 module to the network. The red LED light confirms that the module has established a network signal and is operational. This visual indicator shows that the GSM module is properly integrated and ready to transmit data.

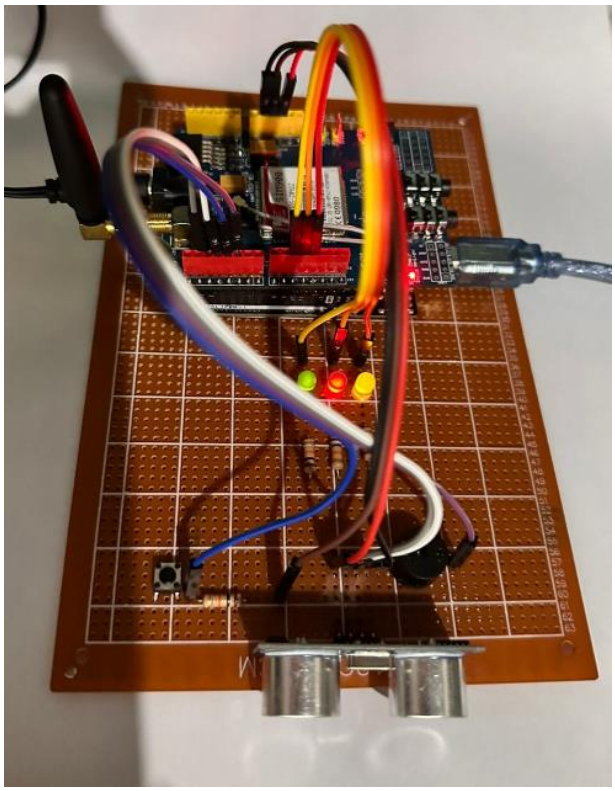

Figure VIII. Programmed implementation.

Figure IX illustrates the detection of a movement at 5 cm, which is within the predefined range of 2 to 100 cm. This distance confirms that the detected object is in the specific range for which the system is designed to trigger alerts. The correct identification of this distance within the set range is crucial for the accurate operation of the system, ensuring that appropriate response measures are activated in emergencies.

```
00:02:21.908 -> distancia en cm: 5
00:02:21.983 -> AT+CREG?
00:02:23.109 -> AT+CREG?
00:02:24.193 -> AT+CREG?
00:02:25.306 -> AT+CREG?
00:02:26.383 -> AT+CREG?
00:02:27.464 -> Realizando llamada...
00:02:27.464 -> ATD0992238855;
00:02:42.478 -> ATH
00:02:44.586 -> AT+CREG?
00:02:45.643 -> Enviando mensaje...
00:02:45.690 -> AT+CMGF=1AT+CMGS="0978603628"
00:02:47.686 -> ADVERTENCIA! Se ha detectado un accidente
00:02:47.771 -> □
00:02:48.770 -> Mensaje Enviado...
```

Figure IX. Collision detection.

Figure X illustrates the complete process that the system follows when detecting a collision using the ultrasonic sensor. When the sensor detects a potential collision, the system immediately activates the emergency protocol, which includes making a call to the pre-configured emergency contact. This call is made to quickly and effectively alert about the incident, ensuring that help is requested without delay and increasing the chances of a timely response to the emergency.

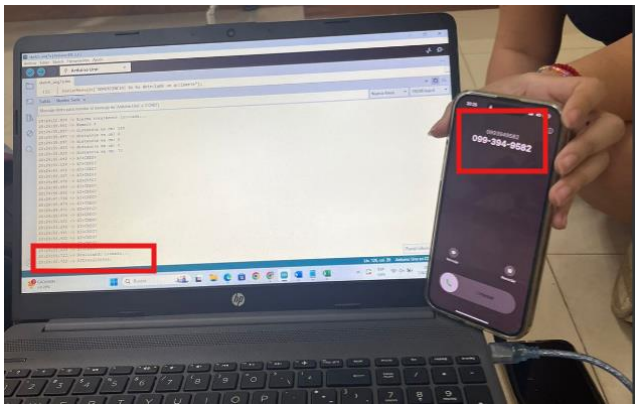

Figure X. Emergency call.

Figure XI illustrates the complete process after making an emergency call. Once the call has been made, the system automatically sends a message to the emergency contact with the text "Warning! An accident has been detected." This notification ensures that the emergency contact is immediately alerted to the critical situation, providing essential information for rapid intervention.

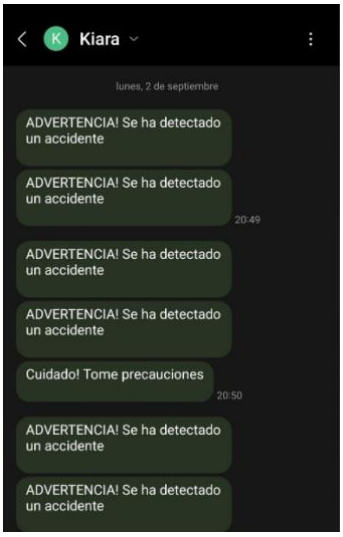

Figure XI. Emergency message.

Figure XII illustrates motion detection at different distances: 127, 123, 124, and 104 cm, all within the preset range of 101 to 150 cm. In these situations, the system is designed to send an alert message to the driver that says, "Watch out! Take precautions." This message aims to warn the driver of a potential impending collision, allowing them to take preventative measures to avoid an accident.

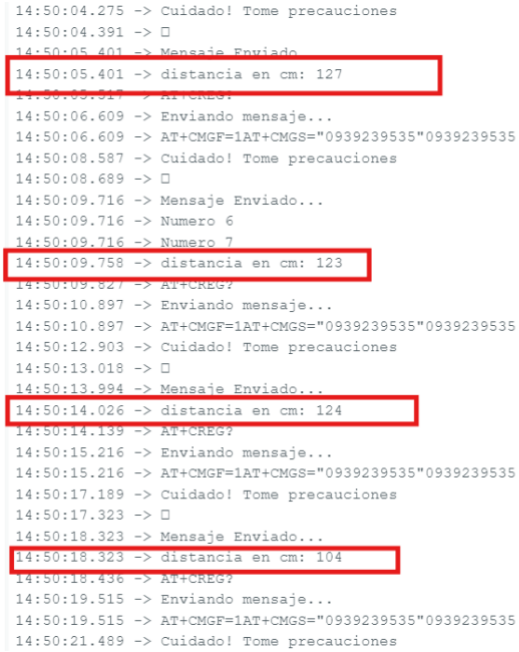

Figure XII. Collision avoidance message.

Figure XIII illustrates that the system sends a warning message to the driver's contact. This message, transmitted automatically, is crucial for the driver to be able to take proper precautions and avoid a potential collision. By receiving this alert, the driver receives real-time information, allowing them to adjust their behavior and improve safety on the road. The figure clearly shows how the system facilitates this vital communication, highlighting its role in accident prevention by enabling a quick and effective response to potentially dangerous situations.

Figure XIII. A collision warning message addressed to the driver.

4. Results. -

4.1 Distance analysis calculations and alert activation. -

Sound Speed Formula:

Distance formula: $$t = \frac{x}{v} \quad (1)$$

Where:

- t: Time it takes for the signal to go and return.
- x: Total distance traveled by the signal (round trip).
- v: Signal propagation speed, which in this case is the speed of sound.

$$v = \frac{340m}{s}$$
$$v = \frac{34000cm}{s} \quad (2)$$

Where:

- v: The speed of sound in the air, expressed in centimeters per second. It is considered 34000 cm/s (equivalent to 340 m/s).

$$t = \frac{\frac{1cm}{34000cm}}{s}$$
$$t = 29{,}411\ \mu s \quad (3)$$

Where:

- This is the conversion of the time it takes for a signal to travel 1 cm (round trip) at a speed of 34000 cm/s. The result is 29,411 microseconds.

The signal goes back and forth therefore, half the distance will be taken.

Distance (cm)= $(Tiempo\ medido(\mu s)\ /29.41\ \mu s * cm)\ /2)$ (4)
Distance (cm) = $(Tiempo\ medido\ (\mu s\ /58.82\ \mu s)$ (5)
Distance (cm) = $Tiempo\ medido\ (\mu s)\ *\ 0.017$ (6)

4.2 Simulation results. - In scenario 1, the moment when a collision occurs is captured within the range of 1 to 100 cm, specifically at 19 cm. At that proximity, the system activates, making a call and sending an SMS to the emergency contact, notifying them of the collision and allowing an immediate response, as visualized in Figure XIV.

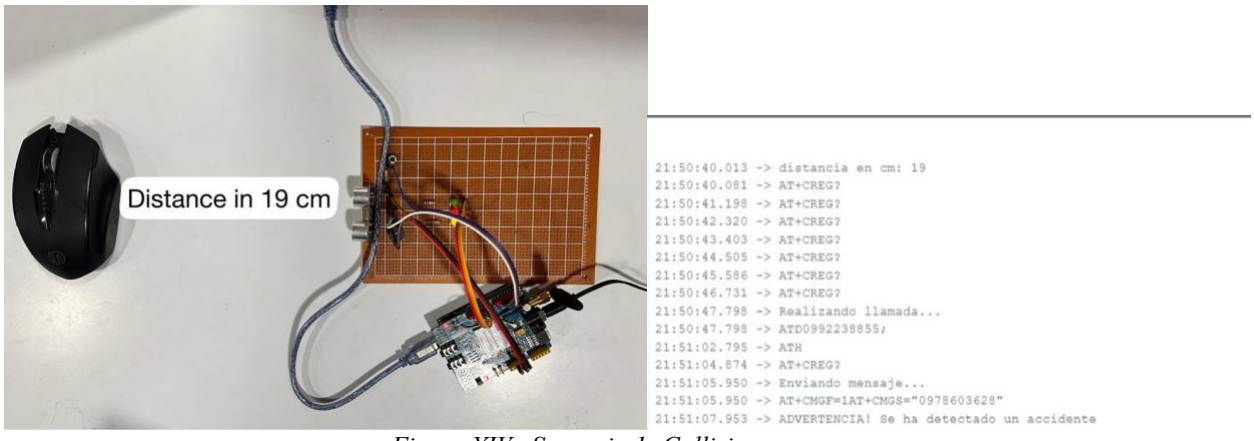

Figure XIV. Scenario 1: Collision message.

Table 1 presents the distances measured by the ultrasonic sensor, calculated using formula (6):

A column labeled "Collision" has been included, indicating whether the system detects a driver's fall at a specific distance. This data is essential for evaluating the system's accuracy and effectiveness in identifying accidents.

The system determines that an accident has occurred when it detects a helmet fall within the predefined range in the programming (2 cm ≤ distance ≤ 100 cm). In this case, an emergency protocol is automatically activated, which includes sending an SMS message and making a call to an emergency contact, alerting them about a potential collision. This process is illustrated in Figures 9, 10, and 11.

Distance (cm) = Measured time (µs) * 0.017	Distance	COLLISION
120	2.04	YES
600	10.20	YES
900	15.31	YES
1200	20.41	YES
1500	25.51	YES
1800	30.61	YES
2100	35.71	YES
2400	40.82	YES
2650	45.07	YES
2950	50.17	YES
3250	55.27	YES
3550	60.37	YES
3850	65.48	YES
4150	70.58	YES
4450	75.68	YES
4750	80.78	YES
5000	85.03	YES
5300	90.14	YES
5600	95.24	YES
5900	100.34	YES

Table 1. Collision results, applying the sound speed formula.

Figure XV provides a graphical representation of the data from Table 1, highlighting the direct relationship between measured time in microseconds and distance travel. To enhance visualization, distances are presented in 5-cm increments.

The graph illustrates that as time increases, distance also increases, suggesting a constant movement or a process in which one variable is directly dependent on the other. Additionally, the figure indicates that when the distance falls within the established range, a collision is detected.

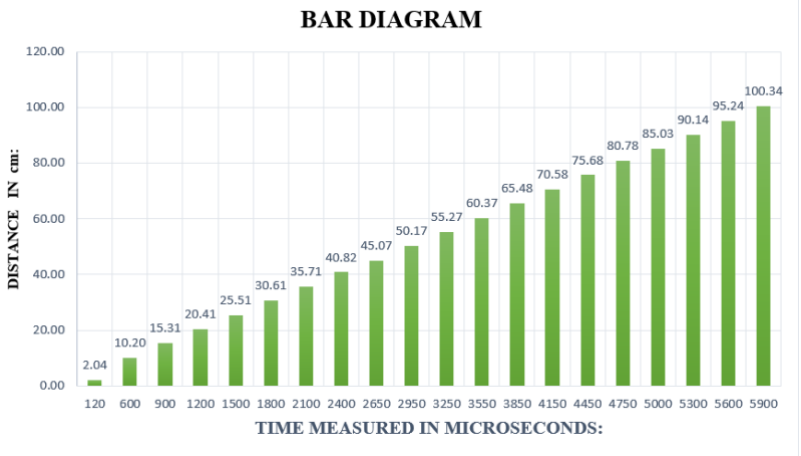

Figure XV. Graphical representation of collision detection.

Scenario 2 shows the moment when the system detects a potential collision at a distance of 114 cm, within the range intended for collision avoidance. In this case, the system proceeds to send a collision avoidance message to the driver to avoid the impact, as presented in Figure XVI.
With the integrated and processed circuit, the emergency alert is detected, reacting immediately to a possible fall.

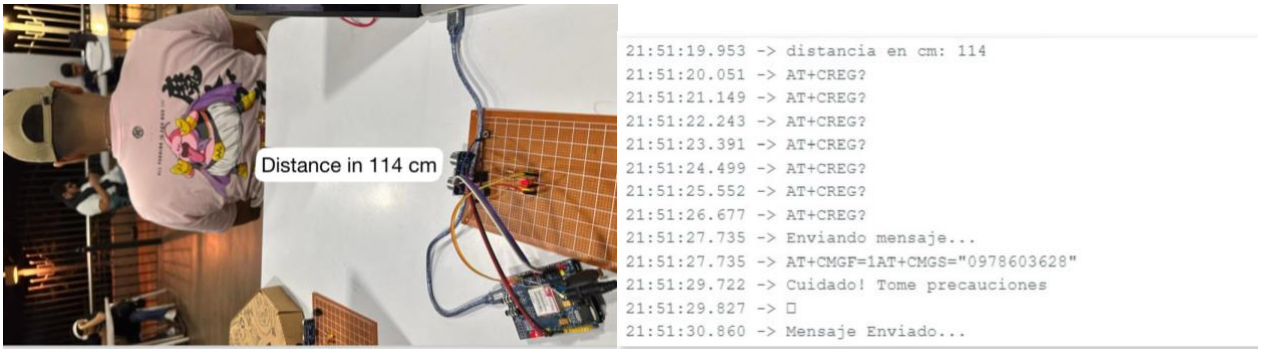

Figure XVI. Scenario 2: Collision avoidance

Table 2 presents the distances measured by the ultrasonic sensor, calculated using formula (6). The system specifically evaluates the distance range defined by the condition "else if (distance > 101 && distance <= 150)", which refers to a proximity zone where the detection of an obstacle does not necessarily imply an immediate collision, but it could represent a potential risk to the driver. Within this range, the system interprets that the driver must remain cautious and be prepared to take corrective actions in case of an emergency.
Consequently, a warning message is triggered to alert the driver about the proximity of the object without a collision occurring. In addition, an audible alarm is activated, reinforcing the visual alert and enhancing the visibility of the impending danger. This system behavior is depicted in Figures 12, 13, 14, and 15, which provide a detailed illustration of how the detection of this intermediate zone triggers the alert mechanisms for the user.

Distance (cm) = Measured time (µs) * 0.017	**DISTANCE (cm)**	**COLLISION**
5950	101.19	YES
6200	105.44	YES
6500	110.54	YES
6800	115.65	YES
7100	120.75	YES
7350	125.00	YES
7650	130.10	YES
7950	135.20	YES
8250	140.31	YES
8550	145.41	YES
8850	150.51	YES

Table 2. Collision avoidance results by applying the sound speed formula.

Figure XVII provides a graphical representation of the data shown in Table 2, illustrating the direct correlation between the distances detected by the system and the time measured in microseconds. This relationship suggests that, as time increases, the distance traveled also increases proportionally, reinforcing the notion that both parameters are closely linked in the proximity measurement process.
To facilitate interpretation, distances are displayed in 5-cm increments, which enhances the visualization of variations within the measurement range. The graph emphasizes that when distances fall within a specific range, a collision avoidance message is triggered, indicating the presence of a potential risk. This preemptive alert is critical for the driver to take the necessary precautions and avoid hazardous situations. The graphical analysis allows for a deeper understanding of how distance and time interact in real-time within the detection process, showcasing the system's effectiveness in identifying potential threats.

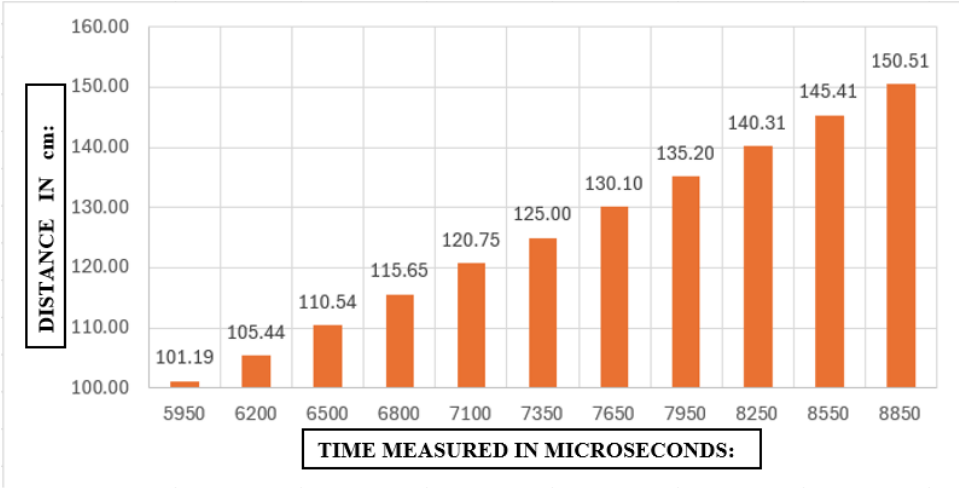

Figure XVII. Graphical representation of collision avoidance.

4.3 Experimental results: Non-collision scenarios. - In Scenario 3 it shows a minimum distance of 0 cm and then a distance of 2 cm, where it begins to detect collisions. It is important to note that the minimum distances range from 0.02 to 1.96 cm, in which the system will not detect falls since they are outside the range established for detection, as shown in Figure XVIII.

Figure XVIII. Scenario 3 Minimum distances.

Figure XIX illustrates a clearly defined trend line, demonstrating that as time, measured in microseconds, increases, the detected distance also increases proportionally. However, distances fall within the range of 0.02 cm to 1.96 cm, which is minimal and indicates that no significant movement is detected. This suggests that at these very short distances, the sensor is unable to register any form of collision or impact, highlighting its limitations in detecting objects within this range.

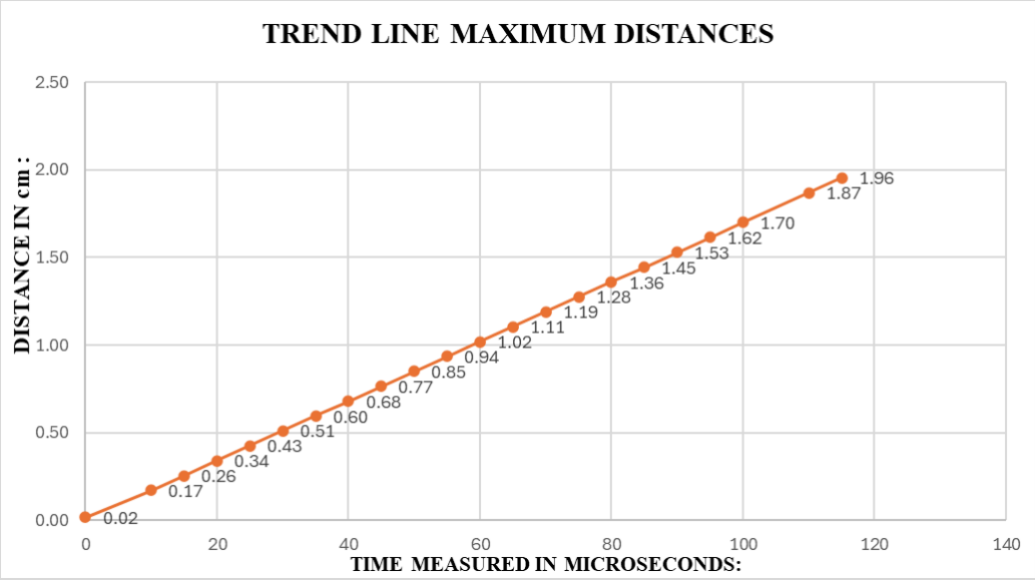

Figure XIX. Graphic representation: No collision at minimum distances.

Scenario 4 has a maximum distance of 174 cm, as shown in Figure XX. It is important to note that the maximum distances range from 151 to 177 cm, where the system will not be able to activate automatic alerts, this is caused because they are outside the range established for detection.

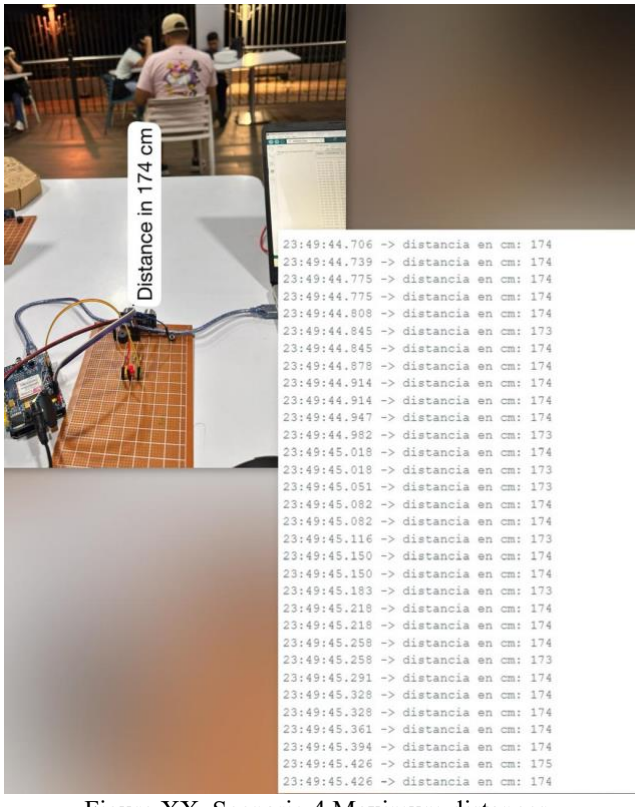

Figure XX. Scenario 4 Maximum distances.

Figure XXI illustrates that at distances between 151 cm and 177 cm, the sensor fails to detect any motion. This observation, also detailed in Table 4, suggests that the sensor's effective range for detecting collisions or impacts does not extend within these distances, highlighting the limits of its detection capabilities outside the defined proximity range for accurate monitoring.

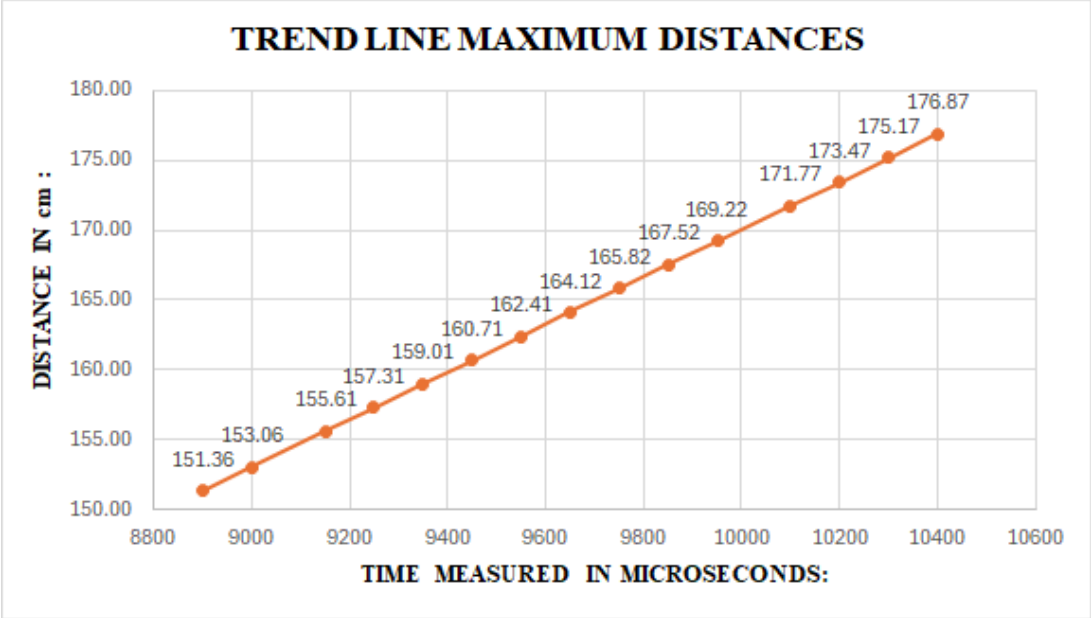

Figure XXI. Graphical representation: No collision at maximum distances.

Table 3 presents the results of 50 tests conducted to evaluate the performance of an emergency communication system based on distance detection. The data includes key aspects such as the distance from the detected object or event (in centimeters), the detection time (in seconds), the signal activation time, the SMS sending time, and the total time from detection to SMS dispatch.

The total time, which is the sum of the individual times for detection, activation, and sending, shows significant variation, ranging from 1.8 seconds at very short distances (e.g., 3 cm) to 10.6 seconds at longer distances (e.g., 149 cm). These variations are critical for assessing the system's efficiency, particularly in emergencies where rapid response is essential. This data helps evaluate the system's ability to process and communicate information effectively in real time, offering insights into the timeliness and reliability of the system's emergency response.

COMMUNICATION EFFICIENCY TABLE					
Test	**Distance (cm)**	**Detection Time(s)**	**Signal(s) activation time**	**SMS Sending Time(s)**	**Total Time(s)**
1	72	3.1	0.52	1.1	4.72
2	30	1.9	0.3	1.2	3.4
3	100	5.9	0.3	1.2	7.4
4	105	6.2	0.25	1.4	7.85
5	32	1.9	0.26	1.2	3.36
6	61	3.6	0.3	1.3	5.2
7	65	3.8	0.3	1.3	5.4
8	70	4.1	0.41	1.3	5.81
9	10	0.6	0.25	1.2	2.05
10	140	8.2	0.5	1.1	9.8
11	109	6.4	0.28	1.2	7.88
12	115	6.8	0.35	1.1	8.25
13	41	2.4	0.4	1.2	4
14	50	2.95	0.41	1.2	4.56
15	25	1.5	0.42	1.2	3.12
16	5	0.3	0.2	1.3	1.8
17	134	7.9	0.5	1.2	9.6

18	52	3.1	0.2	1.1	4.4
19	99	5.85	0.4	1.2	7.45
20	68	4	0.4	1.1	5.5
21	74	4.4	0.35	1.2	5.95
22	31	1.85	0.25	1.3	3.4
23	56	3.3	0.3	1.3	4.9
24	14	0.85	0.35	1.2	2.4
25	21	1.25	0.3	1.2	2.75
26	38	2.25	0.3	1.3	3.85
27	116	6.85	0.25	1.3	8.4
28	121	7.15	0.4	1.2	8.75
29	11	0.65	0.3	1.2	2.15
30	19	1.15	0.41	1.3	2.86
31	17	1	0.26	1.3	2.56
32	3	0.2	0.3	1.3	1.8
33	55	3.25	0.3	1.4	4.95
34	63	3.75	0.4	1.2	5.35
35	102	6	0.5	1.3	7.8
36	112	6.6	0.5	1.3	8.4
37	53	3.15	0.25	1.3	4.7
38	67	3.95	0.3	1.4	5.65
39	36	2.15	0.3	1.3	3.75
40	93	5.5	0.25	1.3	7.05
41	91	5.4	0.3	1.35	7.05
42	75	4.45	0.4	1.4	6.25
43	105	6.2	0.5	1.3	8
44	60	3.55	0.4	1.3	5.25
45	23	1.4	0.2	1.3	2.9
46	4	0.25	0.25	1.3	1.8
47	143	8.45	0.5	1.2	10.15
48	147	8.65	0.5	1.2	10.35
49	149	8.8	0.5	1.3	10.6
50	127	7.5	0.4	1.3	9.2

Table 3. System efficiency in communication.

Figure XXII illustrates the relationship between detected distance and total delay time in the emergency communication system. The blue bars represent the detected distance (in cm), while the orange line indicates the total delay time (in seconds), which includes detection time, signal activation, and SMS dispatch. A trend is observed where, as the detected distance increases, the total delay also tends to rise, which is expected due to the longer processing and transmission duration at greater distances. However, some fluctuations are present, possibly due to environmental factors or system performance variations. This graphical representation helps assess the system's efficiency in detecting and transmitting emergency messages, highlighting the importance of optimizing its performance at greater distances to improve response times in critical situations.

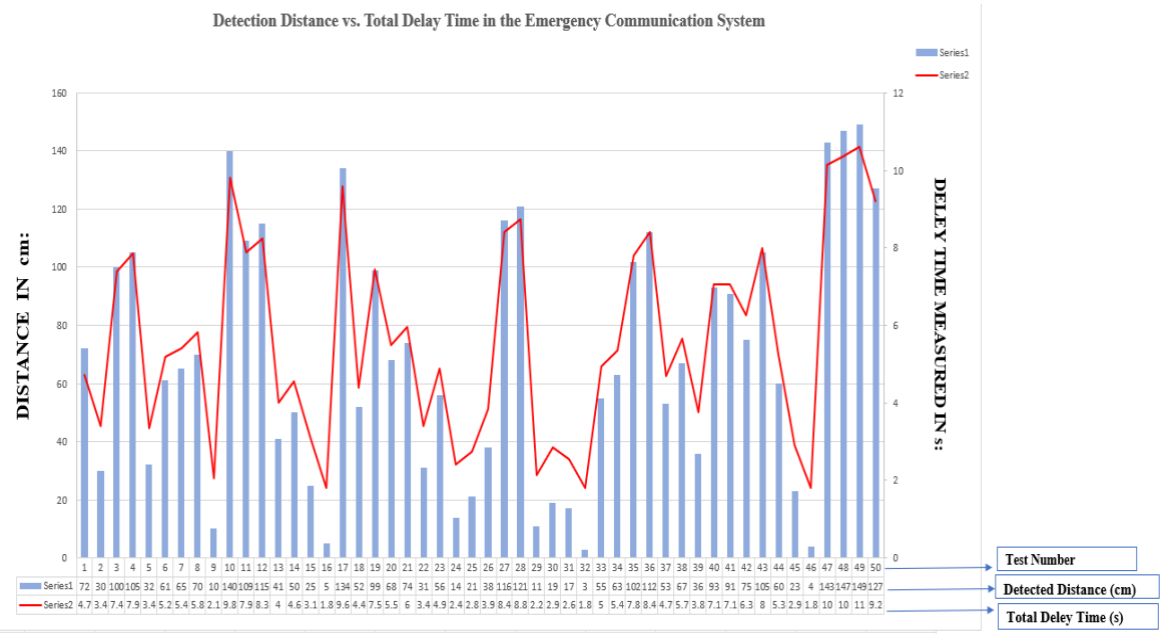

Figure XXII. Graphical representation of the efficiency of the communication system.

The system does not detect distances outside its operating range because its operating range has been strategically defined to ensure accurate and relevant detection in potential collision scenarios. An interval of 2 to 100 cm was established for activating emergency alerts and 101 to 150 cm for preventive warnings, considering reaction times and avoiding false alarms. Although the ultrasonic sensor can measure greater distances, the restriction is due to a design decision oriented to system efficiency and not to hardware limitations. If necessary, parameters in the microcontroller programming could be modified to extend the sensing range, ensuring that the stability and accuracy of the measurements remain within acceptable margins.

To improve coverage without compromising reliability, a possible solution would be the integration of complementary sensors with longer ranges or the implementation of additional technologies, such as LiDAR or machine vision cameras. These systems could provide more advanced detection in dynamic environments and at greater distances, optimizing the system's ability to anticipate and prevent incidents with a greater margin of time.

Table 4 presents the results of tests conducted to evaluate system performance, focusing on accuracy and false positive rate. With a response time between 1.8 and 10.6 seconds, as demonstrated in Table 3, the system showed a 90% correct detection rate, indicating high reliability in identifying obstacles within the range of 2 to 150 cm.

A false positive rate of 10% was observed, attributed to external interference or variations in object reflectivity. To mitigate these errors, filters were implemented in the programming that discards inconsistent readings, stabilizing the measurements. The optimization process will continue to improve accuracy and reliability in future tests.

Performance Metrics Table				
Distance (cm)	True Positives (TP)	False Positives (FP)	Accuracy	False Positive Rate (%)
2-50	48	2	96	4
51-100	45	5	90	10
101-150	40	10	80	20
151-200	38	12	76	24

Table 4. System Performance.

- Definitions:
- True Positives (TP): Cases where the system correctly detects the presence of the object.
- False Positives (FP): Cases where the system detects an object that is not present.
- Accuracy: Calculated as: $\text{Accuracy} = \frac{VP}{VP+FP} \times 100$
- False Positive Rate: Calculated as: $\text{False Positive Rate} = \frac{FP}{VP+FP} \times 100$

5. Discussion. - The paper [27] focused on the implementation of a visible light communication (VLC) system for emergency vehicles, highlighting the transmission and reception of data over a radio frequency link and VLC. While their results demonstrated the feasibility of the system, especially in terms of range (up to 200 meters for radio frequency and 30 cm for VLC), the present study proposes a solution that integrates voice recognition, significantly improving accessibility and interaction without the need for manual intervention.

Both studies seek to improve the efficiency of communication in vehicular emergencies, although from different technological approaches. In this project, an average of 8.24 s can be visualized for sending emergency SMS, which shows that the greater the distance, the longer it takes to send the message. While the VLC system provides an efficient alternative means of data transmission that has a data of 6.4 s, the integration of voice recognition technologies in this study facilitates more intuitive and accessible communication, which is crucial for people with disabilities.

The integration of speech recognition into the proposed system could further improve communication efficiency by eliminating the need for manual intervention, which could be crucial in emergencies where time is of the essence, and the person in need of assistance may be unable to manipulate a device. Additional data would be useful for further analysis, such as SMS sending success rate, speech recognition error rate, and comparison with other communication technologies used in emergency vehicles, such as radio communication systems or satellite communication systems.

The article [28] presents an innovative device that monitors the blood alcohol concentration and heart rate of drivers using advanced sensors and wireless communication technologies. Sensors are a fundamental part of data measurement and frequency monitoring, in this article, unlike the present article, monitors the distance in which one is about to suffer or suffered a collision from the most accurate data was detected at a distance of 100 cm from the surface where in a total of 7.4 seconds of reaction sends an alert message to a third party.

The results of the study show that the device achieves remarkable accuracy in measuring blood alcohol concentration and heart rate, with an average absolute error of 1.61 and a standard deviation that supports the reliability of the data obtained. The processed information is sent through the Node-RED platform for analysis and subsequent early warning in case of detecting dangerous levels of alcohol in the driver's blood. In addition, the importance of 5G network infrastructure to improve system performance in future deployments is highlighted.

In this article, measurements are noted, but through movement at the moment of suffering or about to have a collision, for example, when the circuit detects that it is falling at a distance of 75 cm measured towards the ground, it will issue a message with a total time of 6.25 seconds to send an emergency message to a predetermined contact, on the other hand, when it detects a distance of 112, it will send a warning message to the same intercom user after 8.4 seconds.

Based on voice recognition for vehicular emergency communication, it is compared with state-of-the-art solutions, such as biometric driver monitoring from article [28], highlighting its potential lower cost and ease of implementation. However, its limitations, such as speech recognition accuracy in noisy environments and its focus on post-accident communication, are discussed. Future research is required to improve speech recognition accuracy, integrate it with accident prevention systems, develop more intuitive user interfaces, and test it in real environments.

Both the paper [29] and this article measure the importance of instantaneous and accurate communication and signaling. In the case of vehicular intercoms with voice recognition technology, the goal is to speed up response in traffic emergencies, enabling interaction without requiring manual use and improving accessibility for people with disabilities. Similarly, the motion detection system with ultrasonic sensor HC-SR04 and Arduino seeks to control the capacity in closed environments, alerting in real time about the number of people present and helping to minimize the risk of contagion in closed spaces.

Vehicular intercoms with voice recognition, with state-of-the-art solutions, such as the HC-SR04 ultrasonic sensor motion detection system and Arduino from the article [29]. Both systems share the goal of improving emergency response through instant and accurate communication and signaling. While the system focuses on interaction through voice recognition, the article [29] focuses on capability control in closed environments.

In terms of cost, the proposed system could be more economical than other solutions involving more complex sensors and devices. In terms of accuracy, both systems aim for immediacy in response, although the accuracy of the proposed system will depend on the quality of speech recognition. In terms of implementation feasibility, the proposed system could be easier to integrate into existing vehicles.

In addition, both systems rely on data collection and analysis to improve decision-making. In the context of traffic accidents, the integration of sensors and proper programming allows for determining the distance at which the emergency signal will be activated, with the data obtained with all the simulations that have been performed when a vehicle is close to suffering a collision in a set range of 2-100 cm, a collision message will be executed and executed to a third party as "direct contact or emergency contact."

If a driver has a collision on a road, depending on the distance, the movement will be executed, for example, when the circuit detects the impact at 19 cm, the alert is executed to the nearest relative, friend at 2.86, and if it is only a movement, a caution message will be executed at 149 cm in a total time of 10. 6 seconds, or in another case at 105 cm with a total time of 8 cm, while, in capacity control, data analysis facilitates the display of the number of people present and counts if 10 people entered in an estimated time and alerts on the maximum allowed capacity.

However, common challenges are faced in terms of reliability and adaptability. While vehicular intercoms must be accurate and function in various environments and emergencies with accurate cm and message execution, capacity control systems must be able to operate in different tourist and cultural scenarios, complying with current social distancing rules.

The article [30], which presents a system for monitoring vehicular traffic using technological devices, offers a practical and economical solution for traffic management. The three-tier architecture, which includes a mobile tracking system, an information gathering system, and fog devices, provides a robust platform for recording and analyzing vehicle movement. The accuracy and effectiveness demonstrated by the system in a real-world environment, such as the city of Corfu, highlight its potential to be deployed in various cities to improve traffic management and develop intelligent traffic-related services.

It integrates voice recognition to improve emergency response and vehicular traffic management with the traffic monitoring system of the article [30]. Both share the goal of optimizing traffic management but differ in their approach. The proposed system focuses on communication in emergencies, while the article [30] uses technological devices to monitor traffic. In terms of cost, the proposed system could be more economical than that of the article [30]. In accuracy, both aim to improve efficiency, but the accuracy of the proposed system depends on voice recognition.

In terms of the feasibility of implementation, the proposed system could be easier to integrate into existing vehicles. However, the proposed system has limitations, such as the possible effect of ambient noise on speech recognition accuracy and its focus on post-accident communication. Future research is proposed to improve speech recognition accuracy, integrate the system with accident prevention technologies, develop more intuitive user interfaces, and test in real-world environments.

In the article, the measurement tables are obtained where you can see the time used and the distance to see if a collision is obtained or not and thus manage the traffic emergency, with a distance of 0.03 gives a time of 0.02 therefore, a collision is not opened, with a distance of 0.77 gives a time of 0.45 therefore here a collision will not be realized, nor an emergency message will be sent either. But you get 2.04; the time will take 1.2 where if a vehicular emergency message is sent.

The convergence of these technologies represents a significant advance in vehicle emergency management and traffic monitoring. The integration of advanced communication systems and technology solutions not only improves the effectiveness of response teams but also provides a flexible and accessible platform for managing traffic in real-time. Continued research and development in this field is essential to overcome current challenges and exploit the full potential of these innovations.

5. Conclusions. - The state-of-the-art analysis showed various technologies and components, which allowed us to conclude that the integration of advanced electronic circuits and specialized sensors in this system offers a superior solution in terms of efficiency and reliability. Unlike other systems studied, the proposed design not only ensures secure connections with emergency contacts but also optimizes the response capacity in dangerous situations, sending alerts more quickly and accurately. This advance represents a significant improvement over previous work, underlining the effectiveness of the system in user protection and safety and confirming its relevance and superiority in the context of emerging alert technologies.

The evaluation of the risk prevention circuit carried out through simulations confirmed that the system is effective in detecting falls and potentially dangerous situations. The ultrasonic sensor measures distances and detects collisions,

triggering alerts when predefined criteria are met. Table 1 shows that the system effectively detects collisions at distances ranging from 2.04 cm to 100.34 cm. In addition, simulations show that the system can issue preemptive warnings when it detects objects in a higher risk range, as detailed in Table 2, where distances range from 101.19 cm to 150.51 cm.

However, some limitations in the sensor's detection range were also identified. These limitations correspond to minimum and maximum distances outside the ranges established in the aforementioned tables. This finding underscores the importance of fine-tuning the system to improve its accuracy and ensure that alerts are issued effectively. Figures 19 and 21 show a trend line that shows the minimum distances, ranging from 0.02 cm to 1.96 cm, and the maximum distances, ranging from 151.36 cm to 177.72 cm, where it is shown that the system will not detect collisions or issue collision preventions.

The tests in Table 3 revealed the effectiveness of the emergency communication system based on distance detection. Data from the 50 tests showed that the total time from detection to sending an SMS varies significantly, from 1.8 seconds over very short distances to 10.6 seconds over longer distances. These results underscore the importance of response time in emergencies, where every second is crucial for user safety.

6. Recommendations. - The current system is effective in detecting risk situations and issuing the corresponding alarms. However, by expanding its design, the response to hazardous situations could be optimized. Considering that the SIM900l GSM module would cover up to 8 different contacts. This would make the system more versatile, increasing the likelihood of receiving a quick and appropriate response from multiple users and not specifically from one contact who might not be available at the time of the emergency.

To power the entire circuit through an external source, it is recommended to use a Power Bank that has a capacity of at least 10,000 mAh, with 5 V and 2 A output. This ensures an adequate and stable power supply for the correct operation of the circuit. The incorporation of other types of sensors, such as microphones, cameras, thermometers, ultrasound, proximity sensors, accelerometers, and gyroscopes, could offer new ways to improve the range and accuracy of the system.

In addition, new algorithms can be developed that transform the way data from different sensors is analyzed. This would help reduce false alarms and improve the system's ability to respond to truly emergent situations.

To adapt the vehicular emergency intercom system to blind people, proximity sensors could be integrated into the user's cane, in addition to an audio-guided function using voice recognition and audible notifications. These sensors would detect obstacles and nearby collisions, triggering audible alerts that provide information about the immediate environment.

The use of modern communication systems, such as 5G, would have a major impact on the clarity and speed of alert transmission. The speed of 5G connections would significantly outperform the 4G network, making it easier to send messages more efficiently. These aspects are crucial in hazardous environments where it is vital to address messages quickly to improve response. In addition, the system could automatically send emergency messages in the event of an accident. Benefits include greater autonomy and safety, as visually impaired people would be able to navigate more safely and receive immediate assistance in hazardous situations.

References

[1] M. A. Espinoza-Mina and A. M. Colina-Vargas, “Characterization of traffic accidents for urban road safety,” Revista Facultad de Ingeniería Universidad de Antioquia, Nov. 2023, https://doi.org/10.17533/udea.redin.20231134

[2] A. Carreras-Coch, J. Navarro, C. Sans, and A. Zaballos, “Communication Technologies in Emergency Situations,” Apr. 01, 2022, MDPI. https://doi.org/10.3390/electronics11071155

[3] M. J. Islam, M. N. Pathan, A. Sultana, and A. Rahman, “An IoT-Based Smart Helmet for Riding Security and Emergency Notification,” in Proceedings - 6th International Conference on Electrical Engineering and Information and Communication Technology, ICEEICT 2024, Institute of Electrical and Electronics Engineers Inc., 2024, pp. 1211–1216. https://doi.org/10.1109/ICEEICT62016.2024.10534489

[4] R. Subramaniyan, S. Kumuran, and J. Kathirvelan, “Smart Helmet System with Wireless Communication through GSM,” in 2024 3rd International Conference on Artificial Intelligence for Internet of Things, AIIoT 2024, Institute of Electrical and Electronics Engineers Inc., 2024. https://doi.org/10.1109/AIIoT58432.2024.10574693

[5] S. Goswami, S. Chakraborty, S. Laha, and A. Dhar, “Enhancement of GSM Security using elliptic curve cryptography algorithm,” in Proceedings - 3rd International Conference on Intelligent Systems Modelling and Simulation, ISMS 2012, 2012, pp. 639–644. https://doi.org/10.1109/ISMS.2012.137

[6] G. M. Debele and X. Qian, “AUTOMATIC ROOM TEMPERATURE CONTROL SYSTEM USING ARDUINO UNO R3 AND DHT11 SENSOR,” 2020.

[7] H. J. Santillán Carranza, J. O. Enríquez Sandoval, and J. F. Bonilla Castro, "Development of a Wireless Educational Tool Based on Raspberry Pi," INGENUITY, vol. 7, no. 1, pp. 13–22, Feb. 2024, https://doi.org/10.29166/ingenio.v7i1.5630

[8] B. MertArduino in CircuitsArduino, “Arduino-Ultrasonic Sensor HC-SR04 With Buzzer Introduction: Arduino-Ultrasonic Sensor HC-SR04 With Buzzer.” [Online]. Available: https://www.instructables.com/Arduino-Ultrasonic-Sensor-HC-SR04-With-Buzzer/

[9] C. Vidal-Silva, M. I. Lineros, G. E. Uribe, and C. J. Olmos, “Electronics for everybody using Arduino: Positive experience in the implementation of hardware-software solutions,” Technological Information, vol. 30, no. 6, pp. 377–386, 2019, https://doi.org/10.4067/S0718-07642019000600377

[10] J. A. Marín-Marín, P. A. García-Tudela, and P. Duo-Terrón, “Computational thinking and programming with Arduino in education: A systematic review for secondary education,” Heliyon, vol. 10, no. 8, p. e29177, Apr. 2024, https://doi.org/10.1016/J.HELIYON.2024.E29177

[11] H. Santillán, A. Mantilla, D. Cárdenas, and P. Wong, “Design of a low-cost portable electrocardiograph for telemedicine application,” Engineering Research Report, no. 26, pp. 244–264, Jul. 2024, https://doi.org/10.36561/ing.26.15

[12] M. Nayak and A. K. Dass, “GSM and Arduino based Smart Home Safety and Security System,” https://doi.org/10.5281/zenodo.7610756

[13] P. Jacko et al., “Remote IoT Education Laboratory for Microcontrollers Based on the STM32 Chips,” Sensors, vol. 22, no. 4, Feb. 2022, https://doi.org/10.3390/s22041440

[14] Arulkumar V., Kavin F., Arulkumar D., and Bharathiraja N., “IoT Sensor Data Retrieval and Analysis in Cloud Environments for Enhanced Power Management,” Journal of Advanced Research in Applied Sciences and Engineering Technology, vol. 45, no. 2, pp. 202–213, May 2024.

[15] A. M. Laukkanen, J. Horáček, and V. Radolf, “Buzzer versus water resistance phonation used in voice therapy. Results obtained with physical modeling,” Biomed Signal Process Control, vol. 66, p. 102417, Apr. 2021, https://doi.org/10.1016/J.BSPC.2021.102417

[16] M. P. Valente and I. B. De Paula, “Sensor based on piezo buzzers for simultaneous measurement of fluid viscosity and density,” Measurement, vol. 152, p. 107308, Feb. 2020, https://doi.org/10.1016/J.MEASUREMENT.2019.107308

[17] A. V. Rojas, J. G. Ibarra, A. Y. Nagano, and F. H. B. Santana, "Curing depth of pit and fissure sealants using diode (LED) emitted light at different distances," Mexican Dental Journal, vol. 19, no. 2, pp. 76–80, Apr. 2015, https://doi.org/10.1016/J.RODMEX.2015.05.002

[18] N. Babu Thomas, L. P. Kumar, J. James, and N. A. George, “Trends, progress and future directions of nanomaterial-based sensors: a bibliometric overview,” May 06, 2024, Emerald Publishing. https://doi.org/10.1108/SR-09-2023-0466

[19] M. Fernandez, C. Rodriguez, L. Alonso, and P. J. Oria, "Study of the Influence of Horn Geometry on Radiation Axis Gain of Ultrasonic Sensors in Air," Ibero-American Journal of Automation and Industrial Informatics RIAIVol. 10 No. 4 pp. 441–452, OCT. 2013.

[20] R. Ceres, J. M. Martín, L. Calderón, T. Freire Bastos, and M. Armada, “Environment recognition in welding processes by ultrasonic sensors,” Sens Actuators A Phys, vol. 37–38, no. C, pp. 635–638, Jun. 1993, https://doi.org/10.1016/0924-4247(93)80108-S

[21] L. F. Macea-Mercado, L. Morales, and L. G. Márquez-Díaz, "A Pavement Management System Based on New Technologies for Developing Countries," Engineering, Research and TechnologyVol. 17 No. 2 pp. 223–236, APR. 2016.

[22] N.-P. Ricardo Francisco, "The crest factor trend helps to detect nascent events; electronic circuit, programs, and applications to signals from various fields," Engineering, Research and Technology, vol. 15, no. 1, pp. 63–81, Jan. 2014, https://doi.org/10.1016/S1405-7743(15)30007-X

[23] M. Lohakan and C. Seetao, “Large-scale experiment in STEM education for high school students using artificial intelligence kit based on computer vision and Python,” Heliyon, Vol. 10, No. 10, p. A31366, May 2024.

[24] L. F. Macea-Mercado, L. Morales, and L. G. Márquez-Díaz, "A Pavement Management System Based on New Technologies for Developing Countries," Engineering, Research and TechnologyVol. 17 No. 2 pp. 223–236, APR. 2016.

[25] C. Hurtado, G. Licea, M. García-Valdez, A. Quezada, and M. Castañón-Puga, “Teaching computer programming as a well-defined domain for beginners with protoboard,” in Advances in Intelligent Systems and Computing, Springer, 2020, pp. 262–271. https://doi.org/10.1007/978-3-030-45691-7_25

[26] A. Y. F. Zhu, “Optimizing financial decision-making for emerging adults: A compact Python-based personalized financial projection approach,” Technol Soc, vol. 77, p. 102599, Jun. 2024, https://doi.org/10.1016/J.TECHSOC.2024.102599

[27] M. Lohakan and C. Seetao, “Large-scale experiment in STEM education for high school students using artificial intelligence kit based on computer vision and Python,” Heliyon, Vol. 10, No. 10, p. A31366, May 2024.

Author contribution:
1. Conception and design of the study
2. Data acquisition
3. Data analysis
4. Discussion of the results
5. Writing of the manuscript
6. Approval of the last version of the manuscript

HS has contributed to: 1, 2, 3, 4, 5 and 6.
CL has contributed to: 1, 2, 3, 4, 5 and 6.
KG has contributed to: 1, 2, 3, 4, 5 and 6.
DC has contributed to: 1, 2, 3, 4, 5 and 6.

Acceptance Note: This article was approved by the journal editors Dr. Rafael Sotelo and Mag. Ing. Fernando A. Hernández Gobertti.

Explorando las Profundidades: Reconstrucción de Cuevas y Detección de Murciélagos mediante Imágenes Infrarrojas

Exploring the Depths: Cave Reconstruction and Bat Detection Using Infrared Imaging

Explorando as Profundezas: Reconstrução de Cavernas e Detecção de Morcegos Usando Imagens Infravermelhas

Israel Cruz Rangel[1(*)], José-Ángel Arroyo-Romero [2], Isabel Bárcenas-Reyes[3], José-Joel González-Barbosa[4], Juan Bautista Hurtado-Ramos[5], Francisco-Javier Ornelas-Rodríguez[6], Alfonso Ramírez-Pedraza[7]

Recibido: 11/10/2024 Aceptado: 26/01/2025

Resumen. - Nuestro objetivo es proporcionar información detallada y precisa sobre las cuevas y la dinámica de la población de quirópteros (murciélagos) que las habitan nos permite comprender las dimensiones y requerimientos del hábitat, monitorear tamaños de poblaciones, desarrollar planes de manejo y conservación específicos. Por tanto, aumentamos nuestro entendimiento de los murciélagos con su entorno y mejoramos la prevención de enfermedades zoonóticas. En este artículo presentamos el desarrollo de una plataforma portátil multisensor, compuesta por una cámara RGB, dos cámaras infrarrojas, sensores inerciales y un par de luces infrarrojas. Esta plataforma permite la detección de quirópteros y la reconstrucción de las cuevas donde habitan. Ejecuta un algoritmo en tiempo real, generando un mapa de nube de puntos y facilitando la observación y detección de los quirópteros. La plataforma fue probada en condiciones reales en diferentes cuevas del estado de Guanajuato por personal del "Comité Estatal para el Fomento y la Protección Pecuaria".

Palabras clave: murciélago, reconstrucción 3D, YOLO, conteo automático.

(*) Autor de correspondencia

[1] Maestría en Tecnología Avanzada, Instituto Politécnico Nacional, México, icruzr1900@ipn.alumno.mx, ORCID iD: https://orcid.org/0009-0002-9112-7025

[2] Maestría en Tecnología Avanzada, Instituto Politécnico Nacional, México, jarroyor2100@alumno.ipn.mx, ORCID iD: https://orcid.org/0009-0004-9185-4307

[3] Doctorado en Educación de Facultad de Ciencias Naturales, Universidad Autónoma de Querétaro, México, ibr.mvz@hotmail.com, ORCID iD: https://orcid.org/0000-0001-8386-6560

[4] Doctorado en Ciencias de la Computación y Telecomunicaciones, Instituto Politécnico Nacional, México, jgonzalezba@ipn.mx, ORCID iD: https://orcid.org/0000-0002-6720-8282

[5] Doctorado en Óptica, Instituto Politécnico Nacional, México, jbautistah@ipn.mx, ORCID iD: https://orcid.org/0000-0003-2663-2463

[6] Doctorado en Óptica, Instituto Politécnico Nacional, México, fornelasr@ipn.mx, ORCID iD: https://orcid.org/0000-0003-2465-188X

[7] Doctorado en Tecnología Avanzada, Secretaría de Ciencia, Humanidades, Tecnología e Innovación SECIHTI, México, aramirez_ixm@ipn.mx, ORCID iD: https://orcid.org/0000-0003-0366-6249

Memoria Investigaciones en Ingeniería, núm. 28 (2025). pp. 110-125
https://doi.org/10.36561/ING.28.9
ISSN 2301-1092 • ISSN (en línea) 2301-1106 – Universidad de Montevideo, Uruguay

Summary. - *Our objective is to bring detailed and precise information about caves and the bat's population dynamics which allows to comprehend the habitat's shapes and dimensions, monitor population size, and development of conservation and specific control plans. And facilitate the study of the relations between bats and their environment. Thus, increasing prevention and understanding of zoonotic diseases. In this article we present the development of a portable multi-sensor platform, integrated by a RGB depth camera, two Infra-Red (IR) cameras, and IR illuminators. With an autonomy of two hours. This platform can detect chiroptera (bats) and reconstruct their nesting caves. Performing real time algorithm, to transform the caves into a point cloud, helping in observation and detection of chiroptera. This platform was tested in real conditions with different caves of the Guanajuato state by the personnel of "Comité Estatal para el Fomento y la Protección Pecuaria".*

Keywords: *Bat, 3D reconstruction, YOLO, Automated Counting.*

Resumo *.* ***-*** *Nosso objetivo é trazer informações detalhadas e precisas sobre cavernas e a dinâmica populacional de morcegos, o que permite compreender as formas e dimensões do habitat, monitorar o tamanho populacional e desenvolver planos de conservação e controle específicos. E facilitar o estudo das relações entre morcegos e seu ambiente. Assim, aumentando a prevenção e a compreensão de doenças zoonóticas. Neste artigo, apresentamos o desenvolvimento de uma plataforma multissensor portátil, integrada por uma câmera de profundidade RGB, duas câmeras de infravermelho (IR) e iluminadores IR. Com autonomia de duas horas, esta plataforma pode detectar quirópteros (morcegos) e reconstruir suas cavernas de nidificação. Executando um algoritmo em tempo real, para transformar as cavernas em uma nuvem de pontos, auxiliando na observação e detecção de quirópteros. Esta plataforma foi testada em condições reais com diferentes cavernas do estado de Guanajuato pelo pessoal do "Comité Estatal para o Fomento e a Proteção Pecuária".*

Palavras-chave: *Morcego, reconstrução 3D, YOLO, Contagem Automatizada.*

1. Introducción. - El estudio de quirópteros abarca diversos aspectos biológicos utilizados para el desarrollo de la humanidad como la medicina, modelos bio-inspirados en áreas como la robótica [1] y ecológicos como las cadenas tróficas, los ciclos de polinización [2] y como reservorios microbiológicos. a Los quirópteros intervienen en numerosos ciclos biológicos. Los quirópteros en ocasiones son los únicos polinizadores de varias especies de plantas [3]. Es conocido que los quirópteros usan refugios artificiales como túneles, puentes y minas abandonadas, así como los huecos de los árboles [4]. Sin embargo, algunos estudios ecológicos han demostrado que las características del refugio artificial suelen ser no aptas para la supervivencia de sus colonias, lo cual representa una desventaja para su ciclo reproductivo [5]. Las cuevas son refugios naturales que cuentan con la temperatura y humedad favorable para la supervivencia de los quirópteros, por lo que son hábitats clave para muchas especies de murciélagos durante el tiempo de crianza [6]. En la reciente década y más aún derivado de la pandemia COVID-19, estudiar el estado actual de conservación y las tendencias de población de los quirópteros representa un desafío, principalmente en sus refugios naturales que son entornos de investigación valiosos para mejorar la comprensión sobre la ecología, comportamiento, fisiología y evolución de estas especies y su biodiversidad [7]. Este monitoreo se dificulta más debido a que este tipo de refugios son oscuros y poseen escondrijos, como grietas, cavidades, rocas y paredes con poca inestabilidad estructural, lo que limita el acceso del personal de vigilancia epidemiológica de enfermedades transmitidas por vectores y del personal operativo de vigilancia para la preservación y conservación de los murciélagos. Esto es un factor condicionante para la planificación de las estrategias diagnósticas, preventivas y de control de enfermedades en la salud humana y animal, principalmente la de fauna silvestre como los murciélagos de México [6].

En la reciente década y más aún derivado de la pandemia COVID-19, estudiar el estado actual de conservación y las tendencias de población de los quirópteros representa un desafío, principalmente en sus refugios naturales que son entornos de investigación valiosos para mejorar la comprensión sobre la ecología, comportamiento, fisiología y evolución de estas especies y su biodiversidad [7]. Este monitoreo se dificulta más debido a que este tipo de refugios son oscuros y poseen escondrijos, como grietas, cavidades, rocas y paredes con poca inestabilidad estructural, lo que limita el acceso del personal de vigilancia epidemiológica de enfermedades transmitidas por vectores y del personal operativo de vigilancia para la preservación y conservación de los murciélagos. Esto es un factor condicionante para la planificación de las estrategias diagnósticas, preventivas y de control de enfermedades en la salud humana y animal, principalmente la de fauna silvestre como los murciélagos de México [6]. El monitoreo de los quirópteros y los tipos de refugios que habitan puede ser optimizado con el uso de técnicas de reconstrucción tridimensional como herramientas de planificación de la conservación útiles para detectar refugios naturales con las características estructurales óptimas para el establecimiento o hábitat potencial para los quirópteros [8]. Por ejemplo, el trabajo presentado en [9] muestra cómo se pueden implementar soluciones más tecnificadas a estas problemáticas.

En [10] presentan un estudio tridimensional de cuevas en la naturaleza, los autores buscan la adquisición simplificada de la topografía de cuevas comparando un escáner láser terrestre, un portátil basado en SLAM y una cámara fotográfica. En [11] muestran la importancia de la investigación de cuevas. Los esfuerzos cartográficos tradicionales consumen mucho tiempo y son subjetivos, motivando el desarrollo de técnicas utilizando escáneres terrestres y sistemas LiDAR móviles para la generación de mapas precisos similares a la cartografía tradicional. En [12] muestran dispositivos móviles autónomos en entornos confinados, sistemas de túneles subterráneos y cuevas. Los escenarios sin GPS, requieren técnicas de mapeo foto realistas, realizando simulaciones con un sistema de túneles subterráneos realistas y en escenarios representativos del mundo real. Algunos trabajos realizan aplicaciones terrestres subterráneas y marinas como muestra algunos trabajos realizan aplicaciones terrestres subterráneas y marinas como muestra en [13] evalúa un sistema portátil de mapeo con LiDAR, llamado PoLiMap, que usa un sensor Livox Avia y un algoritmo modificado de FAST-LIO-SLAM. Usado para aplicaciones de entornos como túneles, muestran la importancia y aplicaciones de este tipo de mapas. En [14] presenta el levantamiento arqueológico de una cueva subterránea mediante mapeo tridimensional utilizando 62 escaneos TLS, generando 1.5 mil millones de puntos, y se utilizó el algoritmo Poisson para reconstruir el modelo 3D. utilizando la nube de puntos para un análisis detallado de interés arquitectónico. En [15] presenta el diseño, implementación de un sistema para explorar minas subterráneas inundadas. Utilizando un mapa topológico generado por un módulo de SLAM. Dado que el mapa puede contener errores e incertidumbres, se define una métrica de distancia para la correspondencia de nodos, permitiendo al robot localizarse y moverse en el mapa.

La visión por computadora ha incrementado notablemente su potencial debido a los avances en aprendizaje automático, convirtiéndose en una herramienta cada vez más utilizada por biólogos e investigadores para el estudio de poblaciones animales. Por ejemplo, investigadores en Israel han implementado esta tecnología para contabilizar el número de grullas comunes, utilizando imágenes termográficas captadas desde vehículos aéreos no tripulados (UAVs) [16]. El plumaje de las grullas, al presentar una reflectividad distinta a los cultivos circundantes facilita el conteo mediante el procesamiento de imágenes en infrarrojo lejano (TIR) antes de ser analizadas por la red neuronal YoLo V3. Aunque nuestro enfoque es similar, existen diferencias notables en cuanto al tipo de fauna estudiada y la metodología aplicada. Las grullas son animales de mayor tamaño, y no se ven afectadas significativamente por la presencia de los UAVs, los murciélagos que son objeto de nuestro estudio, su comportamiento se ve alterado ante la presencia de estos dispositivos.

Por otro lado, otro grupo de investigadores ha utilizado imágenes termográficas TIR para observar primates en las copas de los árboles, quienes son visibles debido a la temperatura de sus cuerpos [17]. Este método muestra la utilidad de estudiar la fauna mediante tecnología avanzada, aunque resaltamos que el uso de equipos TIR es considerablemente más costoso en comparación con los equipos NIR más económicos, como las Arducam IR que emplea nuestro sistema.

Un estudio realizado en Nebraska, Estados Unidos, por Hu et al. aborda la complejidad del uso de técnicas de visión por computador y aprendizaje automático para el estudio de ecosistemas, centrándose específicamente en aves de estuario [18]. Este estudio es particularmente interesante debido a su enfoque en el desarrollo de software destinado a facilitar la utilización de la visión por computadora a investigadores de vida silvestre, implementando tecnologías de etiquetado automático y la detección de áreas extensas. Sin embargo, los autores concluyen que es posible que su tecnología no funcione con la misma precisión en diferentes escenarios.

Una aplicación de software para el conteo de murciélagos desarrollada en MatLab fue presentada por Bentley et al. [19]. Sin embargo, esta herramienta también se basa en la colocación de una cámara de imágenes termografías (TIR) en una posición fija, operando bajo el supuesto de que los murciélagos cruzarán su campo visual. McFarlane [20] hace un estudio sobre las poblaciones de murciélagos en las cuevas de Guangtong en Borneo. McFarlane escoge específicamente dichas cuevas porque había estudios previos en ellas, realizan escaneos 3D de las cavernas con un equipo FARO. A partir de estimar el número de murciélagos que pueden estar presentes en función de la densidad de murciélagos por unidad de área, y luego multiplicar esta densidad por el área o volumen total del refugio. También implica contar el número de murciélagos que salen de un refugio. Generalmente, los observadores cuentan manualmente los murciélagos que salen en un periodo de tiempo determinado y luego extrapolan para estimar el tamaño total de la colonia.

Los investigadores en [21] han desarrollado un sistema automatizado de respuesta conductual que integra experimentos de reproducción sonora en estudios con cámaras trampa, las cuales se activan mediante un sensor de movimiento. Esta estrategia, que también activa bocinas, es crucial para observar el comportamiento de los animales salvajes ante sonidos asociados a la caza furtiva, representando una excelente estrategia de ahorro de baterías. En [22] proponen un diseño de hardware específico para el estudio de libélulas en cuerpos de agua, utilizando cámaras trampa centradas en estructuras como postes, facilitando la observación de animales pequeños y rápidos. Esta tecnología es relevante para entender el desempeño de cámaras trampa en la detección de animales pequeños y escurridizos, como los murciélagos, dado que ambos comparten la dificultad de ser detectados debido a su reducido tamaño. En cuanto al conteo de quirópteros, en [23] han diseñado un dispositivo que produce barreras de luz infrarroja, situadas en las oquedades que permiten el ingreso y salida de los murciélagos de sus refugios. Este estudio, realizado en Alemania, se centró en poblaciones hibernantes, una condición que no se aplica a las especies de nuestro estudio, como Desmodus rotundus. Además, el uso de estas barreras luminosas exige un equipo que pueda cubrir completamente la entrada del refugio y que sea adaptable a las variaciones de cada uno, especialmente en entornos silvestres.

Las cámaras tradicionales que proporcionan imágenes RGB presentan problemas de adquisición en el hábitat natural de los quirópteros, ya que estas cámaras tradicionales no funcionan eficazmente en escenarios con ausencia de luz. El uso de sistemas combinados como las cámaras de infrarrojas pueden proporcionar una respuesta en entornos visuales desafiantes. La detección de quirópteros, así como la reconstrucción de las cuevas que son habitadas por estos mamíferos exige que el equipo sea liviano, compacto y portátil.

Este estudio propone un sistema autónomo, ligero y fácil de transportar que cuente con dos funcionalidades principales: 1) la adquisición de imágenes infrarrojas para la detección de murciélagos y 2) la reconstrucción tridimensional de su hábitat que destaque por su capacidad para generar mapas virtuales sin necesidad de referencias.

1.1 Objetivos. -

- Evaluar la efectividad de una cámara infrarroja (IR) en expediciones en cuevas y otros espacios naturales para la detección de quirópteros.
- Obtener imágenes infrarrojas (IR) que puedan ser utilizadas en el entrenamiento de redes neuronales para el conteo automático de quirópteros.
- Obtener imágenes de profundidad que posibiliten la realización de reconstrucciones tridimensionales de las cuevas habitadas por quirópteros.

Dentro de este trabajo, la pregunta de investigación que respondemos es la siguiente: ¿Cómo pueden las tecnologías de imagen infrarroja y de profundidad, junto con redes neuronales, mejorar la detección, monitoreo y modelado de los hábitats de quirópteros en cuevas y otros espacios naturales, asegurando una tasa de detección correcta mínima del 85% en condiciones de funcionamiento?

2. Desarrollo. -

2.1 Descripción del área de estudio. - Un desafío importante en el estudio de cuevas habitadas por quirópteros es la capacidad de acceder a ellas. En el municipio de Xichú en el estado de Guanajuato, México. El Comité Estatal para el Fomento y Protección Pecuaria responsables del control biológico de estas especies necesitan caminar grandes distancias de hasta 14 km, como se muestra en la Figura XII. Regularmente el personal carga con redes de niebla, equipo de seguridad, por lo que el peso del equipo es una condicionante importante. Por esta razón el equipo proporcionado debe ser un sistema de adquisición pequeño, estable y de poco peso que faciliten el trabajo del personal.

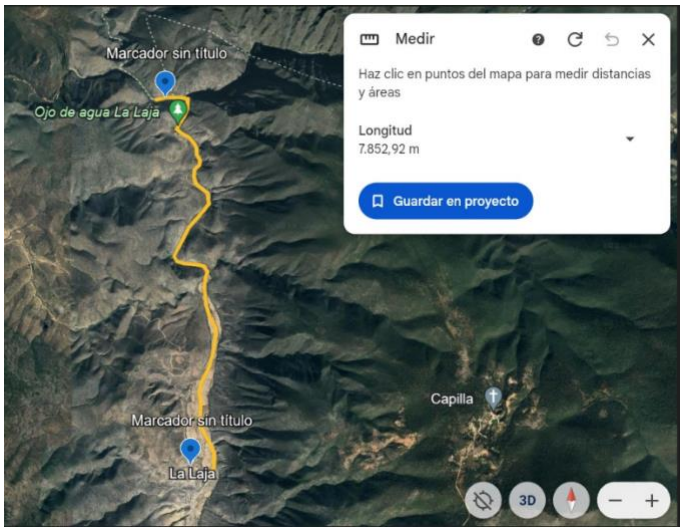

Figura I. Recorrido realizado para llegar al nicho de los murciélagos desde el ultimo acceso vehicular y hasta la entrada a la cueva con la ayuda de un mapa de Google.

Los refugios de anidación de los murciélagos son en su mayor parte de difícil acceso. Aunque se trata en algunos casos de excavaciones a pie de carretera, principalmente minas abandonadas, también hay minas muy internadas en zonas naturales. Muchas veces hay que atravesar caminos irregulares, así como obstáculos peculiares, llámense ríos, arenales, formaciones rocosas, maleza, entre muchos otros. Así mismo, cuando se trata de excavaciones mineras la orografía dentro de las cuevas suele ser bastante transitable. Pero en ocasiones nos topamos con túneles, rocas afiladas y caminos sinuosos e irregulares (ver Figuras II y XII). En el caso de esta expedición, nos topamos además con condiciones de alta humedad en las cuevas, y calor sofocante, por lo que el equipo a utilizar opera correctamente en esas condiciones. El equipo debe estar protegido para soportar golpes y pinchazos puesto que en determinadas zonas de la cueva los espacios son sumamente reducidos, como se muestra en la Figura III. Utilizando un equipo de adquisición equipado con una cámara de profundidad para una reconstrucción tridimensional, un par de cámaras infrarrojas para la detección de quirópteros, un par de luces IR (infrarrojo) proyectando hacia adelante y hacia arriba y sensores inerciales. El estudio de cuevas requiere atención y es peligroso debido al riesgo de lesiones al operar en la oscuridad y la inestabilidad estructural del entorno. Este trabajo compacta las necesidades de realizar observaciones de quirópteros con el análisis del entorno obteniendo un mapa tridimensional de dimensiones conocidas de una cueva, así como la detección de especies que en esta habitan.

Figura II Imágenes de la orografía de Xichú hacia la cueva

Figura III. Las imágenes muestran ejemplos de las condiciones de trabajo dentro de las cuevas de Xichú

2.2 Materiales. - Para el desarrollo de este trabajo construimos un sistema portátil. Se utilizó una estructura equipada con una cámara Intel D435i (es una cámara estereoscópica utiliza dos sensores de profundidad y una cámara RGB para capturar imágenes tridimensionales e IMU integrada). La cámara estereoscópica tiene una resolución de hasta 1280x720 y puede alcanzar hasta 90 FPS en modo de profundidad y hasta 30 fps en modo RGB. La arquitectura multisensor propuesta también cuenta con dos cámaras IR que se conectan a través de un puerto USB 3.0. con una configuración estereoscópica para la detección de quirópteros. Al sistema portátil le incluimos un par de luces infrarrojas. El sistema cuenta con un mini pc Intel i7 a .3.6 GHz con 16 g de memoria RAM con un sistema operativo Ubuntu 20.04 utilizando el entorno de trabajo de ROS (*Robot Operating System*). ROS es una modular que permite crear componentes de software para diferentes tareas, los nodos de software se ejecuten de manera independiente y se comunican entre sí de manera eficiente. La imagen mostrada en la Figura IV muestra un esquema de nuestro sistema. El dispositivo funciona con un banco de energía portátil, asegurando hasta 2 horas de uso continuo. El peso total del dispositivo es 3 kilogramos, y está diseñado para ofrecer adaptabilidad, puede integrar sensores adicionales como se muestra en la Figura. La Figura V muestra la arquitectura propuesta, los componentes utilizados son:

- Monitor touch screen. Esta pantalla nos permite a través del tacto, seleccionar una de las dos funcionalidades propuestas, además de visualizar en tiempo real los resultados tanto de la grabación de imágenes infrarrojas o la reconstrucción tridimensional de la caverna
- Cámara de profundidad D435i. Es una cámara de profundidad que combina sensores IR, una cámara RGB de alta resolución y una unidad de medición inercial (IMU) para capturar datos tridimensionales. Proporciona información detallada de profundidad y movimiento en tiempo real, (ver Figura VI(a)).
- Iluminación IR. La iluminación infrarroja permite iluminar los objetos dentro de la cueva, asegurando que los tipos de objetos sean visibles en la imagen infrarroja capturada con la mejor calidad posible. • Cámaras NIR. El sistema cuenta con un par de cámaras NIR, que nos permiten capturar imágenes en entornos oscuros, como cuevas, sin necesidad de iluminación en el rango visible.
- Convertidor. El sistema de alimentación es de corriente continua (DC) a 12 voltios. Sin embargo, algunos dispositivos funcionan con este voltaje, otros, como la PC, requieren 19 voltios. El convertidor nos permite realizar las adaptaciones de voltaje necesarios.
- Tres bancos de baterías. Las baterías utilizadas son de litio. Un banco de baterías alimenta el sistema de iluminación infrarroja, otro banco suministra energía a la PC, y el último se encarga del monitor. Es importante destacar que el sistema una vez configurado puede funcionar sin necesidad de conectar el monitor.
- PC.: Un equipo de cómputo responsable de almacenamiento y procesamiento de la información adquirida por los sensores, equipada con un procesador AMD Ryzen 7 3750H y 16 GB DDR4 con un sistema operativo Linux.

Figura IV Principales componentes del sistema

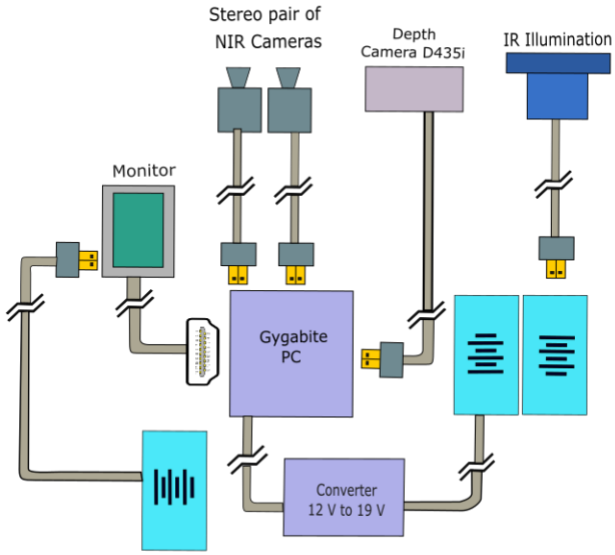

Figura V. Sistema de mapeo tridimensional y detección de Quirópteros

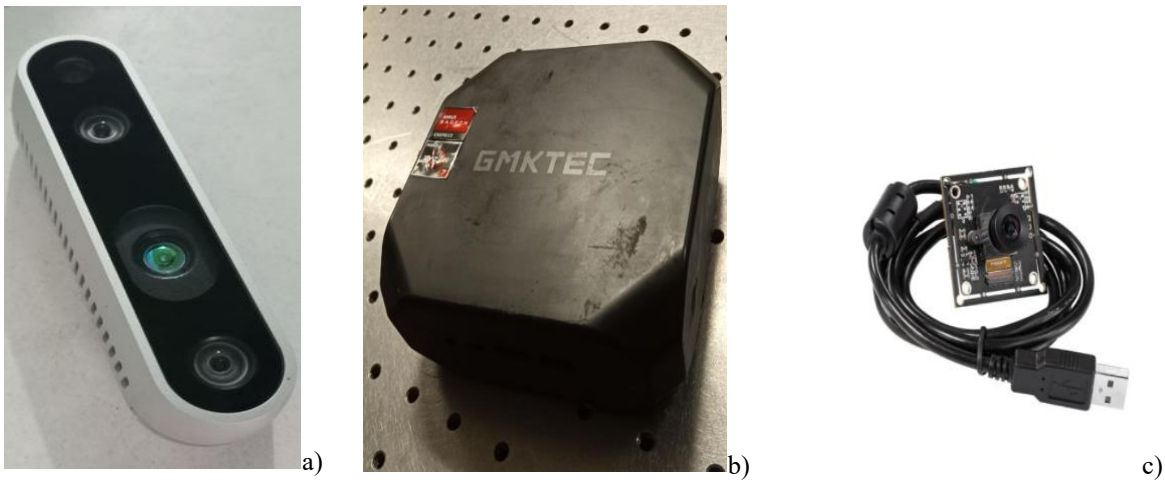

a) b) c)

Figura VI. Principales componentes del sistema a) cámara de profundidad que combina sensores IR, una cámara RGB de alta resolución y una unidad de medición inercial (IMU) para capturar datos tridimensionales. b) muestra una computadora GMXTEC con un procesador AMD Ryzen 7 3750H y 16 GB DDR4 con un sistema operativo Linux.

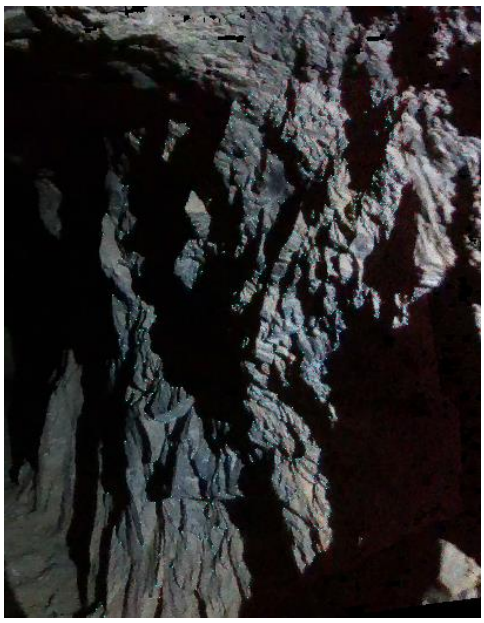

Figura VII. Posiciones de descriptores, puntos en verde, generados para la reconstrucción 3D. Un descriptor en una imagen es una representación matemática de características visuales específicas que permite identificar y comparar partes de la imagen.

2.3 Métodos. - Los métodos seleccionados para el análisis de imágenes fueron elegidos por su afinidad con los sensores utilizados. El Algoritmo 1 describe las etapas de la adquisición de los datos hasta la reconstrucción y detección de quirópteros en cuevas.

La cámara Intel RealSense D435i se calibra utilizando el software Intel RealSense SDK (*Software Development Kit*). La calibración se compone de dos etapas: la calibración intrínseca y extrínseca. La calibración intrínseca corrige las características geométricas y ópticas de la cámara y calibración extrínseca determina la relación espacial entre la cámara y otros sensores o dispositivos lo que garantiza que los datos de la cámara y los sensores estén correctamente alineados. Se capturan imágenes de patrones de calibración del tipo tablero de ajedrez identificado bordes y esquinas. Esto permiten hacer una comparación entre el plano imagen obtenida por la cámara a partir de mundo real. Mientras para los parámetros extrínsecos se realizan rotaciones controladas variando los ángulos del patrón, permitiendo encontrar relaciones de posición en el mundo con las imágenes obtenidas. Para la calibración extrínseca el software de RealSense procesa la información y ajusta para mejorar la precisión y la calidad de los datos capturados.

La reconstrucción 3D es una técnica utilizada para reconstruir un entorno tridimensional a partir de estimar la posición y orientación de una cámara, cambiando la perspectiva con una secuencia de imágenes extraídas a partir de las poses de la cámara. Mediante la calibración de la cámara es posible determinar la posición de la cámara en el mundo a partir de la superposición de fotogramas utilizando como referencia los puntos de interés en las imágenes llamados descriptores. El descriptor en un fotograma es un conjunto de píxeles con valores específicos. Las posiciones de los píxeles en la imagen se utilizan para comparar las intensidades y buscar coincidencias entre fotogramas consecutivos. Posteriormente, se optimiza la nube de puntos utilizando un punto en profundidad proporcionado por la cámara infrarroja, aplicando el método de Levenberg-Marquardt para actualizar la posición de la cámara. En la Figura VII se muestran los descriptores generados sobre la superficie de la cueva.

Para la reconstrucción del entorno tridimensional se realiza lo siguiente: Se captura información de la cámara infrarroja y los sensores inerciales mientras se desplaza el sistema por la cueva por la cueva. Se utilizan herramientas de software como OpenCV, para escalar la imagen. También se utiliza la biblioteca realsense2 para generar descriptores a partir de las esquinas y bordes para poder encontrar las relaciones entre fotogramas consecutivos conociendo. Utilizando los parámetros intrínsecos de la cámara infrarroja, podemos encontrar la dirección de cada descriptor en el mundo real. Los descriptores extraídos tienen como particularidad que puede identificar el mismo descriptor en adquisiciones consecutivas. La identificación del mismo descriptor en dos admisiones consecutivas nos permite calcular la coordenada en profundidad para generar una nube de puntos tridimensional donde D es un valor en profundidad que corresponde a las coordenadas (x, y) consideradas como coordenadas del plano imagen en píxeles como se muestra a continuación (D(x, y)). La ecuación 1 muestra las relaciones entre estos tres parámetros permitiendo un punto que en conjunto formará la nube de puntos que permite reconstruir el objeto tridimensional Punto es = (X, Y, Z).

$$X = \frac{x - c_x \cdot D(x,y)}{f_x}, \qquad Y = \frac{y - c_y \cdot D(x,y)}{f_y}, \quad Z = D(x,y)$$

Los siguientes algoritmos describen la funcionalidad del software desarrollado en el prototipo

Algoritmo 1 Algoritmo de reconstrucción de cuevas y adquisición de datos para el conteo de quirópteros

init ← Encendido de la computadora
while batería OK o Computadora encendida do
    Opción ← Selección reconstrucción 3D o detección de quiópteros
    if Opción = reconstrucción 3D then
        3D_RECONSTRUCTIÓN() usando SLAM (ver algoritmo 2)
    else
        MURCEILAGOS_DETECCIÓN() (ver algoritmo 3)
    end if
    end ← parar el proceso
end while

Algoritmo 2 3D_RECONSTRUCTIÓN. SLAM usando Descriptores de Imágenes Infrarrojas

M ← Inicializar mapa vacío
x_0 ← Inicializar posición inicial de la cámara
Obtener la primera imagen infrarroja I0 y extraer descriptores D0
Guardar D_0 en M
for cada iteración t **do**
    Capturar nueva imagen infrarroja I_t
    Extraer descriptores D_t de la imagen I_t
    Estimación de Movimiento:
    Usar el sistema inercial y sensores del sistema construido para estimar el movimiento $\hat{x}_t$
    Asociación de Características:
    Comparar los descriptores D_t con los descriptores guardados en M
    Si se encuentran características coincidentes, actualizar posición estimada del sistema construido x_t
    Actualización del Mapa:
    if nuevas áreas no mapeadas son observadas **then**
        Actualizar el mapa M con los nuevos descriptores D_t

        Corrección de la Trayectoria:
        Usar técnicas de optimización (Filtro de Kalman) para corregir la estimación de la trayectoria del sistema construido x_t
    end if
end for
Retornar mapa final M y trayectoria estimada del sistema construido

Algoritmo 3 MURCEILAGOS_DETECCIÓN. Reforzamiento del aprendizaje y detección de murciélagos en imágenes infrarrojas con YOLO

Inicializar modelo YOLO preentrenado *model*
Definir porcentaje de imágenes infrarrojas con murciélagos etiquetados para entrenamiento p_{train} y detección p_{detect}
Cargar conjunto de imágenes infrarrojas con murciélagos etiquetados *infrared_dataset*
División del Conjunto de Datos:
Dividir infrared_dataset en train_set y detect_set según ptrain y pdetect:
train_set ← ptrain × infrared_dataset
detect_set ← pdetect × infrared_dataset
Entrenamiento del Modelo:
for cada imagen I en train_set do
    Obtener la anotación de murciélagos para I
    Usar I y su anotación para entrenar el modelo YOLO
    Actualizar pesos del modelo *model*
end for
Detección de Murciélagos en Imágenes Infrarrojas:
Inicializar contador de imágenes con murciélagos detectados correct_detections = 0
Inicializar contador total de imágenes procesadas total_infrared_images = 0

17: **for** cada imagen infrarroja Iir en detect_set **do**
18: Obtener predicciones de YOLO sobre I_{ir}
19: **if** YOLO detecta murciélagos en I_{ir} then
20: Incrementar correct_detections
21: **end if**
22: Incrementar total_infrared_images
23: **end for**
24: **Evaluación de Resultados:**
25: Calcular la tasa de detección como:

$$Detection\ Rate\ = \frac{correct\ detections}{total\ infrared\ images}$$

26: Retornar *Detection Rate* como métrica de detección en imágenes infrarrojas

2.4 Resultados. - En esta sección se muestran los resultados generados del escaneo tridimensional de la cueva y la detección automática de murciélagos. El escaneo permite reconstruir el interior de la cueva, ofreciendo ventajas para los interesados en control y preservación de los quirópteros. Por ejemplo, permite explorar el refugio desde cualquier parte del mundo de forma virtual. El mapeo se genera a partir de una nube de puntos extraída de los fotogramas en tiempo real, se aportan las propiedades de textura y dimensiones. La Figura VIII muestra la reconstrucción basada en una nube de puntos a partir de los fotogramas obtenidos, en ella se muestra una textura bastante buena que permite al usuario darse una idea de lo accidentada que puede estar la cueva, así como las herramientas que podrían implementarse como las redes de niebla por mencionar alguna. En el caso de la imagen, se observa un terreno transitable que permitiría desplazarse de forma convencional manteniendo precauciones en el uso de equipo de protección personal, como cascos para evitar golpes y guantes derivados de la proximidad de las paredes al extraer las dimensiones de la cueva.

La reconstrucción del entorno virtual permite no solo conocer las dimensiones internas de los túneles habitados por quirópteros, también permite conocer algunas características en el que se encuentran los quirópteros, así como conocer las posibles rutas internas e incluso establecer el recorrido óptimo ya que muchos de estos lugares se encuentran conectaos entre sus túneles. La Figura IX muestra la cueva sobre un mallado de un metro por un metro permitiendo encontrar la longitud de la cueva explorado aproximadamente 17 m de longitud. A partir del escaneo de la nube de puntos procesada hemos reconstruido el mapa 3D que contiene un total de 74 fotogramas a partir de imágenes RGB sobrepuestas con la misma cantidad de imágenes IR. El tiempo de procesamiento fuera de línea de aproximadamente 15 segundos.

La Figura X es un ejemplo de imágenes adquiridas por el sistema, se llevó fuera de línea un reforzamiento con YOLO como se muestra en el algoritmo 3. El porcentaje de detección (Detection_rate) es de 70%.

Figura VIII. Reconstrucción 3D de las cuevas

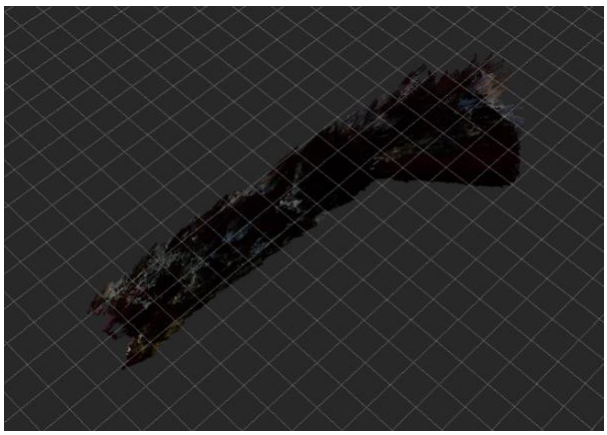

Figura IX. Cueva montada sobre un mallado de 1 m x 1 m a partir de los parámetros extrínsecos e intrínsecos de la cámara

Figura X. Detección automática de murciélagos usando imágenes IR (infra rojas)

2.4.1 Análisis Estadístico. - Para evaluar el desempeño del mapeo y reconstrucción 3D, se tomó en cuenta la precisión de la reconstrucción mediante la reconstrucción del mapa virtual. Se realizó un mapa del entorno sensor láser HER-430. con las siguientes dimensiones 2.5m * 2.5m. En los resultados del mapa obtenido se aprecia mucha similitud con el mapa de referencia del entorno, se realizó un cálculo del RMSE obteniendo un valor de en 11.22mm lo que se considera insignificante para labores de mapeo.

Para evaluar la factibilidad del conteo automático de murciélagos, se entrenaron múltiples versiones de redes neuronales convolucionales con la plataforma Roboflow. Esta plataforma a través de Ultralytics mantiene las versiones más actuales de YOLO, así como modelos propios y basados en la COCO database. Se evaluaron 238 imágenes capturadas de murciélagos en sus refugios naturales capturadas bajo iluminación infrarroja, las cuales fueron aumentadas hasta formar un conjunto de entrenamiento de 840 imágenes. Es decir, procesadas para crear imágenes modificadas que ayudan a no sesgar el entrenamiento, en el sentido de que no se entrene la red con imágenes iguales, sino que hagan acercamientos, cambios en los colores, y agreguen ruido. Lo cual nos permite formar un modelo de inteligencia artificial mucho más robusto. De las 3754 imágenes, conforman: el conjunto de entrenamiento 630, el conjunto de validación 30 y el conjunto de pruebas 54. De esto obtenemos con una precisión de 98.0% para el modelo Roboflow 3.0 Object Detection (Accurate)luego de ser entrenado por 300 épocas. Y dando como resultado la matriz de la figura [F 10] que muestra que se clasificaron correctamente (a través de todas las épocas de entrenamiento) 3754 imágenes, hubo 117 Falsos Negativos y 9 Falsos Positivos.

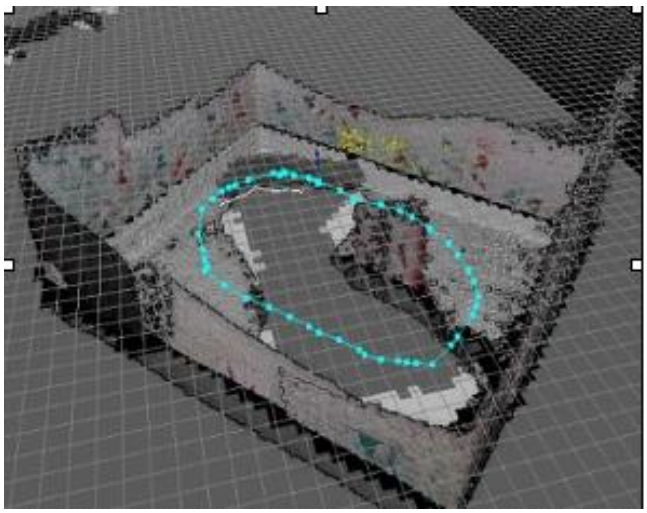

Figura XI.Reconstrucción de una trayectoria

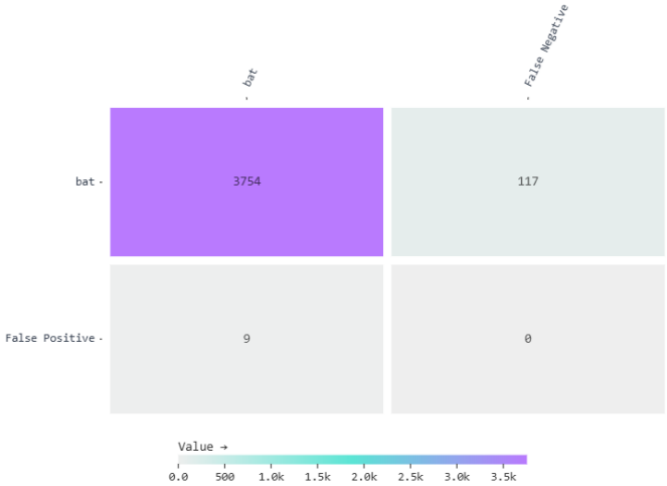

Figura XII.Matriz de confusión de YOLO para detección automática de quirópteros

2.4.2 Trabajos futuros. - En el presente trabajo se busca una arquitectura de adquisición confiable con el propósito de establecer una base de datos de cuevas habitadas por quirópteros, con el objetivo de identificar en el futuro posibles relaciones entre las características de las cuevas y las zonas seleccionadas por estos animales para habitar. Además, se pretende en un futuro cercano explorar la conexión entre el tipo de cueva y las especies de quirópteros que la ocupan. También se proyecta aumentar la cantidad de información disponible mediante la inclusión de mediciones sobre los niveles de oxígeno y otros gases presentes en cada cueva, lo que proporcionará datos más completos y útiles para el Comité Estatal para el Fomento y Protección Pecuaria del estado de Guanajuato, así como para otras entidades del país. Los dispositivos de medición deben ser de bajo consumo y portátiles como el presentado en [24]. Las redes neuronales profundas han demostrados ser eficientes en la clasificación [25], por lo que en trabajos futuros se detectarán murciélagos y serán clasificados.

3. Conclusiones. - El enfoque propuesto se distingue de las soluciones convencionales existentes ya que integra un sistema de detección basado en una configuración estéreo de cámaras infrarrojas funcionando como una cámara trampa que permite conocer dos aspectos funcionales de suma importancia para biólogos y veterinarios. De la experiencia tomada en las visitas a los refugios de los quirópteros, sean cuevas, minas u oquedades, podemos darnos cuenta observamos que el sistema de visión debe ser lo más portátil posible, debido a que los refugios de los murciélagos son de difícil acceso. Los murciélagos son muy veloces, la tasa de cuadros por segundo de captura de las fotografías debe ser alta. Por lo tanto, el sistema podría saturarse fácilmente de fotografías, especialmente considerando que se usaron cámaras en configuración estéreo, entonces, la cantidad de imágenes almacenadas se duplica con cada captura. El prototipo debe contar con discos duros deben ser de gran capacidad de almacenamiento. Al situarse en lugares remotos, todo el sistema debe ser sumamente autónomo. Es decir, debe tener un bajo consumo de baterías, y debe ser fácil de utilizar. Puesto que el tiempo para la captura de imágenes y de la expedición en general suele ser muy limitado. Así como debe de estar perfectamente aislado de agua y polvo y protegido contra golpes y caídas debido a lo accidentado

del terreno. El mapeo 3D es importante ya que facilita el trabajo de biólogos y veterinarios encargados del monitoreo y control de quirópteros. En este trabajo buscamos dar una solución utilizando el equipo portátil que diseñamos. Este paquete permite la reconstrucción de un entorno hostil y la detección de murciélagos por su versatilidad en convertirse un sistema de vigilancia (cámara trampa). Nuestros experimentos muestran que nuestro sistema puede reconstruir las cuevas habitadas por quirópteros y brindar información del entorno para la instalación de redes de niebla y equipo necesario para misiones futura, también nuestro experimento muestra que podemos detectar quirópteros con precisión, aunque actualmente requiere un procesamiento fuera de línea empleando una red YOLO con entrenamiento reforzado para la detección y etiquetado. Sin embargo, la detección de murciélagos está más allá del alcance de este trabajo, pero promete simplificar el trabajo de conteo e identificación de especies de quirópteros generando relaciones con el entorno en el que estas especies habitan en condiciones del mundo real. Consideramos que nuestra propuesta del sistemas y algoritmos puede servir como conjuntos de datos valiosos para futuros trabajos de investigación.

Fondos: Instituto Politécnico Nacional, SIP 20240650

Glosario

- Cuevas (Caves): Espacios subterráneos naturales que sirven como hábitats para diversas especies, incluyendo murciélagos, proporcionando protección y un ambiente ideal para la reproducción.
- Murciélagos (Bats): Quirópteros que desempeñan roles significativos en la ecología, como la polinización y el control biológico de plagas. Habitan en cuevas y son esenciales para el funcionamiento de diversos ecosistemas, a menudo enfrentando condiciones de vida desafiantes.
- Tecnología Infrarroja (Infrared Technology): Tecnología utilizada en el estudio para detectar murciélagos y reconstruir cuevas en condiciones de poca luz, lo que permite la observación y recolección de datos incluso cuando la visibilidad es escasa.
- Reconstrucción 3D (3D Reconstruction): Un proceso que crea un modelo tridimensional de los entornos de las cuevas mediante la captura y el procesamiento de imágenes de diversos sensores.
- Plataforma Multisensores (Multisensor Platform): Un sistema portátil diseñado para combinar cámaras RGB, cámaras infrarrojas, sensores inerciales y luces infrarrojas para detectar murciélagos y mapear las estructuras de las cuevas.
- Algoritmo en Tiempo Real (Real-Time Algorithm): Un algoritmo que procesa los datos a medida que se recopilan para generar un mapa de nubes de puntos con fines de análisis y monitoreo inmediatos.
- Nube de Puntos (Point Cloud): Una colección de puntos de datos en el espacio producida por el proceso de reconstrucción 3D, utilizada para analizar las dimensiones espaciales y las características de la cueva.
- Visión por Computadora (Computer Vision): Un campo interdisciplinario que consiste en permitir que las computadoras interpreten y procesen información visual del mundo, aplicado al estudio de las poblaciones animales.
- Sensor Inercial (Inertial Sensor): Un dispositivo que mide la fuerza específica, la tasa angular y, a veces, el campo magnético que rodea el sensor, contribuyendo al seguimiento de los movimientos y la orientación de la plataforma portátil.
- Cámara Estereoscópica (Stereoscopic Camera): Un sistema de cámaras que utiliza dos o más lentes para capturar imágenes que simulan la visión binocular humana, permitiendo la percepción de profundidad.
- Zoonosis (Zoonotic Diseases): Enfermedades que se transmiten de los animales a los humanos, destacando la importancia de entender las poblaciones de murciélagos para gestionar los riesgos para la salud pública.
- Batería de Litio (Lithium Battery): Baterías recargables utilizadas en la plataforma portátil multisensor, elegidas por su ligereza y alta densidad de energía.

Referencias

[1] J. Colorado, A. Barrientos y C. Rossi, «Músculos inteligentes en robots biológicamente inspirados: Modelado, control y actuación,» *Revista Iberoamericana de Automática e Informática Industrial RIAI,* vol. 8, nº 4, p. 385–396., 2011.

[2] K. F. Darras, M. Balle, W. Xu, Y. Yan, V. G. Zakka, M. Toledo-Hernández, D. Seng, W. Lin, B. Zhang y Z. Lan, «Eyes on nature: Embedded vision cameras for terrestrial biodiversity monitoring,» *Methods in Ecology and Evolution,* vol. 15, nº 12, pp. 2262-2275, 2024.

[3] S. J. Ghanem y C. C. Voigt, «Increasing Awareness of Ecosystem Services Provided by Bats,» *Advances in the Study of Behavior,* vol. 44, pp. 279-302, 2012.

[4] D. Ortiz-Ramírez, C. Lorenzo , E. Naranjo y L. León-Paniagua , «elección de refugios por tres especies de murciélagos frugívoros (Chiroptera: Phyllostomidae) en la Selva Lacandona, Chiapas, México,» *Revista mexicana de biodiversidad,* vol. 77, nº 2, pp. 261-270, 2006.

[5] R. Brigham y B. Fenton, «The influence of roost closure on the roosting and foraging behaviour of Eptesicus fuscus (Chiroptera: Vespertilionidae),» *Canadian Journal of Zoology,* vol. 64, pp. 1128-1133, 2011.

[6] M. Labadie, N. Morand, R. Fabien, G. F. Nguilili, T. N'Kaya, A. Caron y H. De Nys, «Habitat sharing and interspecies interactions in caves used by bats in the Republic of Congo,» *PeerJ,* vol. 13, 2025.

[7] S. Platto, Z. Jinfeng , W. Yanqing, W. Huo y E. Carafoli, «Biodiversity loss and COVID-19 pandemic: The role of bats in the origin and the spreading of the disease,» *Biochemical and Biophysical Research Communications,* vol. 538, pp. 2-13, 2021.

[8] W. Tabib, K. Goel, J. Yao, C. Borium y N. Michael, «Autonomous Cave Surveying With an Aerial Robot,» *IEEE Transactions on Robotics,* vol. 38, nº 2, pp. 1016-1032, 2022.

[9] L. Espinasa, R. Tatarsky, M. Girard y M. Sandone, «Population Size and Spatial Distribution of the Mexican Blind Cavefish (Astyanax) within the Caves,» *Fishes MDPI,* vol. 9, nº 9, p. 334, 2024.

[10] D. Giordan, D. Godone, M. Baldo, M. Piras, N. Grasso y R. Zerbetto, «Survey Solutions for 3D Acquisition and Representation of Artificial and Natural Caves,» *Applied Sciences,* vol. 11, nº 14, 2021.

[11] H. Bravo, E. Lo, H. Moyes, D. Rissolo, S. Montgomery y F. Kuester, «A methodology for cave floor basemap synthesis from point cloud data: a case study of slam-based LiDAR at Las cuevas, Belize,» *ISPRS Annals of the Photogrammetry, Remote Sensing and Spatial Information Sciences,* Vols. 1 de 2X-M-1-2023, pp. 179-186, 2023.

[12] H. Azpúrua, A. Rezende, G. Potje, G. Júnior, R. Fernandes, V. Miranda, L. Filho, J. Domingues, F. Rocha, F. Sousa, L. G. Barros, E. Nascimento, M. Douglas, G. Pessin y G. Freitas, «Towards Semi-autonomous Robotic Inspection and Mapping in Confined Spaces with the EspeleoRobô,» *Journal of Intelligent \& Robotic Systems,* vol. 101, 2021.

[13] P. Trybała, P. Kujawa, K. Romańczukiewicz, A. Smentek y F. Remondino, «Designing and evaluating a portable lidar-based SLAM system,» *The International Archives of the Photogrammetry, Remote Sensing and Spatial Information Sciences,* Vols. %1 de %2XLVIII-1/W3-2023, pp. 191-198, 2023.

[14] I. Marini, C. Caradonna, M. Melis y C. Nardinocchi, «Terrestrial laser scanning for 3D archaeological documentation. The prehistoric Cave of Sa Miniera de Santu Josi (Sardinia, Italy),» *Journal of Physics: Conference Series,* vol. 2204, 2022.

[15] C. Rossi, A. Caro Zapata, Z. Milosevic, R. Suarez y S. Dominguez, «Topological Navigation for Autonomous Underwater Vehicles in Confined Semi-Structured Environments,» *Sensors,* vol. 23, nº 5, 2023.

[16] A. Chen, J. Moran, G. Shoshiani y M. Chater, «Using computer vision, image analysis and UAVs for the automatic recognition and counting of common cranes (Grus grus),» *Journal of Environmental Management,* vol. 328, 2023.

[17] E. Gazagne, R. Gray, R. Ratajszczak, F. Brotcorne y A. Hambuckers, «Unmanned aerial vehicles (UAVs) with thermal infrared (TIR) sensors are effective for monitoring and counting threatened Vietnamese primates,» *Primates Springer,* vol. 64, nº 4, pp. 407-413, 2023.

[18] H. Qiao, L. Zhang, J. Drahota, W. Woldt, D. Varner, A. Bishop, T. LaGrange, C. Neale y Z. Tang, «Combining Multi-View UAV Photogrammetry, Thermal Imaging, and Computer Vision Can Derive Cost-Effective Ecological Indicators for Habitat Assessment,» *Remote Sensing,* vol. 16, nº 6, p. 1081, 2024.

[19] I. Bentley, V. Kuczynska, V. M. Eddington, M. Armstrong y L. N. Kloepper, «BatCount: A software program to count moving animals,» *Public Library of Science San Francisco, CA USA,* vol. 18, nº 3, 2023.

[20] D. McFarlane, G. Van Rentergem, A. Ruina, J. Lundberg y K. Christenson, «Estimating colony size of the wrinkle-lipped bat, Chaerephon plicatus (Chiroptera: Molossidae) at Gomantong, Sabah, by quantitative image analysis,» *Acta Chiropterologica,* vol. 17, nº 1, pp. 171-177, 2015.

[21] J. P. Suraci, M. Clinchy, B. Mugerwa, M. Delsey, D. W. Macdonald, J. Smith, C. C. Wilmers y L. Y. Zanette, «A new Automated Behavioural Response system to integrate playback experiments into camera trap studies,» *Methods in Ecology and Evolution Wiley Online Library,* vol. 8, nº 8, pp. 957-964, 2017.

[22] A. Yoshioka, A. Shimizu, H. Oguma, N. Kumada, K. Fukasawa, S. Jingu y T. Kadoya, «Development of a camera trap for perching dragonflies: a new tool for freshwater environmental assessment,» *PeerJ,* vol. 8, 2020.

[23] G. Krivek, E. Mahecha, F. Meier, G. Kerth y J. van Schaik, «Counting in the dark: estimating population size and trends of bat assemblages at hibernacula using infrared light barriers,» *Animal Conservation Wiley Online Library,* vol. 26, nº 5, pp. 701-713, 2023.

[24] J. A. Tovar-Sánchez, J. F. Arias-Molina, H. A. Milquez-Sanabria y M. A. Mayorga-Castellanos, «Technical Design of a Low-Cost, Portable Methane Quantification System,» *Ingeniería,* vol. 28, 2023.

[25] A.-M. Hernández-Ponce, F.-J. Ornelas-Rodríguez, J.-B. Hurtado-Ramos, P.-A. Ramírez-Pedraza y J.-J. González-Barbosa, «A Semi-Supervised Deep Learning Model for Defective lime Classification,» *Ingeniería e Investigación,* vol. 44, nº 3, pp. 1-14, 2024.

Nota contribución de los autores:

1. Concepción y diseño del estudio
2. Adquisición de datos
3. Análisis de datos
4. Discusión de los resultados
5. Redacción del manuscrito
6. Aprobación de la versión final del manuscrito

ICR ha contribuido en: 1, 2, 3, 4, 5 y 6.
JAAR ha contribuido en: 1, 2, 3, 4, 5 y 6.
IBR ha contribuido en: 1, 2, 3, 4, 5 y 6.
JJGB ha contribuido en: 1, 2, 3, 4, 5 y 6.
JBHR ha contribuido en: 1, 2, 3, 4, 5 y 6.
FJOR ha contribuido en: 1, 2, 3, 4, 5 y 6.
ARP ha contribuido en: 1, 2, 3, 4, 5 y 6.

Nota de aceptación: Este artículo fue aprobado por los editores de la revista Dr. Rafael Sotelo y Mag. Ing. Fernando A. Hernández Gobertti.

Interacción suelo-estructura de una edificación con losa de cimentación por los modelos dinámicos de Barkan y Savinov, Norma Rusa SNIP 2.02.05-87 y Gazetas y Mylonakis

Soil-structure interaction of a building with a foundation slab with the dynamic models of Barkan and Savinov, Russian Standard SNIP 2.02.05-87 and Gazetas and Mylonakis

Interação solo-estrutura de uma edificação com laje de fundação utilizando os modelos dinâmicos de Barkan e Savinov, Norma Russa SNIP 2.02.05-87 e Gazetas e Mylonakis

Juan Contreras [1], Genner Villarreal Castro[2,(*)]

Recibido: 14/10/2024 Aceptado: 26/01/2025

Resumen. - El análisis de la Interacción Dinámica Suelo-Estructura en la respuesta sísmica de edificaciones ha sido objeto de estudio en múltiples investigaciones, destacando su relevancia en la seguridad estructural, especialmente en contextos de alta sismicidad como Perú. Estudios realizados por Villarreal (2023), Braña, Gamón, Fundora y Martínez (2022) señalan que el comportamiento estructural de las edificaciones puede verse modificada al considerar la interacción suelo estructura en el análisis estructural y modelación de edificaciones. Mediante la incorporación de los coeficientes dinámicos obtenidos con las propiedades elásticas del estrato del suelo, es factible determinar si existe alguna variación significativa en el comportamiento estructural del modelo, en ese sentido el presente estudio se propone como objetivo de investigación: determinar si la incorporación de los modelos dinámicos de interacción suelo-estructura de Barkan & Savinov, Norma Rusa SNIP 2.02.05-87 y Gazetas & Mylonakis establecidos en la norma NIST GCR 12-917-21, pueden modificar o influir significativamente en el comportamiento estructural de la edificación para ser consideradas dentro del análisis estructural y posteriormente en la Norma Peruana E030. La edificación considerada para el análisis tiene un sistema estructural por muros absorbentes a cortantes (alta rigidez), y la cimentación es uniforme mediante una losa de cimentación de e=0.40 cm. Mediante el estudio de mecánica de suelos se determinó las propiedades del suelo, categorizando al suelo como S3, con un módulo de elasticidad E_s=1150 ton/m^2 y un coeficiente Poisson μ_(1=) 0.30, la altura del estrato a nivel de cimentación es de 1.20 m. La edificación se ubica en una zona de aceleración pico de 0.25g. Mediante el análisis de los resultados se llegó a demostrar que la estructura al tener alta rigidez no modifica significativamente su periodo, siendo la mayor variación del periodo de 1.60% para el modelo de Barkan & Savinov, seguido del modelo de Gazetas & Mylonakis con 1.42%, en lo concerniente a las derivas se observó un incremento significativo en el nivel en contacto con la cimentación, con un promedio de variación de 16.56% en la dirección XX' más flexible de la edificación, mientras que en la dirección más rígida el incremento fue de 10.50%. Los resultados de las derivas se verificaron mediante un análisis tiempo historia, considerando el Sismo de Lima de Octubre de 1966 y sus dos componentes (EW-NS), verificando que para el caso EW el incremento de la deriva fue de un 16.82%, mientras que para el caso NS se obtuvo un incremento del 16.81%, ambos en la dirección XX'. Con estos resultados se llegó a concluir que existe un incremento significativo en las deformaciones laterales en el nivel que se encuentra en contacto con la losa de cimentación, mientras que la variación en el periodo fundamental y los esfuerzos cortantes no fueron significativas en gran medida por el sistema estructural de muros absorbentes de cortante que presentan una rigidez superior a otros sistemas constructivos.

Palabras clave: modelo ISE dinámico de Barkan y Savinov, modelo ISE dinámico de la norma rusa, modelo ISE dinámico de Gazetas y Mylonakis.

Summary. - *The analysis of the Soil-Structure Dynamic Interaction in the seismic response of buildings has been the subject of study in multiple investigations, highlighting its relevance in structural safety, especially in contexts of high*

(*) Autor de correspondencia

[1] Doctor en Ingeniería, Universidad Nacional del Santa (Perú), juanalbertocontrerasmoreto1207@gmail.com, ORCID iD: https://orcid.org/0000-0003-2048-130X

[2] Doctor en Ingeniería, Universidad de San Martín de Porres (Perú), gvillarrealc@usmp.pe, ORCID iD: https://orcid.org/0000-0003-1768-646X

Memoria Investigaciones en Ingeniería, núm. 28 (2025). pp. 126-153
https://doi.org/10.36561/ING.28.10
ISSN 2301-1092 • ISSN (en línea) 2301-1106 – Universidad de Montevideo, Uruguay

seismicity such as Peru. Studies carried out by Villarreal (2023), Braña, Gamón, Fundora and Martínez (2022) indicate that the structural behavior of buildings can be modified by considering the soil-structure interaction in the structural analysis and modeling of buildings. By incorporating the dynamic coefficients obtained with the elastic properties of the soil stratum, it is feasible to determine if there is any significant variation in the structural behavior of the model, in this sense the present study proposes as a research objective: to determine if the incorporation of the dynamic models of soil structure interaction of Barkan & Savinov, Russian Standard SNIP 2.02.05-87 and Gazetas & Mylonakis established in the NIST GCR 12-917-21 standard, can significantly modify or influence the structural behavior of the building to be considered within the structural analysis and later in the Peruvian standard E030. The building considered for the analysis has a structural system by shear absorbent walls (high rigidity), and the foundation is uniform by means of a foundation slab of e=0.40 cm. Through the study of soil mechanics, the properties of the soil were determined, categorizing the soil as S3, with an elasticity modulus Es=1150 ton/m2 and a Poisson coefficient μ=0.30, the height of the stratum at the foundation level is 1.20 m. The building is located in a peak acceleration zone of 0.25g. Through the analysis of the results, it was demonstrated that the structure having high rigidity does not significantly modify its period, being the greatest variation of the period of 1.60% for the Barkan & Savinov model, followed by the Gazetas & Mylonakis model with 1.42%. Concerning the drifts, a significant increase was observed in the level in contact with the foundation, with an average variation of 16.56% in the most flexible XX' direction of the building, while in the most rigid direction the increase was 10.50%. The results of the drifts were verified through a time history analysis, considering the Lima Earthquake of October 1966 and its two components (EW-NS), verifying that for the EW case the increase in the drift was 16.82%, while for the NS case an increase of 16.81% was obtained, both in the XX' direction. These results led to the conclusion that there was a significant increase in lateral deformations at the level in contact with the foundation slab, while the variation in the fundamental period and shear stresses were not significant, largely due to the structural system of shear-absorbing walls, which have a higher rigidity than other construction systems.

Keywords: *Barkan and Savinov dynamic ISE model, Russian standard dynamic ISE model, Gazetas and Mylonakis dynamic ISE mode*

***Resumo*. -** *A análise da interação dinâmica solo-estrutura na resposta sísmica de edifícios tem sido objeto de estudo em diversas investigações, destacando sua relevância na segurança estrutural, especialmente em contextos de alta sismicidade, como o Peru. Estudos realizados por Villarreal (2023), Braña, Gamón, Fundora e Martínez (2022) indicam que o comportamento estrutural de edifícios pode ser modificado considerando a interação solo-estrutura na análise e modelagem estrutural de edifícios. Ao incorporar os coeficientes dinâmicos obtidos com as propriedades elásticas do estrato do solo, é possível determinar se há alguma variação significativa no comportamento estrutural do modelo, neste sentido o presente estudo propõe como objetivo de pesquisa: determinar se a incorporação dos modelos dinâmicos de interação solo-estrutura de Barkan & Savinov, Norma Russa SNIP 2.02.05-87 e Gazetas & Mylonakis estabelecidos na norma NIST GCR 12-917-21, podem modificar ou influenciar significativamente o comportamento estrutural da edificação a ser considerada na análise estrutural e posteriormente na norma peruana E030. A edificação considerada para a análise possui um sistema estrutural por paredes absorventes de cisalhamento (alta rigidez), e a fundação é uniforme por meio de uma laje de fundação de e=0,40 cm. Por meio do estudo da mecânica dos solos, foram determinadas as propriedades do solo, categorizando-o como S3, com módulo de elasticidade Es=1150 ton/m2 e coeficiente de Poisson μ=0,30, a altura do estrato no nível da fundação é de 1,20 m. O edifício está localizado em uma zona de pico de aceleração de 0,25g. Por meio da análise dos resultados, demonstrou-se que a estrutura com alta rigidez não modifica significativamente seu período, sendo a maior variação do período de 1,60% para o modelo de Barkan & Savinov, seguido pelo modelo de Gazetas & Mylonakis com 1,42%. Em relação aos deslocamentos, observou-se um aumento significativo no nível em contato com a fundação, com variação média de 16,56% na direção XX' mais flexível do edifício, enquanto na direção mais rígida o aumento foi de 10,50%. Os resultados dos desvios foram verificados por meio de uma análise histórica temporal, considerando o Terremoto de Lima de outubro de 1966 e suas duas componentes (EW-NS), verificando-se que para o caso EW o aumento do desvio foi de 16,82%, enquanto para o caso NS obteve-se um aumento de 16,81%, ambos na direção XX'. Esses resultados levaram à conclusão de que houve um aumento significativo das deformações laterais no nível em contato com a laje de fundação, enquanto a variação do período fundamental e das tensões de cisalhamento não foram significativas, em grande parte devido ao sistema estrutural de paredes absorvedoras de cisalhamento, que apresentam maior rigidez do que outros sistemas construtivos.*

Palavras-chave: *Modelo ISE dinâmico de Barkan e Savinov, modelo ISE dinâmico padrão russo, modelo ISE dinâmico de Gazetas e Mylonakis*

1. Introducción. - La interacción dinámica entre el suelo y la estructura es crucial para entender el comportamiento estructural y sísmico en las edificaciones, diversas investigaciones en el tema señalan que las propiedades modales de las estructuras se ven alteradas por la flexibilidad del suelo y la masa del sistema suelo-estructura, dando como resultado frecuencias de vibración más largas lo cual incrementa los periodos debido al comportamiento histerético del suelo, además se ha observado que esta interacción puede alterar los desplazamientos laterales de la edificación, siendo este aspecto dentro del comportamiento estructural uno de los factores que ponen en mayor riesgo a las edificaciones, dado que las deformaciones que se encuentran en el límite inelástico con una breve variación podrían pasar a una condición de deformaciones permanentes e irrecuperables, así Tena-Colunga (2019) consideran que es necesario reflexionar sobre la importancia de modelar las estructuras con Interacción Dinámica Suelo-Estructura, especialmente en suelos blandos en vista que ignorar estos efectos puede llevar a daños irrecuperables y colapsos estructurales. Además, se debe considerar que, en el contexto peruano, esta interacción adquiere una relevancia especial debido a la condición de alta sismicidad del país y la diversidad de tipos de suelo que pueden presentar características complejas, desde suelos blandos hasta rocosos.

Las regiones que colindan con la costa peruana como Cajamarca, se ven aun en mayor riesgo por la alta sismicidad debido a su ubicación frente a la Placa de Nazca que se encuentra en subducción bajo la Placa Sudamericana.

En ese aspecto, la investigación se realizó en el distrito de Jaén, región de Cajamarca, al norte del Perú, cuya naturaleza geológica es característica por la presencia de fallas geológicas y depósitos sedimentarios.
De acuerdo al estudio de mecánica de suelos, se determinó que los suelos en la región son blandos, con depósitos fluvioaluviales compactados de baja rigidez, propios de las zonas de transición entre la Cordillera de los Andes y la llanura Amazónica, un aspecto que añade complejidad a la geología y sismicidad de la zona.

La pseudoaceleración utilizada en el espectro inelástico en la zona fue de 〖S〗_a=0.875 g que se determinó para una estructura con un sistema estructural por muros de corte (factor de reducción R=6) y sin irregularidades, con un suelo clasificado en la norma peruana como S3. Cabe señalar que al espectro para el análisis convencional se le realizó una reducción por sistema estructural obteniendo una seudoaceleración de S_a=0.6563 g.

Los modelos de interacción suelo estructura dinámicos considerados para el análisis fueron tres: Barkan & Savinov, ISE de la Norma Rusa SNIP 2.02.05-87 y Gazetas & Mylonakis considerados en la norma NIST GCR 12-917-21. Para determinar el peso sísmico se consideró las cargas gravitacionales y de servicio de la Norma Peruana E020, para el análisis y parámetros se consideró los criterios de la norma E030 y E060.

2. Fuerzas sísmicas de pseudoaceleración. - El análisis sísmico de la estructura se realizó con un espectro de pseudoaceleración elástico, mediante el procedimiento de análisis modal espectral. De acuerdo a la Norma Técnica Peruana E030, la zona de peligro sísmico está definida como Z2 con un coeficiente de 0.25g. En el estudio de Mecánica de suelos (EMS) y ensayo de penetración estándar ($\overline{N}_{60}$) se clasificó como un suelo tipo S3 con una velocidad promedio de las ondas de corte ($\overline{V}_s$=165 m/s). Por tanto, los parámetros establecidos para el sitio (S,TP,TL) considerados para una zona de riesgo sísmico Z2 son: Factor de suelo $S_2 = 1.40$, periodo corto del estrato $T_p(S) = 1.0$, periodo largo del estrato $T_L(S) = 1.6$.
El cálculo del coeficiente símico $C = 2.5$ se determinó mediante la norma E030, que señala que para todos los casos donde el periodo de la estructura tiene un periodo fundamental menor al periodo corto del estrato del suelo $T < T_P \rightarrow C = 2.5$.
En la *Tabla I* se aprecia los parámetros normativos usados para calcular el coeficiente sísmico C:

Parámetros	Factor
Altura de edificación h_n	18.60
Coeficiente Ct (sistema muros)	60.00
Periodo estático de la edificación T	0.31
T_P (S)	1.00
T_L (S)	1.60
$T < T_P$	Cumple condición

Tabla I.- Parámetros normativos para determinar el coeficiente C

El sistema estructural de la edificación se determinó con un análisis de absorción de cortantes para los muros estructurales y columnas, determinando que las fuerzas cortantes que absorben los muros se encuentran por encima del 70%, por lo cual la estructura es definida como una edificación con un sistema de muros estructurales, sistema al cual le corresponde el factor de reducción de $R = 6.0$ (E030, 2018). La edificación tiene uso "común" y está destinado a vivienda multifamiliar, con un "factor de uso" igual a $U = 1.0$ (E030, 2018).

Con los coeficientes símicos *Z, U, C y S* se procedió a calcular la pseudoaceleración elástica e inelástica, así como el espectro reducido por R, con la ecuación de pseudoaceleración de la norma (E030, 2018).
Al reemplazar los parámetros se obtuvo una pseudoaceleración para el espectro elástico de 0.145833g como se aprecia a continuación:

$$S_a = \frac{ZUCS}{R} = \frac{0.25 * 1 * 2.5 * 1.4}{6} = 0.145833g$$

La pseudoaceleración S_a para el espectro inelástico, con el factor de reducción igual a $R = 1$ es equivalente a una pseudoaceleración de :

$$S_a = 0.145833g * (6) = 0.875\ g$$

Mientras que el espectro inelástico de pseudoaceleración reducido por $0.75 * R = 0.75 * (6)$ para estructuras regulares (E030, 2018) fue equivalente a:

$$S_a = 0.145833g * 0.75(6) = 0.6563\ g$$

En la *Figura I*, se observa los espectros de pseudoaceleración elástico, inelástico y reducido. El espectro inelástico se utilizó para el escalamiento del sismo utilizado en el análisis tiempo historia.

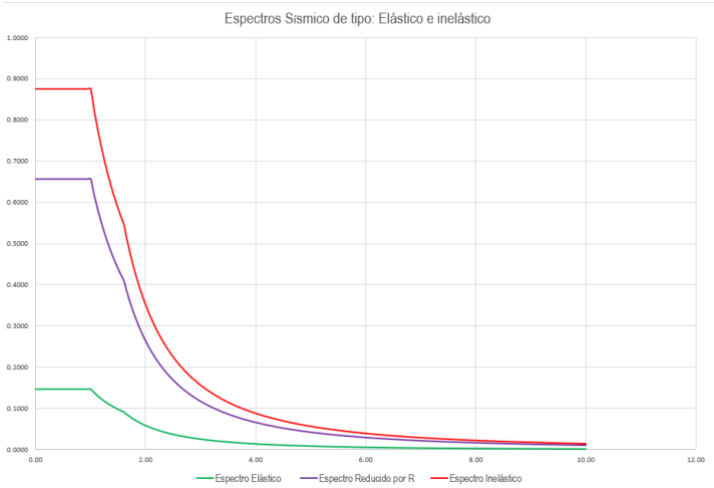

Figura I.- Espectros de seudoaceleración

Para realizar el análisis modal espectral de la estructura, se procedió a cargar el espectro inelástico con una pseudoaceleración $S_a = 0.6563\ g$.

3. Modelado de la estructura. - El modelo matemático de la estructura, se realizó considerando las secciones y materiales de cada elemento estructural como muros, vigas, columnas y losas. En el modelo matemático se consideró los criterios establecidos en la Norma Peruana E030 como por ejemplo el principio de diafragma rígido, brazo rígido, combinación de carga, entre otros.

3.1. Estructura empotrada convencionalmente en la base. - En la *Tabla II* se aprecian las propiedades de los materiales utilizados para el concreto y acero usado en el modelado:

Elementos	Propiedades
Concreto en vigas, columnas, losas	f'c=210 kgf/cm^2
Losa de cimentación e=0.40	f'c=210 kgf/cm^2
Acero (resistencia)	f'y=4200 kgf/cm^2
Módulo de elasticidad Ec	Ec= 2188.20 kgf/mm^2
Coeficiente de Poisson	μ= 0.20
Metro cúbico de concreto (Peso)	γ_{CA}=2.4 tonf/m^3

Tabla II.- Propiedades de Resistencia del concreto

El módulo de elasticidad del material concreto se determinó con la ecuación de la norma ACI 318, al ingresar la resistencia del concreto usado en todos los elementos estructurales, se obtuvo el módulo de elasticidad del concreto:

$$E_c = 15100\sqrt{f'c} = 151\sqrt{210}\ \frac{Kgf}{mm^2} = 2188.20\ kgf/mm^2$$

El modelo estructural combina muros estructurales, losas aligeradas en los niveles superiores y una losa de cimentación de e=0.40 m. Las cargas vivas se determinaron mediante la Norma E020 como se aprecia en la *Tabla III*.

Nivel	**Uso (Servicio)**	**Carga (**tonf/m2)
Azotea	Azotea	0.10
Nivel 01 a Nivel 05	Uso común	0.20
Semisótano	Estacionamiento	0.10

Tabla III.- Cargas vivas asignadas a la edificación

En el modelo se consideró cargas impuestas (sin función estructural) definidas como cargas gravitacionales, calculadas mediante la Norma E020 como tabiquerías ($150\ \frac{kgf}{m^2}$), acabados de piso ($100\ \frac{kgf}{m^2}$) y ladrillos ($60\ \frac{kgf}{m^2}$) en las losas aligeradas.

Las cargas señaladas se añadieron al modelo matemático, asignándolas como carga muerta (CM) y carga viva (CV). Estas cargas se combinaron para determinar el peso sísmico de la edificación mediante la combinación de cargas definidas en la norma E030:

$$P_s = 100\%\ CM + 25\%\ CV$$

Como resultado del modelamiento en la *Figura II* se puede observar el modelo en planta (a) y en vista 3d (b). La estructura tiene una planta típica en todos sus niveles, se aprecian además los muros estructurales encargados de absorber las fuerzas cortantes.

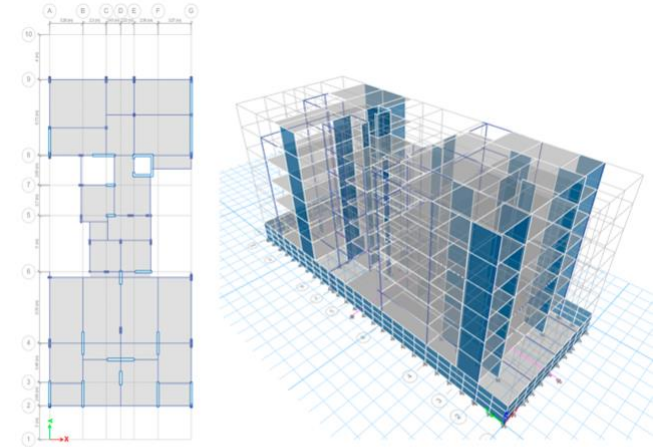

Figura II.- Modelo estructural en planta y vista 3D

Al proceder con el análisis inicial, se obtuvo el periodo de la estructura. En la *Figura III* se muestra el periodo fundamental de la estructura con el análisis modal espectral con la base empotrada. El primer modo de vibración (a) es en la dirección del modelo *XX'* del modelo con $T_1 = 0.554\ s$, el segundo modo de vibración (b) es en la dirección *YY'* del modelo con $T_2 = 0.441\ s$ y el tercer modo de vibración de la estructura es torsional con un periodo de $T_3 = 0.306\ s$ cómo se puede observar en (c). El modelo convencional, cuenta con empotramiento en la cimentación (restricción en los 6 grados de libertad).

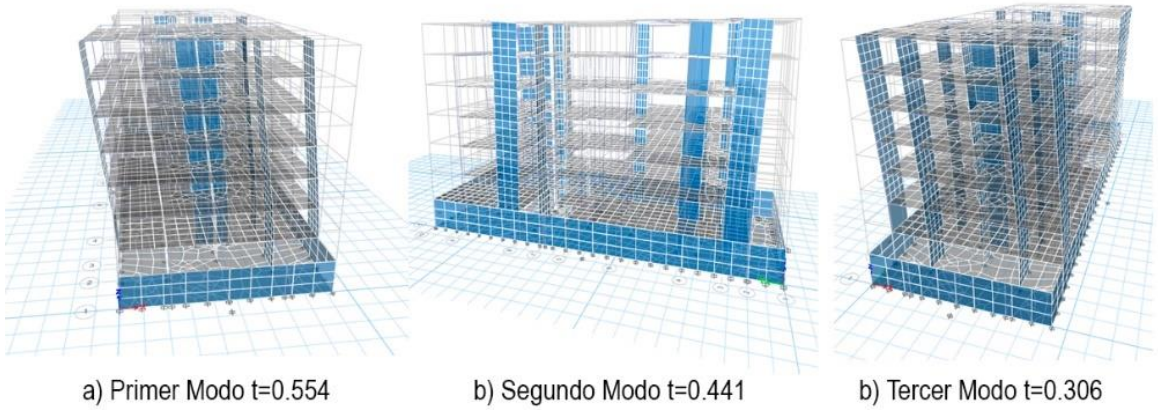

Figura III.- Modos de vibración de la estructura

4. Coeficientes de los modelos dinámicos de interacción suelo estructura. - A diferencia del modelo que considera la base empotrada, los modelos dinámicos de interacción suelo estructura incorporan los coeficientes de rigidez y amortiguamiento en los seis grados de libertad de la cimentación del modelo estructural. La determinación de estos coeficientes se calculó considerando las propiedades obtenidas mediante un estudio de Mecánica de Suelos (EMS), el peso sísmico de la edificación y las dimensiones de la losa de cimentación. Cabe señalar que mediante el estudio (EMS) se tipificó al suelo de cimentación dentro de los suelos flexibles S3 con un sólo estrato, con material blando, con una granulometría conformada por arena media a fina y con las propiedades que se describen a continuación:

- Clasificación del suelo : S3 – Suelo blando
- Tipo de suelo : Arena arcillosa de baja plasticidad
- Velocidad de onda : V_S = 165 m/s
- Módulo de elasticidad del suelo : E_S= 1150tonf/m^2
- Coeficiente de Poisson : μ_1 = 0.30
- Altura de estrato : h_1 = 1.00 m
- Capacidad portante del suelo : q_a = 1.35 kgf/cm^2
- Densidad del suelo : ρ_s = 0.1 tonf.s^2/m^4
- Coeficiente C_0 : C_o = 0.8 kgf/cm^2
- Profundidad de desplante : γ_{CA}= 1.2 m

El peso sísmico de la edificación se determinó mediante la combinación de la Norma E030 (*CM+0.25CV*) para edificaciones comunes obteniendo un peso sísmico P = 2420.38 tonf, como se puede apreciar en la *Tabla IV*.

Nivel	UX (kg)	UY (kg)	Peso (Tonf)
Azotea	157059.67	157059.67	157.06
Story5	312775.15	312775.15	312.78
Story4	338874.36	338874.36	338.87
Story3	338874.36	338874.36	338.87
Story2	338874.36	338874.36	338.87
Story1	338874.36	338874.36	338.87
Semi Sótano	463424.5	463424.5	463.42
Base	131621.34	131621.34	131.62
Peso sísmico sin considerar la losa			2420.38

Tabla IV.- Peso sísmico por piso

Las dimensiones geométricas de la losa de cimentación de la estructura se observan en la *Tabla V*.

Descripción	Detalle
Dirección de la losa (xx')	a = 14 m
Dirección de la losa (yy')	b = 36 m
Área de la losa	A = 504 m^2

Altura de la losa	$e = 0.40$ m
Distancia al centroide de la losa	$d = c/2 = 0.2$ m
Peso del concreto por m3	$\gamma = 2.4$ tonf/m^3
Gravedad	$g = 9.806$ m/s^2

Tabla V.- Dimensiones de la losa

4.1. Propiedades del modelo dinámico de Barkan & Savinov. - Los coeficientes de rigidez del modelo ISE de Barkan & Savinov se obtienen haciendo uso de las masas traslacionales del modelo, respecto a los ejes centroidales *x, y, z* de la estructura. Las masas rotacionales respecto a los ejes de contacto suelo – losa de cimentación se determinaron en los ejes *x', y', z'*. Al peso sísmico de la estructura obtenida mediante la Norma E030 se procedió a añadir el peso de la losa de cimentación mediante:

$$P_{Losa} = \gamma * a.b.c = 483.84\ tonf$$

Las masas traslacionales en la dirección horizontal son iguales $M_t = M_x = M_y = M_z$ por tanto, se tiene:

$$M_t = M_x = M_y = M_z = \frac{\gamma.a.b.c}{g} = 49.341\ \frac{tonf * s^2}{m}$$

Mediante las masas traslacionales del modelo, se procedió a determinar las inercias de masa en las dos direcciones de la estructura:

$$I_{mx} = \frac{M_t * b^2}{12} = 5328.85\ tonf.m.s^2$$
$$I_{my} = \frac{M_t * a^2}{12} = 805.907\ tonf.m.s^2$$

Las inercias de masa rotacionales se determinaron mediante las inercias de masa, como se aprecia en las siguientes ecuaciones:

$$M_{\varphi x'} = M_t.d^2 + I_{mx} = 5330.825\ tonf.m.s^2$$
$$M_{\varphi y'} = M_t.d^2 + I_{my} = 807.88\ tonf.m.s^2$$
$$M_{\psi z'} = M_t.\frac{a^2 + b^2}{12} = 6134.758\ tonf.m.s^2$$

4.1.1 Determinación de los coeficientes de presión estática. - La magnitud de la presión estática del suelo "ρ " de la losa de cimentación de la estructura, y el peso sísmico de la estructura se obtuvo mediante:

$$\rho = \frac{P_{estructura} + P_{losa}}{A_{losa}}$$

Al reemplazar los datos de la tabla, se obtuvo una presión estática del suelo "ρ " de :

$$\rho = \frac{P_{estructura} + P_{losa}}{A_{losa}} = 0.523\ \frac{kgf}{cm^2}$$

Respecto a los coeficientes C_o y ρ_o para un suelo arcilloso de baja plasticidad (tabla 2.1 del libro de Villarreal, 2017), se determinaron los siguientes coeficientes:

$$\rho_o = 0.2\ \frac{kgf}{cm^2}\ \text{y}\ C_o = 0.8\ \frac{kgf}{cm^3}$$

Mediante los datos, se procedió a calcular el coeficiente D_0, obteniendo:

$$D_0 = \frac{1-\mu}{1-0.5\mu}.C_0 = \left(\frac{1-0.30}{1-0.5*0.30}\right) * 0.80 = 0.659\ \frac{kgf}{cm^3}$$

4.1.2 Coeficientes de desplazamiento y compresión. - Mediante los coeficientes de presión estática, se determinó los coeficientes de desplazamiento y compresión en la losa de cimentación de la estructura (Villarreal, 2017) para el modelo de Barkan & Savinov:

$$C_x = D_o\left[1 + \frac{2*(a+b)}{m^{-1}*A_{Losa}}\right].\sqrt{\frac{\rho}{\rho_0}} = 1407.06\ \frac{tonf}{m^3}$$
$$C_y = 1407.06\ \frac{tonf}{m^3}$$

$$C_z = C_o\left[1+\frac{2*(a+b)}{m^{-1}*A_{Losa}}\right].\sqrt{\frac{\rho}{\rho_0}} = 1708.57\ \frac{tonf}{m^3}$$

$$C_{\varphi x} = C_o\left[1+\frac{2(a+3b)}{m^{-1}*A_{Losa}}\right].\sqrt{\frac{\rho}{\rho_0}} = 2115.91\ \frac{tonf}{m^3}$$

$$C_{\varphi y} = C_o\left[1+\frac{2(b+3a)}{m^{-1}*A_{Losa}}\right].\sqrt{\frac{\rho}{\rho_0}} = 1866.98\ \frac{tonf}{m^3}$$

4.1.3 Coeficientes de rigidez de Barkan & Savinov. - Los coeficientes de rigidez lateral, se determinaron mediante las ecuaciones de rigidez $K_x, K_y\ y\ K_z$ (Villarreal, 2017), obteniendo:

$$K_x = C_x A = \ 1407.06\ \frac{tonf}{m^3} * 504\ m^2 = 709.157\ \frac{tonf}{mm}$$

$$K_y = C_y A = \ 1407.06\ \frac{tonf}{m^3} * 504\ m^2 = 709.157\ \frac{tonf}{mm}$$

$$K_z = C_z A = \ 1708.57\ \frac{tonf}{m^3} * 504\ m^2 = 861.12\ \frac{tonf}{mm}$$

Para los coeficientes de rigidez rotacionales se determinó las inercias, como se observa:

$$I_x = \frac{a^3 * b}{12} = 8232\ m^4$$

$$I_y = \frac{a * b^3}{12} = 54432\ m^4$$

Los coeficientes de rigidez rotacionales del modelo son los siguientes:

$$K_{\varphi x} = C_{\varphi x} I_x = \ 115173340174.254\ \frac{tonf.mm}{rad}$$

$$K_{\varphi y} = C_{\varphi y} I_y = \ 15368991472.055\ \frac{tonf.mm}{rad}$$

4.1.4 Incorporación de los coeficientes de Barkan & Savinov en el modelo. - Los coeficientes calculados se ingresaron mediante un elemento estructural de tipo resorte definido como *Point Spring*. En la *Figura IV* se observa el modelo con los coeficientes de Barkan-Savinov asignados. Los coeficientes se procedieron a incorporar mediante el comando *Assign/Point Spring* en la losa de cimentación que previamente fue discretizada. Las propiedades se ingresaron en losas discretizadas en un modelo 2D que se utiliza frecuentemente en sistemas de interacción suelo-estructura (Obinna, 2022).

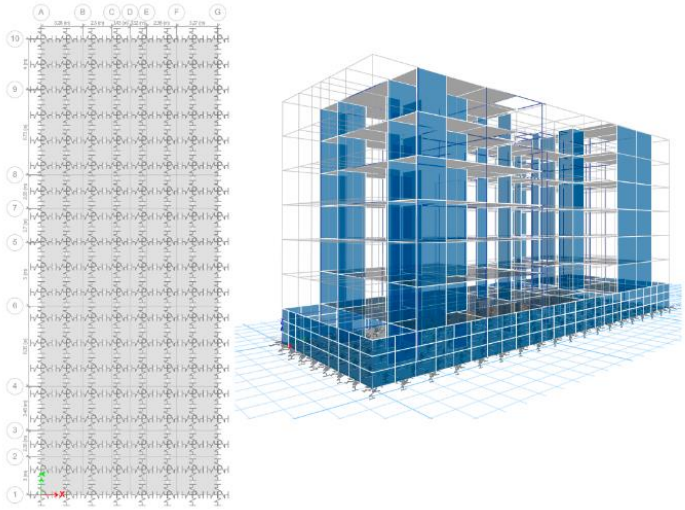

Figura IV.- Modelo con los coeficientes de Barkan – Savinov

4.2. Modelo dinámico de la Norma Rusa SNIP 2.02.05-87. - Villarreal (2023) considera que la característica elástica de la cimentación se puede determinar mediante el "coeficiente de compresión elástica uniforme", que se puede determinar mediante la siguiente ecuación:

$$C_z = b_o E\left(1 + \sqrt{\frac{A_{10}}{A_{losa}}}\right)$$

Donde, se considera los siguientes parámetros:

$$b_0 = 1.2 * m^{-1} \text{ (para suelos arcillosos según el EMS)}$$
$$A_{10} = 10m^2$$
$$E = 1150\ \frac{tonf}{m^2}$$
$$A_{Losa} = 504\ m^2$$

Mediante los parámetros señalados, el coeficiente de compresión elástica C_z de la Norma Rusa se determinó obteniendo:

$$C_z = 1.2 * 1150\left(1 + \sqrt{\frac{10m^2}{504m^2}}\right) = 1574.385\ \frac{tonf}{m^3}$$

Mediante el coeficiente de compresión elástica C_z, se determinaron los coeficientes de desplazamiento elástico uniforme, mediante las siguientes ecuaciones:

$$C_x = 0.7 * C_z = 1102.07\ \frac{tonf}{m^3}$$
$$C_{\varphi x} = C_{\varphi y} = 2 * C_z = 3148.77\ \frac{tonf}{m^3}$$
$$C_{\varphi x} = C_{\varphi y} = 2 * C_z = 3148.77\ \frac{tonf}{m^3}$$
$$C_{\psi z} = C_z = 1574.38\ \frac{tonf}{m^3}$$

4.2.1 Calculo de los coeficientes de rigidez. - Los coeficientes de rigidez de compresión elástica uniforme $K_x, K_y. K_z$; y los coeficientes de rigidez rotacionales como $K_{\varphi x}$, $K_{\varphi y}$, $K_{\psi z}$; se calcularon previamente. Los coeficientes de rigidez se calcularon mediante las siguientes ecuaciones:

$$K_x = C_x A = \ 546.443\ \frac{tonf}{mm}$$
$$K_y = C_x A = \ 555.443\ \frac{tonf}{mm}$$
$$K_z = C_z A = \ 793.49\ \frac{tonf}{mm}$$

Para los coeficientes de rigidez rotacionales se calcularon las inercias, mediante las siguientes ecuaciones:

$$I_x = \frac{a^3 * b}{12} = 8232\ m^4$$
$$I_y = \frac{a * b^3}{12} = 54432\ m^4$$
$$I_z = \frac{a^3 * b}{12} + \frac{a * b^3}{12} = 62664\ m^4$$

Por tanto, calculando los coeficientes de rigidez rotacionales, se obtuvo:

$$K_{\varphi x} = C_{\varphi x} I_x = 171{,}393{,}900.741\ tonf.m/rad$$
$$K_{\varphi y} = C_{\varphi y} I_y = 25{,}920{,}682.519\ tonf.m/rad$$
$$K_{\psi z} = C_{\psi z} I_y = 98{,}657{,}291.63\ tonf.m/rad$$

4.2.2 Amortiguamiento relativo para vibraciones verticales. - Para calcular la amortiguación relativa para vibraciones verticales β_z :

$$\gamma_{ts} = 0.7 \quad \text{(Para suelos arcillosos)}$$

Se consideró el Q_{adm} según el estudio de mecánica de suelos como:

$$R = 0.915 \ \frac{kgf}{cm^2}$$

Determinando la presión estática media ρ_m del suelo se obtuvo:

$$\rho_m = \gamma_{ts} * R = 6.405 \ \frac{tonf}{m^2}$$

Considerando el valor adimensional C_{zp}:

$$C_z = 1574.08 \ \frac{tonf}{m^3}$$

Se obtuvo como amortiguamiento relativo vertical:

$$\beta_z = 2.\sqrt{\frac{E}{C_z * p_m}} = 2.\sqrt{\frac{1150}{1574.38 * 6.405}} = 0.675$$

Con los amortiguamientos relativos para vibraciones verticales, se calcularon los amortiguamientos críticos:

$$\beta_x = 0.6 * \beta_z = 0.405$$
$$\beta_y = 0.6 * \beta_z = 0.405$$
$$\beta_{\varphi x} = 0.5 * \beta_z = 0.338$$
$$\beta_{\varphi y} = 0.5 * \beta_z = 0.338$$
$$\beta_{\psi z} = 0.3 * \beta_z = 0.203$$

Mediante el cálculo del amortiguamiento crítico obtenido, se procede a determinar los amortiguamientos efectivos en el suelo, mediante las siguientes ecuaciones:

$$B_x = 2 * \beta_x * \sqrt{K_x * M_x} = 4243.158 \ tonf.s/m$$
$$B_y = 2 * \beta_y * \sqrt{K_y * M_y} = 4243.158 \ tonf.s/m$$
$$B_z = 2 * \beta_z * \sqrt{K_z * M_z} = 8452.573 \ \ tonf.s/m$$
$$B_{\varphi x} = 2 * \beta_{\varphi x} * \sqrt{K_{\varphi x} * M_{\varphi x'}} = 645621.656 \ tonf.s.m$$
$$B_{\varphi y} = 2 * \beta_{\varphi y} * \sqrt{K_{\varphi y} * M_{\varphi y'}} = 97741.7 \ tonf.s.m$$
$$B_{\psi z} = 2 * \beta_{\psi z} * \sqrt{K_{\psi z} * M_{\psi z'}} = 315280.967 \ tonf.s.m$$

4.2.3 Incorporación de los coeficientes de la Norma Rusa SNIP 2.02.05-87. - La incorporación de los coeficientes de rigidez y amortiguamiento se realizó mediante el comando *Spring Properties / Área Spring Property*. En la *Figura V* se aprecia la incorporación de las propiedades determinadas para el modelo dinámico con los coeficientes de la norma rusa.

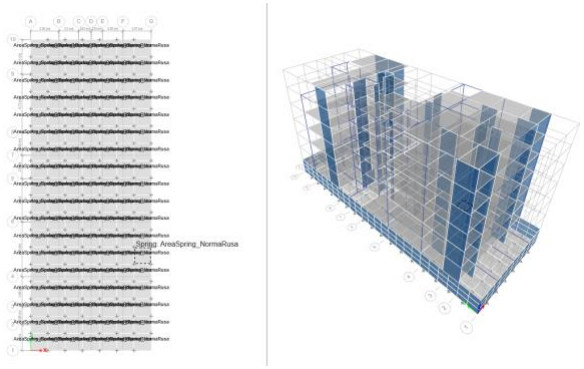

Figura V.- Modelo con los coeficientes de la Norma Rusa

4.3. Coeficientes del modelo dinámico de Gazetas & Mylonakys. - Los modelos dinámicos de Gazetas (1991) y Mylonakys et al. (2006) requieren de los parámetros obtenidos mediante el EMS, donde se determinó que el suelo se categoriza como un suelo S3, por la velocidad de propagación de la onda de corte Vs en los estratos.

$$Vs = 165\ \frac{m}{s}$$

$\mu = 0.30$ (Coeficiente de Poisson del suelo)

$$g = 9806\ \frac{m}{s^2}$$

$$\gamma = 19\ \frac{kN}{m^3}$$

En base a esos datos se calculó el módulo de corte del suelo máximo.

$G_{max} = \frac{\gamma}{g} * Vs^2 = 52.75\ MPa$ (Módulo de corte del suelo)

$B = 7.00\ m$ ($\frac{a}{2}$ medida del lado menor al centroide)

$L = 18.00\ m$ ($\frac{b}{2}$ medida del lado mayor al centroide)

Las inercias de la losa de cimentación utilizadas fueron:

$$I_x = \frac{(2 * L)^3 * (2 * B)}{12} = 54432\ m^4$$

$$I_y = \frac{(2 * L) * (2 * B)^3}{12} = 8232\ m^4$$

$J = I_z = I_x + I_y = 62664.5\ m^4$ (Define el momento polar de inercia)

El módulo de corte del suelo G_m se obtuvo mediante:

$$G_m = G_{max} * 0.3433 = 18.108\ MPa$$

Con estos parámetros se procedió a determinar los coeficientes de rigidez traslacional, los factores de rigidez por empotramiento, los factores modificatorios de la rigidez dinámica y amortiguamiento, amortiguamiento por radiación de la estructura, mediante las ecuaciones elásticas de la Norma NIST GCR 12-917-21 como se describe a continuación.

4.3.1 Coeficientes de rigidez traslacional y torsional. - Los coeficientes de rigidez traslacional y torsional se determinaron mediante los coeficientes de rigidez traslacional y rotacional (*Figura VI*) en los ejes z, y, x, calculados mediante las ecuaciones de la tabla 2-2a incluidas en la Norma NIST GCR 12-917-21.

Gazetas (1991); Mylonakis et al. (2006)

$$K_{z,sur} = \frac{2GL}{1-\nu}\left[0.73+1.54\left(\frac{B}{L}\right)^{0.75}\right]$$

$$K_{y,sur} = \frac{2GL}{2-\nu}\left[2+2.5\left(\frac{B}{L}\right)^{0.85}\right]$$

$$K_{x,sur} = K_{y,sur} - \frac{0.2}{0.75-\nu}GL\left(1-\frac{B}{L}\right)$$

$$K_{zz,sur} = GJ_t^{0.75}\left[4+11\left(1-\frac{B}{L}\right)^{10}\right]$$

$$K_{yy,sur} = \frac{G}{1-\nu}\left(I_y\right)^{0.75}\left[3\left(\frac{L}{B}\right)^{0.15}\right]$$

$$K_{xx,sur} = \frac{G}{1-\nu}\left(I_x\right)^{0.75}\left(\frac{L}{B}\right)^{0.25}\left[2.4+0.5\left(\frac{B}{L}\right)\right]$$

Figura VI.- Soluciones elásticas para rigidez estática (Tabla 2-2a)

Con las ecuaciones se procedió a calcular los respectivos coeficientes de rigidez traslacional y rotacional:

Traslación en el eje z:

$$K_{z,sur\_gm} = \left(\frac{2 * Gm * L}{1 - \mu}\right) * \left(0.73 + 1.54 * \left(\frac{B}{L}\right)^{0.75}\right) = 155{,}803.791 \ \frac{tonf}{m}$$

Traslación en el eje y:

$$K_{y,sur\_gm} = \left(\frac{2 * Gm * L}{2 - \mu}\right) * \left(2 + 2.5 * \left(\frac{B}{L}\right)^{0.85}\right) = 134{,}490.879 \ \frac{tonf}{m}$$

Traslación en el eje x:

$$K_{x,sur} = \left(\frac{Gm * B}{2 - \mu}\right) * (6.8 * \left(\frac{L}{B}\right)^{0.65} + 2.4) = 124{,}539.842 \ \frac{tonf}{m}$$

Torsión en torno al eje z:

$$K_{zz,sur\_gm} = (Gm * J^{0.75}) * \left(4 + 11 * \left(1 - \frac{B}{L}\right)^{10}\right) = 292{,}609{,}657.093 \ \frac{kN.m}{rad}$$

Rotación en torno al eje y:

$$K_{yy,sur\_gm} = \left(\frac{Gm}{1 - \mu}\right) * {I_x}^{0.75} * \left(\frac{L}{B}\right)^{0.25} * \left(2.4 + \left(\frac{B}{L}\right)\right) = 302{,}869{,}323.78 \ \frac{kN.m}{rad}$$

Rotación en torno al eje x:

$$K_{xx,sur\_gm} = \left(\frac{Gm}{1 - \mu}\right) * {I_y}^{0.75} * \left(3 * \left(\frac{L}{B}\right)^{0.15}\right) = 77{,}277{,}492.743 \ \frac{kN.m}{rad}$$

4.3.2 Factores para la corrección de rigidez por empotramiento. - Para el cálculo de los factores para la corrección de rigidez por empotramiento, traslación en el eje x, y, z (η_z, η_y, η_x) y corrección para la torsión en los ejes x, y, z ($\eta_{zz}, \eta_{yy}, \eta_{xx}$), se consideró la altura de la cimentación y la altura del empotramiento, con los siguientes valores.

$$D = 1.20 \ m$$
$$dw = 0.40 \ m$$
$$Zw = 0.6 \ m$$
$$Aw = 2 * (2B + 2L) * dw = 40m^2$$

En la F*igura VII* se aprecia el resumen de los factores de corrección traslacional y torsional (tabla 2-2b) de la Norma NIST GCR 12-917-21

Gazetas (1991); Mylonakis et al. (2006)

$$\eta_z = \left[1 + \frac{D}{21B}\left(1 + 1.3\frac{B}{L}\right)\right]\left[1 + 0.2\left(\frac{A_w}{4BL}\right)^{2/3}\right]$$

$$\eta_y = \left(1 + 0.15\sqrt{\frac{D}{B}}\right)\left[1 + 0.52\left(\frac{z_w A_w}{BL^2}\right)^{0.4}\right]$$

Same equation as for η_y, but A_w term changes for $B \neq L$

$$\eta_{zz} = 1 + 1.4\left(1 + \frac{B}{L}\right)\left(\frac{d_w}{B}\right)^{0.9}$$

$$\eta_{yy} = 1 + 0.92\left(\frac{d_w}{B}\right)^{0.6}\left[1.5 + \left(\frac{d_w}{D}\right)^{1.9}\left(\frac{B}{L}\right)^{-0.6}\right]$$

$$\eta_{xx} = 1 + 1.26\frac{d_w}{B}\left[1 + \frac{d_w}{B}\left(\frac{d_w}{D}\right)^{-0.2}\sqrt{\frac{B}{L}}\right]$$

Figura VII.- Factores de corrección (Tabla 2-2b)

En la *Tabla VI* se muestran los factores de corrección traslacional y torsional calculados, mediante las ecuaciones de la Norma NIST GCR 12-917-21:

η_{z_gm}	η_{y_gm}	η_{x_gm}	η_{zz_gm}	η_{yy_gm}	η_{xx_gm}
1.05	1.152	1.126	1.148	1.284	1.075

Tabla VI.- Factores de corrección

4.3.3 Factores modificatorios de la rigidez dinámica y amortiguamiento. - Se determinó los factores modificatorios de la rigidez dinámica y amortiguamiento por radiación de ondas considerado en las funciones de impedancia para la losa de cimentación y la frecuencia de vibración del suelo, como se aprecia a continuación:

$$w = 1.61 * \frac{2\pi}{s} = 10.116\ \frac{rad}{s}$$

$$\alpha_0 = w * \frac{B}{Vs} = 0.429$$

$$\psi = \sqrt{\frac{2*(1-\mu)}{1-2\mu}} = 1.871, donde\ maximo\ valor\ \psi = 2.5$$

En la Figura VIII se aprecian las ecuaciones de los factores modificatorios utilizados en modelo ISE de Gazetas & Mylonakys.

Surface Stiffness Modifiers

$$\alpha_z = 1.0 - \left[\frac{\left(0.4 + \frac{0.2}{L/B}\right)a_0^2}{\left(\frac{10}{1+3(L/B-1)}\right) + a_0^2}\right]$$

$$\alpha_y = 1.0$$

$$\alpha_x = 1.0$$

$$\alpha_{zz} = 1.0 - \left[\frac{\left(0.33 - 0.03\sqrt{L/B-1}\right)a_0^2}{\left(\frac{0.8}{1+0.33(L/B-1)}\right) + a_0^2}\right]$$

$$\alpha_{yy} = 1.0 - \left[\frac{0.55a_0^2}{\left(0.6 + \frac{1.4}{(L/B)^3}\right) + a_0^2}\right]$$

$$\alpha_{xx} = 1.0 - \left[\frac{\left(0.55 + 0.01\sqrt{L/B-1}\right)a_0^2}{\left(2.4 - \frac{0.4}{(L/B)^3}\right) + a_0^2}\right]$$

Figura VIII.- Factores modificatorios (Tabla 2-3a)

En la *Tabla VII* se aprecia los factores modificadores de rigidez dinámica y coeficientes de amortiguamiento por radiación para cimentaciones rígidas obtenidos con las ecuaciones de Gazetas & Mylonakys de la Tabla 2-3a de la Norma NIST GCR 12-917-21.

α_z	α_y	α_x	α_{zz}	α_{yy}	α_{xx}
0.906	1.00	1.00	0.869	0.883	0.961

Tabla VII.- Factores modificatorios de rigidez

Mediante los factores modificatorios y los coeficientes de rigidez sin empotramiento, se procedió a calcular el amortiguamiento por radiación de ondas crítico sin considerar el empotramiento.

4.3.4 Coeficientes de amortiguamiento por radiación. - Al determinar los factores modificatorios, se pudo determinar los coeficientes de rigidez corregidos por el empotramiento de la cimentación en el suelo. Los coeficientes de amortiguamiento por radiación se determinaron mediante las ecuaciones de la *Figura IX* de la Norma NIST GCR 12-917-21.

Radiation Damping

$$\beta_z = \left[\frac{4\psi(L/B)}{(K_{z,sur}/GB)}\right]\left[\frac{a_0}{2\alpha_z}\right]$$

$$\beta_y = \left[\frac{4(L/B)}{(K_{y,sur}/GB)}\right]\left[\frac{a_0}{2\alpha_y}\right]$$

$$\beta_x = \left[\frac{4(L/B)}{(K_{x,sur}/GB)}\right]\left[\frac{a_0}{2\alpha_x}\right]$$

$$\beta_{zz} = \left[\frac{(4/3)\left[(L/B)^3+(L/B)\right]a_0^2}{(K_{zz,sur}/GB^3)\left[\left(\frac{1.4}{1+3(L/B-1)^{0.7}}\right)+a_0^2\right]}\right]\left[\frac{a_0}{2\alpha_{zz}}\right]$$

$$\beta_{yy} = \left[\frac{(4\psi/3)(L/B)^3 a_0^2}{\left(\frac{K_{yy,sur}}{GB^3}\right)\left[\left(\frac{1.8}{1+1.75(L/B-1)}\right)+a_0^2\right]}\right]\left[\frac{a_0}{2\alpha_{yy}}\right]$$

$$\beta_{xx} = \left[\frac{(4\psi/3)(L/B)a_0^2}{(K_{xx,sur}/GB^3)\left[\left(2.2-\frac{0.4}{(L/B)^3}\right)+a_0^2\right]}\right]\left[\frac{a_0}{2\alpha_{xx}}\right]$$

Figura IX.- Amortiguamiento por radiación (Tabla 2-3a)

Mediante los factores modificadores de rigidez dinámica y coeficientes de amortiguamiento por radiación para cimentaciones rígidas se procedió a calcular el amortiguamiento por radiación de ondas crítico sin considerar el empotramiento, en los ejes traslacionales x, y, z. Así como para el amortiguamiento por radiación de ondas en el eje torsional y rotacionales. (ver ecuaciones en tabla 2-3a de la Norma NIST GCR 12-917-21). En la *Tabla VIII* se aprecia los coeficientes de amortiguamiento por radiación calculados.

β_z	β_y	β_x	β_{zz}	β_{yy}	β_{xx}
0.417	0.234	0.253	0.055	0.059	0.059

Tabla VIII.- Coeficientes de amortiguamiento por radiación

4.3.5 Coeficientes de rigidez dinámica corregidos. - Los coeficientes de rigidez corregidos por el empotramiento de la cimentación en el suelo para Gazetas y Mylonakis se determinaron mediante las siguientes ecuaciones:

$$K_{z\_e\_gm} = K_{zsur\_gm} * \eta_{z\_gm} * \alpha_z = 148.156\ \frac{tonf}{mm}$$

$$K_{x\_e\_gm} = K_{xsur\_gm} * \eta_{x\_gm} * \alpha_x = 140.269\ \frac{tonf}{mm}$$

$$K_{y\_e\_gm} = K_{ysur\_gm} * \eta_{y\_gm} * \alpha_y = 154.885\ \frac{tonf}{mm}$$

$$K_{zz\_e\_gm} = K_{zz,sur\_gm} * \eta_{zz_{gm}} * \alpha_{zz} = 32{,}800{,}214.597\ \frac{tonf.mm}{rad}$$

$$K_{xx\_e\_gm} = K_{xx,sur\_gm} * \eta_{xx_{gm}} * \alpha_{xx} = 8{,}978{,}468.754\ \frac{tonf.mm}{rad}$$

$$K_{yy\_e\_gm} = K_{yy,sur\_gm} * \eta_{yy_{gm}} * \alpha_{yy} = 38{,}598{,}531.764\ \frac{tonf.m}{rad}$$

4.3.6 Amortiguamiento crítico corregido. - Mediante las rigideces corregidas, se procedió a determinar los amortiguamientos críticos por radiación de ondas corregidas por el empotramiento para Gazetas & Mylonakis, mediante las ecuaciones que se aprecian en la *Figura X*:

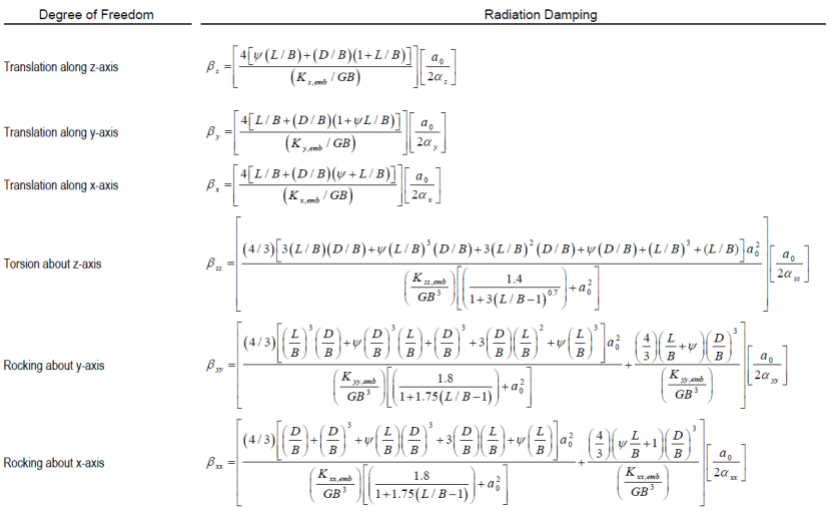

Figura X.- Amortiguamiento por radiación (Tabla 2-3b)

Mediante los coeficientes de rigidez dinámica corregidos, se procedió a calcular los factores modificadores de rigidez dinámica y relaciones de amortiguamiento por radiación por el empotramiento de la cimentación, como se aprecia en la tabla IX (ver ecuaciones en tabla 2-3b de la norma NIST GCR 12-917-21)

β_{z_e}	β_{y_e}	β_{x_e}	β_{zz_e}	β_{yy_e}	β_{xx_e}
0.494	0.282	0.291	0.085	0.066	0.039

Tabla IX.- Amortiguamiento crítico corregido

4.3.7 Coeficiente de Amortiguamiento por radiación de ondas. - Los valores efectivos del amortiguamiento, sin considerar el empotramiento se calculan considerando el amortiguamiento crítico obtenido y la frecuencia de vibración mediante las siguientes ecuaciones:

$$C_{z\_gm} = \frac{2 * K_{z,sur\_gm} * (0.05 + \beta_z)}{w} = 14.38\ s.\frac{tonf}{mm}$$

$$C_{y\_gm} = \frac{2 * K_{y,sur\_gm} * (0.05 + \beta_y)}{w} = 7.547\ s.\frac{tonf}{mm}$$

$$C_{x\_gm} = \frac{2 * K_{x,sur\_gm} * (0.05 + \beta_x)}{w} = 7.448\ s.\frac{tonf}{mm}$$

$$C_{zz\_gm} = \frac{2 * K_{zz,sur\_gm} * (0.05 + \beta_{zz})}{w} = 683{,}121.718\ m.s.\frac{tonf}{rad}$$

$$C_{yy\_gm} = \frac{2 * K_{yy,sur\_gm} * (0.05 + \beta_{yy})}{w} = 731{,}002.477\ m.s.\frac{tonf}{rad}$$

$$C_{xx\_gm} = \frac{2 * K_{xx,sur\_gm} * (0.05 + \beta_{xx})}{w} = 187{,}819.041\ m.s.\frac{tonf}{rad}$$

Estos valores efectivos del amortiguamiento, se procedieron a corregir por el empotramiento con las rigideces de Gazetas & Mylonakis, mediante las siguientes ecuaciones:

$$C_{z\_e\_gm} = \frac{2 * K_{z\_e\_gm} * (0.05 + \beta_{z\_e})}{w} = 15.938\ s.\frac{tonf}{mm}$$

$$C_{y\_e\_gm} = \frac{2 * K_{y\_e\_gm} * (0.05 + \beta_{y\_e})}{w} = 10.157\ s.\frac{tonf}{mm}$$

$$C_{x\_e\_gm} = \frac{2 * K_{x\_e\_gm} * (0.05 + \beta_{x\_e})}{w} = 9.445\ s.\frac{tonf}{mm}$$

$$C_{zz\_e\_gm} = \frac{2 * K_{zz\_e\_gm} * (0.05 + \beta_{zz\_e})}{w} = 874198.393 \ m.s.\frac{tonf}{rad}$$
$$C_{yy\_e\_gm} = \frac{2 * K_{yy\_e\_gm} * (0.05 + \beta_{yy\_e})}{w} = 884764.407 \ m.s.\frac{tonf}{rad}$$
$$C_{xx\_e\_gm} = \frac{2 * K_{xx\_e\_gm} * (0.05 + \beta_{xx\_e})}{w} = 157133.341 \ m.s.\frac{tonf}{rad}$$

4.3.8 Incorporación de la rigidez y amortiguamiento del modelo de Gazetas & Mylonakys. - Las propiedades de rigidez y amortiguamiento que se obtuvieron con las ecuaciones de Gazetas y Mylonakis se asignaron mediante la propiedad de *Area Spring* como se muestra en la figura XI.

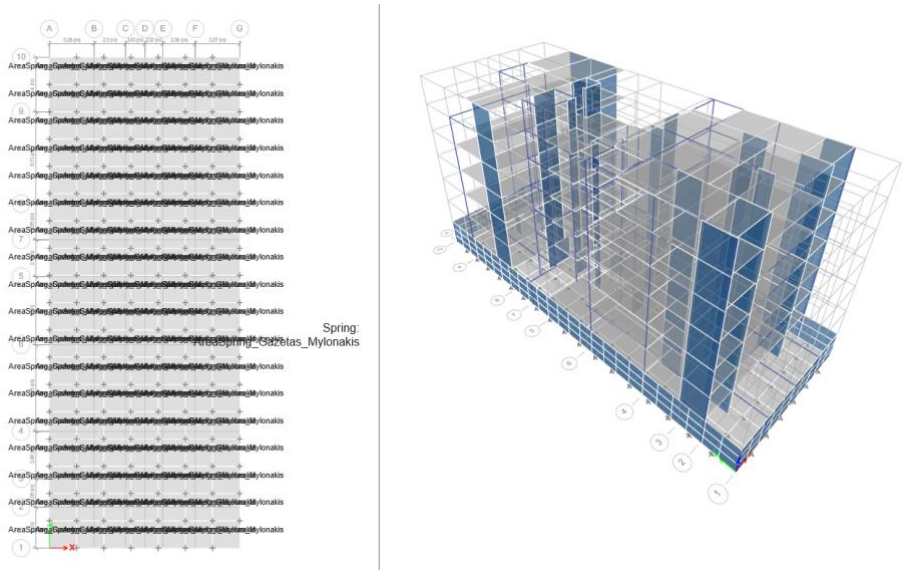

Figura XI.- Modelo con los coeficientes de Gazetas & Mylonakis

5. Resultados del análisis de los modelos con los coeficientes dinámicos. - Los resultados del análisis modal espectral de la estructura con la base empotrada convencionalmente y los modelos dinámicos de interacción suelo-estructura, se muestran a continuación en los cuadros comparativos que se describen a continuación.

5.1. Variación del periodo con los modelos dinámicos de ISE. - La interacción suelo estructura con los modelos dinámicos puede modificar el periodo de vibración de la estructura por el incremento del amortiguamiento, sin embargo, se debe considerar que la frecuencia de vibración de la estructura además se encuentra definido por la rigidez de los elementos estructurales como columnas y muros estructurales. En los modelos se procedió a incorporar los coeficientes de rigidez y amortiguamiento de cada modelo dinámico de interacción suelo-estructura y se llegó a determinar que la variación en el periodo fundamental de la edificación es mínima y se puede considerar que no es significativa.

En la *Tabla X* se muestran los periodos obtenidos para el modelo empotrado y los modelos con los coeficientes dinámicos. Para la comparación se consideró los dos periodos traslacionales y el periodo rotacional.

Modo	Modelo Empotrado	Modelo Dinámico de Barkan-Savinov	Modelo Dinámico de la Norma Rusa	Modelo Dinámico de Gazetas-Mylonakis
1	0.554	0.563	0.558	0.562
2	0.441	0.446	0.443	0.445
3	0.306	0.309	0.308	0.309

Tabla X.- Periodos de la estructura con los coeficientes ISE

En la *Tabla XI* se muestran los periodos fundamentales obtenidos para los modelos con los coeficientes dinámicos, se aprecia que la variación para el modelo de Barkan y Savinov el periodo se incrementó en 1.60%, en el modelo de la Norma Rusa fue de 0.72% y en el modelo de Gazetas & Mylonakis el periodo se incrementó en un 1.42%.

Modo	% de variación con el Modelo Dinámico de Barkan-Savinov	% de variación con el Modelo Dinámico de la Norma Rusa	% de variación con el Modelo Dinámico de Gazetas-Mylonakis
1	1.60%	0.72%	1.42%
2	1.12%	0.45%	0.90%
3	0.97%	0.65%	0.97%

Tabla XI.- Porcentajes de variación de los periodos

En la *Figura XII* se aprecia la tendencia de los periodos de las estructuras con los modelos dinámicos y el modelo con base fija, las curvas son similares debido a que las variaciones en el periodo de la edificación no fueron significativas, este resultado se puede explicar por el sistema estructural de la edificación que fue propuesta en base a muros de corte que incorporan una rigidez superior a los demás sistemas.

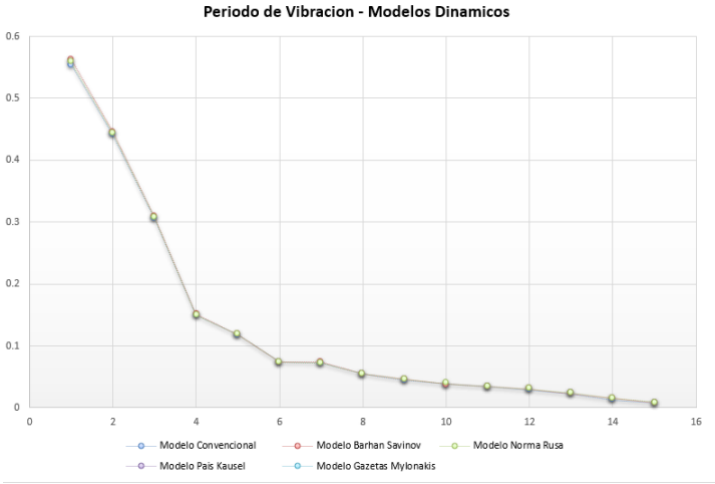

Figura XII.- Periodos obtenidos con el análisis convencional y modelos dinámicos de ISE.

5.2. Derivas de entrepiso con los modelos dinámicos de ISE. - Las derivas de entrepiso son uno de los indicadores principales del comportamiento estructural de la edificación, el incremento de las derivas puede dar lugar a deformaciones inelásticas y permanentes en la estructura. En este aspecto se determinó las derivas de la estructura con el modelo convencional empotrado y con los modelos de interacción suelo-estructura. Las derivas de entrepiso en la dirección *XX'* para el modelo convencional y los modelos con interacción dinámica suelo-estructura se muestran en la *Tabla XII*.

Nivel	Modelo Convencional	Barkan Savinov	Norma Rusa	Gazetas & Mylonakis
Azotea	0.0042	0.0043	0.0043	0.0042
Story5	0.0044	0.0046	0.0045	0.0045
Story4	0.0040	0.0041	0.0040	0.0040
Story3	0.0043	0.0044	0.0043	0.0043
Story2	0.0040	0.0042	0.0041	0.0041
Story1	0.0030	0.0032	0.0031	0.0032
Semi Sótano	0.0008	0.0010	0.0009	0.0010

Tabla XII.- Derivas en la dirección XX'

Las derivas de entrepiso en la dirección *YY'* para el modelo convencional y los modelos con interacción dinámica suelo-estructura se muestran en la *Tabla XIII*.

Nivel	Modelo Convencional	Barkan Savinov	Norma Rusa	Gazetas & Mylonakis
Azotea	0.0017	0.0017	0.0017	0.0017
Story5	0.0017	0.0018	0.0017	0.0017
Story4	0.0019	0.0019	0.0019	0.0019
Story3	0.0019	0.0019	0.0019	0.0019
Story2	0.0016	0.0017	0.0017	0.0016

Story1	0.0010	0.0011	0.0011	0.0011
Semi Sótano	0.0001	0.0001	0.0001	0.0001

Tabla XIII.- Derivas en la dirección YY'

En la *Tabla XIV* se muestran los porcentajes de variación en las derivas en la dirección *XX'* comparativamente para los modelos dinamicos de interaccion suelo-estructura en referencia al modelo convencional con base empotrada. Para el modelo de Barkan y Savinov, se observa un incremento en la deriva de 20.04% en el semi sotano de la estructura (nivel en contacto con la losa de cimentacion), para el caso de la Norma Rusa el porcentaje de incremento en la deriva fue de 11.52%, mientras que para Gazetas y Mylonakis la variacion fue del 18.12%. El promedio de variación de los tres modelos en el modelo con empotramiento convencional fue de 16.56%. Cabe señalar que la direccion *XX*' de la estructura es la dirección con menor rigidez del modelo estructural.

Nivel	Barkan Savinov	Norma Rusa	Gazetas & Mylonakis	Promedio
Azotea	3.34%	1.24%	0.55%	1.71%
Story5	3.44%	1.30%	0.79%	1.85%
Story4	3.44%	1.27%	1.09%	1.93%
Story3	3.62%	1.40%	1.37%	2.13%
Story2	4.25%	1.77%	2.02%	2.68%
Story1	6.29%	2.93%	4.07%	4.43%
Semi Sótano	20.04%	11.52%	18.12%	16.56%

Tabla XIV.- Porcentaje de variación en las derivas en la dirección XX'

En la *Tabla XV* se muestran los porcentajes de variación en las derivas en la dirección *YY'* utilizando los modelos dinamicos de interaccion suelo-estructura en comparacion al modelo con la base empotrada. En los resultados para el modelo de Barkan y Savinov se observa un incremento en la deriva de 10.53% en el semi sotano de la estructura, en el modelo con los coeficientes de la Norma Rusa el porcentaje de incremento en la deriva fue de 8.68%, mientras que para Gazetas & Mylonakis el incremento fue del 12.30%. El promedio de variación de los tres modelos en comparacion al modelo con empotramiento convencional fue de 10.50%. Cabe señalar que la direccion *YY'* de la estructura es la dirección con mayor rigidez del modelo estructural.

Nivel	Barkan Savinov	Norma Rusa	Gazetas & Mylonakis	Promedio
Azotea	1.81%	0.74%	0.25%	0.77%
Story5	1.67%	0.69%	0.31%	0.69%
Story4	1.61%	0.67%	0.32%	0.65%
Story3	1.63%	0.70%	0.24%	0.70%
Story2	1.88%	0.89%	0.02%	0.93%
Story1	2.77%	1.49%	0.96%	1.74%
Semi Sótano	10.53%	8.68%	12.30%	10.50%

Tabla XV.- Porcentaje de variación en las derivas en la dirección YY'

En la *Figura XIII* se observa las derivas de la estructura con el análisis convencional y las derivas con los modelos dinámicos de interacción suelo-estructura. Se aprecia que al incorporar los modelos de ISE las derivas se incrementan significativamente, este resultado se explica porque la incorporación de los coeficientes de rigidez y amortiguamiento en la cimentación modifican el comportamiento estructural de la edificación generando más deformación en el nivel de contacto con el suelo.

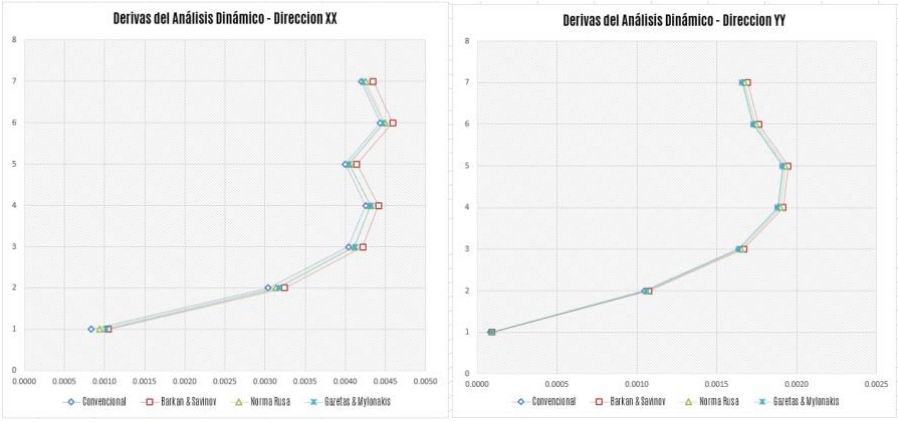

Figura XIII.- Derivas obtenidos con el análisis convencional y modelos dinámicos de ISE.

5.3. Esfuerzos cortantes con los modelos dinámicos de ISE. - Los modelos de interacción suelo-estructura pueden variar los esfuerzos cortantes en cada uno de los niveles de los modelos estructurales. Los esfuerzos cortantes obtenidos en la dirección *XX'* para el modelo convencional con la base empotrada y los modelos con interacción dinámica se muestran en la *Tabla XVI.*

Nivel	Modelo Convencional (tonf)	Barkan Savinov (tonf)	Norma Rusa (tonf)	Gazetas & Mylonakis (tonf)
Azotea	46.17	46.65	46.05	43.98
Story5	109.65	111.01	109.98	108.17
Story4	163.87	165.98	164.50	162.43
Story3	205.44	208.32	206.41	204.33
Story2	234.93	238.57	236.24	234.12
Story1	252.28	256.72	253.97	251.83
Semi Sótano	260.95	266.23	263.03	261.09

Tabla XVI.- Fuerzas cortantes en la dirección XX'

Los esfuerzos cortantes obtenidos en la dirección *YY'* para el modelo convencional con la base empotrada y los modelos con interacción dinámica se muestran en la *Tabla XVII.*

Nivel	Modelo Convencional (tonf)	Barkan Savinov (tonf)	Norma Rusa (tonf)	Gazetas & Mylonakis (tonf)
Azotea	47.48	47.34	47.15	45.63
Story5	115.94	115.66	115.53	113.01
Story4	170.15	169.72	169.53	166.33
Story3	210.04	209.42	209.24	205.56
Story2	237.80	237.00	236.73	232.40
Story1	252.99	252.00	251.56	246.66
Semi Sótano	261.41	260.58	258.92	255.91

Tabla XVII.- Fuerzas cortantes en la dirección YY'

En la *Tabla XVIII* se muestran los porcentajes de variación en las cortantes en la dirección XX*'* para los modelos dinamicos de interaccion suelo-estructura en referencia al modelo con la base empotrada. Para el modelo de Barkan y Savinov, se observa un incremento de 2.02% en el semi sotano de la estructura (nivel en contacto con la losa de cimentacion), para el caso de la Norma Rusa el porcentaje de incremento en la cortante fue de 0.80%, mientras que para Gazetas & Mylonakis la variacion fue del 4.98% en el último nivel, estos resultados determinan que los esfuerzos cortantes se incrementan, sin embargo no son significativos.

Nivel	Barkan Savinov	Norma Rusa	Gazetas & Mylonakis
Azotea	1.04%	0.26%	4.98%
Story5	1.24%	0.30%	1.37%

Story4	1.29%	0.38%	0.89%
Story3	1.40%	0.47%	0.55%
Story2	1.55%	0.56%	0.35%
Story1	1.76%	0.67%	0.18%
Semi Sótano	2.02%	0.80%	0.05%

Tabla XVIII.- Porcentaje de variación en las cortantes en la dirección XX'

En la *Tabla XIX* se muestran los porcentajes de variación en las cortantes en la dirección *YY'*. Para los modelos dinamicos de interaccion suelo-estructura, se obtuvo para el modelo de Barkan y Savinov, se observa un incremento poco significativo de 0.32% en el semi sotano de la estructura, para el modelo de la Norma Rusa el porcentaje de incremento en los esfuerzos cortantes fue de 0.95%, mientras que para Gazetas & Mylonakis el incremento fue del 2.15% en el nivel en contacto con el suelo.

Nivel	Barkan Savinov	Norma Rusa	Gazetas & Mylonakis
Azotea	0.30%	0.69%	4.04%
Story5	0.24%	0.36%	2.59%
Story4	0.26%	0.37%	2.30%
Story3	0.29%	0.38%	2.18%
Story2	0.34%	0.45%	2.32%
Story1	0.39%	0.57%	2.57%
Semi Sótano	0.32%	0.95%	2.15%

Tabla XIX.- Porcentaje de variación en las cortantes en la dirección YY'

6. Resultados de los modelos ISE dinámicos mediante un análisis tiempo historia. - El procedimiento analítico de análisis tiempo historia en las estructuras, es un método numérico utilizado para evaluar la respuesta dinámica de las estructuras bajo cargas variables en el tiempo que se presentan en un sismo real. Mediante este método analítico en la dinámica estructural, se aplica una simulación de fuerzas y desplazamientos variables en el tiempo, que pueden ser tomados de registros sísmicos reales o simulados; mediante los métodos de superposición modal o integración directa, se procede a evaluar la deformación, tensión y aceleración en la estructura a lo largo del tiempo, como consecuencia de la aplicación de estas fuerzas variables.

Según lo que señala la Norma peruana E030, en el Art. 30, el análisis tiempo historia puede ser usado como un procedimiento complementario al análisis modal espectral, usando para ello acelerogramas reales o simulaciones con sus dos componentes EW (Este-Oeste) y NS (Norte-Sur). Los registros sísmicos deben estar escalados al espectro de diseño o al espectro con un sismo máximo considerado, teniendo en cuenta un factor de reducción R=1.

En el análisis complementario de tiempo historia de los modelos dinámicos con interacción suelo-estructura se utilizó el sismo de Lima ocurrido en octubre de 1966. A continuación, se muestra en la *Tabla XX* los detalles técnicos del evento sísmico.

Ficha Técnica de Sismo de Lima de 1966	
Estación donde se registró el sismo	Parque de la Reserva
Fecha del evento sísmico	17 de Octubre de 1966
Profundidad del sismo	25 km
Magnitud en Escala de Richter	8.1 Mb
Numero de registros (Analógico)	3283
Pico de aceleración componente EW	-180.56 cm/s2
Pico de aceleración componente NS	-268.24 cm/s2
Frecuencia e Intervalo de registro	0.02s

Tabla XX.- Datos técnicos del evento sísmico de Lima 1966

El sismo seleccionado se procedió a escalar a un espectro de escalamiento con un factor de reducción R=1, considerando las recomendaciones de la Norma técnica peruana E030. En la *Figura XIV* se aprecia los componentes del sismo de Lima EW y NS, en la imagen superior se observa el registro original y en la imagen inferior el sismo después del escalamiento.

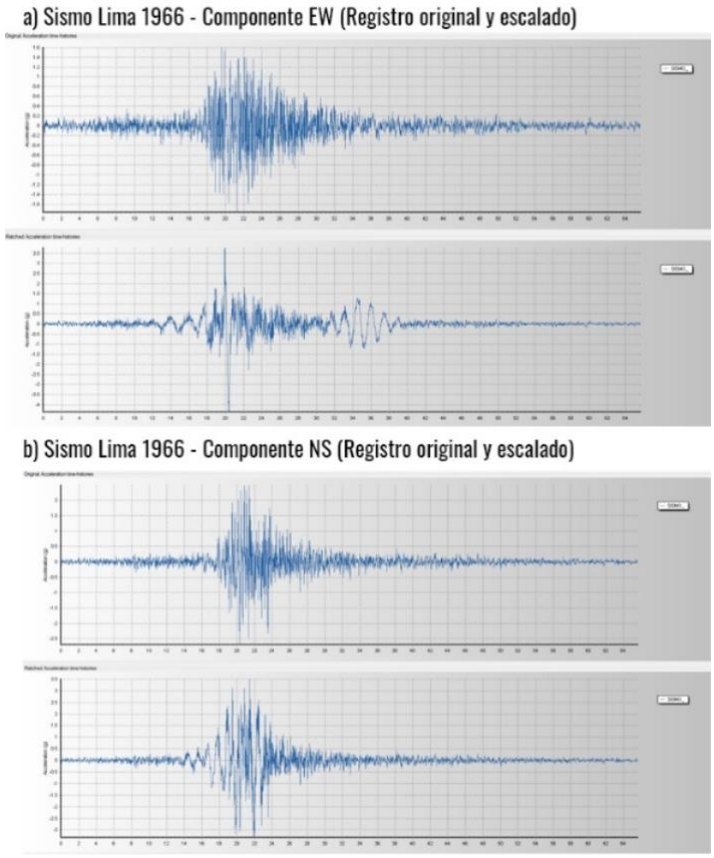

Figura XIV.- Componentes EW-NS del sismo de Lima 1966, original y escalado

En la *Tabla XXI* se muestra la aceleración de los registros escalados al espectro inelástico, considerando el sismo de diseño.

Sismo de Lima 1966	Aceleración original		Aceleración escalada	
	EW	NS	EW	NS
Aceleración máxima (m/s2)	1.8056	2.6824	4.3146	3.432
Aceleración en unidades de g	0.18g	0.27g	0.44g	0.35g

Tabla XXI.- Resultados del escalamiento del evento sísmico de Lima 1966

Los registros escalados generaron cuatro casos de análisis por cada modelo con interacción suelo estructura. El sismo de Lima EW – componente EW aplicado en la dirección *XX'* y en la dirección *YY'*.

Las derivas de entrepiso en la dirección *XX'* mediante el análisis tiempo historia obtenidos para el modelo con base empotrada y los modelos con interacción dinámica suelo-estructura se muestran en la *Tabla XXII*.

Nivel	Modelo Convencional	Barkan Savinov	Norma Rusa	Gazetas & Mylonakis
Azotea	0.0046	0.0049	0.0047	0.0048
Story5	0.0052	0.0055	0.0053	0.0054
Story4	0.0053	0.0056	0.0054	0.0054
Story3	0.0058	0.0061	0.0059	0.0060
Story2	0.0056	0.0060	0.0058	0.0058
Story1	0.0044	0.0047	0.0045	0.0046
Semi Sótano	0.0012	0.0015	0.0014	0.0015

Tabla XXII.- Derivas con análisis Tiempo Historia. Sismo de Lima 1966 – EW, en la dirección XX'

Las derivas de entrepiso en la dirección *YY'* mediante el análisis tiempo historia obtenidos para el modelo con base empotrada y los modelos dinámicos con interacción suelo-estructura se muestran en la *Tabla XXIII*.

Nivel	Modelo Convencional	Barkan Savinov	Norma Rusa	Gazetas & Mylonakis
Azotea	0.0015	0.0016	0.0015	0.0015
Story5	0.0016	0.0016	0.0016	0.0015
Story4	0.0018	0.0018	0.0018	0.0017
Story3	0.0018	0.0018	0.0018	0.0018
Story2	0.0016	0.0016	0.0016	0.0016
Story1	0.0011	0.0011	0.0011	0.0011
Semi Sótano	0.0001	0.0001	0.0001	0.0001

Tabla XXIII.- Derivas con análisis Tiempo Historia. Sismo de Lima 1966 – EW, en la dirección YY'

En la *Tabla XXIV* se muestran los porcentajes de variación en las derivas en la dirección *XX'* para los modelos dinamicos de interaccion suelo-estructura. Para el modelo de Barkan y Savinov, se observa un incremento en la deriva de 19.90 % en el semi sotano de la estructura (nivel en contacto con la losa de cimentacion), para el caso de la Norma Rusa el porcentaje de incremento en la deriva fue de 11.66%, mientras que para Gazetas y Mylonakis la variacion fue del 18.89%, el promedio de variación de los tres modelos en el modelo con empotramiento convencional fue de 16.82%.

Nivel	Barkan Savinov	Norma Rusa	Gazetas & Mylonakis	Promedio
Azotea	5.85%	3.13%	3.54%	4.17%
Story5	5.80%	3.04%	3.50%	4.12%
Story4	5.05%	1.91%	2.77%	3.25%
Story3	5.38%	2.36%	3.17%	3.63%
Story2	5.53%	1.97%	3.19%	3.56%
Story1	6.32%	3.01%	4.60%	4.65%
Semi Sótano	19.90%	11.66%	18.89%	16.82%

Tabla XXIV.- Porcentaje de variación en las derivas. Sismo de Lima 1966 – EW, en la dirección XX'

En la *Tabla XXV* se muestran los porcentajes de variación en las derivas en la dirección *YY'* utilizando los modelos dinamicos de interaccion suelo-estructura. En los resultados para el modelo de Barkan y Savinov se observa un incremento en la deriva de 7.22% en el semi sotano de la estructura, en el modelo con los coeficientes de la Norma Rusa el porcentaje de incremento en la deriva fue de 5.59%, mientras que para Gazetas & Mylonakis el incremento fue del 7.85%. El promedio de variación de los tres modelos en comparacion al modelo con empotramiento convencional fue de 6.89%.

Nivel	Barkan Savinov	Norma Rusa	Gazetas & Mylonakis	Promedio
Azotea	4.26%	2.50%	1.83%	2.86%
Story5	0.17%	1.23%	2.56%	1.21%
Story4	0.28%	0.84%	1.82%	0.98%
Story3	0.00%	0.61%	1.39%	0.67%
Story2	0.46%	0.30%	0.80%	0.21%
Story1	1.38%	0.37%	0.27%	0.68%
Semi Sótano	7.22%	5.59%	7.85%	6.89%

Tabla XXV.- Porcentaje de variación en las derivas. Sismo de Lima 1966 – EW, en la dirección YY'

En la *Figura XV* se aprecia los resultados de las derivas con el análisis tiempo historia, en la estructura con la base empotrada y con los coeficientes dinámicos de interacción suelo-estructura. El sismo usado en este caso fue el Sismo de Lima 1966 – componente EW, los resultados muestran un incremento de las derivas en la dirección *XX' y* dirección *YY'*.

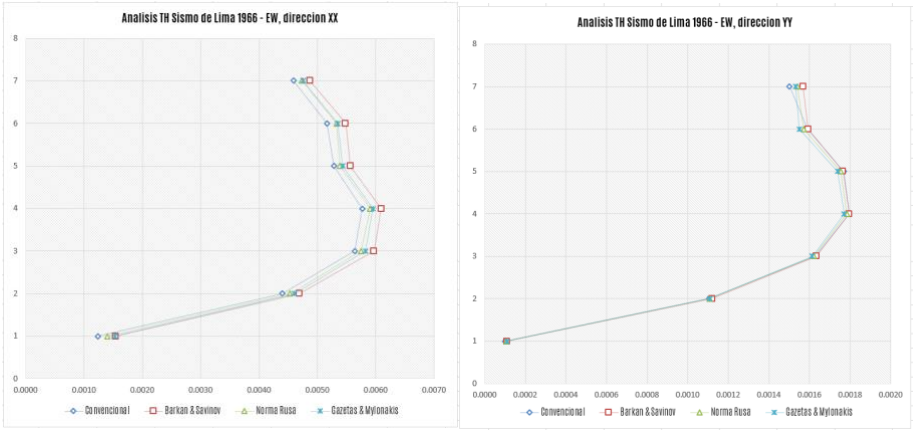

Figura XV.- Derivas obtenidos con el sismo de Lima 1966, componente EW

Los resultados para el caso del componente NS del sismo de Lima de 1966 se muestran en las tablas siguientes. Las derivas de entrepiso en la dirección *XX'* mediante el análisis tiempo historia obtenidos para el modelo con base empotrada y los modelos dinámicos con interacción suelo-estructura se muestran en la *Tabla XXVI.*

Nivel	Modelo Convencional	Barkan Savinov	Norma Rusa	Gazetas & Mylonakis
Azotea	0.0042	0.0046	0.0043	0.0044
Story5	0.0047	0.0050	0.0047	0.0048
Story4	0.0046	0.0046	0.0046	0.0044
Story3	0.0048	0.0049	0.0048	0.0047
Story2	0.0047	0.0049	0.0048	0.0048
Story1	0.0037	0.0040	0.0039	0.0039
Semi Sótano	0.0011	0.0014	0.0012	0.0013

Tabla XXVI.- Derivas con análisis Tiempo Historia. Sismo de Lima 1966 – NS, en la dirección XX'

Las derivas de entrepiso en la dirección *YY'* mediante el análisis tiempo historia obtenidos para el modelo con base empotrada y los modelos dinámicos con interacción suelo-estructura se muestran en la *Tabla XXVII.*

Nivel	Modelo Convencional	Barkan Savinov	Norma Rusa	Gazetas & Mylonakis
Azotea	0.0012	0.0013	0.0013	0.0013
Story5	0.0013	0.0014	0.0013	0.0013
Story4	0.0014	0.0015	0.0014	0.0014
Story3	0.0014	0.0014	0.0014	0.0014
Story2	0.0012	0.0012	0.0012	0.0012
Story1	0.0007	0.0008	0.0008	0.0008
Semi Sótano	0.0001	0.0001	0.0001	0.0001

Tabla XXVII.- Derivas con análisis Tiempo Historia. Sismo de Lima 1966 – NS, en la dirección YY'

En la *Tabla XXVIII* se muestran los porcentajes de variación en las derivas en la dirección *XX'* para los modelos dinamicos de interaccion suelo-estructura. Para el modelo de Barkan y Savinov, se observa un incremento en la deriva de 20.65% en el semi sotano de la estructura (nivel en contacto con la losa de cimentacion), para el caso de la Norma Rusa el porcentaje de incremento en la deriva fue de 11.92%, mientras que para Gazetas y Mylonakis la variacion fue del 17.86%, el promedio de variación de los tres modelos en el modelo con empotramiento convencional fue de 16.81%.

Nivel	Barkan Savinov	Norma Rusa	Gazetas & Mylonakis	Promedio
Azotea	10.00%	2.50%	5.46%	5.99%
Story5	5.78%	1.28%	2.90%	3.32%
Story4	0.31%	1.19%	4.65%	1.26%
Story3	1.31%	0.79%	1.20%	0.22%

Story2	5.20%	2.34%	2.38%	3.31%
Story1	7.17%	3.42%	4.04%	4.88%
Semi Sótano	20.65%	11.92%	17.86%	16.81%

Tabla XXVIII.- Porcentaje de variación en las derivas. Sismo de Lima 1966 – NS, en la dirección XX'

En la *Tabla XXIX* se muestran los porcentajes de variación en las derivas en la dirección *YY'* utilizando los modelos dinamicos de interaccion suelo-estructura en comparacion a la estructura con base empotrada convencionalmente. En los resultados para el modelo de Barkan y Savinov se observa un incremento en la deriva de 16.53% en el semi sotano de la estructura, en el modelo con los coeficientes de la Norma Rusa el porcentaje de incremento en la deriva fue de 12.17%, mientras que para Gazetas & Mylonakis el incremento fue del 15.48%. El promedio de variación de los tres modelos en comparacion al modelo con empotramiento convencional fue de 14.73%.

Nivel	Barkan Savinov	Norma Rusa	Gazetas & Mylonakis	Promedio
Azotea	4.97%	2.35%	2.58%	3.30%
Story5	4.77%	2.29%	2.43%	3.16%
Story4	4.93%	2.32%	2.63%	3.29%
Story3	4.99%	2.40%	2.74%	3.38%
Story2	5.18%	2.49%	3.04%	3.57%
Story1	5.16%	2.51%	3.32%	3.66%
Semi Sótano	16.53%	12.17%	15.48%	14.73%

Tabla XXIX.- Porcentaje de variación en las derivas. Sismo de Lima 1966 – NS, en la dirección YY'

En la *Figura XVI* se aprecia los resultados de las derivas con el análisis tiempo historia, en la estructura con la base empotrada y con los coeficientes dinámicos de interacción suelo-estructura. El sismo usado en este caso fue el Sismo de Lima 1966 – componente NS, los resultados muestran las derivas en la dirección *XX' y* dirección *YY'*. Se observa un incremento de las derivas significativo en la base de la edificación, los resultados en el análisis tiempo historia confirman los resultados obtenidos mesdiante el analisis modal espectral.

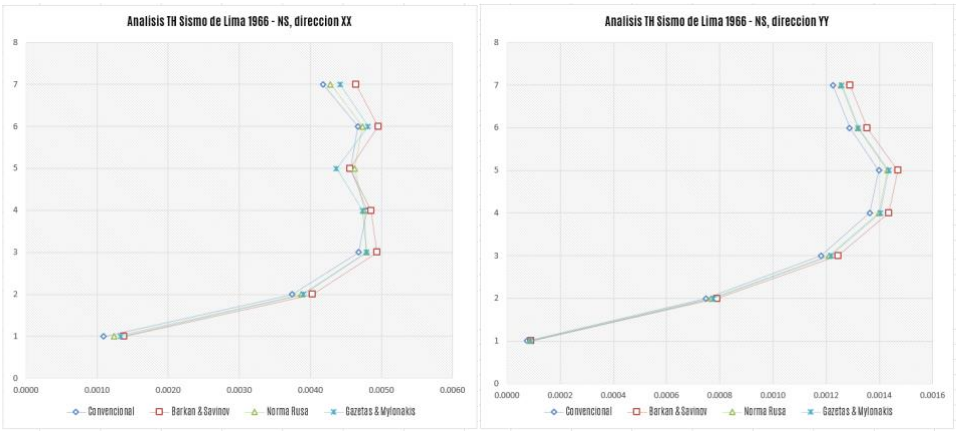

Figura XVI.- Derivas obtenidos con el sismo de Lima 1966, componente NS

7. Conclusiones

- El estudio inicia con el análisis de una edificación con un sistema estructural predominante en muros estructurales, utilizando un procedimiento convencional analítico modal espectral con el supuesto hipotético que la cimentación en contacto con el suelo es empotrada tal como lo señala la normativa peruana E030. Mediante un estudio de mecánica de suelos se procedió a determinar las propiedades del estrato que subyace a la cimentación, dichas propiedades se usaron para calcular los coeficientes de interacción suelo-estructura para los modelos ISE de Barkan y Savinov, Norma Rusa SNIP 2.02.05-87 y Gazetas & Mylonakis, al incorporar los coeficientes en los modelos respectivos se llegó a determinar que estos modelos de ISE tienen efectos importantes sobre el comportamiento estructural de la edificación, siendo la deriva el indicador principal que muestra un incremento en todos los casos de análisis. Mediante un análisis tiempo historia considerando el sismo de Lima de 1966 se verificó que los resultados concuerdan con los resultados obtenidos mediante el procedimiento analítico modal espectral.

- Mediante la incorporación de los coeficientes dinámicos de interacción suelo-estructura en el análisis estructural, se demostró que existe una modificación en las frecuencias de vibración del modelo estructural, una variación del periodo en un rango menor al 5% en comparación al modelo estructural con un análisis convencional que considera la base con restricción a desplazamientos en sus ejes traslacionales y rotacionales. El resultado obtenido se debe en gran medida al grado de rigidez de la estructura, que lo clasifica como una estructura con un sistema de muros estructurales, dentro de los modelos dinámicos de interacción suelo-estructura se apreció un incremento del periodo en 1.6% para el modelo de Barkan y Savinov, lo que permite determinar que la variación en este indicador del comportamiento estructural no es significativa.

- En lo concerniente a los esfuerzos cortantes se apreció un incremento no significativo con los modelos dinámicos de interacción suelo-estructura. La máxima variación obtenida fue del 4.04% para el modelo de Gazetas & Mylonakis en el último nivel de la estructura. La incorporación de los coeficientes de interacción dinámica suelo-estructura confirmaron el incremento de esfuerzos, sin embargo, para la zona de aceleración sísmica Zona 2 no se consideran significativas.

- En las derivas de entrepiso de la estructura provocadas por las deformaciones laterales, la incorporación de los coeficientes dinámicos de interacción suelo-estructura confirmaron un incremento significativo en el nivel 1 o semisótano, variando en la dirección *XX'* de la estructura en un 20.04% para el modelo dinámico de Barkan y Savinov, para el modelo con los coeficientes de la Norma Rusa fue de 11.52%, mientras que en el modelo con los coeficientes de Gazetas & Mylonakis se obtuvo un incremento de 18.12%. En la dirección *YY'* de la edificación se obtuvo un incremento de 10,53% para el modelo dinámico de Barkan y Savinov, para el modelo de la Norma Rusa se obtuvo un incremento en 8.68%, mientras que en el modelo con los coeficientes de Gazetas & Mylonakis se obtuvo un incremento de 12.30%. En un análisis modal espectral se determinó que el incremento de las derivas es significativo, al considerar la interacción suelo-estructura con los modelos dinámicos.

- En el análisis tiempo historia con el sismo de Lima – 1966 para el caso de análisis con el componente EW, la incorporación de los coeficientes dinámicos de interacción suelo-estructura confirmaron un incremento significativo en el nivel 1 o semisótano. En la dirección *XX'* de la estructura se apreció un incremento de 19.90% para el modelo dinámico de Barkan y Savinov, para el modelo con los coeficientes de la Norma Rusa fue de 11.66%, mientras que en el modelo con los coeficientes de Gazetas & Mylonakis se obtuvo un incremento de 18.89%. En la dirección *YY'* de la edificación se obtuvo un incremento de 7.22% para el modelo dinámico de Barkan y Savinov, para el modelo de la Norma Rusa se obtuvo un incremento en 5.59%, mientras que en el modelo con los coeficientes de Gazetas & Mylonakis se obtuvo un incremento de 7.85%. Los resultados confirman el resultado obtenido con el método modal espectral, siendo la variación promedio en la dirección *XX´* de un 16.82%.

- En el análisis tiempo historia con el sismo de Lima – 1966 para el caso de análisis con el componente NS, la incorporación de los coeficientes dinámicos de interacción suelo-estructura confirmaron un incremento significativo en el nivel 1 o semisótano. En la dirección *XX'* de la estructura se apreció un incremento de 20.65% para el modelo dinámico de Barkan y Savinov, para el modelo con los coeficientes de la Norma Rusa fue de 11.92%, mientras que en el modelo con los coeficientes de Gazetas & Mylonakis se obtuvo un incremento de 17.86%. En la dirección *YY'* de la edificación se obtuvo un incremento de 16.53% para el modelo dinámico de Barkan y Savinov, para el modelo de la Norma Rusa se obtuvo un incremento en 12.17%, mientras que en el modelo con los coeficientes de Gazetas & Mylonakis se obtuvo un incremento de 15.48%. Los resultados para este caso de análisis tiempo historia confirman el resultado obtenido con el método modal espectral, siendo la variación promedio en la dirección *XX´* de un 16.81%.

- Mediante los resultados obtenidos por el procedimiento modal espectral y análisis tiempo historia en la estructura, se demuestra que la incorporación de los modelos dinámicos de interacción suelo-estructura modifican el comportamiento estructural significativamente, específicamente en las derivas en el nivel que se encuentra en contacto directo con la losa de cimentación, Ccorratgé, Martínez y Cobelo (2022) refuerzan estos resultados al demostrar que la consideración de la interacción dinámica suelo-estructura genera incrementos en los desplazamientos en el tope de la edificación y en las derivas por piso, lo que podría llevar a un desempeño estructural menos favorable, entrando en rangos de pre-colapso y colapso.

- Se concluye que la utilización de los modelos dinámicos de interacción suelo-estructura exigen a la estructura a una mayor deformación lateral, resultado que coincide con las investigaciones realizadas por autores diversos como Villarreal (2023), Morales y Espinoza (2020), Acuña y Molina (2023) quienes llegan a concluir que un

efecto del uso de los modelos de interacción suelo-estructura es un incremento en las derivas de la estructura, lo cual puede ser una diferencia para que una edificación pase del rango elástico al inelástico.

8. Recomendaciones

- Mediante los resultados obtenidos se llegó a determinar que los modelos de ISE dinámicos incrementan las derivas de la estructura principalmente en el nivel que está en contacto con la cimentación, modificando el comportamiento estructural de la edificación. Los resultados obtenidos mediante el uso de los coeficientes dinámicos de interacción suelo-estructura, muestran resultados con un mayor grado de realidad en el modelamiento, por lo cual es recomendable considerar la incorporación de la interacción dinámica suelo-estructura en la Norma Peruana de Diseño Sismorresistente E030.

- Considerando que la interacción suelo-estructura con los modelos dinámicos de Barkan y Savinov, Norma Rusa y Gazetas & Mylonakis, en un suelo flexible afectan con mayor incidencia en el nivel más bajo, es necesario considerar investigaciones similares en estructuras que puedan presentar irregularidades de rigidez en ese nivel como piso blando, estructuras con sistemas aporticados y estructuras con sistemas duales de columnas y muros estructurales.

- Es recomendable considerar modelos dinámicos de interacción suelo-estructura con procedimientos analíticos de tiempo historia con diversos sismos que puedan ser representativos para la zona sísmica en estudio. Considerando que los resultados obtenidos pueden ser más exigentes para procedimientos de análisis no lineal y no líneal por integración directa.

- Es recomendable considerar el estudio de los modelos dinámicos de interacción suelo-estructura en edificaciones reales, como colegios, escuelas y hospitales, en vista que cada tipología presenta una variedad de sistemas estructurales diferentes por su uso, por lo cual mediante la incorporación de los modelos ISE se puede señalar en que tipologías pueden ser de uso obligatorio y normativo.

Referencias

[1] *Acuña, F. & Molina, C. Efectos de la interacción suelo estructura (ISE) en una edificación de 5 pisos tipo pórtico en concreto reforzado sobre suelo blando (arcilla) típico en la ciudad de Montería – Córdoba.* 2023. Revista Ciencia latina, Vol. 7 Núm. 4 (2023)

[2] Braña, P. Gamón, R, Fundora, Nelson, & Martínez, J. *Influence of Height in the Consideration of the Dynamic Soil-structure Interaction in Buildings with dual Typology Located in Areas of High SeismicHazard*. Journal of earthquake engineering, 2022, vol. 26, no. 5, p. 1234-1256.

[3] Ccorratgé, Z. Martínez, J y Cobelo, W. *Influencia de la interacción dinámica suelo-estructura en el mecanismo de colapso y nivel de desempeño de edificaciones de hormigón armado*. 2022. Revista de Ingeniería Sísmica, p. 41-53.

[4] García, J. Ramsés, J. & Fernández, L. *Efecto de la Interacción Suelo- Estructura en la detección de daño, usando el método de rigideces base*. 2011 Sociedad Mexicana de Ingeniería Sísmica. XVIII Congreso nacional de Ingeniería Sísmica.

[5] Morales, L. & Espinoza, A. *Influencia de la interacción suelo estructura (ISE) de cimentaciones superficiales en suelos no cohesivos en el comportamiento estructural de una edificación de 8 pisos y un subsuelo*. 2020. Revista Ingenio, N.º 1 vol. 3 (2020)

[6] MVCS (Ministerio de Vivienda, Construcción y Saneamiento). *Norma E020. Cargas*. Lima - Perú

[7] MVCS (Ministerio de Vivienda, Construcción y Saneamiento). *Norma E030. Diseño Sismorresistente*. Lima - Perú.

[8] MVCS (Ministerio de Vivienda, Construcción y Saneamiento). *Norma E060. Concreto Armado*. Lima - Perú.

[9] NIST GCR 12-917-21. *Soil-Structure Interaction for Building Structures. 2012*, National Institute of Standards and Technology Engineering Laboratpory Gaithersburg. California, USA.

[10] Tena, A. *Interacción suelo-estructura: reflexiones sobre su importancia en la respuesta dinámica de estructuras durante sismos*. Revista Internacional de Ingeniería de Estructuras, 2019, Vol. 24, Nro. 2, p. 141-165.

[11] Obinna, U. *Modelling of Soil- Structure Interaction*. 2022, Structville Integrated Services Limited. USA. https://structville.com/2022/03/modelling-of-soil-structure-interaction.html#google_vignette

[12] Villarreal, G. *Interacción Sísmica Suelo-Estructura en Edificaciones con Plateas de cimentación. 2017*, Primera edición. Lima, Perú.

[13] Villarreal, G. *Soil-Structure Interaction in Buildings*. 2023, Revista Internacional de Ingeniería de Estructuras. Vol. 28, 2, 103-125(2023)

[14] Villarreal, G. Interacción Sísmica Suelo-Estructura en Edificaciones con zapatas aisladas. 2009, Primera edición. Lima, Perú.

[15] Villarreal, G. & Aguila, C. *Soil-structure interaction and its influence on the seismic response of rc buildings*. Revista Internacional de Ingeniería de Estructuras, 2021, vol. 14, no. 2, p. 55-73.

Nota contribución de los autores:

1. Concepción y diseño del estudio
2. Adquisición de datos
3. Análisis de datos
4. Discusión de los resultados
5. Redacción del manuscrito
6. Aprobación de la versión final del manuscrito

JC ha contribuido en: 1, 2, 3, 4, 5 y 6.
GVC ha contribuido en: 1, 2, 3, 4, 5 y 6.

Nota de aceptación: Este artículo fue aprobado por los editores de la revista Dr. Rafael Sotelo y Mag. Ing. Fernando A. Hernández Gobertti.

An IoT-Based Autonomous Waiter Robot

Un robot camarero autónomo basado en IoT

Um robô garçom autónomo baseado em IoT

Sadiq Ur Rehman[1(*)]

Recibido: 17/10/2024 Aceptado: 26/01/2025

Summary. - The widespread adoption of automation and robotics across various sectors has driven innovations in service delivery, particularly in the hospitality industry. This paper presents the design, development, and implementation of an IoT-based waiter robot aimed at enhancing efficiency and customer satisfaction in restaurants. The robot employs an ESP32 microcontroller, ultrasonic sensors, and a touchscreen interface for autonomous navigation, order processing, and food delivery. Unlike traditional path-planning approaches, this robot adapts dynamically to its environment, offering flexibility and reliability in service. Detailed evaluations demonstrate the system's effectiveness in optimizing operations, reducing delays, and improving overall customer experience. The proposed solution is cost-effective and scalable, making it suitable for diverse restaurant settings.

Keywords: IoT, ESP32, Robot, Automation, Ultrasonic Sensors, Real-time Navigation

(*) Corresponding author.

[1] Ph.D., Assistant Professor, FEST, Hamdard University (Pakistan), sadiq.rehman@hamdard.edu.pk,
ORCID iD: https://orcid.org/0000-0002-6308-450X

Memoria Investigaciones en Ingeniería, núm. 28 (2025). pp. 154-167
https://doi.org/10.36561/ING.28.11
ISSN 2301-1092 • ISSN (en línea) 2301-1106 – Universidad de Montevideo, Uruguay

Resumen. - *La adopción generalizada de la automatización y la robótica en varios sectores ha impulsado innovaciones en la prestación de servicios, particularmente en la industria hotelera. Este artículo presenta el diseño, desarrollo e implementación de un robot camarero basado en IoT destinado a mejorar la eficiencia y la satisfacción del cliente en restaurantes. El robot emplea un microcontrolador ESP32, sensores ultrasónicos y una interfaz de pantalla táctil para navegación autónoma, procesamiento de pedidos y entrega de alimentos. A diferencia de los enfoques tradicionales de planificación de rutas, este robot se adapta dinámicamente a su entorno, ofreciendo flexibilidad y confiabilidad en el servicio. Las evaluaciones detalladas demuestran la eficacia del sistema para optimizar las operaciones, reducir los retrasos y mejorar la experiencia general del cliente. La solución propuesta es rentable y escalable, lo que la hace adecuada para diversos entornos de restaurantes.*

Palabras clave: *IoT, ESP32, Robot, Automatización, Sensores ultrasónicos, Navegación en tiempo real.*

Resumo. ***-*** *A adoção generalizada da automação e da robótica em vários setores impulsionou inovações na prestação de serviços, especialmente na indústria hoteleira. Este artigo apresenta o projeto, desenvolvimento e implementação de um robô garçom baseado em IoT que visa aumentar a eficiência e a satisfação do cliente em restaurantes. O robô emprega um microcontrolador ESP32, sensores ultrassônicos e uma interface touchscreen para navegação autônoma, processamento de pedidos e entrega de alimentos. Ao contrário das abordagens tradicionais de planejamento de trajetória, este robô se adapta dinamicamente ao seu ambiente, oferecendo flexibilidade e confiabilidade no serviço. Avaliações detalhadas demonstram a eficácia do sistema na otimização das operações, na redução de atrasos e na melhoria da experiência geral do cliente. A solução proposta é econômica e escalável, tornando-a adequada para diversos ambientes de restaurantes.*

Palavras-chave: *IoT, ESP32, Robô, Automação, Sensores Ultrassônicos, Navegação em Tempo Real.*

1. Introduction. - Technological advancements have significantly transformed various industries, leading to the integration of robots into daily operations. In healthcare, robots assist in delicate surgeries, while in manufacturing, they optimize production lines from assembly to packaging [1, 2]. Recently, the service sector has embraced robotics, introducing IoT-based waiter robots to revolutionize dining experiences in restaurants, coffee shops, and similar setups [3]. These robots aim to improve order processing efficiency, ensure timely food delivery, and navigate safely through congested aisles. Furthermore, they provide restaurant owners with opportunities to reduce operational costs and enhance employee productivity, creating a seamless and technologically advanced customer experience [4].

Conventional food delivery systems in restaurants rely heavily on human labor, resulting in inefficiencies such as delayed service, order mix-ups, and high operating costs. These limitations underscore the need for automated solutions. Leveraging IoT technology enables real-time data transfers, paving the way for autonomous systems capable of performing tasks without human intervention [5-9]. This study proposes an IoT-based waiter robot to address these challenges by integrating advanced navigation algorithms, real-time obstacle avoidance, and decision-making processes. Table 1 compares existing waiter robots, emphasizing their features and limitations.

Feature	Robo Waiter	Savioke Relay	Bear Robotics Penny	Pudu Bot	Bella Bot
Manufacturer	Robo Waiter	Savioke	Bear Robotics	Pudu Tech	Pudu Tech
Country	Denmark	USA	USA	China	China
Navigation System	Lidar	Lidar, Camera	Lidar, Camera	Lidar, Camera	Lidar, Camera
Interaction Method	Buttons	Touch Screen	Touch Screen, Voice	Touch Screen	Touch Screen, Voice
Payload Capacity	2 kg	5 kg	12 kg	30 kg	10 kg
Battery Life	8 hours	24 hours	12 hours	10-12 hours	12-16 hours
Charging Time	2 hours	2 hours	4 hours	4 hours	4 hours
Max Speed	0.5 m/s	1.1 m/s	0.9 m/s	1.2 m/s	1.2 m/s
Obstacle Detection	Basic IR sensor	Advanced sensor	Advanced sensor	Advanced sensor	Advanced sensor
Connectivity	Bluetooth	Wi-Fi	Wi-Fi, Bluetooth	Wi-Fi	Wi-Fi
Cost	Low	High	Medium	Medium	Medium
Additional Features	Basic voice responses	Can call the elevator, SLA	Advanced voice recognition	Multi-robot collaboration	Facial recognition, AI
Application	Simple table service	Hotel service, Delivery	Restaurant service	Restaurant service	Restaurant service

Table I. Comparison table for different bots

Following are the key contributions of our work.

1. Combining IoT technologies with robotics and real-time data processing.
2. Significantly improves service efficiency and reduces operational delays.
3. Features a scalable architecture that adapts to various restaurant sizes and needs.

Recent advancements in waiter robots reflect substantial progress in automation, efficiency, and technology integration. Table 2. Demonstrate the comparative analysis of significant studies and technological improvement in comparison to the proposed model

References	Limitations	Proposed Work
[10]	Robots followed only designated paths with IR sensor arrays; and high-voltage HUB motors.	Utilized lithium-ion batteries for better energy efficiency; implemented advanced mapping for improved navigation.
[11]	Used RFID tags for table identification.	Adopted advanced mapping for flexible and efficient table navigation.

[12]	RFID is used for order management, but it has limited obstacle-detection and path-finding capabilities.	Enhanced with ultrasonic sensors for obstacle detection; used mapping for path finding; integrated order processing and billing.
[13]	Designed an IoT-based robot with real-time tracking and mobile app control.	Showcased ESP32's real-time capabilities and ease of integration with mobile apps.

Table II. Comparative analysis of significant studies and technological improvement

The remainder of this paper is organized as follows: Section II describes the Proposed Architectural Model and Methodology of the system. Section III presents the results and discussion, highlighting the system's performance. Finally, Section IV concludes the paper with a summary of the key findings and the implications for the future of automated restaurant services.

2. Proposed Architectural Model and Methodology. - The development of the IoT-based waiter robot involved a series of well-structured steps to ensure its efficiency and reliability. The robot's architecture and specifications are illustrated in the block diagram in Figure I and the system process diagram in Figure III.

2.1 System Overview. - The IoT-based waiter robot's architecture integrates hardware and software components to ensure autonomous navigation and efficient task execution. For the robot, the ESP32 microcontroller [14] is used for its multi-functionality and an in-built Wi-Fi module which is very essential in IoT and is used to control robots, appliances, and other attributes to ensure perfect interaction between the robot, the kitchen, and the customers.

For navigation and obstacle detection purposes, the robot uses ultrasonic sensors with a range of up to 21 meters which allows the robot to smoothly operate at the restaurants. Further, using the TCRT5000 infrared sensor [15], the robot can identify when the trays placed for the customer's food have been taken and only then return to the kitchen.

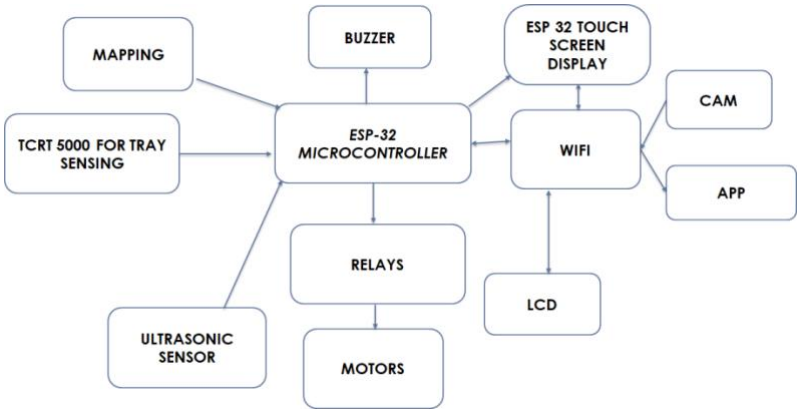

Figure I. Block Diagram

The robot has a touch-based LCD, with ESP32 (connections can be seen in Figure II) at the customer interface and the kitchen interface. In the kitchen, such a display gives instructions to the robot to move to the customer's table to take an order. Once at the customer's table, the robot provides the customer with the menu where the customer makes his/her order which is sent back to the kitchen through the WiFi. The chef then prepares the order and places it on the robot's tray.

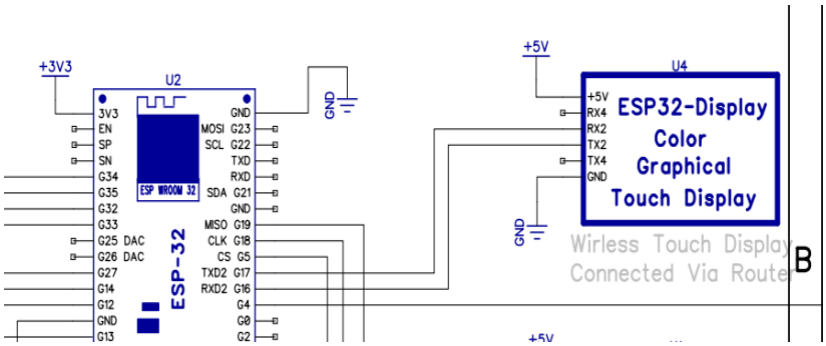

Figure II. Connection of ESP 32 with TOUCH LCD

Upon order completion, the chef commands the robot to deliver the meal to the customer. The robot uses its ultrasonic sensors to navigate, halting if an obstacle is detected until the path is clear. After the customer takes their meal, detected by the TCRT5000 sensor, the robot returns to its initial position in the kitchen, ready for the next task.

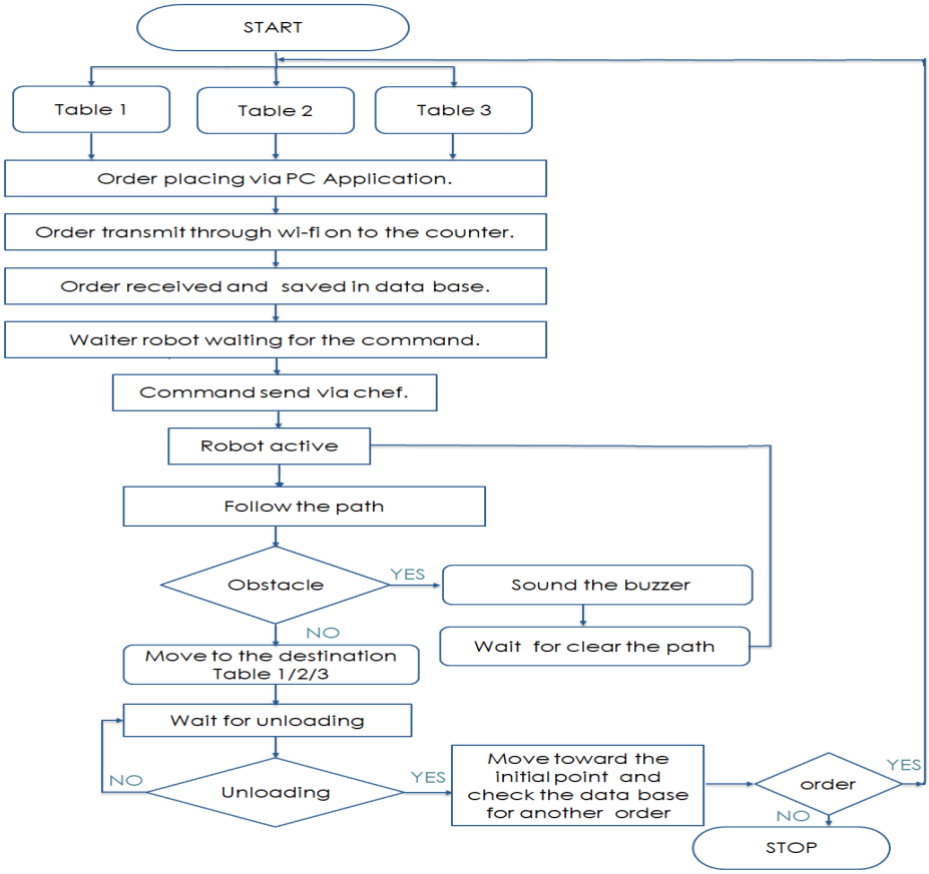

Figure III. System Process Diagram

The robot is powered by a 24V lithium-ion battery, which provides energy to the DC-geared motors [16] through a 4-channel relay module. The relay module, connected to the ESP32, allows precise control of the robot's movements (see Figure IV).

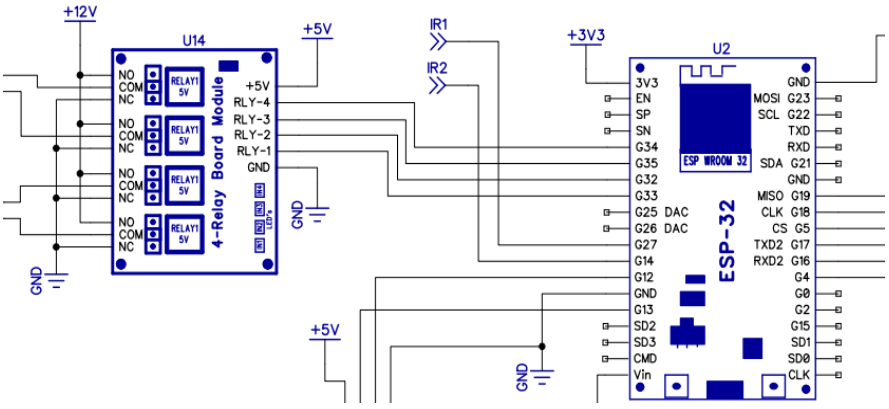

Figure IV. Connection of ESP 32 with relay

The robot's base is constructed from an 8mm steel laminated sheet, chosen for its durability and cost-effectiveness. Measuring 20 inches by 15 inches, the base supports all components and ensures stability during movement (in Figure Va). It houses the battery mechanism, which includes four Li-ion batteries, and a buck converter that steps down the voltage from 16V DC to 3-5V for various components (in Figure Vb).

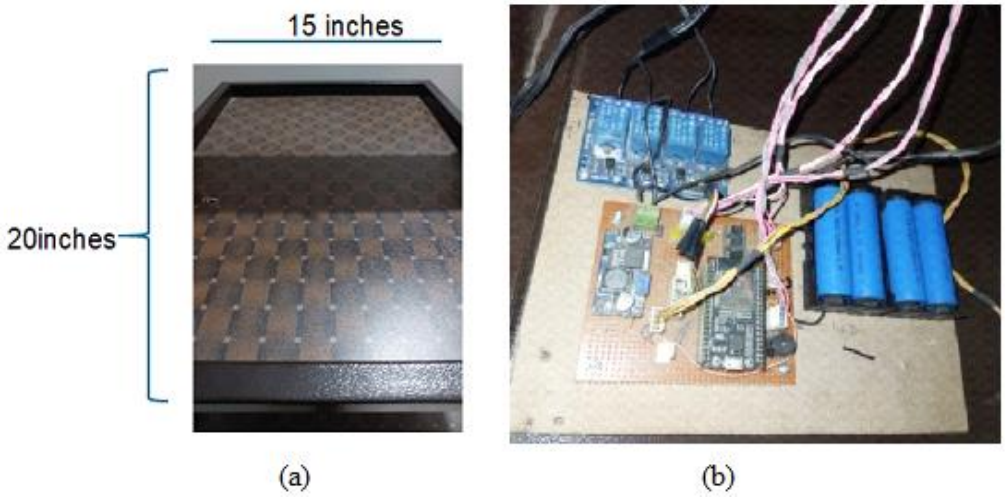

Figure V. (a) Dimension of the base, (b) Base circuitry

On top of the robot, a 2.8-inch ESP32 touch display LCD, with resolutions between 240x320 and 480x320 pixels, enables user interaction and order placement. A webcam is also installed to monitor the robot's position and detect obstacles, allowing real-time visibility of any obstructions (see Figure VI).

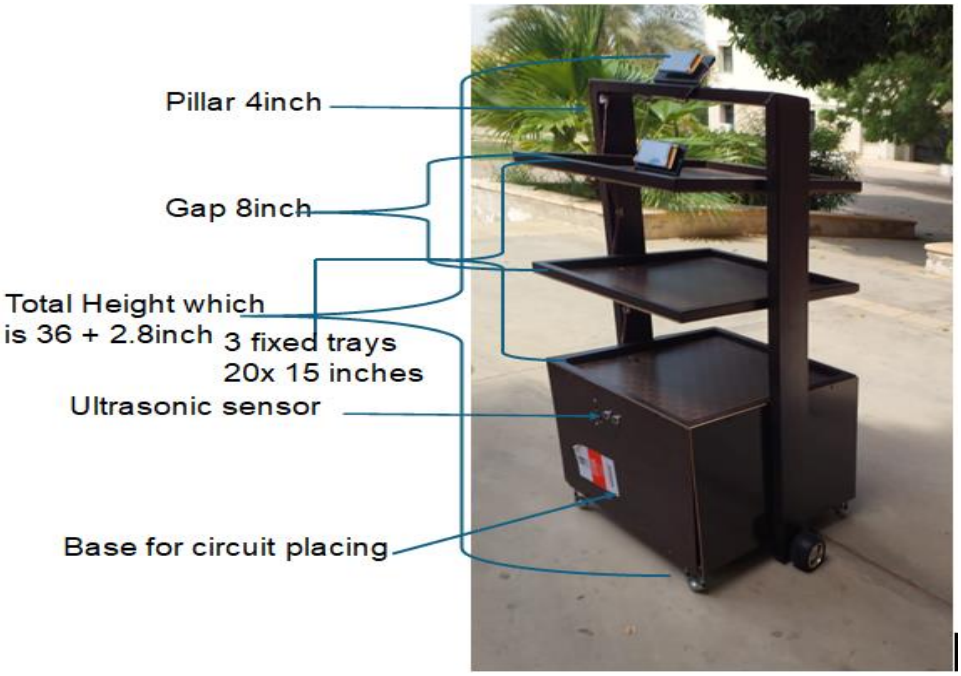

Figure VI. Structure with dimensions

2.2 Navigation Algorithm. - The robot employs an A* path-planning algorithm to ensure optimal navigation in dynamic environments. The algorithm processes input from ultrasonic sensors to identify obstacles and dynamically adjust the robot's trajectory. The A* algorithm calculates the shortest path based on cost functions that account for distance, obstacle proximity, and time. The robot's movement is controlled by precise motor commands derived from these calculations.

2.3 Software Architecture and Real-Time Obstacle Avoidance. - The IoT-based waiter robot is designed with a robust software architecture consisting of three primary modules: the Data Acquisition Module, the Processing Unit, and the Communication Module. The Data Acquisition Module is responsible for continuously gathering sensor data, such as distance measurements and tray status, while the Processing Unit handles the navigation algorithm, processes sensor inputs, and generates motor control commands. The Communication Module facilitates Wi-Fi connectivity, enabling interaction between the robot, the kitchen interface, and the customer touchscreen. This integrated system allows for real-time data processing and dynamic decision-making. Furthermore, the robot's obstacle avoidance system employs ultrasonic sensors to detect potential collisions. Upon detection, the A* algorithm recalculates the robot's path to avoid obstacles, and the motor controller adjusts the movement accordingly. Continuous monitoring ensures that the robot can navigate efficiently and reliably, even in crowded environments.

3. Results and Discussion. - In the kitchen setup, an ESP32-controlled display allows the chef to dispatch the robot to the customer's table to take an order. Upon arrival, a display on the robot presents menu options categorized as follows: Appetizers (FOOD A), Desserts (FOOD B), and Grilled Items (FOOD C) as shown in Figure VII. The customer makes their selection through the display (Figure VIII and Figure IX), which is then transmitted to the kitchen display via Wi-Fi. After placing the order, the display shows a "Thank You" message (Figure X), and the robot returns to the kitchen. The chef prepares the meal, places it on the robot's tray, and commands the robot to deliver it to the customer's table.

Figure VII. Chefs command the robot to take the order

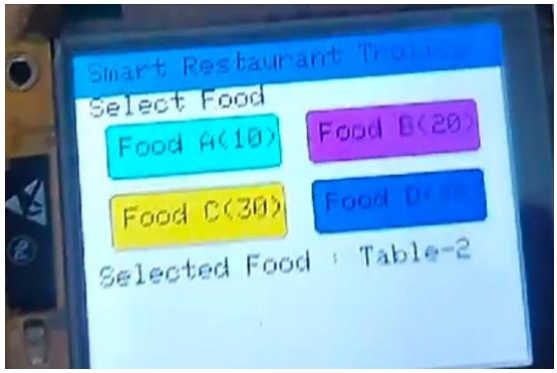

Figure VIII. Menu Display

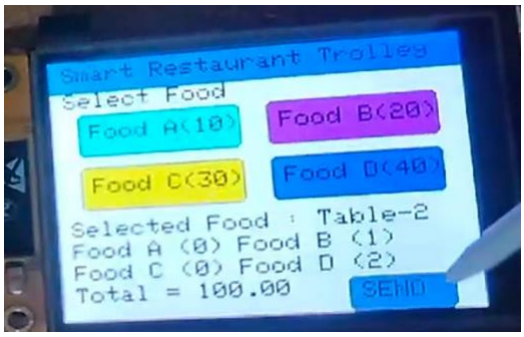

Figure IX. Selection of Food by the customer

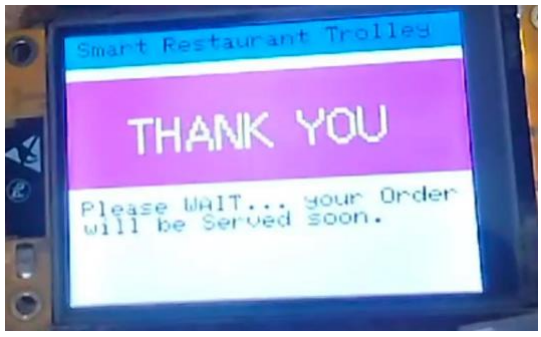

Figure X. After taking the order

During meal delivery, the robot follows the command from the chef to navigate to the customer's table. Once there, the customer retrieves the meal trays, and the TCRT 5000 sensor detects the tray's removal, signaling that the meal has been received. The ultrasonic sensor continuously scans for obstacles, with the robot stopping and sounding a buzzer if an obstacle is detected, resuming its journey only when the path is clear. After the customer has taken their meal, the TCRT 500 sensor confirms the absence of the tray, prompting the robot to return to its original position in the kitchen, ready for its next task.

For the robot's movement, we selected wheels with a diameter of 4 inches (see Table III). Using smaller wheels than this diameter would cause the robot to slip on the surface, leading to increased power consumption during rotation. On the other hand, using larger wheels would raise the cost and result in higher power usage, making the 4-inch diameter an optimal choice for balancing performance and efficiency.

Name of Equipment	Circumference of Wheel (cm)	RPM	RPS	Time (sec)	Distance (cm)	Speed (cm/sec)	Accuracy Based on Perfect Turning
Wheel (Gear Motor)	31.92	15	0.3	60	479.04	7.984	Best
Wheel (Gear Motor)	31.92	20	0.3	45	479.04	10.645	Better
Wheel (Gear Motor)	31.92	25	0.4	36	479.04	13.324	Very Good
Wheel (Gear Motor)	31.92	30	0.5	30	479.04	15.968	Good

Table III. Wheel configuration

The robot has been tested across various testing scenarios to validate its performance. Some of the key scenarios include the following,

3.1 Load Vs Ampere. - It is observed that the IoT Base Waiter Robot's current consumption varied with different weight loads. Specifically, with a load of approximately 2 kg, the robot drew 1.68 mA. When the weight was increased to around 4 kg, the current consumption rose to 1.75 mA. With a maximum load of 6 kg, the current increased further to 1.91 mA. These findings are illustrated in Figure XI.

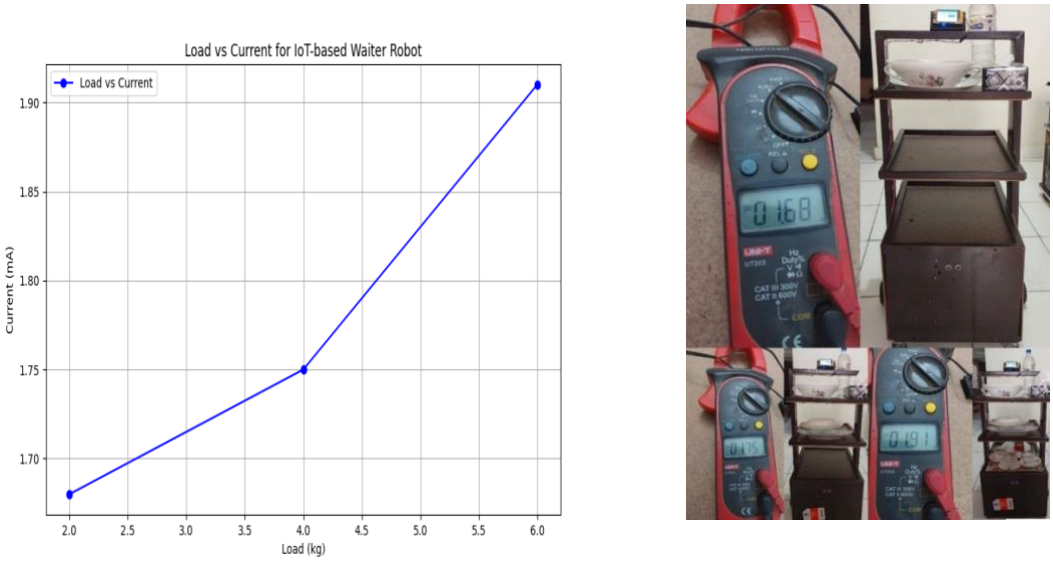

Figure XI. Comparison of Load Vs Amp for the proposed system model

3.2 Distance over time. - The performance of the robot under varying weight loads was assessed by measuring the distance covered over time (see Figure XII). With a 2 kg load, the robot traveled 2.17 meters in 20 seconds. Increasing the weight to 4 kg resulted in a distance of 1.78 meters covered in 20 seconds. At the maximum load of 6 kg, the robot covered 1.50 meters in 20 seconds.

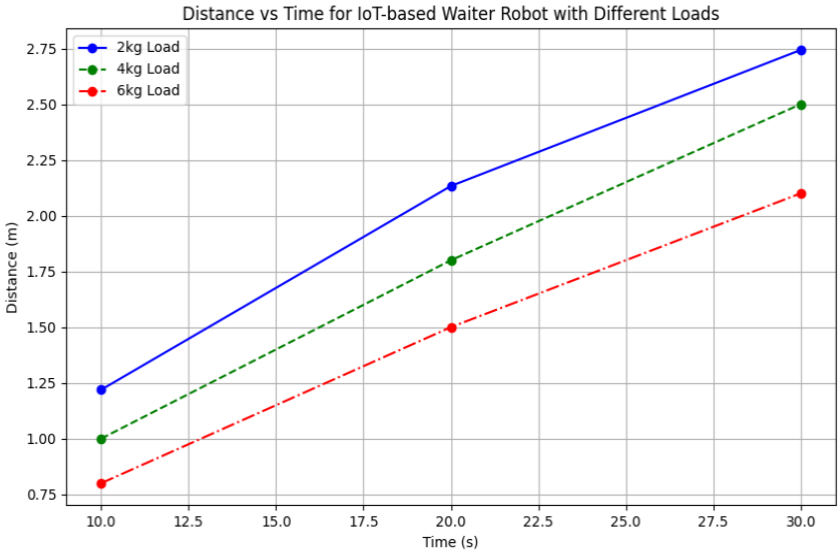

Figure XII. Comparison of distance covered over time for the proposed system model

3.3 Speed Vs torque. - Table IV shows the statistical relationship between speed and torque for the IoT-based waiter robot under different weight loads (2 kg, 4 kg, and 6 kg). It highlights an inverse relationship: as torque increases (due to heavier loads or higher resistance), the robot's speed decreases. The yellow line (2 kg) indicates the highest speed at lower torque (see Figure XIII), while the red line (6 kg) shows the lowest speed, reflecting the significant impact of heavier loads. This analysis demonstrates the robot's load-dependent performance, providing insights into optimizing its operation for varying weights.

Weight (kg)	Speed (m/s)	Torque (Nm)
2	1.5	0.5
2	1.2	0.7
2	1.0	0.9
4	1.2	0.8
4	1.0	1.0
4	0.8	1.2
6	1.0	1.1
6	0.8	1.3
6	0.6	1.5

Table IV. Speed vs Torque

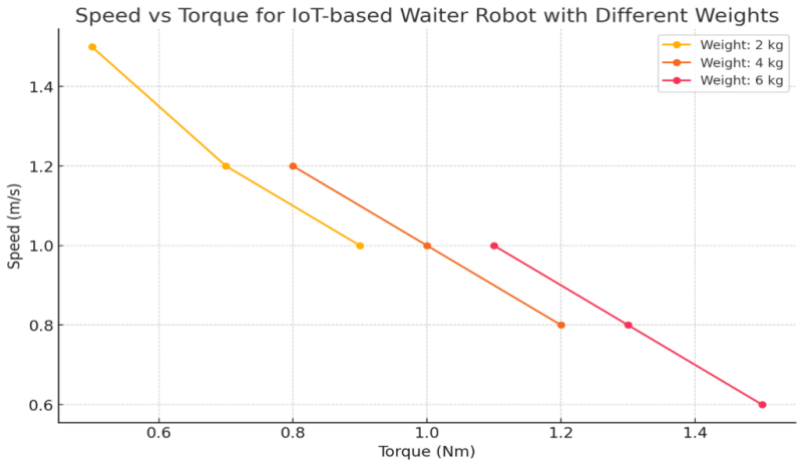

Figure XIII. Speed vs torque

There are a lot of other parameters that were considered during the testing of this prototype system. The graphs in Figure XIV, we obtain as the result of those tests in which we kept the 4 Kg weight constant. It can be seen that the graph of battery life versus distance traveled shows a sharp decline in battery life as distance increases, indicating higher energy consumption over longer trips and the need for efficient power management. Similarly, the response time improves with more orders, while success rates decrease as obstacle density increases, underscoring the need for advanced navigation algorithms. Customer satisfaction rises with service speed but plateaus beyond an optimal point, and energy consumption increases significantly with heavier loads. Higher network latency reduces navigation accuracy, while increased bandwidth reduces processing time, though improvements diminish after a certain point. Idle time decreases with longer working hours, and collision rates rise at moderate speeds but decline at higher speeds. Maintenance costs increase with usage duration, highlighting the importance of proactive maintenance strategies.

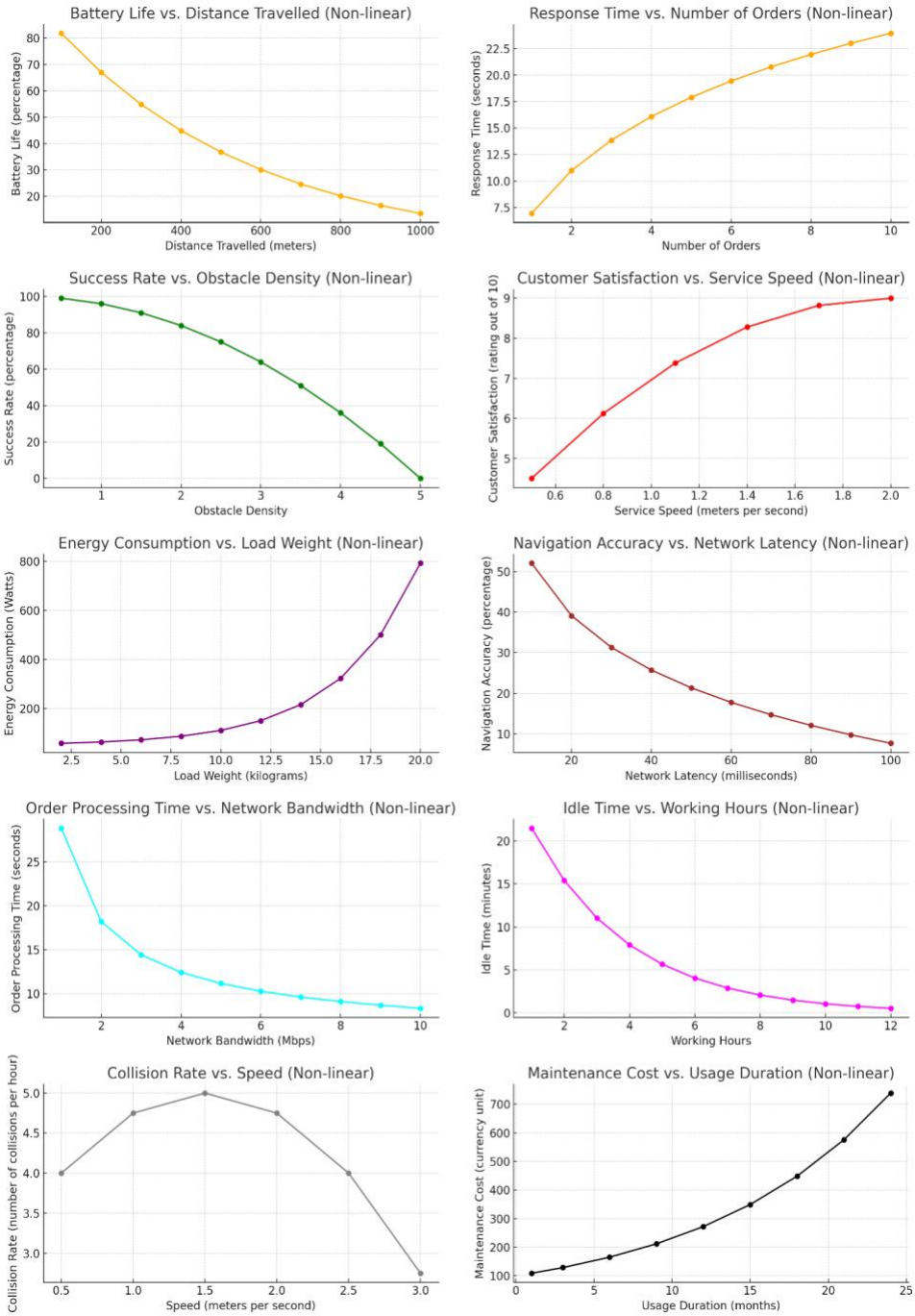

Figure XIV. Comparison of different parameters for the proposed system model

4. Conclusion and Future Work. - The IoT-based waiter robot proposed in this study can potentially transform the restaurant business positively. The system which operates with the ESP32 microcontroller and is utilized with the help of modern sensors and convenient interfaces helps increase the level of service, decreasing the time of service and, thus, increasing satisfaction of the customers. The self-orienting capability, real-time computing, and modularity of the designed robot enable it to be easily integrated into various restaurant contexts and thus economically efficient. Future upgrades would bring enhancements like SLAM for better navigation of the floor and introducing enhanced customer interaction as other enhancements would improve the efficiency of the robot and the service it provides. These enhancements coupled with the possibility of payment system integration distinguish the adaptability of the system as well as the application of IoT and robotics in revitalizing the processing of meals and the food chain.

References

[1] Rehman, S.U., Ahmed, S.B. and Raza, M.H., "Real-Time Protocols for Communication and Collaboration Environments in Telemedical Applications". Sir Syed University Research Journal of Engineering & Technology, 11(01), 2021. https://doi.org/10.33317/ssurj.307

[2] Keshvarparast, A., Battini, D., Battaia, O. and Pirayesh, A. "Collaborative robots in manufacturing and assembly systems: literature review and future research agenda". Journal of Intelligent Manufacturing, 35(5), pp.2065-2118, 2024. https://doi.org/10.1007/s10845-023-02137-w

[3] Bilancia, P., Schmidt, J., Raffaeli, R., Peruzzini, M. and Pellicciari, M., "An overview of industrial robots control and programming approaches". Applied Sciences, 13(4), p.2582, 2023. https://doi.org/10.3390/app13042582

[4] Ivanov, S. and Webster, C, "Restaurants and robots: public preferences for robot food and beverage services". Journal of Tourism Futures, 9(2), pp.229-239, 2023. https://doi.org/10.1108/JTF-12-2021-0264

[5] Molinillo, S., Rejón-Guardia, F. and Anaya-Sánchez, R., "Exploring the antecedents of customers' willingness to use service robots in restaurants". Service Business, 17(1), pp.167-193, 2023. https://doi.org/10.1007/s11628-022-00509-5

[6] Rehman, S.U., Mustafa, H. and Larik, A.R., "IoT based substation monitoring & control system using arduino with data logging", 4th International Conference on Computing & Information Sciences (ICCIS), pp. 1-6. IEEE., 2021,

[7] Rehman, S.U. and Khan, A., "Integrating IoT Technology for Improved Distribution Transformer Monitoring and Protection". Electrical, Control and Communication Engineering, 19(1), pp.22-28, 2023. https://doi.org/10.2478/ecce-2023-0004

[8] Rehman, S.U., Mustafa, H., Shaikh, M.A. and Memon, S., "Towards Sustainable Energy Storage: A Low-Cost IoT Solution for Real-time Monitoring of Lead-Acid Battery Health". Memoria Investigaciones en Ingeniería, (26), pp.202-212, 2024. https://doi.org/10.36561/ING.26.12

[9] Shakir, M., Karim, S., Memon, S., Rehman, S.U. and Mustafa, H, "An improvement in IoT-based smart trash management system using Raspberry Pi", International Journal of Computational Vision and Robotics, 14(2), pp.191-201, 2024. https://doi.org/10.1504/IJCVR.2024.136997

[10] Mohammadnejad, A. and Zade, H.T. "Design and modeling of a waiter robot". 13th International Conference on Information and Knowledge Technology (IKT), pp 1-7, IEEE., 2022.

[11] Hwang, J., Kim, H., Kim, J.J. and Kim, I., "Investigation of perceived risks and their outcome variables in the context of robotic restaurants". Journal of Travel & Tourism Marketing, 38(3), pp.263-281, 2021. https://doi.org/10.1080/10548408.2021.1906826

[12] Akhund, T.M.N.U., Siddik, M.A.B., Hossain, M.R., Rahman, M.M., Newaz, N.T. and Saifuzzaman, M., "IoT Waiter Bot: a low cost IoT based multi functioned robot for restaurants". 8th international conference on reliability, infocom technologies and optimization (Trends and Future Directions)(ICRITO) (pp. 1174-1178). IEEE, 2020. https://doi.org/10.1109/ICRITO48877.2020.9197920

[13] Gautam, K., Sharma, A.K., Nandal, A., Dhaka, A., Seervi, G. and Singh, S. "Internet of Things (IoT)-based smart farming system: A broad study of emerging technologies". In Internet of Things and Fog Computing-Enabled Solutions for Real-Life Challenges (pp. 39-60). CRC Press. 2022. https://doi.org/10.1201/9781003230236

[14] Cameron, N.. "ESP32 Microcontroller". In ESP32 Formats and Communication: Application of Communication Protocols with ESP32 Microcontroller (pp. 1-54). Berkeley, CA: Apress, 2023. https://doi.org/10.1007/978-1-4842-9376-8_1

[15] Rahmawati, T., Tasyakuranti, A.N., Sumarti, H. and Kusuma, H.H., "Development of Non-Invasive Cholesterol Monitoring System Using TCRT5000 Sensor with Android Compatibilt"y. Jurnal Fisika, 13(2), 2023. https://doi.org/10.15294/jf.v13i2.45044

[16] Singh, A., Deore, S., Khandare, L., Shinde, S., Rane, P. and Nangare, R., “Speed and Direction Control of DC Geared Motor Using WiFi Module”. International Research Journal of Innovations in Engineering and Technology, 8(3), p.358, 2024. https://doi.org/10.47001/IRJIET/2024.803055

Author contribution:
1. Conception and design of the study
2. Data acquisition
3. Data analysis
4. Discussion of the results
5. Writing of the manuscript
6. Approval of the last version of the manuscript

SUR has contributed to: 1, 2, 3, 4, 5 and 6.

Acceptance Note: This article was approved by the journal editors Dr. Rafael Sotelo and Mag. Ing. Fernando A. Hernández Gobertti.

Two-Dimensional Numerical Analysis on the Double Shear Specimens of Timber-Concrete Composite Structures: Effects of Screw Dimensions and Timber Density

Análisis Numérico Bidimensional de Especímenes de Doble Corte en Estructuras Compuestas de Madera y Concreto: Efectos de las Dimensiones del Tornillo y la Densidad de la Madera

Análise Numérica Bidimensional em Especificações de Cisalhamento Duplo de Estruturas Compostas de Madeira e Concreto: Efeitos das Dimensões dos Parafusos e da Densidade da Madeira

L. Jun En[1(*)], M. A. Mohd Snin[2], S. N. Fatimah Ghazali[3], N. A. Fatihah Mokhtar[4], M. Ikmal Zainal[5], R. Suryavarman[6]

Recibido: 29/10/2024 Aceptado: 28/01/2025

Summary. - This study investigates the behaviour of screw connections in timber-concrete composite (TCC) structures using two-dimensional finite element modelling with LUSAS software. The research focuses on the shear force capacity and stiffness of screws arranged in a parallel 90-degree formation within a double shear test configuration. A comprehensive review of the literature provided the necessary data on embedment strengths of screws in timber and concrete. Finite element simulations of TCC structures were conducted and validated against previous experimental findings. The analysis examined how variations in screw diameter, depth, and timber density impact connection performance. Results indicate that a 10 mm diameter screw with a 100 mm embedment depth and timber density of 476 kg/m³ achieves a shear force capacity of 11.80 kN, a maximum displacement of 16.48 mm, and a stiffness of 701 N/mm. Reducing the screw diameter to 8 mm and 6 mm results in lower shear capacities of 9.45 kN and 7.07 kN, with corresponding stiffness of 574 N/mm and 438 N/mm. Similarly, decreasing the screw depth to 80 mm and 60 mm reduces shear capacities to 9.34 kN and 7.01 kN, with stiffness of 572 N/mm and 437 N/mm, respectively. Increasing the timber density to 600 kg/m³ improves the shear force capacity to 14.70 kN and the stiffness to 980 N/mm. The findings demonstrate that larger screw diameters, greater embedment depths, and higher timber densities significantly enhance the shear force capacity and stiffness of screw connections in TCC structures. The main finding of this research is the identification of the failure mode of screw connections, which is influenced by the properties of the timber, concrete, and screw. When the concrete strength surpasses the timber strength, failure occurs due to timber crushing, while screw deformation and timber crushing are expected when interaction stresses exceed the yield stress in the timber-screw interface. This study provides critical insights for optimizing screw connections in TCC designs and contributes to the development of more effective design codes for timber-concrete composites.

Keywords: Timber structures; Timber concrete composite; Screw connections; Embedment strength

(*) Corresponding author.

[1] Undergraduate student, School of Civil Engineering, Universiti Sains Malaysia (Malaysia), junen@student.usm.my, ORCID iD: https://orcid.org/0009-0009-3614-4069

[2] Undergraduate student, School of Civil Engineering, Universiti Sains Malaysia (Malaysia), ceamirul@usm.my, ORCID iD: https://orcid.org/0000-0003-4521-6238

[3] Undergraduate student, School of Civil Engineering, Universiti Sains Malaysia (Malaysia), imahghazali@student.usm.my, ORCID iD: https://orcid.org/0009-0003-8305-1021

[4] Undergraduate student, School of Civil Engineering, Universiti Sains Malaysia (Malaysia), ainnafatihah@student.usm.my, ORCID iD: https://orcid.org/0009-0002-6635-9713

[5] Undergraduate student, School of Civil Engineering, Universiti Sains Malaysia (Malaysia), ikmalzainal@student.usm.my, ORCID iD: https://orcid.org/0009-0005-2593-7750

[6] Master student, KPR Institute of Engineering and technology (India), suryaram2001@gmail.com, ORCID iD: https://orcid.org/0009-0003-9877-5655

Memoria Investigaciones en Ingeniería, núm. 28 (2025). pp. 168-182
https://doi.org/10.36561/ING.28.12
ISSN 2301-1092 • ISSN (en línea) 2301-1106 – Universidad de Montevideo, Uruguay

Resumen. - *Este estudio investiga el comportamiento de las conexiones por tornillos en estructuras compuestas de madera y concreto (TCC) utilizando modelado de elementos finitos bidimensionales con el software LUSAS. La investigación se centra en la capacidad de fuerza de corte y rigidez de los tornillos dispuestos en una formación paralela de 90 grados dentro de una configuración de prueba de corte doble. Una revisión exhaustiva de la literatura proporcionó los datos necesarios sobre las resistencias de incrustación de los tornillos en madera y concreto. Se realizaron simulaciones de elementos finitos de estructuras TCC, las cuales fueron validadas con base en hallazgos experimentales previos. El análisis examinó cómo las variaciones en el diámetro del tornillo, la profundidad y la densidad de la madera afectan el rendimiento de la conexión. Los resultados indican que un tornillo de 10 mm de diámetro con una profundidad de incrustación de 100 mm y densidad de madera de 476 kg/m³ alcanza una capacidad de fuerza de corte de 11,80 kN, un desplazamiento máximo de 16,48 mm y una rigidez de 701 N/mm. La reducción del diámetro del tornillo a 8 mm y 6 mm da lugar a capacidades de corte más bajas de 9,45 kN y 7,07 kN, con una rigidez correspondiente de 574 N/mm y 438 N/mm. De manera similar, la reducción de la profundidad del tornillo a 80 mm y 60 mm reduce las capacidades de corte a 9,34 kN y 7,01 kN, con rigidez de 572 N/mm y 437 N/mm, respectivamente. El aumento de la densidad de la madera a 600 kg/m³ mejora la capacidad de fuerza de corte a 14,70 kN y la rigidez a 980 N/mm. Los hallazgos demuestran que diámetros de tornillos más grandes, mayores profundidades de incrustación y mayores densidades de madera mejoran significativamente la capacidad de fuerza de corte y la rigidez de las conexiones por tornillos en estructuras TCC. El principal hallazgo de esta investigación es la identificación del modo de fallo de las conexiones por tornillos, que está influenciado por las propiedades de la madera, el concreto y el tornillo. Cuando la resistencia del concreto supera la resistencia de la madera, la falla ocurre debido al aplastamiento de la madera, mientras que se espera la deformación del tornillo y el aplastamiento de la madera cuando las tensiones de interacción superan la tensión de fluencia en la interfaz madera-tornillo. Este estudio proporciona información crucial para optimizar las conexiones por tornillos en el diseño de TCC y contribuye al desarrollo de códigos de diseño más efectivos para compuestos de madera y concreto.*

Palabras clave: *Estructuras de Madera, Compuestos de Madera y Concreto, Conexiones*

Resumo**. -** *Este estudo investiga o comportamento das conexões por parafusos em estruturas compostas de madeira e concreto (TCC) utilizando modelagem de elementos finitos bidimensionais com o software LUSAS. A pesquisa foca na capacidade de força de cisalhamento e rigidez dos parafusos dispostos em uma formação paralela de 90 graus dentro de uma configuração de teste de cisalhamento duplo. Uma revisão abrangente da literatura forneceu os dados necessários sobre as resistências de incrustação de parafusos em madeira e concreto. Simulações de elementos finitos de estruturas TCC foram conduzidas e validadas com base em resultados experimentais anteriores. A análise examinou como variações no diâmetro do parafuso, profundidade e densidade da madeira impactam o desempenho das conexões. Os resultados indicam que um parafuso de 10 mm de diâmetro com 100 mm de profundidade de incrustação e densidade de madeira de 476 kg/m³ atinge uma capacidade de força de cisalhamento de 11,80 kN, um deslocamento máximo de 16,48 mm e uma rigidez de 701 N/mm. A redução do diâmetro do parafuso para 8 mm e 6 mm resulta em capacidades de cisalhamento mais baixas de 9,45 kN e 7,07 kN, com rigidez correspondente de 574 N/mm e 438 N/mm. Da mesma forma, a diminuição da profundidade do parafuso para 80 mm e 60 mm reduz as capacidades de cisalhamento para 9,34 kN e 7,01 kN, com rigidez de 572 N/mm e 437 N/mm, respectivamente. Aumento da densidade da madeira para 600 kg/m³ melhora a capacidade de força de cisalhamento para 14,70 kN e a rigidez para 980 N/mm. Os resultados demonstram que diâmetros maiores de parafusos, maiores profundidades de incrustação e maiores densidades de madeira aumentam significativamente a capacidade de força de cisalhamento e a rigidez das conexões por parafusos em estruturas TCC. A principal conclusão desta pesquisa é a identificação do modo de falha das conexões por parafusos, que é influenciado pelas propriedades da madeira, do concreto e do parafuso. Quando a resistência do concreto supera a resistência da madeira, ocorre falha devido ao esmagamento da madeira, enquanto a deformação do parafuso e o esmagamento da madeira são esperados quando as tensões de interação excedem a tensão de escoamento na interface madeira-parafuso. Este estudo fornece informações críticas para otimizar as conexões por parafusos no design de TCC e contribui para o desenvolvimento de códigos de projeto mais eficazes para compostos de madeira e concreto.*

Palavras-chave: *Estruturas de madeira; Composto de madeira e concreto; Conexões por parafuso; Força de embutimento*

1. Introduction. - Timber-Concrete Composite (TCC) structural system integrates timber and concrete elements to enhance efficiency and durability, aiming to optimize the structural integrity and performance of composite beams. TCC systems are versatile and adaptable, capable of supporting substantial loads and stresses. The primary goal of TCC technology is to improve the overall strength and efficiency of structures through a robust structural connection between timber and concrete components [3, 8, 12, 14]. Various shear connectors, such as screws, bolts, nails, mesh plates, and steel plates, can be used to connect timber and concrete elements [4, 7, 18]. Screws are particularly prevalent as shear connectors in these systems. Design standards for timber-to-timber structures are available in many countries, offering guidelines for the effective use of these connectors, such as those provided by Eurocode 5 - Design of timber structures [6]. However, while Eurocode 5 provides design standards for timber-to-timber connections, it has certain limitations when applied to timber-concrete composite structures. Shear connections are essential for providing ductility in TCC systems, with design parameters such as strength, stiffness, deflection, and configuration being critical to their overall performance [1, 5, 15, 16]. Research has demonstrated that the shear force capacity $F_{V,R}$ and stiffness Ks of these systems are significantly affected by the material properties of timber, concrete, and fasteners [9, 17]. According to Eurocode 5, the strength of screw connections is influenced by both embedment strength and withdrawal strength [6, 13]. While Eurocode 5 provides guidelines for the embedment strength of vertical screw connections in TCC, it has limitations regarding the stiffness formula, as it depends on the types of timber, screw properties, and concrete properties used in TCC structures. In this context, the stiffness of screw connections in TCC structures is assumed to be twice that of screw connections in TTC structures. According to Eurocode 5, the failure of these connections is also influenced by the properties of the timber, concrete, and screw. Therefore, the failure modes of screw connections in TCC structures must be explored to determine whether the screw connection will fail due to screw snapping, withdrawal from the timber, or withdrawal from the concrete. To better understand how the failure of screw connections and embedment strength affect the strength and stiffness of these connections, this study conducted a numerical analysis of screw connections in TCC structures, utilizing a database of previous TCC structures that employed screw connections.

2. Aims of research. -This study aims to determine how the screw, timber, and concrete properties of TCC structures influence the shear force capacity and stiffness of the connection. It is expected that an increase in the diameter and length of the screw will enhance the shear force capacity and stiffness of the connection in TCC structures. Additionally, it is anticipated that higher timber density will improve the shear force capacity of the connections. Furthermore, the failure mode of the screw connections is dependent on the properties of the screw, timber, and concrete. Therefore, this study aims to achieve two main objectives:

- Validation of Double Shear Test Models: To validate finite element models used for double shear testing by comparing the results with established experimental data from previous studies.

- Analysis of Local Shear Connection Behaviour: To investigate the local behaviour of shear connections within TCC structures. This involves assessing the influence of varying timber densities and screw dimensions on connection performance and identifying associated failure mechanisms.

To fulfil these objectives, the study employs the finite element method using LUSAS software to construct a two-dimensional model grounded in prior experimental work as discussed in section of methodology. The model examines different timber densities and screw sizes to evaluate their effects on connection behaviour and to elucidate potential failure modes.

3. Methodology. - This research utilized the finite element method (FEM) with LUSAS software version 21 to model a double shear test involving screw connections [10]. The model was developed based on existing literature and previous research. To validate the model, the shear force capacity and stiffness obtained from the simulations were compared with data from earlier studies to assess the adequacy of the results. Subsequently, the study explored variations in material properties, including timber density, and screw dimensions, to examine their effects on the shear connections. This involved modifying these parameters and investigating their impact on the local behaviour of timber-concrete connections. Finally, the results were analysed and discussed to provide insights into the performance and behaviour of the connections under different conditions. Figure I shows the flowchart of this research.

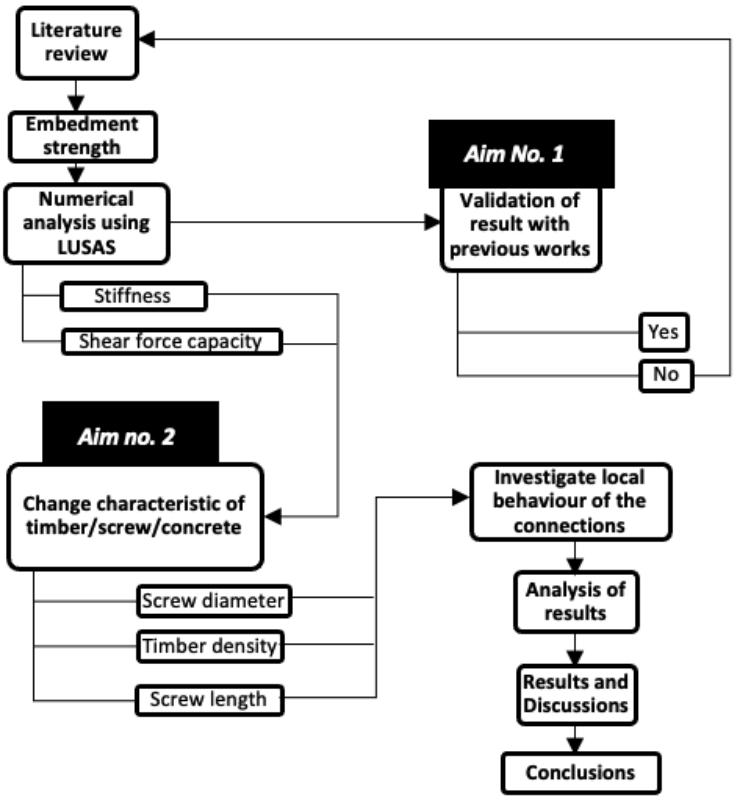

Figure I.- Flow chart of the research

3.1. Double shear test specimens physical and mechanical properties for finite element modelling. - This research utilized the data sample from the double shear test of screw connections in timber-concrete structures as reported by Manojlović et al. [11]. Figure II illustrates the dimensions of the screw and double shear specimen (2a) and the specimen prior to testing (2b). All material properties used in this research are detailed in Table 1. These physical and mechanical properties serve as the baseline for modelling of double shear specimen. Material properties for timber, concrete, and screws were defined using isotropic material models. For concrete, the material properties included a Young's modulus E_c of 30,000 N/mm², Poisson's ratio v_c of 0.2, mass density ρ_c of 2.4×10^{-6} t/mm² and compressive strength f_c of 55 MPa. Timber properties were set with a Young's modulus E_t of 13,000 N/mm², Poisson's ratio v_t of 0.2, mass density of 0.447×10^{-6} t/mm², and compressive strength f_t of 24 MPa. For the screws, the material was also defined isotopically with a Young's modulus E_s of 210,000 N/mm², Poisson's ratio v_s of 0.3, mass density ρ_s of 0.89×10^{-6} t/mm², and tensile strength of 695 MPa. The load was applied at the top of the timber member in the double shear test, simulating typical loading conditions for these connections.

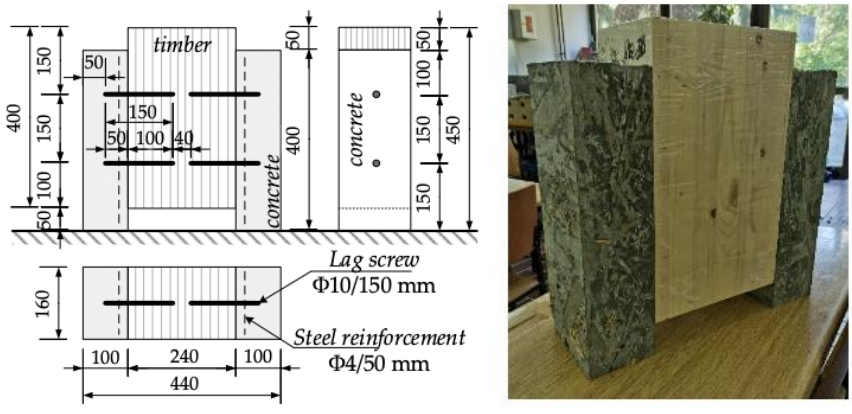

(a) (b)

Figure II.- Sample used for FE Modelling (a) Details dimensions of screw connections in double shear specimen and (b) double shear specimen before tested [11]

Materials	Properties	Mean Value
Glulam GL24	Compressive strength, f_t	24 MPa
Concrete	Cubic compressive strength f_c	55 MPa
Screw	Tensile strength f_u	695 MPa

Table I.- Material properties of the specimens [11]

3.2 Tools and platform. - This study utilized the LUSAS Modeller software, available in the Computer Lab at the Universiti Sains Malaysia (USM), Engineering Campus. The modelling process involved several critical steps. Specifically, the double shear specimens were modelled on only one side due to symmetry considerations. For meshing, the timber surface was represented using plane strain elements with a quadrilateral shape and quadratic interpolation, employing a regular mesh approach to ensure accuracy. Concrete surfaces were similarly meshed with plane stress elements and quadratic interpolation, also utilizing a regular mesh. Screws were modelled as bar elements with quadratic interpolation and divided into four segments. Interface and delamination properties were defined by specifying line elements with plane strain characteristics for the interface and manually assigning the interaction between timber and concrete.

For the geometric properties, the model encompassed screw, timber, and concrete components. Screws were represented as geometric lines with bar properties, where the cross-sectional area was calculated using $A = 2\pi r^2$. For two screws, this resulted in a total cross-sectional area of 157.08 mm^2. The geometric surfaces for timber and concrete were defined with a thickness of approximately 160 mm (see Figure IIa). This setup ensured that the model accurately represented the spatial dimensions and properties of the materials involved in the timber-concrete composite structure.

3.3 Embedment strength model as interface material. - The initial phase of this research involved a comprehensive literature review to gather the necessary properties of timber and concrete for use in numerical analysis. Key parameters required for modelling include embedment strength and maximum displacement. These parameters are essential for defining the interface material between the screw and timber/concrete. According to the LUSAS software guidelines, the interface material between two different materials can be characterized by a linear decrease in strength with increasing applied stress in the opening or tearing directions, reflecting a weakening connection, as illustrated in Figure III. The maximum value of the stress in Figure III also known as initiation stress,τ. Ben et al. [2] and Manojlović et al. [11] report that the embedment strength of the screw $f_{h,t}$ in glulam GL24 is 36.1 MPa, with a maximum displacement δ_{max} of approximately 15 mm. The value of initiation stress in the modelling were used to determine the fracture energy by calculating the area under the curve of embedment strength versus displacement, as shown in the graph provided by Manojlović et al. [11] in Figure IV. For the screw embedded in the concrete component, the embedment strength $f_{h,c}$ was calculated using the formula suggested by Mohd Snin and Kassem [13], as presented in Equation 1. The fracture energy was then determined from the area under this curve, with the initiation stress set at 46.75 MPa. In the modelling process, the interface material was assigned to line elements.

Consequently, the initiation stresses for both the timber and concrete interfaces with the screw needed to be multiplied by a correction factor, as well as by the circumference $C=2\pi r$ of the screw's circular cross-section, to accurately represent the stress along the line as presented in Equation 2. Analysis revealed that applying a correction factor of 5 was necessary to align the results with experimental findings. This adjustment accounts for the use of line elements to represent the screw in the two-dimensional analysis. Table 2 shows the details of the data to calculate initiation stress and fracture energy for baseline model. Next, assign the master element for the timber and concrete where the screw will be located as presented in Figure Va. Set the slave element assignment for the screw by configuring the selection memory. After establishing the master and slave assignments, drag the interface element by selecting the slave assignment. Combine the timber and concrete components by first making them unmergeable (see Figure Vb). Position the screw within the timber and concrete. Finally, assign the material properties for the timber, concrete, and screw.

$$f_{h,c} = 0.85 f_c \ \textbf{(N/mm}^2\textbf{)} \quad (1)$$

$$\tau = f_{h,c} \ or \ f_{h,t} \ . (2\pi r) . 5 \ \textbf{(N/mm)} \quad (2)$$

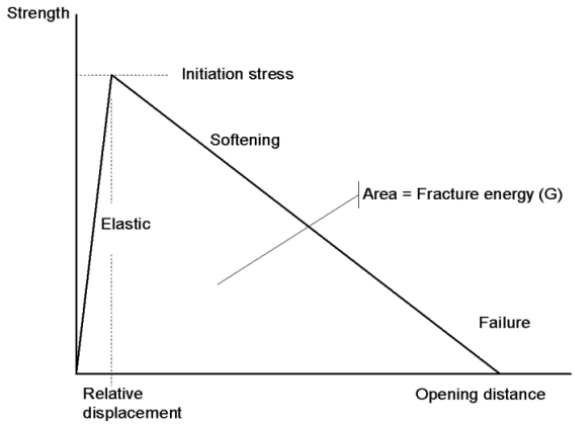

Figure III.- Material properties of interface element

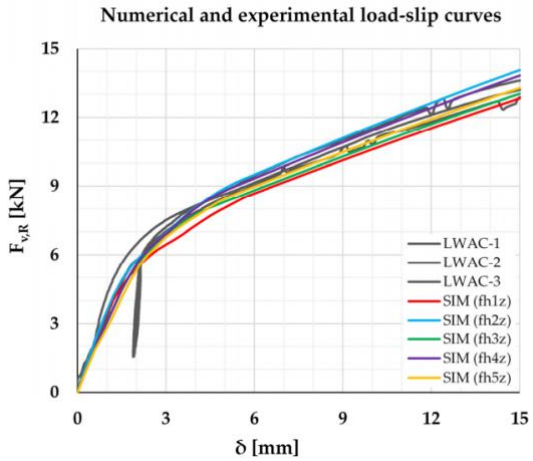

Figure IV.- Embedment strength against displacement used as the data for FE modelling from Manojlović et al. [11]

Part	Embedment strength (N/mm^2)	Initiation stress [Eq.2] (N/mm)	Fracture energy [Area under the graph] (J/mm^2)
Screw to timber	36.1	5667	84975
Screw to concrete	46.75	17150	17150

Table II.- Initiation stress and fracture energy for interface material

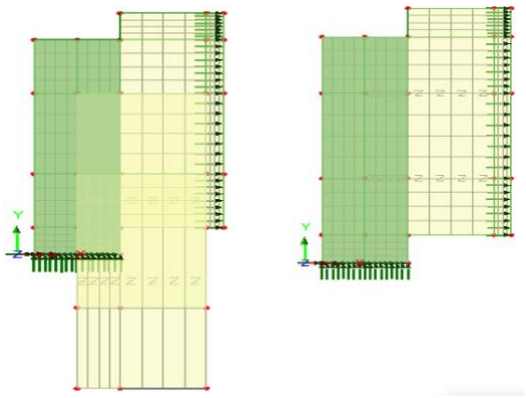

(a) (b)

Figure V.- Process to assign the interface element between screw to timber/concrete. (a) Master (on timber/concrete) and slave (on screw) assignment and (b) Completed assignment of interface element

After modelling the double shear test for timber-concrete composite structures, the resulting graph of shear force capacity versus displacement can be generated. Compare this graph with those from Manojlović et al. [11]. If the results from the modelling significantly differ from those in the reviewed articles, recheck the properties and materials entered into the LUSAS software to ensure they match those reported by Manojlović et al. [11]. Additionally, examine the local behaviour of the screw within the timber and concrete surfaces. Displacement and deformation should be clearly observable from the results. Next, modify the characteristics of the timber, concrete, or screw, such as timber density or screw diameter, and observe any changes in the behaviour of deformation within the TCC structures. Finally, analyse all the results from the modelling, and provide a discussion and recommendations based on these results.

4. Result and Discussion. -

4.1 Validation of the results. - After completing the modeling process, a graph comparing shear force capacity versus displacement was simulated, as shown in Figure VI. This figure illustrates a comparison between the results of this study and the previous findings of Manojlović et al. [11]. The details of the comparison between the experiment are provided in Table III, and these results are also compared with the theoretical values from Eurocode 5. Specifically, the shear force capacity of the TCC structure (per screw) in this study is 11.80 kN, and the stiffness is approximately 701 N/mm (calculated based on the slope of the graph). In comparison, Manojlović et al. [11] reported a shear force capacity of 10.65 kN and a stiffness of approximately 2889 N/mm. The percentage difference in shear force capacity is approximately 10.79%, while the percentage difference in stiffness is about -74%. The significant deviation in stiffness between the numerical value from this study and the experimental value from Manojlović et al. [11] is attributed to the bond strength model used in this study, which assumes linear properties, as shown in Figure III. This model results in a linear behavior of the bond between the screw and timber/concrete in the numerical analysis. However, validation of the failure mode of the screw connection has been conducted to support the results of this numerical study.

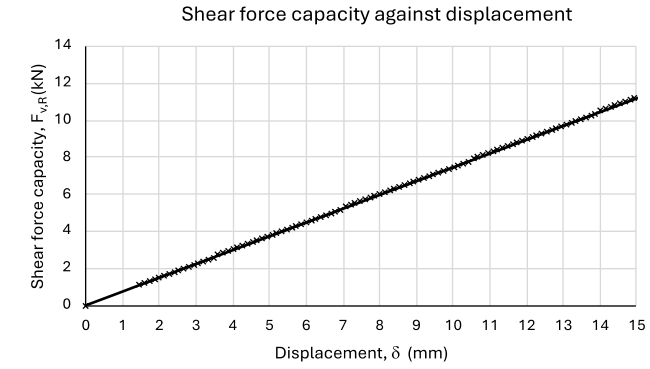

(a)

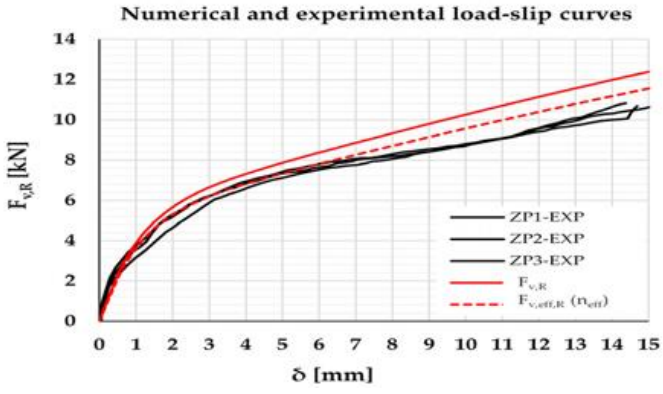

(b)

Figure VI.- Graph of shear force capacity against displacement (a) Numerical analysis in this study and (b) Experimental and Numerical works from Manojlović et al. [11]

Parameter	Method	Mean	Deviations [%]
Shear force capacity (N)	Experiment	10,650	-
	Theoretical (Eurocode 5)	10,491	-2.44
	Numerical from this study	11,800	10.79
Stiffness (N/mm)	Experiment	2889	-
	Theoretical (Eurocode 5)	6975	141.43
	Numerical from this study	750	-74

Table III.- Comparison of shear force capacity and stiffness between these numerical results to experimental work and theoretical formula from Eurocode 5.

Moreover, the results can be further validated by comparing the screw failure observed in the modelling with failure images from previous studies. Specifically, Figure VII illustrates screws being pushed out from the timber, which is consistent with the failure patterns shown in Figure VIII a) from prior research. This comparison reveals similar crushing deformation of the timber and bending deformation of the lag screw. Additionally, the push-out failure mechanism observed in this study aligns with the mechanisms described in previous works. Hammad et al. (2024) stated that the failure mode of the screw inside the timber involves two plastic hinges, as shown in Figure VIII b), which appear before the screw breaks. In the current study, the model also showed the formation of double hinges on the screw, as shown in Figure VII.

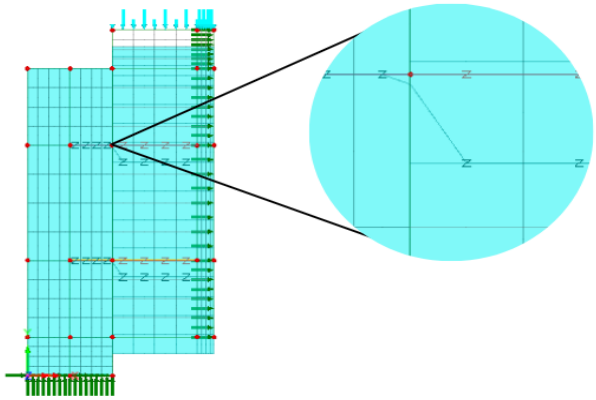

Figure VII.- The failure mode of the screw for TCC-structure from modelling

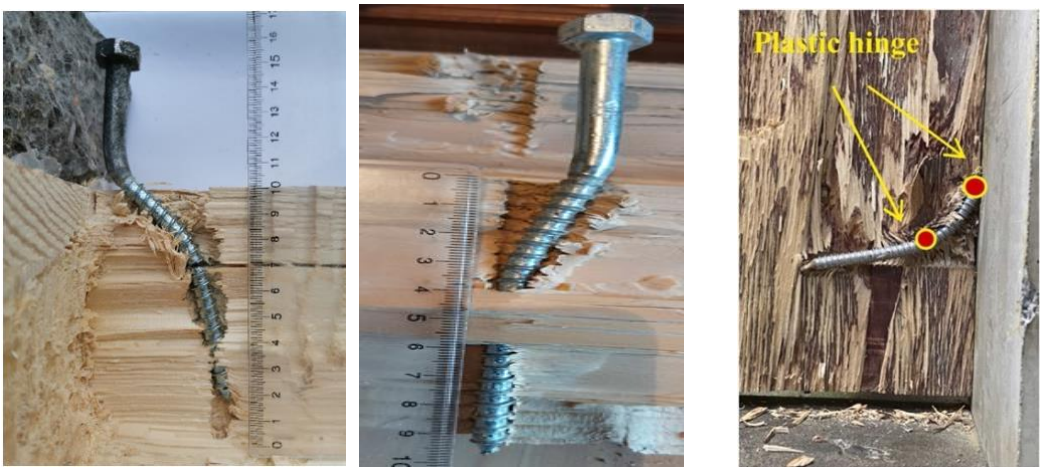

(a) (b)

Figure VIII.- The failure mode of pushing out specimen and crushing deformation of timber a) Minoljovic et al. [11] b)Hammad et al. [20]

4.2 Local behaviour of the screws. - Since the strength of the connection in TCC structures depends on the interaction between the timber and the screw, as well as the concrete and the screw, the discussion focuses on these types of

interactions. After modelling with LUSAS software, the local behaviour of the screw can be assessed from the contour patterns of stresses on the screw and the interaction between the screw to timber and concrete. Prior to failure, a screw progresses through several stages: elastic deformation, yielding, strain hardening, reaching ultimate strength, and eventual failure. Initially, the screw deforms elastically under applied load, returning to its original shape once the load is removed, as described by Hooke's Law. When the load increases and the screw reaches its yield point, plastic deformation begins, resulting in permanent changes. Subsequently, strain hardening may occur, enhancing the material's strength and resistance to further deformation, thus allowing it to support greater loads. The ultimate strength represents the maximum load the structure can withstand before failure mechanisms take over and this stage often includes necking, a localized reduction in cross-sectional area. Failure may occur in the interaction due to either a snapped screw or the withdrawal of the screw, which can happen in the timber or the concrete. The withdrawal of the screw is related to the stress at the interface between the screw and the timber, as well as between the screw and the concrete. As shown in Figure IX, the interfaces between the screw and timber, and the screw and concrete, are modeled to fail in a debonding manner. Failure occurs when the structure can no longer support the load, leading to breakage or collapse. Ductile materials undergo significant plastic deformation before failure, while brittle materials fail abruptly with minimal plastic deformation. This discussion refers to the initiation stress at the interfaces between the screw and timber/concrete, which are 5667 N/mm² and 11328 N/mm², respectively, with the screw strength being 250 N/mm², as presented in Figure IX.

At a load factor of 10 kN (per side), the stresses on the interface between screw and timber are approximately 2400 N/mm², and between screw and the concrete, they are about 4800 N/mm². No deformation or failure is observed in the screw, concrete, or timber at this load. When the load factor increases to 18 kN (per side), stresses rise to about 8640 N/mm² between screw and timber interface, while in the concrete, they reach approximately 4320 N/mm². These interface stresses remain below the yield stresses, indicating that the structure can still withstand additional force. At a load factor of 23.6 kN (per side), as presented in Figure VII, which corresponds to the shear force capacity of the model, the stresses at the screw-timber interface are approximately 5664 N/mm², while at the screw-concrete interface, they are about 11328 N/mm².The initial embedment strength of the screw in timber, considered its yield stress, is around 5665 N/mm². Thus, as the stresses exceed this yield stress, deformation of the screw and timber crushing are expected. However, the initial embedment strength of the screw in concrete is about 17175 N/mm². The stresses between screw and concrete the interface remain below this yield stress, so no deformation occurs in the concrete. This mechanism is similar to that observed by Mohd Snin et al. [13], where the failure of the screw involved it being withdrawn from the timber but remaining in the concrete. Very little deformation occurred in the part of the screw embedded in the concrete. From the model in this study, it was found that the initiation stress applied to the interface between the concrete and screw was 2 times higher compared to the timber-to-screw interface. This makes the bond between the concrete and the screw very strong.

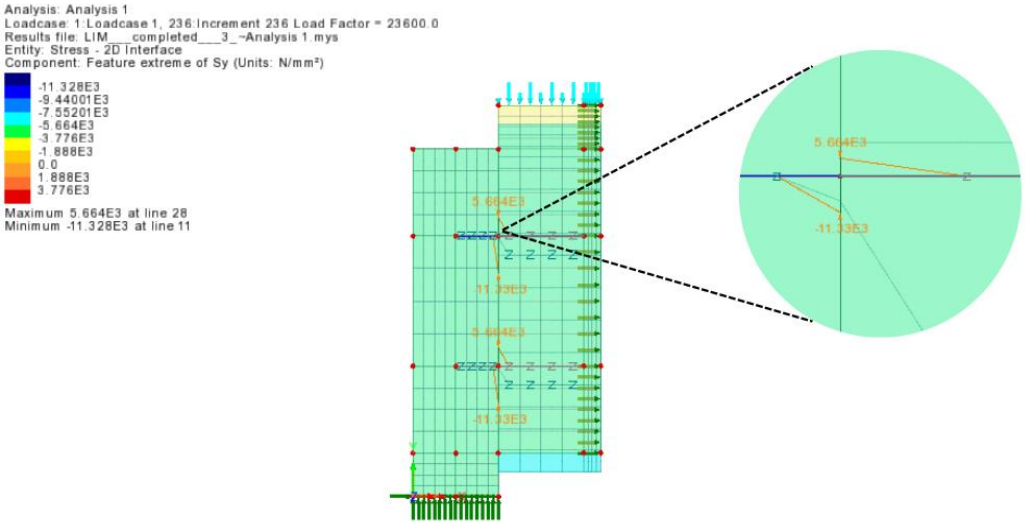

Figure IX.-Interface stresses of the screw at maximum load factor of 23.6 kN (per side)

4.3 Effects of diameter of screws on shear force capacity. - This section examines the impact of screw diameter on the shear force capacity and stiffness of connections. A plot of shear force capacity versus displacement, categorized by screw diameters of 6 mm, 8 mm, and 10 mm, is presented in Figure X. The data indicate that the 10 mm screw exhibited the highest shear force capacity at 11.8 kN, followed by the 8 mm and 6 mm screws with capacities of 9.47

kN and 7.07 kN, respectively. *Table IV* details the shear force capacity and stiffness for each screw diameter and their correlation with initiation stress and fracture energy. This is supported by the research conducted by Long et al. (2022), which found that a larger diameter size increased the embedment strength of the screw connection by 30%. The increased shear force capacity with larger screw diameters is attributed to the greater cross-sectional area, which enhances the screw's ability to withstand shear stresses. This improvement facilitates more effective shear load transfer across concrete and timber layers. Larger diameter screws generally support heavier loads and exhibit increased stress endurance, thereby enhancing the composite structure's shear capacity. Additionally, the stiffness of the joint between concrete and timber is improved with larger screws, resulting in reduced relative displacements and better composite action. This improved mechanical coupling between concrete and timber leads to enhanced frictional resistance at the interface and more even distribution of shear forces, reducing the likelihood of local failures. In summary, larger screw diameters correlate with higher initiation stress, increased fracture energy, and improved shear force capacity. This, in turn, results in a higher stiffness and greater rigidity of the TCC structure, strengthening the overall connection.

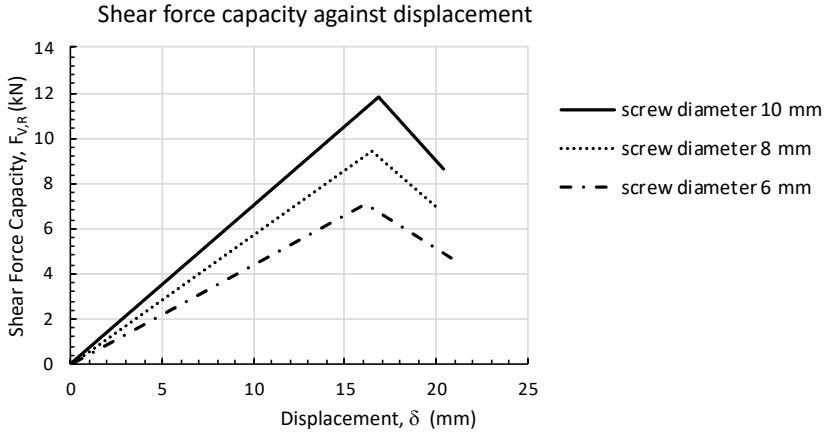

Figure X.- Shear force capacity against displacement with different screw diameter (per screw)

Diameter of screw (mm)	Initiation stress (N/mm)	Fracture energy (J/mm^2)	Shear force capacity (kN)	Stiffness (slope of the graph) (N/mm)
6	3402	51035	7.07	438
8	4536	68040	9.45	574
10	5665	84975	11.80	701

*Table IV***.-** *Summary of comparison of the results based on different screw diameter (per screw)*

4.4 Effects of depth of screws in timber on shear force capacity. - This section investigates the effect of screw length on the shear force capacity and stiffness of connections using an 8 mm diameter screw. Shear force capacity versus displacement for screw embedded in timber lengths of 60 mm, 80 mm, and 100 mm is illustrated in Figure XI. The data reveal that the 100 mm screw embedded in timber length achieved the highest shear force capacity at 11.8 kN, followed by the 80 mm and 60 mm screws, with capacities of 9.43 kN and 7.01 kN, respectively. Table 4 presents the shear force capacity and stiffness associated with each screw embedded in timber length. This matches the study performed by Ribeiro et al. (2018), which found that increasing the screw depth can enhance the withdrawal strength of the screw due to the larger contact area between the timber and the screw. Similar to this study, increased embedment depth improves the screw's resistance to shear forces by providing a larger surface area in contact with the timber. This deeper engagement reduces the likelihood of localized failures by distributing the load over a broader area. Consequently, a deeper screw results in a stronger connection between concrete and timber, facilitating more efficient shear force transfer and enhancing the composite structure's overall shear capacity. The rigidity of the joint, measured by the stiffness, improves with greater screw length. A longer screw, being more deeply embedded, creates a stiffer bond, reducing relative movement (displacement) between the concrete and timber layers under load. This increased resistance to deformation results in a lower slip and a higher stiffness, indicating a more robust connection. In summary, increased screw length enhances shear force capacity and stiffness, leading to greater rigidity and a stronger connection in the TCC structure. The deeper the screw is embedded in the timber, the more effective the load distribution and connection strength, resulting in improved structural performance.

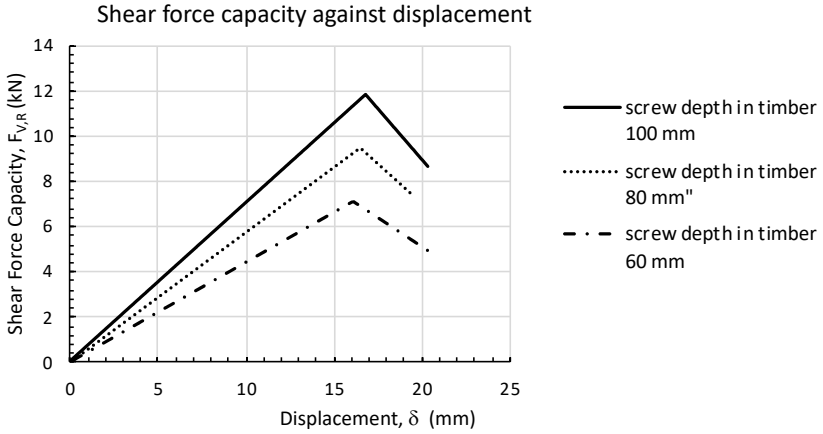

Figure XI.- Shear force capacity against displacement with different screw depth in timber (per screw)

Depth of screw in timber (mm)	Shear force capacity (kN)	Stiffness (Slope of the graph) (N/mm)
60	7.01	437
80	9.43	572
100	11.80	701

Table IV.- Summary of comparison of the results based on different screw depth in timber (per screw)

4.5 Effects of timber density on the shear force capacity. -This section examines the influence of timber density on the shear force capacity and stiffness of connections using an 8 mm diameter and 150 mm length screw. Figure XII presents the relationship between shear force capacity and displacement for timber densities of 476 kg/m³ (typically softwood) and 600 kg/m³ (typically hardwood). The data indicate that the timber with a density of 600 kg/m³ achieved the highest shear force capacity of 14.7 kN, compared to 11.8 kN for the 476 kg/m³ density. This was also found by Ribeiro et al. (2018), who reported that a higher density of timber increased the bond strength between the screw and the timber. Cabrera et al. (2022) also found that the higher density of Beech species increased the embedment strength of the screw when compared to Poplar species, which has a lower density. Higher-density timber, being more rigid and strong, enhances the shear force capacity of the TCC structure as it better withstands the forces imparted by screws or connectors (see Table V for details of strength and stiffness). In contrast, lower-density timber is less rigid and weaker, reducing its capacity to resist shear stresses. Connectors such as screws or dowels perform more effectively in higher-density timber due to the material's increased resistance to pull-out and embedment forces, thereby improving overall shear capacity. Lower-density timber, with its tendency for easier embedment and pull-out, may not support connections as effectively, diminishing shear force capability. Higher-density timber also leads to stronger connections that deform less under load. This reduced deformation results in less relative movement or displacement between the concrete and timber layers, thereby increasing the stiffness. The improved performance of connectors in higher-density timber further enhances load transmission and composite action, resulting in an increased stiffness. In summary, higher timber density correlates with greater shear force capacity and stiffness, leading to increased rigidity and stronger connections in TCC structures.

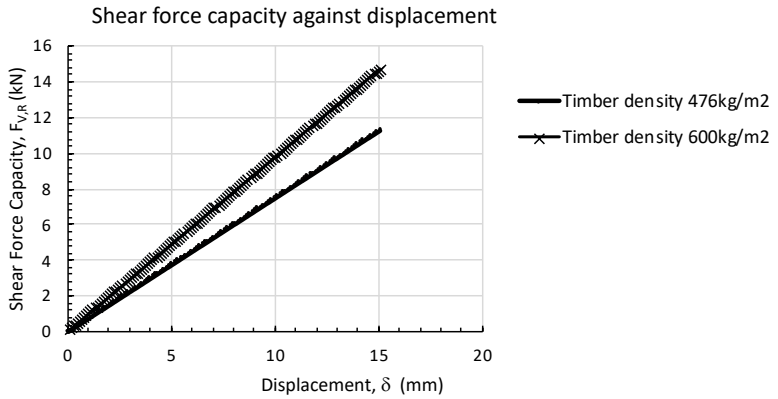

Figure XII.- Shear force capacity against displacement for two different timber density (per screw)

Timber density (kg/m^3)	Shear force capacity (kN)	Stiffness (Slope of the graph) (N/mm)
476	11.80	701
600	14.70	980

Table V.- Summary of the comparison of the results based on different timber density (per screw)

5. Limitations and Future Work. - This research is limited to a two-dimensional analysis, with a focus on the failure mode of the screw connection influenced by the material and geometric properties of the screw, timber, and concrete. The discussion also emphasizes global behavior, such as shear force capacity and stiffness, which are affected by the material properties of the screw, timber, and concrete. Future work should address local characteristics, such as the plastic hinges that may form due to shear forces, influencing the embedment and withdrawal strength of the screw. However, this would require experimental work to observe the actual shape of the screw after failure. By examining the details of the plastic hinge formation on the screw, it would be possible to measure and correlate this with the shear strength of the screw connection.

6. Conclusions.- This study successfully met its objectives of validating double shear test models and analyzing local shear connection behaviour in timber-concrete composite (TCC) structure. The finite element models used for simulating double shear tests demonstrated quite similar results when compared to experimental data. The simulation results for shear force capacity was within 10% of the experimental values reported by Manojlović et al. [11]. The study also found that increasing the screw diameter to 10 mm significantly improved shear force capacity and stiffness, thereby enhancing the structural performance of the connections. Greater embedment depths (100 mm) resulted in higher shear force capacity and improved stiffness, indicating better load distribution and reduced localized failures. A higher timber density (600 kg/m³) increased both shear force capacity and stiffness compared to lower-density timber (476 kg/m³), highlighting the benefit of using denser timber for stronger connections. The most significant finding of this research is the identification of the failure mode of the screw connections. The study revealed that the failure of screw connections depends on the properties of the timber, concrete, and screw. When the concrete strength exceeds the timber strength, failure occurs due to timber crushing. In the interaction between timber and screw, when the interaction stresses exceed the yield stress, screw deformation and timber crushing are expected. These results underscore the critical role of screw dimensions and timber density in optimizing the performance of shear connections in TCC structures. The insights gained offer valuable guidance for both practical engineering applications and future research in the field. Lastly, Table VI shows the summary of the findings for this research

Parameter	Key Finding		
	Details	Shear force capacity	Stiffness
Screw diameter	6 mm	low	low
	8 mm	medium	medium
	10 mm	high	high
Screw length	60 mm	low	low
	80 mm	medium	medium
	100 mm	high	high
Timber density	476 kg/m^3	low	low
	600 kg/m^3	high	high

Table VI.- Summary of findings according to different variable in screw and timber properties

Acknowledgements.- The authors acknowledge the funding received from the Universiti Sains Malaysia under the short-term grant (304/PAWAM/6315691) which helped in supporting this research.

References

[1] Bajzecerova, V., Kovac, M., & Kanocz, J. (2018). Structural analysis of cross-laminated timber slabs subjected to bending – state of the art. Selected Scientific Papers - Journal of Civil Engineering, 13(1), 133–140. https://doi.org/10.1515/sspjce-2018-0027

[2] Ben, Q., Dai, Y., Chen, S., Shi, B., & Yang, H. (2022). Shear performances of shallow notch-screw connections for timber-concrete composite (TCC) floors. BioResources, 17(2), 3278–3290. https://doi.org/10.15376/biores.17.2.3278-3290

[3] Buka-Vaivade, K. (2022). Development of Innovative Rational Timber-Concrete Composite Structures. https://doi.org/10.7250/9789934228452

[4] Daňková, J. (2014). Timber - Concrete Structural Element with Glued Steel Mesh. Advanced Materials Research, 1000, 91–96. https://doi.org/10.4028/www.scientific.net/amr.1000.91

[5] Du, H., Hu, X., Sun, Z., & Fu, W. (2020). Shear stiffness of inclined screws in timber–concrete composite beam with timber board interlayer. Advances in Structural Engineering, 23(16), 3555–3565. https://doi.org/10.1177/1369433220940814

[6] CEN, European Committee for Standardization, (2020). Eurocode 5. Design of Timber Structures. https://doi.org/10.3403/ddenv1995-1

[7] Füchslin, M., Grönquist, P., Stucki, S., Mamie, T., Kelch, S., Burgert, I., & Frangi, A. (2023). PUSH-OUT TESTS OF WET-PROCESS ADHESIVE-BONDED BEECH TIMBER-CONCRETE AND TIMBER-POLYMER-CONCRETE COMPOSITE CONNECTIONS. World Conference on Timber Engineering (WCTE 2023). https://doi.org/10.52202/069179-0422

[8] Johari, I.B., Mohd Snin, M.A.B., Senin, S.F.B. & Mohamad Rashid, M.R.B. (2023). Screw Connection Systems in Timber-Concrete Composite Structures: A Literature Review. *Tehnički vjesnik, 30* (4), 1336-1346. https://doi.org/10.17559/TV-20220820075553

[9] Hammad, M. W., Valipour, H. R., & Foster, S. J. (2024). Timber-concrete composites (TCC) floors subjected to hogging moment. Engineering Structures, 303, 117488. https://doi.org/10.1016/j.engstruct.2024.117488
LUSAS. (2024). *LUSAS Modeller manual* (Version 21). LUSAS.

[10] Manojlović, D., Rašeta, A., Vukobratović, V., Čeh, A., Kozarić, L., Jovanović, Đ., & Starčev-Ćurčin, A. (2023). Simulation of Load–Slip Capacity of Timber–Concrete Connections with Dowel-Type Fasteners. Buildings, 13(5), 1171. https://doi.org/10.3390/buildings13051171

[11] Miotto, J. L., & Dias, A. A. (2015). Structural efficiency of full-scale timber–concrete composite beams strengthened with fiberglass reinforced polymer. Composite Structures, 128, 145–154. https://doi.org/10.1016/j.compstruct.2015.03.054

[12] Mohd Snin, M. A., & Kassem, M. M. (2023). Novel Use of Scanning Methods to Investigate the Performance of Screw Connections in Timber-Concrete Composite Structures. *Advances in Civil Engineering*, *2023*, 1–17. https://doi.org/10.1155/2023/4176805

[13] Müller, K., & Frangi, A. (2021). Micro-notches as a novel connection system for timber-concrete composite slabs. Engineering Structures, 245, 112688. https://doi.org/10.1016/j.engstruct.2021.112688

[14] Moshiri, F., Shrestha, R., & Crews, K. (2014). The Predictive Model for Stiffness of Inclined Screws as Shear Connection in Timber-Concrete Composite Floor. Materials and Joints in Timber Structures, 443–453. https:/doi.org/10.1007/978-94-007-7811-5_40

[15] PHAM, V. S. (2022). Shear Behavior of Different Connections for Cross-Laminated Timber-Concrete Composite Floor. SSRN Electronic Journal. https://doi.org/10.2139/ssrn.4229164

[16] Pyykkö, J., & Svensson, S. (2024). Load-bearing capacity of slender dowel-type fasteners in Timber-Concrete Composite connections. Engineering Structures, 316, 118556. https://doi.org.10.1016/j.engstruct.2024.118556
Winder, S., Chapman, D., Papastavrou, P., Smith, S., & McRobie, A. (2023). Prefabricated Timber Concrete Composites. World Conference on Timber Engineering (WCTE 2023), 3091–3100. https://doi.org/10.52202/069179-0403

[17] Cabrera, G., Moltini, G., & Baño, V. (2022). Embedment Strength of Low- and Medium-Density Hardwood Species from Spain. Forests, 13(8), 1154. https://doi.org/10.3390/f13081154

[18] Hammad, M. W., Valipour, H. R., & Foster, S. J. (2024). Timber-concrete composites (TCC) floors subjected to hogging moment. Engineering Structures, 303, 117488. https://doi.org/10.1016/j.engstruct.2024.117488

[19] Long, W., Ou, J., Sun, X., Huang, X., He, M., & Li, Z. (2022). Experimental study on the embedment strength of smooth dowels inserted in cross-laminated timber narrow side. Journal of Wood Science, 68(1). https://doi.org/10.1186/s10086-022-02055-0

[20] Ribeiro, M. L., Del Menezzi, C., Siqueira, M. L., & Melo, R. R. (2018). Effect of Wood Density And Screw Length on The Withdrawal Resistance of Tropical Wood. Nativa, 6(4), 402–406. https://doi.org/10.31413/nativa.v6i4.5638

Author contribution:
1. Conception and design of the study
2. Data acquisition
3. Data analysis
4. Discussion of the results
5. Writing of the manuscript
6. Approval of the last version of the manuscript

LJE has contributed to: 1, 2, 3, 4, 5 and 6.
MAMS has contributed to: 1, 2, 3, 4, 5 and 6.
SNFG has contributed to: 1, 2, 3, 4, 5 and 6.
NAFM has contributed to: 1, 2, 3, 4, 5 and 6.
MIZ has contributed to: 1, 2, 3, 4, 5 and 6.
RS has contributed to: 1, 2, 3, 4, 5 and 6.

Acceptance Note: This article was approved by the journal editors Dr. Rafael Sotelo and Mag. Ing. Fernando A. Hernández Gobertti.

Eficiencia de la lombriz roja californiana en la biorremediación de suelos contaminados con hidrocarburos

Efficiency of the Californian red earthworm in the bioremediation of soils contaminated with hydrocarbons

Eficiência da minhoca vermelha da Califórnia na biorremediação de solos contaminados com hidrocarbonetos

Samuel Baldeon Coronado[1(*)], Kettly Baltazar Torres[2] , Jhon Patrick Ríos Bartra[3]

Recibido: 12/11/2024 Aceptado: 26/01/2025

Resumen. - En los últimos años, el Perú ha enfrentado un incremento significativo de pasivos ambientales relacionados con hidrocarburos, lo que representa un grave problema para el medio ambiente (Bazán et al., 2024). Esta investigación evaluó la eficiencia de la lombriz roja californiana (Eisenia fetida) en la biorremediación de suelos contaminados, comparando su capacidad para reducir los niveles de contaminación con los Estándares de Calidad Ambiental (ECA) establecidos para suelos. Se empleó un diseño experimental factorial 3x3, con tres niveles de tratamiento y tres repeticiones, y se aplicó la prueba ANOVA para el análisis estadístico de los resultados. Los resultados revelaron una eficiencia en la biorremediación de suelos contaminados por diesel. En el tratamiento con 10 lombrices, se encontraron diferencias significativas, destacando el tratamiento A3 (3.06 ml) como el más eficiente. En contraste, para los tratamientos con 20 y 30 lombrices, no se observaron diferencias significativas. Los análisis gráficos indican que la cantidad de lombrices y la concentración de diésel influyen en la eficiencia del proceso, siendo más efectivas en concentraciones moderadas (A2) y menos eficientes a niveles más altos. En conclusión, la lombriz roja californiana muestra un potencial significativo en la biorremediación de suelos contaminados con hidrocarburos, siendo más eficiente en menores concentraciones (A1 y A2), mientras que a concentraciones más altas (A3) se observa una saturación en su capacidad de procesamiento.

Palabras clave: Eficiencia; lombriz roja californiana, biorremediación; suelos contaminados; hidrocarburos.

(*) Autor de correspondencia

[1] Bachiller, Universidad Peruana Unión, Facultad de Ingeniería y Arquitectura, samuelbaldeon@upeu.edu.pe, ORCID iD: https://orcid.org/0009-0008-0644-6034

[2] Bachiller, Universidad Peruana Unión, Facultad de Ingeniería y Arquitectura, katerinbaltazar@upeu.edu.pe, ORCID iD: https://orcid.org/0000-0002-1132-2115

[3] Magister, Universidad Peruana Unión, Facultad de Ingeniería y Arquitectura, jhon.rios@upeu.edu.pe, ORCID iD: https://orcid.org/0000-0002-1439-6291

Memoria Investigaciones en Ingeniería, núm. 28 (2025). pp. 183-192
https://doi.org/10.36561/ING.28.13
ISSN 2301-1092 • ISSN (en línea) 2301-1106 – Universidad de Montevideo, Uruguay

Summary. - *In recent years, Peru has faced a significant increase in environmental liabilities related to hydrocarbons, which represents a serious problem for the environment (Bazán et al., 2024). This research evaluated the efficiency of the Californian red earthworm (Eisenia fetida) in the bioremediation of contaminated soils, comparing its ability to reduce contamination levels with the Environmental Quality Standards (ECA) established for soils. A 3x3 factorial experimental design was used, with three treatment levels and three repetitions, and the ANOVA test was applied for the statistical analysis of the results. The results revealed an efficiency in the bioremediation of soils contaminated by diesel. In the treatment with 10 worms, significant differences were found, highlighting treatment A3 (3.06 ml) as the most efficient. In contrast, for treatments with 20 and 30 worms, no significant differences were observed. The graphical analyzes indicate that the number of worms and the concentration of diesel influence the efficiency of the process, being more effective at moderate concentrations (A2) and less efficient at higher levels. In conclusion, the Californian red earthworm shows significant potential in the bioremediation of soils contaminated with hydrocarbons, being more efficient at lower concentrations (A1 and A2), while at higher concentrations (A3) a saturation is observed in its processing capacity.*

Keywords: *Efficiency; Californian red worm, bioremediation; contaminated soils; hydrocarbons.*

Resumo**. -** *Nos últimos anos, o Peru tem enfrentado um aumento significativo nos passivos ambientais relacionados a hidrocarbonetos, o que representa um sério problema para o meio ambiente (Bazán et al., 2024). Esta pesquisa avaliou a eficiência da minhoca vermelha da Califórnia (Eisenia fetida) na biorremediação de solos contaminados, comparando sua capacidade de reduzir os níveis de contaminação com os Padrões de Qualidade Ambiental (ECA) estabelecidos para solos. Foi utilizado um delineamento experimental fatorial 3x3, com três níveis de tratamento e três repetições, e o teste ANOVA foi aplicado para a análise estatística dos resultados. Os resultados revelaram uma eficiência na biorremediação de solos contaminados por diesel. No tratamento com 10 minhocas, foram encontradas diferenças significativas, destacando o tratamento A3 (3,06 ml) como o mais eficiente. Em contrapartida, para os tratamentos com 20 e 30 minhocas, não foram observadas diferenças significativas. As análises gráficas indicam que o número de minhocas e a concentração de diesel influenciam a eficiência do processo, sendo mais eficaz em concentrações moderadas (A2) e menos eficiente em níveis mais elevados. Conclui-se que a minhoca vermelha da Califórnia apresenta potencial significativo na biorremediação de solos contaminados com hidrocarbonetos, sendo mais eficiente em concentrações mais baixas (A1 e A2), enquanto em concentrações mais elevadas (A3) observa-se uma saturação em sua capacidade de processamento.*

Palavras-chave: *Eficiência; verme vermelho da Califórnia, biorremediação; solos contaminados; hidrocarbonetos.*

1. Introducción. - En los últimos años, el Perú ha enfrentado un aumento significativo de pasivos ambientales generados por la contaminación por hidrocarburos, lo cual representa una grave amenaza para el medio ambiente [1]. De acuerdo con un informe del Organismo de Evaluación y Fiscalización Ambiental (OEFA), se han identificado un total de 3,231 pasivos ambientales en el sector hidrocarburos, de los cuales 151 son considerados de alto riesgo, 1,997 de riesgo medio y 1,083 de bajo riesgo. Asimismo, se han clasificado 61 pasivos con alto riesgo para la salud, 35 para el medio ambiente y 123 para la seguridad [2].

Un caso alarmante se ha presentado en la Amazonía peruana, donde se han registrado cerca de 500 derrames de petróleo en las últimas dos décadas, principalmente debido a fallas operativas y al deterioro de la infraestructura tanto en los yacimientos como en el oleoducto que atraviesa la selva. Estas situaciones han provocado numerosas protestas por parte de las comunidades indígenas, que demandan compensación y medidas de remediación por los impactos ambientales en los cuerpos de agua, la flora y fauna, así como en su entorno social [3]. Un ejemplo notable es el derrame en Loreto, donde más de cien barriles de petróleo, operados por Petroperú, afectaron a 1,230 familias indígenas debido a la ruptura del oleoducto, permitiendo que el crudo se desplazara desde la Amazonía hasta la costa del océano Pacífico, alterando diversos factores ambientales [4].

La contaminación por hidrocarburos tiene un efecto adverso en la fertilidad del suelo, provocando toxicidad directa en los organismos, disminuyendo la retención de humedad y nutrientes, aumentando la compactación del suelo, y alterando su pH y salinidad [5]. En ese sentido, la utilización de lombrices para remediar suelos contaminados por hidrocarburos es una alternativa económica y ecológica que mejora la calidad del suelo sin generar residuos peligrosos, esta técnica sostenible es clave para innovar en la protección del medio ambiente [6].

Ante este panorama, es fundamental considerar alternativas de biorremediación para restaurar las áreas afectadas. Por lo tanto, esta investigación se centró en el uso de lombrices de tierra como agentes de remediación, evaluando su efectividad en la recuperación de suelos contaminados por hidrocarburos mediante la medición de su impacto en la calidad del suelo.

2. Materiales y métodos

2.1 Área de estudio. - El suelo utilizado para la experimentación controlada con hidrocarburos fue extraído de las áreas disponibles de la Universidad Peruana Unión, ubicada en el Jr. Los Mártires 214, urbanización Santa Lucía, distrito de Morales, provincia de San Martín, región San Martín. La Figura I muestra el mapa de ubicación del área de estudio."

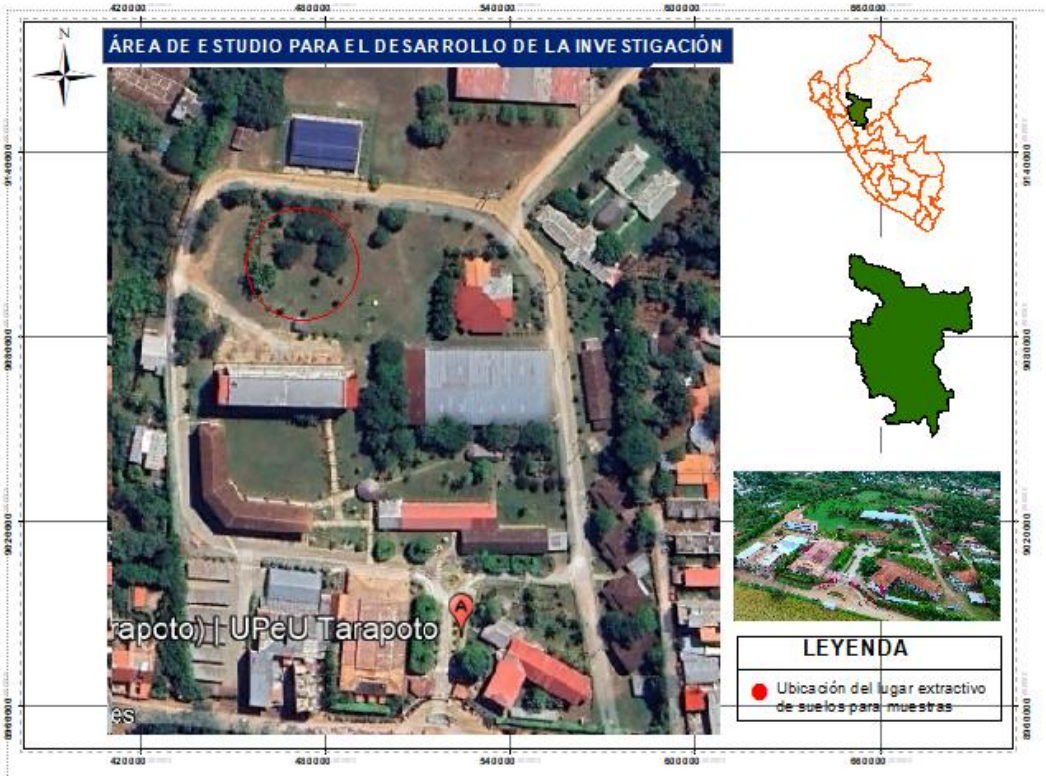

Figura I. Ubicación del lugar de estudio

Asimismo, el tratamiento del suelo contaminado con hidrocarburos se realizó a escala de laboratorio utilizando lombrices rojas californianas *(Eisenia foetida)* bajo condiciones controladas. Este experimento se llevó a cabo en el laboratorio de la Universidad Peruana Unión, lo que permitió asegurar la precisión en el manejo de las variables ambientales y obtener resultados confiables sobre la efectividad de la biorremediación.

2.2 Diseño metodológico. - El diseño metodológico utilizado fue experimental, debido a la manipulación de la variable independiente para analizar su efecto en la variable dependiente. Asimismo, se utilizó un diseño factorial 3x3, con tres niveles de tratamiento y tres repeticiones, lo que permitió identificar las combinaciones óptimas y evaluar la interacción entre las variables bajo el mismo control.

2.3 Diseño muestral. - Para la investigación, se seleccionó 30 kg de suelo extraídos del territorio de la Universidad Peruana Unión como población de estudio. Asimismo, se aplicó un muestreo aleatorio simple, garantizando que cada unidad de suelo contaminado tuviera la misma posibilidad de ser asignada a los diferentes tratamientos del diseño factorial. Este método facilitó la obtención de una muestra representativa, permitiendo hacer conclusiones confiables sobre los efectos de variables como la dosis de diésel, la cantidad de lombrices y el tiempo de recuperación en la regeneración del suelo contaminado.

2.4 Técnicas de recolección de datos. - La recolección y análisis de las muestras se llevaron a cabo mediante el acondicionamiento de 27 maceteros, cada uno con un volumen de 30 kg de suelo contaminado con hidrocarburos. En estos maceteros, se distribuyeron lombrices en tres grupos de tratamiento, con 10, 20 y 30 unidades respectivamente. El periodo de evaluación se estableció en 15 días, tiempo suficiente para observar el impacto de las diferentes cantidades de lombrices en la remediación del suelo. Este diseño experimental permitió evaluar de manera precisa la efectividad de las lombrices en la recuperación del suelo contaminado con diesel.

2.5 Análisis estadístico. - Para el análisis estadístico de los resultados obtenidos se consideró los requisitos de normalidad y homogeneidad de varianzas, posteriormente se realizó la prueba de ANOVA para realizar las comparaciones de los tratamientos, finalmente se realizó la prueba tukey para aquellos tratamientos que superaron el valor de 0.05, a fin de conocer el mejor la mejor eficiencia de las cantidades representativas de las lombrices rojas californianas.

3. Resultados. - En la Tabla I se presentan los valores obtenidos a partir del análisis de laboratorio realizado a las muestras de suelos contaminados con diferentes dosis de diésel y cantidades variables de lombrices rojas californianas. Los resultados muestran la concentración de hidrocarburos en mg/kg.

Concentración de diesel (ml)		N° de lombrices rojas californianas	Repeticiones			$\bar{x}$
			R1 (mg/kg)	R2 (mg/kg)	R3 (mg/kg)	
		10 unidades	71.888	80.199	78.289	76.8
A1	**1.02**	20 unidades	119.739	120.722	118.82	119.8
		30 unidades	182.35	180.292	115.251	159.3
		10 unidades	90.765	89.566	85.199	88.5
A2	**2.04**	20 unidades	117.533	123.143	120.198	120.3
		30 unidades	150.663	150.029	149.914	150.2
		10 unidades	111.863	114.128	113.386	113.1
A3	**3.06**	20 unidades	120.882	118.122	115.343	118.1
		30 unidades	171.723	172.135	169.183	171.0

Tabla I. Resultados de laboratorio sobre la recuperación de suelos contaminados con hidrocarburos utilizando lombrices rojas californianas.

En la Tabla II se presentan los resultados del análisis de varianza (ANOVA) para el uso de 10, 20 y 30 unidades de lombrices rojas californianas en la biorremediación de suelos contaminados con hidrocarburos. Los resultados indican que, con 10 unidades de lombrices, se obtuvo un P-Valor de 0.000, lo que evidencia una diferencia estadísticamente significativa entre los tratamientos. En consecuencia, se realizó la prueba de Tukey para identificar el tratamiento que mostró los mejores resultados, como se detalla en la Tabla III.

En contraste, para el tratamiento con 20 unidades de lombrices, se obtuvo un P-Valor de 0.531, lo que indica que no existe una diferencia significativa entre los tratamientos, y por lo tanto, no fue necesario aplicar la prueba de Tukey. De manera similar, el tratamiento con 30 unidades de lombrices mostró un P-Valor de 0.546, evidenciando nuevamente

la ausencia de diferencias significativas, por lo cual tampoco se requirió la prueba de Tukey.

	FV	Suma de cuadrados	GL	M.C	F	P-Valor
10 U	Entre grupos	2063.378	2	1031.689	107.230	0.000
	Dentro de grupos	57.728	6	9.621		
	Total	2121.105	8			
20 U	Entre grupos	7.720	2	3.860	0.704	0.531
	Dentro de grupos	32.899	6	5.483		
	Total	40.619	8			
30 U	Entre grupos	653.121	2	326.561	0.672	0.546
	Dentro de grupos	2917.718	6	486.286		
	Total	3570.840	8			

Tabla II. Resultados del análisis de varianza (ANOVA) para el uso de 10, 20 y 30 unidades de lombrices rojas californianas en el tratamiento del suelo.

Al aplicar la prueba de Tukey para el tratamiento con 10 unidades de lombrices, se identificaron tres grupos. Los resultados muestran que el uso de 10 unidades no logra reducir eficientemente la cantidad de diésel en proporción al incremento en las dosis aplicadas

Concentración Diesel	N	Grupos		
		1	2	3
A1 (1.02 ml)	3	76.79200		
A2 (2.04 ml)	3		88.51000	
A3 (3.06 ml)	3			113.12567
Sig.		1.000	1.000	1.000

Tabla III. Resultados de la prueba de Tukey en la biorremediación de suelos contaminados con hidrocarburos utilizando 10 unidades de lombrices rojas californianas.

En los siguientes gráficos se muestra la eficiencia de la lombriz roja californiana en la biorremediación de suelos contaminados con hidrocarburos.

En la figura II se muestra, que los valores de concentración en el suelo siguen aumentando a mayor cantidad de diésel, lo cual indica que las 10 u de lombrices no están reduciendo eficazmente la cantidad de diésel proporcional al incremento en las dosis aplicadas.

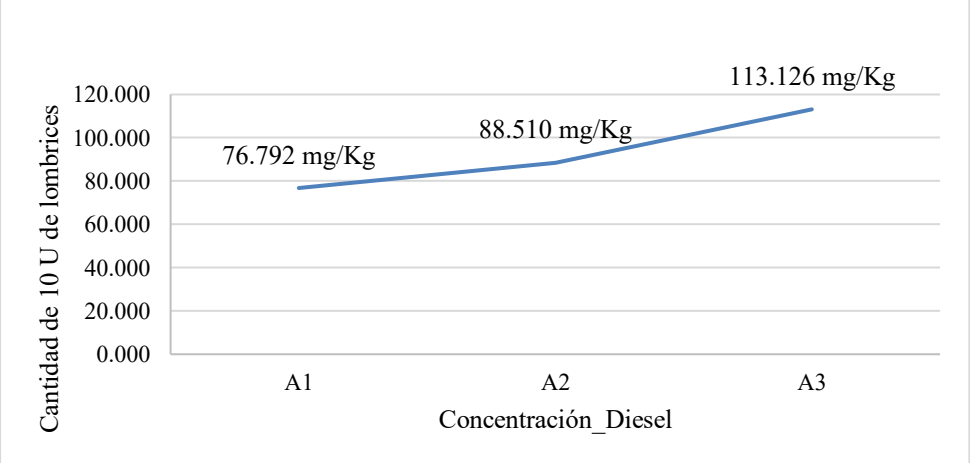

Figura II. Eficiencia del empleo de 10 u de lombriz roja californiana en la biorremediación de suelos contaminados con diesel

En la Figura III se muestra un comportamiento no lineal en la concentración de diésel tras la biorremediación con 20 lombrices. La tendencia describe un aumento inicial en la concentración de diésel de A1 a A2, seguido por una disminución en A3, por lo que el empleo de 20 u de lombrices es más eficiente en la biorremediación en concentraciones de 3.06 ml de diesel en un periodo de estudio de 15 días.

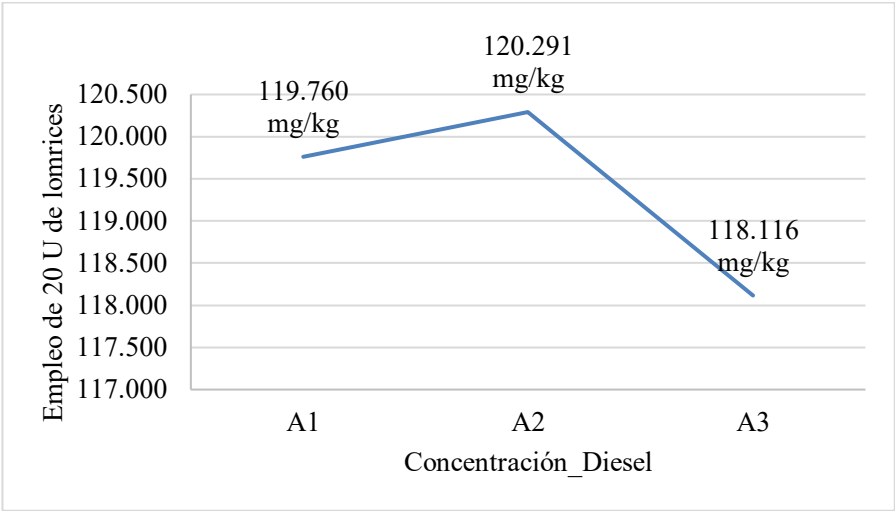

Figura III. Eficiencia del empleo de 20 u de lombriz roja californiana en la biorremediación de suelos contaminados con diesel

La Figura IV muestra una curva en "U", que indica un comportamiento no lineal entre la concentración de diésel y la eficiencia del empleo de 30 u de lombrices en la biorremediación. La concentración disminuye de A1 a A2, pero luego aumenta en A3. Las lombrices son más efectivas en el tratamiento A2, donde las concentraciones de diésel están dentro de su rango óptimo de procesamiento. En A3, la eficiencia disminuye, posiblemente debido a una saturación en su capacidad de remediación.

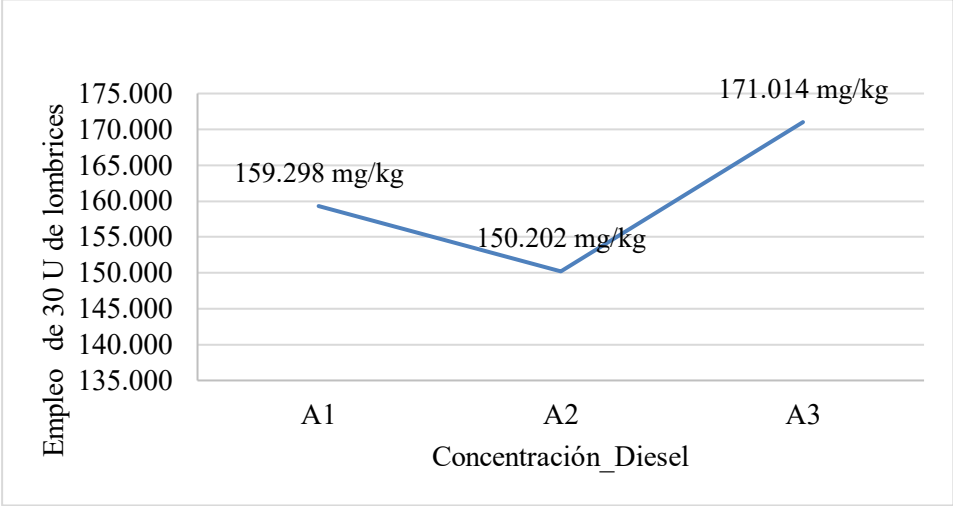

Figura IV. Eficiencia del empleo de 30 u de lombriz roja californiana en la biorremediación de suelos contaminados con diesel.

4. Discusiones. - Los resultados muestran que el empleo de 10 lombrices rojas californianas *(Eisenia fetida)* no está reduciendo eficazmente la cantidad de diésel en proporción al incremento en las dosis aplicadas. En cuanto a la utilización de 20 lombrices, el proceso de biorremediación fue más eficiente en concentraciones de 3.06 ml de diésel durante un periodo de estudio de 15 días. Para el caso de 30 lombrices, la concentración de diésel disminuyó del tratamiento A1 a A2, pero luego aumentó en A3. Las lombrices fueron más efectivas en A2, donde las concentraciones de diésel estaban dentro de su rango óptimo de procesamiento, aunque en A3 la eficiencia disminuyó, debido a una saturación en su capacidad de remediación. En ese sentido, Acuña et al., (2021) [7] reportaron que las lombrices rojas

californianas tienen un rendimiento decreciente en concentraciones elevadas de hidrocarburos. En su estudio las lombrices mostraron alta eficiencia en la degradación de hidrocarburos de fracción C10-C28 en concentraciones bajas y moderadas, pero en concentraciones más altas el porcentaje de remediación disminuyó, por lo que concuerda con los resultados obtenidos, donde las lombrices muestran mayor eficiencia en concentraciones moderadas y una saturación en concentraciones altas.

Por otro lado, Flores et al. (2021) [8] observaron que la capacidad de las lombrices para la biorremediación de suelos contaminados con diésel es limitada en concentraciones elevadas, ya que las lombrices se ven negativamente afectadas debido a la saturación, lo que reduce su eficiencia. Este hallazgo concuerda con Ortega y Quiroga (2019) [9], quienes destacaron que los mejores resultados en la biorremediación se obtienen en concentraciones moderadas de diésel. De manera similar, Ojeda y Córdova (2023) [10] reportaron que la eficiencia de las lombrices disminuye significativamente cuando las concentraciones de diésel superan ciertos límites, subrayando la importancia de mantener cantidades moderadas de contaminante para maximizar la efectividad del proceso.

5. Conclusiones. -

- El empleo de 10 unidades de lombrices rojas californianas en la biorremediación de suelos contaminados revela que, a medida que se incrementa la cantidad de diésel aplicado, también aumenta su concentración en el suelo. Esto indica que las lombrices no están reduciendo de manera efectiva la cantidad de diésel en proporción al aumento de las dosis aplicadas.

- El empleo de 20 unidades de lombrices rojas californianas en la biorremediación de suelos contaminados revela que, no es uniforme y podría estar influenciada por la cantidad de diésel. El incremento en A2 señala una saturación en la capacidad de las lombrices, pero la disminución en A3 muestra que es más eficiente en concentraciones más altas o con más tiempo de exposición.

- El empleo de 30 unidades de lombrices rojas californianas en la biorremediación de suelos contaminados revela que, las lombrices rojas californianas tienen un comportamiento variable en función de la concentración de diésel en el suelo. Son más efectivas en la biorremediación en el tratamiento A2, pero su eficiencia disminuye en concentraciones más altas (A3). Este comportamiento está relacionado con la capacidad de tolerancia de las lombrices al diésel y su habilidad para procesar el contaminante.

Referencias

[1] Acuña S, Celedonia & Muñoz (2021). Reducción de hidrocarburos (fracción c10- c28) de petróleo en suelos contaminados por hidrocarburos con el uso de la lombriz roja californiana (Eisenia foetida) en el distrito de Huancavelica. Universidad Nacional de Huancavelica.

[2] Bazán S, Morales R, Rengifo G, & Valdivia (2024). Pasivos ambientales del subsector hidrocarburos y sitios impactados: Un análisis de su situación actual y perspectiva. Gaceta Científica, 10 (2), 53–63. https://doi.org/10.46794/gacien.10.2.2167

[3] Barbaran C (2017). Reducción de Cromo en suelos contaminados por agroquímicos utilizando lombrices de tierra (Eisenia foetida) en el Centro Poblado Huarabi- Canta; 2017. 1, 1(1-14).

[4] Buenestado C (2020). Diseño de Experimentos: Diseño Factorial. En Diseño de Experimentos.

[5] Bunge, M. (2007). La investigación científica (4ta. Ed). Siglo XXI.

[6] Caján, A. Pascual & Anco (2021). Efecto eco toxicológico del cloruro de potasio sobre la lombriz roja californiana (Eisenia foetida). Revista del Instituto de investigación de la Facultad de minas, metalurgia y ciencias geográficas, 24(47), Article 47. https://doi.org/10.15381/iigeo.v24i47.20658

[7] Cépeda, A. L., & Lossio, M. Z. (2024). La sombra de los hidrocarburos en el Perú. 56.

[8] Chen, M., Xu, P., Zeng, G., Yang, C., Huang, D., & Zhang, J. (2015). Bioremediation of soils contaminated with polycyclic aromatic hydrocarbons, petroleum, pesticides, chlorophenols and heavy metals by composting: applications, microbes and future research needs. Biotechnology Advances, 33(6), 745-755. https://doi.org/10.1016/j.biotechadv.2015.05.003.

[9] Cruz N, Meléndez J, & Castañeda E (2021). Biorremediación con vermicomposta en la contaminación del suelo producida por hidrocarburos. 7.

[10] Flores J, Nuñez C, & Diaz L (2021). Growth of the californian red worm (Eisenia Foetida) in vermicomposting process of diesel contaminated soil. International Journal of Environmental Research and Public Health, 18(5), 2226. https://doi.org/10.3390/ijerph18052226

[11] Gavilánez L, Freddy (2021). Diseños y análisis estadísticos para experimentos agrícolas. Ediciones Díaz de Santos.

[12] Katherine, C. S. D., Antonio, V. M. L., & David, A. M. W. (2020). Aplicación de sustratos orgánicos en la cría de la lombriz roja californiana (Eisenia foetida) para la producción de alimento animal. Conciencia Digital, 3(3.1), Article 3.1. https://doi.org/10.33262/concienciadigital.v3i3.1.1354

[13] Lin, Z., Zhen, Z., Ren, L., Yang, J., Luo, C., Zhong, L., ... Zhang, D. (2018). Effects of two ecological earthworm species on atrazine degradation performance and bacterial community structure in red soil. Chemosphere, 196, 467-475. https://doi.org/10.1016/j.chemosphere.2017.12.177

[14] Ojeda M, Córdova B, Álvarez R, López L, Martínez G., & Morales (2023). Remediación de suelos contaminados con hidrocarburos empleando sustancias húmicas de vermicomposta. Terra Latinoamericana, 41. https://www.redalyc.org/journal/573/57375131033/html/

[15] Ortega O & Quiroga D (2019). Evaluación de la eficiencia de tres procesos de biorremediación en suelos contaminados con petróleo, mediante la determinación de la concentración letal 50 (CL50) en la lombriz californiana, Eisenia Foetida (lombricidae) [Bachelor thesis, Universidad Santo Tomás]. https://repository.usta.edu.co/handle/11634/19059

[16] Rodríguez (2018). Efecto del humus de lombriz en la remoción de suelos contaminados con crudo de petróleo. Ucayali, Perú. Universidad Nacional de Ucayali.

http://repositorio.unu.edu.pe/bitstream/hansdle/UNU/4047/000003720T_Ambiental.pdf.sequence=1&isAllowed=y

[17] Vargas M (2018). Efecto de diésel como contaminante del suelo en el crecimiento del Frijol Castilla o caupi, (Vigna unguiculata L) Distrito de Yarinacocha, Provincia de Coronel Portillo, Región Ucayali. 2018. 1, 1-54.

Nota contribución de los autores:

1. Concepción y diseño del estudio
2. Adquisición de datos
3. Análisis de datos
4. Discusión de los resultados
5. Redacción del manuscrito
6. Aprobación de la versión final del manuscrito

SBC ha contribuido en: 1, 2, 3, 4, 5 y 6.
KBT ha contribuido en: 1, 2, 3, 4, 5 y 6.
JPRB ha contribuido en: 1, 2, 3, 4, 5 y 6.

Nota de aceptación: Este artículo fue aprobado por los editores de la revista Dr. Rafael Sotelo y Mag. Ing. Fernando A. Hernández Gobertti.

Application of Six Sigma Methodology for Enhancement of Soft Plastic Extrusion Process

Aplicación de la metodología Seis Sigma para la mejora del proceso de extrusión de plásticos blandos

Aplicação da Metodologia Seis Sigma para Aprimoramento do Processo de Extrusão de Plástico Macio

Muhammad Mansoor Uz Zaman Siddiqui[1(*)], Adeel Tabassum[2]

Recibido: 12/11/2024 Aceptado: 28/01/2025

Summary. - The gasket manufacturing process in "Company A" faced significant challenges and inefficiencies because of high rejection rates and variation in extrusion machine, magnetic insertion machine and welding machine's performance. All three machines were consistently generating major rejections on a daily basis including a high volume of purging rejections from the PVC soft extrusion machine, excessive trimming of oversized magnets during the magnetic insertion process, and significant rejection due to poor joint strength in the welding process of PVC profiles. In order to address these underlying issues, Six Sigma DMAIC (Define, Measure, Analyze, Improve, Control) methodology was employed in order to decrease rejection/waste, increase process efficiency and decrease defects of all three machines. The study involved process mapping, cause and effect analysis, quality function deployment (QFD) and statistical process tools such as ANOVA, regression and Cp/Cpk analysis. Root causes were identified and targeted improvements based on the data were introduced including optimized production planning, machine parameter optimization and standardization, improvement of production execution planning and storage availability, temperature controls on welding machines and encoder wheel knurling for magnetic insertion machine. The main objectives were to deal with problems including material waste, variance in magnetic strip size, issues in welding machines and frequent machine stoppages caused by improper production scheduling because of improper availability of storage space for batch production independent of door pre-assembly plan. Following implementation, results show a considerable decrease in extrusion machine rejection %age from 12% to 4.06%, a reduction in purging waste from 17 kg/day to 6.9 kg/day and an increase in machine efficiency from 50.1% to 83.3%. Furthermore, welding machine rejection %age fell from 7% to 3.7% as a result of enhanced temperature management and equipment maintenance. Size variation issue in magnet insertion machine was resolved by knurling of encoder wheel. Overall, these changes resulted in an annual cost savings of roughly 1.5 million PKR for the extrusion process and 1.2 million from magnet insertion machine. The significance of this project originates from its potential to streamline the gasket production process by reducing waste and faults while increasing machine efficiency. The results offer a replicable framework that can be employed across wide range of manufacturing industries for quality improvement and cost optimization.

Keywords: Gasket manufacturing, DMAIC methodology, Six sigma, Process optimization, waste reduction, sustainable production, ANOVA, Statistical process control.

Resumen. - *El proceso de fabricación de juntas en la "Empresa A" se enfrentaba a importantes desafíos e ineficiencias debido a las altas tasas de rechazo y a la variación en el rendimiento de las máquinas de extrusión, inserción magnética y soldadura. Las tres máquinas generaban rechazos importantes a diario, incluyendo un alto volumen de rechazos por purga de la máquina de extrusión blanda de PVC, un recorte excesivo de imanes de gran tamaño durante el proceso de inserción magnética y un rechazo significativo debido a la baja resistencia de las uniones en el proceso de soldadura de los perfiles de PVC. Para abordar estos problemas subyacentes, se empleó la metodología Six Sigma DMAIC (Definir, Medir, Analizar, Mejorar, Controlar) con el fin de reducir el rechazo/desperdicio, aumentar la*

(*) Corresponding author.

[1] Master of Engineering, Department of Industrial Engineering, NEDUET (Pakistan), 2023phdmnf1@student.uet.edu.pk, ORCID iD: https://orcid.org/0009-0007-8992-7601

[2] Mechanical Engineer, Department of Mechanical Engineering, NUST (Pakistan), adeeltabassum1@gmail.com, ORCID iD: https://orcid.org/0009-0006-9375-1090

Memoria Investigaciones en Ingeniería, núm. 28 (2025). pp. 193-221
https://doi.org/10.36561/ING.28.14
ISSN 2301-1092 • ISSN (en línea) 2301-1106 – Universidad de Montevideo, Uruguay

eficiencia del proceso y disminuir los defectos en las tres máquinas. El estudio incluyó el mapeo de procesos, el análisis de causa y efecto, el despliegue de la función de calidad (QFD) y herramientas estadísticas de proceso como ANOVA, regresión y análisis Cp/Cpk. Se identificaron las causas raíz y se introdujeron mejoras específicas basadas en los datos, incluyendo la planificación optimizada de la producción, la optimización y estandarización de los parámetros de la máquina, la mejora de la planificación de la ejecución de la producción y la disponibilidad de almacenamiento, los controles de temperatura en las máquinas de soldar y el moleteado de la rueda del codificador para la máquina de inserción magnética. Los principales objetivos fueron abordar problemas como el desperdicio de material, la variación en el tamaño de la banda magnética, los problemas en las máquinas de soldar y las frecuentes paradas de la máquina causadas por una programación de producción incorrecta debido a la disponibilidad inadecuada de espacio de almacenamiento para la producción por lotes independientemente del plan de premontaje de la puerta. Después de la implementación, los resultados muestran una disminución considerable en el porcentaje de rechazo de la máquina de extrusión del 12% al 4,06%, una reducción en el desperdicio de purga de 17 kg/día a 6,9 kg/día y un aumento en la eficiencia de la máquina del 50,1% al 83,3%. Además, el porcentaje de rechazo de la máquina de soldar disminuyó del 7% al 3,7% como resultado de una mejor gestión de la temperatura y el mantenimiento del equipo. El problema de variación de tamaño en la máquina de inserción de imanes se resolvió mediante el moleteado de la rueda del codificador. En general, estos cambios resultaron en un ahorro anual de aproximadamente 1,5 millones de rupias pakistaníes (PKR) en el proceso de extrusión y 1,2 millones en la máquina de inserción de imanes. La importancia de este proyecto radica en su potencial para optimizar el proceso de producción de juntas, reduciendo el desperdicio y los fallos, a la vez que aumenta la eficiencia de la máquina. Los resultados ofrecen un marco replicable que puede emplearse en una amplia gama de industrias manufactureras para mejorar la calidad y optimizar los costes.

Palabras clave: *Fabricación de juntas, metodología DMAIC, Six sigma, Optimización de procesos, reducción de desperdicios, producción sustentable, ANOVA, Control estadístico de procesos.*

Resumo. - *O processo de fabricação de juntas na "Empresa A" enfrentou desafios e ineficiências significativos devido às altas taxas de rejeição e à variação no desempenho da máquina de extrusão, da máquina de inserção magnética e da máquina de solda. Todas as três máquinas geravam consistentemente grandes rejeições diariamente, incluindo um alto volume de rejeições por purga da máquina de extrusão de PVC macio, corte excessivo de ímãs superdimensionados durante o processo de inserção magnética e rejeição significativa devido à baixa resistência da junta no processo de soldagem de perfis de PVC. Para abordar essas questões subjacentes, a metodologia Six Sigma DMAIC (Definir, Medir, Analisar, Melhorar, Controlar) foi empregada para diminuir a rejeição/desperdício, aumentar a eficiência do processo e diminuir os defeitos das três máquinas. O estudo envolveu mapeamento de processos, análise de causa e efeito, implantação da função de qualidade (QFD) e ferramentas estatísticas de processo, como ANOVA, regressão e análise Cp/Cpk. As causas-raiz foram identificadas e melhorias direcionadas com base nos dados foram introduzidas, incluindo planejamento de produção otimizado, otimização e padronização dos parâmetros da máquina, melhoria do planejamento da execução da produção e disponibilidade de armazenamento, controles de temperatura em máquinas de solda e recartilhamento da roda do encoder para máquina de inserção magnética. Os principais objetivos eram lidar com problemas incluindo desperdício de material, variação no tamanho da tira magnética, problemas em máquinas de solda e paradas frequentes de máquinas causadas por programação de produção inadequada devido à disponibilidade inadequada de espaço de armazenamento para produção em lote independente do plano de pré-montagem da porta. Após a implementação, os resultados mostram uma redução considerável na porcentagem de rejeição da máquina de extrusão de 12% para 4,06%, uma redução no desperdício de purga de 17 kg/dia para 6,9 kg/dia e um aumento na eficiência da máquina de 50,1% para 83,3%. Além disso, a porcentagem de rejeição da máquina de solda caiu de 7% para 3,7% como resultado do gerenciamento aprimorado de temperatura e manutenção do equipamento. O problema de variação de tamanho na máquina de inserção magnética foi resolvido pelo recartilhamento da roda do codificador. No geral, essas mudanças resultaram em uma economia de custos anual de aproximadamente 1,5 milhão de PKR para o processo de extrusão e 1,2 milhão da máquina de inserção magnética. A importância deste projeto se origina de seu potencial para agilizar o processo de produção de juntas, reduzindo desperdícios e falhas, enquanto aumenta a eficiência da máquina. Os resultados oferecem uma estrutura replicável que pode ser empregada em uma ampla gama de indústrias de manufatura para melhoria de qualidade e otimização de custos.*

Palavras-chave: *Fabricação de juntas, metodologia DMAIC, Seis sigma, otimização de processos, redução de desperdícios, produção sustentável, ANOVA, controle estatístico de processos.*

1. Introduction. - The manufacturing sector constantly strives to minimize rejection and rework during production while simultaneously enhancing production efficiency and product quality (A Paramasivam, 2022). Six sigma methodology (Tjahjono, 2010) (Hill, 2017) (S. Reosekar) (Patel, 2021) in its essence was first introduced in 1986 by Bill smith and Mikel harry, the two engineers from Motorola in 1986. The term "Six Sigma" originates from a statistical concept that describes a process with no more than 3.4 defects per million opportunities (Noori, 2018). Six sigma methodology (Macias-Aguayo, Garcia-Castro, Barcia, McFarlane, & Abad-Moran, 2022) as evident from its name is a six step-based data driven approach which aim to reduce the defects and variability in manufacturing process by using statistical tools and techniques (Yang C-C, 2022). It is a systematic approach and since its implementation by companies across various manufacturing fields, has shown that it is enhances the production process efficiency by reduction in defects and optimization of manufacturing process and as a result of this it increases customer (internal and external) satisfaction (McDermott, et al., 2022). Companies have been able to save huge amount of money by reduction in defects in products and increase in efficiency of production process (Alarcón, Calero, Pérez-Huertas, & Martín-Lara, 2023) (Ndrecaj, Mohamed Hashim, Mason-Jones, Ndou, & Tlemsani, 2023). The most common six sigma methodology that is being used in manufacturing sector is DMAIC and it stands for define, measure, analyze, improve and control (Monika Smętkowska B. M., 2018). It is a closed loop process in which impact of improvement measures is evaluated and improved until the desired results are obtained. After achieving the desired results final phase is control which is of utmost importance as continuous improvement is only possible if is sustainable over longer durations. This DMAIC approach is applicable in broad range of industries including manufacturing, software, sales, quality, service and marketing (LM, 2022).

Gaskets that are produced through extrusion process are very critical part of refrigerator product as they provide sealing of freezer and refrigerator compartments from the atmosphere thus keeping the cooling inside the refrigerator. The profile is made up of polyvinyl chloride (PVC) (Lewandowski & Skórczewska, 2022) material and it contains a magnet that is inserted into the profile before the joining process at the welding station. The magnet ensures the door remains securely locked and airtight due to its strong attraction to the paint-coated material (PCM) side panel. If any issues arise with the magnet, such as being too short, broken, or wavy, or if the profile welding joint opens due to transportation or poor welding, hot air can enter the freezer or refrigerator compartment. This results in poor insulation from the surrounding atmosphere. Quality of the gasket has direct impact on energy efficiency, compressor life, refrigerator's performance and preservation of food.

1.1 Problem statement. - Refrigerator gasket manufacturing process in the company A (for confidentiality reason) has been facing lots of challenges regarding rejection and rework issues during extrusion process for gasket profile manufacturing from PVC material, size variation issue during magnet cutting and magnet insertion station and poor PVC weld joints issue. These issues not only increase process waste at the gasket manufacturing station, leading to significant costs for Company A, but also negatively impact the efficiency of the gasket manufacturing process.

1.2 Objectives. - Objectives of implementation of six sigma methodology on gasket extrusion process are as under:

1- Improve efficiency and productivity of the extrusion process of gasket profile manufacturing process
2- Reduction in rejection and rework of gaskets
3- Enhance the quality and consistency of the gasket profiles
4- Cost savings by waste minimization
5- Reduction in magnet wastage because of size variation issue
6- Reduction in rejection and rework at welding machine station

2. Literature review. - In recent years, global economic landscape is going through one of the toughest times because of rising material costs, fluctuation in demand, more competition from emerging markets (Most. Asikha Aktar, 2021). These issues lead to increase in manufacturing cost and reduction in profit margins as product prices can only be increased up to a certain because purchasing power of general public is also going down (Bailey, 2016). So, in order to make the business sustainable, increase profit margins and bring the cost of manufacturing down, more and more companies from different fields are employing six sigma methodologies in their manufacturing setup (Muraliraj). Six sigma offers a systematic, data driven framework that helps companies identify inefficiencies, rejection and rework reasons, things impacting the quality of the product thereby enabling the company to take corrective measures to resolve these issues leading to increase in cost savings and profit margins even in uncertain economic environment. The application of Six Sigma has produced notable non-financial and financial benefits/results for numerous Fortune 500 firms (Wasage, 2016). Allied Signal, General Electric, Raytheon, Bank of America, Bechtel, Caterpillar and Motorola are a few of these businesses. By applying the six-sigma methodology, these businesses have drastically decreased their defect rates and multiplied their profits by many folds (T. Costa F. S., 2017). Numerous studies have demonstrated the importance of Six Sigma and Lean techniques in driving quality improvements and minimizing

process variability. Smętkowska and Mrugalska (2018) successfully applied Six Sigma DMAIC to reduce rejection rates in manufacturing operations (Monika Smętkowska B. M., 2018). Similarly, Macias-Aguayo et al. (2022) stressed the use of Six Sigma and Industry 4.0 principles to improve operational efficiency (Jaime Macias-Aguayo, 2022). T. Costa et al. (2017) used Six Sigma to optimize extrusion processes in tire manufacture, resulting in considerable defect reduction, demonstrating the applicability of this methodology to extrusion-based industries such as gasket production (T. Costa F. S., 2017). Furthermore, Hassan Araman et al. (2023) shed light on six sigma and gasket materials' performance, emphasizing the need of exact dimensional control and structural integrity in preserving refrigerator insulation and energy efficiency (Araman, 2023).

This literature clearly establishes the applicability of Six Sigma in gasket extrusion processes, specifically for identifying root causes of quality issues, improving dimensional accuracy and ensuring overall product integrity and process stability. Six sigma methodologies can be applied across any manufacturing industry. Building upon these insights, the current study applies Six Sigma principles to a real-time manufacturing process of soft plastic gaskets, aiming for practical process enhancements and measurable outcomes.

There are several other key philosophies in the manufacturing industry, such as Lean Manufacturing and Six Sigma. Six Sigma is a data-driven methodology that utilizes statistical tools to minimize defects and reduce process variability. Whereas Lean Manufacturing primarily focuses on eliminating waste and improving process flow. Lean practices typically target Ohno's seven types of waste to enhance production efficiency. Six sigma uses DMAIC methodology in which multiple statistical tools are used during different phases in order to achieve the desired result. All those tools will be discussed in the methodology section in detail. Six Sigma is a statistical term that represents a process in which minimal defects occur. "Sigma" (σ) stands for a process's standard deviation in Six Sigma terminology. A process that achieves a Six Sigma level is said to produce less than 3.4 defects per million opportunities (DPMO), which is an indication of almost perfect quality. This yield %age is equal to 99.9997% error-free output (Raman Sharma, 2018).

Sigma Level	DPMO	Yield
6	3.4	99.9997%
5.5	32	99.9987%
5	233	99.9770%
4.5	1350	99.8700%
4	6210	99.3800%
3.5	22750	97.7000%
3	66807	93.3000%
2.5	158655	84.1000%
2	308538	69.1000%
1.5	500005	50.0000%
1	691462	30.9000%
0.5	841345	15.9000%

Table 1 Sigma level and comparative values of DPMO and Yield %age

Values in Table 1 represents that as sigma level increases defects per million opportunities decreases and yield %age (defect free units) increases. This means that if 1 million parts are produced, the DPMO (defects per million opportunities) represents the number of defective parts out of those 1 million. The yield percentage indicates the %age of the parts produced without any defects.

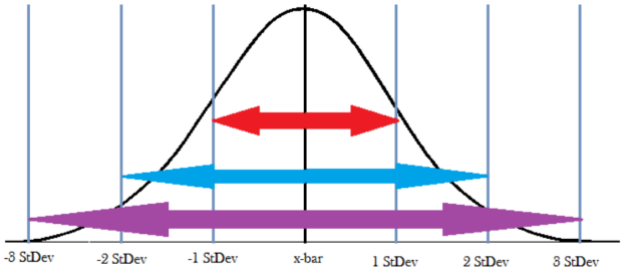

Figure I. Normal distribution curve or Bell curve

The X-bar line in Figure represents that normal data is distributed symmetrically around mean. A normal curve is useful for determining the probability that a given data point in a population will fall within a certain range of the distribution (Amaral, 2022).

The X-bar line in Figure represents the mean and normal data is formed symmetrically around it. A normal curve is useful for determining the chance that a given data point in a population will fall within a certain range of the distribution. Red arrow covers ±1σ from mean and (σ = standard deviation) represents that 68.26% of all data points falls within this range. Blue arrow covers ±2σ from mean and it represents that 95.46% of all data points falls within this range. The purple arrow covers ±3σ from mean and it represents that 99.7% of data points fall in this range. In a perfect bell curve mean median and mode of the data set are same and located at the peak of the curve. The ends of normal distribution curve are known as tails, and these represents extreme values in a data set. In six sigma defects normally fall in these tails. Six sigma practitioners can determine the process capability (Cp & Cpk) which shows how well the process is performing relative to specification limits.

Gasket is an integral part of refrigerator product (Guoqiang Liu, A review of refrigerator gasket: Development trend, heat and mass transfer characteristics, structure and material optimization, 2021) which help keep the refrigerator freezer and refrigerator compartment insulated from environment. Gasket profile is manufactured from the polyvinyl chloride (PVC) material through the extrusion process. Extrusion process is a manufacturing technique in which a material is heated according to the required specifications in a barrel which is then forced through a die to achieve the required profile (Guoqiang Liu, Research on test method of heat transfer coefficient for refrigerator gasket, 2020). After exiting of PVC profile from die it is shifted to cooling station through conveyors where it is cooled down through water jets. These profiles are then shifted to cutting station where they are cut to desired length as per requirement. These profiles are then later on moved to stock area and then as per requirement to magnet insertion machine area where magnets are inserted into the profile as per the required length. After this step all these profiles are moved from magnet insertion machine to welding area where these profiles are inserted into the die, joined by heating them up to required temperature and then die is closed resulting in a joint formation. All these processes are very critical with many potential modes of failures which will be discussed in later part of the paper (Tianyang Zhao, 2024).

2.1 Research gap. - The revenue generated by refrigerator manufacturing industry worldwide is estimated to 121 billion USD. Being a billion-dollar industry, no research has been conducted on combined optimization of extrusion, magnet insertion and welding process. In this project six sigma methodology will be systematically applied in order to identify the key problems in the whole gasket manufacturing process. These defects/problems will then be later addressed by using six sigma DMAIC methodology.

2.2 Significance of the study. - Implementing Six Sigma in optimizing the gasket manufacturing process is highly significant, especially in the context of current economic challenges where high manufacturing costs and price increases are unsustainable. This optimization will enhance process efficiency, reduce rejections & rework thus lowering the overall manufacturing cost of the gaskets. Additionally, it will lead to a reduction in defects, both internally and at the customer end. Furthermore, this project will set a benchmark for the refrigerator manufacturing industry, demonstrating the value of applying Six Sigma methodology not only in gasket production but potentially across all manufacturing processes.

3. Methodology. - In order to carry out this research work, six sigma DMAIC methodology was adopted. DMAIC is a systematic problem-based and customer centric data/target-oriented approach consisting of five basic steps. Those steps/phases are defined phase, measure phase, analyze phase, improve phase and control phase. Define was started by making a project charter in which objective of the project, goals, deliverables and problem statement were defined. Whole gasket extrusion manufacturing process was mapped by using SIPOC diagram (Supplier, Inputs, Process, Outputs, Customer). VOC (voice of customer) vs VOB (voice of business) analysis was done in order to list down the common requirements of customer (internal) and business. FMEA (Failure mode effect analysis) was conducted to identify initial potential failures, evaluate and prioritize risks and suggesting potential solutions/action plan for prevention of those failures in gasket extrusion manufacturing process. Re FMEA will be done at a later stage again in order to evaluate the performance of the project. In second measure phase, data of extrusion machine production, magnetic strip rejection/scrap and welding machines rejection and rework was gathered in order to measure the current process performance and set the baseline for improvements in coming phase. In the third phase i.e., the analysis phase, analysis of top problems was conducted and for this purpose detailed cause and effect diagram were made, and top five problems were prioritized by performing pareto analysis. Quality function deployment (QFD) tool was used to prioritize customer requirements and to their relationship with functional requirement for better finished product.

3.1 Define Phase. - Define phase is one of the first steps in DMAIC methodology. This phase focused on gathering insights from various stakeholders specifically customer, process owner (production team). This helped in identifying critical issues in the gasket manufacturing area. First step in define phase to make a project charter in which objectives, goals, project deliverables, in-scope, out-scope and problem statement were defined.

3.2 Problem Statement. - In the Year 2023, 27,283 gaskets rejected out of 2,84,477 gaskets produced at Gasket Manufacturing Area. Out of these 27,283 rejected gaskets, 7267 gaskets were crushed, and 20,016 gaskets were scrapped. The rejection ratio stands at 9.57% and by 15 kg of average value of purging waste for 287 days, this costed company 3.5 million rupees. As 1.95" magnetic strips get rejected per each profile leading to further cost of 0.96 million rupees. If these issues persist, this could result in a potential loss of 4.5 million rupees to the company in 2024. Now in order to assist planning and keep the track of project during its various phases, a Gantt chart was setup with deadlines of the project phase wise. Gantt chart is available in Figure .

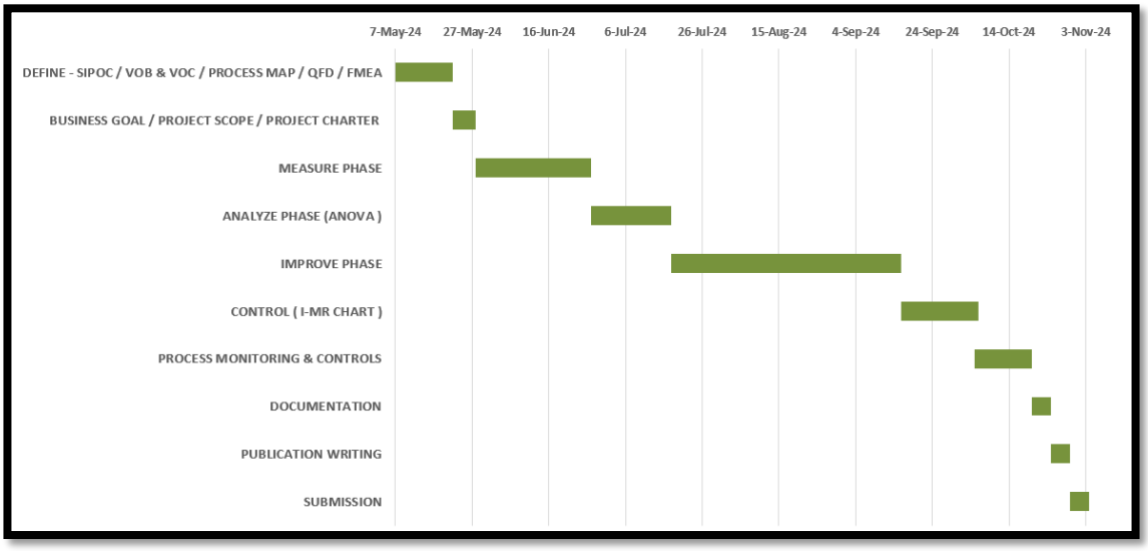

Figure II. Gantt chart with project milestones and deadlines.

Understanding the voice of customer and voice of business was absolutely necessary in order to identify the most important things related to gasket manufacturing process from customer and management point of view. VOB vs VOC was prepared, and intersection points were considered as goals of the projects. VOB vs VOC is shown in Figure .

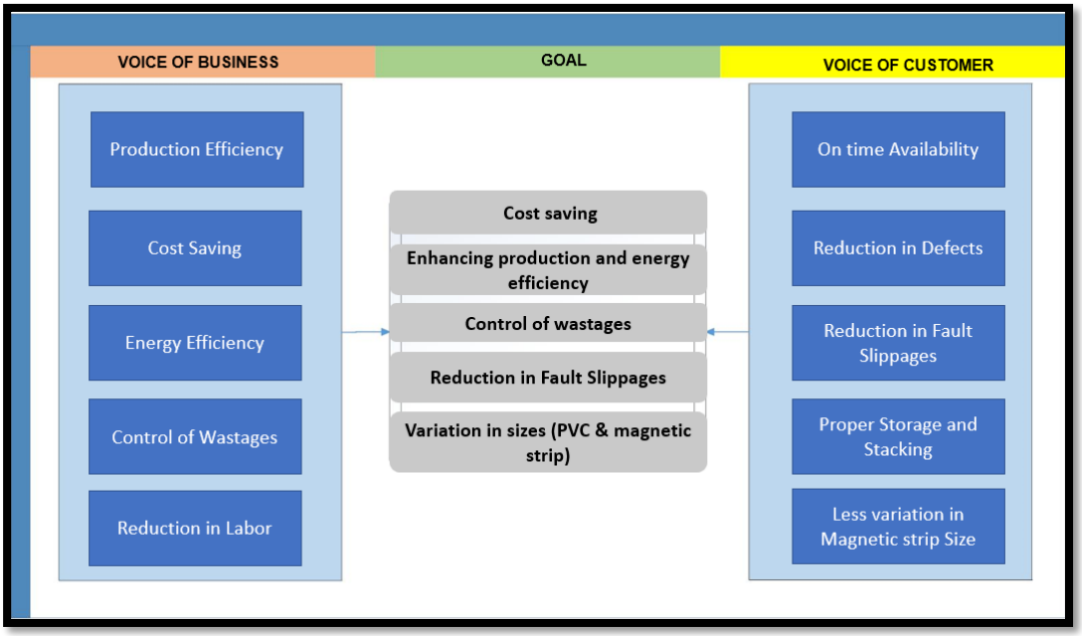

Figure III. Voice of business (VOB) vs Voice of Customer (VOC).

In this comparison of VOB (Voice of the Business) and VOC (Voice of the Customer), common goals were identified that were important to both the immediate customer, the door assembly line and management. Key objectives included cost savings, improving production efficiency, optimizing machine energy consumption, controlling waste, minimizing defects passed to the customer and reducing variations in the sizes of PVC profiles and magnetic strips.
After that a SIPOC (supplier-input-process-output-customer) was plotted in order to identify all the suppliers (internal and external), inputs, process mapping, outputs and customer (internal). SIPOC is used to understand the process components and relevance as it is a simple tool. This was developed through brainstorming session with the project team and process owner (production team). SIPOC diagram is available in Figure .

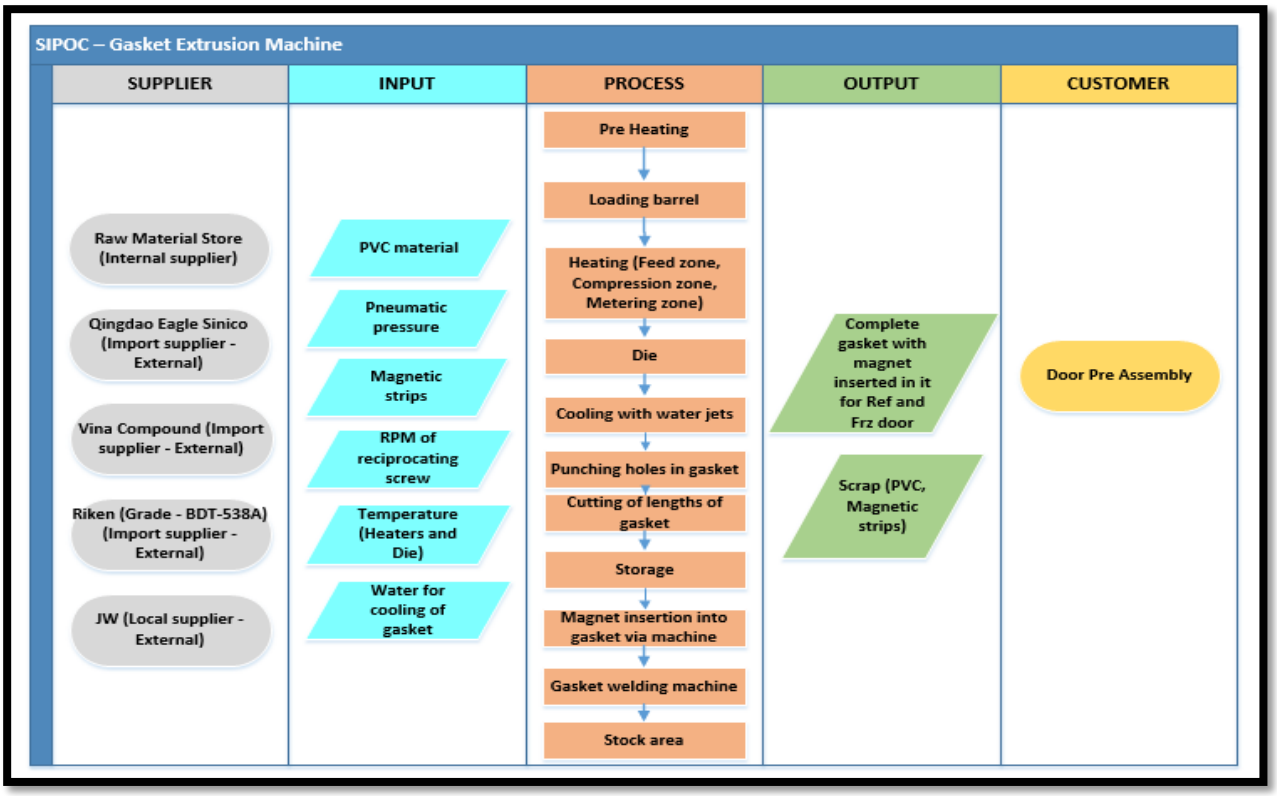

Figure IV. SIPOC of gasket manufacturing process.

In the SIPOC, the process was clearly outlined, with both internal and external suppliers and all process inputs identified. The outcomes, including the finished product and scrap, were also defined, along with the customer, Door Pre-Assembly. This tool enables a comprehensive understanding of all aspects related to the process and helps in identifying critical elements. It provides a foundation for process improvement and acts as a starting point for more detailed analysis in the later stages of the DMAIC methodology.

Visually representing each stage of the gasket manufacturing process, from the input of raw materials to the output of the finished product, is known as process mapping. This involves mapping the extrusion of PVC profiles to inserting magnetic strips in PVC profiles and then welding of these gasket profiles. This process map makes it easy to see how steps in manufacturing link to one another. Now in order to get the clear representation of the workflow and for identification of bottlenecks and inefficiencies, process map was developed and can be seen in Figure .

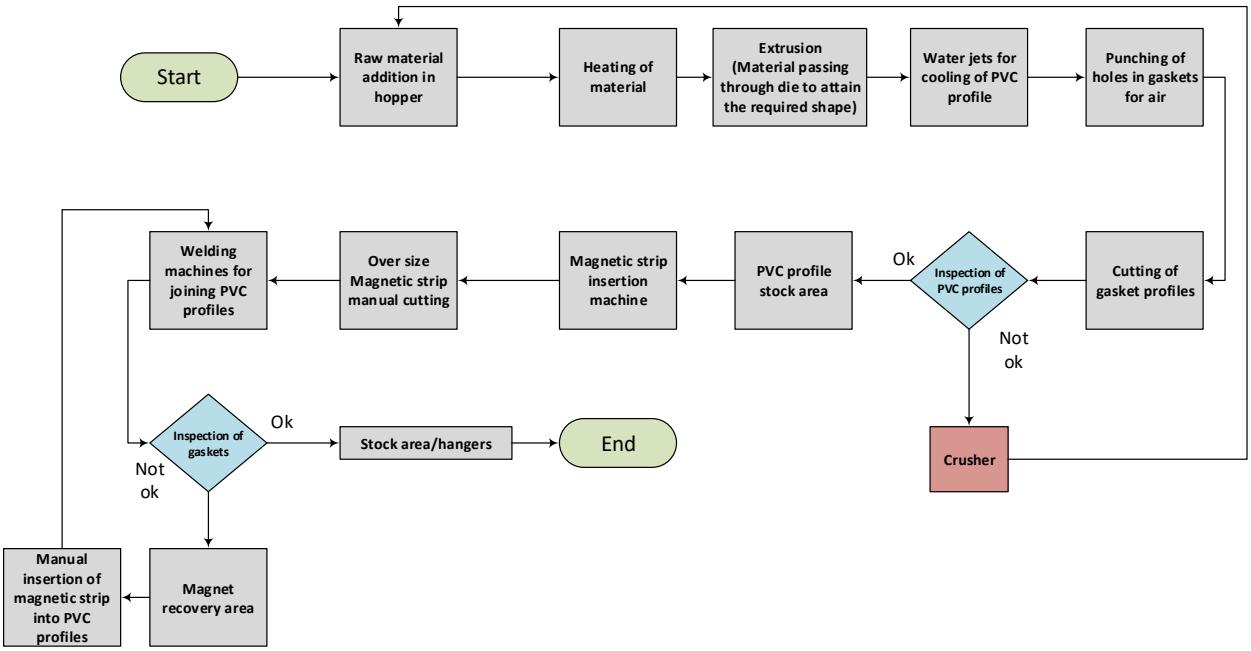

Figure V. Process map of gasket manufacturing process.

3.3 Measure Phase. - Measuring the process's current performance is the main goal of the DMAIC Measure phase. Data is gathered during this phase to measure important metrics about rejection, cycle time, production rates and other important parameters, as well as to provide a baseline for the process. Data was collected from quality inspection reports, production monitoring reports, operator check sheets and from machine logs. In order to ensure the integrity of the analysis and remove any biases in the data, several statistical tools were employed. These tools will be discussed in detail in later section of ANOVA. Prior to making any modifications, it is important to know how the process is working in order to enable more accurate analysis in later phases. In the measure phase, data of gasket manufacturing process was gathered in order to set the baseline of the gasket manufacturing process and identify all the issues and inefficiencies by analyzing the data gathered through check sheets. Gasket manufacturing process was divided into three processes; extrusion of soft PVC (polyvinyl chloride) material in order to make gasket profiles, magnet insertion station and welding station of PVC profiles. For all these three processes, data on machine actual production, rejection reasons, loss time in hours, machine efficiency and parameters monitoring were collected. Extrusion machine efficiency monitoring report is available in Table

Sr. No	Date	Standard Working time	Total Standard Production (kg)	Total Actual Production (kg)	Efficiency
1	10th July, 2024	11	495	51	10%
2	12th July, 2024	16	720	341	47%
3	13th July, 2024	19	855	348	41%
4	15th July, 2024	16	720	416	58%
5	16th July, 2024	22	990	487	49%
6	19th July, 2024	19	855	402	47%
7	20th July, 2024	19	855	477	56%
8	21st July, 2024	19	855	516	60%
9	22nd July, 2024	19	855	436	51%
10	23rd July, 2024	19	855	298	35%
11	24th July, 2024	19	855	454	53%
12	26th July, 2024	19	855	434	51%
13	27th July, 2024	22	990	471	48%

14	28th July, 2024	16	720	350	49%
15	29th July, 2024	19	855	340	40%
16	30th July, 2024	19	855	390	46%
17	31st July, 2024	16	720	415	58%
18	1st Aug, 2024	22	990	550	56%
19	2nd Aug, 2024	16	720	570	79%
20	3rd Aug, 2024	16	720	520	72%
21	4th Aug, 2024	16	720	400	56%
22	5th Aug, 2024	19	855	391	46%
23	6th Aug, 2024	19	855	371	43%
24	7th Aug, 2024	19	855	250	29%
25	8th Aug, 2024	19	855	378	44%
26	9th Aug, 2024	16	720	421	58%
27	10th Aug, 2024	16	720	413	57%
28	11th Aug, 2024	16	720	401	56%
29	12th Aug, 2024	16	720	397	55%
30	13th Aug, 2024	16	720	386	54%

Table II. Extrusion machine efficiency monitoring report.

Extrusion machine rejection data is mentioned in the Table .

Sr. No	Date	Standard Working time (hours)	Total Standard Production (kg)	Total Actual Production (kg)	Rejection %age	Total Rejection (kg)
1	10th July, 2024	11	495	51	88%	45
2	12th July, 2024	16	720	341	12%	40
3	13th July, 2024	19	855	348	13%	44
4	15th July, 2024	16	720	416	12%	48
5	16th July, 2024	22	990	487	12%	57
6	19th July, 2024	19	855	402	9%	37
7	20th July, 2024	19	855	477	6%	30
8	21st July, 2024	19	855	516	11%	58
9	22nd July, 2024	19	855	436	12%	52
10	23rd July, 2024	19	855	298	18%	54
11	24th July, 2024	19	855	454	12%	54
12	26th July, 2024	19	855	434	6%	27
13	27th July, 2024	22	990	471	9%	42
14	28th July, 2024	16	720	350	13%	45
15	29th July, 2024	19	855	340	12%	41
16	30th July, 2024	19	855	390	11%	43
17	31st July, 2024	16	720	415	12%	49
18	1st Aug, 2024	22	990	550	7%	38
19	2nd Aug, 2024	16	720	570	12%	70
20	3rd Aug, 2024	16	720	520	15%	78
21	4th Aug, 2024	16	720	400	14%	54
22	5th Aug, 2024	19	855	391	9%	35

23	6th Aug, 2024	19	855	371	12%	46
24	7th Aug, 2024	19	855	250	16%	41
25	8th Aug, 2024	19	855	378	11%	42
26	9th Aug, 2024	16	720	421	11%	45
27	10th Aug, 2024	16	720	413	8%	35
28	11th Aug, 2024	16	720	401	10%	39
29	12th Aug, 2024	16	720	397	13%	53
30	13th Aug, 2024	16	720	386	15%	56
		Grand Total		12076	11.6%	1398

Table III. Extrusion machine rejection data

Welding machines efficiency monitoring report is mentioned in the Table .

Sr. No	Date	Standard Working hours (hrs.)	Total No. of Machines	Total UPH	Actual Production	Standard Production	Efficiency
1	10th July, 2024	11	5	200	1255	2200	57%
2	12th July, 2024	11	5	200	970	2200	44%
3	13th July, 2024	22	10	400	1610	4400	37%
4	15th July, 2024	22	8	320	1848	3520	53%
5	16th July, 2024	8	4	160	1004	1280	78%
6	19th July, 2024	22	8	320	2053	3520	58%
7	20th July, 2024	19	9	360	2485	3360	74%
8	21st July, 2024	22	8	320	2270	3520	64%
9	22nd July, 2024	11	3	120	1046	1320	79%
10	23rd July, 2024	22	7	280	2085	3080	68%
11	24th July, 2024	22	7	280	1764	3080	57%
12	26th July, 2024	22	7	280	2078	3080	67%
13	27th July, 2024	22	7	280	1626	3080	53%
14	28th July, 2024	19	7	280	1416	2720	52%
15	29th July, 2024	22	7	280	1676	3080	54%
16	30th July, 2024	11	4	160	1004	1760	57%
17	31st July, 2024	22	7	280	2376	3080	77%
18	1st Aug, 2024	22	6	240	1790	2640	68%
19	2nd Aug, 2024	11	4	160	1108	1760	63%
20	3rd Aug, 2024	11	4	160	986	1760	56%
21	4th Aug, 2024	11	4	160	1120	1760	64%
22	5th Aug, 2024	11	5	200	385	2200	18%
23	6th Aug, 2024	11	4	160	419	1760	24%
24	7th Aug, 2024	11	4	160	944	1760	54%
25	8th Aug, 2024	11	5	200	1222	2200	56%
26	9th Aug, 2024	11	4	160	328	1760	19%
27	10th Aug, 2024	11	4	160	525	1760	30%
28	11th Aug, 2024	11	4	160	929	1760	53%
29	12th Aug, 2024	11	4	160	885	1760	50%
30	13th Aug, 2024	11	4	160	508	1760	29%

Table

Sr. No	Date	Standard Working hours (hrs.)	Total No. of Machines	Total UPH	Actual Production	Standard Production	Efficiency
1	10th July, 2024	11	5	200	1255	2200	57%
2	12th July, 2024	11	5	200	970	2200	44%
3	13th July, 2024	22	10	400	1610	4400	37%
4	15th July, 2024	22	8	320	1848	3520	53%
5	16th July, 2024	8	4	160	1004	1280	78%
6	19th July, 2024	22	8	320	2053	3520	58%
7	20th July, 2024	19	9	360	2485	3360	74%
8	21st July, 2024	22	8	320	2270	3520	64%
9	22nd July, 2024	11	3	120	1046	1320	79%
10	23rd July, 2024	22	7	280	2085	3080	68%
11	24th July, 2024	22	7	280	1764	3080	57%
12	26th July, 2024	22	7	280	2078	3080	67%
13	27th July, 2024	22	7	280	1626	3080	53%
14	28th July, 2024	19	7	280	1416	2720	52%
15	29th July, 2024	22	7	280	1676	3080	54%
16	30th July, 2024	11	4	160	1004	1760	57%
17	31st July, 2024	22	7	280	2376	3080	77%
18	1st Aug, 2024	22	6	240	1790	2640	68%
19	2nd Aug, 2024	11	4	160	1108	1760	63%
20	3rd Aug, 2024	11	4	160	986	1760	56%
21	4th Aug, 2024	11	4	160	1120	1760	64%
22	5th Aug, 2024	11	5	200	385	2200	18%
23	6th Aug, 2024	11	4	160	419	1760	24%
24	7th Aug, 2024	11	4	160	944	1760	54%
25	8th Aug, 2024	11	5	200	1222	2200	56%
26	9th Aug, 2024	11	4	160	328	1760	19%
27	10th Aug, 2024	11	4	160	525	1760	30%
28	11th Aug, 2024	11	4	160	929	1760	53%
29	12th Aug, 2024	11	4	160	885	1760	50%
30	13th Aug, 2024	11	4	160	508	1760	29%

Table IV. Welding machine efficiency monitoring report.

Welding machines rejection data is attached in Table .

Sr. No	Date	Standard Working hours (hours)	Actual Production (Nos)	Standard Production (Nos)	Rejection Quantity	Rejection %age
1	10th July, 2024	11	1255	2200	90	7%
2	12th July, 2024	11	970	2200	80	8%

3	13th July, 2024	22	1610	4400	70	4%
4	15th July, 2024	22	1848	3520	85	5%
5	16th July, 2024	8	1004	1280	101	10%
6	19th July, 2024	22	2053	3520	109	5%
7	20th July, 2024	19	2485	3360	105	4%
8	21st July, 2024	22	2270	3520	95	4%
9	22nd July, 2024	11	1046	1320	87	8%
10	23rd July, 2024	22	2085	3080	115	6%
11	24th July, 2024	22	1764	3080	111	6%
12	26th July, 2024	22	2078	3080	102	5%
13	27th July, 2024	22	1626	3080	104	6%
14	28th July, 2024	19	1416	2720	110	8%
15	29th July, 2024	22	1676	3080	95	6%
16	30th July, 2024	11	1004	1760	90	9%
17	31st July, 2024	22	2376	3080	89	4%
18	1st Aug, 2024	22	1790	2640	112	6%
19	2nd Aug, 2024	11	1108	1760	120	11%
20	3rd Aug, 2024	11	986	1760	131	13%
21	4th Aug, 2024	11	1120	1760	87	8%
22	5th Aug, 2024	11	385	2200	55	14%
23	6th Aug, 2024	11	419	1760	41	10%
24	7th Aug, 2024	11	944	1760	31	3%
25	8th Aug, 2024	11	1222	2200	59	5%
26	9th Aug, 2024	11	328	1760	67	20%
27	10th Aug, 2024	11	525	1760	61	12%
28	11th Aug, 2024	11	929	1760	80	9%
29	12th Aug, 2024	11	885	1760	71	8%
30	13th Aug, 2024	11	508	1760	51	10%

Table V. Welding m/c's rejection data.

Magnet that is inserted into PVC profile before welding is one of the most critical stations as far as oversized magnet strip rejection per profile is concerned. Its data is gathered and is present in the Table .

Sr. No	Date	Standard Working hours (hours)	Actual Production (Nos)	Rejection per profile (m)	Rejection per gasket (m)	Total rejection of magnet per day (m)	Total rejection magnet per day (kg)
1	10th July, 2024	11	1255	0.044	0.176	221	13
2	12th July, 2024	11	970	0.044	0.176	171	10
3	13th July, 2024	22	1610	0.044	0.176	283	17
4	15th July, 2024	22	1848	0.044	0.176	325	20
5	16th July, 2024	8	1004	0.044	0.176	177	11
6	19th July, 2024	22	2053	0.044	0.176	361	22
7	20th July, 2024	19	2485	0.044	0.176	437	26
8	21st July, 2024	22	2270	0.044	0.176	400	24
9	22nd July, 2024	11	1046	0.044	0.176	184	11
10	23rd July, 2024	22	2085	0.044	0.176	367	22

11	24th July, 2024	22	1764	0.044	0.176	310	19
12	26th July, 2024	22	2078	0.044	0.176	366	22
13	27th July, 2024	22	1626	0.044	0.176	286	17
14	28th July, 2024	19	1416	0.044	0.176	249	15
15	29th July, 2024	22	1676	0.044	0.176	295	18
16	30th July, 2024	11	1004	0.044	0.176	177	11
17	31st July, 2024	22	2376	0.044	0.176	418	25
18	1st Aug, 2024	22	1790	0.044	0.176	315	19
19	2nd Aug, 2024	11	1108	0.044	0.176	195	12
20	3rd Aug, 2024	11	986	0.044	0.176	174	10
21	4th Aug, 2024	11	1120	0.044	0.176	197	12
22	5th Aug, 2024	11	385	0.044	0.176	68	4
23	6th Aug, 2024	11	419	0.044	0.176	74	4
24	7th Aug, 2024	11	944	0.044	0.176	166	10
25	8th Aug, 2024	11	1222	0.044	0.176	215	13
26	9th Aug, 2024	11	328	0.044	0.176	58	3
27	10th Aug, 2024	11	525	0.044	0.176	92	6
28	11th Aug, 2024	11	929	0.044	0.176	164	10
29	12th Aug, 2024	11	885	0.044	0.176	156	9
30	13th Aug, 2024	11	508	0.044	0.176	89	5

*Every gasket has 4 profiles
*1-meter magnet = 60 gm

Table VI. Magnet insertion machine data

3.4 Analyze Phase. - FMEA (Failure Modes and Effects Analysis) is a tool used in the Six Sigma methodology to identify probable failure modes in the production process and evaluate their impact on product quality. FMEA helps in the identification of potential flaws such as size variances, joining problems or material issues by examining crucial steps including PVC extrusion, magnetic strip insertion and welding of gasket profiles. For this gasket manufacturing process, a detailed FMEA was developed in which teams prioritized process improvements by using the risk priority number (RPN) that was assigned on factors including severity, occurrence and detection. This is in line with Six Sigma's objective of reducing variances and improving quality by ensuring defect reduction, process optimization and overall product reliability. FMEA is available in Figure

Sr. No	Process steps	Potential failure mode	Potential effects	Severity	Failure causes	Occurrence	Current controls	Detection	Risk Profile Number RPN	Recommended actions
1	Pre-Heating in Oven	Improper heating	Moisture Issue Warpage Crack formation Bubble formation	5	Thermocouple issue Heater issue Un even temperature distribution	3	Temperature monitoring	4	60	1- Thermoregulator should be present for temperature control 2- Uniform heating should be present
2	Material (PVC) loading in hopper	Improper heater temp set at Feed zone	Accumulation of PVC material in the hopper base	8	Premature heating in Feed zone temperatures	2	Training of machine operators	3	48	Training of machine operators
3	Extrusion - Feed zone	Material clogging Poor material melting	In consistent flow of material	7	1- Improper temperature settings 2- Heater malfunction	6	1- Regular cleaning of hopper 2- Temperature monitoring and visual inspection of gasket	3	126	1- Monitoring of temperature and Gasket 2 Regular cleaning
4	Extrusion - Compression zone	1- Uneven compression 2- Over heating	1- In consistent gasket thickness 2- Burnt section of gasket	7	1- In correct temperature settings 2- Excessive friction between screw and barrel 3- Material quality issue	3	1- Regular maintenance 2- Temperature monitoring	3	63	1- Machine health review (screw, heaters, pressures etc)
5	Extrusion - metering zone	1- Flow inconsistencies 2- Die Swell	1- Dimensional inaccuracy 2- Excessive material expansion	7	1- Variations in screw speed or partial blockage 2- Material properties issue	3	1- Reguar maintenance 2- Material quality check	4	84	1- Reguar maintenance 2- Material quality check
6	Cooling	Slow cooling of gasket because of higher temp of water	Warpage, shrinkage	6	1- Improper cooling rate 2- Water temperature too high	2	Chiller water temperature monitoring	3	36	1- Adjust chiller temperature
7	Profile Formation at Die	1- Improper profile of gasket 2- Bubble formation in gasket profile	1- Material waprapage 2- Bubble formation on gasket	7	1- Improper cooling rate 2- Moisture issue	3	1- Chiller water temperature monitoring 2- Pre-heating of material	3	63	1- Adjust chiller temperature 2- Pre-heating of material
8	Cutting	Un even cutting	Improper joints formation	8	1- Blade wear 2- Blade misalignment	4	Visual inspection of gasket and blades	3	96	1- Regular maintenance of cutting assembly (blade checks, alignment etc)
9	Magnet insertion	1- Magnet cutting size variation 2- Magnet manual cutting issue	Manual cutting of magnet - Loss in productivity and improper joints during welding	8	1- Machine settings issue	4	Visual inspection	2	64	Preventive machine maintenance
10	Manual cutting of magnet	Un even cutting	Improper joints formation	8	1- Variation in magnet cutting machine 2- Manual cutting of magnet by worker	6	Visual inspection	3	144	Preventive machine maintenance
11	Welding	Weak weld joints Gasket joint overlap Gasket joint hole	1- Gasket joint tear 2- Imrproper fitting	8	1- In correct weld temperatures 2- Alignement issues during welding	7	1- Temperature checks 2- Alignment checks	4	224	1- Implement precise temperature control 2- Alignment fixtures
12	Storage	Waviness issue because of improper storage	Gaps and waviness issue after assembly	10	Storage/stacking on floor	7	1- Storage on hangers	3	210	1- Enhanced monitoring 2- Training of production workers 3-Design new hangers for storage

Figure VI. Failure modes and effect analysis

Objective of cause-and-effect diagram was to determine the root causes of the problems as well as sources of inefficiencies and variations in the manufacturing process. After analyzing the data collected in the measure phase and potential causes and failure modes in FMEA, fishbone diagram of complete gasket manufacturing process was developed. Fishbone or cause and effect diagram is mentioned in the Figure below.

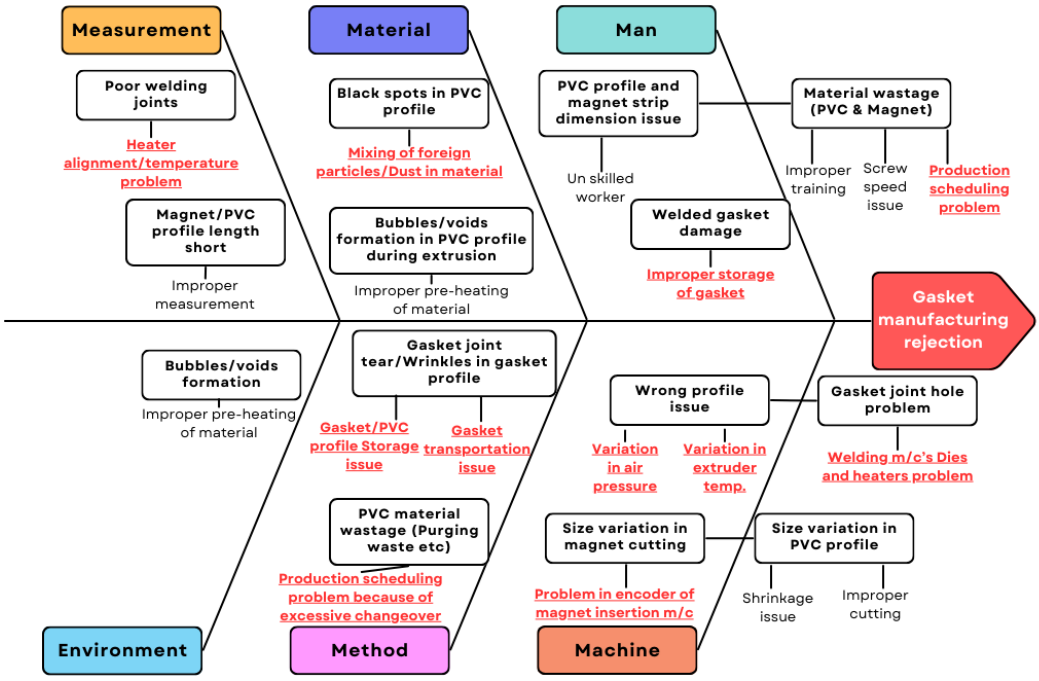

Figure VII. Cause-and-effect diagram.

In the gasket manufacturing process, several key factors contributing to high rejection rates were identified. These included improper storage and transportation systems, issues with welding dies and heaters, inaccurate cutting of the magnetic strip, poor quality PVC material and frequent color changes during gasket profile production. Together, these issues were leading to inefficiencies and increased rejection rates during the gasket manufacturing process.

Now cause and effect matrix was developed in order to prioritize the identified causes based on their impact on critical customer requirements. It can be seen in Figure .

Cause and Effect Matrix

Project: Gasket Manufacturing Process | Correlation: 9: High | 3: Medium | 1: Low | 0: No correlation

Sr. No	Causes Variables (Xs) ↓ / Effects Variables (Ys)	1 Dust in Material	2 Excessive changeover in extrusion m/c	3 Purging Waste	4 Wrong profile	5 Size variation in magnetic strip	6 Holes in gasket joints	7 Rejection of Gasket	Weighted Score (X)	%	Rank	Status (critical, potential, or eliminated)
	Importance to customer (1-10)	10	5	5	1	9	9	9				
1	Production Scheduling	0	9	9	9	0	0	9	180	11.5%	6	Critical
2	Extruder Temperature	0	3	9	9	0	0	0	69	4.4%	7	Eliminated
3	Air Pressure	0	1	1	9	0	0	3	46	2.9%	10	Eliminated
4	Screw speed	0	3	9	0	0	0	0	60	3.8%	9	Eliminated
5	PVC profile cutter	0	3	0	0	0	3	3	69	4.4%	7	Eliminated
6	Magnet strip cutting machine	0	0	0	0	9	9	9	243	15.6%	5	Critical
7	Welding m/c heaters	0	9	9	9	0	9	9	261	16.7%	4	Critical
9	Welding m/c dies	0	9	9	9	9	9	9	342	21.9%	1	Critical
11	Storage	3	9	9	9	0	9	9	291	18.6%	3	Critical
13	PVC material quality	9	9	9	9	0	3	9	297	100.0%	2	Critical
	Weighted Score (Y)	120	275	320	63	162	378	540	1561			
Comments/Conclusion:	Rank	6	4	3	7	5	2	1				

Figure VIII. Cause-and-Effects Matrix

In cause-and-effect matrix, critical causes were prioritized based on their impact on critical customer requirements. Critical causes that were identified were production scheduling issue, magnet strip cutting machine variation issue, welding machine heaters and dies health issue, improper storage for gaskets and PVC profiles issue and PVC material quality issue that impacts on the final product quality.

After that QFD was developed based on the cause-and-effect diagram and cause and effect matrix in order to link customer requirements with technical requirements that need improvement. QFD is available in Figure .

Quality Function Deployment

Project title: Gasket Ectrusion
Project leader: Adeel Tabassum
Date: 06-Jul-24

Relationships: 9 Strong | 3 Moderate | 1 Weak | 0 None

	1: low, 5: high Customer importance rating	Functional Requirements (How's) → / Customer Requirements - (What's) ↓	Raw Material	Production Scheduling of extrusion m/c	Trained Labour	Welding m/c health (heaters and dies)	Extrusion Machine Health	Extrusion machine Parameters	PVC Profile cutting m/c	Magnet cutting machine	Storage of gasket	Weighted Score
1	5	Timely delivery of gaskets	1	9	9	9	3	3	9	9	1	265
2	5	Reduction in defects	1	9	3	9	9	3	9	9	9	305
3	5	Reduction in fault slippages	0	0	1	1	3	3	9	9	9	175
4	4	Flexible	9	0	0	0	0	0	0	0	0	36
5	4	No Dust	9	0	0	0	0	0	0	0	9	72
6	2	Propper Storage and stacking	1	9	3	0	0	0	3	3	9	56
7	5	Magnetic strip size variation	1	1	3	0	0	0	0	9	0	70
8												0
9												0
		Technical importance score	89	113	86	95	75	45	141	186	149	979
		Importance %	9%	12%	9%	10%	8%	5%	14%	19%	15%	100%
		Priorities rank	6	4	7	5	8	9	3	1	2	

Figure IX. Quality function deployment (QFD)

After analyzing the data from the previous year (2023) using the Pareto principle, the results are illustrated in the Figure , Figure and Table below.

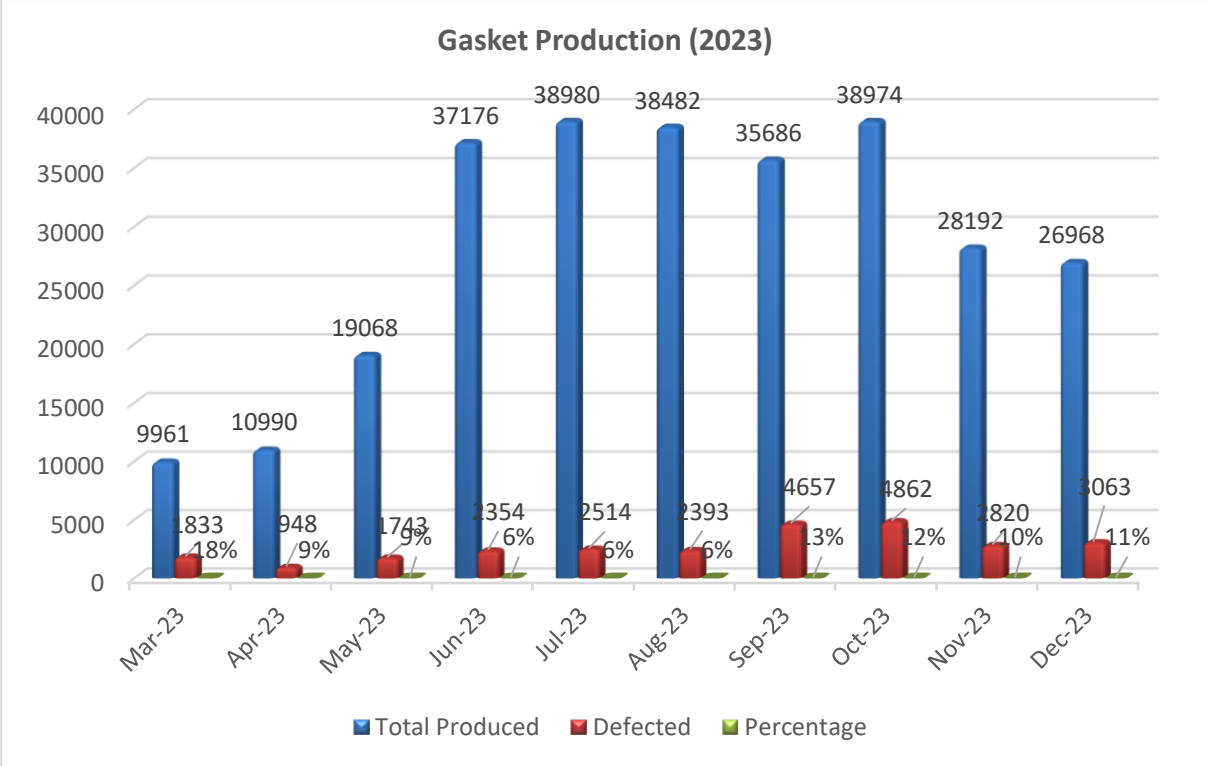

Figure X. Gasket production and rejection data of 2023.

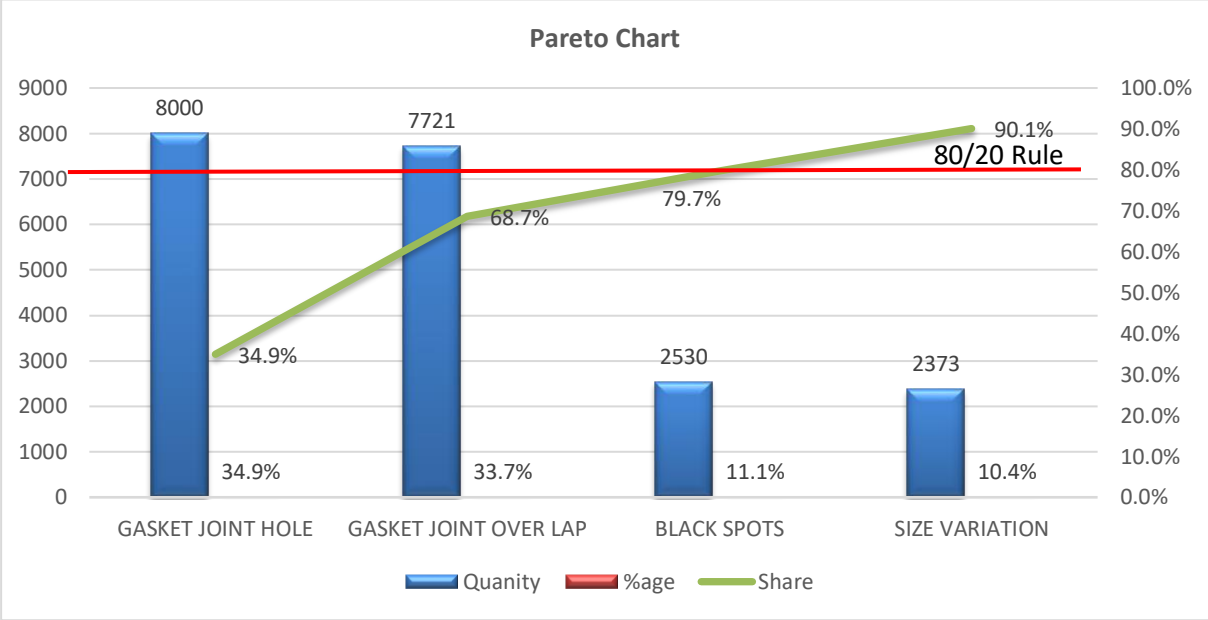

Figure XI. Pareto analysis of the data of 2023.

Problem	Quantity	%age	Cause of the defect
GASKET JOINT HOLE	8000	29%	Welding M/C
GASKET JOINT OVER LAP	7721	28%	
GASKET PROFILE WRONG	4893	18%	Extrusion Machine
BLACK SPOTS	2530	9%	Material
SIZE VARIATION	2373	9%	Extrusion Machine

Table VII. Cause of defect identification based on 2023 data.

Summary of the data that was gathered in measure phase is mentioned in Table , Table and Table .

PVC Extrusion M/c Data				
Sr. No	Total Production (kg)	Efficiency	Rejection Qty. (kg)	Rejection %age
1	12076	50%	1398	12%

Table VIII. Summary of PVC Extrusion machine data.

Welding M/c's Data				
Sr. No	Total Production	Efficiency	Rejection Qty.	Rejection %age
1	39,715	54%	2604	7%

Table IX. Summary of welding machine's data.

Magnet insertion m/c data			
Sr. No	Total Production of gaskets	Total Rejection of magnet (kg)	Average Rejection per day (kg)
1	39,715	419	14

Table X. Summary of magnet insertion m/c data.

3.5 ANOVA. - ANOVA (Analysis of Variance) is used on the data collected during the measure phase of the gasket manufacturing process to evaluate whether there are statistically significant differences between the means of various groups or factors that may be impacting the process. In the measure phase data was gathered in order to better understand the variability in the gasket production process, such as differences in total rejection, purging rejection, machine parameter settings, variation in production plan and machine efficiency. ANOVA allows manufacturers to determine which factors have a major impact on the quality or performance of their gaskets. This analysis aids in identifying sources of variation that must be addressed during the improve phase of the process.

The "Total Rejection" data's normality was thoroughly tested in this study using four statistical tests: the Kolmogorov-Smirnov test, the Kolmogorov-Smirnov test with Lilliefors correction, the Shapiro-Wilk test and the Anderson-Darling test. The Kolmogorov-Smirnov test produced a statistic of 0.09 and a p-value of 0.982, suggesting no significant departure from a normal distribution. Similarly, the Kolmogorov-Smirnov test with Lilliefors correction, which accounts for small sample sizes, yielded a statistic of 0.09 and a p-value of 1, providing additional support for the normality assumption. The Shapiro-Wilk test, which is known for being effective with small to intermediate sample sizes, yielded a statistic of 0.97 and a p-value of 0.606, supporting the conclusion of normality. Finally, the Anderson-Darling test, which is especially sensitive to tail deviations, returned a statistic of 0.24 and a p-value of 0.779, suggesting no significant departure from normalcy. Collectively, these tests provide strong evidence that the "Total Rejection" data follows a normal distribution, supporting the use of parametric statistical approaches in following investigations. Data is mentioned in Table

Normality tests	Statistics	p
Kolmogorov-Smirnov	0.09	0.982
Kolmogorov-Smirnov (Lilliefors Corr.)	0.09	1
Shapiro-Wilk	0.97	0.606
Anderson-Darling	0.24	0.779

Table XI. Tests for normal distribution of Total Rejection.

The Durbin-Watson test was used to determine whether the regression model's residuals had autocorrelation. The test produced a statistic of 2.37, which is near to the ideal value of two, indicating no significant first-order autocorrelation.

The corresponding p-value of 0.348, which is greater than the conventional significance level of 0.05, supports this result by indicating that the null hypothesis of no autocorrelation cannot be discarded. The autocorrelation coefficient of -0.24 suggests a small negative connection between residuals, although it is not statistically significant. Overall, the results indicate that the residuals are independent, and the regression model meets the requirement of no autocorrelation. This discovery improves the trustworthiness of the regression analysis and its conclusions and is mentioned in Table

Autocorrelation	Statistics	p
-0.24	2.37	0.348

Table XII. Durbin-Watson-Test

Now multicollinearity test was performed. It is used to confirm that the regression model is reliable and valid by determining whether the predictor variables were significantly linked with one another. Multicollinearity can generate a number of problems in regression analysis, including exaggerated standard errors of coefficient estimates, incorrect significance tests, and difficulties evaluating each predictor's unique contributions. Multicollinearity, which happens when predictor variables in a regression model are highly correlated, can impair model dependability by increasing the variance of coefficient estimates and making it harder to analyze each predictor's individual effect. To diagnose multicollinearity, two crucial metrics are commonly used: tolerance and the Variance Inflation Factor (VIF). Tolerance levels less than 0.10 or VIF values greater than 10 are typically regarded indicators of problematic multicollinearity. In this analysis, the Tolerance and VIF values for all predictors, such as "purging rejection" (Tolerance = 0.81, VIF = 1.23), "Gasket size variation issue" (Tolerance = 0.88, VIF = 1.14), and "machine stop for lunch break" (Tolerance = 0.63, VIF = 1.58), are well within acceptable ranges. None of the predictors have Tolerance values less than 0.10 or VIF values greater than 10, indicating that multicollinearity is not a major concern in this model. This implies that the predictors are sufficiently independent, and the regression analysis can proceed without concern for multicollinearity influencing the results. Results are available in Table .

Model	Tolerance	VIF
Purging rejection	0.81	1.23
Gasket size variation issue	0.88	1.14
Color changeover rejection	0.68	1.47
Pre-heating	0.58	1.73
Machine parameter setting	0.7	1.44
Machine stop - No plan	0.67	1.49
Machine stop - Gasket color change	0.49	2.02
Machine stop for lunch break	0.63	1.58

Table XIII. Multicollinearity test.

Now model summary and ANOVA table were prepared from regression analysis in order to evaluate the performance of the model. The regression analysis showed a robust association between predictors and the dependent variable ($R = 0.91$ and $R^2 = 0.84$), accounting for 84% of the variation. The improved R^2 (0.76) verified the model's robustness, and the standard error of 5.9 indicated acceptable prediction accuracy. The ANOVA findings ($F = 10.86$, $p < .001$) showed the model's overall significance. This investigation confirmed the model's fit and predictive capability, indicating its suitability for evaluating variable relationships. It confirmed that the predictors together had a significant effect on the dependent variable. Above mentioned values are available in Table 2 and Table.

R	R^2	Adjusted R^2	Standard error of the estimate
0.91	0.84	0.76	5.9

Table 2 Model summary

Model	df	F	p
Regression	8	10.86	<.001

Table XV. ANOVA.

Now Pareto diagram was prepared in order to identify and prioritize the most significant factors that results in the instability of the process leading it to deviate from mean and perform erratically. This pareto diagram (Figure) will also validate the significant factors diagnosed in the previous mentioned tools like cause-and-effect diagram, cause and effect matrix, quality function deployment and FMEA.

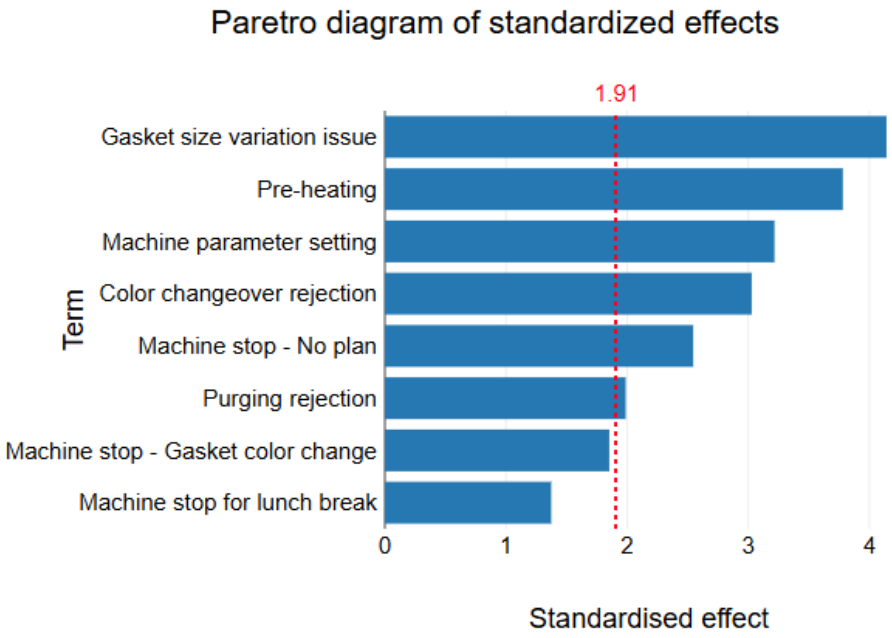

Figure XII. Pareto diagram of standardized effects.

In this pareto diagram, factors such as gasket size variation issue, pre-heating, machine parameter setting, color changeover rejection, machine stop – no plan, purging rejection were evaluated and then ranked for their impact. This highlights the ones that require immediate attention and will yield maximum results with optimized allocation of resources.

3.6 Improve Phase. - The goal of improve phase is to implement the solutions of the problems/causes that were identified in the analyze phase. This involves designing and testing the suggested improvements of the problems to enhance efficiency, reduce defects and variations in the manufacturing process. Detailed solutions to each cause identified in analyze phase are given below in Table .

Sr. No	Problem	Root cause	Suggestions for improvement
1	Purging Waste & Wrong profile issue	Excessive changeover issue	1- Gasket manufacturing plan should be independent from DPA plan 2- Gasket production planning should be done as per stock area 3- Stock area for PVC profiles should be designed in such a way that extrusion machine must not be used for production every single day. Batch production planning should be done
2	Magnetic Strip cutting Waste	Cutting machine sensors not ok	1-In first step, knurling of encoder wheel as grooves on the wheel are practically eliminated 2- If problem of size variation is not resolved then secondly will remove the mechanical delay between the rocker arm and limit switch 3- In case the problem is still not resolved then will replace the existing the encoder with rotary increment encoder
		Manual Cutting	4- For a temporary solution, manual cutting should be done as we are already performing this process at later stage
3	Welding Joints	Welding Dies health issue	1-Repairing of Dies
		Uncontrolled heaters temperatures for welding	2- Usage of K type thermocouples with microsensor to control the temperature 3- Replacing the existing filament type electric heaters with tube type electric heaters
		Storage issue for finished gasket	4-Use trollies or hangers for transportation 5-Improve design of Hangers
4	Black spots	Dust in Crush	1-Use less crush or no crush
		Foreign particles mixing in virgin material	2- Supplier material evaluation should be done

Table XVI. Suggestions for improvements for gasket manufacturing process.

Detailed feasibility analysis of the improvements mentioned in Table was performed. Cost of these improvements is mentioned in Table , Table and Table .

Item	Price (PKR)
Price of Thermocouple	2500
Price of MAX6675	2350
Price of Arduino UNO	2000
Cost of single setup	6850
Total No. of welding Machines	8
Total Cost	54,800

Table XVII. Welding machine heaters temperature controller.

Item	Quantity
Number of coils on each hanger	50
Cost of improvement on each hanger	50
(scrap metal will be used - Cost is of labor and welding)	50
Total Cost	75000

Table XVIII. Redesigning of hangers for gasket storage.

Item	Quantity with 1 m/c production (PKR)
Cost of each box (PKR)	5,000
Total Cost (PKR)	90,000

Table XIX. Construction of wooden boxes for PVC profile storage.

3.7 Control phase. - After the implementation of improvement suggestions that were mentioned in improve phase, control phase in the gasket manufacturing process focuses on sustaining the improvements made in previous stages to guarantee consistent product quality with little variance. Control mechanisms are put in place during this phase to keep an eye on important process variables like material wastage control by controlled production scheduling, controlling of defects related to welding machines, controlling the defects related to storage of gaskets and PVC profiles, extrusion machine parameters and magnetic strip insertion precision. Control charts are used to monitor these variables over 30 days of time in order to identify any deviations. Remapping of process was done in order to improve the existing setup. Summary of extrusion machine data is available in the Table below.

PVC Extrusion M/c Data (After Improvement) Date = 20th Aug, 2024 – 10th Sep, 2024				
Sr. No	Total Actual Production (kg)	Efficiency %age	Total Rejection (kg)	Rejection %age
1	13200	83.2%	536	4.06%

PVC Extrusion M/c Data (Before Improvement)				
Sr. No	Total Production (kg)	Efficiency	Rejection Qty. (kg)	Rejection %age
1	12076	50%	1398	12%

Table XX. Summary of extrusion m/c data (Before vs After Improvement).

In this research, Cp and Cpk (Statistical Process Control metrics) were used to evaluate the process's capability before and after making modifications to the gasket manufacturing process. These indices were used for studying how modifications affected production efficiency, rejection %age, and purge rejection. Cp assesses the process's potential capability by comparing its spread to the specification limitations, whereas Cpk accounts for process centering, providing information about how well the process mean aligns with the target. Before improvement, the process had low Cp and negative Cpk values, indicating inadequate capability and a considerable variation from the target values.

The findings show that effectiveness of the improvement steps taken on manufacturing line in increasing production efficiency, lowering rejection rates, and reducing purge rejection, resulted in a more capable and stable manufacturing process that revolves around.
Cp and Cpk calculation of before and after improvements are mentioned in Table and Table.

Parameters	Production Efficiency	Rejection %age	Purging rejection
Target	80%	4.0%	7
+ Tol	20%	0.5%	3
- Tol	5%	0.5%	3
USL	100%	4.5%	10
LSL	75%	3.5%	4
AVE	48%	13.1%	14
MAX	61%	88.4%	21
MIN	10%	4.6%	4
USL-LSL	25%	1.0%	6
s	9.7%	15.4%	4
CpU	1.785	-0.19	-0.40
CpL	-0.926	0.21	0.94
Cp	0.429	0.01	0.27
Cpk	-0.926	-0.19	-0.40

Table XXI. Cp & Cpk calculations of gasket manufacturing process - Before improvement.

Parameters	Production Efficiency	Rejection %age	Purging rejection
Target	80%	4%	7.000
+ Tol	20%	0.5%	3.000
- Tol	5%	0.5%	3.000
USL	100%	4.5%	10.000
LSL	75%	3.5%	4.000
AVE	83%	4.1%	6.852
MAX	90%	4.3%	8.000
MIN	78%	3.7%	5.000
USL-LSL	25%	1.0%	6.000
s	2.8%	0.1%	0.972
CpU	1.996	1.023	1.080
CpL	0.975	1.290	0.979
Cp	1.486	1.157	1.029
Cpk	0.975	1.023	0.979

Table XX. Cp & Cpk calculations of gasket manufacturing process - After improvement.

I-MR control chart of production efficiency, rejection %age and purging rejection are given below and explained in detail.

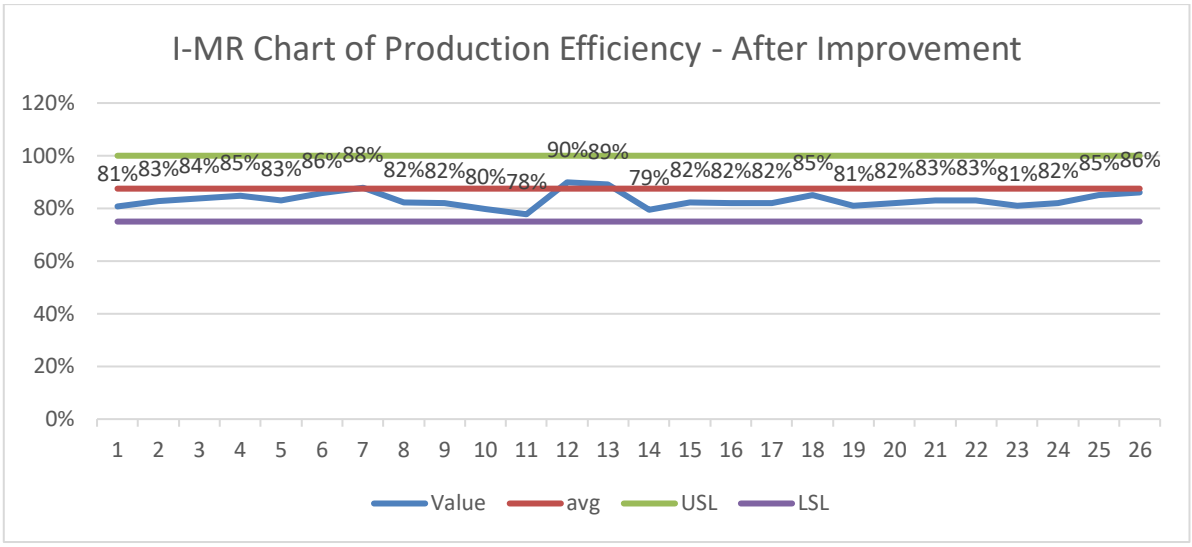

Figure XIII. I-MR control chart of purging rejection after improvement.

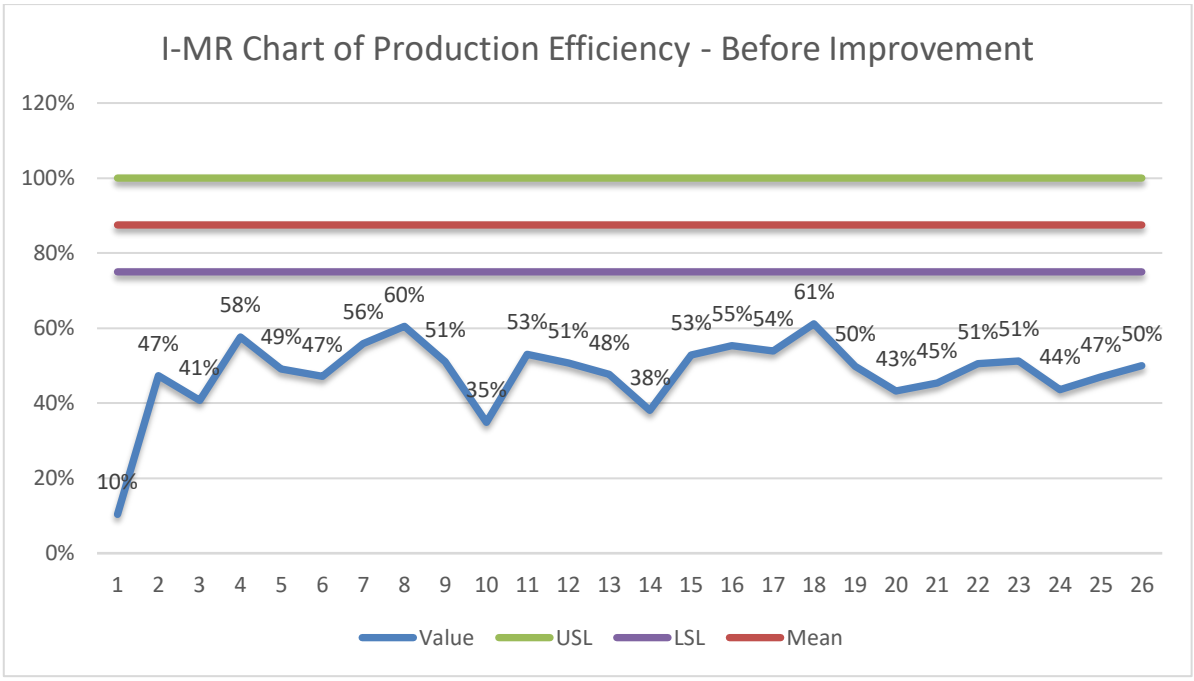

Figure XIV. I-MR control chart of purging rejection before improvement

As it can be seen in **Error! Reference source not found.** and **Error! Reference source not found.** that average rejection reduced from 17 kg/day to 6.9 kg/day. Average rejection per day dropped from 47 kg to 24 kg just because of improving production planning and storage area for PVC profiles. Cost of PVC material per kg is 395 PKR including energy consumption and labor cost per day. This results in a saving of 5,135 PKR per day just from extrusion machine. This amounts to 1.5 million PKR per year from one extrusion machine only.

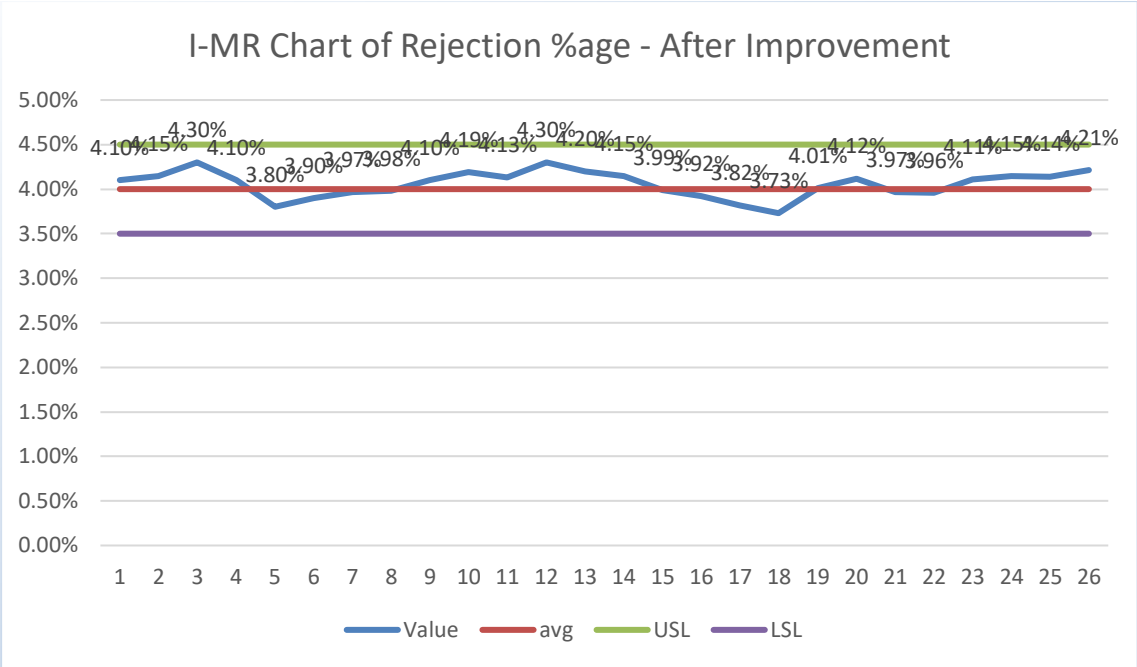

Figure XV. I-MR chart of date vs rejection %age after improvement.

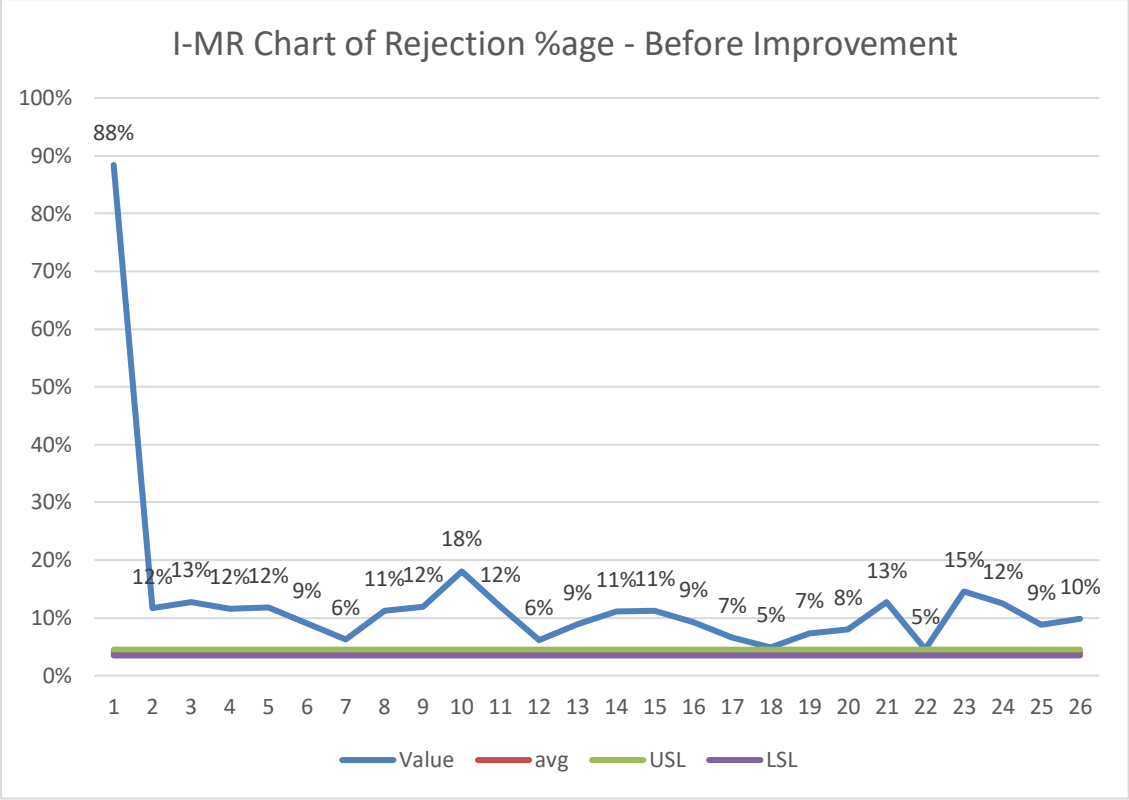

Figure XVI. I-MR control chart of date vs rejection %age before improvement.

The graphs in Figure and Figure show a significant reduction in the average rejection %age, dropping from 12% to 4.06%. This substantial decline in rejection %age is primarily due to increased productivity. The boost in production and decrease in stoppage times led to a reduction in purging rejection and machine setup rejection, ultimately contributing to the overall decrease in the rejection %age.

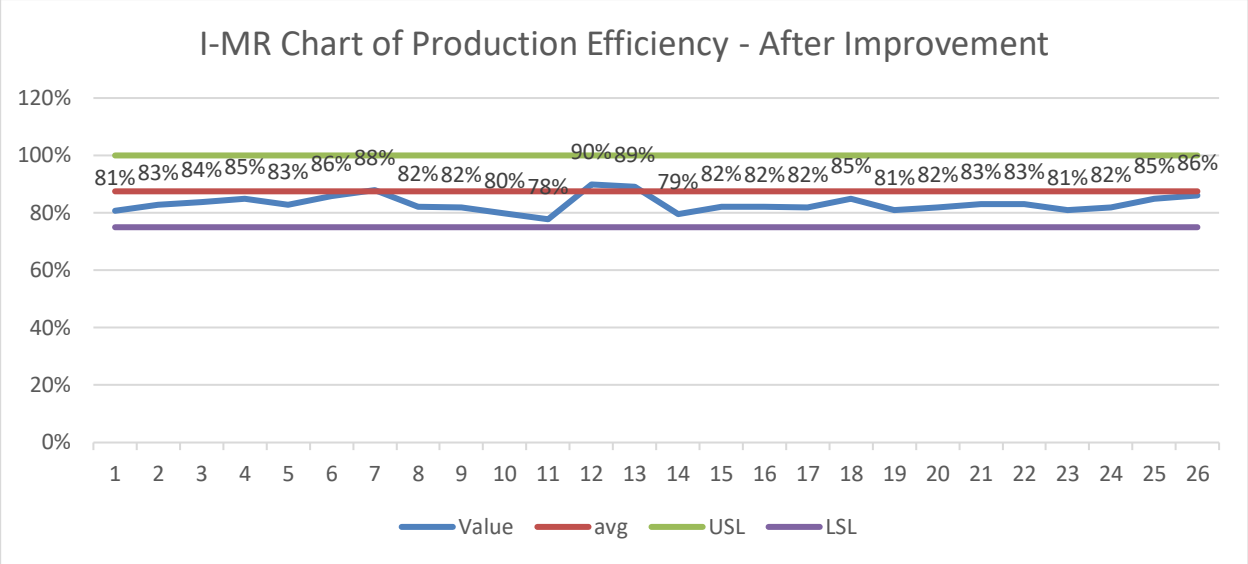

Figure XVII. I-MR control chart of efficiency after improvement.

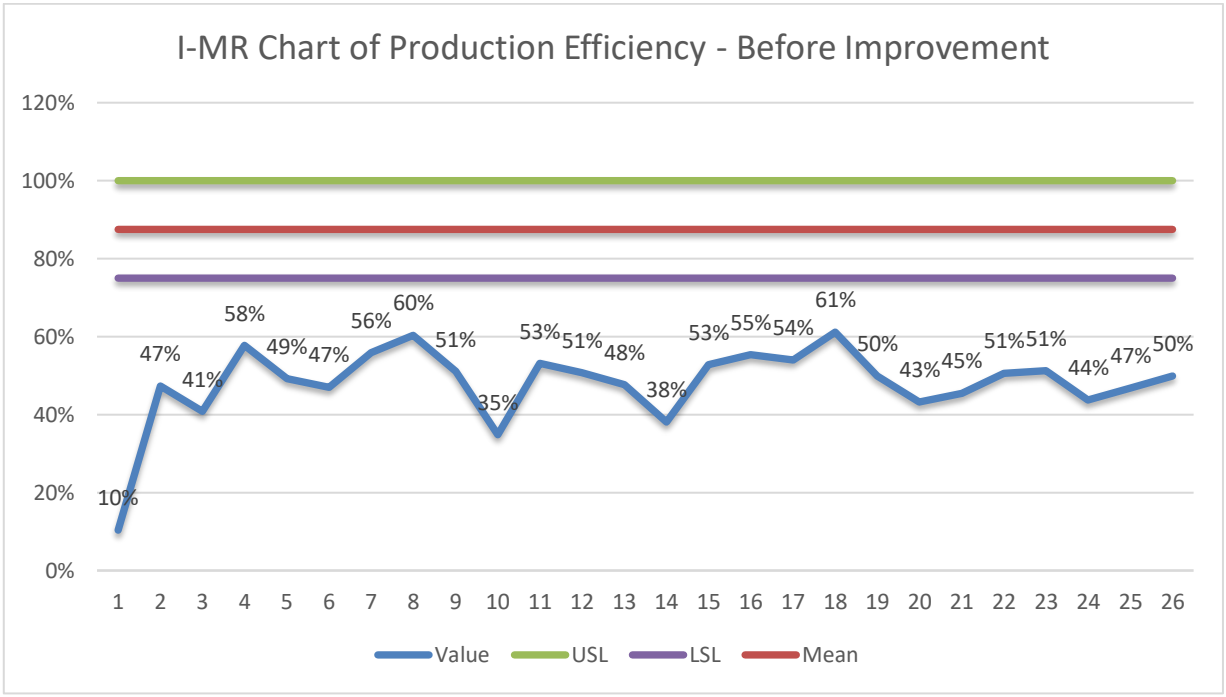

Figure XVIII. I-MR control chart of production efficiency before improvement.

It can be seen from the Figure and Figure that efficiency of extrusion machine increased from 50.1% to 83.3% which is a huge change. This was only possible by reducing the number of changeovers and stoppage times.

Rejection because of size variation in magnet cutting machine issue was resolved after the knurling of encoder wheel. Average value of magnetic strip rejection per day was 14 kg. At a cost of 17 PKR/meter and 1 meter of magnet weighs 60 gm. This saves company almost 1.2 million PKR in 1 year (300 working days).

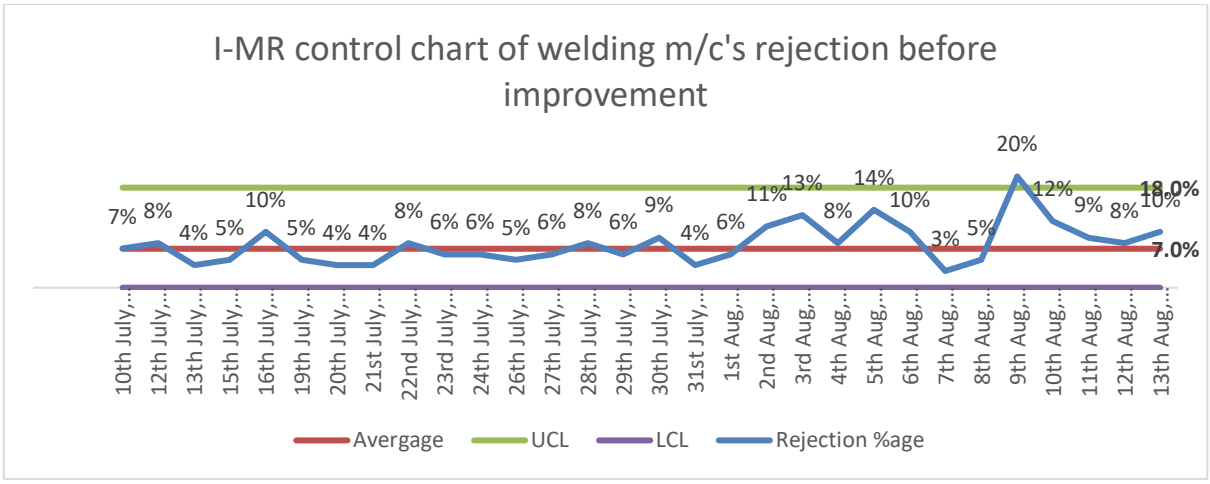

Figure XIX. I-MR control chart of welding m/c's rejection before improvement.

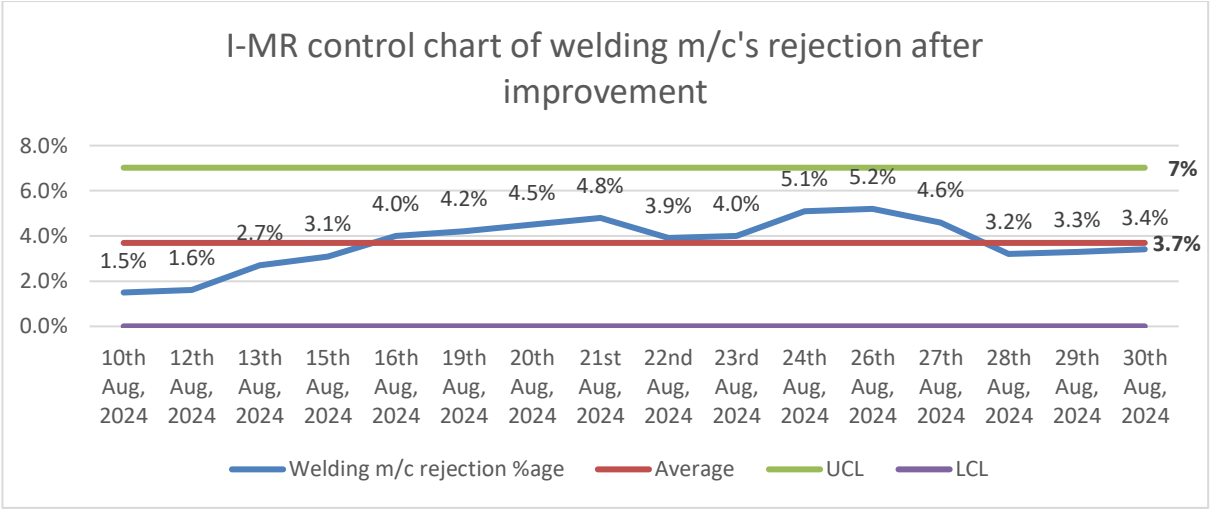

Figure XX. I-MR control chart of welding m/c's rejection after improvement.

It can be seen in Figure and Figure that average welding rejection was reduced from 7% to 3.7%. This happened because of implementing temperature controller for heaters and repairing of dies. Efficiency monitoring report was not prepared for welding m/c's as their plan is dependent upon door pre-assembly and production on welding machines start and stop based on the requirement of door pre-assembly.

4. Conclusion. - The six-sigma project, based on DMAIC methodology, for gasket manufacturing process has resulted in significant improvement in gasket manufacturing process resulting in increase in efficiency, waste reduction, process improvement thus improving the overall product quality.

4.1 PVC extrusion machine. - The overall rejection %age of the extrusion machine decreased significantly from 12% to 4.06%. The average purging rejection per day was reduced from 17 kg to 6.9 kg and the total daily rejection dropped from 47 kg to 24 kg. This reduction translates into a savings of 5,135 PKR per day, amounting to 1.5 million PKR annually (based on 300 working days). Additionally, the efficiency of the extrusion machine improved from 50.1% to 83.3%, marking a substantial increase in productivity. Also, next month plan was completed in 20 days thus saving a considerable amount of energy cost, labour cost and other costs associated with it.

4.2 Magnet insertion m/c. - There was loss of 14 kg of magnet per day and as 1-meter magnet weighs 60 gm so there was a loss of 233.3 meters of magnet per day. This loss was reduced to zero by knurling of encoder wheel thus saving company 1.2 million rupees in one year (300 working days) at a cost of 17 PKR/meter.

4.3 Welding m/c's. - Since the welding machines operate based on the requirements of the door pre-assembly process, the rejection %age of the welding machines was monitored after the improvements were implemented. The rejection

rate dropped from 7% to 3.7%, primarily due to enhancements in the temperature control of the welding heaters and repairs to the dies, which contributed to better overall performance and reduced defects.

In conclusion this six-sigma project not only achieved significant improvements in gasket manufacturing process by optimizing the production process and production scheduling by developing the storage area of gasket profiles in order to smoothen the production of extrusion machine and remove it dependency on door pre-assembly plan because of absence of storage space. Also, a significant problem was resolved by knurling of encoder wheel at magnet insertion station by improving the threading of encoder wheel so that it can accurately read the length of magnet during production. Major issues of welding machines were resolved by adding a temperature controller for heater and repairing of dies. In addition to these changes, comprehensive operator training sessions were conducted, and Standard Operating Procedures (SOPs) were established to guide production execution and quality inspection processes. As a result of this final product is improved significantly along with process. By continuing to monitor and control these improvements can be sustained as there is not ample time available for preventive maintenance because of extrusion m/c production plan completion before time with at least 10 days to spare.

References

[1] A Paramasivam, P. V. (2022). Manufacturing process rejection analysis of heavy duty gear reduction starter motor. *Materials Today: Proceedings, 59*(2), 1295-1300. doi:doi.org/10.1016/j.matpr.2021.11.520

[2] Alarcón, F., Calero, M., Pérez-Huertas, S., & Martín-Lara, M. (2023). State of the Art of Lean Six Sigma and Its Implementation in Chemical Manufacturing Industry Using a Bibliometric Perspective. *applied sciences, 13*(12). doi:doi.org/10.3390/app13127022

[3] Amaral, M. T. (2022). Growth curves with multivariate θ generalized normal distribution for cardiac dysfunction in rats. *Communications in Statistics: Case Studies, Data Analysis and Applications, 6*(2), 615-627. doi:doi.org/10.1080/23737484.2020.1752848

[4] Araman, H. a. (2023). A case study on implementing Lean Six Sigma: DMAIC methodology in aluminum profiles extrusion process. *The TQM Journal, 35*(2), 337-365. doi:https://doi.org/10.1108/TQM-05-2021-0154

[5] Bailey, D. C.-L. (2016). Challenging the age of austerity: Disruptive agency after the global economic crisis. *Comparative European Politics, 16*, 9-31. doi:doi.org/10.1057/s41295-016-0072-8

[6] Guoqiang Liu, G. Y. (2020). Research on test method of heat transfer coefficient for refrigerator gasket. *International Journal of Refrigeration, 110*, 106-120. doi:doi.org/10.1016/j.ijrefrig.2019.11.007

[7] Guoqiang Liu, G. Y. (2021). A review of refrigerator gasket: Development trend, heat and mass transfer characteristics, structure and material optimization. *Renewable and Sustainable Energy Reviews, 144*. doi:doi.org/10.1016/j.rser.2021.110975

[8] Hill, J. T.-J.-K. (2017). The implementation of a Lean Six Sigma framework to enhance operational performance in an MRO facility. *Production & Manufacturing Research, 6*(1), 26-48. doi:doi.org/10.1080/21693277.2017.1417179

[9] Jaime Macias-Aguayo, L. G.-C. (2022). Industry 4.0 and Lean Six Sigma Integration: A Systematic Review of Barriers and Enablers. *Applied sciences, 12*(22). doi:https://doi.org/10.3390/app122211321

[10] Lewandowski, K., & Skórczewska, K. (2022). A Brief Review of Poly(Vinyl Chloride) (PVC) Recycling. *polymers, 14*(15). doi:doi.org/10.3390/polym14153035

[11] LM, M. (2022). Define, Measure, Analyze, Improve, Control (DMAIC) Methodology as a Roadmap in Quality Improvement. *Global Journal on Quality and Safety in Healthcare, 5*(2), 44-46. doi:doi.org/10.36401/JQSH-22-X2

[12] Macias-Aguayo, J., Garcia-Castro, L., Barcia, K., McFarlane, D., & Abad-Moran, J. (2022). Industry 4.0 and Lean Six Sigma Integration: A Systematic Review of Barriers and Enablers. *applied sciences, 12*(22). doi:doi.org/10.3390/app122211321

[13] McDermott, O., Antony, J., Bhat, S., Jayaraman, R., Rosa, A., Marolla, G., & Parida, R. (2022). Lean Six Sigma in Healthcare: A Systematic Literature Review on Challenges, Organisational Readiness and Critical Success Factors. *processes, 10*(10). doi:doi.org/10.3390/pr10101945

[14] Monika Smętkowska, B. M. (2018). Using Six Sigma DMAIC to Improve the Quality of the Production Process: A Case Study. *Procedia - Social and Behavioral Sciences, 238*, 590-596. doi:doi.org/10.1016/j.sbspro.2018.04.039

[15] Monika Smętkowska, B. M. (2018). Using Six Sigma DMAIC to Improve the Quality of the Production Process: A Case Study. *Procedia - Social and Behavioral Sciences, 238*, 590-596. doi:https://doi.org/10.1016/j.sbspro.2018.04.039

[16] Most. Asikha Aktar, M. M.-A. (2021). Global economic crisis, energy use, CO2 emissions, and policy roadmap amid COVID-19. *Sustainable Production and Consumption, 26*, 770-781. doi:doi.org/10.1016/j.spc.2020.12.029

[17] Muraliraj, J. Z. (n.d.). Annotated methodological review of Lean Six Sigma. *International Journal of Lean Six Sigma, 9*(1), 2-49. doi:doi.org/10.1108/IJLSS-04-2017-0028

[18] Ndrecaj, V., Mohamed Hashim, M., Mason-Jones, R., Ndou, V., & Tlemsani, I. (2023). Exploring Lean Six Sigma as Dynamic Capability to Enable Sustainable Performance Optimisation in Times of Uncertainty. *sustainability, 15*(23). doi:doi.org/10.3390/su152316542

[19] Noori, B. a. (2018). Development of Six Sigma methodology to improve grinding processes: A change management approach. *International Journal of Lean Six Sigma, 9*(1), 50-63. doi:doi.org/10.1108/IJLSS-11-2016-0074

[20] Patel, A. a. (2021). Critical review of literature on Lean Six Sigma methodology. *International Journal of Lean Six Sigma, 12*(3), 627-674. doi:doi.org/10.1108/IJLSS-04-2020-0043

[21] Raman Sharma, P. G. (2018). SIX SIGMA DMAIC METHODOLOGY IMPLEMENTATION IN AUTOMOBILE INDUSTRY: A CASE STUDY. *Journal of manufacturing engineering, 13*(1), 42-50.

[22] S. Reosekar, R. a. (n.d.). Six Sigma methodology: a structured review. *International Journal of Lean Six Sigma, 5*(4), 392-422. doi:doi.org/10.1108/IJLSS-12-2013-0059

[23] T. Costa, F. S. (2017). Improve the extrusion process in tire production using six sigma methodology. (1104-1111, Ed.) *Procedia manufacturing, 13*. doi:doi.org/10.1016/j.promfg.2017.09.171

[24] T. Costa, F. S. (2017). Improve the extrusion process in tire production using Six Sigma methodology. *Procedia Manufacturing, 13*, 1104-1111. doi:https://www.sciencedirect.com/science/article/pii/S2351978917308090

[25] Tianyang Zhao, G. L. (2024). Effect of structural improvement of gaskets on the heat leakage load and energy consumption of the refrigerator. *Energy, 300*. doi:doi.org/10.1016/j.energy.2024.131430

[26] Tjahjono, B. B. (2010). Six Sigma: a literature review. *International Journal of Lean Six Sigma, 1*(3). doi:doi.org/10.1108/20401461011075017

[27] Wasage, C. (2016). Implementation of Six Sigma Projects in Fortune 500 companies. *Journal of Modern Accounting and Auditing, 12*(4), 208-216. doi:doi.org/10.17265/1548-6583/2016.04.002

[28] Yang C-C, J. Y.-T.-C. (2022). The Development of the New Process of Design for Six Sigma (DFSS) and Its Application. *Sustainability, 14*(15). doi:doi.org/10.3390/su14159294

Author contribution:
1. Conception and design of the study
2. Data acquisition
3. Data analysis
4. Discussion of the results
5. Writing of the manuscript
6. Approval of the last version of the manuscript

MMUZS has contributed to: 1, 2, 3, 4, 5 and 6.
AT has contributed to: 1, 2, 3, 4, 5 and 6.

Acceptance Note: This article was approved by the journal editors Dr. Rafael Sotelo and Mag. Ing. Fernando A. Hernández Gobertti.

Parametric Optimization of Electric Discharge Machining for AISI 1045 Steel: A Comprehensive Study

Optimización paramétrica del mecanizado por electroerosión para acero AISI 1045: un estudio exhaustivo

Otimização Paramétrica da Usinagem por Eletroerosão para Aço AISI 1045: Um Estudo Abrangente

Muhammad Mansoor Uz Zaman Siddiqui[1(*)], Syed Amir Iqbal[2], Ali Zulqarnain[3], Adeel Tabassum[4]

Recibido: 20/11/2024 Aceptado: 02/03/2025

Summary. - This study investigates the optimization of Electric Discharge Machining (EDM) parameters for AISI 1045. It is a medium carbon steel which is commonly used in automotive and aerospace industries because of its balanced strength, toughness and machinability. However, achieving optimal machining efficiency with excellent surface finish in short time and without wasting excess material with EDM remains a challenge at large. The research focuses on optimizing key EDM input parameters like current (LV), voltage (HV), pulse on time (Ton) and pulse off time (Toff), to improve machining time (Tm), material removal rate (MRR), electrode wear rate (EWR), surface roughness (Ra) and base radius (R). Full factorial design and Response Surface Methodology (RSM) were used to conduct experiments, and ANOVA was employed to identify the most significant factors influencing the output responses. Multi-objective optimization was performed through the desirability function and the findings were validated by repeated experiments. The results showed that pulse on time (Ton), its interaction with pulse off time (Toff) and the three-factor interaction between current (LV), Ton and Toff were the most significant factors affecting machining performance. Optimizing these parameters reduced machining time (Tm) to 623.21 seconds thus significantly improving EDM efficiency. The material removal rate (MRR) was maximized at 0.0173 g/min resulting in considerable increase in material removal efficiency. The electrode wear rate (EWR) was minimized to 0.0088 g/min, which prolongs electrode life and reduces operational costs. Surface roughness (Ra) was improved to 0.0253 mm, ensuring a high-quality surface finish. The base radius (R) was successfully optimized to 1.5298 mm, aligning closely with the desired target of 1.5 mm thus ensuring dimensional accuracy. This investigative study of optimization of parameters for EDM of AISI 1045 material is extremely significant for automotive and aerospace industries that rely on precision machining, as the optimized EDM parameters lead to improved efficiency, reduced material waste and enhanced product quality. These findings offer valuable insights for improving EDM processes, particularly in sectors requiring complex geometries and high precision, such as automotive and aerospace manufacturing.

Keywords: Electric Discharge Machining; AISI 1045; Parametric Optimization; Material Removal Rate; Electrode Wear Rate; Surface Roughness; Machining Time; Response Surface Methodology; ANOVA; Base Radius

Resumen. - *Este estudio investiga la optimización de los parámetros de mecanizado por descarga eléctrica (EDM) para AISI 1045. Es un acero de carbono medio que se utiliza comúnmente en las industrias automotriz y aeroespacial debido a su resistencia, tenacidad y maquinabilidad equilibradas. Sin embargo, lograr una eficiencia de mecanizado óptima con un excelente acabado superficial en poco tiempo y sin desperdiciar material sobrante con EDM sigue*

(*) Corresponding author.

[1] Master of Engineering, Department of Industrial Engineering, University of Engineering & Technology (Pakistan), 2023phdmnf1@student.uet.edu.pk,
ORCID iD: https://orcid.org/0009-0007-8992-7601

[2] Dean, Department of Industrial & Manufacturing Engineering, NEDUET (Pakistan), deanmme@neduet.edu.pk,
ORCID iD: https://orcid.org/0000-0002-6812-6238/

[3] Director Industrial Liaison, Department of Industrial & Manufacturing Engineering, NEDUET (Pakistan), dil@neduet.edu.pk,
ORCID iD: https://orcid.org/0000-0003-2762-5409

[4] Mechanical Engineer, Department of Mechanical Engineering, NUST (Pakistan), adeeltabassum1@gmail.com,
ORCID iD: https://orcid.org/0009-0006-9375-1090

siendo un desafío en general. La investigación se centra en la optimización de los parámetros de entrada clave de EDM como la corriente (LV), el voltaje (HV), el tiempo de activación del pulso (Ton) y el tiempo de desactivación del pulso (Toff), para mejorar el tiempo de mecanizado (Tm), la tasa de remoción de material (MRR), la tasa de desgaste del electrodo (EWR), la rugosidad superficial (Ra) y el radio base (R). Se utilizaron el diseño factorial completo y la Metodología de Superficie de Respuesta (RSM) para realizar experimentos y se empleó ANOVA para identificar los factores más significativos que influyen en las respuestas de salida. Se realizó una optimización multiobjetivo a través de la función de deseabilidad y los hallazgos se validaron mediante experimentos repetidos. Los resultados mostraron que el tiempo de activación del pulso (Ton), su interacción con el tiempo de desactivación del pulso (Toff) y la interacción de tres factores entre la corriente (LV), Ton y Toff fueron los factores más significativos que afectaron el rendimiento del mecanizado. La optimización de estos parámetros redujo el tiempo de mecanizado (Tm) a 623,21 segundos, mejorando así significativamente la eficiencia de la electroerosión. La tasa de eliminación de material (MRR) se maximizó a 0,0173 g/min, lo que resultó en un aumento considerable en la eficiencia de eliminación de material. La tasa de desgaste del electrodo (EWR) se minimizó a 0,0088 g/min, lo que prolonga la vida útil del electrodo y reduce los costos operativos. La rugosidad superficial (Ra) se mejoró a 0,0253 mm, lo que garantiza un acabado superficial de alta calidad. El radio base (R) se optimizó con éxito a 1,5298 mm, alineándose estrechamente con el objetivo deseado de 1,5 mm, lo que garantiza la precisión dimensional. Este estudio de investigación sobre la optimización de parámetros para la electroerosión de material AISI 1045 es fundamental para las industrias automotriz y aeroespacial que dependen del mecanizado de precisión, ya que la optimización de los parámetros de la electroerosión mejora la eficiencia, reduce el desperdicio de material y mejora la calidad del producto. Estos hallazgos ofrecen información valiosa para mejorar los procesos de electroerosión, especialmente en sectores que requieren geometrías complejas y alta precisión, como la fabricación automotriz y aeroespacial.

Palabras clave: *Mecanizado por electroerosión; AISI 1045; Optimización paramétrica; Tasa de remoción de material; Tasa de desgaste de electrodos; Rugosidad superficial; Tiempo de mecanizado; Metodología de superficie de respuesta; ANOVA; Radio base*

Resumo. - *Este estudo investiga a otimização dos parâmetros de usinagem por descarga elétrica (EDM) para AISI 1045. É um aço de médio carbono comumente usado nas indústrias automotiva e aeroespacial devido à sua resistência, tenacidade e usinabilidade equilibradas. No entanto, atingir a eficiência de usinagem ideal com excelente acabamento superficial em curto espaço de tempo e sem desperdiçar excesso de material com EDM continua sendo um grande desafio. A pesquisa se concentra na otimização dos principais parâmetros de entrada de EDM, como corrente (LV), tensão (HV), tempo de pulso ligado (Ton) e tempo de pulso desligado (Toff), para melhorar o tempo de usinagem (Tm), taxa de remoção de material (MRR), taxa de desgaste do eletrodo (EWR), rugosidade da superfície (Ra) e raio da base (R). O planejamento fatorial completo e a Metodologia de Superfície de Resposta (RSM) foram usados para conduzir experimentos e ANOVA foi empregada para identificar os fatores mais significativos que influenciam as respostas de saída. A otimização multiobjetivo foi realizada por meio da função de desejabilidade e os resultados foram validados por experimentos repetidos. Os resultados mostraram que o tempo de pulso ligado (Ton), sua interação com o tempo de pulso desligado (Toff) e a interação de três fatores entre corrente (LV), Ton e Toff foram os fatores mais significativos que afetaram o desempenho da usinagem. A otimização desses parâmetros reduziu o tempo de usinagem (Tm) para 623,21 segundos, melhorando significativamente a eficiência da EDM. A taxa de remoção de material (MRR) foi maximizada em 0,0173 g/min, resultando em um aumento considerável na eficiência da remoção de material. A taxa de desgaste do eletrodo (EWR) foi minimizada para 0,0088 g/min, o que prolonga a vida útil do eletrodo e reduz os custos operacionais. A rugosidade da superfície (Ra) foi melhorada para 0,0253 mm, garantindo um acabamento superficial de alta qualidade. O raio da base (R) foi otimizado com sucesso para 1,5298 mm, alinhando-se estreitamente com o alvo desejado de 1,5 mm, garantindo assim a precisão dimensional. Este estudo investigativo sobre a otimização de parâmetros para eletroerosão do material AISI 1045 é extremamente significativo para as indústrias automotiva e aeroespacial que dependem de usinagem de precisão, visto que os parâmetros otimizados de eletroerosão levam a uma maior eficiência, redução do desperdício de material e melhoria da qualidade do produto. Essas descobertas oferecem insights valiosos para o aprimoramento dos processos de eletroerosão, particularmente em setores que exigem geometrias complexas e alta precisão, como a indústria automotiva e aeroespacial.*

Palavras-chave: *Usinagem por Descarga Elétrica; AISI 1045; Otimização Paramétrica; Taxa de Remoção de Material; Taxa de Desgaste do Eletrodo; Rugosidade da Superfície; Tempo de Usinagem; Metodologia de Superfície de Resposta; ANOVA; Raio da Base.*

1. Introduction. - The machining techniques that are generally used in the industry can be categorized into conventional and non-conventional methods. The conventional machining process removes material from a workpiece using mechanical techniques such as cutting, shearing, and abrasion. The techniques used can be milling, grinding, drilling and turning (1). When the conventional machining techniques are applied, hard tools are used to shape the workpiece to the required size and surface finish. Conversely, the non-conventional machining methods use alternative techniques that are dependent on sources of high energy or other methods that can support in removal of material from the workpiece. These methods include water jet machining (2), ultrasonic machining (3) (4), laser cutting (5) (6), electrical discharge machining (EDM) (7) (8) and electrochemical machining (9) (10). The common applications for the non-conventional machining processes are hard materials, complex geometries and those areas where the conventional processes lose their effect. The parts produced are relatively accurate machined flexibly when these techniques are utilized.

There's always a need for usage of versatile materials that can be used for a wide range of applications in which the material should show a balance between toughness, strength and wear resistance. Electric Discharge Machining (EDM) is particularly well-suited for machining AISI 1045 due to its ability to handle hard materials and complex geometries without inducing mechanical stress. AISI 1045 is a medium carbon steel with a moderate carbon content (0.43-0.5%) and is widely used in industries requiring high strength and wear resistance, such as automotive and aerospace. However, its hardness makes it challenging to machine using conventional methods, especially for intricate shapes and tight tolerances. EDM is a contact less process and uses electrical impulses to erode material, making it ideal for such applications. Additionally, EDM provides excellent surface finish quality, reducing the need for post-processing steps like polishing or grinding. These advantages make EDM the preferred choice for machining AISI 1045 in precision-critical applications.

Electrical Discharge Machining (EDM) is particularly well-suited for machining AISI 1045 due to the material's properties and the unique capabilities of the EDM process. AISI 1045, a medium-carbon steel, is known for its good tensile strength and wear resistance, making it a popular choice for components such as gears, shafts, and machinery parts. However, its hardness and toughness can pose challenges for conventional machining methods, especially when intricate shapes or fine surface finishes are required. EDM, being a non-contact machining process that uses electrical discharges to remove material, is ideal for such scenarios. It can efficiently machine hard materials like AISI 1045 without inducing mechanical stress or tool wear, which are common issues in traditional machining. This makes EDM a preferred method for achieving precise geometries and high-quality surface finishes on AISI 1045 components.

There are several industrial applications of AISI 1045 material which includes construction usage, tool and die making, automotives industry and agriculture. In industrial applications, this material is used to make shafts, gears and couplings, bolts and studs, crankshafts and connecting rods etc. In construction applications, its usage comes for those structural components where a balance between strength and toughness is the task. In the dies and tools where wear resistance and medium strength is required, this material is utilized. In automotive industry, this material is used to manufacture axles as well as engine components (11). Similarly, it is used to produce components which are assembled in agricultural machinery. This material has also found its way in the nuclear industry (12).

In EDM process, the manufacturing is carried out via electric discharge to obtain the desired shape. It works on the workpiece as the material is eroded thermally. For usage of EDM on AISI 1045, it is preferable in some circumstances which encompass a number of factors. The need for EDM on this material arises when the geometries are complex as EDM is capable of producing intricate shapes with fine details that are not possible with conventional methods. Also, when thin walls and sharp corners are required, EDM supports prevention of deformation in the components. AISI 1045 is good at heat treatment hardening as it becomes wear resistant at the same time it's a challenge to machine it uses conventional cutting processes (13). EDM is capable to machine this material with minimal tool wear. EDM on AISI 1045 is also needed when there are tight tolerances and high precision to produce exact dimensions in critical parts. After optimizing the input parameters and output responses, this manufacturing procedure reduces the need for final processing steps like polishing or grinding. Since EDM is a non-contact process, deflection of tool and wearing can be eliminated as it happens when processing hard materials conventionally. EDM also has better accessibility and reaches internal cavities where conventional machining process doesn't support.

The advantages of using EDM on AISI 1045 are quite impressive. There isn't any mechanical stress as there isn't any type of direct contact between the electrode and workpiece as EDM is capable to machine hard materials with high accuracy and precision with excellent surface finish due to which multiple and additional process requirements as in non-conventional machining are eliminated (14). The application of EDM on AISI 1045 includes die and mold making for injection molding as well as metal forming and stamping (15). Its's application in tool and die industry for

customized jigs and fixtures preparation is also noticeable (16). It is also used for rapid prototyping where complex geometries are required. It can also be utilized in preparation of surgical instruments and medical implants in medical devices (17). Most importantly, in automotive and aerospace industry, AISI 1045 is the choice for intricate parts manufacturing for engines and also precision components (18).

EDM process has its own set of limitations which are an area of interest for researchers (19). EDM usually has a slower rate when it comes to material removal i.e. MRR thus resulting in higher machining times (Tm). The conventional processes are much faster in terms of material removal rate. Secondly, the initial setup cost of EDM is much higher as compared to conventional subtractive manufacturing techniques. Material should also be electrically conductive in order to be used for EDM. On reviewing the literature, it came to the authors' knowledge that a very limited work has been carried out on AISI 1045 when it comes to die sinking EDM process as most of the research work is carried out with wire EDM (20) or conventional machining processes (21). Haron et al had performed experiment with varying copper electrode diameter (9.5, 12 and 20 mm) and current value (3.5 and 6.5 A) to determine the optimum value of material removal rate (MRR) and electrode wear rate (EWR) (22). Kumar and Agarwal had performed machining parameters optimization for surface roughness in the EDM processing of AISI 1045 (23). There seemed a need to carry out a comprehensive study to determine the effect of various input parameters including current (LV), voltage (HV), pulse on time (Ton) and pulse off time (Toff) and monitor the various output parameters including MRR, EW, machining time (Tm), base radius (R) and machined surface roughness (Ra) and optimize them accordingly. For large scale manufacturers and designers, all output responses like Machining time (Tm), material removal rate (MRR), electrode wear rate (EWR), surface roughness (Ra), base radius (R) are of extreme importance and compromise on any of the responses means major loss in productivity or product quality. Currently there is no single study present at this point of time where the afore mentioned parameters and their output responses have been considered in totality when the EDM process of AISI 1045 is considered (24) (8) (25) (20) (26). This is of great importance for manufacturers in automotive engine manufacturing, dies and mold makers, aerospace industry, bio medical machine manufacturing etc. The current experimental research for optimizing the parameters was carried out in a meticulous setting and results of the study were positive.

2. Materials and methods. -

2.1 Materials. - AISI-1045 is a low-cost alloy suitable for most engineering and construction applications. It is a medium carbon steel with adequate strength and toughness characteristics and is valuable for induction or flame hardened components and can provide a typical surface hardness of up to 58 HRC. The typical applications include construction applications, bolts, axles, connecting rods, pins, rams, studs spindles, ratchets etc.

The authors have used copper electrode as it is a good performer in surface finishing and quality compared to graphite. When using a graphite electrode, increased tool wear and poor surface quality are observed (27). The dielectric used in the experiment is kerosene oil. K., Masoud Pour & S. Ehsan Layegh (2022) have conducted a study to optimize MRR, Ra and surface topography on tool steels including AISI 1045 under the influence of ZnO nanoparticles. The study concluded that the optimized values for input factors AISI 1045 had been achieved using 2 g of the ZnO nanoparticles that had reduced the Ra by 16.66% (18).

In the current research, the experimentation has been carried out in a controlled environment with lower levels of input factors, these resulted in positive output. The results will be discussed in detail in the results section.

The chemical composition of AISI-1045 is listed in Table

Element	%
Carbon (C)	0.45
Manganese (Mn)	0.75
Silicon (Si)	0.25
Sulphur (S)	0.05 max.
Phosphorous (P)	0.05 max.
Iron (Fe)	Balance

Table I. Chemical Composition of AISI 1045.

When transistorized, pulse-type power supplies, either electrolytic or pure were developed, the metallic electrode that became preferable was copper as copper along with specific levels of power supply supports in low burning due to wear. If graphite is consumed in the same setting, the tool wear is high. Moreover, for advanced power supply circuits with polishing performed, copper is compatible. Copper produces a good surface finish due to its structural integrity

compared to the counterpart graphite. This property further resists DC arcing where flushing is poor. On a wire EDM, Female electrodes are commonly utilized in copper for usage in reverse burning punches and cores in the sinker EDM (25) (26).

2.2 Methods. - In this study, the researchers had planned the experiments to optimize the output responses like machining time (Tm), material removal rate (MRR), electrode wear rate (EWR), surface roughness (Ra) and base radius (R) using design of experiments (DOE) and Response Surface Methodology (RSM).

2.2.1 Design of experiments (DOE). - Planning any data collection activities in the face of variability, whether or not the experimenter has complete control, is known as design of experiments (DOE). It entails a group of tests or a sequence of tests in which the input variables of a system or process are purposefully changed. The goal is to methodically monitor and pinpoint the reasons for variations in the output responses (28).

2.2.2 Response Surface Methodology (RSM). - It is a statistical and mathematical method for optimizing processes and determining the correlations between numerous input factors and one or more output replies. It is especially effective for modeling and analyzing issues whose outcomes are influenced by multiple variables. RSM combines experimental design, regression analysis and optimization approach to create a mathematical model (usually a second-order polynomial) that predicts response behavior based on input elements. The method aids in determining ideal conditions for processes and is frequently used in engineering, manufacturing and other sectors to increase efficiency, product quality and performance.

3. Experimental Methodology. - The experimental design was based on the Design of Experiment (DOE) technique, especially a full factorial design. This method enables a thorough examination of the essential effects and interactions among the four selected input parameters: pulse on time (Ton), pulse off time (Toff), current (LV) and voltage (HV). Each of these parameters was examined at two different levels, high and low, allowing for a thorough examination of their effect on output responses. Values of the input parameters are mentioned in the Table .

Factor	Levels	No. of Levels
Workpiece	AISI 1045	1
Pulse on time (T_{on})	4 µs, 6.5µs	2
Pulse off time (T_{off})	5.5 µs, 6.5 µs	2
Current (LV)	30 A, 50 A	2
Voltage (HV)	0.3 V, 0.7 V	2

Table II. Values of input parameters along with levels.

Pulse on time (Ton) was chosen because it directly affects the energy delivered to the workpiece during each pulse. Longer pulse durations result in higher energy input consequently resulting in increased material removal rate but this can also lead to higher electrode wear and surface roughness. In order to optimize all the output lower Ton values (4 µs and 6.5 µs) were selected to minimize electrode wear and reduce excessive heat generation, which is crucial for precision applications. Similarly, pulse off time (Toff) was included because it controls the cooling time between pulses. A slightly higher Toff (5.5 µs and 6.5 µs) was chosen to enhance flushing efficiency, ensuring better debris removal and maintaining process stability. This helps prevent short circuits and improves surface finish. The study avoided very low Toff values, as they could lead to insufficient cooling and debris removal, causing instability in the machining process.

Current (LV) was another critical parameter selected for optimization because it influences the intensity of the electrical discharge. The study chose current levels of 30 A and 50 A to balance power consumption and material removal efficiency. Lower currents (30 A) are more energy-efficient and suitable for fine machining, while higher currents (50 A) increase MRR but may also increase electrode wear and surface roughness. Very high currents were avoided because they could lead to excessive electrode wear and thermal damage, while very low currents might result in insufficient material removal, making the process inefficient. Voltage (HV) was also included because it affects the spark gap and the energy of each discharge. The study selected lower voltage levels (0.3 V and 0.7 V) to reduce thermal damage and improve surface finish. Lower voltages are more suitable for precision machining, as they help achieve finer surface finishes and tighter tolerances. Higher voltages were not considered because they could lead to larger craters on the workpiece surface, increasing surface roughness and reducing dimensional accuracy.

Other parameters, such as electrode material and dielectric fluid, were kept constant to isolate the effects of the primary electrical parameters under investigation. Copper electrodes were chosen because they are known for their good surface finish and lower wear rates compared to graphite electrodes, which tend to produce poorer surface quality and are less suitable for precision applications. Kerosene was selected as the dielectric fluid due to its effectiveness in flushing debris and cooling the workpiece and electrode. Other dielectric fluids, such as deionized water or oil-based fluids, were not considered because kerosene is widely used in EDM processes and provides a good balance between cost and performance. The duty factor, which is the ratio of Ton to the total cycle time, was indirectly controlled by the selection of Ton and Toff. The study did not explicitly vary the duty factor as a separate parameter because it is linked to Ton and Toff. The chosen Ton and Toff values already provided a reasonable range of duty factors (38% to 54%), which were sufficient to study the effects on machining performance. Parameters such as flushing pressure was not varied in this study. Flushing pressure is crucial for debris removal. It was kept constant because the focus was on optimizing electrical parameters rather than mechanical factors. The study assumed a constant flushing pressure that was sufficient to maintain process stability.

Based on these input parameters, basic experimental runs were performed and data of output responses against input factors were recorded. These basic experimental runs are mentioned in Table III. Basic experimental runs for AISI-1045 on Table .

3.1 Workpiece preparation. - The workpieces (Figure) used in these experiments consisted of two grounded blocks, each with dimensions of 100 x 10 x 20 mm, secured in place using dowel pins. Electrode is of copper material (Figure). Dielectric is of kerosene + C10 material.

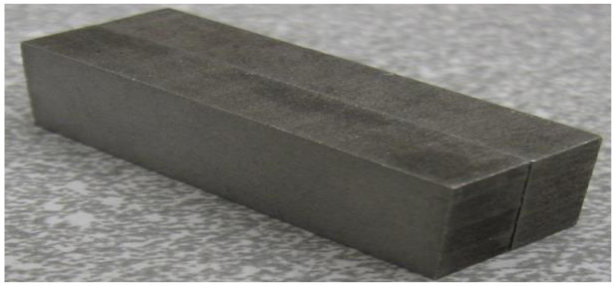

Figure I. Parted Workpiece Snapshot before Machining.

Figure II. Copper Electrode Tip at 17 X prior to Machining.

3.2 Equipment used:

- EDM machine = Genspark E5B1041
- Weighing scale = AND GF-200 with least count of 0.001 g
- Surface roughness tester = Wilson Wolpert CM T2
- Microscope = Stereo microscope with 45X magnification with CMOS chip

EDM machine is available in Figure , weighing scale in Figure , surface roughness tester in Figure and microscope in Figure .

Figure III. Genspark E5B1041.

Figure IV. Precision weighing scale AND GF-200.

Figure V. Surface Roughness Tester WW CM T2.

Figure VI. Stereo microscope.

EWR was calculated using the equation mentioned below in Equation 1:

$$EWR = \frac{Eb - Ea}{Tm} \ (g/\text{min})$$

Equation 1 Equation to calculate electrode wear rate

MRR was calculated using the equation mentioned below in Equation 2:

$$MRR = \frac{Wb - Wa}{Tm} \ (g/\text{min})$$

Equation 2 Equation to calculate material removal rate

3.3 Objectives. - The objectives of this experimental study are as follows:
1. To reduce the machining time (Tm) for AISI 1045 steel via the EDM technique.
2. To improve the material removal rate (MRR) during EDM machining of AISI 1045 steel.
3. To reduce the electrode wear rate (EWR) when treating AISI 1045 steel using EDM.
4. To improve surface roughness (Ra) on AISI 1045 steel with EDM.
5. Minimize variations in the base radius (R) of AISI 1045 steel machined with EDM.

3.4 Analysis of Variance (ANOVA). - The experimental data that was performed on the basis of basic experimental runs as mentioned in Table was examined by using statistical techniques and conclusions were drawn based on the significance of the components and their interactions. A 95% confidence interval was used and factors with the p-values less than 0.05 were considered as significant. The normal plot of standardized effects was used to distinguish between significant and non-significant components, whilst residual plots evaluated the model's fit. After that the model was then refitted by removing the non-significant factors and a revised ANOVA table was created. Now this revised ANOVA table consists of only significant factors and all non-significant factors are eliminated in order to better understand the impact of input factors on output responses. Main effect plot and interaction plots were also created. A high slope in the main effects plot showed significant factors, while non-parallel lines in the interaction plot indicated significant relationships at the factor level. The Response Optimizer tool was used to perform optimization, with targets such as response minimization, maximization or equating established. The desirability function was studied by specifying lower, target and upper bounds, with a desirability (d) value near to 1 indicating that the response is close to the target. The results (Table and Table) produced optimal values for the major factors, their response values and the desirability factor. The findings were validated by replicating the studies and the optimal solutions were put into practice. Detailed experimental results and replicates are available in Appendix 7 and Appendix 8.

4. Results and Discussion. -

4.1 Experimental results and analysis. -

4.1.1 Optimized results for machining time (Tm). - The machining time (Tm) for AISI 1045 was optimized using ANOVA in Minitab in which all the input factors were considered and their interaction with output responses were calculated to determine significant causes to the variation in machining time. The purpose of this investigation was to reduce machining time thereby increasing the efficiency of the EDM process. All detailed graphs and table are present in Appendix 2. Machining pictures of electrode and workpiece are given in Appendix 9 and Appendix 10.

Initially all input parameters like pulse on time (Ton), pulse off time (Toff), current (LV) and voltage (HV) were considered along with their interactions with output response of machining time. Significant factors were identified using p-value and a 0.05 threshold for significance was considered. The p-value is used to determine the statistical significance of each input factor and their interactions. A p-value less than 0.05 indicates that the factor or interaction has a significant effect on the machining time (Tm). The ANOVA Table and normal probability plots (Figure and Figure) and residual plots (Figure and Figure) showed that the input factor i.e. pulse on time (Ton), interaction between pulse on time (Ton) and pulse off time (Toff) (Ton*Toff) and the three-factor interaction between LV, Ton and Toff (LV*Ton*Toff) were statistically significant in terms of their influence on the output response which is machining time. These significant input factors p-values are listed below (Table):

- Ton = 0.000
- Ton*Toff = 0.021
- LV*Ton*Toff = 0.024

The interaction between Ton and Toff is significant because it represents the balance between energy input and cooling time. Longer Ton increases the energy delivered per pulse, leading to higher material removal rates (MRR), but it also generates more heat, which can increase electrode wear and surface roughness. Toff, on the other hand, provides time for cooling and debris removal. The study found that specific combinations of Ton and Toff can optimize MRR while minimizing electrode wear and surface roughness. For example, a longer Ton combined with a slightly longer Toff can enhance material removal efficiency without causing excessive heat buildup or debris accumulation. This interaction highlights the need to carefully balance energy input and cooling to achieve optimal machining performance.

This three-factor interaction is significant because it reflects the combined effect of current, pulse duration, and cooling time on machining performance. Higher current (LV) increases the intensity of the electrical discharge, leading to higher MRR, but it also increases electrode wear and surface roughness. When combined with longer Ton, the energy input is further amplified, which can lead to excessive material removal and thermal damage if not balanced with an appropriate Toff. The study found that optimizing this three-factor interaction can significantly reduce machining time

(Tm) while maintaining acceptable levels of electrode wear and surface finish. For instance, a higher current combined with longer Ton and a slightly longer Toff can maximize material removal efficiency while ensuring sufficient cooling and debris removal. This interaction underscores the importance of coordinating current, pulse duration, and cooling time to achieve a balance between productivity and quality.

The model was then refitted by eliminating non-significant factors as mentioned in Table . The revised model in main effect plot (Figure) and residual plot (Figure) showed that both the model and the major factors Ton, Ton*Toff and LV*Ton*Toff were still significant.

For machining time optimization, the target value was set to '0', while the upper bound value was set at 343 seconds, which reflected the shortest observed machining time during the experiment. The desirability function in Figure was used to calculate the optimized values of the machining time. The desirability function's target was set at '0' for machining time to minimize processing duration, as shorter machining times are desirable for industrial efficiency. The resulting desirability value (d = 0) suggested that the response (Tm) was far from the target value, implying that the target of '0' was unsuitable for this particular response. The response was much below the highest limit (343 seconds), resulting in a lower desirability. If the target had been set closer to 600 seconds with a larger upper bound (e.g., 1000 seconds), the desirability would have approached one, indicating a greater alignment with the optimization goal.

For the optimized value of output response of Tm, following values of input factors came out to be significant where lowest machining time was achieved.
Current (LV) = 30 A; Pulse on time (Ton) = 6.5 µs and pulse off time (Toff) = 5.0 µs.
The minimal machining time for these optimized parameters was found to be 623.2083 seconds.

Significant input factors that were calculated for output response of machining time shows both direct and inverse relation Tm. Pulse on time (Ton) was found to be directly proportional to Tm and this shows that as Ton will increase machining time will also increase which is understandable as longer Ton increases the energy input each for pulse thus increasing the machining time. On the other hand, the interaction between Ton and pulse off time (Toff) (Ton*Toff) showed a complex relationship because certain combinations of these two parameters resulted in shorter machining times. Furthermore, the three-factor interaction (LV*Ton*Toff) showed that when current is considered along with pulse on and off times overall machining time will reduce because more material will be removed from workpiece surface as current is higher along with increased pulse duration. These interactions show that the Tm is highly sensitive to both individual factors and their interactions and this suggests that the input parameters interactions must be carefully adjusted to get the best and optimized results.

4.1.2 Optimized results for material removal rate (MRR). - The optimization of material removal rate (MRR) for AISI 1045 was carried out using ANOVA in Minitab. All input factors, including pulse on time (Ton), pulse off time (Toff), current (LV) and voltage (HV) were considered with the goal of maximizing MRR. Significant factors were identified by examining the p-values in the ANOVA table, with a significance threshold of 0.05. All tables and figures are present in Appendix 3.

From the ANOVA Table and the normal probability plot (Figure and Figure) and residual plot (Figure and Figure), Ton and the interaction between Ton and Toff (Ton*Toff) were considered to be significant factors that are affecting MRR. The p-values of significant factors are listed below (Table):

- Ton = 0.000
- Ton*Toff = 0.034

Following this, the model was refitted by excluding non-significant factors and focusing only on Ton and Ton*Toff interaction as mentioned in Table .

Now the main effects plot in Figure and interaction plot in Figure for MRR were prepared. The main effects plot showed a steep slope for means showing the importance of Ton and Ton*Toff. Additionally, the interaction plot revealed non-parallel lines, highlighting the significant interaction between Ton and Toff in calculating MRR.

The desirability function is a widely used approach in multi-objective optimization to convert multiple response variables into a single composite desirability score, ranging from 0 (least desirable) to 1 (most desirable). In the optimization of Material Removal Rate (MRR) for EDM machining of AISI 1045, the desirability function was employed to determine the best combination of pulse on time (Ton) and pulse off time (Toff) that maximizes MRR while ensuring process stability and efficiency. For the optimization of MRR, the target value was set to '1', while the

lower bound was set at 0.0304 g/min, which represented the maximum observed MRR during the experiment. The desirability function (Figure) was used to assess how closely the optimized values aligned with the target. A desirability value of d = 0 indicated that the response (MRR) was far from the set target of '1', suggesting that this target was unrealistic for the given response. The response was much lower than the upper limit (0.0304 g/min), resulting in a lower desirability. Had the target been set closer to 0.02 g/min with a lower upper limit (e.g., 0.001 g/min), the desirability would have approached one, indicating better alignment with the optimization objective.

The optimization process resulted in the following significant input factor values for maximizing MRR:

- Ton (Pulse on time): 6.5 µs
- Toff (Pulse off time): 5.5 µs

On these optimized settings, the maximum MRR achieved was 0.0173 g/min, which reflects the optimized material removal under the given experimental conditions. This optimization highlights the critical influence of both Ton and its interaction with Toff on the material removal rate during EDM machining of AISI 1045 steel.

Ton and MRR are directly proportional to each other because higher energy cycle will lead to more material removed from the workpiece leading to higher MRR. While on the other hand interaction between Ton and Toff is complex in nature. As Ton increased material removal rate, optimal time is needed so that the workpiece temperature of that particular section cools down but not completely solidified between pulses ensuring efficient material removal.

4.1.3 Optimized results for electrode wear rate (EWR). - The analysis of Electrode Wear Rate (EWR) for AISI 1045 was carried out using ANOVA in Minitab. All input factors were considered including pulse on time (Ton), pulse off time (Toff), current (LV) and voltage (HV). The objective of this analysis was to minimize the EWR thereby increasing electrode life and improving overall machining efficiency. Significant factors affecting EWR were identified by evaluating the p-values from the ANOVA table, with a threshold of 0.05 indicating statistical significance. All detailed graphs and table are present in Appendix 4.

ANOVA Table , normal probability plot (Figure) and residual plot (Figure and Figure) showed that Ton was the only significant factor affecting EWR and its p-value was 0.001 (Table). Now the model was refitted by excluding all the non-significant factors and only Ton as the primary influencing variable. The p-values in the revised ANOVA Table confirmed that the refitted model, as well as the factor Ton, were statistically significant in determining the variation in EWR.

Now the main effects plot (Figure) and interaction plot (Figure) were prepared for EWR. The main effects plot showed a steep slope thus confirming the significance of Ton in influencing EWR. The interaction plot further showed non-parallel lines meaning that interactions among other factors did not contribute significantly to EWR. This established the fact that Ton as the key variable in this analysis.

For optimization of EWR, the target value was set to '0', while the upper bound value was established at 0.00551 g/min, which represented the minimum observed EWR in the experiments. The desirability function (Figure) was utilized to determine how closely the optimized values aligned with the desired target. A desirability value of d = 0 showed that the response (EWR) was far from the set target of '0', highlighting that this target was not practically attainable for this specific response. The actual EWR was much below the upper bound, resulting in a lower desirability score. If the target had been set closer to 0.009 g/min and the upper bound set to a larger value (e.g., 0.01 g/min), the desirability would have approached one, signaling better alignment with the optimization goal.

Through the optimization process, the significant input factor (Ton) was determined to have the following optimized value for minimizing EWR:

- Pulse on time (Ton) = 4.0 µs

With this optimized Ton value, the minimum EWR was calculated to be 0.0088 g/min, reflecting the ideal electrode wear rate achievable under these experimental conditions. This optimization highlights the critical role of Ton in controlling electrode wear, as shorter pulse durations reduce electrode erosion, lowering the wear rate during EDM machining of AISI 1045 steel. Optimized results for surface roughness (Ra)

The surface roughness (Ra) for AISI 1045 was analyzed using ANOVA in Minitab. The goal was to minimize the surface roughness, thus improving the surface quality of the workpiece. All input factors, including voltage (HV), pulse on time (Ton), pulse off time (Toff) and current (LV) were initially considered to identify significant input factors

that can have possible impact on the output response i.e. surface roughness. The analysis was conducted by assessing p-values from the ANOVA table, with a significance threshold set at 0.05. All detailed graphs and table are present in Appendix 5.

ANOVA table (Table), normal probability plot (Figure and Figure) and residual plot (Figure and Figure) showed that the three-way interaction between HV, Ton and Toff (HV*Ton*Toff) was a significant factor affecting surface roughness (Ra) and its p-value came out to be 0.039 (Table). Now the model was refitted (Table) by removing non-significant factors, retaining only this three-way interaction as a significant input factor. The p-values from the revised ANOVA table confirmed that the refitted model and the interaction HV*Ton*Toff remained significant for surface roughness.

The interaction between voltage, Ton, and Toff is significant because it influences the spark gap and the energy distribution during the EDM process. Lower voltages (HV) reduce the spark gap and the energy of each discharge, leading to finer surface finishes but potentially lower MRR. When combined with longer Ton, the energy input is increased, which can improve MRR but may also increase surface roughness if not balanced with an appropriate Toff. The study found that optimizing this interaction can minimize surface roughness (Ra) by controlling the energy delivered to the workpiece. For example, a lower voltage combined with longer Ton and a slightly longer Toff can achieve a smoother surface finish by reducing the size of the craters formed during machining. This interaction highlights the need to carefully adjust voltage, pulse duration, and cooling time to achieve the desired surface quality.

Now the main effects plot (Figure) and interaction plot (Figure) were prepared. The main effects plot showed steep slopes of the means, proving the importance of the HV*Ton*Toff interaction on surface roughness. Additionally, the interaction plot exhibited non-parallel lines, confirming that the interaction between these three factors had a significant impact on the output response of Ra.

For optimizing Ra, the target value was set to '0' and the upper bound value was fixed at 0.01 mm, representing the minimum observed value of surface roughness in the experiment. The desirability function (Figure) was applied to check how closely the optimized values aligned with the desired target. A desirability value of d = 0 indicated that the response (Ra) was far from the target of '0', suggesting that the target was not feasible for this response. The response was much lower than the upper bound (0.01 mm), resulting in lower desirability. If the target had been set closer to 0.025 mm, with a larger upper bound (e.g., 0.05 mm), the desirability would have approached one, indicating a more realistic optimization scenario.

Based on this optimization, the following input factors were identified as the optimal values for minimizing surface roughness (Ra):

- Voltage (HV) = 0.70 V
- Pulse on time (Ton) = 6.50 µs
- Pulse off time (Toff) = 6.50 µs

With these optimized values, the minimum surface roughness (Ra) achieved was calculated to be 0.0253 mm. This showed the effectiveness of optimizing these specific parameters for improving surface quality. The interaction of HV, Ton and Toff shows that when voltage and pulse times are balanced, the energy delivered during the machining process becomes more controlled, leading to smaller crater formation and resulting in a smoother surface finish and reduced roughness.

4.1.4 Optimized results for base radius (R). - The base radius (R) for AISI 1045 steel was analyzed using ANOVA in Minitab. The goal was to optimize the output response i.e. base radius. All input factors were considered initially including pulse on time (Ton), pulse off time (Toff) and current (LV. The p-values from the ANOVA Table were assessed, with a threshold of 0.05 for significance. All detailed graphs and table are present in Appendix 6.

Both the ANOVA table (Table), normal probability plot (Figure and Figure) showed that the interaction between LV and Toff (LV*Toff), as well as the three-factor interaction LV, Ton and Toff (LV*Ton*Toff) were significant factors effecting the base radius. The p-values of significant factors are listed below (Table):

- LV*Toff = 0.037
- LV*Ton*Toff = 0.010

The interaction between current and Toff is significant because it reflects the relationship between the intensity of the electrical discharge and the cooling time. Higher currents increase the energy of each spark, leading to higher MRR

but also higher electrode wear and surface roughness. When combined with a longer Toff, the cooling time is increased, which can help mitigate the thermal effects of higher currents. The study found that this interaction is particularly important for achieving dimensional accuracy (base radius, R). For example, a higher current combined with a slightly longer Toff can improve material removal efficiency while ensuring sufficient cooling to maintain dimensional accuracy. This interaction emphasizes the need to balance current and cooling time to achieve both productivity and precision.

Now the model (Table) was refitted by eliminating the non-significant factors thus keeping only the significant interactions. The p-values from the refitted ANOVA table confirmed that the revised model and these significant interactions remained statistically valid for optimizing the base radius (R).

After identifying the significant factors, the main effects plot (Figure) and interaction plot (Figure) were generated. The main effects plot displayed a steep slope of means, emphasizing the importance of the interactions between LV, Ton and Toff on the base radius. Similarly, the interaction plot showed non-parallel lines, confirming that the interactions between current, pulse on time and pulse off time had a significant impact on the output response (R).

For optimization, the target value for the base radius was set at 1.5 mm, with an upper bound of 1.55 mm and a lower bound of 1.45 mm, reflecting the desired dimensions of the electrode. The desirability function (Figure) was applied to assess the closeness of the optimized values to the target. A desirability value of d = 0.40233 indicated that the response (R) was about 40% closer to the target, showing a moderate alignment with the desired value of 1.5 mm.
Based on the optimization analysis, the following input parameters were determined to be optimal for achieving the desired base radius:

- LV (Current): 30 A
- Ton (Pulse on time): 6.5 µs
- Toff (Pulse off time): 5.5 µs

With these optimized input values, the base radius (R) was calculated to be 1.5298 mm, indicating a close match to the target radius. The interactions between LV, Ton and Toff show that when the current and pulse times are balanced, the material removal process is controlled more precisely thus enabling the electrode to achieve a base radius near the desired dimensions. The non-parallel lines in the interaction plot further reinforce that these factors do not operate independently, but in combination, they significantly influence the output response.

5. Conclusions. - This study aimed to optimize the electrical discharge machining (EDM) process for AISI 1045 steel. A strict focus was on optimization of key output parameters such as machining time (Tm), material removal rate (MRR), electrode wear rate (EWR), surface roughness (Ra) and base radius (R) by. By employing ANOVA analysis in Minitab, significant input factors, including pulse on time (Ton), pulse off time (Toff), current (LV) and voltage (HV), along with their interactions, were systematically analyzed to identify their impact on the five output responses mentioned above. The results of this investigative study provide key insights into how each of these input parameters impact on the five output responses, both individually and in combination, thereby contributing to a more efficient and controlled manufacturing process with the final product being manufactured in less time with reduced material wastages of both workpiece and electrodes and having excellent surface finish. Machining pictures of electrode and workpiece are given in Appendix 9 and Appendix 10.

The optimization of machining time revealed that pulse on time (Ton), its interaction with pulse off time (Ton*Toff) and the three-factor interaction between current, pulse on and pulse off times (LV*Ton*Toff) were the most significant factors affecting Tm. The optimized values of Ton = 6.5 µs, Toff = 5.0 µs and LV = 30A resulted in a minimal machining time of 623.2083 seconds. This showed that while Ton is directly proportional to machining time, specific interactions with Toff and LV can lead to significant reductions in machining time by increasing material removal efficiency.

Similarly, the optimization of the material removal rate (MRR) showed that Ton and the Ton*Toff interaction were significant factors. The optimized parameters, Ton = 6.5 µs and Toff = 5.5 µs, resulted in a maximum MRR of 0.0173 g/min. The relationship between Ton and MRR was found to be directly proportional. This means that with longer pulse durations and higher energy input will lead to more material removal. However, the interaction with Toff required precise timing to ensure that sufficient material was removed without cooling down or solidifying between pulses thus showing the complexity of achieving maximum MRR.

Electrode wear rate (EWR) optimization highlighted that pulse on time (Ton) was the sole significant factor influencing EWR. The optimized value of Ton = 4.0 µs yielded a minimal EWR of 0.0088 g/min, showcasing that shorter pulse durations reduce electrode erosion and prolong electrode life. This result emphasizes the importance of balancing Ton to minimize wear while maintaining machining efficiency.

Surface roughness (Ra) analysis revealed that the interaction between voltage (HV), Ton and Toff (HV*Ton*Toff) was critical in determining surface quality. The optimized values of HV = 0.7V0 V, Ton = 6.5 µs and Toff = 6.5 µs achieved a minimum Ra of 0.0253 mm. This optimization demonstrated that fine control over these interactions reduces crater formation during machining, leading to smoother surface finishes.

Lastly, the base radius (R) optimization showed that the interaction between current (LV) and pulse off time (Toff) (LV*Toff), as well as the three-factor interaction between LV, Ton and Toff (LV*Ton*Toff), were significant in achieving the desired base radius. The optimized values of LV = 30A A, Ton = 6.5 µs and Toff = 5.5 µs resulted in a base radius of 1.5298 mm, closely aligning with the target of 1.5 mm. These findings demonstrate that the precise adjustment of current and pulse timing significantly enhances the dimensional accuracy of the electrode.

In conclusion, this research provides a comprehensive optimization framework for EDM machining of AISI 1045 steel, addressing the critical parameters that influence machining efficiency, quality and precision. By understanding the complex interactions between input parameters, this study offers valuable guidelines for achieving desired machining outcomes while minimizing defects and inefficiencies. The application of these findings in industrial EDM processes can lead to significant improvements in productivity, material usage and overall machining quality.

6. Limitations of the study. - The study has several limitations, including its focus on only four input parameters (Ton, Toff, LV, HV) and AISI 1045 steel, which limits its applicability to other materials and conditions. It did not explore factors like flushing pressure, electrode geometry, or dielectric fluid variations, nor did it consider surface integrity aspects such as recast layer thickness or residual stresses. The experiments were conducted under controlled laboratory conditions, potentially limiting real-world applicability, and the reliance on statistical methods like RSM may not capture complex, non-linear interactions. Additionally, the study did not address economic or environmental impacts, such as cost-effectiveness or the use of kerosene as a dielectric fluid, nor did it compare EDM with other machining methods. These limitations suggest areas for future research to enhance the study's robustness and industrial relevance.

References

[1] *A Review of Recent Application of Machining Techniques, based on the Phenomena of CNC Machining Operations.* I.P. Okokpujie, C.A. Bolu, O.S. Ohunakin, E.T. Akinlabi, D.S. Adelekan. s.l. : Elsevier, 2019, Procedia Manufacturing, Vol. 35, pp. 1054-1060. ISSN 2351-9789.

[2] *Improving the machining performance of polymer hybrid composite by abrasive water jet machining for precise machining.* Kumar, K. Nirmal, and P. Dinesh Babu. s.l. : Springer Nature, 2024, Arabian Journal for Science and Engineering. 2191-4281.

[3] *Ultrasonic machining: a case study.* Gilmore, Randy. 1-2, s.l. : Elsevier, 1991, Journal of Materials Processing Technology, Vol. 28, pp. 139-148. ISSN 0924-0136.

[4] *Mechanical behavior of carbon fiber-reinforced plastic during rotary ultrasonic machining.* Abdelkader Slimane, Mohammed Chaib, Sidahmed Slimane, Sidahmed Dahmane, Anas Abderrahmane Lahouel, Ahmed Guelailia, Kaddour Bahram, Said Kebdani & Benattou Bouchouicha. 11, s.l. : Springer Nature, 2024, The International Journal of Advanced Manufacturing Technology, Vol. 130, pp. 5345-5357. 1433-3015.

[5] *A comprehensive review of studying the influence of laser cutting parameters on surface and kerf quality of metals.* Muhammad Alsaadawy, Montasser Dewidar, Ahmed Said, Ibrahem Maher & Taher A. Shehabeldeen. 3, s.l. : Springer Nature, 2024, The International Journal of Advanced Manufacturing Technology, Vol. 130, pp. 1039-1074.

[6] *Innovation Study for Laser Cutting of Complex Geometries with Paper Materials.* A. Happonen, A. Stepanov, H. Piili, A. Salminen. s.l. : Elsevier, 2015, Physics Procedia, Vol. 78, pp. 128-137. ISSN 1875-3892.

[7] *Electric Discharge Machining of Ti6Al4V ELI in Biomedical Industry: Parametric Analysis of Surface Functionalization and Tribological Characterization.* Farooq, Muhammad Umar, Saqib Anwar, Haider Ali Bhatti, M. Saravana Kumar, Muhammad Asad Ali, and Muhammad Imam Ammarullah. 12, s.l. : MDPI, 2023, Materials, Vol. 16. 1996-1944.

[8] *Optimization design for die-sinking EDM process parameters employing effective intelligent method.* Van Tron Tran, Minh Huy Le,Minh Thai Vo,Quoc Trung Le,Van Huong Hoang,Ngoc-Thien Tran,Van-Thuc Nguyen,Thi-Anh-Tuyet Nguyen,Hoai Nam Nguyen,Van Thanh Tien NguyenORCID Icon &Thanh Tan Nguyen. 2, s.l. : Taylor & Francis, 2023, Cogent engineering, Vol. 10.

[9] *Experimental Study on Electrochemical Machining with Electrolyte Confined by Absorption Material.* Wataru Natsu, Junfeng He, Yu Iwanaga. s.l. : Elsevier, 2020, Procedia CIRP, Vol. 87, pp. 263-267.

[10] *A review on recent achievements and challenges in electrochemical machining of tungsten carbide.* Mohammed Asmael, Amin Memarzadeh. 1, s.l. : Queens University Belfast, 2023, Archives of Advanced Engineering Science, Vol. 2, pp. 1-23.

[11] *To Study the Effect of Process Parameters for Minimum Surface Roughness of Cylindrical Grinded AISI 1045 Steel.* Singh, T., Goyal, K., Kumar, P. 3, s.l. : Horizon Research Publishing Corporation, 2014, Manufacturing Science and Technology, Vol. 2, pp. 56-61.

[12] *Surface texturing of the carbon steel AISI 1045 using femtosecond laser in single pulse and scanning regime.* Stašić J, Gaković B, Perrie W, Watkins K, Petrović S, Trtica M. 1, s.l. : Elsevier, 2011, Applied Surface Science, Vol. 258, pp. 290-296. ISSN 0169-4332.

[13] *A Review of Electrode Manufacturing Methods for Electrical Discharge Machining: Current Status and Future Perspectives for Surface Alloying.* Garba, E., et al. 9, s.l. : MDPI, 2023, Machines, Vol. 11. 906.

[14] *Experimental Investigations of Surface Modification of AISI 1045 Die Steel by Electro Discharge Machining Process.* Harjot Singh, S.S. Banwait. 4, s.l. : Science and Education Publishing Co., 2016, American Journal of Mechanical Engineering, Vol. 4, pp. 131-141.

[15] *Prediction and optimization of performance measures in electrical discharge machining using rapid prototyping tool electrodes.* Mahapatra, Anshuman Kumar Sahu & Siba Sankar. s.l. : Springer Nature, 2021, Journal of Intelligent Manufacturing, Vol. 32, pp. 2125-2145.

[16] *Reviewing performance measures of the die-sinking electrical discharge machining process: challenges and future scopes.* Shastri, R.K., et al. 384, s.l. : MDPI, 2022, Nanomaterials, Vol. 12.

[17] *Process optimization for rapid manufacturing of complex geometry electrical discharge machining electrode.* Singh J, Pandey PM. 1, s.l. : Sage Journals, 2020, Proceedings of the Institution of Mechanical Engineers, Part C: Journal of Mechanical Engineering Science, Vol. 231, pp. 66-81.

[18] *Influence of ZnO nanoparticle addition and spark peak current on EDM process of AISI 1045, AISI 4140, and AISI D3: MRR, surface roughness, and surface topography.* K., Masoud Pour & S. Ehsan Layegh. s.l. : Springer Nature, 2022, The International Journal of Advanced Manufacturing Technology , Vol. 122, pp. 3703-3724.

[19] *Electrical Discharge Machining (EDM): A Review.* Banu, A., & Ali, M. Y. 1, s.l. : Deer Hill Publications, 2016, International Journal of Engineering Materials and Manufacture, Vol. 1, pp. 3-10. E-ISSN: 0128-1852.

[20] *Wire EDM process optimization for machining AISI 1045 steel by use of Taguchi method, artificial neural network and analysis of variances.* Ahmed A. A. Alduroobi, Alaa M. Ubaid, Maan Aabid Tawfiq & Rasha R. Elias. 6, s.l. : Springer Nature, 2020, International Journal of System Assurance Engineering and Management , Vol. 11, pp. 1314-1338. 0976-4348.

[21] *Study on AISI1045 material for various applications: an over view.* Vishnuja, U., Bhaskar, GB. 2, s.l. : Research India Publivcations, 2018, International Journal of Engineering and Manufacturing, Vol. 8, pp. 125-144. ISSN 2249-3115.

[22] *Investigation on the influence of machining parameters when machining tool steel using EDM.* C.H. Che Haron, B.Md. Deros, A. Ginting, M. Fauziah. 1, s.l. : Elsevier, 2001, Journal of Materials Processing Technology, Vol. 116, pp. 84-87.

[23] *Optimization of Machining Parameters for Surface Roughness in EDM of AISI 1045 Based on Taguchi Technique.* Agarwal, Subodh Kumar and Sanjay. Vancouver, British Columbia, Canada : ASME, 2012. ASME International Mechanical Engineering Congress & Exposition. Vol. 3. ISBN: 978-0-7918-4427-4.

[24] *Optimization of wire electric discharge machining (WEDM) process parameters for AISI 1045 medium carbon steel using Taguchi design of experiments.* Zaman, Uzair Khaleeq uz, Usman Ahmed Khan, Shahid Aziz, Aamer Ahmed Baqai, Sajid Ullah Butt, Danish Hussain, Ali Siadat, and Dong Won Jung. 21, s.l. : MDPI, 2022, Materials, Vol. 15. 7846.

[25] *Variation of surface roughness on electrical discharge machining die sinking caused of different electrode material, current, and on Time.* Darsin, M., Y. Hermawan, and A. Rachmat. Bali, Indonesia : Asian Federation of Biotechnology, 2011. 12th International Conference on Quality in Research. pp. 956-961. ISSN 114-1284.

[26] *Application of Response Surface Methodology For Determining MRR and TWR Model In Die Sinking EDM of AISI 1045 Steel.* M. B. Patel, P. K. Patel, J. B. Patel, B. B. Patel. 6, 2012, International Journal of Engineering Research and Applications, Vol. 2, pp. 1227-1231. ISSN: 2248-9622.

[27] *Analysis of material removal rate and electrode wear in sinking EDM roughing strategies using different graphite grades.* F Klocke, M Schwade, A Klink, D Veselovac. [ed.] J.-P. Kruth B. Lauwers. Leuven, Belgium : Elsevier, 2013. Proceedings of the Seventeenth CIRP Conference on Electro Physical and Chemical Machining (ISEM). Vol. 6, pp. 163-167. ISSN 2212-8271.

[28] *Modeling and analysis of MRR, EWR and surface roughness in EDM milling through response surface methodology.* Khan, A.K.M. Asif Iqbal and Ahsan Ali. 4, s.l. : Science Publications, 2010, American Journal of Engineering and Applied Sciences, Vol. 3, pp. 611-619. ISSN 1941-7020 .

Appendix 1

RUN	LV	HV	PULSE ON TIME	PULSE OFF TIME
1	0.3	30	4	5.5
2	0.7	30	4	5.5
3	0.3	50	4	5.5
4	0.7	50	4	5.5
5	0.3	30	6.5	5.5
6	0.7	30	6.5	5.5
7	0.3	50	6.5	5.5
8	0.7	50	6.5	5.5
9	0.3	30	4	6.5
10	0.7	30	4	6.5
11	0.3	50	4	6.5
12	0.7	50	4	6.5
13	0.3	30	6.5	6.5
14	0.7	30	6.5	6.5
15	0.3	50	6.5	6.5
16	0.7	50	6.5	6.5

Table III. Basic experimental runs for AISI-1045

Appendix 2

Factorial Fit: Tm versus HV, LV, Ton, Toff

Estimated Effects and Coefficients for Tm (coded units)

Term	Effect	Coef	SE Coef	T	P
Constant		845.6	24.05	35.16	0.000
HV	23.5	11.7	24.05	0.49	0.629
LV	-60.8	-30.4	24.05	-1.26	0.215
Ton	-261.0	-130.5	24.05	-5.43	0.000
Toff	21.0	10.5	24.05	0.44	0.666
HV*LV	-7.5	-3.8	24.05	-0.16	0.876
HV*Ton	-29.2	-14.6	24.05	-0.61	0.548
HV*Toff	-1.0	-0.5	24.05	-0.02	0.984
LV*Ton	-76.0	-38.0	24.05	-1.58	0.124
LV*Toff	85.6	42.8	24.05	1.78	0.085
Ton*Toff	113.3	56.6	24.05	2.36	0.025
HV*LV*Ton	-19.5	-9.8	24.05	-0.41	0.687
HV*LV*Toff	21.0	10.5	24.05	0.44	0.665
HV*Ton*Toff	-40.5	-20.2	24.05	-0.84	0.407
LV*Ton*Toff	-110.4	-55.2	24.05	-2.29	0.028
HV*LV*Ton*Toff	-53.8	-26.9	24.05	-1.12	0.272

S = 166.624 R-Sq = 61.28% R-Sq(adj) = 43.13%

Analysis of Variance for Tm (coded units)

Source	DF	SeqSS	Adj SS	Adj MS	F	P
Main Effects	4	873413	873413	218353	7.86	0.000
2-Way Interactions	6	322167	322167	53694	1.93	0.105
3-Way Interactions	4	175730	175730	43932	1.58	0.203
4-Way Interactions	1	34723	34723	34723	1.25	0.272
Residual Error	32	888437	888437	27764		
Pure Error	32	888437	888437	27764		
Total	47	2294469				

Unusual Observations for Tm

Obs	StdOrder	Tm	Fit	SE Fit	Residual	St Resid
9	9	495.00	821.67	96.20	-326.67	-2.40R
36	36	1231.00	907.00	96.20	324.00	2.38R

R denotes an observation with a large standardized residual.

Table IV. ANOVA Table of Tm for AISI-1045 considering all factors.

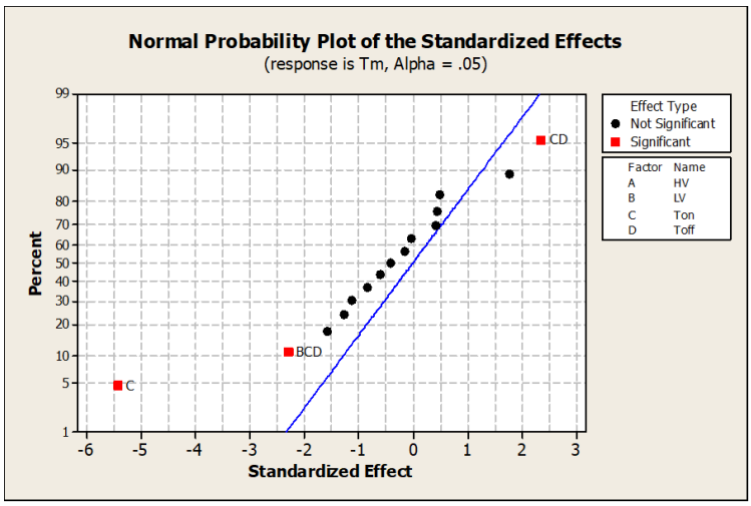

Figure VII. Normal Probability Plot of the standardized effects of Tm for AISI-1045 considering all factors.

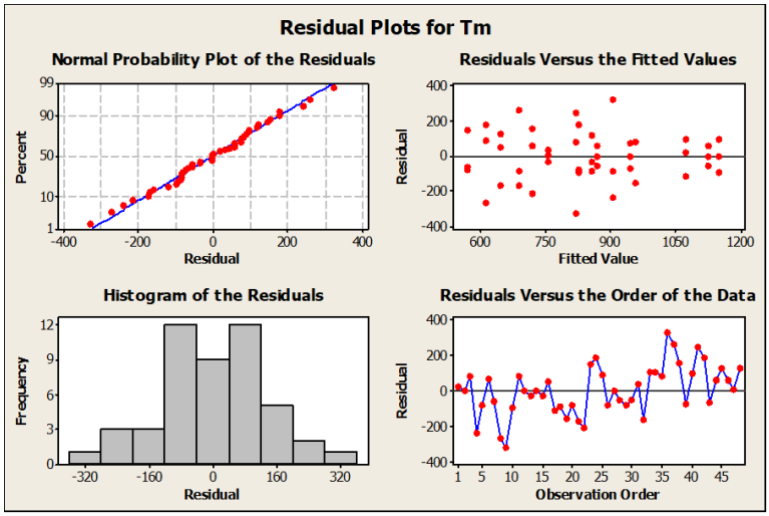

Figure VIII. Residual Plot of Tm for AISI-1045 considering all factors.

Factorial Fit: Tm versus LV, Ton, Toff

Estimated Effects and Coefficients for Tm (coded units)

Term	Effect	Coef	SE Coef	T	P
Constant		845.6	23.65	35.76	0.000
LV	-60.8	-30.4	23.65	-1.29	0.206
Ton	-261.0	-130.5	23.65	-5.52	0.000
Toff	21.0	10.5	23.65	0.44	0.660
Ton*Toff	113.3	56.6	23.65	2.40	0.021
LV*Ton*Toff	-110.4	-55.2	23.65	-2.33	0.024

S = 163.841 R-Sq = 50.86% R-Sq(adj) = 45.01%

Analysis of Variance for Tm (coded units)

Source	DF	Seq SS	AdjSS	MS	F	P
Main Effects	3	866810	866810	288937	10.76	0.000
2-Way Interactions	1	154020	154020	154020	5.74	0.021
3-Way Interactions	1	146192	146192	146192	5.45	0.024
Residual Error	42	1127448	1127448	26844		
Lack of Fit	2	157216	157216	78608	3.24	0.050
Pure Error	40	970233	970233	24256		
Total	47	2294469				

Unusual Observations for Tm

Obs	StdOrder	Tm	Fit	SE Fit	Residual	St Resid
4	4	668.00	1022.80	59.92	-354.80	-2.33R
9	9	495.00	942.40	55.34	-447.40	-2.90R

R denotes an observation with a large standardized residual.

Estimated Coefficients for Tm using data in uncoded units

Term	Coef
Constant	3833.95
LV	7.22155
Ton	-648.183
Toff	-454.867
Ton*Toff	103.663
LV*Ton*Toff	-0.325750

Table V. ANOVA Table of Tm for AISI-1045 considering significant factors.

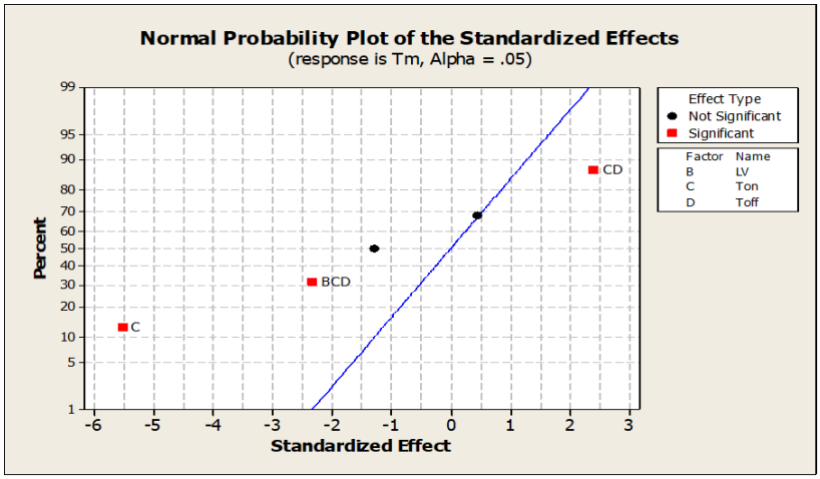

Figure IX. Normal Probability Plot of the standardized effects of Tm for AISI-1045 considering significant factors.

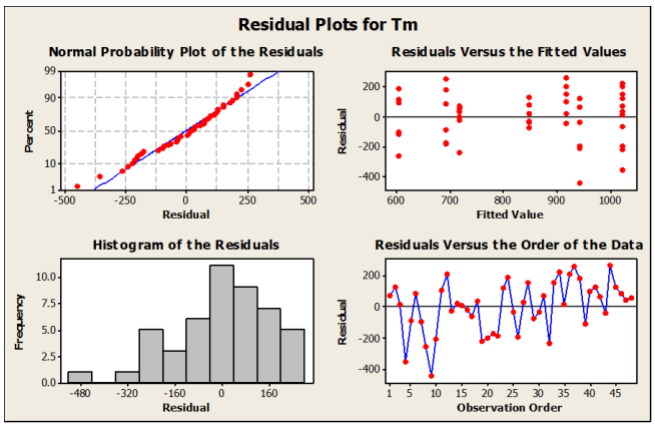

Figure X. Residual Plot of Tm for AISI-1045 considering all factors.

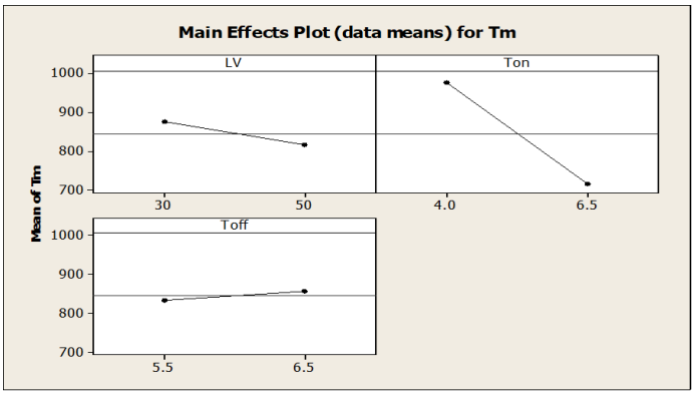

Figure XI. Main Effects Plot of Tm for AISI-1045 considering significant factors.

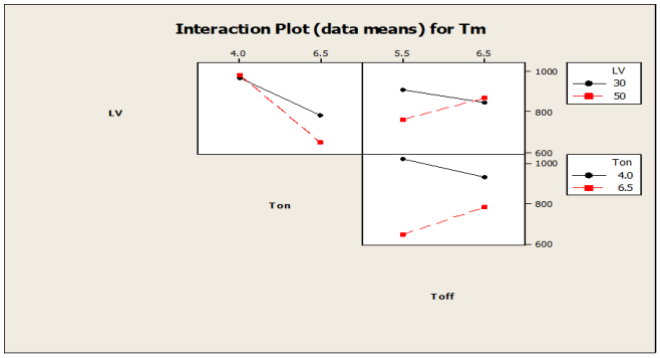

Figure XII. Residual Plot of Tm for AISI-1045 considering Ton & LV.

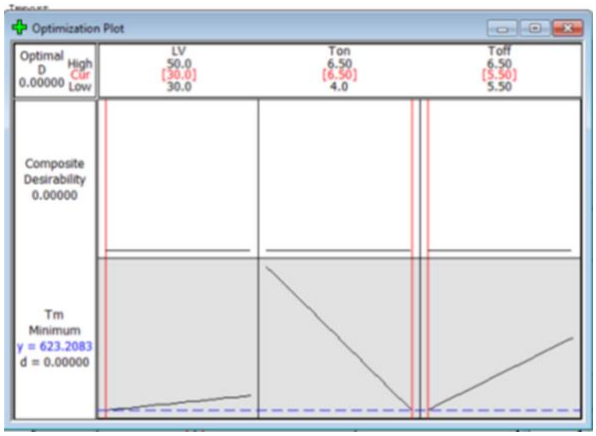

Figure XIII. Optimization Plot of Tm for AISI-1045 for significant factors

Appendix 3

Factorial Fit: MRR versus HV, LV, Ton, Toff

Estimated Effects and Coefficients for MRR (coded units)

Term	Effect	Coef	SE Coef	T	P
Constant		0.012883	0.000575	22.41	0.000
HV	0.000160	0.000080	0.000575	0.14	0.890
LV	0.001598	0.000799	0.000575	1.39	0.174
Ton	0.004607	0.002304	0.000575	4.01	0.000
Toff	-0.001590	-0.000795	0.000575	-1.38	0.176
HV*LV	0.000896	0.000448	0.000575	0.78	0.441
HV*Ton	0.000844	0.000422	0.000575	0.73	0.468
HV*Toff	-0.000010	-0.000005	0.000575	-0.01	0.993
LV*Ton	0.001988	0.000994	0.000575	1.73	0.093
LV*Toff	-0.001694	-0.000847	0.000575	-1.47	0.151
Ton*Toff	-0.002541	-0.001271	0.000575	-2.21	0.034
HV*LV*Ton	0.000405	0.000202	0.000575	0.35	0.727
HV*LV*Toff	0.000083	0.000041	0.000575	0.07	0.943
HV*Ton*Toff	0.000814	0.000407	0.000575	0.71	0.484
LV*Ton*Toff	0.000966	0.000483	0.000575	0.84	0.407
HV*LV*Ton*Toff	0.000795	0.000397	0.000575	0.69	0.495

S = 0.00398335 R-Sq = 50.71% R-Sq(adj) = 27.60%

Analysis of Variance for MRR (coded units)

Source	DF	Seq SS	Adj SS	Adj MS	F	P
Main Effects	4	0.00031597	0.00031597	0.00007899	4.98	0.003
2-Way Interactions	6	0.00017753	0.00017753	0.00002959	1.86	0.118
3-Way Interactions	4	0.00002120	0.00002120	0.00000530	0.33	0.853
4-Way Interactions	1	0.00000758	0.00000758	0.00000758	0.48	0.495
Residual Error	32	0.00050775	0.00050775	0.00001587		
Pure Error	32	0.00050775	0.00050775	0.00001587		
Total	47	0.00103002				

Unusual Observations for MRR

Obs	StdOrder	MRR	Fit	SE Fit	Residual	StResid
8	8	0.031840	0.019720	0.002300	0.012120	3.73R
24	24	0.012790	0.019720	0.002300	-0.006930	-2.13R

R denotes an observation with a large standardized residual.

Table VI. ANOVA Table of MRR for AISI-1045 considering all factors.

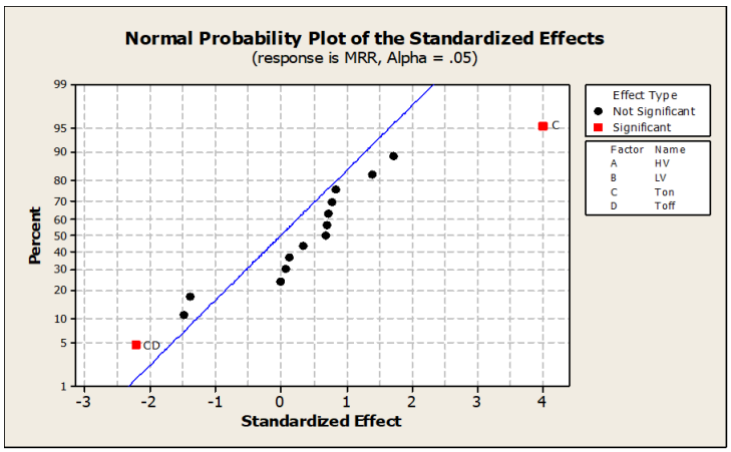

Figure XIV. Normal Probability Plot of the standardized effects of MRR for AISI-1045 considering all factors.

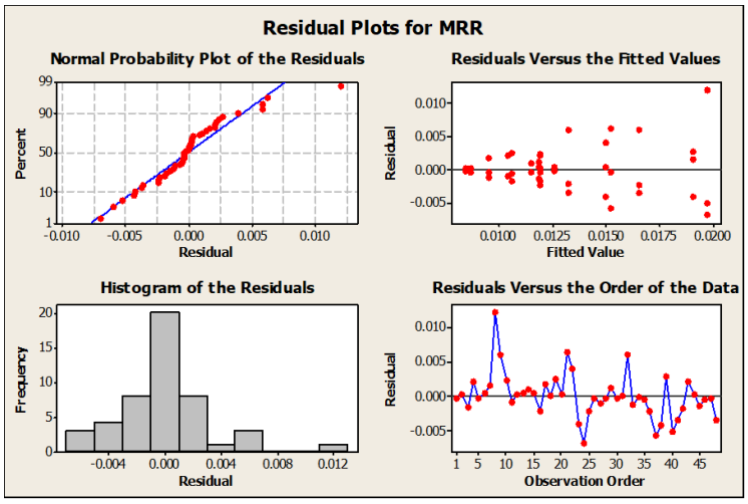

Figure XV. Residual Plot of MRR for AISI-1045 considering all factors.

Factorial Fit: MRR versus Ton, Toff

Estimated Effects and Coefficients for MRR (coded units)

Term	Effect	Coef	SE Coef	T	P
Constant		0.012883	0.000562	22.92	0.000
Ton	0.004607	0.002304	0.000562	4.10	0.000
Toff	-0.001590	-0.000795	0.000562	-1.41	0.164
Ton*Toff	-0.002541	-0.001271	0.000562	-2.26	0.029

S = 0.00389492 R-Sq = 35.20% R-Sq(adj) = 30.78%

Analysis of Variance for MRR (coded units)

Source	DF	Seq SS	Adj SS	Adj MS	F	P
Main Effects	2	0.00028502	0.00028502	0.00014251	9.39	0.000
2-Way Interactions	1	0.00007750	0.00007750	0.00007750	5.11	0.029
Residual Error	44	0.00066750	0.00066750	0.00001517		

Pure Error	44	0.00066750	0.00066750	0.00001517	
Total	47	0.00103002			

Unusual Observations for MRR

Obs	StdOrder	MRR	Fit	SE Fit	Residual	StResid
8	8	0.031840	0.017252	0.001124	0.014588	3.91R
9	9	0.019150	0.011055	0.001124	0.008095	2.17R
32	32	0.022470	0.013121	0.001124	0.009349	2.51R
37	37	0.009300	0.017252	0.001124	-0.007952	-2.13R

R denotes an observation with a large standardized residual.

Estimated Coefficients for MRR using data in uncoded units

Term	Coef
Constant	-0.0512942

Table VII. ANOVA Table of MRR for AISI-1045 considering significant factors.

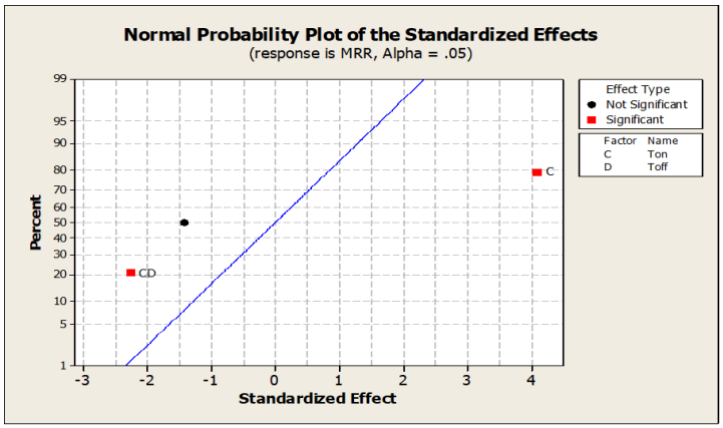

Figure XVI. Normal Probability Plot of the standardized effects of MRR for AISI-1045 considering significant factors

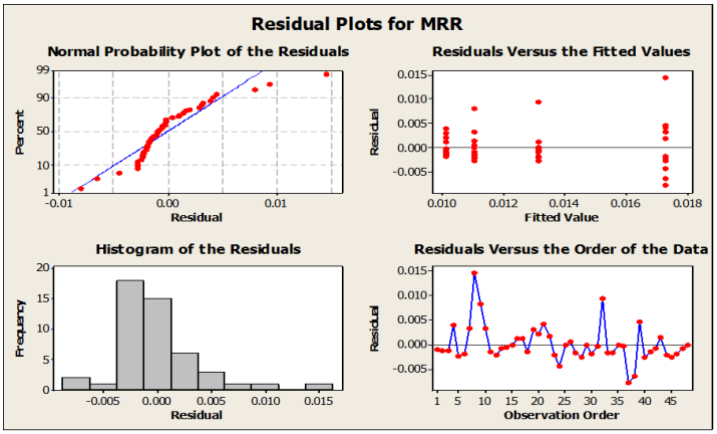

Figure XVII. Residual Plot of MRR for AISI-1045 considering all factors.

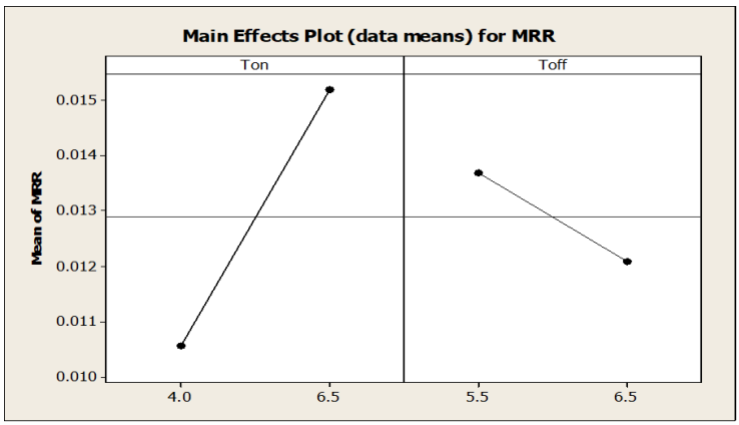

Figure XVIII. Main Effects Plot of MRR for AISI-1045 considering significant factors.

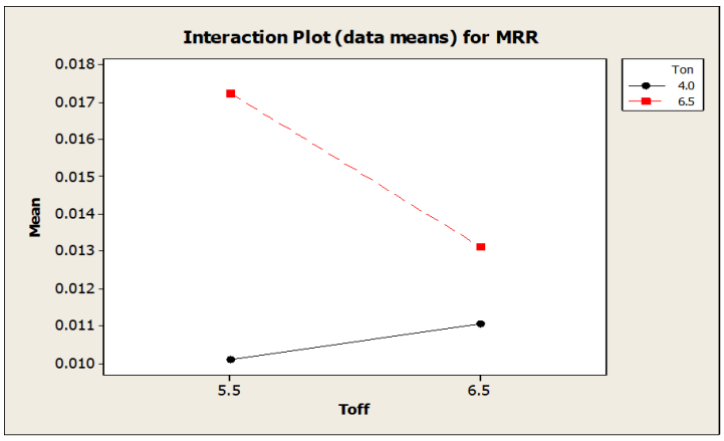

Figure XIX. Residual Plot of MRR for AISI-1045 considering Ton & LV.

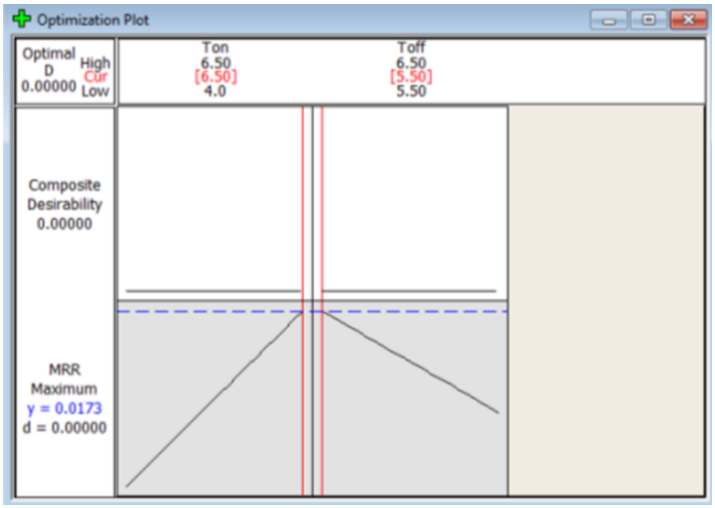

Figure XX. Optimization Plot of MRR for AISI-1045 for significant factors.

Appendix 4

Factorial Fit: EWR versus HV, LV, Ton, Toff

Estimated Effects and Coefficients for EW (coded units)

Term	Effect	Coef	SE Coef	T	P
Constant		0.010172	0.000382	26.66	0.000
HV	-0.000559	-0.000279	0.000382	-0.73	0.469
LV	0.001468	0.000734	0.000382	1.92	0.063
Ton	0.002742	0.001371	0.000382	3.59	0.001
Toff	-0.000344	-0.000172	0.000382	-0.45	0.655
HV*LV	0.000028	0.000014	0.000382	0.04	0.971
HV*Ton	0.000919	0.000459	0.000382	1.20	0.238
HV*Toff	0.000263	0.000131	0.000382	0.34	0.733
LV*Ton	0.001214	0.000607	0.000382	1.59	0.122
LV*Toff	-0.001214	-0.000607	0.000382	-1.59	0.122
Ton*Toff	-0.001386	-0.000693	0.000382	-1.82	0.079
HV*LV*Ton	0.000284	0.000142	0.000382	0.37	0.713
HV*LV*Toff	0.000583	0.000291	0.000382	0.76	0.451
HV*Ton*Toff	0.000227	0.000114	0.000382	0.30	0.768
LV*Ton*Toff	0.001205	0.000603	0.000382	1.58	0.124
HV*LV*Ton*Toff	-0.000048	-0.000024	0.000382	-0.06	0.950

S = 0.00264388 PRESS = 0.000503286
R-Sq = 48.87% R-Sq(pred) = 0.00% R-Sq(adj) = 24.90%

Analysis of Variance for EW (coded units)

Source	DF	Seq SS	Adj SS	Adj MS	F	P
Main Effects	4	0.00012125	0.00012125	0.00003031	4.34	0.006
2-Way Interactions	6	0.00006938	0.00006938	0.00001156	1.65	0.165
3-Way Interactions	4	0.00002310	0.00002310	0.00000577	0.83	0.518
4-Way Interactions	1	0.00000003	0.00000003	0.00000003	0.00	0.950
Residual Error	32	0.00022368	0.00022368	0.00000699		
Pure Error	32	0.00022368	0.00022368	0.00000699		
Total	47	0.00043744				

Unusual Observations for EW

Obs	StdOrder	EW	Fit	SE Fit	Residual	St Resid
8	8	0.019770	0.013577	0.001526	0.006193	2.87R
9	9	0.016610	0.011313	0.001526	0.005297	2.45R

R denotes an observation with a large standardized residual.

Table VIII. ANOVA Table of EWR for AISI-1045 considering all factors.

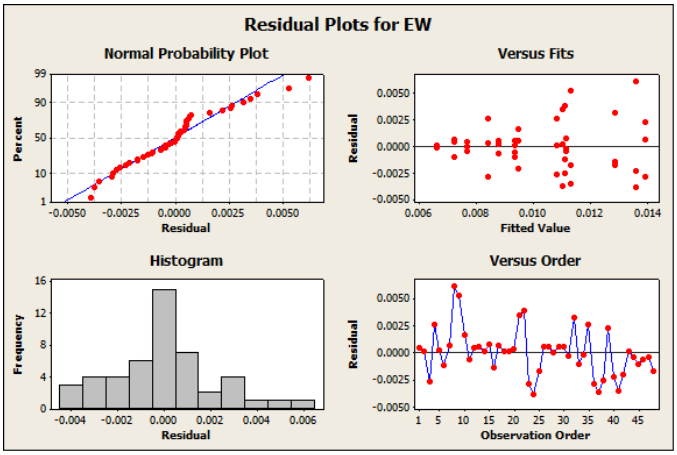

Figure XXI. Residual Plot of EW for AISI-1045 considering all factors.

Factorial Fit: EWR versus Ton

Estimated Effects and Coefficients for EW (coded units)

Term	Effect	Coef	SE Coef	T	P
Constant		0.010172	0.000397	25.65	0.000
Ton	0.002742	0.001371	0.000397	3.46	0.001

S = 0.00274739 PRESS = 0.000378065
R-Sq = 20.63% R-Sq(pred) = 13.57% R-Sq(adj) = 18.90%

Analysis of Variance for EW (coded units)

Source	DF	Seq SS	Adj SS	Adj MS	F	P
Main Effects	1	0.00009023	0.00009023	0.00009023	11.95	0.001
Residual Error	46	0.00034722	0.00034722	0.00000755		
Pure Error	46	0.00034722	0.00034722	0.00000755		
Total	47	0.00043744				

Unusual Observations for EW

Obs	StdOrder	EW	Fit	SE Fit	Residual	St Resid
8	8	0.019770	0.011543	0.000561	0.008227	3.06R
9	9	0.016610	0.008801	0.000561	0.007809	2.90R

R denotes an observation with a large standardized residual.

Estimated Coefficients for EW using data in uncoded units

Term	Coef
Constant	0.00441392
Ton	0.00109683

Table IX. Table of EWR for AISI-1045 considering significant factors.

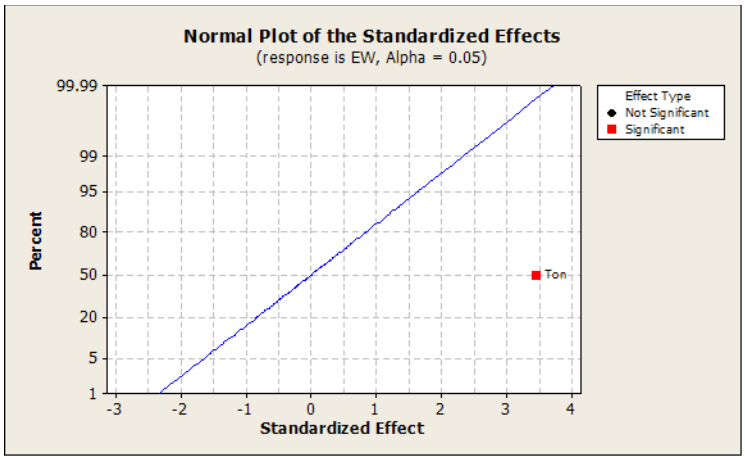

Figure XXII. Normal Probability Plot of the standardized effects ofAISI-1045 for AISI 1045 considering significant factors.

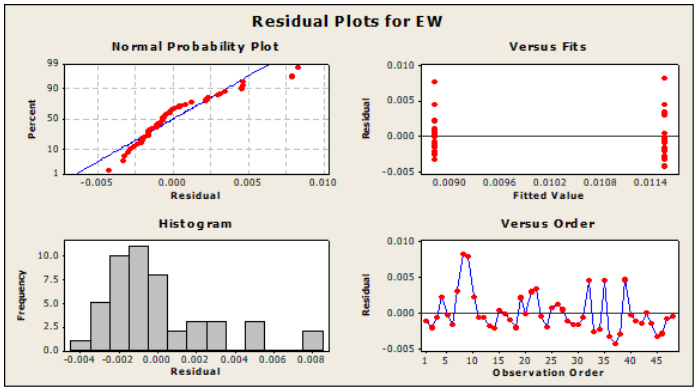

Figure XXIII. Residual Plot of EWR for AISI-1045 considering all factors.

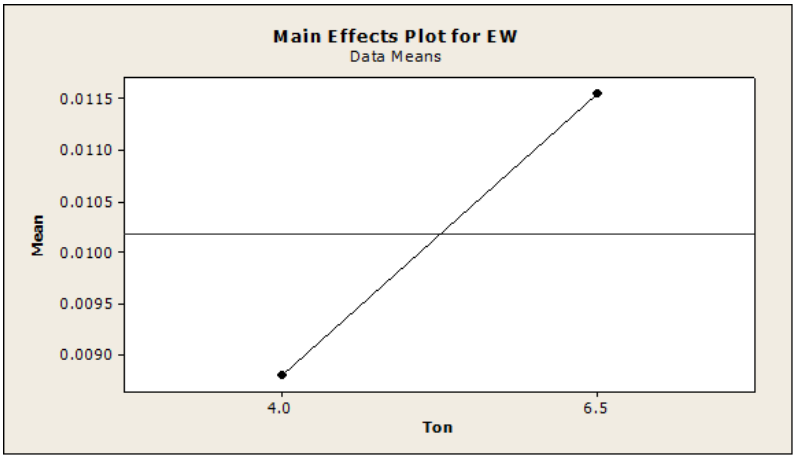

Figure XXIV. Main Effects Plot of EWR for AISI-1045 considering significant factors.

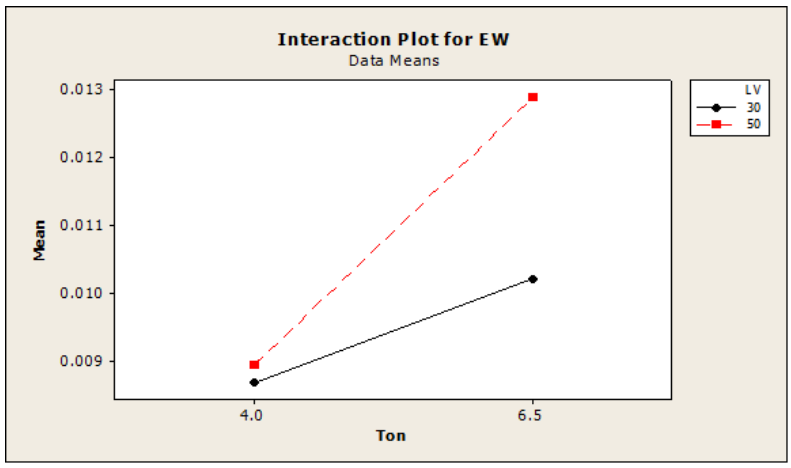

Figure XXV. Residual Plot of EWR for AISI-1045 considering Ton & LV.

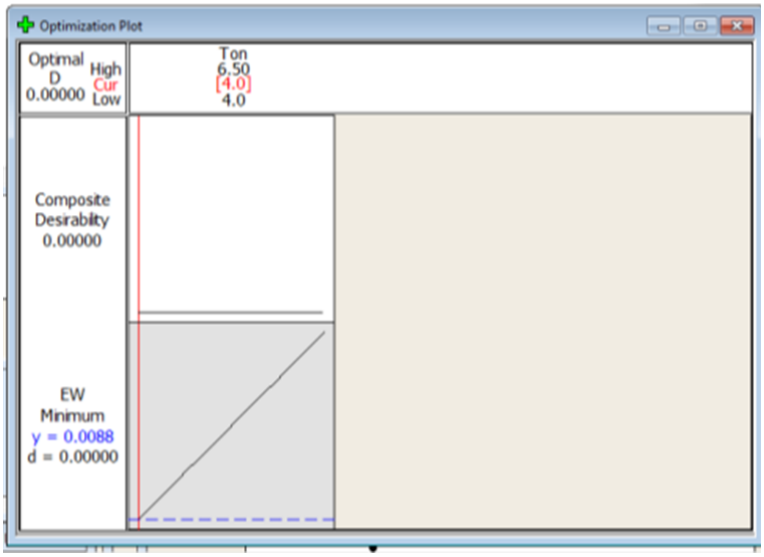

Figure XXVI. Optimization Plot of EWR for AISI-1045 for significant factors.

Appendix 5

Factorial Fit: Ra versus HV, LV, Ton, Toff

Estimated Effects and Coefficients for Ra (coded units)

Term	Effect	Coef	SE Coef	T	P
Constant		0.03696	0.004893	7.55	0.000
HV	0.00167	0.00083	0.004893	0.17	0.866
LV	-0.00367	-0.00183	0.004893	-0.37	0.710
Ton	-0.00175	-0.00088	0.004893	-0.18	0.859
Toff	-0.00217	-0.00108	0.004893	-0.22	0.826
HV*LV	0.00675	0.00337	0.004893	0.69	0.495
HV*Ton	0.01433	0.00717	0.004893	1.46	0.153
HV*Toff	0.01158	0.00579	0.004893	1.18	0.245
LV*Ton	0.01183	0.00592	0.004893	1.21	0.235
LV*Toff	0.00358	0.00179	0.004893	0.37	0.717
Ton*Toff	0.00483	0.00242	0.004893	0.49	0.625
HV*LV*Ton	-0.00908	-0.00454	0.004893	-0.93	0.360
HV*LV*Toff	-0.01467	-0.00733	0.004893	-1.50	0.144
HV*Ton*Toff	-0.02108	-0.01054	0.004893	-2.15	0.039
LV*Ton*Toff	-0.00858	-0.00429	0.004893	-0.88	0.387
HV*LV*Ton*Toff	0.01050	0.00525	0.004893	1.07	0.291

S = 0.0339027 PRESS = 0.0827565
R-Sq = 33.03% R-Sq(pred) = 0.00% R-Sq(adj) = 1.63%

Analysis of Variance for Ra (coded units)

Source	DF	Seq SS	Adj SS	Adj MS	F	P
Main Effects	4	0.0002878	0.0002878	0.00007194	0.06	0.992
2-Way Interactions	6	0.0067369	0.0067369	0.00112282	0.98	0.457
3-Way Interactions	4	0.0097896	0.0097896	0.00244740	2.13	0.100
4-Way Interactions	1	0.0013230	0.0013230	0.00132300	1.15	0.291
Residual Error	32	0.0367807	0.0367807	0.00114940		
Pure Error	32	0.0367807	0.0367807	0.00114940		
Total	47	0.0549179				

Unusual Observations for Ra

Obs	StdOrder	Ra	Fit	SE Fit	Residual	StResid
1	1	0.042000	0.098333	0.019574	-0.056333	-2.04R
17	17	0.230000	0.098333	0.019574	0.131667	4.76R
24	24	0.111000	0.055000	0.019574	0.056000	2.02R
33	33	0.023000	0.098333	0.019574	-0.075333	-2.72R

R denotes an observation with a large standardized residual.

Table X. ANOVA Table of Ra for AISI-1045 considering all factors.

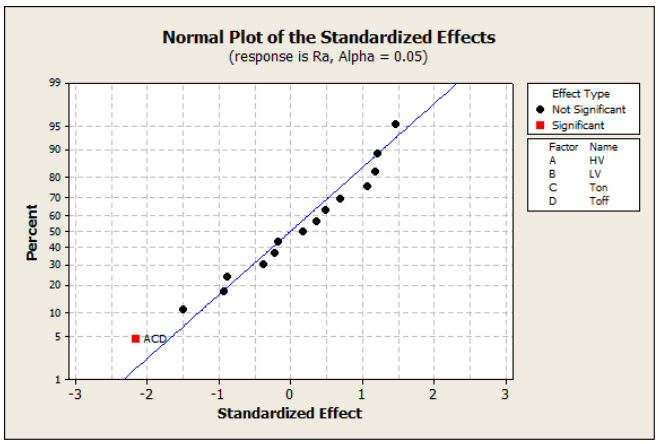

Figure XXVII. Normal Probability Plot of the standardized effects of Ra for AISI-1045 considering all factors.

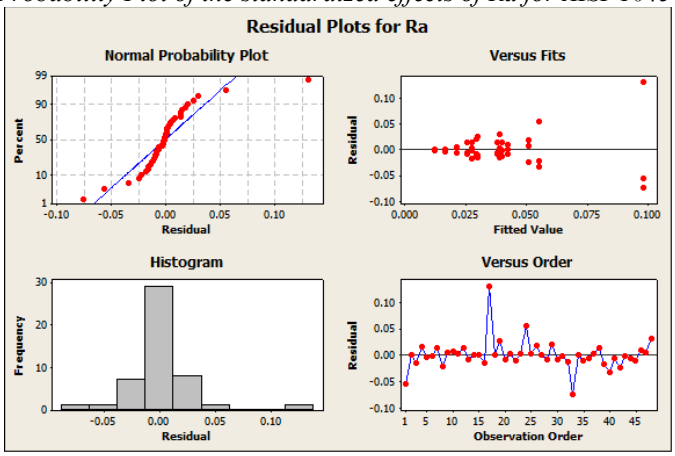

Figure XXVIII. Residual Plot of Ra for AISI-1045 considering all factors.

Factorial Fit: Ra versus HV, Ton, Toff

Estimated Effects and Coefficients for Ra (coded units)

Term	Effect	Coef	SE Coef	T	P
Constant		0.03696	0.004895	7.55	0.000
HV	0.00167	0.00083	0.004895	0.17	0.866
Ton	-0.00175	-0.00088	0.004895	-0.18	0.859
Toff	-0.00217	-0.00108	0.004895	-0.22	0.826
HV*Ton*Toff	-0.02108	-0.01054	0.004895	-2.15	0.037

S = 0.0339142 PRESS = 0.0616278
R-Sq = 9.94% R-Sq(pred) = 0.00% R-Sq(adj) = 1.57%

Analysis of Variance for Ra (coded units)

Source	DF	Seq SS	Adj SS	Adj MS	F	P
Main Effects	3	0.0001264	0.0001264	0.00004214	0.04	0.990
3-Way Interactions	1	0.0053341	0.0053341	0.00533408	4.64	0.037
Residual Error	43	0.0494574	0.0494574	0.00115017		
Lack of Fit	3	0.0043558	0.0043558	0.00145192	1.29	0.292

Pure Error	40	0.0451017	0.0451017	0.00112754	
Total	47	0.0549179			

Unusual Observations for Ra

ObsStdOrder	Ra	Fit	SE Fit	Residual	St Resid
17	17	0.230000	0.048625	0.010946	0.181375	5.65R

R denotes an observation with a large standardized residual.

* NOTE * Estimated regression coefficients in uncoded units are not available because the model is non-hierarchical.

Table XI. ANOVA Table of Ra for AISI-1045 considering significant factors.

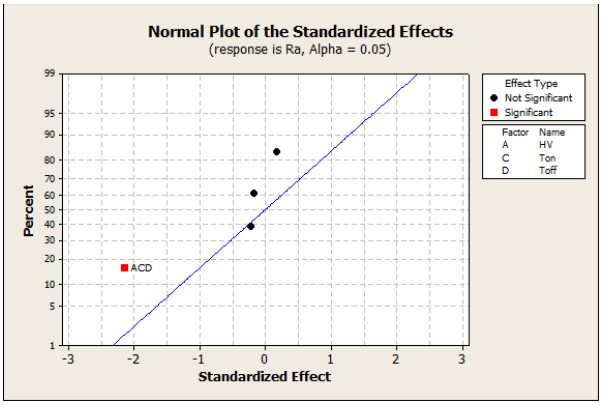

Figure XXIX. Normal Probability Plot of the standardized effects of Ra for AISI-1045 considering significant factors.

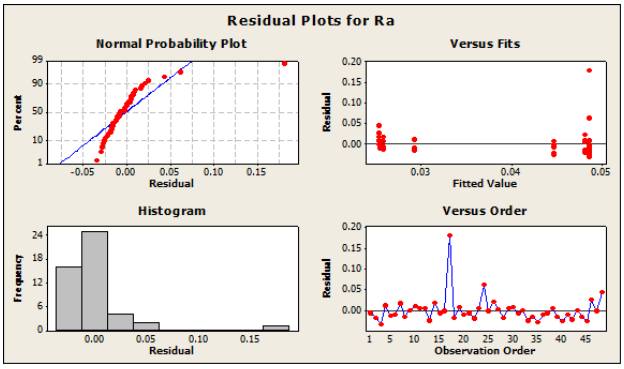

Figure XXX. Residual Plot of Ra for AISI-1045 considering significant factors.

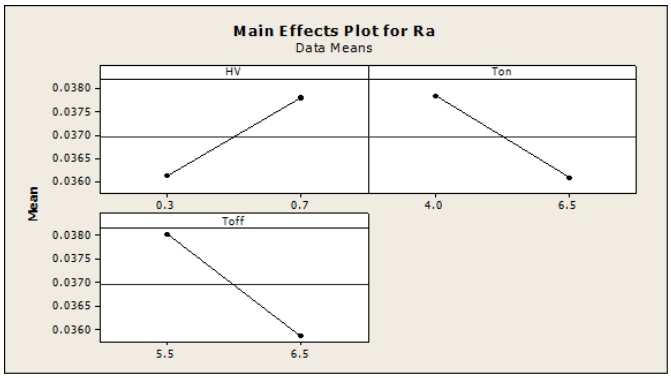

Figure XXXI. Main Effects Plot of Ra for AISI-1045 considering significant factors.

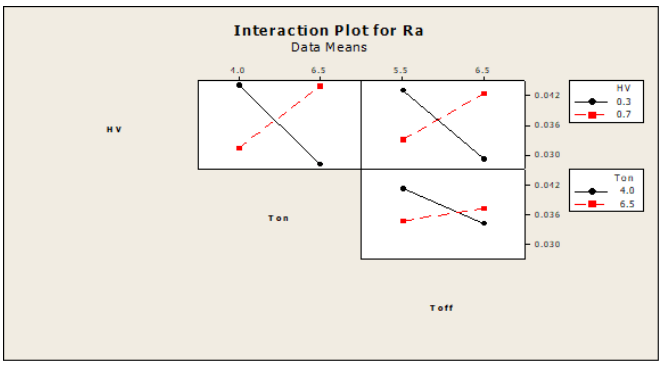

Figure XXXII. Residual Plot of Ra for AISI-1045 considering HV, Ton &Toff.

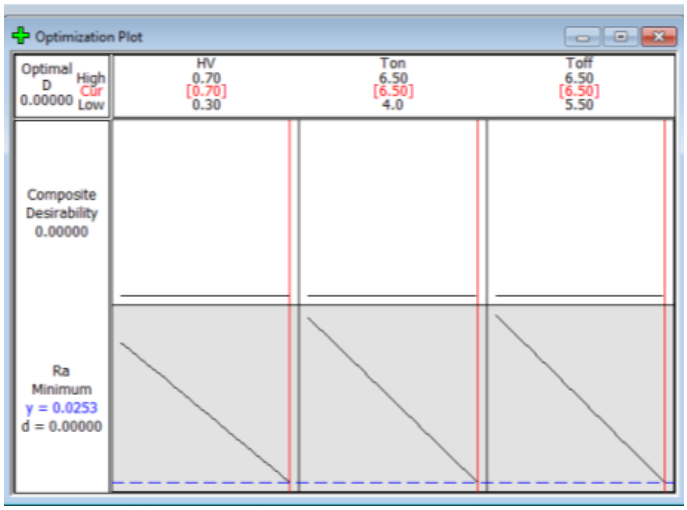

Figure XXXIII. Optimization Plot of Ra for AISI-1045 for significant factors.

Appendix 6

Factorial Fit: R versus HV, LV, Ton, Toff

Estimated Effects and Coefficients for R (coded units)

Term	Effect	Coef	SE Coef	T	P
Constant		1.55752	0.004904	317.62	0.000
HV	-0.00396	-0.00198	0.004904	-0.40	0.689
LV	0.00754	0.00377	0.004904	0.77	0.448
Ton	0.00304	0.00152	0.004904	0.31	0.758
Toff	0.00246	0.00123	0.004904	0.25	0.804
HV*LV	-0.00196	-0.00098	0.004904	-0.20	0.843
HV*Ton	0.00421	0.00210	0.004904	0.43	0.671
HV*Toff	-0.00521	-0.00260	0.004904	-0.53	0.599
LV*Ton	0.00304	0.00152	0.004904	0.31	0.758
LV*Toff	-0.02138	-0.01069	0.004904	-2.18	0.037
Ton*Toff	0.00096	0.00048	0.004904	0.10	0.923
HV*LV*Ton	0.01504	0.00752	0.004904	1.53	0.135
HV*LV*Toff	0.01046	0.00523	0.004904	1.07	0.294
HV*Ton*Toff	-0.00487	-0.00244	0.004904	-0.50	0.623
LV*Ton*Toff	-0.02704	-0.01352	0.004904	-2.76	0.010
HV*LV*Ton*Toff	-0.00271	-0.00135	0.004904	-0.28	0.784

S = 0.0339739 PRESS = 0.0831045
R-Sq = 35.60% R-Sq(pred) = 0.00% R-Sq(adj) = 5.41%

Analysis of Variance for R (coded units)

Source	DF	Seq SS	Adj SS	Adj MS	F	P
Main Effects	4	0.0010541	0.0010541	0.00026352	0.23	0.920
2-Way Interactions	6	0.0061888	0.0061888	0.00103147	0.89	0.511
3-Way Interactions	4	0.0130878	0.0130878	0.00327194	2.83	0.040
4-Way Interactions	1	0.0000880	0.0000880	0.00008802	0.08	0.784
Residual Error	32	0.0369353	0.0369353	0.00115423		
Pure Error	32	0.0369353	0.0369353	0.00115423		
Total	47	0.0573540				

Unusual Observations for R

Obs	StdOrder	R	Fit	SE Fit	Residual	St Resid
21	21	1.58300	1.52533	0.01961	0.05767	2.08R
36	36	1.61200	1.53567	0.01961	0.07633	2.75R

R denotes an observation with a large standardized residual.

Table XII. ANOVA Table of R for AISI-1045 considering all factors.

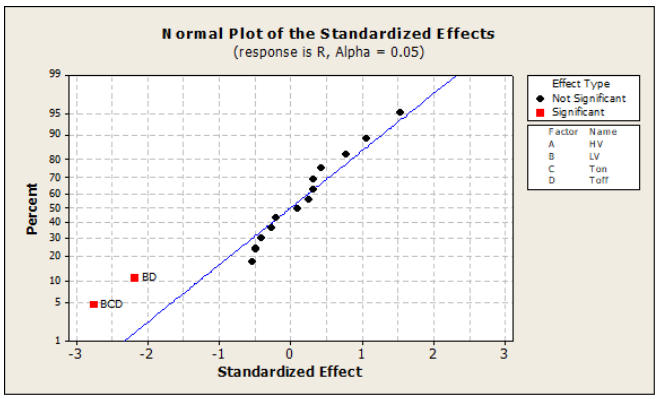

Figure XXXIV. Normal Probability Plot of the standardized effects of R for AISI-1045 considering all factors.

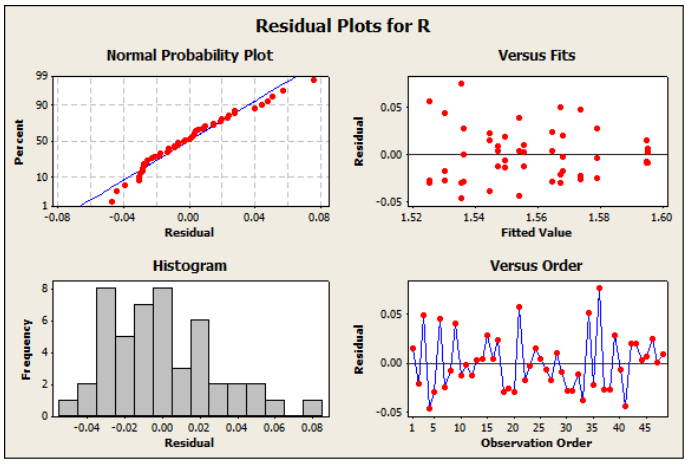

Figure XXXV. Residual Plot of R for AISI-1045 considering all factors.

Factorial Fit: R versus LV, Ton, Toff

Estimated Effects and Coefficients for R (coded units)

Term	Effect	Coef	SE Coef	T	P
Constant		1.55752	0.004577	340.30	0.000
LV	0.00754	0.00377	0.004577	0.82	0.415
Ton	0.00304	0.00152	0.004577	0.33	0.741
Toff	0.00246	0.00123	0.004577	0.27	0.790
LV*Toff	-0.02138	-0.01069	0.004577	-2.34	0.024
LV*Ton*Toff	-0.02704	-0.01352	0.004577	-2.95	0.005

S = 0.0317093 PRESS = 0.0551578
R-Sq = 26.37% R-Sq(pred) = 3.83% R-Sq(adj) = 17.60%

Analysis of Variance for R (coded units)

Source	DF	Seq SS	Adj SS	Adj MS	F	P
Main Effects	3	0.0008661	0.0008661	0.00028869	0.29	0.834
2-Way Interactions	1	0.0054827	0.0054827	0.00548269	5.45	0.024

3-Way Interactions	1	0.0087750	0.0087750	0.00877502	8.73	0.005
Residual Error	42	0.0422302	0.0422302	0.00100548		
Lack of Fit	2	0.0001220	0.0001220	0.00006102	0.06	0.944
Pure Error	40	0.0421082	0.0421082	0.00105270		
Total	47	0.0573540				

Unusual Observations for R

Obs	StdOrder	R	Fit	SE Fit	Residual	St Resid
3	3	1.62200	1.55571	0.01121	0.06629	2.23R
4	4	1.48900	1.55571	0.01121	-0.06671	-2.25R
34	34	1.61800	1.55383	0.01121	0.06417	2.16R

R denotes an observation with a large standardized residual.

* NOTE * Estimated regression coefficients in uncoded units are not available because the model is non-hierarchical.

Table XIII. ANOVA Table of R for AISI-1045 considering significant factors.

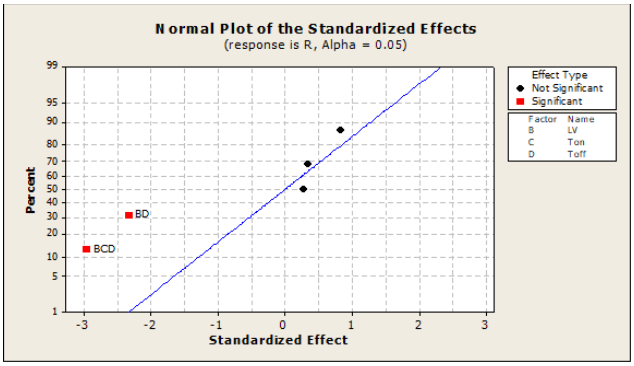

Figure XXXVI. Normal Probability Plot of the standardized effects of R for AISI-1045 considering significant factors.

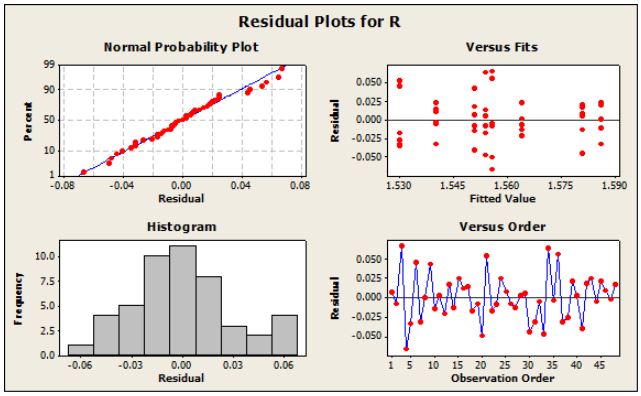

Figure XXXVII. Residual Plot of R for AISI-1045 considering all factors.

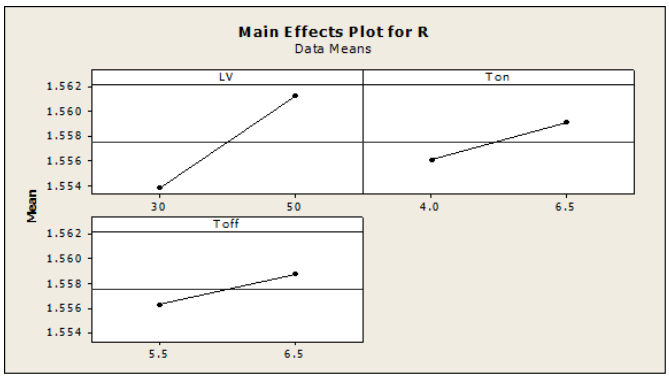

Figure XXXVIII. Main Effects Plot of R for AISI-1045 considering significant factors.

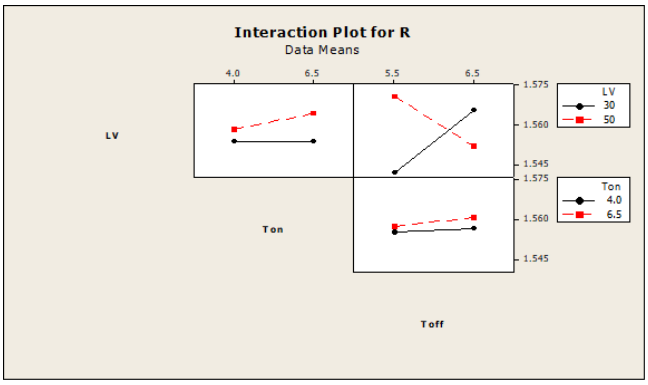

Figure XXXIX. Residual Plot of R for AISI-1045 considering Ton, Toff& LV.

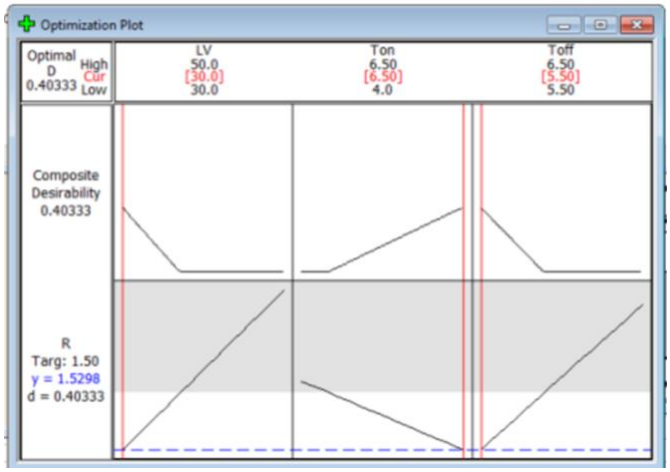

Figure XL. Optimization Plot of R for AISI-1045 for significant factors

Appendix 7

Run Order	HV	LV	T_{on}	T_{off}	Work Piece Material	E_a	W_a	Duty Factor %
1	0.3	30	4	5.5	AISI-1045	9.356	258.952	42%
2	0.7	30	4	5.5	AISI-1045	9.216	258.786	42%
3	0.3	50	4	5.5	AISI-1045	9.705	258.62	42%
4	0.7	50	4	5.5	AISI-1045	9.565	258.468	42%
5	0.3	30	6.5	5.5	AISI-1045	9.833	258.312	54%
6	0.7	30	6.5	5.5	AISI-1045	9.712	258.163	54%
7	0.3	50	6.5	5.5	AISI-1045	9.382	257.965	54%
8	0.7	50	6.5	5.5	AISI-1045	9.259	257.792	54%
9	0.3	30	4	6.5	AISI-1045	9.389	257.61	38%
10	0.7	30	4	6.5	AISI-1045	9.252	257.452	38%
11	0.3	50	4	6.5	AISI-1045	9.172	257.28	38%
12	0.7	50	4	6.5	AISI-1045	9.034	257.12	38%
13	0.3	30	6.5	6.5	AISI-1045	9.787	256.953	50%
14	0.7	30	6.5	6.5	AISI-1045	9.652	256.785	50%
15	0.3	50	6.5	6.5	AISI-1045	9.505	256.606	50%
16	0.7	50	6.5	6.5	AISI-1045	9.362	256.452	50%
17	0.3	30	4	5.5	AISI-1045	12.067	261.575	42%
18	0.7	30	4	5.5	AISI-1045	11.941	261.397	42%
19	0.3	50	4	5.5	AISI-1045	9.585	261.249	42%
20	0.7	50	4	5.5	AISI-1045	9.439	261.076	42%
21	0.3	30	6.5	5.5	AISI-1045	9.223	260.91	54%
22	0.7	30	6.5	5.5	AISI-1045	9.098	260.725	54%
23	0.3	50	6.5	5.5	AISI-1045	9.622	260.565	54%
24	0.7	50	6.5	5.5	AISI-1045	9.49	260.386	54%
25	0.3	30	4	6.5	AISI-1045	9.519	260.217	38%

26	0.7	30	4	6.5	AISI-1045	9.375	260.052	38%
27	0.3	50	4	6.5	AISI-1045	8.112	259.909	38%
28	0.7	50	4	6.5	AISI-1045	7.966	259.763	38%
29	0.3	30	6.5	6.5	AISI-1045	9.219	259.615	50%
30	0.7	30	6.5	6.5	AISI-1045	9.092	259.448	50%
31	0.3	50	6.5	6.5	AISI-1045	9.199	259.297	50%
32	0.7	50	6.5	6.5	AISI-1045	9.056	259.131	50%
33	0.3	30	4	5.5	AISI-1045	12.453	249.045	42%
34	0.7	30	4	5.5	AISI-1045	12.332	248.884	42%
35	0.3	50	4	5.5	AISI-1045	12.398	248.713	42%
36	0.7	50	4	5.5	AISI-1045	12.167	248.542	42%
37	0.3	30	6.5	5.5	AISI-1045	12.706	248.345	54%
38	0.7	30	6.5	5.5	AISI-1045	12.591	248.198	54%
39	0.3	50	6.5	5.5	AISI-1045	18.431	248.042	54%
40	0.7	50	6.5	5.5	AISI-1045	18.299	247.864	54%
41	0.3	30	4	6.5	AISI-1045	12.718	247.694	38%
42	0.7	30	4	6.5	AISI-1045	12.58	247.524	38%
43	0.3	50	4	6.5	AISI-1045	13.194	247.354	38%
44	0.7	50	4	6.5	AISI-1045	13.064	247.172	38%
45	0.3	30	6.5	6.5	AISI-1045	12.272	246.999	50%
46	0.7	30	6.5	6.5	AISI-1045	12.137	246.83	50%
47	0.3	50	6.5	6.5	AISI-1045	12.041	246.66	50%
48	0.7	50	6.5	6.5	AISI-1045	11.905	246.506	50%

Table XIV. Experimental inputs for AISI-1045 material with three replicates.

Appendix 8

Run Order	Tm (sec)	MRR (g/min)	EW (g/min)	Base (mm)	Radius	Surface (R_a) (mm)	Roughness
1	1094	0.0091	0.00768	1.56		0.042	
2	1149	0.00867	0.00674	1.546		0.012	
3	1034	0.00882	0.00812	1.622		0.014	
4	668	0.01401	0.01105	1.489		0.04	
5	602	0.01485	0.01126	1.495		0.013	
6	779	0.01525	0.00986	1.575		0.038	
7	505	0.02055	0.01461	1.554		0.042	
8	343	0.03184	0.01977	1.586		0.033	
9	495	0.01915	0.01661	1.594		0.026	
10	729	0.01416	0.01111	1.536		0.057	
11	1021	0.0094	0.00811	1.566		0.029	
12	1124	0.00891	0.00817	1.543		0.052	
13	822	0.01226	0.00985	1.598		0.02	
14	867	0.01239	0.00941	1.568		0.043	
15	720	0.01283	0.01192	1.564		0.038	
16	694	0.01418	0.01141	1.551		0.023	
17	957	0.01116	0.0079	1.568		0.23	
18	1055	0.00842	0.00671	1.537		0.011	
19	800	0.01298	0.01095	1.548		0.056	
20	822	0.01212	0.00869	1.506		0.017	
21	517	0.02147	0.01451	1.583		0.018	
22	506	0.01897	0.01494	1.513		0.028	
23	719	0.01494	0.01102	1.576		0.031	
24	793	0.01279	0.00968	1.61		0.111	
25	904	0.01095	0.00956	1.558		0.024	
26	745	0.01152	0.00999	1.543		0.069	
27	943	0.00929	0.00929	1.55		0.027	
28	1069	0.00831	0.00769	1.566		0.03	
29	772	0.01298	0.00987	1.586		0.05	
30	813	0.01114	0.00989	1.536		0.033	
31	789	0.01262	0.01087	1.508		0.036	
32	478	0.02247	0.01607	1.535		0.025	
33	1173	0.00824	0.00619	1.506		0.023	
34	1248	0.00822	0.00644	1.618		0.013	
35	1036	0.0099	0.01338	1.551		0.019	
36	1231	0.0096	0.00551	1.612		0.019	
37	948	0.0093	0.00728	1.498		0.018	
38	872	0.01073	0.00853	1.503		0.054	
39	490	0.0218	0.01616	1.607		0.01	

40	702	0.01453	0.01128	1.588	0.021
41	1066	0.00957	0.00777	1.51	0.014
42	1007	0.01013	0.00739	1.569	0.026
43	874	0.01249	0.00892	1.588	0.026
44	1182	0.00878	0.00726	1.558	0.032
45	976	0.01039	0.0083	1.601	0.018
46	928	0.01099	0.00873	1.589	0.051
47	756	0.01222	0.01071	1.537	0.043
48	772	0.01298	0.01111	1.556	0.069

Table XV. Experimental Responses for AISI-1045along with three Replicates.

Appendix 9. - The AISI-1045 workpiece surface outline images were taken at a magnification level of 22X

Experimental Runs	**Replicate # 1**	**Replicate # 2**	**Replicate # 3**
1			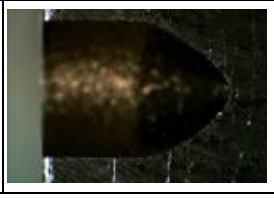
T_{on} = 4µs,T_{off}5.5 µs,Duty Factor = 42%, HV = 0.3V, LV = 30A			
2		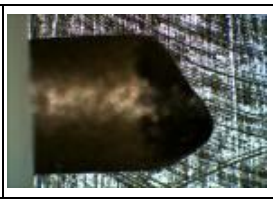	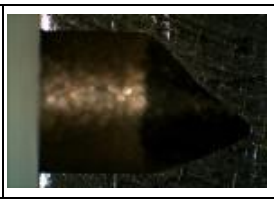
T_{on} = 4µs,T_{off}5.5 µs,Duty Factor = 42%, HV = 0.7V, LV = 30A			
3		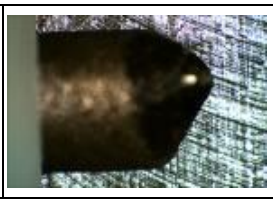	
T_{on} = 4µs,T_{off}5.5 µs,Duty Factor = 42%, HV = 0.3V, LV = 50A			
4	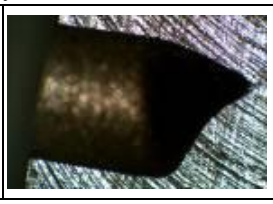	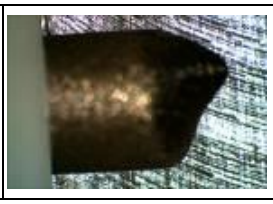	
T_{on} = 4µs,T_{off}5.5 µs,Duty Factor = 42%, HV = 0.7V, LV = 50A			
5			
T_{on} = 6.5µs,T_{off}5.5 µs,Duty Factor = 54%, HV = 0.3V, LV = 30A			
6	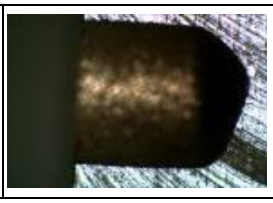	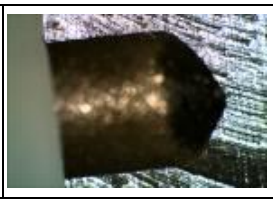	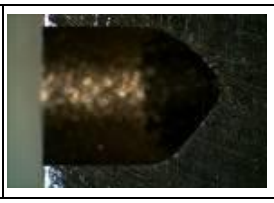
T_{on} = 6.5µs,T_{off}5.5 µs,Duty Factor = 54%, HV = 0.7V, LV = 30A			
7		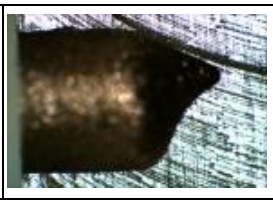	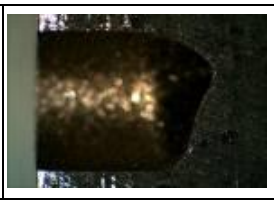

Experimental Runs	**Replicate # 1**	**Replicate # 2**	**Replicate # 3**
T_{on} = 6.5µs,T_{off}5.5 µs,Duty Factor = 54%, HV = 0.3V, LV = 50A			
8			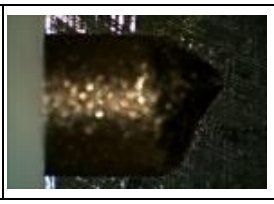
T_{on} = 6.5µs,T_{off}5.5 µs,Duty Factor = 54%, HV = 0.7V, LV = 50A			
9		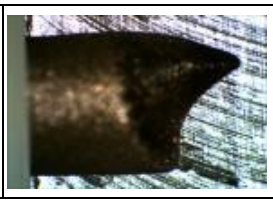	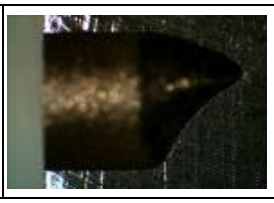
T_{on} = 4µs,T_{off}6.5 µs,Duty Factor = 38%, HV = 0.3V, LV = 30A			
10	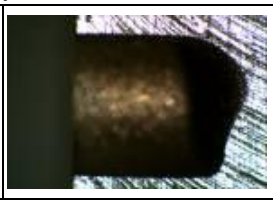	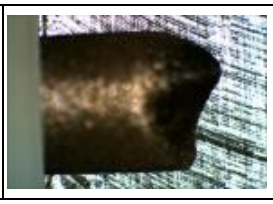	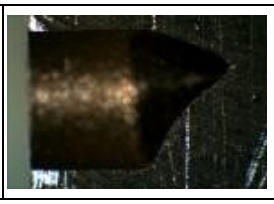
T_{on} = 4µs,T_{off}6.5 µs,Duty Factor = 38%, HV = 0.7V, LV = 30A			
11	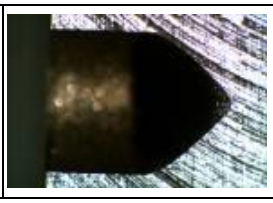	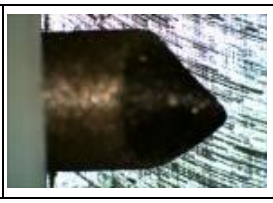	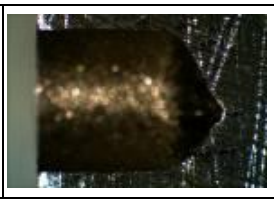
T_{on} = 4µs,T_{off}6.5 µs,Duty Factor = 38%, HV = 0.3V, LV = 50A			
12	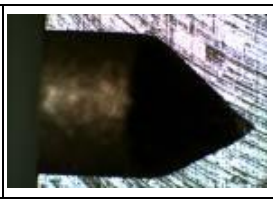	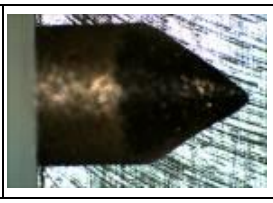	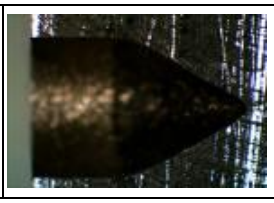
T_{on} = 4µs,T_{off}6.5 µs,Duty Factor = 38%, HV = 0.7V, LV = 50A			
13			
T_{on} = 6.5µs,T_{off}6.5 µs,Duty Factor = 50%, HV = 0.3V, LV = 30A			
14	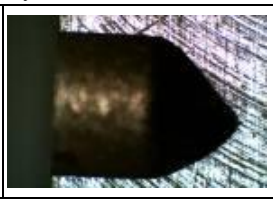	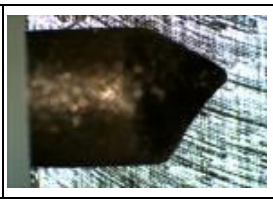	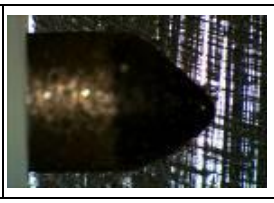
T_{on} = 6.5µs,T_{off}6.5 µs,Duty Factor = 50%, HV = 0.7V, LV = 30A			

Experimental Runs	**Replicate # 1**	**Replicate # 2**	**Replicate # 3**
15			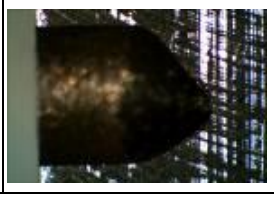
T_{on} = 6.5µs,T_{off}6.5 µs,Duty Factor = 50%, HV = 0.3V, LV = 50A			
16	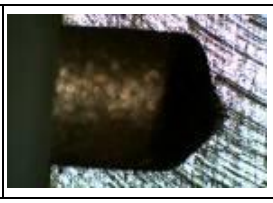	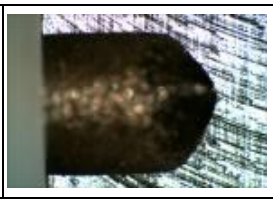	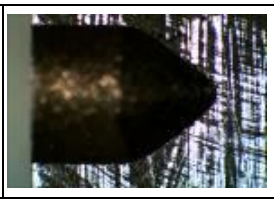
T_{on} = 6.5µs,T_{off}6.5 µs,Duty Factor = 50%, HV = 0.7V, LV = 50A			

Table XVI. AISI 1045 Workpiece Outline 22X.

Appendix 10. - The electrode images that machined AISI-1045 were taken at a magnification level of 20 X

Experimental Runs	**Replicate # 1**	**Replicate # 2**	**Replicate # 3**
1			
T_{on} = 4µs,T_{off}5.5 µs,Duty Factor = 42%, HV = 0.3, LV = 30			
2		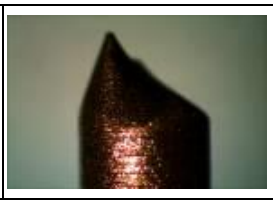	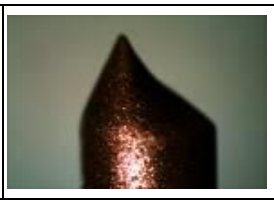
T_{on} = 4µs,T_{off}5.5 µs,Duty Factor = 42%, HV = 0.7, LV = 30			
3	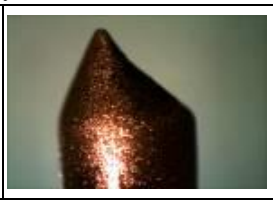	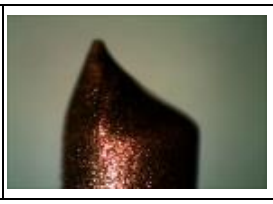	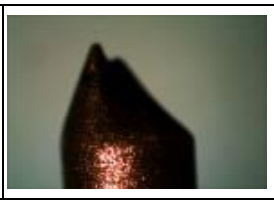
T_{on} = 4µs,T_{off}5.5 µs,Duty Factor = 42%, HV = 0.3, LV = 50			
4	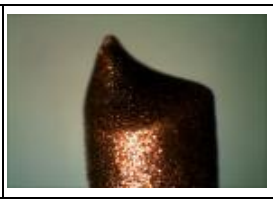		
T_{on} = 4µs,T_{off}5.5 µs,Duty Factor = 42%, HV = 0.7, LV = 50			
5	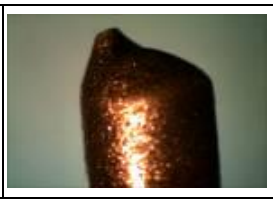	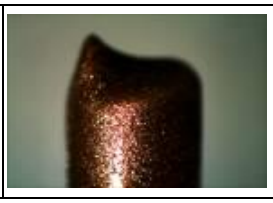	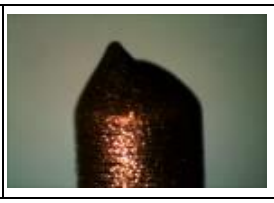
T_{on} = 6.5µs,T_{off}5.5 µs,Duty Factor = 54%, HV = 0.3, LV = 30			
6	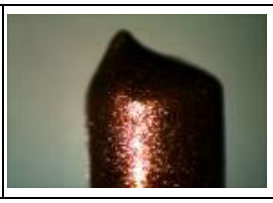	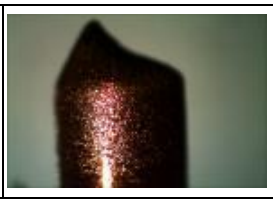	
T_{on} = 6.5µs,T_{off}5.5 µs,Duty Factor = 54%, HV = 0.7, LV = 30			
7	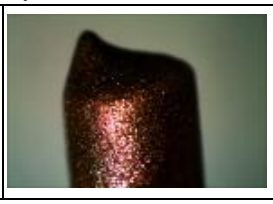		
T_{on} = 6.5µs,T_{off}5.5 µs,Duty Factor = 54%, HV = 0.3, LV = 50			

Experimental Runs	Replicate # 1	Replicate # 2	Replicate # 3
8	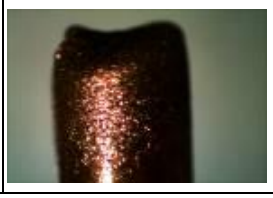		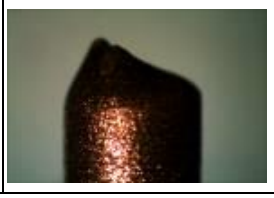
T_{on} = 6.5µs,T_{off}5.5 µs,Duty Factor = 54%, HV = 0.7, LV = 50			
9		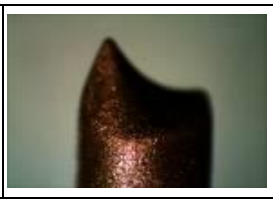	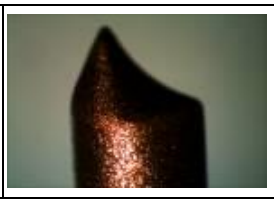
T_{on} = 4µs,T_{off}6.5 µs,Duty Factor = 38%, HV = 0.3, LV = 30			
10	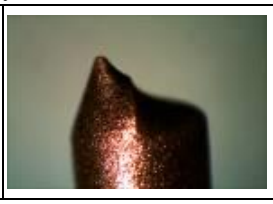	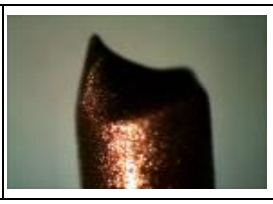	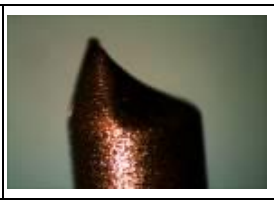
T_{on} = 4µs,T_{off}6.5 µs,Duty Factor = 38%, HV = 0.7, LV = 30			
11	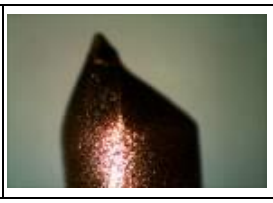	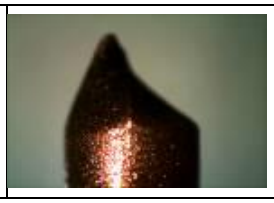	
T_{on} = 4µs,T_{off}6.5 µs,Duty Factor = 38%, HV = 0.3, LV = 50			
12			
T_{on} = 4µs,T_{off}6.5 µs,Duty Factor = 38%, HV = 0.7, LV = 50			
13			
T_{on} = 6.5µs,T_{off}6.5 µs,Duty Factor = 50%, HV = 0.3, LV = 30			
14		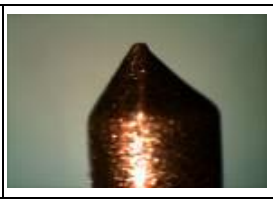	
T_{on} = 6.5µs,T_{off}6.5 µs,Duty Factor = 50%, HV = 0.7, LV = 30			

Experimental Runs	**Replicate # 1**	**Replicate # 2**	**Replicate # 3**
15			
T_{on} = 6.5µs,T_{off}6.5 µs,Duty Factor = 50%, HV = 0.3, LV = 50			
16			
T_{on} = 6.5µs,T_{off}6.5 µs,Duty Factor = 50%, HV = 0.7, LV = 50			

Table XVII. AISI 1045– Copper Electrode – 20 X.

Author contribution:
1. Conception and design of the study
2. Data acquisition
3. Data analysis
4. Discussion of the results
5. Writing of the manuscript
6. Approval of the last version of the manuscript

MMUZS has contributed to: 1, 2, 3, 4, 5 and 6.
SAI has contributed to: 1, 2, 3, 4, 5 and 6.
AZ has contributed to: 1, 2, 3, 4, 5 and 6.
AT has contributed to: 1, 2, 3, 4, 5 and 6.

Acceptance Note: This article was approved by the journal editors Dr. Rafael Sotelo and Mag. Ing. Fernando A. Hernández Gobertti.

Direct Air Carbon Capture Using Metal-Organic Frameworks (MOFs): Techno-Economic Performance of Temperature Vacuum Swing Adsorption (TVSA) Systems

Captura directa de carbono en el aire mediante estructuras metalorgánicas (MOF): Rendimiento técnico-económico de los sistemas de adsorción por oscilación de temperatura y vacío (TVSA)

Captura direta de carbono no ar usando estruturas metal-orgânicas (MOFs): desempenho técnico-econômico de sistemas de adsorção por oscilação de temperatura e vácuo (TVSA)

Haider Ali[1(*)], Duraid Uddin[2], Asad A. Naqvi[3], Umair Naeem[4], Nomaan Akhtar[5], Saqib Shams[6], Ali Karim[7]

Recibido: 20/11/2024 Aceptado: 02/03/2025

Summary. - Direct Air Carbon Capture (DACC) technology is used to remove CO_2 directly from the atmosphere, helping tackle climate change and excessive greenhouse gas emissions efficiently. In this study, a techno-economic analysis of DACC has been carried out, including its working mechanisms, energy needs, and costs, as well as a summary of the current research status. This research compares two leading metal-organic frameworks (MOFs) — MIL-101(Cr)-PEI-800 and mmen-Mg_2(dobpdc) — focusing on their energy consumption, CO_2 adsorption, and cost. This study investigates the performance of these MOFs in a temperature vacuum swing adsorption (TVSA) process, which cyclically varies temperature and pressure to capture CO_2 and regenerate adsorbents. Among all materials, mmen-Mg_2(dobpdc) achieves the best performance with a much higher capacity and a favourable nonlinear isotherm shape, indicating significantly improved efficiency and lower energy input. DACC systems based on advanced MOFs hold great promise for minimizing non-point source emissions and should thus be considered essential components of a climate change mitigation strategy. This study contributes to direct future research and development toward more efficient and cost-effective MOFs in DACC applications.

Keywords: Direct Air Carbon Capture, Temperature Vacuum Swing Adsorption, Metal-Organic Framework.

(*) Corresponding author.

[1] Researcher, Department of Mechanical Engineering, NEDUET (Pakistan), haider.ali@neduet.edu.pk
ORCID iD: https://orcid.org/0000-0001-8242-3696

[2] Researcher, Department of Mechanical Engineering, NEDUET (Pakistan), duraid_uddin2000@yahoo.com,
ORCID iD: https://orcid.org/0009-0009-4351-1162

[3] Researcher, Department of Mechanical Engineering, NEDUET (Pakistan), asadakhter@neduet.edu.pk,
ORCID iD: https://orcid.org/0000-0001-6290-3115

[4] Student, Department of Mechanical Engineering, NEDUET (Pakistan), umairnaeem139@gmail.com,
ORCID iD: https://orcid.org/0009-0003-0763-4081

[5] Student, Department of Mechanical Engineering, NEDUET (Pakistan), nomaan.akhtar2@gmail.com,
ORCID iD: https://orcid.org/0009-0007-2969-675X

[6] Student, Department of Mechanical Engineering, NEDUET (Pakistan), saqibshams200204@gmail.com,
ORCID iD: https://orcid.org/0009-0009-3932-6095

[7] Student, Department of Mechanical Engineering, NEDUET (Pakistan), alikarimptcl@gmail.com,
ORCID iD: https://orcid.org/0009-0008-0495-0237

Memoria Investigaciones en Ingeniería, núm. 28 (2025). pp. 269-286
https://doi.org/10.36561/ING.28.16
ISSN 2301-1092 • ISSN (en línea) 2301-1106 – Universidad de Montevideo, Uruguay

Resumen. - *La tecnología de Captura Directa de Carbono en el Aire (DACC) se utiliza para eliminar CO_2 directamente de la atmósfera, lo que contribuye a combatir eficientemente el cambio climático y las emisiones excesivas de gases de efecto invernadero. En este estudio, se realizó un análisis tecnoeconómico de la DACC, incluyendo sus mecanismos de funcionamiento, necesidades energéticas y costes, así como un resumen del estado actual de la investigación. Esta investigación compara dos estructuras metalorgánicas (MOF) líderes —MIL-101(Cr)-PEI-800 y mmen-Mg_2(dobpdc)—, centrándose en su consumo energético, adsorción de CO_2 y coste. Este estudio investiga el rendimiento de estas MOF en un proceso de adsorción por oscilación de temperatura y vacío (TVSA), que varía cíclicamente la temperatura y la presión para capturar CO_2 y regenerar los adsorbentes. Entre todos los materiales, mmen-Mg_2(dobpdc) alcanza el mejor rendimiento, con una capacidad mucho mayor y una forma de isoterma no lineal favorable, lo que indica una eficiencia significativamente mejorada y un menor consumo de energía. Los sistemas DACC basados en MOF avanzados son muy prometedores para minimizar las emisiones de fuentes no puntuales y, por lo tanto, deberían considerarse componentes esenciales de una estrategia de mitigación del cambio climático. Este estudio contribuye a orientar la investigación y el desarrollo futuros hacia MOF más eficientes y rentables en aplicaciones DACC.*

Palabras clave: *Captura directa de carbono en aire, adsorción por oscilación de temperatura y vacío, estructura metalorgánica.*

Resumo. - *A tecnologia de Captura Direta de Carbono no Ar (DACC) é usada para remover CO_2 diretamente da atmosfera, ajudando a combater as mudanças climáticas e as emissões excessivas de gases de efeito estufa de forma eficiente. Neste estudo, foi realizada uma análise técnico-econômica do DACC, incluindo seus mecanismos de funcionamento, necessidades energéticas e custos, bem como um resumo do status atual da pesquisa. Esta pesquisa compara duas estruturas metal-orgânicas (MOFs) líderes — MIL-101(Cr)-PEI-800 e mmen-Mg_2(dobpdc) — com foco em seu consumo de energia, adsorção de CO_2 e custo. Este estudo investiga o desempenho dessas MOFs em um processo de adsorção por oscilação de temperatura e vácuo (TVSA), que varia ciclicamente a temperatura e a pressão para capturar CO_2 e regenerar adsorventes. Entre todos os materiais, o mmen-Mg_2(dobpdc) atinge o melhor desempenho com uma capacidade muito maior e uma forma isotérmica não linear favorável, indicando eficiência significativamente melhorada e menor consumo de energia. Os sistemas DACC baseados em MOFs avançados são bastante promissores para minimizar as emissões de fontes difusas e, portanto, devem ser considerados componentes essenciais de uma estratégia de mitigação das mudanças climáticas. Este estudo contribui para direcionar futuras pesquisas e desenvolvimentos em direção a MOFs mais eficientes e econômicos em aplicações DACC.*

Palavras-chave: *Captura direta de carbono no ar, adsorção por oscilação de temperatura e vácuo, estrutura metal-orgânica.*

1. Introduction. - In recent years, there has been a continuous debate about humanity's contribution to the rise of atmospheric greenhouse gases and the resulting global warming. While the exact causal relationship is still under discussion, it is now widely accepted that human activities have significantly increased these gases in the atmosphere [1]. Human activities generate greenhouse gases (GHGs) in the atmosphere, primarily carbon dioxide (CO_2), methane (CH_4), chlorofluorocarbons (CFCs), and nitrous oxide (N_2O). These gases significantly contribute to global warming, which is one of the most pressing environmental threats facing humanity today. Among these GHGs, CO_2 has the largest impact, accounting for about 55% of the observed greenhouse effect and global warming. The emissions from thermal power plants (TPPs) are a major source of CO_2, as approximately 30% of the world's fossil fuel consumption is dedicated to power generation, leading to substantial CO_2 emissions [2]. The ongoing rise in atmospheric GHGs concentrations is the most significant factor driving global warming. Since the onset of industrialization, the substantial release of CO_2 from human activities has played a major role in enhancing the greenhouse effect, becoming a pressing environmental issue that requires urgent attention. Additionally, other gases, such as methane (CH_4), nitrous oxide (N_2O), and ozone-depleting substances (ODSs), including fluorinated gases, also contribute to climate change [3], [4]. The current level of CO_2 in the atmosphere is over 400 ppm and rising by about 2 ppm per year, mainly due to burning fossil fuels [5]. The International Energy Agency reports that more than two-thirds of greenhouse gas emissions and over 80% of carbon dioxide emissions stem from energy-related activities. The global CO_2 emissions grew by an average of 2.6% annually. Many studies have documented the statistics and detrimental effects of global warming, revealing that around 60% of the planet is now facing unprecedented high temperatures each year [6].

Currently, the most prevalent techniques for capturing CO_2 from gas mixtures include absorption, membrane separation, and low-temperature CO_2 capture. Absorption typically involves using solvents that selectively absorb CO_2 from flue gases, making it effective for large-scale industrial applications. Membrane separation utilizes selective permeability to separate CO_2 from other gases, offering a more energy-efficient and compact alternative. Low-temperature CO_2 capture, on the other hand, leverages cryogenic processes to condense and separate CO_2 from gas streams, which can be particularly advantageous in high-purity applications. Each of these methods presents unique advantages and challenges, making them suitable for different operational contexts and carbon capture goals [7].

Fossil fuels will continue to be a major energy source, so we need technologies to capture and store CO_2 directly from the air, which is known as Direct Air Capture (DAC). Traditional carbon capture methods target specific sources like power plants, but DAC can capture CO_2 from any location, making it more versatile. There has been research into various DAC methods, including using solutions like sodium hydroxide [8]. However, these can be expensive and energy intensive.

More recent studies have focused on using solid materials called Metal-Organic Frameworks (MOFs), which are more efficient in capturing CO_2. Metal-organic frameworks (MOFs) offer numerous significant benefits that make them highly attractive for a range of applications, particularly in gas separation, storage, and catalysis. One of their standout features is their exceptionally high surface area, which enhances their capacity for gas adsorption and storage, making them efficient materials for capturing gases like CO_2 and hydrogen. Additionally, the tunability of MOFs allows for easy modification of their structural and chemical properties by altering the metal ions or organic linkers used in synthesis, enabling the design of materials tailored to specific applications, such as selective gas separation. Their highly porous structure facilitates efficient gas diffusion and adsorption, which is crucial for processes like carbon capture and air purification. Furthermore, their lightweight nature is advantageous in applications where weight is a concern, such as gas storage for transportation [7], [9]. Two promising MOFs are MIL-101(Cr)-PEI-800 and mmen-Mg2(dobpdc), which are known for their high capacity to adsorb CO_2 and their stability [8].

Solid adsorbents like MOFs can capture CO_2 through processes that use temperature and pressure changes. Studies have shown that these materials can be effective and potentially less costly than liquid solutions [10]. The research also explores different designs to improve efficiency, such as using monolith structures, which reduce pressure drops and increase mass transfer rates. Steam can be used as a stripping agent to regenerate the adsorbents, and some experiments have shown that certain adsorbents can withstand repeated cycles of adsorption and desorption using steam [11].

This paper evaluates the economic and energy performance of DAC using MIL-101(Cr)-PEI-800 and mmen-Mg2(dobpdc) in a temperature vacuum swing adsorption (TVSA) process. The study aims to optimize the conditions for DAC and guide future materials development to improve performance. Numerical models are used to analyze the effect of air and steam velocity on the system's CO_2 capture efficiency.

2. Methodology. - The study focuses on Direct Air Carbon Capture (DACC) technology using solid adsorbents and emphasizes the importance of material selection in its performance and cost-effectiveness, as illustrated in Figure I. Two metal-organic frameworks (MOFs), MIL-101(Cr)-PEI-800 and mmen-Mg2(dobpdc), are evaluated for their CO_2 capture capabilities. These MOFs are crucial because they offer high surface areas and tunable pore structures that enhance CO_2 adsorption, making them suitable for DACC applications. The study explores how these materials are used in monolithic contactors, structures designed to maximize the contact surface between the adsorbent and air. These contactors play a vital role in improving CO_2 capture efficiency by reducing pressure drops and increasing the adsorption rate, which leads to better overall performance in capturing atmospheric CO_2.

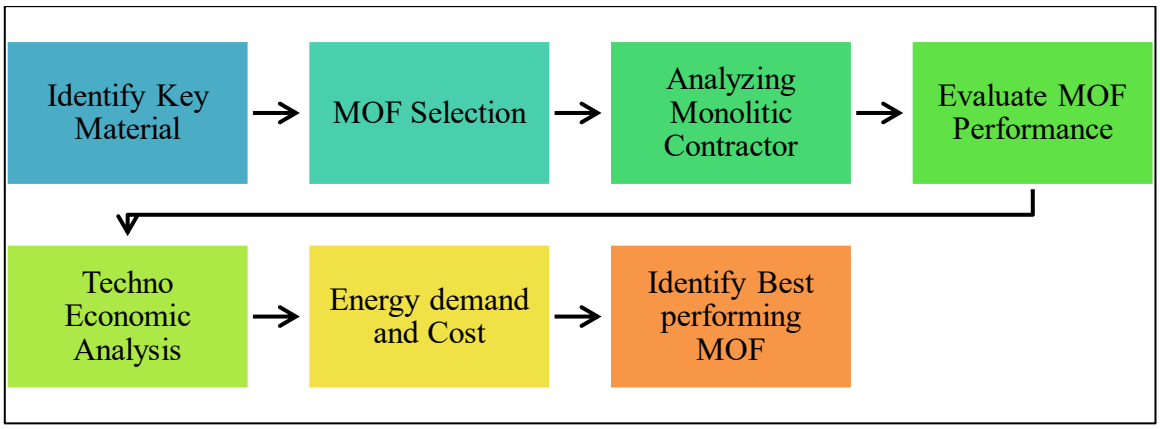

Figure I. Methodology of Study

The effectiveness of monolithic contactors is highlighted, as they allow for more efficient airflow and CO_2 adsorption, making them a viable option for large-scale DACC operations. In terms of cost evaluation, the study examines the energy demands and overall expenses of implementing these MOFs in a DACC system. mmen-Mg2(dobpdc) emerges as the more effective and cost-efficient material due to its higher CO_2 adsorption capacity and favorable non-linear isotherm behavior, which allows it to perform better under varying conditions. This material also requires less energy for regeneration compared to MIL-101(Cr)-PEI-800, making it a superior option for reducing CO_2 emissions. Overall, mmen-Mg_2(dobpdc) demonstrates better performance and economic viability, positioning it as a promising material for future DACC applications.

A TVSA-based DAC system is presented by Sinah [12] to compare the performance of two MOF sorbents, namely, MIL-101-(Cr)-PEI800 and mmen-Mg_2(dobpdc). The monolith channel/ as shown in Figure II, through which the reactant, i.e., air flow, is assumed to be cylindrical for analysis. Each of these channels is coated with an absorbent film. The characteristics of the monolith channel are presented in Table I.

Table 1: Parameters of Monolith Channel

Parameters of Monolith Channel [12]	
Absorbent film Thickness	60 microns
Diameter of Monolith Channel	1270 microns
Cell Density	400 cpsi

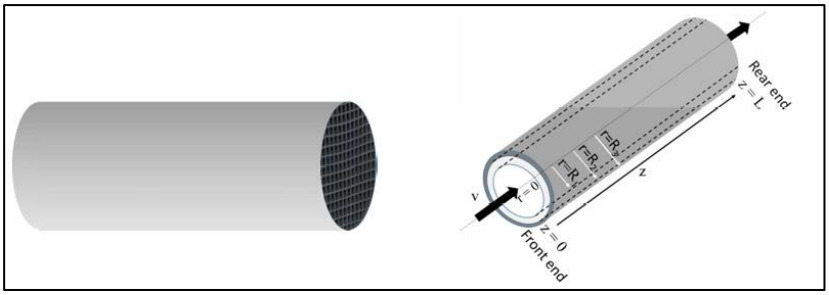

Figure II. Monolith channel [12]

The process (as illustrated in Figure 3) consists of the following five steps.

1. Air at ambient conditions (298K, 1 atm., 25% Relative Humidity) enters the channel. The CO_2 concentration in the air is assumed to be 400 ppm. Adsorption of CO_2 by the film begins in this step.
2. The second step involves the evacuation of air from the channel. This is done mainly to prevent the amine groups in the MOFs from being oxidized at high temperatures. The channel at the front end is closed and is evacuated by the use of a vacuum pump. The step continues until the oxygen concentration falls below 4%.
3. The third step involves pressurizing the channel to prevent any backflow of air (oxygen) from the rear end. This is done by closing the rear end and passing saturated steam at 1 atm through the front end.
4. Desorption occurs in step four by temperature swing. The rear end of the channel is opened, and saturated steam at 1 atm is fed to the channel from the front end. The steam condenses on the surface of the absorbent, increasing its temperature.
5. The last step involves cooling the system down to 348K from the desorption temperature of 373K. This is done to prevent the oxidative degeneration of the amine groups in the MOF. The vacuum pump is used for cooling using evaporating the water vapours out of the channel. As in the evacuation step, the front of the channel is closed, and pressure is dropped at the rear.

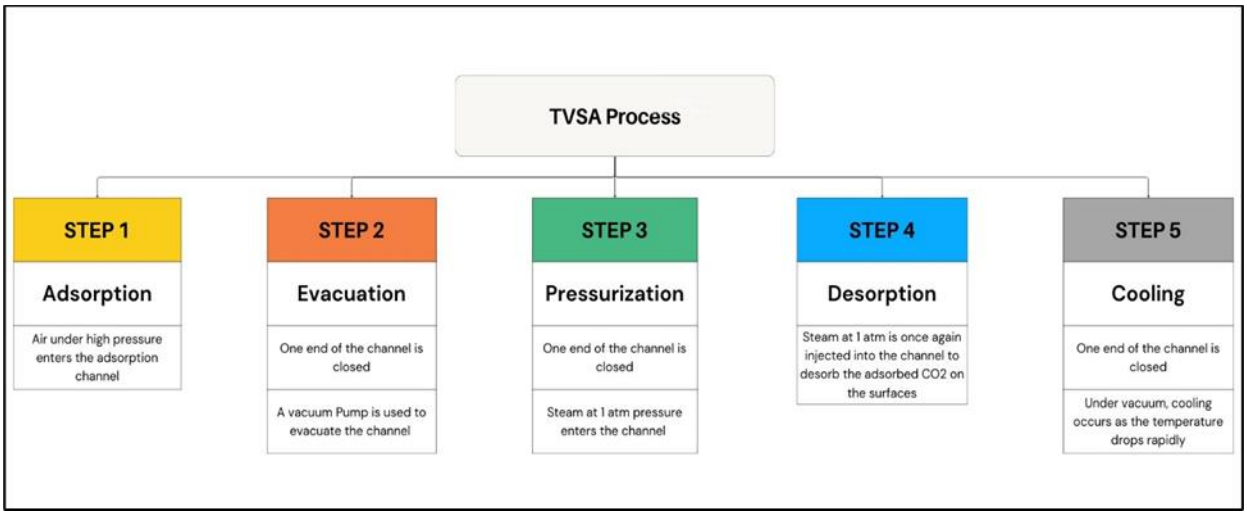

Figure III. Process Flow of TVSA.

3. Background. -

3.1 Air Capture System. - The research by J. K. Stolaroff et al. [13] explores the feasibility of capturing carbon dioxide (CO_2) directly from ambient air using a sodium hydroxide (NaOH) spray-based system. This approach is distinct from traditional methods that capture CO_2 from large, stationary sources such as power plants. The primary advantage of capturing CO_2 from ambient air is the potential to address emissions from diffuse sources and even past emissions. This can be particularly useful in achieving significant reductions in atmospheric CO_2 levels to mitigate climate change effects [14].

3.1.1 Process Overview. -

System Description. - The system involves spraying a solution of NaOH into the air, where it reacts with CO_2 to form sodium carbonate (Na_2CO_3). The CO_2-laden solution is then processed to regenerate NaOH and capture pure CO_2, which can be sequestered or utilized in various applications.

Contractor Design. - The contactor is the component where air interacts with the NaOH solution to absorb CO_2. Different designs for contactors include convection towers, open pools, and packed scrubbing towers [15]. This study focuses on a spray-based contractor.

- **Spray-Based Contactor:** The system utilizes fine spray nozzles to create a mist of NaOH solution that increases the contact surface area between the air and the absorbing liquid. A critical aspect of the design is managing drop coalescence, which can reduce the efficiency of CO_2 absorption [16].

The description of Direct Air Capture using the wet scrubbing method is given in Table II.

Aspect	Details
CO_2 Capture Method	Direct capture from ambient air using wet scrubbing
Absorbent Used	Sodium hydroxide (NaOH)
Recovery Process	Two-step precipitation and crystallization followed by customization with sodium tri-titanate
Energy Requirement	Approximately 50% less high-grade heat than conventional; lower maximum temperature required
Contactor Design	Packed scrubbing towers or open towers with NaOH spray
Advantages	Reduces CO_2 systematically from dispersed emissions, substantial cost reduction, pure CO_2 stream generated

Table II. DAC using wet scrubbing method [17]

3.1.2 Temperature Swing Adsorption. - Temperature Vacuum Swing Adsorption (TVSA) combines temperature and vacuum swings, which significantly lowers the energy required for the desorption process compared to TSA, which relies solely on heating. This makes TVSA more energy efficient. The comparison of different CO_2 capture methods is given in Table IV.

Method	Process Description	Efficiency	Advantages	Disadvantages	Key References
TVSA (Temperature Vacuum Swing Adsorption)	Involves the adsorption of CO_2 at lower temperatures and desorption at higher temperatures under vacuum conditions.	High	High working capacity, lower energy consumption compared to TSA.	Requires precise temperature control and vacuum systems.	[18], [19]
TSA (Temperature Swing Adsorption)	Adsorption of CO_2 occurs at ambient temperature and desorption at elevated temperatures.	Moderate to High	Simple setup, effective for large-scale applications.	Higher energy consumption due to heating requirements.	[20], [21]
Capture from Ambient Air Using Sodium Hydroxide Spray	Involves spraying a sodium hydroxide solution to capture CO_2 from ambient air, forming sodium carbonate.	Variable	Effective for low CO_2 concentrations, can be integrated with existing systems.	Chemical handling and disposal issues, lower efficiency for high CO_2 concentrations.	[13]
Electrochemical Conversion	Electrochemical reduction of CO_2 to valuable products using electrical energy	Moderate to high	Produces high-value chemicals and fuels, potential for integration with renewable energy sources	Complex catalyst development, high energy consumption, scalability challenges	[22]

Table III. Different CO_2 Capture Methods.

The addition of vacuum swing in TSA reduces the desorption time, leading to shorter cycle times and higher throughput. This efficiency can result in lower operational costs and improved overall process economics. TVSA systems typically produce high-purity CO_2 streams due to the effective desorption facilitated by vacuum. This high purity can be advantageous for subsequent CO_2 utilization or sequestration. It has a lower environmental impact as it requires less water compared to the NaOH spray method, which involves significant water use and potential chemical

handling issues. This makes the process more sustainable and environmentally friendly. TVSA is more cost-effective, especially for large-scale applications, due to its lower energy requirements and efficient operation. While initial capital costs for vacuum equipment may be higher, the long-term savings in operational costs make it a better economic choice.

Temperature Swing Adsorption (TSA) is a cyclic process used for the capture of CO_2 and other gases; details are given in Table 5. It leverages temperature changes to adsorb and desorb gases from solid adsorbents.

i. Adsorption. - During the adsorption phase, a gas mixture containing CO_2 is passed through an adsorbent bed. Materials like zeolites, activated carbons, and MOFs are used due to their high surface area and selective adsorption properties. The CO_2 molecules adhere to the surface of the adsorbent at lower temperatures, while other gases pass through the bed. This selective adsorption is influenced by the adsorbent's affinity for CO_2 and its operating temperature [23], [24].

ii. Heating. - Once the absorbent bed is saturated with CO_2, the heating phase begins. The bed is heated, typically using steam or other heat sources, to increase the temperature. This heat causes the CO_2 molecules to desorb from the adsorbent surface. The efficiency of this step depends on the thermal properties of the adsorbent and the design of the heating system. Effective heat integration can significantly lower the energy penalty associated with this step [23], [24].

iii. Desorption. - As the temperature rises, the CO_2 is released from the adsorbent. This desorption process generates a concentrated CO_2 stream, which can be captured and stored. The purity and recovery rate of CO_2 depend on the adsorbent material and the operational parameters of the TSA cycle. MOFs, for example, have shown promising results due to their tunable properties and high selectivity for CO_2 [23], [24].

iv. Cooling. - After desorption, the adsorbent bed is cooled down to its initial temperature, readying it for the next cycle. Cooling can be achieved through heat exchange with ambient air or other cooling media. Efficient cooling ensures that the adsorbent retains its adsorption capacity for subsequent cycles [23], [24].

Step	Description
1. Adsorption	CO_2 laden gas is passed through the adsorbent bed, where CO_2 is selectively adsorbed at a lower temperature. The bed typically contains materials like zeolites, activated carbons, or metal-organic frameworks (MOFs)
2. Heating	The adsorbent bed is heated to desorb the captured CO_2. This step increases the temperature of the bed to release the CO_2, making the adsorbent ready for the next cycle
3. Desorption	CO_2 is released from the adsorbent material due to the increased temperature. This step produces a concentrated stream of CO_2, which can be captured for further use or storage

Table V. TSA Process Steps [25]

3.2 Evaluating Metal-Organic Frameworks (MOFs) for CO_2 Capture. - Two MOFs, Zn4O(BTB)2 (MOF-177) and Mg2(dobdc) (Mg-MOF-74), were evaluated. Mg-MOF-74 demonstrated a higher working capacity and selectivity for CO_2 over N_2, which is critical for efficient CO_2 capture [26].

The study analyzed CO_2 adsorption isotherms at various temperatures, revealing that Mg2(dobdc) had superior performance, including a high working capacity of 17.6 wt% at 200°C. The presence of strong CO_2 adsorption sites in Mg-MOF-74 was crucial for its effectiveness in TSA processes [26].

3.3 Electrochemical Conversion. - The electrochemical conversion of CO_2 involves using electrical energy to drive chemical reactions that transform CO_2 into valuable products such as hydrocarbons, alcohols, and other chemicals. This process typically takes place in an electrochemical cell consisting of a cathode, an anode, and an electrolyte [22], [27].

i. Cathode Reactions. - At the cathode, CO_2 molecules are reduced to form products such as carbon monoxide (CO), formate, methanol, methane, ethylene, and other hydrocarbons. The specific product depends on the catalyst used and the operating conditions, such as potential and electrolyte composition.

The reduction of CO_2 involves multiple electron and proton transfer steps, making it a complex process. Effective catalysts are crucial to enhance selectivity and efficiency towards desired products [22], [27].

ii. Anode Reactions. - At the anode, water is typically oxidized to produce oxygen gas (O_2) and protons (H^+). This oxidation reaction provides the necessary protons and electrons for the reduction reactions at the cathode.

The overall efficiency of the process depends on the ability of the anode to facilitate the oxygen evolution reaction (OER) efficiently [22], [27].

iii. Electrolyte. - The electrolyte facilitates the movement of ions between the cathode and anode. It can be an aqueous solution, solid oxide, or ionic liquid, depending on the specific electrochemical system.

The choice of electrolyte affects the conductivity, stability, and overall efficiency of the electrochemical cell [22], [27].

iv. Metallic Catalysts. - Transition metals such as copper, silver, gold, and zinc are commonly used as catalysts for CO_2 reduction. Copper, in particular, is known for its ability to produce a wide range of hydrocarbons and alcohols.

Alloying and modifying these metals with other elements can enhance their catalytic properties and product selectivity [22], [27].

v. Metal-Organic Frameworks (MOFs). - MOFs are a class of porous materials that have shown promise as catalysts for CO_2 electroreduction. Their high surface area and tunable chemical environment make them suitable for optimizing catalytic activity and selectivity.

MOFs can be functionalized with various active sites to target specific reduction pathways [28].

vi. Electrocatalyst Optimization. - Research focuses on optimizing the structure, composition, and morphology of electrocatalysts to improve their performance. This includes developing nanostructured catalysts, bimetallic systems, and hybrid materials that combine the advantages of different components [28].

3.4 Mathematical Modelling of the TVSA system. - The following assumptions were made to develop the mathematical model:

- Air is considered to have oxygen and nitrogen components in addition to the CO_2 (and 25% relative humidity), and the saturated steam is pure.
- Ideal gas law and ideal mixtures are assumed for the non-condensable components [29].
- Temperature and concentration variations are neglected in the radial direction in the adsorbent film and monolith wall leading to a lumped model in the radial coordinate for these model elements [30].
- Adsorbent film thickness is uniform in the axial direction [31].
- During the desorption step, condensed water does not penetrate inside the MOF pores due to the high flow rate of desorbed CO_2 from the MOF pores in the opposing direction. Thus, heat is conducted into the MOF and wall and is not transferred by diffusion of steam within the MOF phase following steam condensation [32], [33].
- Heat loss from the channel is negligible during all steps of the cycle

The pressure drop across the channel is given by the Hagen Poiseuille equation:

$$\Delta P = \frac{8L\mu v}{R_1^2} \tag{1}$$

where, L = length of the channel
v = velocity of gas inside the channel
μ = gaseous viscosity
R_1 = Channel Inner Radius

The other source of pressure drop is due to drag on the system, which is assumed to be negligible as compared to pressure drop by Hagen- Poiseuille Equation [eqn. (1)].

The CO_2 absorption rate is approximated by the linear driving force model as given by:

$$\frac{\partial \mathbf{Q_{CO2}}}{\partial \mathbf{t}} = \mathbf{k}(\mathbf{Q_{CO2}^{eq}} - \mathbf{Q_{CO2}}) \tag{2}$$

Where, Q_{CO2} = absorbed CO_2 concentration
Q_{CO2}^{eq} = equilibrium concentration of CO_2
k = overall mass transfer coefficient

The mass transfer coefficient is calculated by the method proposed by A Sinha [12], which gives the final equation as:

$$\mathrm{k_m} = \frac{\mathrm{h_g M_{H_2 0}}}{\mathrm{C_{p,g} M_g y_{lm} Le_{H_2 0}^{2/3}}} \tag{3}$$

where, h_g = convective heat transfer coefficient of moist air
$M_{H_2 0}$ = Molar mass of water vapor
$c_{p,g}$ = Specific heat of moist air
M_g = Molar mass of air
y_{lm} = Log Mean Mole Fraction
$Le_{H_2 0}$ = Lewis number of H_2O
y_{lm} = Log mean mole fraction

$$y_{lm} = \frac{y_{ni} - y_{nb}}{\ln\left(\frac{y_{ni}}{y_{nb}}\right)} \tag{4}$$

Where, y_{ni} = mole fraction of the non-condensable gases at the gas film interface
y_{bi} = mole fraction in the bulk flow

The concentration at the interface is assumed to be in equilibrium with pure liquid water and thus estimated using the Antoine equation [eqn. (6)]:

$$-D_{H_2 O} \frac{\partial y}{\partial x} \tag{5}$$

$$C_{H_2 O}^{i} = \frac{\exp\left[a - \left(\frac{b}{T_g + c}\right)\right]}{R T_g} \tag{6}$$

where, $C_{H_2 O}^{i}$ = saturation concentration of water vapor in the MOF channel interface
a, b, c = Antoinne constants

The heat of absorption of CO_2 is determined using the Clausius−Clapeyron equation.

$$\ln\frac{P_2}{P_1} = \frac{\Delta H}{R}\left(\frac{1}{T_1} - \frac{1}{T_2}\right) \tag{7}$$

The heat of absorption of CO_2 is calculated at 25°C, 50°C and 75°C

The system design specifications and mass and heat transfer properties are tabulated in Table VI and Table VII, respectively.

Name	Symbol	Value	Unit
Air thermal conductivity	k_g	0.0257	$W/m.K$
Air heat capacity	$C_{p,g}$	1003	$J/kg.K$
Air density	ρ_g	1.1839	kg/m^3
Adsorbent Thermal Conductivity	k_{ads}	0.32	$W/m.K$
Adsorbent Heat Capacity	$C_{p,ads}$	892.5	$J/kg.K$
Adsorbent Density	ρ_{ads}	500	kg/m^3
Wall Thermal Conductivity	k_{wall}	1.6	$W/m.K$
Wall Heat Capacity	$C_{p,wall}$	840	$J/kg.K$
Wall density	ρ_{wall}	2050	kg/m^3
Antoine Constants	a, b, c	5.2,1733.9, -39.5	-

Table VI. Properties of the TVSA CO_2 Capture System [12].

Parameter	Value
D_g (m)	0.000016
h (W/m^2-K)	75
$T_{ambient}$	298
C_{CO2o} (mol/m^3)	0.016
C_{inerto} (mol/m^3)	40.88
ΔH (J/mol)	55000
ΔH (J/mol)	70000
A_1 (m)	0.00063
A_2 (m)	0.00052

Table VII. Heat and Mass Transfer Properties [12]

3.5 Estimating Energy Requirements

1) Electrical energy is required for the running of the fan. Higher air flow rates cause a larger pressure drop across the channel.
2) Energy required by the vacuum pump to decrease the pressure inside the channel.
3) Energy is required to provide sensible heat to the adsorbent.
4) Use of vacuum pumps to lower the partial pressure of water vapour.

The efficiency of the pump is considered to be 85 % [12]. The equations for the energy requirement for the various components are given in Table VII.

Components	Energy requirement (Joules per mole of CO_2)
Electrical energy for blowers	$E_1 = \frac{\Delta PQ.t}{N}$
Adsorbent sensible heat	$E_2 = \frac{mads\ Cads}{LN} \int_{t=tstep\ 4}^{tstep\ 5} \int_{z=0}^{L} (\frac{dTads}{dt}\ dz)dt$
Monolithic wall sensible heat	$E_3 = \frac{mads\ Cwall}{LN} \int_{t=tstep\ 4}^{tstep\ 5} \int_{z=0}^{L} (\frac{dTwall}{dt}\ dz)dt$
CO_2 desorption heat	$E_4 = \Delta H$
Electrical energy for vacuum Pump	$E_5 = -\frac{P_1 V_1^{\gamma}}{N_m} \frac{(V_2^{1-\gamma} - V_1^{\gamma})}{1-\gamma}$
Energy in uncondensed steam	$E_6 = \frac{2\pi L'}{N_m} \int_{t=tstep4}^{tstep5} (\int_{r=0}^{R1} v_{step4} r C_{H2O}(L) dr\ )\ dt$

Table VIII. Energy Requirements [12]

3.6 Economic Modelling of the System

- O&M cost of the device (includes energy, loading and unloading of a sorbent (**$N_{O\&M}$**))
- Scrap value of the sorbent at the end of its lifetime (**N_S**)
  N_S = Sorbent Price **V_s** + Installation cost **I_s**
- The amount spent on the hardware is taken into consideration; hence, the running expense is the capital cost of the plant **N_{BoP}**.

For NPV of a DAC system:

$$NPV_0 = N_{rev} - (N_{O\&M} + N_{BoP} + N_S) \quad (8)$$

The net present value of the system has to be zero or greater than zero at some point during the operation.

To find $t_{life,}$ the first derivative of the NPV equation concerning time must be zero:

$$@t = t_{life}\ \frac{dNPV_0}{dt} = n_{rev} - (n_{O\&M} + N_{BoP}) = 0 \quad (9)$$

Revenue generated per unit of time can be calculated as,

$$n_{rev}(t) = \frac{PC_0}{t_{cycle}} e^{\frac{-t}{\tau D}} e^{\frac{-t}{\tau M}} \quad (10)$$

where **P** is the market price of carbon dioxide per unit mass, $\mathbf{C_0}$ is the initial capacity of sorbent (the amount of CO_2 captured per cycle), and $\mathbf{t_{cycle}}$ is the duration of one loading/unloading cycle. **D** is the time constant of the sorbent capacity degradation, and **M** is a time constant that accounts for the time value of money. The costs of MIL-101(Cr)-PEI-800 and mmen-Mg2 (dobpdc) are taken as $15/kg and $50/kg, respectively taken from local market survey.

In summary, achieving economic viability for a Direct Air Capture (DAC) device necessitates meeting the conditions outlined in Equations (8), (9) and (10). While equation (9) allows for the calculation of the device's lifetime, a positive value for t_{life} does not automatically ensure a positive Net Present Value (NPV).

4. Results and Discussions. - The flow of CO2 through the material is shown in Figure 4, which shows how quickly CO_2 starts to pass through the material without being captured. For MIL-101(Cr)-PEI-800, CO_2 breaks through earlier, meaning this material gets saturated faster and starts letting CO_2 through sooner, while for mmen-Mg2(dobpdc), CO_2 breaks through later, indicating this material can capture more CO_2 before it gets saturated. At a time, step of approximately 4200s, the concentration stays constant since most of the CO_2 is adsorbed on the surface by the adsorbent.

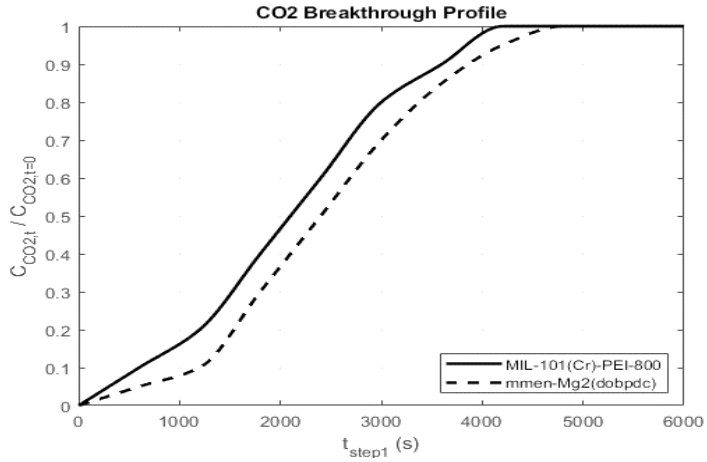

Figure IV. CO_2 breakthrough curve.

The holding time of CO_2 for each material is shown in Figure 5. From where one can conclude that since mmen-Mg_2(dobpdc) has a higher capacity of approximately 2.9 mmol/g, so it can hold more CO_2 while MIL-101(Cr)-PEI-800 has a lower capacity of approximately 1.2 mmol/g, so it holds less CO_2. In simple terms, mmen-Mg2(dobpdc) is better at capturing and holding more CO_2 for a longer time compared to MIL-101(Cr)-PEI-800.

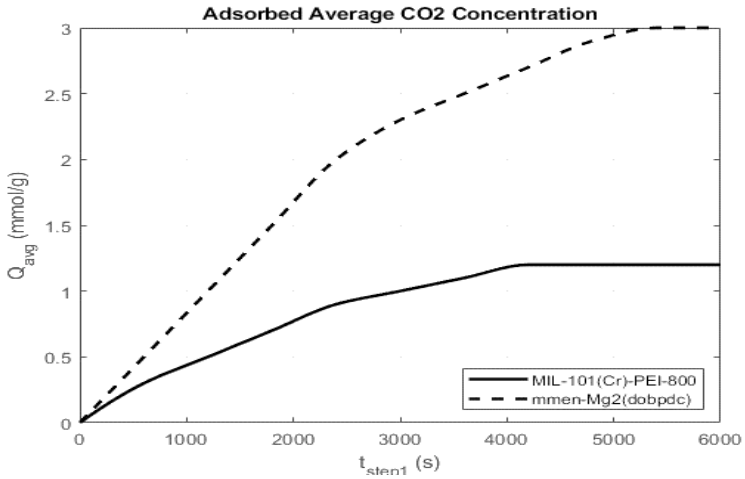

Figure V. Adsorbed average CO_2 concentration.

Energy requirements of the both MOFs mmen-Mg2 (dobpdc) and MIL-101 (Cr)-PEI-800 are given in Figure VI and Figure VII, respectively. Since the thermal efficiency was taken to be 85% [12], the minimum primary combustion energy requirements for the MIL-101(Cr)-PEI-800 and mmen-Mg2 (dobpdc) adsorbents are around 0.150 MJ/mole and 0.125 MJ/mole.

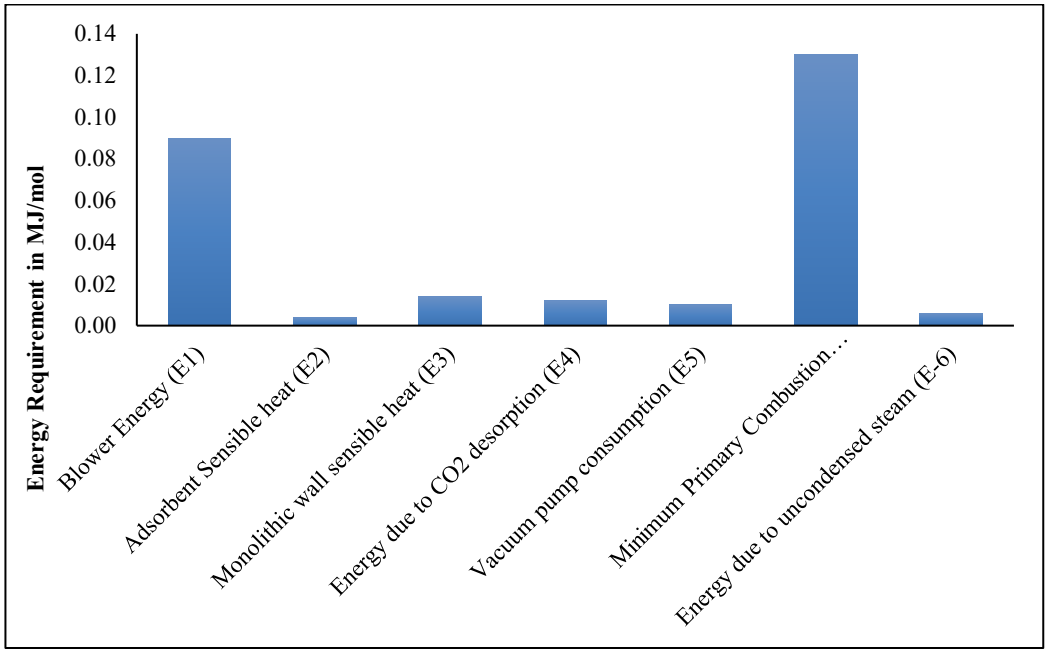

Figure VI. Energy requirements for mmen-Mg2 adsorbent.

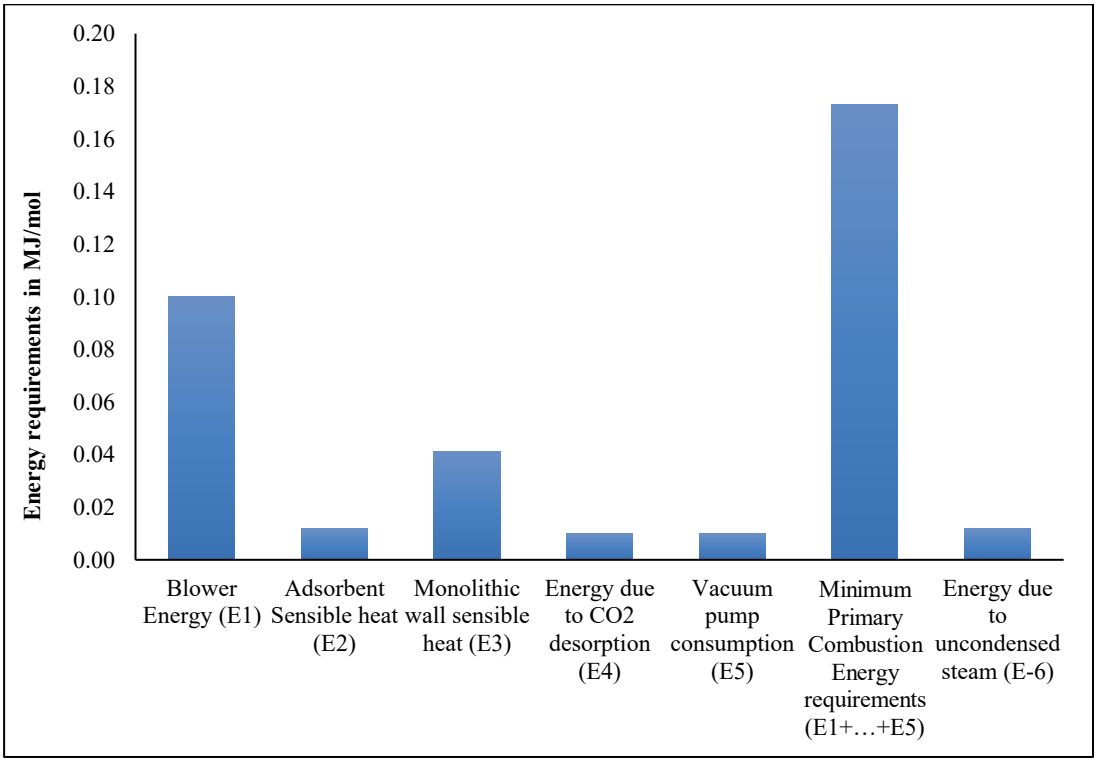

Figure VII. Energy requirements for MIL-101 (Cr)-PEI-800 adsorbent.

The cost comparison of both MOFs is shown in Figure 6. The curve shows the cost components for MIL-101(Cr)-PEI-800 and mmen-Mg-2(dobpdc), indicating that mmen-Mg-2(dopdc) generally incurs lower costs in key areas such as steam and blower operation. Specifically, MIL-101(Cr)-PEI-800 shows higher costs for blower Opex and steam, suggesting it is less economical in operational expenditure. While both materials have similar costs for monoliths and

vacuum pump Capex, mmen-Mg-2(dobpdc) offers cost savings in most categories, highlighting it as the more cost-effective option for these processes.

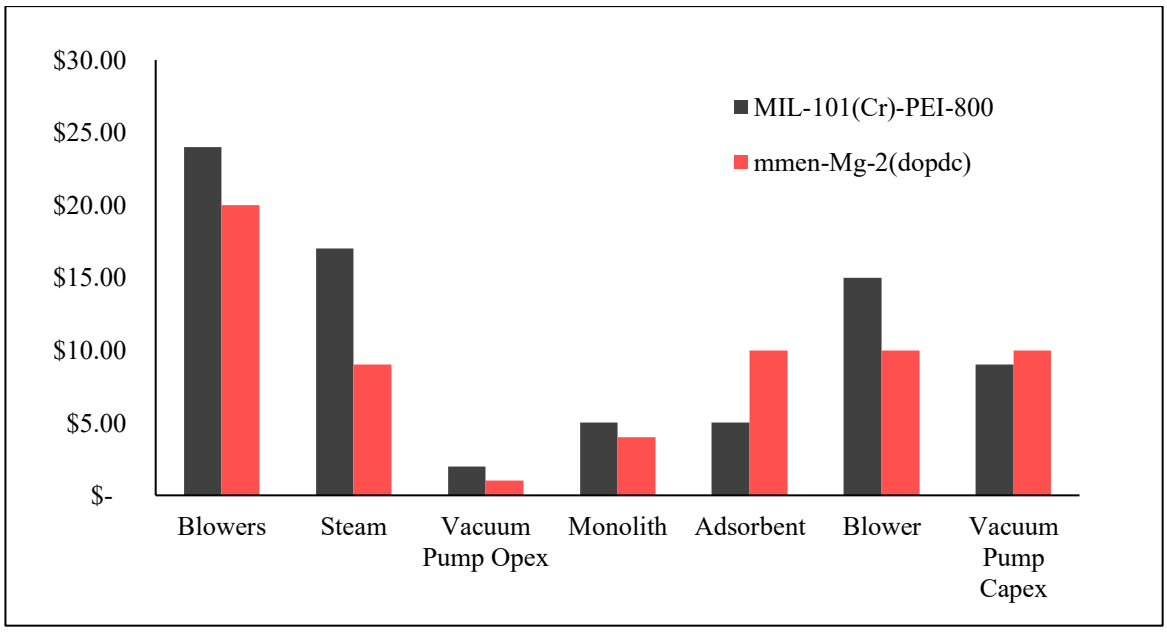

Figure VIII. Cost comparison between both adsorbents.

The Figure 7 looks at how the cost of the Direct Air Capture (DAC) process changes with different steam velocities for two materials MIL-101(Cr)-PEI-800 and mmen-Mg2(dobpdc). The curve shows that cost is the strong function of steam velocity. For MIL-101(Cr)-PEI-800, the cheapest operation is found at a steam velocity of 0.04 m/s while for mmen-Mg2(dobpdc), the lowest cost is at a steam velocity of about 0.06 m/s.

The study performed an analysis to find the best adsorption and desorption times by varying certain parameters and keeping the air velocity constant at 3 m/s. For this analysis, the steam velocity was kept at the optimal points identified (0.04 m/s for MIL-101(Cr)-PEI-800 and 0.06 m/s for mmen-Mg_2(dobpdc)). This helps to optimize the DAC process for cost and efficiency.

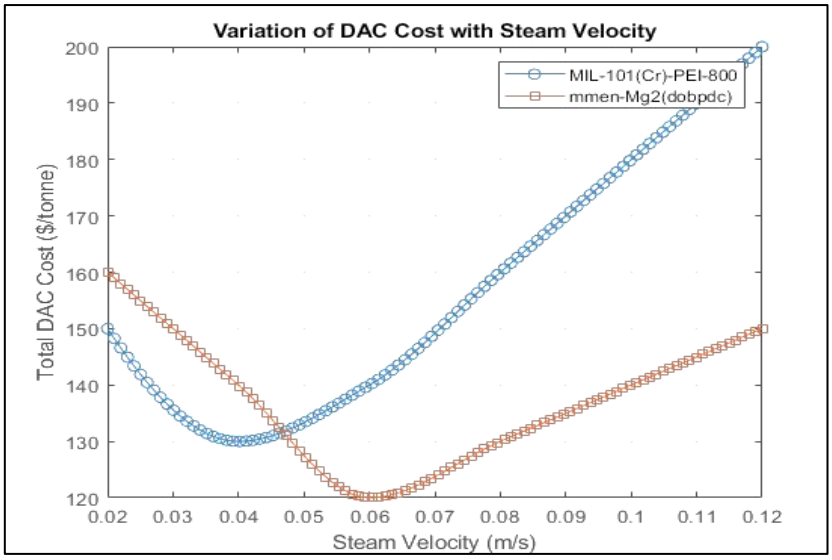

Figure IX. Total DAC Cost v/s Steam velocity.

MOF-based adsorbents, such as mmen-Mg_2(dobpdc), can potentially reduce energy demands and operational costs in DACC systems. However, transitioning these materials from lab-scale success to industrial deployment requires addressing unresolved challenges. These include energy-intensive synthesis (e.g., solvent reliance, high-temperature

activation), mechanical brittleness during pelletization (critical for industrial reactor integration), and stability under cyclic TVSA conditions, where thermal degradation or moisture sensitivity could compromise long-term performance. It also requires advancements in scalable synthesis methods like continuous flow reactors [34]. A thorough understanding of how MOFs integrate into different CO2 capture technologies and regeneration processes [35], and the effective use of computational tools for material design and performance prediction under realistic operating conditions [36]. Addressing these multifaceted challenges is crucial for transitioning the promise of MOFs into practical, large-scale solutions for carbon capture.

5. Conclusion. - This study investigates the performance of a TVSA (Temperature Vacuum Swing Adsorption) process for Direct Air Capture (DAC) of CO_2 using two advanced materials, MIL-101(Cr)-PEI-800 and mmen-Mg2(dobpdc). The latter material demonstrated superior CO_2 adsorption capacity (2.9 mmol/g compared to 1.2 mmol/g for MIL-101(Cr)-PEI-800). Key optimizations included air and steam flow rates, with 3 m/s airflow and steam velocities of 0.04 m/s for MIL-101(Cr)-PEI-800 and 0.06 m/s for mmen-Mg2(dobpdc). Energy requirements were minimized to below the CO_2 combustion energy, and costs were estimated at $77-142 per tonne for MIL-101(Cr)-PEI-800 and $64-194 per tonne for mmen-Mg2(dobpdc). Future improvements could include using solar energy and enhancing material stability, aiming to further optimize energy efficiency and reduce costs in scalable DAC solutions. The thickness of the adsorbent film is crucial in determining energy costs, as a thicker film captures more CO_2, thereby reducing the energy required for the desorption step. Maintaining a normal air flow rate is essential, since higher air flow rates would lead to CO_2 bypassing the adsorbent without being captured. It was observed that increasing air velocity beyond 3 m/s does not enhance adsorption. Additionally, utilizing a solar thermal cycle to produce steam can further decrease the system's overall energy cost.

On the other hand, the economic modelling of the Direct Air Capture (DAC) system includes the operation and maintenance (O&M) costs, which cover energy and the loading/unloading of the sorbent ($\mathbf{N_{O\&M}}$), and the scrap value of the sorbent at the end of its lifetime ($\mathbf{N_S}$). The scrap value ($\mathbf{N_S}$) is calculated as the sum of the sorbent price ($\mathbf{V_s}$) and the installation cost ($\mathbf{I_s}$). The hardware cost is also considered, making the capital cost of the plant ($\mathbf{N_{BoP}}$) part of the running expenses. The net present value (NPV) of the DAC system is determined by eq (8). For the system to be economically viable, the NPV must be zero or greater at some point during operation. To find the lifetime ($\mathbf{t_{life}}$) of the system, the first derivative of the NPV equation with respect to time is set to zero in eq (9). Key takeaways include that the NPV starts negatively due to the initial sorbent cost, increases with revenue from captured CO_2, and $\mathbf{t_{life}}$ is the point where the NPV reaches its maximum. The revenue generated per unit of time is calculated using eq (10).

The economic analysis indicates that MOFs can significantly reduce storage costs compared to traditional methods. The study evaluated the lifecycle costs of MOF-based storage systems and found that they offer competitive advantages in terms of both capital and operational expenses. This makes MOFs a cost-effective option for carbon capture.

Acknowledgment. - The Authors acknowledge the support provided by Sindh Higher Education Commission through the project SRSP/NPS SC. & Tech-09/314/2023-24.

References

[1] R. A. Kerr, "It's Official: Humans Are Behind Most of Global Warming," Science, vol. 291, no. 5504, pp. 566–566, Jan. 2001, doi: 10.1126/science.291.5504.566A.

[2] A. Kaithwas, M. Prasad, A. Kulshreshtha, and S. Verma, "Industrial wastes derived solid adsorbents for CO2 capture: A mini review," Chem. Eng. Res. Des., vol. 90, no. 10, pp. 1632–1641, Oct. 2012, doi: 10.1016/j.cherd.2012.02.011.

[3] S. A. Montzka, E. J. Dlugokencky, and J. H. Butler, "Non-CO2 greenhouse gases and climate change," Nature, vol. 476, no. 7358, pp. 43–50, Aug. 2011, doi: 10.1038/nature10322.

[4] R. Checa-Garcia, K. P. Shine, and M. I. Hegglin, "The contribution of greenhouse gases to the recent slowdown in global-mean temperature trends," Environ. Res. Lett., vol. 11, no. 9, p. 094018, Sep. 2016, doi: 10.1088/1748-9326/11/9/094018.

[5] J. G. Canadell et al., "Contributions to accelerating atmospheric CO 2 growth from economic activity, carbon intensity, and efficiency of natural sinks," Proc. Natl. Acad. Sci., vol. 104, no. 47, pp. 18866–18870, Nov. 2007, doi: 10.1073/pnas.0702737104.

[6] Y. Wu, J. Xu, K. Mumford, G. W. Stevens, W. Fei, and Y. Wang, "Recent advances in carbon dioxide capture and utilization with amines and ionic liquids," Green Chem. Eng., vol. 1, no. 1, pp. 16–32, Sep. 2020, doi: 10.1016/j.gce.2020.09.005.

[7] J. Zhang, S. Wang, X. Cheng, C. Chen, L. Zhang, and Z. Wang, "Design strategies and advantages of metal-organic frameworks@ lignocellulose-based composite aerogel for CO2 capture: A review," Sep. Purif. Technol., vol. 356, p. 129878, Apr. 2025, doi: 10.1016/j.seppur.2024.129878.

[8] A. Sodiq et al., "A review on progress made in direct air capture of CO2," Environ. Technol. Innov., vol. 29, p. 102991, Feb. 2023, doi: 10.1016/j.eti.2022.102991.

[9] M. Liu et al., "Recent advances and principles of metal–organic framework for the detection of chloramphenicol: Perspectives and challenges," Microchem. J., vol. 207, p. 111878, Dec. 2024, doi: 10.1016/j.microc.2024.111878.

[10] Y. An et al., "The stability of MOFs in aqueous solutions—research progress and prospects," Green Chem. Eng., vol. 5, no. 2, pp. 187–204, Jun. 2024, doi: 10.1016/j.gce.2023.07.004.

[11] I. K. Shah, P. Pre, and B. J. Alappat, "Steam Regeneration of Adsorbents: An Experimental and Technical Review," Chem. Sci. Trans., vol. 2, no. 4, Oct. 2013, doi: 10.7598/cst2013.545.

[12] A. Sinha, L. A. Darunte, C. W. Jones, M. J. Realff, and Y. Kawajiri, "Systems Design and Economic Analysis of Direct Air Capture of CO2 through Temperature Vacuum Swing Adsorption using MIL-101(Cr)-PEI-800 and mmen-Mg2(dobpdc) MOF Adsorbents".

[13] J. K. Stolaroff, D. W. Keith, and G. V. Lowry, "Carbon dioxide capture from atmospheric air using sodium hydroxide spray: Supporting Information".

[14] "Sodium Hydroxide-Based CO2 Direct Air Capture for Soda Ash Production─Fundamentals for Process Engineering | Industrial & Engineering Chemistry Research." Accessed: Sep. 25, 2024. [Online]. Available: https://pubs.acs.org/doi/10.1021/acs.iecr.3c00357

[15] K. Heidel, D. Keith, A. Singh, and G. Holmes, "Process design and costing of an air-contactor for air-capture," Energy Procedia, vol. 4, pp. 2861–2868, Jan. 2011, doi: 10.1016/j.egypro.2011.02.192.

[16] P. Tabarzadi and A. Ghaemi, "Modeling and optimization of CO2 capture in spray columns via artificial neural networks and response surface methodology," Case Stud. Chem. Environ. Eng., vol. 10, p. 100783, Dec. 2024, doi: 10.1016/j.cscee.2024.100783.

[17] M. Mahmoudkhani and D. W. Keith, "Low-energy sodium hydroxide recovery for CO2 capture from atmospheric air—Thermodynamic analysis," Int. J. Greenh. Gas Control, vol. 3, no. 4, pp. 376–384, Jul. 2009, doi: 10.1016/j.ijggc.2009.02.003.

[18] W. R. Lee et al., "Exceptional CO 2 working capacity in a heterodiamine-grafted metal–organic framework," Chem. Sci., vol. 6, no. 7, pp. 3697–3705, 2015, doi: 10.1039/C5SC01191D.

[19] L. A. Darunte, K. S. Walton, D. S. Sholl, and C. W. Jones, "CO2 capture via adsorption in amine-functionalized sorbents," Curr. Opin. Chem. Eng., vol. 12, pp. 82–90, May 2016, doi: 10.1016/j.coche.2016.03.002.

[20] D. Wu et al., "Thermodynamic complexity of carbon capture in alkylamine-functionalized metal–organic frameworks," J. Mater. Chem. A, vol. 3, no. 8, pp. 4248–4254, Feb. 2015, doi: 10.1039/C4TA06496H.

[21] Z. Yuan, M. R. Eden, and R. Gani, "Toward the Development and Deployment of Large-Scale Carbon Dioxide Capture and Conversion Processes," Ind. Eng. Chem. Res., vol. 55, no. 12, pp. 3383–3419, Mar. 2016, doi: 10.1021/acs.iecr.5b03277.

[22] "Maximum and Comparative Efficiency Calculations for Integrated Capture and Electrochemical Conversion of CO2 | ACS Energy Letters." Accessed: Sep. 24, 2024. [Online]. Available: https://pubs.acs.org/doi/10.1021/acsenergylett.3c02489

[23] L. Joss, M. Hefti, Z. Bjelobrk, and M. Mazzotti, "On the Potential of Phase-change Adsorbents for CO2 Capture by Temperature Swing Adsorption," Energy Procedia, vol. 114, pp. 2271–2278, Jul. 2017, doi: 10.1016/j.egypro.2017.03.1375.

[24] A. Ntiamoah, J. Ling, P. Xiao, P. A. Webley, and Y. Zhai, "CO2 Capture by Temperature Swing Adsorption: Use of Hot CO2-Rich Gas for Regeneration," Ind. Eng. Chem. Res., vol. 55, no. 3, pp. 703–713, Jan. 2016, doi: 10.1021/acs.iecr.5b01384.

[25] E. S. Sanz-Pérez, C. R. Murdock, S. A. Didas, and C. W. Jones, "Direct Capture of CO 2 from Ambient Air," Chem. Rev., vol. 116, no. 19, pp. 11840–11876, Oct. 2016, doi: 10.1021/acs.chemrev.6b00173.

[26] J. A. Mason, K. Sumida, Z. R. Herm, R. Krishna, and Jeffrey. R. Long, "Evaluating metal–organic frameworks for post-combustion carbon dioxide capture via temperature swing adsorption," Energy Environ. Sci., vol. 4, no. 8, p. 3030, 2011, doi: 10.1039/c1ee01720a.

[27] "Electrochemical Approaches for CO2 Conversion to Chemicals: A Journey toward Practical Applications | Accounts of Chemical Research." Accessed: Sep. 25, 2024. [Online]. Available: https://pubs.acs.org/doi/10.1021/acs.accounts.1c00674

[28] "Techno-economic Analysis of Metal–Organic Frameworks for Hydrogen and Natural Gas Storage | Energy & Fuels." Accessed: Sep. 24, 2024. [Online]. Available: https://pubs.acs.org/doi/10.1021/acs.energyfuels.6b02510

[29] T. Ahmed, "Chapter 3 - Natural Gas Properties," in Equations of State and PVT Analysis (Second Edition), T. Ahmed, Ed., Boston: Gulf Professional Publishing, 2016, pp. 189–238. doi: 10.1016/B978-0-12-801570-4.00003-9.

[30] M. S. Shafeeyan, W. M. A. Wan Daud, and A. Shamiri, "A review of mathematical modeling of fixed-bed columns for carbon dioxide adsorption," Chem. Eng. Res. Des., vol. 92, no. 5, pp. 961–988, May 2014, doi: 10.1016/j.cherd.2013.08.018.

[31] J. L. Plawsky, M. Ojha, A. Chatterjee, and P. Wayner, "Review of the effects of surface topography, surface chemistry, and fluid physics on evaporation at the contact line," Chem. Eng. Commun., vol. 196, pp. 658–696, May 2009, doi: 10.1080/00986440802569679.

[32] "Water and Metal–Organic Frameworks: From Interaction toward Utilization | Chemical Reviews." Accessed: Sep. 25, 2024. [Online]. Available: https://pubs.acs.org/doi/10.1021/acs.chemrev.9b00746

[33] “CO2 capture materials: a review of current trends and future challenges - ScienceDirect.” Accessed: Sep. 25, 2024. [Online]. Available: https://www.sciencedirect.com/science/article/pii/S2589234723001690

[34] J. L. Woodliffe et al., “Continuous flow synthesis of MOF UTSA-16(Zn), mixed-metal and magnetic composites for CO2 capture – toward scalable manufacture,” J. Environ. Chem. Eng., vol. 12, no. 6, p. 114167, Dec. 2024, doi: 10.1016/j.jece.2024.114167.

[35] M. Kong et al., “A review on development of post-combustion CO2 capture technologies: Performance of carbon-based, zeolites and MOFs adsorbents,” Fuel, vol. 371, p. 132103, Sep. 2024, doi: 10.1016/j.fuel.2024.132103.

[36] Z. Deng and L. Sarkisov, “Multi-Scale Computational Design of Metal–Organic Frameworks for Carbon Capture Using Machine Learning and Multi-Objective Optimization,” Chem. Mater., vol. 36, no. 19, pp. 9806–9821, Oct. 2024, doi: 10.1021/acs.chemmater.4c01969.

Author contribution:
1. Conception and design of the study
2. Data acquisition
3. Data analysis
4. Discussion of the results
5. Writing of the manuscript
6. Approval of the last version of the manuscript

MMUZS has contributed to: 1, 2, 3, 4, 5 and 6.
AT has contributed to: 1, 2, 3, 4, 5 and 6.

Acceptance Note: This article was approved by the journal editors Dr. Rafael Sotelo and Mag. Ing. Fernando A. Hernández Gobertti.

On-Time Delivery Improvement in an Injection Molding Process Applying a Problem-Solving Approach Based on Lean-Sigma and the MSA Effect

Mejora del índice de Entregas a Tiempo en un Proceso de Moldeo por Inyección de Plástico Utilizando un Enfoque Orientado a la Solución de Problemas Basado en Lean-Sigma y el Efecto del Sistema de Medición

Melhorar a Taxa de Entrega Pontual num Processo de Moldagem por Injeção de Plástico Utilizando uma Abordagem Orientada para o Problema Lean-Sigma e o Efeito do Sistema de Medição

Omar Celis-Gracia[1], Jorge Luis García-Alcaraz [2(*)], Fabiola Hermosillo-Villalobos[3]

Recibido: 21/01/2025 Aceptado: 02/03/2025

Summary. - Mexico's manufacturing industry is vital to the global economy. This industry has recently faced challenges due to the COVID-19 pandemic and globalized markets. Some developed countries can adopt innovative technologies; however, Mexico focuses on improving production processes with little investment, combined with existing resources and technology. Mexican companies use improvement techniques such as Six Sigma and Lean Manufacturing to achieve this goal. This study reports a method called Lean-Sigma that, unlike traditional methods that take months or even years to solve a problem, our method offers results in weeks, avoiding waste generation and speeding up decision-making. The proposed method consists of the following phases: identifying and measuring the problem, analyzing the root cause, developing a solution, and verifying the solution and control plan. The main characteristic of this approach is that it acts at the speed of Lean and uses engineering tools to solve problems and to demonstrate how the measurement system error could affect the achievement of the single-minute exchange of die (SMED). To validate the proposed method, a case study is presented in a plastic injection molding process in a manufacturing company located in Ciudad Juárez (Chihuahua, México), which has a late delivery rate that causes delays in the final assembly lines. Implementing the suggested strategy increased on-time deliveries from 77% to 99.36% in six weeks.

Keywords: Lean-Sigma, problem-solving, SMED, OTD, MSA.

(*) Corresponding author.

[1] PhD Student, Department of Electrical Engineering and Computer Science, Universidad Autónoma de Ciudad Juárez (México), al232735@alumnos.uacj.mx, ORCID iD: https://orcid.org/0000-0003-2061-3384

[2] Full-Time Professor PhD, Department of Industrial Engineering and Manufacturing, Universidad Autónoma de Ciudad Juárez (México), jorge.garcia@uacj.mx, ORCID iD: https://orcid.org/0000-0002-7092-6963

[3] PhD Student, Department of Electrical Engineering and Computer Science, Universidad Autónoma de Ciudad Juárez (México), al232735@alumnos.uacj.mx, ORCID iD: https://orcid.org/0000-0003-1644-7598

Memoria Investigaciones en Ingeniería, núm. 28 (2025). pp. 287-302
https://doi.org/10.36561/ING.28.17
ISSN 2301-1092 • ISSN (en línea) 2301-1106 – Universidad de Montevideo, Uruguay

Resumen. - *La industria manufacturera de México es vital para la economía mundial. Esta industria ha enfrentado recientemente algunos retos debido a la pandemia COVID-19 y a la globalización de los mercados. Algunos países desarrollados pueden adoptar tecnologías innovadoras; sin embargo, en México, la atención se centra en la mejora de los procesos de producción con poca inversión, combinada con los recursos y la tecnología existentes. Las empresas mexicanas utilizan técnicas de mejora como Seis Sigma y Manufactura Esbelta para lograr este objetivo. Este estudio reporta un método denominado Lean-Sigma que, a diferencia de los métodos tradicionales que tardan meses o incluso años en resolver un problema, nuestro método ofrece resultados en semanas, evitando la generación de desperdicios y agilizando la toma de decisiones. El método propuesto consta de las siguientes fases: identificación y medición del problema, análisis de la causa raíz, desarrollo de una solución y verificación de la solución y del plan de control. La principal característica de este enfoque es que actúa a la velocidad de Lean y utiliza herramientas de ingeniería para resolver problemas, así como para demostrar cómo el error del sistema de medición podría afectar a la consecución del cambio de troquel en un minuto (SMED). Para validar el método propuesto, se presenta un caso de estudio en un proceso de moldeo por inyección de plástico en una empresa manufacturera ubicada en Ciudad Juárez (Chihuahua México), la cual tiene una tasa de entrega tardía que ocasiona retrasos en las líneas de ensamble final. La aplicación de la estrategia sugerida aumentó las entregas a tiempo del 77% al 99,36% en seis semanas.*

Palabras clave: *Lean-Sigma, Solución de Problemas, SMED, Entregas a Tiempo, MSA.*

Resumo. - *A indústria transformadora do México é vital para a economia global. Esta indústria tem enfrentado recentemente alguns desafios devido à pandemia da COVID-19 e aos mercados globalizados. Alguns países desenvolvidos podem adotar tecnologias inovadoras; no entanto, no México, a tónica é colocada na melhoria dos processos de produção com pouco investimento, combinada com os recursos e a tecnologia existentes. As empresas mexicanas utilizam técnicas de melhoria como o Six Sigma e o Lean Manufacturing para atingir este objetivo. Este estudo relata um método chamado Lean-Sigma que, ao contrário dos métodos tradicionais que levam meses ou mesmo anos para resolver um problema, o nosso método oferece resultados em semanas, evitando a geração de resíduos e acelerando a tomada de decisões. O método proposto consiste nas seguintes fases: identificação e medição do problema, análise da causa raiz, desenvolvimento de uma solução e verificação da solução e do plano de controlo. A principal caraterística desta abordagem é que actua à velocidade do Lean e utiliza ferramentas de engenharia para resolver problemas, bem como para demonstrar de que forma o erro do sistema de medição pode afetar a realização da troca de moldes num minuto (SMED). Para validar o método proposto, é apresentado um estudo de caso num processo de moldagem por injeção de plástico numa empresa de produção localizada em Ciudad Juárez (Chihuahua, México), que tem uma taxa de entrega tardia que causa atrasos nas linhas de montagem finais. A implementação da estratégia sugerida aumentou a pontualidade das entregas de 77% para 99,36% em seis semanas.*

Palavras-chave: *Lean-Sigma, Resolução de problemas, SMED, Entrega atempada, MSA.*

1. Introduction. - The On-time delivery is a challenge faced by manufacturing companies today, negatively impacting product quality, customer satisfaction, and overall organizational efficiency [1]. According to Kholil et al. [2], the internal factors make this a difficult challenge to solve, including internal process capabilities, maintenance strategies, and supply chain coordination. However, external factors, such as the COVID-19 pandemic, have also caused the closure of raw material manufacturing companies worldwide, delaying supply and reducing the time required for transformation into finished products [3][4].

Horzela & Semrau [5] stated that one of the factors that contribute negatively to on-time delivery is the machine availability, which is a critical factor in ensuring on-time delivery in the manufacturing industry. Trakulsunti et al. [6] stated that by maintaining high levels of machine availability, minimizing downtime, and effectively managing production schedules, manufacturers can improve their ability to meet customer demands, fulfill delivery commitments and remain competitive. To achieve increased machine availability, companies must work on becoming more flexible and with little economic investment; therefore, they use continuous improvement (CI) approaches [7], [8], which play a crucial role in organizations [9].

Furthermore, CI initiatives, such as Total Quality Management, Lean Manufacturing (LM), and Six Sigma (SS), are critical in achieving flexibility [10]. These initiatives emphasize the importance of process improvement, employee training, and flexible production processes as key elements [11]. The benefits of such CI programs are that they enable organizations to adapt to changing and uncertain environments, stabilizing performance on the one hand and improving adaptability to change on the other [12]. This adaptability is critical for organizations to remain flexible in dynamic market conditions [13][14].

To improve flexibility and operate in a more stable state, responding to changing market demands and conditions, companies use approaches such as Lean Six Sigma (LSS) and Lean-Sigma (LS) [15]. The LSS approach is a process improvement methodology that combines the principles of Lean Manufacturing and Six Sigma [16]. This is because by integrating Lean's focus on waste reduction and value creation with the data-driven analytical tools and problem-solving methodologies of Six Sigma, organizations improve process performance, efficiency, and customer satisfaction [17]. On the other hand, LS differs in the problem-solving-oriented approach, which provides results in a short period, unlike LSS, which is more oriented to CI projects that can take, on average, 12 months to obtain results and determine if decisions have been correct [18].

In Mexico, using these continuous improvement tools is of great importance as it is a country with a developed manufacturing sector that contributes to the national economy. For example, by 2023, there were 579,828 companies in the manufacturing sector in the country, of which 486 were in the state of Chihuahua and 330 in Ciudad Juarez, representing 70% of the total in the entire state. These companies generate approximately 3 million jobs nationwide, 500,000 in Chihuahua state and more than 300,000 in Ciudad Juarez. This means that 60% of jobs in this sector in the state are generated in Ciudad Juarez, representing 11% at the national level [19]. Therefore, it is important to examine the industrial sector.

Currently, some publications demonstrate how these CI tools are used and the advantages they provide to the organization, such as Estrada-Orantes et al. [16] show an application of the LS approach in a manufacturing company dedicated to the production of plastic components by injection, where one of the machines that made up the process experienced difficulties in meeting on-time deliveries with a highly demanded product Initially, 99% of the product had burs (excess material) on one side, and an operator was removed manually, representing a rework; thus, the process's Cpk index was -1.64, out of the specification limits. The LS approach solves the problem using process mapping, root cause analysis, brainstorming, five whys, design of experiments (DOE), and Kaizen.

On the other hand, Gracia & Moctezuma [17] present another application of LS in a gear and chain assembly process; the process had problems with on-time deliveries due to the addition of a new model, and a daily shipment sequence was required, gaining greater flexibility. Initially, the process had an on-time delivery rate of 66%, and by applying the LS, a work team was integrated to solve the problem. Using LM tools, the production line was balanced using takt time calculation and just in time (JIT) to increase productivity from 1.8 to 2.5 pieces/min*man, which positively impacted the manufacturing lead time from 26.07 to 17 seconds, equivalent to a 35% improvement. Consequently, the percentage of on-time deliveries increased from 66% to 100%, and the sequence of shipments complied with. This approach solved the problem within four weeks, and the process capability increased from 2.6 to 3.4 sigmas.

Condé et al. [20] show an LSS approach through the Define, Measure, Analyze, Improve, Control (DMAIC) methodology, employing a design of experiments to reduce defects in an automotive company. First, the main defects

and factors that result in nonconforming parts in the casting and machining processes are identified. The design of experiments allowed for an increase in the quality level from 3.4 to 4 sigma's, which is an acceptable sustainable level. This indicates that LSS increases the quality levels of the process. However, it is necessary to wait six months to see the results, which generates the company incurring poor quality costs during that time.

Based on the previously mentioned applications, it is concluded that traditional continuous improvement approaches such as LSS and SS provide good results to organizations with efficiency, delivery, quality, and cost problems; however, the time required to provide acceptable results averages between six and 12 months, which has a negative impact on the costs and performance metrics of the organization. Furthermore, while the improvements achieved are acceptable, the original philosophy of these approaches, which is to bring processes to Six Sigma levels, has not been achieved. This approach stands out for LS and presents a more attractive form for companies because of its reaction time. It acts at the speed of lean, identifies the causes of problems, and resolves them in weeks, preventing companies from continuing to generate waste.

Therefore, this study aims to present the application of Lean Sigma in a manufacturing process with a problem-solving approach using industrial engineering principles. The novelty of this study is that results can be obtained in weeks, but it also shows that the error percentage of the measurement system could result in a milestone in achieving SMED. By solving the problem quickly, manufacturing companies can be flexible and cope with external factors, such as changes in demand, by improving on-time delivery rates and increasing customer satisfaction.

This case study was conducted in a company that manufactures gasoline pumps in the automotive sector. The demand for the plastic injection molding process fluctuated, and the number of parts delivered to the final assembly process was insufficient. This caused line stoppages and delayed deliveries to customers. The process of interest had 20 plastic injection molding machines, where the noncompliance rate ranged between 20% and 30%, resulting in late deliveries and high costs owing to low machine availability.

After this introduction, section two includes the methodology for this research. Section three discusses the results, section four reports the conclusions, and section five presents some of the limitations and future research.

2. Methodology. - The methodology used in this research is based on the DMAIC cycle and the Lean-Sigma approach, which consists of 5 stages, as shown in Figure I, which includes the steps and engineering tools used.

2.1 Step 1: Identify and measure the problem. - This step aims to define and delimit the problem and obtain initial data from the production process under initial conditions to determine the condition of the problem in terms of process capability. It starts with the formation of a multidisciplinary team dedicated full-time to the problem under analysis so that personnel from different departments can contribute ideas from different perspectives. Including the production supervisor, process engineer, manufacturing engineer, quality engineer, planning, and, if possible, at least two operators who perform the operation function are recommended. Once the work team is formed, it meets to identify and delimit the problem, using elements of a Project charter and defining the fundamental aspects, which include the Macro problem statement, project objective, project scope and limits, response variable, conditions, magnitude, performance, period, and specifications. This allows us to have a clear vision of the problem and to obtain important data, mainly to define the response variable that needs to be improved.

Subsequently, the work team collected initial data on the identified response variable. The data collection consists of obtaining the reports of the last weeks, where the value or performance of the response variable can be visualized, and tests are performed to confirm the normality of the data. If they are not normal, it is necessary to determine the type of distribution they follow for better analysis. Next, a control chart is created for individual data using Minitab software to analyze the trends and behavior of the response variable; however, the work team continues to monitor it to see trends and relate the out-of-control points with special events that occur in a specific period. Subsequently, a capability analysis is performed using the previously collected data and the specification limits to determine the parts per million defects and observe the size of the problem.

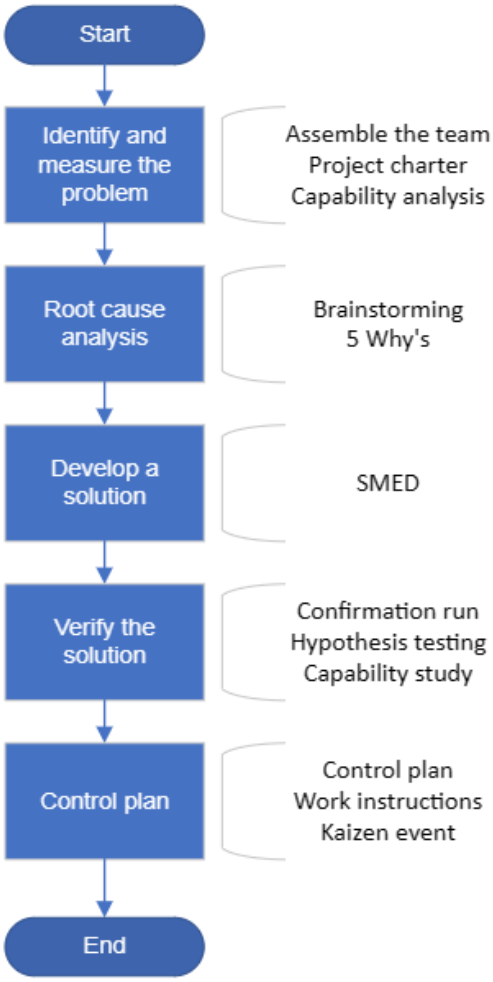

Figure I.- Flowchart of the proposed methodology based on the Lean-Sigma approach [16].

2.2 Step 2: Root cause analysis. - Once the problem is identified and the magnitude of the problem is determined, the team finds the potential causes that are generating the problem. First, the team engaged in brainstorming, where each participant brainstormed why the problem occurred, and the round continued until the ideas were exhausted. The moderator then refined the ideas to eliminate repeated ideas. With the list of ideas reduced, the nominal group technique was used to weigh ideas for each participant. Once the ideas have been weighed, the sum of the ideas is obtained, and the idea with the highest score is chosen. Finally, the 5 whys technique is applied, which consists of asking five times why the problem occurs, and the technique is stopped once a cause is found that does not point to a person or a department but is a cause that is under the control of the team and can provide a solution.

2.3 Step 3: Develop a solution. - Once the root cause is identified, a lean manufacturing or Six Sigma tool is used to solve the problem. In this case, the selected tool was SMED, which reduced the model to less than ten minutes. SMED is a Lean Manufacturing tool that reduces model changeover or setup times. This tool follows a well-structured methodology consisting of four phases, as Figure II illustrates.

Figure II.- Stages for the SMED Technique.

The purpose of the preliminary stage is to document the activities involved in the model change, which is performed by mapping the process. It is recommended that a video of the process be captured to perform a detailed analysis, where the activities and times are recorded. Once the activities are identified and listed, the next step is to classify them into two categories based on their current performance and not on how they should be or are believed to be. This classification is based on both internal and external activities.

The external activity is performed while the equipment is still operating or has not finished producing the previous model. In contrast, internal activity is necessary when the equipment is stopped. Subsequently, in step two, the activities that can be eliminated because they are considered unnecessary or wasteful are identified, and the internal activities that can be carried out externally are listed. In this step, checklists can be developed to validate that external activities have been completed before the machine is stopped. Finally, in stage three, an action plan is made to work on process improvements that require investment to reduce the time of internal activities, some of which can be to perform activities simultaneously, purchase more tools, design and implement fixtures, and poka yokes, among others.

Once the SMED technique was implemented, the team monitored the duration of the model changeover time. It makes a control chart comparing before and after to determine if there is a significant reduction.

2.4 Step 4: Verify the solution. - This step is of great importance because it validates that the tool implemented in the previous step is practical for the response variable. After improvements were made, data were collected on the response variable, and a 2-sample T statistical test was performed at a 95% confidence level.

2.5 Control plan. - Finally, in this step, we carry out Kaizen events to train personnel in the new tool implemented in step three. In addition, work instructions, procedures, standards, and process control plans are modified as applicable.

3. Results and Discussion. - This section is divided into sections based on the information reported.
3.1. Identifying and measuring the problem. The following information was obtained during the team meeting, during which important aspects of the problem were defined.

- Macro Problem Statement: The production schedule in the molding area is not followed. On average, 30% of the time, the program is not completed on time, resulting in delayed delivery to the internal customer.
- Project Goal: To reduce schedule noncompliance from 30% to 15%.
- Project scope and limits: The project was conducted in a plastic injection molding area.
- Response variable: Y=Compliance with production schedule. A defect occurs when scheduled production is not 100%.
- Conditions: Defects occur on different days of the week and in different months. Magnitude: The cost of non-compliance with the production program in March 2024 amounts to $31,000, and a projection shows that the annual cost amounts to $372,000.
- Performance: The measurement scale was equivalent to the % of compliance with the program.
- Period: It was estimated that defects generally occur when downtime is triggered.
- Specifications: Compliance with the program should exceed 99.2%.

It is important to note that the company's goal of achieving an on-time delivery rate above 99.2% was unmet, and the annual loss was $372,000.

Next, the work team collected information on the on-time delivery rate using six months of production reports. A total of 120 data points were plotted weekly, resulting in 24 subgroups. The data was then subjected to a normality test, as shown in Figure III. A p-value above 0.100 indicated that the data was normal.

Figure III.- Normality test of the initial data for compliance with the production program.

Once the normality of the data was confirmed, a control chart was created to observe the behavior of compliance with the production program to observe trends, as shown in Figure IV, where the on-time delivery rate was within statistical control and exhibited normal behavior. It can also be seen that, on average, the compliance rate was 77.42%, with behavior ranging from 63.89% to 90.95%. With this data, in the worst-case scenario, the molding process delivered 37% fewer parts required by the following process, affecting the final assembly lines.

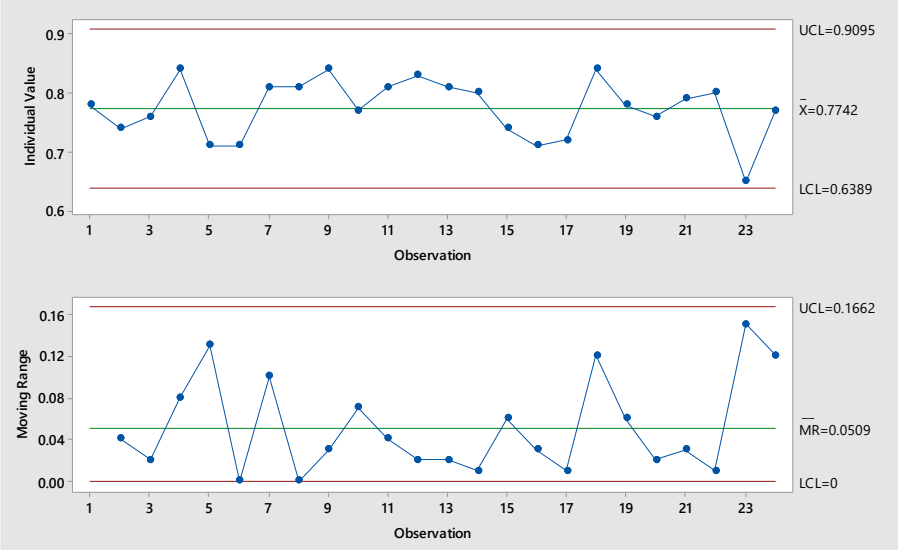

Figure IV.- Control chart of initial data regarding compliance with the production program.

Based on the company's goal of 99.2% compliance, a capability study was conducted to determine the process's sigma level and existing defective parts per million (DPPM). Figure V shows the analysis from which the following can be concluded: the process's initial C_{pk} is -1.61, which means that 100% of the time, the level of compliance was outside the goal set by the company; therefore, the initial sigma level can be set equal to zero.

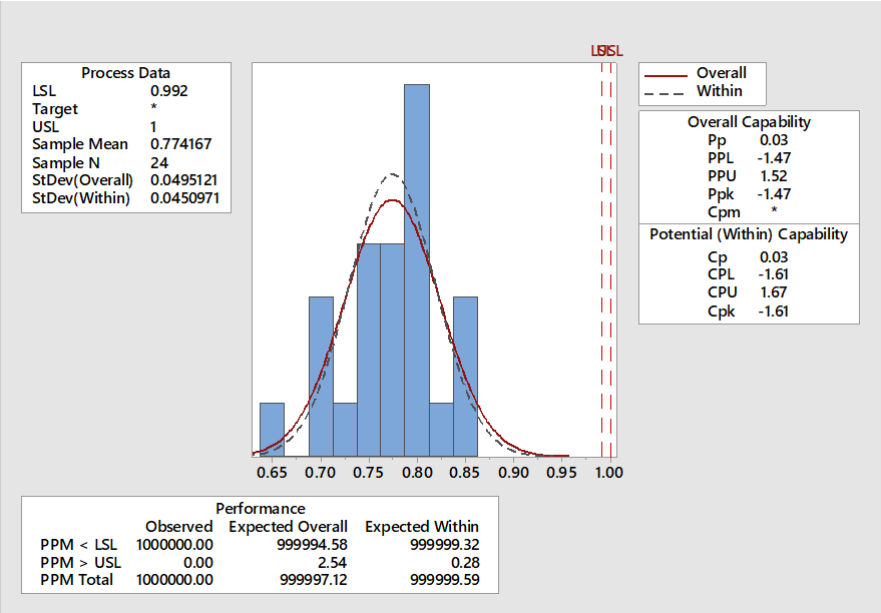

Figure V.- Process capability analysis performed on the OTD under initial conditions.

3.2. Root cause analysis. - Based on the information obtained and analyzed, basic quality tools were used to determine the root cause of the problem. First, the production area's multidisciplinary team, consisting of the production supervisor, group leader, maintenance technician, quality engineer, industrial engineer, tool crib technician and two equipment technicians, met to brainstorm ideas. Approximately 30 ideas were generated, some of which are listed in Table I.

No.	Idea
1	The machine does not achieve the production rate
2	Quality defects
3	Tool damaged
4	Training
5	Changeover time
6	Scheduling fluctuations
7	The production Schedule is not being followed
8	Missing materials
9	Failure in the dryers
10	Absenteeism

Table I.- Ideas generated by the multidisciplinary team

The team used the nominal group technique with a generated list of ideas, and each member assigned weights to the ideas. Table II shows the scores for each of the ideas, and it was found that the time required to change the model was the major contributor to not delivering on time.

No.	Idea	Score
1	The machine does not achieve the production rate	16
2	Quality defects	30
3	Tool damaged	1
4	Training	1
5	**Changeover time**	**40**
6	Scheduling fluctuations	28

7	The production Schedule is not being followed	19
8	Missing materials	0
9	Failure in the dryers	0
10	Absenteeism	0

Table II.- List of ideas with weights when applying the nominal group technique.

The team decided to focus primarily on problems with high model changeover times, which scored 40; therefore, it collected data on model changeover times in minutes in the production area. Figure VI presents the data collected for 280 events.

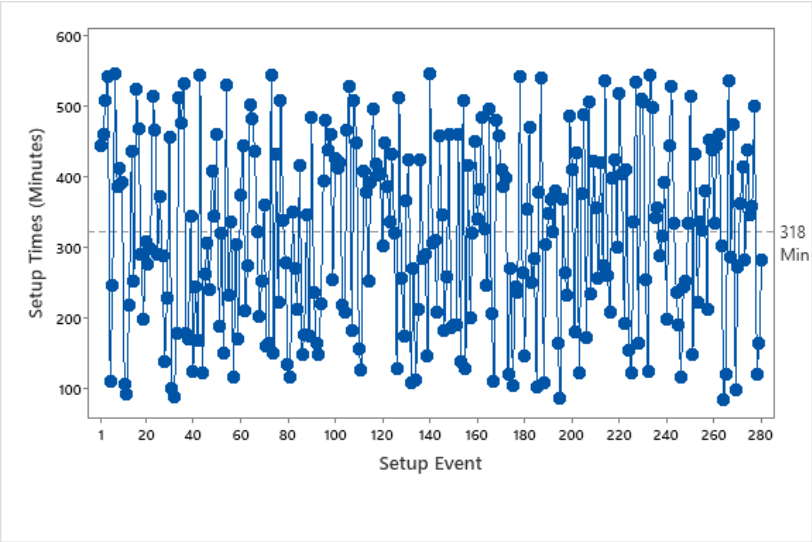

Figure VI. - Model changeover times under initial conditions.

The average changeover time was 318 min (~ 5 h). This indicates that more than half of the workday shift is lost when a model change is made, resulting in lower production and efficiency. Therefore, there is a correlation between high model change times and on-time deliveries owing to the loss of time available on the production line.

3.3. Develop a solution. - Once the root cause of the problem has been identified, the team discussed possible lean tools to counteract the adverse effects of model change over time. It identified the single-minute exchange of die (SMED) tool, a lean manufacturing tool that seeks to reduce setup and model changeover times to less than 10 min. Four phases of the SMED technique are described, and the results are shown below.

3.3.1. Identify model change activities. - The main purpose of this step is to identify the activities involved during a changeover; to do so, different model changes were analyzed. The changeover process was mapped to one of the machines, selecting one of the models that, according to the team's experience, generated the most problems, causing the setup time to increase up to 8 hours in the worst-case scenario. Once the process is mapped, the activities were identified and are listed in Table III.

No.	Activity Description	Time in Minutes
1	Go to the tool room to get the mold cavity and tools	13
2	Turn off heaters	3
3	Waiting to release a crane	35
4	Go to the tool room to get tools	15
5	Place holder and attach mold to the crane	4
6	Go to the tool room to get support to replace	17
7	Go to the tool room to get hoses	15
8	Disconnect hoses and clean	33

9	Place locks on the mold	2
10	Take off eight supports	11
11	Open the clamp and disassemble the arrow	16
12	Take down the mold	3
13	Put in place next to the mold	6
14	Close clamps	3
15	Place supports on the mold (2)	6
16	Open the clamp and install the arrow	2
17	Install six supports to the mold	27
18	Take off holders to the crane and detach the mold.	1
19	Upload the program	2
20	Open the mold and adjust	4
21	Install 40 hoses	30
22	Go to the tool room to get a zip tie	16
23	Install the zip tie	6
24	Change the fixture to the robot	4
25	Adjust the water level	5
26	Review and fix the leakage	1
27	Go to the tool room to get resin to purge the machine	27
28	Preheat and purge	30
29	Make parts for setup validation	10
	Total Time in Minutes	347

Table III.- Documentation of changeover activities under initial conditions.

Some of the most relevant aspects to mention in this step are that, as shown in Table III, 29 activities can be identified in the model-change process. Similarly, it can be observed that the model changeover time is 347 min, equivalent to 5.78 hours, considering that the shift is 9 hours. This means that approximately 64.25% of the machine time is unavailable for production because of this increase in setup times, resulting in the company's current symptoms, that is, noncompliance with deliveries to the assembly lines.

3.3.2. Separate internal and external activities. - Once the process has been mapped and the activities involved have been identified, the work team classified each activity as internal or external. In this case, during the analysis, it was identified that all activities were performed internally, that is, while the equipment was stopped.

3.3.3. Convert internal activities into external. The team analyzed each activity in detail to convert those that can be performed externally before the equipment is stopped. Figure VII shows in the left graph that 24.1% of the activities can be performed externally, resulting in a ~39.8% reduction of the total changeover time, as shown in the right chart.

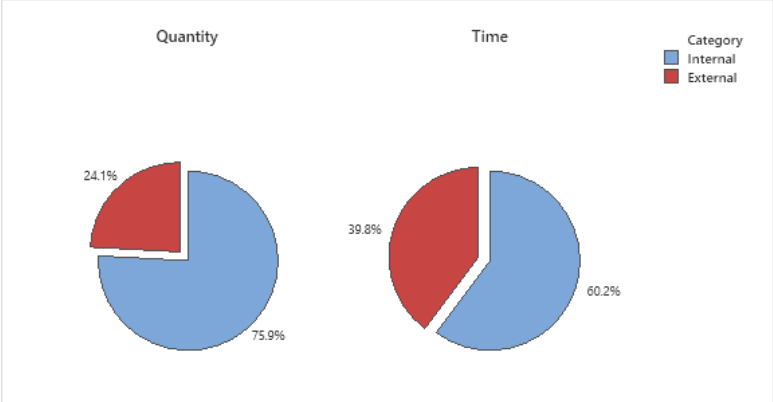

Figure VII.- Impact of converting internal into external in the total changeover time.

Using the fundamental principle of converting internal activities into external ones, the model changeover time for the analyzed setup was reduced from 347 to 209 min, which represents a decrease of approximately 40%. In addition, there were 7 external and 22 internal activities.

A setup preparation checklist was developed to list all necessary activities to achieve activity conversion. The tools must be available before the previous model's production ends. This ensures that when the machine stops, everything is available and within the reach of an efficient setup change. This step implemented a checklist and monitored the setup times to ensure that external activities were prepared before executing a model change.

3.3.4. Reduce internal activities. - Because the proportion of internal activities was still considerably high (76%), the team worked on reducing the time spent on internal activities in this phase. For this, the team proposed strategies such as developing fixtures, executing activities in parallel, and standardizing and documenting model change activities. Once these activities were implemented, the model change time was monitored for two weeks, collecting 25 data points, and a before vs. after graph was made.

As shown in Figure VIII, once the SMED technique was implemented, the model changeover times were reduced by approximately 73%, from 344.6 to 92.7 min on average.

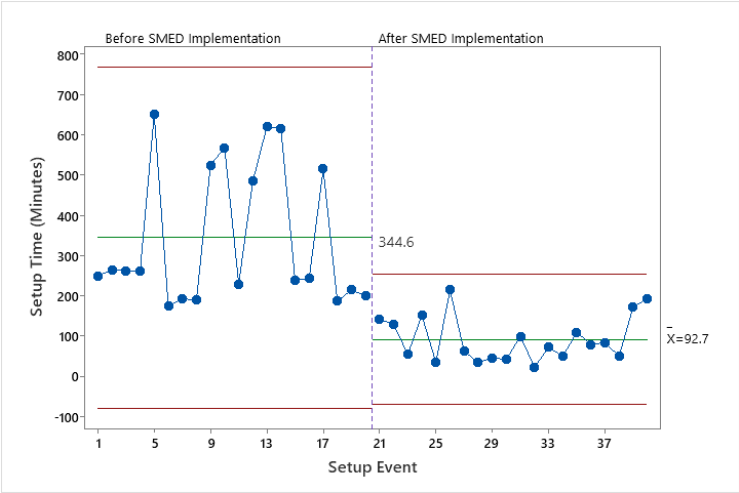

Figure VIII.- Control chart of setup time before and after the SMED Implementation

Even though the model change was reduced to 92.7 min on average, this value is still well above the SMED technique. Therefore, the team investigated why this was considerably high. After a brainstorming session, it was found that the first part of releases consumed 40% of the model changeover time. This was because of the multiple quality rejections of the parts.

When investigating the root cause of the high rate of rejections, it was identified that the measurements varied owing to various factors. Therefore, the team decided to conduct a measurement system analysis (MSA) on different days involving the personnel and instruments used in the release of the machine. The results of the MSA error and the sigma level of the corresponding day are presented in Table IV, which was used to perform a regression analysis in Minitab. Figure IX shows the regression analysis and the corresponding equation.

Day	% Error (X)	Sigma Level (Y)
1	31.72	1.044
2	39.91	0.771
3	23.99	2.246
4	29.82	0.872
5	31.81	0.021
6	40.78	0.472
7	30.03	1.891

Day	% Error (X)	Sigma Level (Y)
11	25.98	2.363
12	25.33	2.56
13	30.66	1.002
14	29.4	1.302
15	36.68	0.448
16	35.58	0.139
17	33.43	0.774

8	23.23	1.98	18	20.68	2.017
9	20.76	2.676	19	40.12	0.683
10	23.23	1.973	20	17.38	2.702

Table IV.- Error of the measurement system and sigma level

The measurement system error had a significant variation, and it had a relationship with the quality level of the process. Regression analysis shows an R-squared value of 71.2%, which means that the measurement system error explains 71.2% of the process's sigma level value.

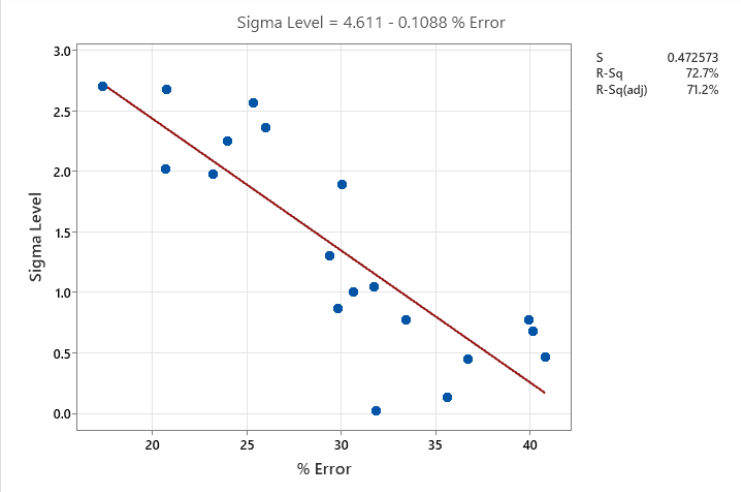

Figure IX.- Regression analysis using the Measurement error (x) vs the Sigma level (y).

3.4. Verify the solution. - Once the solution was developed and implemented, an experimental design was conducted to verify the impact of the model change on compliance with the production schedule. For this purpose, data on compliance with the production schedule was taken for two weeks, and then a comparison was made using a 2-sample t-test in Minitab software. The results are presented in Table V.

	Sample	N	Mean	StDev	SE Mean
	Before	24	0.7742	0.0495	0.010
	After	22	0.9936	0.0162	0.0035
Null hypothesis	H_0: $\mu_1 - \mu_2 \geq 0$				
Alternative hypothesis	H_1: $\mu_1 - \mu_2 < 0$				

Table V.- 2 Sample test and hypothesis tests to validate the solution.

Based on the confirmation run and hypothesis test shown in Table V, it is concluded that the model change time is directly correlated to the compliance with the production schedule. Once the solution was implemented, compliance with the production schedule increased from 77% to 99.36%.

3.5. Control plan. - As the last step of the proposed methodology, a series of Kaizen-type events involving staff from all shifts involved in the model changes were carried out. These events were theoretical-practical training given to quality, maintenance, production, manufacturing and test engineering to notify them about the implemented improvements and the new work method for standardization. Initially, there was no properly documented method to perform the changeover process; after implementing the SMED technique, a work instruction was developed, including a sequential flow with tools, materials and information needed before and after the changeover initiation. It is important to mention that the kaizen events were carried out using the Gemba approach. To monitor and react on time, a board was placed next to the machines to document the setup times, including the challenges and milestones found during the process. Also, an Andon was implemented with a color code properly defined to visually identify the machine's status and support immediately in case any showstopper appears.

4. Discussion of results and conclusions. - The initial information showed that the analyzed plastic injection process had a sigma level of zero, initially having a production schedule compliance rate of 77% on average, below the company's goal. Using the proposed methodology based on Lean sigma, it is concluded that the root cause of the problem was that model changeover times sometimes shoot up to 8 hours, affecting the availability of machinery and flexibility and the ability of the process to adapt to fluctuations in demand. The SMED technique was used to reduce model changeover times and achieve a 75% reduction in setup times, with the fundamental principle of converting internal activities into external ones. In the solution verification step, it was possible to demonstrate that there was a correlation between the reduction of model changes and compliance with the production schedule according to the 2-sample-t test; it was demonstrated with a confidence level of 95% that compliance with the schedule was increased from 77% to 99.36%.

This case study was carried out over eight weeks, solving the root problem with an approach where the contribution or novelty lies in the fact that this approach is oriented to solving problems at the speed of lean, unlike traditional Six Sigma approaches, where projects are based on annual savings and on average improvements can be seen between 6 and 12 months. It is important to mention that companies need to solve problems quickly to reduce Lead time; for example, Kulkarni et al. [22] show an application of traditional Six Sigma, where a company is scraping 10% of the daily production which represents a loss of $10K daily that means a total loss of $200,000 per month, using the traditional approach which took eight months to solve the problem this represented a total loss of over a million dollars compared to the proposed method which would have a loss of $300,000. Guleria et al. [23] applied the traditional Lean Six Sigma approach, showing results in eight months; in this case, the company lost $800,000 versus $150,000 if the proposed approach had been used.

Another scientific contribution proposed by this research is the correlation between the measurement system error and the sigma level of the process, which was presented in the phase of reduction of internal activities of the SMED technique. However, the team managed to reduce the model change time significantly. It was observed that it was still high, so it was decided to investigate in more detail, finding that the root cause was the high rate of rejection, and it was found that the error in the measurement system was an important contributor. It is concluded that the measurement system explains 71.2% of the fluctuation in the sigma level of the process, which means that the measurement system does not correctly classify good and bad parts; bad parts are accepted, and good parts can be rejected. This finding opens a line of research focused on further studying the relationship between these two components and strategies to counteract the error in the measurement system so that the quality of the processes is maintained at acceptable levels. Considering this case study, the measurement system error is ~ 29%; this value means that, on average, 29% of the time, parts are categorized incorrectly; in other words, 29% percent of the parts are rejected and scrapped when these are acceptable. This error can represent a high contribution to the increase of the manufacturing costs of the company, considering only one part number with a scrap cost of $10.53, considering a monthly production of 25,000, if the worst scenario is assumed that 29% of the parts are scrapped because of the error of the measurement system this could be an annual cost of ~$900,000.

This methodology and its approach, including the engineering tools used, can be applied to any manufacturing company around the world. It includes fabrication, powder coating, final assembly, metals, molding, and PCBAs, among other processes.

5. Limitations and future research. - It is important to mention that this research was carried out using a plastic injection molding process; however, the methodology can be used in any manufacturing process. One of the limitations is that for its implementation, the work team must be led by a person with knowledge of Lean and Six Sigma topics, preferably a Black Belt, to be able to guide and direct the team in the right direction and with an analytical and statistical approach. Likewise, it should be noted that a multidisciplinary work team must be dedicated and committed because it requires time to achieve the expected results. The proposed approach initially focused on addressing the main cause of the problem; it is recommended to continue applying the approach to address other identified causes to improve the process continuously. In future research, it is recommended that the effect of the measurement system analysis be investigated at the sigma level of the process to quantify and develop a solution for this cause of variation.

References

[1] M. Bhargava and S. Gaur, "Process Improvement Using Six-Sigma (DMAIC Process) in Bearing Manufacturing Industry: A Case Study," in IOP Conference Series: Materials Science and Engineering, IOP Publishing Ltd, Jan. 2021. doi: 10.1088/1757-899X/1017/1/012034.

[2] M. Kholil, J. Haekal, A. Suparno, D. S. Oktaandhini, and T. Widodo, "Lean Six sigma Integration to Reduce Waste in Tablet coating Production with DMAIC and VSM Approach in Production Lines of Manufacturing Companies," International Journal Of Scientific Advances, vol. 2, no. 5, 2021, doi: 10.51542/ijscia.v2i5.8.

[3] D. Zhang, S. Chen, and Y. Xu, "Study on the improvement of single minute exchange of die based on lean production," in Seventh International Conference on Electromechanical Control Technology and Transportation (ICECTT 2022), SPIE, 2022, pp. 101–110. doi: 10.1117/12.2645572.

[4] K. F. Barcia, L. Garcia-Castro, and J. Abad-Moran, "Lean Six Sigma Impact Analysis on Sustainability Using Partial Least Squares Structural Equation Modeling (PLS-SEM): A Literature Review," Sustainability (Switzerland), vol. 14, no. 5, 2022, doi: 10.3390/su14053051.

[5] A. Horzela and J. Semrau, "Using Tools to Improve Logistics and Production Processes in a Selected Construction Company," European Research Studies Journal, 2021, doi: 10.35808/ersj/2100.

[6] Y. Trakulsunti, J. Antony, R. Jayaraman, and G. Tortorella, "The application of operational excellence methodologies in logistics: a systematic review and directions for future research," Total Quality Management and Business Excellence, vol. 34, no. 5–6, pp. 538 – 557, 2023, doi: 10.1080/14783363.2022.2071695.

[7] S. S. Chakravorty and D. N. Hales, "Sustainability of process improvements: an application of the experiential learning model (ELM)," Int J Prod Res, vol. 55, no. 17, pp. 4931 – 4947, 2017, doi: 10.1080/00207543.2016.1277278.

[8] A. C. Tonini, M. De Mesquita Spínola, and F. J. B. Laurindo, "Six sigma and software development process: DMAIC improvements," in Portland International Conference on Management of Engineering and Technology, 2006, pp. 2815 – 2823. doi: 10.1109/PICMET.2006.296875.

[9] R. L. Matthews and P. E. Marzec, "Continuous, quality and process improvement: disintegrating and reintegrating operational improvement?," Total Quality Management and Business Excellence, vol. 28, no. 3–4, pp. 296 – 317, 2017, doi: 10.1080/14783363.2015.1081812.

[10] H. Lebovits and J. Teal, "Considering Equity in Public Process Improvement Trainings," Public Integrity, vol. 22, no. 6, pp. 555 – 574, 2020, doi: 10.1080/10999922.2020.1719807.

[11] M. A. S. Ribeiro, A. C. O. Santos, G. da F. de Amorim, C. H. de Oliveira, R. A. da Silva Braga, and R. S. Netto, "Analysis of the implementation of the single minute exchange of die methodology in an agroindustry through action research," Machines, vol. 10, no. 5, p. 287, 2022, doi: https://doi.org/10.3390/machines10050287.

[12] J. Nikolić, M. Dašić, and M. Đapan, "Smed as an indispensable part of lean manufacturing in the small and medium enterprises.," International Journal for Quality Research, vol. 17, no. 1, 2023, doi: 10.24874/IJQR17.01-16.

[13] P. Teixeira, J. C. Sá, F. J. G. Silva, L. P. Ferreira, G. Santos, and P. Fontoura, "Connecting lean and green with sustainability towards a conceptual model," J Clean Prod, vol. 322, p. 129047, 2021, doi: 10.1016/J.JCLEPRO.2021.129047.

[14] J. L. García-Alcaraz, G. Alor-Hernández, C. Sánchez-Ramírez, E. Jiménez-Macías, J. Blanco-Fernández, and J. I. Latorre-Biel, "Mediating role of the six sigma implementation strategy and investment in human resources in economic success and sustainability," Sustainability (Switzerland), vol. 10, no. 6, 2018, doi: 10.3390/su10061828.

[15] A. Al-Atiyat, A. O. Ojo, and P. C.-H. Soh, "Impact of six sigma critical success factors on productivity improvement through absorptive capacity in the manufacturing industry in Saudi Arabia," International Journal of Productivity and Quality Management, vol. 32, no. 4, pp. 536 – 556, 2021, doi: 10.1504/IJPQM.2021.114267.

[16] F. Estrada-Orantes and N. Alba-Baena, "Creating the lean-sigma synergy," in Lean manufacturing in the developing world: methodology, case studies and trends from latin America, 2014, pp. 117–134. doi: https://doi.org/10.1007/978-3-319-04951-9_6.

[17] O. C. Gracia and J. A. T. Moctezuma, "Implementación de la metodología Lean Sigma en un proceso de ensamble de engranes y cadenas: Caso de estudio," CULCyT: Cultura Científica y Tecnológica, vol. 19, no. 3, pp. 23–32, 2022, doi: https://doi.org/10.20983/culcyt.2022.3.2.3.

[18] O. Celis-Gracia, J. L. García-Alcaraz, F. J. Estrada-Orantes, L. Avelar-Sosa, N. G. Alba-Baena, and F. Hermosillo-Villalobos, "Reduction of Setup Times in a Metal Fabrication Company Using a Lean-Sigma Approach," Enfoque UTE, vol. 15, no. 3, pp. 41–48, Jun. 2024, doi: 10.29019/enfoqueute.1027.

[19] "Index." Accessed: Jan. 29, 2024. [Online]. Available: https://index.org.mx/

[20] G. C. P. Condé and J. C. de Toledo, "Continuous Improvement Related Performance: A Bibliometric Study and Content Analysis," in Springer Proceedings in Mathematics and Statistics, G. dos Reis J.C., M. F. F.G., and V. J. M., Eds., Springer, 2023, pp. 211 – 222. doi: 10.1007/978-3-031-47058-5_17.

[21] S. D. Kulkarni et al., "Enhancing the process capability of machining process of boring tool holder by application of six sigma methodology," Mater Today Proc, vol. 52, pp. 329–338, 2022, doi: 10.1007/978-3-319-92267-6_45.

[22] P. Guleria, A. Pathania, S. Sharma, and J. C. Sá, "Lean six-sigma implementation in an automobile axle manufacturing industry: A case study," Mater Today Proc, vol. 50, pp. 1739–1746, Jan. 2022, doi: 10.1016/J.MATPR.2021.09.177.

Author contribution:
1. Conception and design of the study
2. Data acquisition
3. Data analysis
4. Discussion of the results
5. Writing of the manuscript
6. Approval of the last version of the manuscript

OCS has contributed to: 1, 2, 3, 4, 5 and 6.
JLGA has contributed to: 1, 2, 3, 4, 5 and 6.
FHV has contributed to: 1, 2, 3, 4, 5 and 6.

Acceptance Note: This article was approved by the journal editors Dr. Rafael Sotelo and Mag. Ing. Fernando A. Hernández Gobertti.

Evaluación de los factores de riesgos psicosociales y la incidencia en el desempeño laboral de los trabajadores de la Municipalidad Distrital de Yuracyacu

Evaluation of psychosocial risk factors and their impact on the work performance of the workers of the District Municipality of Yuracyacu

Avaliação dos factores de risco psicossocial e do seu impacto no desempenho profissional dos trabalhadores do Município de Yuracyacu

Abner Jesús García Castillo[1(*)], Emérida Noemí Meza Pérez[2] , Betsabeth Teresa Padilla Macedo[3]

Recibido: 11/02/2025 Aceptado: 26/01/2025

Resumen. - El objetivo de esta investigación es evaluar la incidencia de los factores de riesgo psicosociales en el desempeño laboral de los trabajadores de la Municipalidad Distrital de Yuracyacu. Se utilizó una versión corta y adaptada del cuestionario de factores de riesgos psicosociales de la Superintendencia de Seguridad Social y el Instituto Sindical de Trabajo, Ambiente y Salud. Este cuestionario está integrado por 20 ítems y 5 dimensiones. El desempeño laboral se evaluó bajo un cuestionario de 21 ítems, donde cada ítem tiene 5 opciones de respuesta del tipo Likert. Luego, se empleó la prueba de normalidad de Shapiro-Wilk y la prueba de correlación de Pearson para procesar los datos estadísticos. Los resultados muestran que las dimensiones de los factores de riesgo psicosocial son altos, debido a que, en las dimensiones de trabajo activo y desarrollo de habilidades, apoyo social en la empresa y calidad de liderazgo y compensaciones se reveló que el 100% de los trabajadores presentaron un nivel de exposición psicosocial más desfavorable para la salud. Los niveles de desempeño laboral mostraron que el 31% de los encuestados tiene un alto nivel y el 24% tiene un bajo nivel. Finalmente, los resultados estadísticos arrojaron una correlación de -0.819, el cual indica una relación negativa fuerte entre los factores de riesgo psicosociales y el desempeño laboral. Es decir, a mayor presencia de factores de riesgo psicosociales, menor es el desempeño laboral.

Palabras clave: Factores de riesgo psicosocial; desempeño laboral; ISTAS21.

(*) Autor de correspondencia

[1] Bachiller en Ingeniería Ambiental. Universidad Peruana Unión, abnergarciaa98@gmail.com,
ORCID iD: https://orcid.org/0009-0001-2123-1081

[2] Bachiller en Ingeniería Ambiental. Universidad Peruana Unión, emeridameza23@gmail.com,
ORCID iD: https://orcid.org/0000-0001-6155-2552

[3] Maestro en Educación con mención en Investigación y Docencia Universitaria. Universidad Peruana Unión, padilla@upeu.edu.pe,
ORCID iD: https://orcid.org/0000-0002-3299-8202

Memoria Investigaciones en Ingeniería, núm. 28 (2025). pp. 303-310
https://doi.org/10.36561/ING.28.18
ISSN 2301-1092 • ISSN (en línea) 2301-1106 – Universidad de Montevideo, Uruguay

Summary. - *The objective of this research is to evaluate the impact of psychosocial risk factors on the job performance of employees at the District Municipality of Yuracyacu. A short and adapted version of the psychosocial risk factors questionnaire from the 'Superintendencia de Seguridad Social' (Social Security Superintendence) and the 'Instituto Sindical de Trabajo, Ambiente y Salud' (Trade Union Institute for Work, Environment and Health) was used. This questionnaire consists of 20 items and 5 dimensions. Job performance was assessed using a 21-item questionnaire, where each item had 5 Likert-scale response options. Subsequently, the Shapiro-Wilk test and Pearson's correlation test were applied to process the statistical data.*

The results show that the dimensions of psychosocial risk factors were high, as the dimensions of 'active work and skill development,' 'social support in the company and leadership quality' and 'compensations' revealed that 100% of workers exhibited a psychosocial exposure level more unfavorable to health. Regarding job performance levels, 31% of respondents had an elevated level of performance, while 24% had a low level of it. Finally, the statistical results showed a correlation of -0.819, indicating a strong negative relationship between psychosocial risk factors and job performance. In other words, the greater the presence of psychosocial risk factors, the lower the job performance.

Keywords: *Psychosocial risk factors; occupational performance; ISTAS21.*

Resumo**.** ***-*** *O objetivo desta pesquisa é avaliar a incidência dos fatores de risco psicossociais no desempenho laboral dos trabalhadores da Municipalidade Distrital de Yuracyacu. Utilizou-se uma versão curta e adaptada do questionário de fatores de risco psicossociais da Superintendência de Segurança Social e do Instituto Sindical de Trabalho, Ambiente e Saúde. Este questionário é composto por 20 itens e 5 dimensões. O desempenho laboral foi avaliado mediante um questionário de 21 itens, onde cada item possui 5 opções de resposta do tipo Likert. Em seguida, empregou-se o teste de normalidade de Shapiro-Wilk e o teste de correlação de Pearson para processar os dados estatísticos. Os resultados mostram que as dimensões dos fatores de risco psicossocial são altas, pois nas dimensões de trabalho ativo e desenvolvimento de habilidades, apoio social na empresa e qualidade de liderança e compensações, revelou-se que 100% dos trabalhadores apresentaram um nível de exposição psicossocial mais desfavorável para a saúde. Os níveis de desempenho laboral mostraram que 31% dos entrevistados têm um alto nível e 24% têm um baixo nível. Finalmente, os resultados estatísticos apresentaram uma correlação de -0,819, o que indica uma forte relação negativa entre os fatores de risco psicossociais e o desempenho laboral. Ou seja, quanto maior a presença de fatores de risco psicossociais, menor é o desempenho laboral.*

Palavras-chave: *Factores de risco psicossociais; desempenho profissional; ISTAS21.*

1. Introducción. - En la actualidad, las empresas buscan obtener un alto desempeño de sus colaboradores, representando así un aspecto esencial para lograr la productividad idónea y alcanzar las metas trazadas. La actividad laboral de las personas ha transformado al mundo; sin embargo, ha sido influenciada por la globalización y el avance tecnológico, los cuales, a su vez, han afectado las estructuras del empleo y las condiciones del trabajo, ocasionando así que el entorno laboral se haya vuelto más exigente. Estas condiciones generan factores psicosociales negativos que amenazan a la salud, originando enfermedades y accidentes laborales. Como consecuencia se obtiene un deficiente rendimiento laboral [1].

Así mismo, para alcanzar el desempeño laboral adecuado es importante contar con un ambiente laboral agradable, así como tomar en cuenta la situación personal del trabajador, su cultura y sus necesidades [2]. El buen desempeño de los colaboradores es directamente proporcional con las condiciones laborales adecuadas que brinda el empleador [3].

En ese sentido, la OMS manifiesta que el trabajo es considerado como una actividad beneficiosa para la salud mental del ser humano, pero si dentro de esta actividad se presenta un ambiente laboral negativo, podría generar problemas de salud en los trabajadores y disminuir la productividad [4]. Asimismo, la Organización Internacional del Trabajo, sostiene que el entorno laboral con atmósfera negativa podría generar estrés, ansiedad y depresión en niveles extremos [5]. Estos problemas de salud se pueden vincular directamente con los riesgos psicosociales afectando así el equilibrio y la salud mental de los colaboradores, lo cual favorece el desarrollo de enfermedades ocupacionales.

El trabajo en una entidad del Estado tiene altas exigencias laborales, tales como turnos rotativos, horas extras y el cumplimiento de indicadores de productividad. Lo mencionado afecta el desempeño laboral y la salud de los trabajadores. Por ello, esta investigación tiene como propósito identificar los factores de riesgo psicosocial y determinar la incidencia en el desempeño laboral de los trabajadores de la Municipalidad Distrital de Yuracyacu.

2. Metodología. -

2.1. Diseño Metodológico. - Esta investigación es de carácter aplicativo con un enfoque cuantitativo, del tipo no experimental y descriptiva correlacional, en donde no se manipulan las variables. Dicho de otro modo, se describe la correlación entre variables mediante razones cruzadas de acuerdo con lo establecido en los objetivos del estudio, teniendo como base la medición numérica [6].

2.2. Diseño muestral. -

2.2.1. Población. - La población está conformada por 31 trabajadores de la Municipalidad Distrital de Yuracyacu.

Criterios de inclusión:

- Trabajadores que se encuentren laborando en la Municipalidad Distrital de Yuracyacu.
- Experiencia profesional de 1 año en adelante.
- Trabajadores que deseen participar en el estudio sin ser obligados a hacerlo.

Criterios de exclusión:

- Trabajadores que recién inician sus actividades en la Municipalidad Distrital de Yuracyacu.
- Experiencia menor a 1 año.
- Trabajadores contratados bajo modalidad de terceros.
- Trabajadores que no deseen participar en el estudio.

2.2.2. Muestra. - La muestra es no probabilística de tipo causal para conocer el comportamiento de todos los indicadores a evaluar en cada uno de los empleados. Siguiendo los criterios de exclusión, la muestra es de 29 colaboradores de la Municipalidad Distrital de Yuracyacu, siendo esta cantidad válida y suficiente para esta investigación porque cumple con la condición de representatividad, homogeneidad y adecuación al diseño estadístico.

2.2.3. Unidad de análisis. - Un trabajador de la Municipalidad Distrital de Yuracyacu que cumple con los criterios de inclusión.

2.3. Técnicas de recolección de datos. - Se utilizó como técnica un procedimiento conocido como encuesta, en donde la valoración de cada ítem fue medida teniendo en cuenta la escala de Likert. Tiene características de indagación, exploración y recolección de datos, considerando ítems que analizan de manera directa o indirecta a los individuos que

representan la unidad de análisis. Se llevaron a cabo dos cuestionarios que miden los factores de riesgos psicosociales y el desempeño laboral.

El cuestionario de factores de riesgos psicosociales tiene como fuente el manual de la Superintendencia de Seguridad Social y el Instituto Sindical de Trabajo, Ambiente y Salud, del cual se tomó la versión corta, adecuada y validada [7]. Está integrada por 20 preguntas agrupadas en 5 dimensiones con alternativas de respuesta de opción múltiple. La categorización de los criterios de la variable de riesgos psicosociales se describe en la Tabla I.

Dimensión	Nivel de riesgo		
	Bajo	Medio	Alto
Exigencias psicológicas	0-8	9-11	12-20
Trabajo activo y desarrollo de habilidades	0-5	6-8	9-20
Apoyo social en la empresa	0-3	4-6	7-20
Compensaciones	0-2	3-5	6-12
Doble presencia	0-1	2-3	4-8
Total	0-19	24-33	38-80

Tabla I. Categorización de los riesgos psicosociales.

El desempeño laboral se evalúa bajo un cuestionario que está integrado por 21 ítems las cuales tienen 5 opciones en respuesta tipo Likert cada una: nunca, casi nunca, a veces, casi siempre y siempre [7], cuya categorización se detalla en la Tabla II.

	Alto	Medio	Bajo
Desempeño laboral a nivel general	71-105 pts.	50-70 pts.	21-49 pts.

Tabla II. Desempeño laboral.

2.4. Técnicas estadísticas para el procesamiento de la información. – Luego de la recolección de datos, se realizó la evaluación estadística mediante el programa SPSS (*Statistical Package for Social Sciences*) versión 25.

En la estadística descriptiva se emplearon tablas de doble entrada con frecuencias simples y porcentajes. Para la estadística diferencial se utilizó la prueba de normalidad de Shapiro-Wilk y la prueba de correlación de Pearson el cual permitió relacionar las dos variables.

3. Resultado y Discusión. - De acuerdo con el procesamiento de datos, se obtuvieron los siguientes resultados:

3.1 Resultado 1. - Factores de riesgo psicosociales de los trabajadores de la Municipalidad Distrital de Yuracyacu.

FACTORES DE RIESGO PSICOSOCIALES	CALIFICACIÓN	
Exigencias psicosociales	Verde	7
	Amarillo	9
	Rojo	13
Trabajo activo y desarrollo de habilidades	Verde	0
	Amarillo	0
	Rojo	29
Apoyo social en la empresa y calidad de liderazgo	Verde	0
	Amarillo	0
	Rojo	29
Compensaciones	Verde	0
	Amarillo	0
	Rojo	29
Doble presencia	Verde	18
	Amarillo	9
	Rojo	2

Tabla III. Factores de riesgo psicosociales de los trabajadores de la Municipalidad Distrital de Yuracyacu.

De acuerdo con el manual ISTAS 21 (COPSOQ), los intervalos de puntuaciones de la Tabla III, se interpretan como: verde (nivel de exposición más favorable para la salud), amarillo (nivel de exposición psicosocial intermedio) y rojo (nivel de exposición psicosocial más desfavorable para la salud).

En ese sentido, en la calificación de las dimensiones de la variable "factores de riesgos psicosociales", se observa que la puntuación de la dimensión exigencias psicosociales mostraron que 7 trabajadores presentan un nivel favorable, 9 presentaron un nivel intermedio y 13 colaboradores presentaron un nivel desfavorable para la salud. Estos datos evidenciaron que las actividades laborales de los trabajadores de la Municipalidad Distrital de Yuracyacu requieren atención permanente, toma de decisiones difíciles y desgaste emocional.

Por otro lado, las dimensiones de "trabajo activo y desarrollo de habilidades", "apoyo social en la empresa y calidad de liderazgo" y "compensaciones" evidenciaron que el 100% los trabajadores presentan un nivel desfavorable para la salud. Esto es debido a la carga de trabajo asignado, falta de apoyo de su superior y el temor a que no se les renueve el contrato, al igual que la investigación de Soliz, donde sus hallazgos mostraron que el 90% de los colaboradores tuvieron niveles altos de estrés, a causa de la incertidumbre de los trabajadores sobre la extensión de su contrato laboral y el trato de la jefatura [8].

Finalmente, la dimensión "doble presencia" mostró que 18 trabajadores obtuvieron el nivel favorable y solo 2 presentaron un nivel desfavorable para la salud.

3.2 Resultado 2. - Nivel de desempeño laboral de los trabajadores de la Municipalidad Distrital de Yuracyacu.

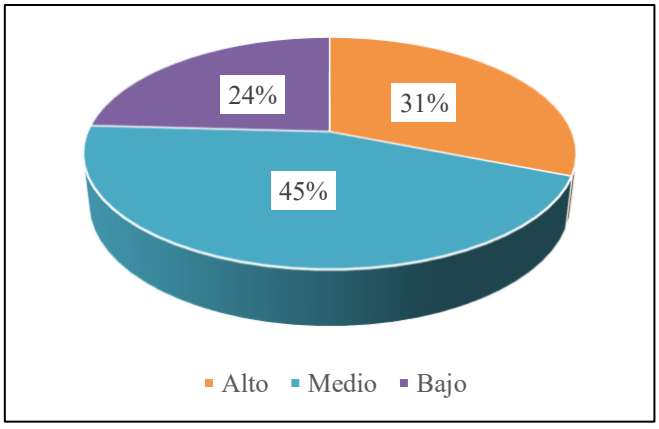

Figura I. Nivel del desempeño laboral.

La figura 1 muestra el nivel del desempeño laboral de los colaboradores de la Municipalidad Distrital de Yuracyacu, donde se observa que el 45% de los trabajadores obtuvieron un nivel medio, el 31% nivel alto y 24% nivel bajo. En relación con ello, los resultados guardan similitud con el estudio de Quiroz y Mamani, donde predomina un nivel medio del 57.3% de desempeño laboral [9].

3.3 Resultado 3. - Identificación de la incidencia de los factores de riesgo psicosociales en el desempeño laboral de los trabajadores de la Municipalidad Distrital de Yuracyacu.

CORRELACIÓN DE PEARSON			
		Desempeño laboral	Factores de riesgo psicosociales
Desempeño laboral	Correlación de Pearson	1	-,819**
	Sig. (bilateral)		,000
	N	29	29
Factores de riesgo psicosociales	Correlación de Pearson	-,819**	1
	Sig. (bilateral)	,000	
	N	29	29

Tabla IV. Correlación de Pearson de las variables.

En la Tabla IV, se observa que el coeficiente de correlación de Pearson es de -0.819, el cual indica una relación negativa fuerte entre los factores de riesgo psicosociales y el desempeño laboral. Esto significa que, a mayor presencia de

factores de riesgo psicosociales, menor es el desempeño laboral. Además, el valor de significancia bilateral es nulo (p = 0.000), lo cual sugiere que esta relación es estadísticamente significativa. Los resultados se asemejan a los obtenidos en los estudios de Aguilar y Lora, en donde se obtuvo una correlación de Spearman igual a -0.886, comprobando así que cuando aumenta el factor de riesgo psicosocial, los niveles de desempeño laboral disminuyen [7].

3. Conclusiones. - Al realizar la investigación, se pudo comprobar que las dimensiones de los factores de riesgo psicosocial se encuentran en un nivel alto, debido a que en tres dimensiones: trabajo activo y desarrollo de habilidades, apoyo social en la empresa y calidad de liderazgo y compensaciones mostró que el 100% de los trabajadores presentaron un nivel de exposición psicosocial desfavorable para la salud. En cuanto a la dimensión de exigencias psicosociales y doble presencia solo 7 y 18 trabajadores respectivamente, se encuentran un nivel de exposición psicosocial favorable para la salud.

Por otro lado, los niveles de desempeño laboral mostraron que el 31% de los trabajadores tienen un alto nivel y el 24% un bajo nivel. Estos resultados evidencian que solo el 31% de trabajadores realizan sus actividades de manera eficaz, eficiente y productiva.

Finalmente, los resultados estadísticos revelaron una relación negativa fuerte entre los factores de riesgo psicosociales y el desempeño laboral. Esto significa, que un aumento en los riesgos psicosociales está asociado a una disminución en el desempeño laboral. Esto destaca y subraya la importancia de gestionar estos factores con el objetivo de optimizar el rendimiento organizacional.

4. Limitaciones y recomendaciones. - Dentro de las limitaciones se destaca el tamaño de la muestra, ya que al ser un tamaño reducido limita la generalización de los resultados en comparación a una población más amplia, no obstante, esto no es un factor que influye en el procesamiento de datos. Por lo que se recomienda que en estudios donde se cuente con una muestra pequeña, se asegure que se cumpla con los criterios de inclusión y representatividad.

Por otro lado, se identificó que las dimensiones empleadas no incluyen factores que pueden influir en los resultados, por ende, se recomienda hacer una investigación más exhaustiva y detallada de las dimensiones, involucrando otros factores como procedencia cultural, historial laboral o expectativas personales.

Referencias

[1] M. M. Díaz Orihuela, J. V. Chávez Sosa, L. V. Castillo Zamora, D. L. Marquez Arcce, J. D. Tantajulca Zuta y D. B. Santamaría Gutiérrez, «Factores psicosociales y rendimiento laboral en colaboradores de una institución educativa privada, Lima, 2021,» Revista Cuidarte, vol. 14, nº 3, pp. 1-11, 2023.

[2] W. d. J. González García y R. Vilchez Pirela, «Factores del desempeño laboral del personal administrativo en universidades nacionales experimentales,» Pensamiento y Gestión, nº 51, pp. 1-21, 2021.

[3] E. Bohórquez, M. Pérez, W. Caiche y A. Benavides Rodríguez, «La motivación y el desempeño laboral: El capital humano como factor clave en una organización,» Universidad y Sociedad, vol. 12, nº 3, pp. 385-390, 2020.

[4] OMS, «Salud mental: fortalecer nuestra respuesta,» Organización Mundial de la Salud, 17 junio 2022. [En línea]. Available: https://www.who.int/es/news-room/fact-sheets/detail/mental-health-strengthening-our-response/?gad_source=1&gclid=CjwKCAiAlJKuBhAdEiwAnZb7lbuXHsaChxa-IkxdEI-FudM-sYb_z6WlLmH6ir6qoM5iYy7wXVH-ahoC6PYQAvD_BwE. [Último acceso: 10 Enero 2025].

[5] OIT, «Nota informativa sectorial de la OIT,» Organización Internacional del Trabajo, Ginebra, 2020.

[6] R. Hernández Sampieri, C. Fernández Collado y P. Baptista Lucio, Metodología de la investigación, México D.F.: McGRAW-HILL / INTERAMERICANA EDITORES, S.A. DE C.V, 2014.

[7] A. Aguilar Velásquez y M. G. Lora Loza, «Factores de riesgos psicosociales y desempeño laboral en trabajadores atendidos en Policlínico de una empresa minera del Sur Peruano, 2021,» Universidad César Vallejo, pp. 1-105, 2022.

[8] R. L. Soliz Baldomar, «El impacto de los factores de riesgo psicosocial en trabajadores del sector industrial,» Trascender, contabilidad y gestión, vol. 7, nº 20, pp. 71-78, 2022.

[9] E. C. Quiroz Risco y D. A. Mamani Chullunquia, «Factores de riesgo psicosocial y el desempeño laboral de los trabajadores de la Municipalidad Provincial de Trujillo,2020» Universidad Privada Antenor Orrego, pp. 68, 2020.

Nota contribución de los autores:

1. Concepción y diseño del estudio
2. Adquisición de datos
3. Análisis de datos
4. Discusión de los resultados
5. Redacción del manuscrito
6. Aprobación de la versión final del manuscrito

AJGC ha contribuido en: 1, 2, 3, 4, 5 y 6.
ENMP ha contribuido en: 1, 2, 3, 4, 5 y 6.
BTPM ha contribuido en: 1, 2, 3, 4, 5 y 6.

Nota de aceptación: Este artículo fue aprobado por los editores de la revista Dr. Rafael Sotelo y Mag. Ing. Fernando A. Hernández Gobertti.

Evolución de la Metrología Eléctrica en Uruguay
Parte I: Desde sus inicios hasta la primera mitad del siglo XX

Evolution of electrical metrology in Uruguay
Part I: Beginnings up to the first half of the 20th century

Evolução da metrologia elétrica no Uruguai
Parte I: Dos primórdios à primeira metade do século XX

Daniel Slomovitz [1(*)]

Recibido: 02/06/2025 Aceptado: 22/06/2025

Resumen. - Las mediciones eléctricas experimentaron un desarrollo significativo desde el inicio de las aplicaciones eléctricas, tanto en el campo de la energía como en el de las comunicaciones. Los primeros cables telegráficos submarinos impulsaron el desarrollo de galvanómetros y puentes de medición de resistencia. A su vez, la expansión de la energía eléctrica estimuló avances en las mediciones de tensión, corriente y potencia.
En Uruguay, los primeros pasos se dieron con la implementación de cursos universitarios sobre estos temas, la creación de laboratorios y el inicio de la investigación y el desarrollo. Esto fue impulsado principalmente por la Facultad de Ingeniería de la Universidad de la República y la empresa eléctrica estatal UTE.
Este trabajo, dividido en dos partes, presenta en esta primera parte los desarrollos entre los comienzos hasta la década de 1960. Fue durante este período que se consolidó la estructura de los laboratorios nacionales y se definieron las normas básicas para las magnitudes más relevantes para el país. En una segunda parte se analizará el desarrollo de las mediciones eléctricas desde esa época hasta la actualidad.

Palabras clave: Patrón, galvanómetro, voltímetro, calibración, historia.

(*) Autor de correspondencia
[1] Profesor, Instituto de Ingeniería Eléctrica, UDELAR (Uruguay), dslomo@gmail.com,
ORCID iD: https://orcid.org/0000-0003-0909-6443

Memoria Investigaciones en Ingeniería, núm. 28 (2025). pp. 311-329
https://doi.org/10.36561/ING.28.19
ISSN 2301-1092 • ISSN (en línea) 2301-1106 – Universidad de Montevideo, Uruguay

Summary. - *Electrical measurements have undergone significant development since the beginning of electrical applications, both in the fields of energy and communications. The first submarine telegraph cables prompted the development of galvanometers and resistance measurement bridges. In turn, the expansion of electrical power systems stimulated advances in voltage, current, and power measurements.*

In Uruguay, the first steps were taken with the implementation of university courses on these topics, the creation of laboratories, and the initiation of research and development activities. This was driven primarily by the Faculty of Engineering of the University of the Republic and the public electric utility UTE.

This work, divided into two parts, presents in this first part the developments between the beginning until the 1960s. It was during this period that the structure of national laboratories was consolidated and basic standards for the most relevant quantities for the country were defined. In a second part we will analyze the development of electrical measurements from that time to the present.

Keywords: *Standard, galvanometer, voltmeter, calibration, history.*

Resumo. ***-*** *As medições elétricas passaram por um desenvolvimento significativo desde o início das aplicações elétricas, tanto na área de energia quanto na de comunicações. Os primeiros cabos telegráficos submarinos impulsionaram o desenvolvimento de galvanômetros e pontes de medição de resistência. Por sua vez, a expansão da energia elétrica impulsionou avanços nas medições de tensão, corrente e potência.*

No Uruguai, os primeiros passos foram dados com a implementação de cursos universitários sobre essas disciplinas, a criação de laboratórios e o início da pesquisa e desenvolvimento. Isso foi impulsionado principalmente pela Faculdade de Engenharia da Universidade da República e pela empresa elétrica estatal UTE.

Esta primeira parte abrange o período até a década de 1960. Foi durante esse período que a estrutura dos laboratórios nacionais foi consolidada e os padrões básicos para as grandezas mais relevantes para o país foram definidos. A segunda parte analisará o desenvolvimento das medições elétricas desde então até o presente.

Palavras-chave: *Padrão, galvanômetro, voltímetro, calibração, histórico.*

1. Introducción. - Uno de los primeros instrumentos de medición eléctrica fue el galvanómetro. Este permitió medir corrientes y tensiones con muy alta sensibilidad. Estaba basado en los trabajos de Oersted y Ampère, que demostraron la íntima relación entre la electricidad y el magnetismo. Su desarrollo comenzó con el descubrimiento del desvío de la aguja de una brújula por efecto de la corriente circulante en un conductor adyacente (Figura I).

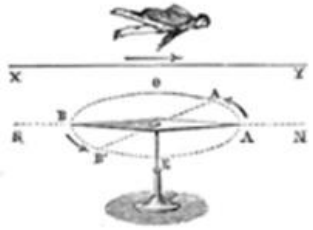

Figura I. Relación entre corrientes y magnetismo [1].

Un invento clave fue realizado por Johann Schweigger en 1820 [2], arrollando el alambre en una bobina que multiplicaba la acción de un solo conductor. Nombró a este instrumento Galvanómetro, en honor a Galvani quien realizó los primeros experimentos de los efectos de la electricidad. Siguientes avances fueron hechos por Johann Christian Poggendorff en 1821, James Cumming en 1821 [3], Leopoldo Nobili en 1828 y William Sturgeon en 1836. La figura II muestra la propuesta de Cumming. Consta de una bobina rectangular, magnificadora del efecto producido por un solo conductor, y una brújula, como elemento sensible al campo magnético.

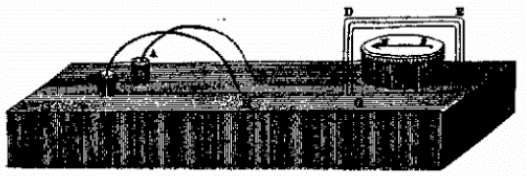

Figura II. Primeros galvanómetros. Propuesta de Cumming [3].

En el año 1856, William Thomson (posteriormente Lord Kelvin) inventa el galvanómetro marino [4], de muy alta sensibilidad, con un haz de luz como indicador y un blindaje magnético que independiza su funcionamiento de condiciones externas (figura III). Su denominación se debió a su aplicación, relacionada con la telegrafía intercontinental mediante los recientes tendidos de cables submarinos. La gran longitud de los mismos y los efectos de sus impedancias atenuaban significativamente las señales lo cual requería gran sensibilidad de los detectores.

Figura III. Galvanómetro marino de Thomson (The Science Museum Group).

Posteriores avances se debieron a Jacques-Arsène d´Arsonval y Marcel Deprez en 1882. Los galvanómetros se siguieron usando como los instrumentos de medida de mayor sensibilidad hasta mediados del siglo XX (figura IV). Una relevante línea de investigación, respecto a estos instrumentos, se desarrolló en Uruguay, tal como se analiza en próximas secciones.

Figura IV. Galvanómetros modernos (Laboratorio de UTE).

A comienzos del siglo XIX se desarrolla el primer elemento tecnológico eléctrico de alto impacto social: la telegrafía. Samuel Morse, en 1836 presentó el primer telégrafo con un código simple, digital, binario, que sólo requería de un hilo para su trasmisión, pues para el retorno se usaba la tierra. En esa época estaban disponibles los elementos básicos, una fuente de corriente continua (pila eléctrica, Volta, 1800) y como detectores, los galvanómetros. El desarrollo de ambos dispositivos posibilitó conectar América con Europa mediante cables submarinos (Cyrus Field, 1854).

Uno de los grandes problemas en estos cables fue las fallas producidas por deterioro de la aislación. Las reparaciones de cables sumergidos en el fondo marino requerían detectar el punto de falla. Para esta tarea, se designó una comisión en Gran Bretaña, que entre otros la integraba el físico e inventor Charles Wheatstone. Su análisis derivó en el desarrollo de puentes de medida de resistencia, con los cuales se podía determinar el largo del cable desde su inicio hasta el punto de falla. Esto fue clave para el desarrollo de los puentes de medida, en particular el que lleva su nombre. La figura V muestra un puente Wheatstone de 1907.

Figura V. Puente Wheatstone (Leeds and Northrup).

El impacto en Uruguay de estos avances en metrología eléctrica, así como desarrollos locales en formación académica, creación de laboratorios e investigación, se vería recién entrado el siglo XX. Significativos esfuerzos, tanto de instituciones académicas como de empresas industriales, condujeron a adelantos que tuvieron repercusión internacional, lo cual se discute en las siguientes secciones.

2. Inicio de planes de formación académica. - Los primeros registros de enseñanza relacionados con medidas eléctricas datan de fines del siglo XVIII, en la recién creada Facultad de Matemáticas de la Universidad del Uruguay, y en la Facultad de Medicina por las aplicaciones de la electricidad en esta rama [5]. En particular se menciona la existencia de un gabinete de física industrial que contaba con una mesa de medidas eléctricas, dos galvanómetros, una brújula de senos y diversas pilas, entre otros elementos. La enseñanza formal de la electrotecnia, con capítulos específicos de metrología eléctrica, comenzó con el plan de estudios de 1906. Un detallado análisis histórico de los distintos planes de estudios, hasta la década de 1940, fue elaborado por Segismundo Gerszonowicz [6], quien citaremos numerosas veces en las siguientes secciones. El plan de 1906, por primera vez incluía un curso especifico de "Nociones de Electrotécnica", en el quinto año. 1910 fue el primer año en que se dictó este curso. Este contenía un capítulo de Unidades de Medida y otro sobre Aparatos de Medida, el que incluía patrones y los medidores básicos de corriente, tensión, potencia y resistencia, así como contadores de energía. En 1914 se agregan al programa clases de laboratorio. Desde la perspectiva actual, resulta raro cómo no se incluyeron, desde el inicio, clases prácticas en una asignatura que está centrada en la experimentación. Como elemento curioso, a visitas actuales, incluía una práctica de calibración de amperímetros por el método electrolítico. Textualmente, "*Este experimento consiste en medir una corriente eléctrica por la cantidad de cobre depositado por ella durante un tiempo determinado*."

En 1927, ya en la existente Facultad de Ingeniería (de aquí en adelante FING), se amplía la temática, abarcando: patrones, galvanómetros, amperímetros electrodinámicos, balanzas, amperímetros térmicos, voltímetros electrodinámicos, voltímetros electrostáticos, medidas de resistencia, puente Wheatstone, resistencia de

galvanómetros, resistencia interna de pilas, medidas de potenciales, medidas de capacidad, medidas de energía eléctrica, de rendimientos y medidas fotométricas.

Un programa más completo aún se estableció en 1931, elaborado por el Ing. Clemente Vercesi. En particular, el curso de Medidas eléctricas se amplió según el programa siguiente (textual).

1. Aparatos de medida. Clasificación, dispositivos de lectura, suspensiones, sensibilidad, amortiguación, galvanómetros, aproximación de los métodos, errores.
2. Medidas de resistencia. Distintos métodos, pequeñas resistencias, grandísimas resistencias, aislación, resistencias líquidas.
3. Medidas de cantidad e intensidad. Galvanómetro, galvanómetro balístico, voltámetros, balanzas, amperímetros, transformadores de intensidad.
4. Medidas de f.e.m. Electrómetros, potenciómetros, vólmetros, transformadores de tensión.
5. Medidas de capacidad e inductancia. Métodos directos, por comparación, patrones.
6. Medidas magnéticas. Intensidad de campos, curva de magnetización, pérdidas.
7. Medidas de potencia. Wáttmetros, circuitos de corriente continua y alterna, potencia, factor de potencia.
8. Circuitos trifásicos. Definiciones, sistemas simétricos y disimétricos, equilibrados y desequilibrados, componentes simétricas, métodos de los 2 wáttmetros y de las 4 lecturas, magnitudes monofásicas equivalentes.
9. Ensayos de sobrecalentamiento. Objeto y duración, medida de las temperaturas, método de circulación, ensayos equivalentes.

Con pequeñas variaciones, este programa siguió vigente hasta la década de 1940, años en que Segismundo Gerszonowicz introduce complementos, y sobre todo una filosofía de enseñanza diferente. Según sus propias palabras [6] *"...con el fin de escapar a la rutina y poder guiar a los estudiantes más íntimamente en el estudio, pensamos dedicar parte o la totalidad del semestre del 6° año (electrotécnica III) al estudio a fondo, con ayuda de artículos originales, trabajos especiales de laboratorio y taller, proyectos, etc. de un solo tema, que variará por completo de un año a otro.*" El programa propuesto (textual), en la temática de medidas eléctricas, fue el siguiente.

1. Errores y correcciones-Unidades, medidas absolutas de resistencia e intensidad, patrones, aparatos de medida, galvanómetros de corriente continua y alterna, aparatos de cero, oscilógrafos, reógrafo, aparatos industriales, registradores.
2. Medidas de resistencias- Medida de grandes resistencias.
3. Medidas de f.e.m-Electrómetros-métodos diversos de medida de la ddp-Potenciómetros de corriente continua y alterna, aplicación a 1a calibración de aparatos de medida.
4. Medidas de capacidades-Coeficientes de inducción mutua y de self inducción, diversos métodos de medida. con estudio particular de puentes en corriente alterna.
5. Medidas de frecuencia-Distintos métodos, frecuencímetro.
6. Medidas del factor de potencia, fasímetro.
7. Medidas de potencia-Medidas en corriente continua y alterna monofásica, diversos métodos, wáttmetros, corrientes parásitas. Análisis de forma de onda.
8. Medida del factor de forma.
9. Medidas de cantidad de electricidad y de energía-Corriente continua: contadores de cantidad de energía, calibrado, ensayos diversos. Corriente alterna: contadores de energía, monofásicos y polifásicos, distintos tipos, calibrado, otros ensayos, contadores de energía reactiva, de energía aparente. Contadores especiales, instalaciones de alta tensión.
10. Medidas magnéticas-Campos débiles, campos fuertes, histéresis, curva de imantación. Permeámetros, pérdidas, aparato Epstein, otros métodos.
11. Medidas en alta tensión-Materiales, estudio de los aisladores y de los cables.

Este programa se complementaba con la realización de proyectos que los estudiantes realizarían parcialmente en el Instituto y parte en sus casas, trabajando en grupos.

En cuanto a facilidades de laboratorio, estas eran muy escasas y según relato de esa época: "*Tan solo en la década de 1930 el instrumental fue incrementado con la adquisición de algunos aparatos, calificados de interesantes como un oscilador 10 a 17000 p/s, un oscilógrafo catódico incompleto, etc. pero con todo, el Laboratorio era extremadamente pobre*". En años siguientes, este laboratorio mejoró, lo cual se discute en la siguiente sección.

Hacia la década de 1950, el programa fue ampliado incluyendo varios ítems sobre determinación de características de

instrumentos y calibración de los mismos. Esto incluía: métodos de determinación de la resistencia y sensibilidad de galvanómetros, diversos métodos de medición de resistencias, calibración de óhmetros, voltímetros, vatímetros y contadores de energía, mediciones de inductancia y capacidad con puentes de alterna, entre otros.

3. Investigación y desarrollo. - En las décadas de 1940 y 1950, impulsado por Segismundo Gerszonowicz, se realizaron múltiples desarrollos sobre aparatos de medida en FING, publicando múltiples artículos. Entre los años 1946 y 1948 dictó conferencias en universidades norteamericanas y viajó frecuentemente a Francia. En esa época fue nombrado "Fellow" del IEEE, el mayor grado que dicha institución otorga. Su destacada actuación merece la inclusión de una breve biografía [7]. Nació en 1909 en Polonia y se graduó de Ingeniero en 1930 en el Instituto Politécnico de Grenoble, Francia. A partir de ese año trabajó en el Laboratorio de Ensayos Mecánicos y Físicos de Materiales de ese Instituto. En 1936 viajó a Uruguay contratado por FING para desempeñarse como Director del recién creado Instituto de Electrotecnia. Se casó, en 1938, con Delia Maggiolo, con quien tuvo un hijo, Jorge, a quien le debo gran parte de la información sobre sus actuaciones. Según su relato, *"…la situación de pre-guerra fue determinante en su decisión de dejar Europa.*" El resto de su familia murió en la guerra. Segismundo Gerszonowicz murió el 10 de julio de 1953 a la temprana edad de 44 años. Aun así, dio un gran impulso a la tecnología de las mediciones eléctricas en Uruguay.

3.1 Galvanómetros. - En los laboratorios de corrientes débiles, tal como se los denominaba en las primeras épocas, los galvanómetros eran un elemento clave para múltiples sistemas de medida. La figura VI muestra uno de tales equipos. El sistema motor, integrado por un cuadro bobinado móvil y un imán fijo, estaba unido a un pequeño espejo que reflejaba la luz de una linterna y proyectaba el haz en una escala ubicada a una distancia del orden del metro. Este sistema amplificaba las pequeñas desviaciones del espejo.

Figura VI. Sistema móvil de galvanómetro de alta sensibilidad (Laboratorio de UTE).

Sus principales problemas se centraban en lograr alta sensibilidad con cortos tiempos de respuesta transitoria. Al ser un sistema oscilatorio electo-mecánico, existe una relación entre sus parámetros eléctricos y mecánicos. Aspectos generales fueron estudiados y documentados en varios trabajos. Uno de sus parámetros fundamentales era el punto de pasaje de respuesta oscilatoria a exponencial-amortiguada, lo cual depende, entre otros parámetros, de su resistencia. En [8] se muestran métodos para la determinación de dicha resistencia critica. Otros estudios abarcaron el retorno a cero de la indicación [9].

Una aplicación diferente corresponde al galvanómetro balístico. En este caso, el instrumento cumple una función de integración, relacionada con la máxima indicación del movimiento transitorio. Cubría campos específicos, como la determinación de propiedades ferromagnéticas [10-12].

En mediciones de alterna, se usaban los llamados galvanómetros de resonancia y de cuerda (figura VII) [13-16]. El sistema móvil resonaba a una frecuencia similar a la de la red, igual a la frecuencia de la señal, logrando así una gran sensibilidad. Mediante una perilla, se podía ajustar ligeramente la frecuencia de resonancia para ajustarla a la frecuencia específica de la señal. Otros tipos de galvanómetros fueron analizados en [17].

Figura VII. Galvanómetro de resonancia para corriente alterna (Laboratorio de UTE)

Como compendio de estos múltiples trabajos, Segismundo Gerszonowicz publicó un tratado de unas 400 páginas sobre galvanómetros en 1943 [18], el más amplio que se haya escrito sobre el tema (figura VIII), una de las pocas referencias latinoamericanas, y quizás la única en español, que figuraba en esas épocas en la bibliografía de países altamente desarrollados. Un detalle que muestra la relevancia internacional que tuvieron sus trabajos en este tema, son las notas de agradecimiento a Segismundo Gerszonowicz, realizadas por varios autores que citaron sus publicaciones, tales como Forest Harris del Laboratorio Nacional de Estados Unidos (NBS) [19], y Charles Dawes [20].

Figura VIII. Tratado sobre galvanómetros, escrito por Segismundo Gerszonowicz [18].

Todavía, hasta la década de 1970, existían en Uruguay galvanómetros en operación tanto en FING como en el Laboratorio de UTE (empresa de energía eléctrica estatal del Uruguay). Pero, su obsolescencia ya fue evidente a partir de la aparición de los primeros instrumentos digitales.

3.2 Laboratorios. - El primer elemento patrón del que se obtuvo referencia, es un resistor de 1 Ω, marca Siemens and Halske, fechado en 1907, propiedad del laboratorio de UTE (figura IX).

Figura IX. Patrón de resistencia fechado en 1907 (Laboratorio de UTE).

Esto muestra que ya existían laboratorios de calibraciones y mediciones de alta precisión en esos años, probablemente ligados a la incipiente expansión de la energía eléctrica en el país. En forma simultánea, se disponía de variados instrumentos de medida. Existen referencias de la existencia en el país de amperímetros de esa época, pero las referencias más antiguas en otras magnitudes, que se han podido ubicar, datan de 1930. La figura X muestra un miliamperímetro fechado en 1906 y un vatímetro, en 1930.

Figura X. Izquierda: Miliamperímetro d´Arsonval - 1906 (izquierda, colección personal). Vatímetro - 1930 (derecha, Laboratorio de UTE).

Los primeros laboratorios, de los que se tiene registro, se crearon en UTE en 1938 y en FING en 1939. Las figuras XI y XII muestran una vista parcial de los laboratorios de FING [21]. Estos inicialmente incluían un área de corrientes continuas y otra de corrientes alternas. En la figura XI se aprecia un galvanómetro de espejo y su escala remota (a la derecha). En la foto de la figura XII se reproduce la instalación de medidas de corriente alterna, con un oscilador a válvulas, patrones de inductancia, y un galvanómetro de vibración tipo Campbell.

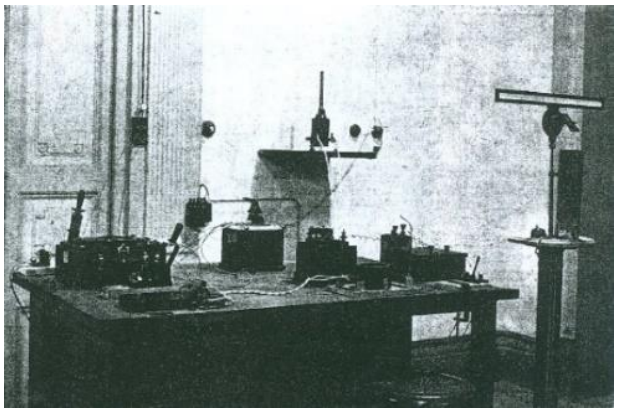

Figura XI. Vista parcial del Laboratorio de Medidas de FING (1939) [21].

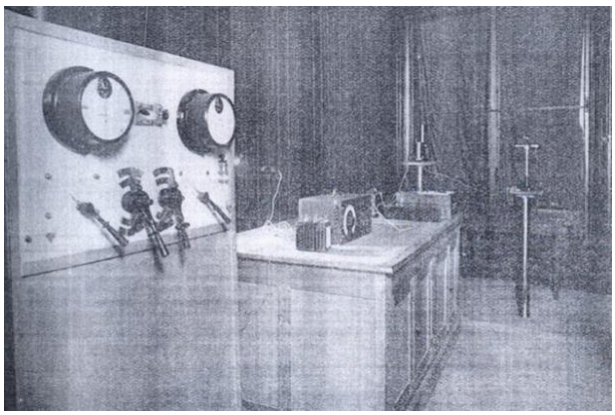

Figura XII. Laboratorio de corriente alterna de FING, incluyendo oscilador a válvulas, patrones de inductancia, y galvanómetro de vibración (1939) [21].

Un reporte posterior muestra el desarrollo de este laboratorio en el año 1953 [22] (Figura XIII).

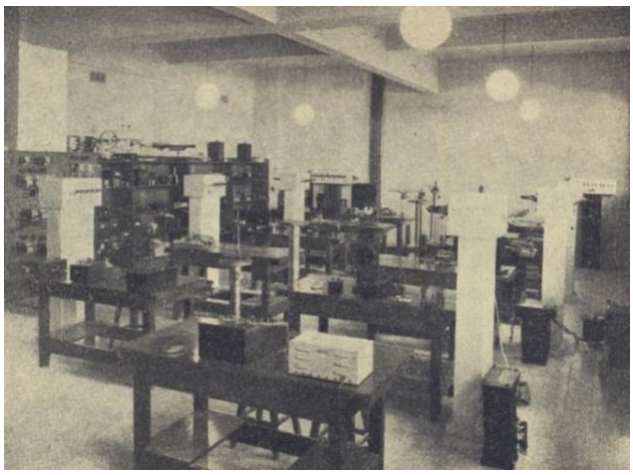

Figura XIII. Laboratorio de medidas eléctricas de FING, año 1953 [22].

Ya contaba con amperímetros, voltímetros y vatímetros de alta precisión para la época (exactitud 0.25 %) y patrones de resistencia entre 0.1 mΩ y 10 kΩ, inductancia entre 1 mH y 1 H, así como pilas patrones Weston de 1.018 V. Entre los galvanómetros se desatacaba un galvanómetro Siemens-Halske con sensibilidades de 0.25 nA y 1.6 μV. Entre los puentes de medición se contaba con un puente Thompson para medidas de pequeñas resistencias y un puente Heaviside-Campbell para las medidas de inductancias. En esa época estaban en uso los oscilógrafos de bucle, que registraban las ondas en papel, permitiendo el registro simultáneo de varios fenómenos. Poseía un equipo de este tipo, marca Westinghouse de 7 bucles, dos de ellos vatimétricos. Los servicios prestados incluían la calibración de contadores de energía, así como de diversos instrumentos de medida.

En la década de 1950, en FING, se desarrolló un laboratorio de alta tensión [22]. Este comprendía un equipo de impulso Westinghouse de tipo Marx, de 1 MV, con sistema de registro formado por un divisor de tensión capacitivo y un oscilógrafo electrónico que permitía registrar fenómenos desde tiempos de 1 μs (figura XIV), y un equipo de alterna de la misma marca, de dos transformadores en cascada, que llegaba hasta 500 kV, con posibilidad de variar la frecuencia entre 40 Hz y 100 Hz (figura XV). Un explosor de esferas completaba la instalación. Este equipamiento estuvo en funcionamiento hasta la década de 1980, cuando fue parcialmente desmantelado.

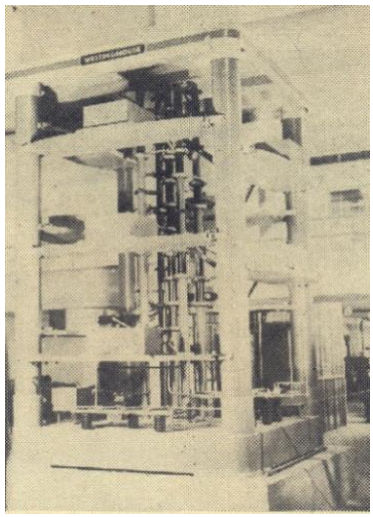

Figura XIV. Generador de impulso sistema Marx, laboratorio de alta tensión de FING, año 1953 [22].

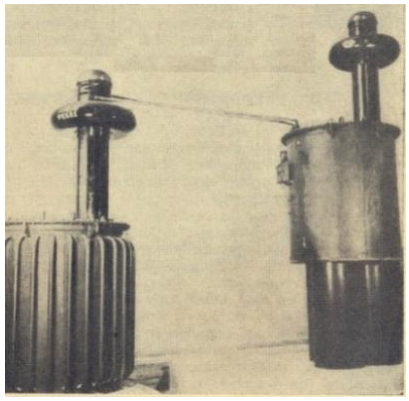

Figura XV. Transformadores del equipo de 500 kV. Laboratorio de alta tensión de FING, año 1953 [22].

Por su lado, la empresa eléctrica, antes de la década de 1930 ya poseía un laboratorio. Esta empresa fue creada por ley el 21 de octubre de 1912, denominándose entonces "Administración General de Usinas Eléctricas del Estado" (UEE), estableciéndose el monopolio estatal de la generación, trasmisión y distribución de electricidad [23]. Sobre este laboratorio la única referencia que se pudo rescatar es que su área era de unos 900 m^2. Registros documentados comienzan recién en 1938, cuando se inauguró el nuevo edificio para los laboratorios, cito en la calle Paraguay 2385, donde aun actualmente se encuentra con más de 2000 m^2 [24]. La figura XVI muestra la inauguración del mismo, con su personal, más aquellos relacionados con su construcción. En la figura XVII aparece una vista panorámica del mismo desde la calle Paraguay, en el año de su inauguración.

Figura XVI. Inauguración del Laboratorio de UTE - 1938.

Figura XVII. Edificio del Laboratorio de UTE - 1938.

Este laboratorio comprendía las áreas de mecánica, química y eléctrica. En lo referente a metrología eléctrica, contaba con un área de calibración de instrumentos, con una mesa marca AEG que incluía fuentes, patrones de resistencia y tensión, y puentes de medida (Figura XVIII).

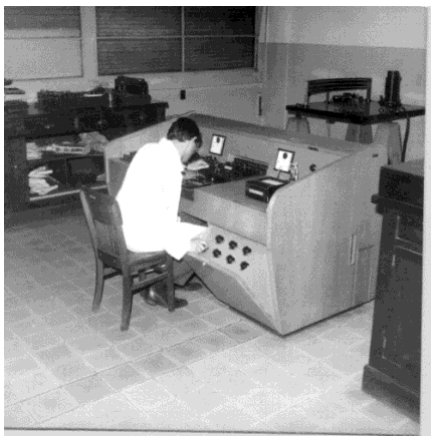

Figura XVIII. Mesa de calibración de instrumentos de medida del Laboratorio de UTE, en operación hasta la década del 1970.

Permitía la calibración de voltímetros, amperímetros y vatímetros, hasta clase 0.2. La limitación era que los instrumentos debían ser aptos para alterna y continua, dado que la mesa solo admitía calibración en corriente continua. Este equipo estuvo en funcionamiento hasta finales de la década de 1970, cuando se desarrollaron sistemas de calibración específicos para corriente alterna. La sala contenía diversos galvanómetros y puentes, así como un instrumento universal Cambridge (al fondo, a la derecha, de la foto) que podía medir tensión, corriente y potencia, con muy alta precisión. El elemento móvil estaba adosado a un espejo, y su escala luminosa medía 3 metros efectivos. Estaba construida en tres niveles. Cuando el haz luminoso llegaba a un extremo de uno de los niveles, aparecía en el siguiente, al comienzo, debido a que tenía tres linternas desplazadas sobre su mesa. Para evitar el efecto de vibraciones del piso, toda la estructura se apoyaba en tres grandes patas de hormigón. Su caja de control, con los ajustes de tensión y corriente, se muestra en la figura XIX.

Figura XIX. Caja de control del instrumento universal Cambridge (Laboratorio de UTE).

Otra área estaba dedicada a la calibración de medidores de energía (figura XX). Varias mesas de instrumentos permitían calibrar una gran cantidad de contadores simultáneamente, necesario por la alta demanda de la empresa.

Figura XX. Sala de calibración de medidores de energía del laboratorio de UTE.

También contaba de una sala para la calibración de transformadores de medida, con patrones y un puente que todavía continúa funcionando (figura XXI).

Figura XXI. Sala de calibración de transformadores de medida del Laboratorio de UTE. Década de 1940.

En el área de la alta tensión, desde su inauguración, UTE ya poseía un pequeño laboratorio con equipamiento de alterna hasta 100 kV (figura XXII). Prácticamente se mantuvo igual hasta fines de la década de 1970, cuando fue ampliada y equipada con nuevos aparatos.

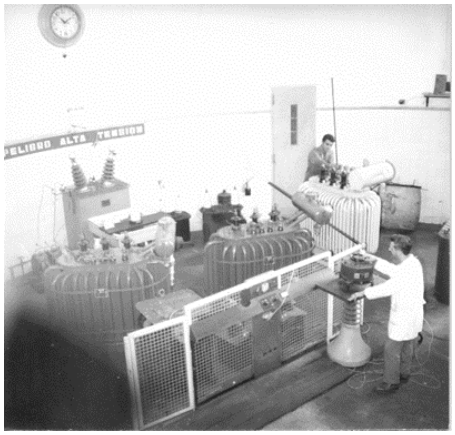

Figura XXII. Sala de alta tensión del Laboratorio de UTE. Década de 1940.

Un tercer laboratorio eléctrico se creó por la Ley N° 13 318 en 1964, con el nombre de Laboratorio de Análisis y Ensayos (LAE), cambiándose a LATU (Laboratorio Tecnológico del Uruguay) en 1975. El propósito inicial fue de control de la calidad de los productos de exportación. Recién en 1982 se crea un área de metrología, debido a la aprobación de la Ley Nacional de Metrología (15298/82). Esta le asignó al LATU la responsabilidad del mantenimiento, custodia y diseminación de los patrones nacionales de medida. Es así que el LATU, hasta hoy, mantiene la trazabilidad a patrones primarios de medición con niveles de incertidumbre acordes con los requerimientos del país. En ese entonces, el área de metrología eléctrica contaba con patrones de resistencia, puentes de medida de resistencia y fuentes de tensión patrones basadas en pilas Weston. Mediante un convenio con UTE, en 1999 concede a esta empresa la custodia de los Patrones Eléctricos Nacionales, convirtiéndose el laboratorio de UTE en Laboratorio Designado Nacional.

3.3 Patrones. - Como se describió anteriormente, desde principios del siglo XX hay registro de la existencia de patrones de unidades eléctricas en UTE. También en FING existían patrones fechados en la primera mitad del siglo XX. En esos tiempos, las principales magnitudes necesarias para el mantenimiento de patrones fueron resistencia y tensión. A partir de ellas, se derivaban otras, como corriente y potencia.

3.3.1 Resistencia. - Los resistores patrones, basados en la resistencia de aleaciones, como la manganina, constituyeron los patrones primarios de resistencia. Los modelos del tipo Thomas de 1 ohm (figura XXIII) son los más estables. A partir de ellos se establecen los valores de toda la escala de resistencia. Ya hacia la mitad del siglo XX, tanto UTE como LATU poseían varias unidades de estos resistores, los cuales constituían el Patrón Nacional de Resistencia. Aun actualmente, siguen en operación.

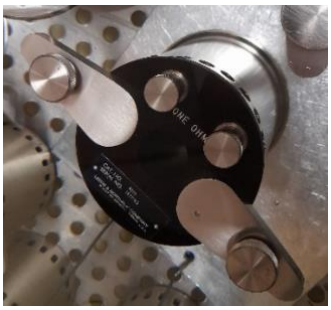

Figura XXIII. Resistor patrón tipo Thomas (Laboratorio de UTE).

3.3.2. Tensión continua. - En 1893, Edward Weston presentó una patente por una pila patrón electroquímica que generaba un voltaje muy estable de 1.0183 V a 20 °C (figura XXIV). Su diseño incluía un ánodo y un cátodo formado por amalgamas de cadmio y mercurio. La estructura de la pila consistía en una ampolla de vidrio con forma de H, con contactos eléctricos de platino ubicados en la base.

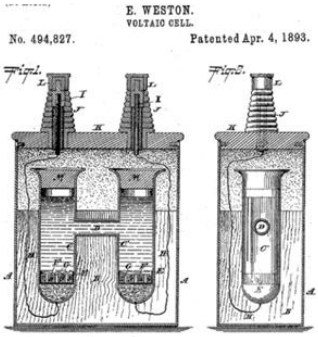

Figura XXIV. Pila patrón propuesta por Weston en 1893.

Estas pilas, si bien eran muy estables en el tiempo, tenían muy alta dependencia con la temperatura, eran muy afectadas por golpes o sacudidas, así como por el consumo de corriente. Aun así, los tres laboratorios antes mencionados poseían varios ejemplares, que estuvieron en uso hasta la década de 1980 (figura XXV).

Figura XXV. Pila patrón tipo Weston (Laboratorio de UTE).

3.3.3 Otras magnitudes. - Complementaban el equipamiento de medida, patrones de capacidad e inductancia (figura XXVI), así como diversos puentes de medida [25].

Figura XXVI. Patrón de capacidad de 1 μF (Laboratorio de UTE).

La Figura XXVII muestra un puente Schering de la marca Trüb-Täuber, todavía en servicio hacia fines del siglo XX. Fue diseñado para medidas de capacidad en alta tensión, a la frecuencia de la red, con un capacitor patrón, aislado en aire, de 100 kV (foto a la derecha).

Figura XXVII. Puente Schering de la marca Trüb-Täuber y capacitor patrón de alta tensión (Laboratorio de UTE).

En relación a la magnitud tiempo-frecuencia, una detallada descripción del desarrollo de patrones de frecuencia en Uruguay puede verse en [26]. A modo de resumen, los principales hitos fueron los siguientes. El Laboratorio de UTE, en la década de 1960, poseía un reloj patrón de péndulo (figura XXVIII). Su estabilidad era de unos 3 segundos por año. Estaba encerrado en un recipiente hermético, y un ajuste muy fino de su frecuencia se realizaba variando la presión interior del aire.

Figura XXVIII. Reloj patrón de péndulo Clemenes Riefler (Laboratorio de UTE).

En esa misma década, en FING se desarrolló un patrón de frecuencia electrónico basado en un cristal de cuarzo y tubos de vacío [27]. Su circuito principal se reproduce en la Figura XXIX.

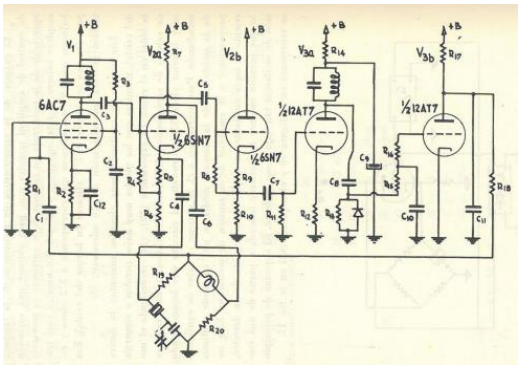

Figura XXIX. Patrón de frecuencia basado en un cristal de cuarzo y electrónica con tubos de vacío, desarrollado por FING en 1966 [27].

La estabilidad alcanzada fue del orden de 0.5 segundos por año. Este constituyó el inicio de desarrollos locales en esta área. Posteriores mejoras se lograron con desarrollos basados en relojes atómicos.

4. Sistemas de unidades. - Existen registros de unidades de medida ya en el antiguo Egipto. Sin embargo, el primer acuerdo internacional sobre este tema debió esperar hasta 1875. En ese año se firmó en Paris, por diecisiete estados,

la llamada Convención del Metro, con el fin de establecer una organización que garantizara la compatibilidad de las mediciones en todo el planeta. Así mismo, se definieron los patrones de masa y longitud, prototipos de los cuales fueron entregados a los países firmantes. Uruguay adhirió al tratado en 1908. Dentro de la estructura, se creó el Bureau Internacional de Pesas y Medidas (BIPM), con funciones de laboratorio en el cual se realizarían calibraciones, se mantendrían los patrones y se organizarían rondas de intercomparaciones. El gobierno francés donó el Pabellón de Breteuil para uso de esta organización (figura XXX), que se encontraba en situación ruinosa. Posteriormente fue remodelado y ampliado y es el actual lugar de funcionamiento de esta organización.

Figura XXX. Pabellón de Breteuil en 1875 (contribución de Luis Mussio, OIML)

Respecto a la incorporación de otras magnitudes, los sistemas de unidades incorporaron el tiempo, con lo cual se satisfacían los requerimientos de la mecánica. La discusión posterior se centró en cuál sería la magnitud a adicionar para contemplar el electromagnetismo. Había acuerdo en que alcanzaría una magnitud independiente adicional, pero siguieron complicadas discusiones sobre cuál debería ser la cuarta unidad. Ya en 1889, Sir Arthur William Rucker había propuesto incorporar, en lugar de una magnitud, una constante, la permeabilidad del vacío. Puede parecer raro que un sistema de unidades este basado en constantes universales, pero debe tenerse en cuenta que en conjunto con ecuaciones de leyes de la física es posible relacionar distintas magnitudes. Esta propuesta fue refrendada el Sub-Comité de Magnitudes y Unidades Eléctricas y Magnéticas de la Comisión Electrotécnica Internacional en 1930. Esto se derivó al Comité Consultivo de Electricidad del BIPM para que decidiera entre las unidades de coulomb, ampere, volt, ohm, farad, henry, weber. El Comité, en cambio, prefería la constante citada, pero dado que no figuraba en la lista, votó por el ohm.

Un detallado análisis de las distintas propuestas y resoluciones, así como su propia opinión, fueron publicados por Segismundo Gerszonowicz en 1939 y 1941 [28-29], dado que hasta esas fechas no se había decidido sobre este tema. Según cita textual decía: "*Esperamos que el Congreso Sudamericano de Ingeniería se unirá a nuestro punto de vista y pedirá a los organismos internacionales habilitados que se active la discusión del asunto en vista de su resolución definitiva*," lo que lamentablemente no ocurrió hasta 1960. En este año, la 11ª Conferencia General de Pesas y Medidas definió el sistema de unidades electromecánico formado por las magnitudes de longitud, masa, tiempo e intensidad, equivalente a las primeras propuestas de asignar un valor a la constante de permeabilidad magnética. Quedaban así también definido el volt, ohm y watt, como lo muestra la figura XXXI. Las unidades de capacidad e inductancia también quedaron definidas a partir de las cuatro básicas citadas.

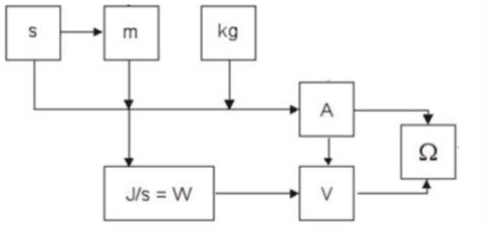

Figura XXXI. Sistema de unidades definido por el BIPM en 1960.

5. Conclusiones. - El desarrollo de la metrología eléctrica en Uruguay, desde comienzos del siglo XX hasta mediados del mismo muestra una evolución que acompañó al avance mundial. Comenzaron cursos universitarios sobre mediciones eléctricas, se crearon laboratorios, tanto en el ámbito universitarios como en el industrial. La Facultad de Ingeniería de la Universidad de la República desempeñó un papel fundamental en la formación académica en esta disciplina, desde 1906. Figuras destacadas como el Ing. Segismundo Gerszonowicz lideraron investigaciones originales, publicando textos que alcanzaron reconocimiento internacional.

En paralelo, la empresa estatal UTE desarrolló un laboratorio que fue pionero en la implementación y uso de patrones eléctricos y aparatos de medida. Con la posterior creación del laboratorio LATU, se consolidó la estructura metrológica del Uruguay.

Esta primera etapa sentó las bases para el desarrollo posterior de la metrología eléctrica en Uruguay, que continuaría su evolución con la aparición de nuevas tecnologías, instrumentos digitales y su inserción en redes internacionales tales como el Sistema Interamericano de Metrología (SIM) y el Bureau Internacional de Pesas y Medidas (BIPM), lo cual será desarrollado en una segunda parte de este trabajo.

Referencias

[1] A. Guillermin, El mundo físico Montaner y Simon Editores, Barcelona, 1893.

[2] J. S. C. Schweigger, Nachricht von der neuesten galvanischen Entdeckung, Journal für Chemie und Physik, 1820, vol. 29: p. 1–17.

[3] J. Cumming, On the Connexion of Galvanism and Magnetism, Transactions of the Cambridge Philosophical Society, 1821, vol. 1, p. 269–279,

[4] W. Thomson, On the Electromotive Force of Voltaic Combinations, Proceedings of the Royal Society of London, 1856, vol. 8, p. 546–550.

[5] Anales de la universidad, Tomo XI, 1901, p. 699.

[6] S. Gerszonowicz, Historia de la enseñanza de la electrotécnica en la Facultad
de Ingeniería de Montevideo, Boletín de la Facultad de Ingeniería, 1940, vol. 5, no 9, p. 513-525, Disponible en https://www.fing.edu.uy/biblioteca/revistas/198217.pdf.

[7] D. Slomovitz, Mediciones eléctricas, IEEE, 2004, CD ROM, ISBN 07803-8395-8.

[8] S. Gerszonowicz, Sobre la determinación directa y semidirecta de la resistencia crítica de los galvanómetros, Boletín de la Facultad de Ingeniería, 1938, p.453-459.

[9] S. Gerszonowicz, Estudio del retorno al cero de los galvanómetros, Boletín de la Facultad de Ingeniería y Ramas Anexas, FIRA, 1939, vol. 4, no 8, p. 460-471.

[10] D. Maggiolo de Gerszonowicz y S. Gerszonowicz, Expresión analítica aproximada de la curva Sq(R) del balístico y su aplicación a algunas medidas rápidas, Boletín de la Facultad de Ingeniería FIRA, 1940, vol. 5, no 9, p. 496-502. Disponible en https://www.fing.edu.uy/biblioteca/revistas/198738.pdf

[11] S. Gerszonowicz, Sobre la corrección debida a los efectos termoeléctricos en las medidas balísticas, Revista Electrotécnica, 1941, Buenos Aires.

[12] S. Gerszonowicz, Galvanómetro balístico. Fluxímetro, Publicaciones. Series Textos y complementos, Laboratorios, 1941, p.56.

[13] S. Gerszonowicz, Galvanómetro de resonancia, Publicación del Instituto de Electrotécnica, 1942, no 5, p. 45. Disponible en https://www.fing.edu.uy/biblioteca/bibliografias/200554.pdf

[14] S. Gerszonowicz, El aparato de cuerda como galvanómetro de resonancia, Serie II: Trabajos del Instituto de Electrotécnica, 1941.

[15] S. Gerszonowicz, Galvanómetros de cuerda y de bucle, Publicación del Instituto de Electrotécnica, 1942, no 7, p.22. Disponible en https://www.fing.edu.uy/biblioteca/bibliografias/200373.pdf

[16] S. Gerszonowicz, El aparato de cuerda como galvanómetro de resonancia, Revista Electrotécnica, 1943, Buenos Aires.

[17] S. Gerszonowicz, Electrodinamómetros, galvanómetros de inducción, de hierro, térmicos, Publicación del Instituto de Electrotécnica, 1943, no 8, p. 34. Disponible en https://www.fing.edu.uy/biblioteca/bibliografias/560249.pdf

[18] S. Gerszonowicz, Galvanómetros y oscilógrafos, Lit. e Imp. del Comercio, Montevideo, 1943. Disponible en https://www.fing.edu.uy/biblioteca/bibliografias/200377.pdf

[19] F. Harris, Electrical Measurements, Wiley, p. ix, 1952.

[20] C. Dawes, A course in electrical engineering, vol. II, Alternating currents, McGraw-Hill Book Company, 1946.

[21] S. Gerszonowicz, Los nuevos laboratorios del Instituto de Electrotécnica, Boletín de la Facultad de Ingeniería, 1939, vol. 4, no 7, p. 417-427, Disponible en https://www.fing.edu.uy/biblioteca/revistas/198222.pdf

[22] A. Cisa, Los laboratorios del Instituto de Electrotécnica de la Facultad de Ingeniería y Ramas Anexas, Boletín de la Asociación Uruguaya para el Progreso de la Ciencia, 1953, vol. 2, no 3, p. 18-26. Disponible en https://www.fing.edu.uy/biblioteca/revistas/424537.pdf

[23] A. Waiter, Trayectoria tecnológica, aspectos económicos e institucionales: inicios de la generación de energía eléctrica en Uruguay, Revista uruguaya de historia económica, 2020, no 18, p. 36-51. Disponible en https://www.audhe.org.uy/publicaciones/index.php/RUHE/article/view/20/24

[24] Se inauguró el nuevo laboratorio, La revista de la UTE, 1938, no 15, p. 6-8. Disponible en https://archive.org/details/35-la-revista-de-la-ute-uruguay-abril-1938-n-15/page/5/mode/2up

[25] D. Maggiolo de Gerszonowicz, Sensibilidad del puente de Wheatstone, Boletín de la Facultad de Ingeniería, 1943, vol. 2, no 4, p. 293-309. Disponible en https://www.fing.edu.uy/biblioteca/revistas/198741.pdf

[26] L. Trigo, A. García, y D. Slomovitz, Desarrollo de patrones de tiempo y frecuencia en Uruguay, Memoria investig. ing. (Facultad Ing., Univ. Montev.), 2023, no 25, p. 72–89.

[27] R. P. Iribarren, V. Herrero, Desarrollo de un patrón de un patrón de frecuencia con oscilador de Meacham a cristal, en cámara termostática de precisión, Boletín de la facultad de Ingeniería y Agrimensura, Montevideo, 1966, vol. IX, no 27, p. 821-854.

[28] S. Gerszonowicz, Sobre la cuarta unidad fundamental en electrotécnica, Boletín de la Facultad de Ingeniería, 1939, vol. 4, no 7, p. 428-434 y vol. 5, no 9, p. 428-492. Disponible en https://www.fing.edu.uy/biblioteca/revistas/198221.pdf

[29] S. Gerszonowicz, Unidades eléctricas y fotométricas, Lit. e Imp. del Comercio, Montevideo, 1941. Disponible en https://www.fing.edu.uy/biblioteca/bibliografias/198229.pdf

Nota contribución de los autores:

1. Concepción y diseño del estudio
2. Adquisición de datos
3. Análisis de datos
4. Discusión de los resultados
5. Redacción del manuscrito
6. Aprobación de la versión final del manuscrito

DS ha contribuido en: 1, 2, 3, 4, 5 y 6.

Nota de aceptación: Este artículo fue aprobado por los editores de la revista Dr. Rafael Sotelo y Mag. Ing. Fernando A. Hernández Gobertti.

Lista de Autores – Memoria Investigaciones en Ingeniería (Número 28).

List of Authors – Memoria Investigaciones en Ingenieria (Volume 28).

MIIUM28-08: Polymer Pathways: A sustainable approach to plastic waste disposition.
Prof. Ifrah Asif, NED University of Engineering and Technology (Pakistan).
Prof. Eylia Abbas Jafri, NED University of Engineering and Technology (Pakistan).
Prof. Bushra Fatima, NED University of Engineering and Technology (Pakistan).
Mehak Fatima Aamir, NED University of Engineering and Technology (Pakistan).

MIIUM28-10: Enhanced Mobility Aid for the Visually Impaired: An Ultrasonic Sensor and Arduino-Based Smart Walking Stick
Prof. Shahzor Memon, Hamdard University (Pakistan).
Eng. Mirza Muhammad Aamir, Pakistan Water & Power Development Authority (Pakistan).
Dr. Prof. Sadiq Ur Rehman, Hamdard University (Pakistan).
Prof. Halar Mustafa, Hamdard University (Pakistan).
Prof. Muhammad Shakir Sheikh, Szabist University (Pakistan).

MIIUM28-12: Design and Development of IoT-based Harvesting Robo-Vec.
Dr. Prof. Sadiq Ur Rehman, Hamdard University (Pakistan).
Dr. Prof. Yasmin Abdul Wahab, Universiti Malaya (Malaysia).

MIIUM28-13: Post Weld Quenching Impact on Microstructure and Mechanical Properties (Tensile, Impact, Hardness) of High-Strength Low-Alloy Steel.
Dr. Atif Shazad, NED University of Engineering and Technology (Pakistan).
Prof. Muhammad Uzair, NED University of Engineering and Technology (Pakistan).

MIIUM28-14: Mechanical Characterization of Post weld quenched Al 6082-T6 TIG welded Joints.
Dr. Atif Shazad, NED University of Engineering and Technology (Pakistan).
Prof. Muhammad Uzair, NED University of Engineering and Technology (Pakistan).
Junaid Jadoon, Pakistan Institute of Engineering & Applied Sciences (Pakistan).
Muhammad Saleem Khan, NED University of Engineering and Technology (Pakistan).

MIIUM28-15: Interacción Suelo-Estructura de una edificación con losa de cimentación con los modelos estáticos de Winkler y Pasternak.
Dr. Juan Contreras, Universidad Nacional del Santa (Perú).
Dr. Genner Villarreal Castro, Universidad de San Martín de Porres (Perú).

MIIUM28-16: Design of a vehicular emergency intercom system using electronic circuits and sensors.
MSc Holger Santillán, Salesian Polytechnic University (Ecuador).
Eng. Carolina López, Salesian Polytechnic University (Ecuador).
Eng. Kiara García, Salesian Polytechnic University (Ecuador).
MSc David Cárdenas, Salesian Polytechnic University (Ecuador).

MIIUM28-17: Explorando las Profundidades: Reconstrucción de Cuevas y Detección de Murciélagos mediante Imágenes Infrarrojas

MSc Israel Cruz Rangel, Instituto Politécnico Nacional (México).
MSc José-Ángel Arroyo-Romero, Instituto Politécnico Nacional (México).
Dr. Isabel Bárcenas-Reyes, Instituto Politécnico Nacional (México).
Dr. José-Joel González-Barbosa, Instituto Politécnico Nacional (México).
Dr. Juan Bautista Hurtado-Ramos, Instituto Politécnico Nacional (México).
Dr. Francisco-Javier Ornelas-Rodríguez, Instituto Politécnico Nacional (México).
Dr. Alfonso Ramírez-Pedraza, Secretaría de Ciencia, Humanidades, Tecnología e Innovación (México).

MIIUM28-18: Interacción suelo-estructura de una edificación con losa de cimentación por los modelos dinámicos de Barkan y Savinov, Norma Rusa SNIP 2.02.05-87 y Gazetas y Mylonakis.

Dr. Juan Contreras, Universidad Nacional del Santa (Perú).
Dr. Genner Villarreal Castro, Universidad de San Martín de Porres (Perú).

MIIUM28-19: An IoT-Based Autonomous Waiter Robot.

Dr. Prof. Sadiq Ur Rehman, Hamdard University (Pakistan).

MIIUM28-21: Two-Dimensional Numerical Analysis on the Double Shear Specimens of Timber-Concrete Composite Structures: Effects of Screw Dimensions and Timber Density

L. Jun En, Universiti Malaya (Malaysia).
M. A. Mohd Snin, Universiti Malaya (Malaysia).
S. N. Fatimah Ghazali, Universiti Malaya (Malaysia).
N. A. Fatihah Mokhtar, Universiti Malaya (Malaysia).
M. Ikmal Zainal, Universiti Malaya (Malaysia).
R. Suryavarman, KPR Institute of Engineering and Technology (India).

MIIUM28-22: Eficiencia de la lombriz roja californiana en la biorremediación de suelos contaminados con hidrocarburos.

Samuel Baldeon Coronado, Universidad Peruana Unión (Perú).
Kettly Baltazar Torres, Universidad Peruana Unión (Perú).
MSc Jhon Patrick Ríos Bartra, Universidad Peruana Unión (Perú).

MIIUM28-23: Application of Six Sigma Methodology for Enhancement of Soft Plastic Extrusion Process.

MSc Muhammad Mansoor Uz Zaman Siddiqui, NED University of Engineering and Technology (Pakistan).
Eng. Adeel Tabassum, NED University of Engineering and Technology (Pakistan).

MIIUM28-24: Parametric Optimization of Electric Discharge Machining for AISI 1045 Steel: A Comprehensive Study.

MSc Muhammad Mansoor Uz Zaman Siddiqui, NED University of Engineering and Technology (Pakistan).
Prof. Syed Amir Iqbal, NED University of Engineering and Technology (Pakistan).
Eng. Ali Zulqarnain, NED University of Engineering and Technology (Pakistan).
Eng. Adeel Tabassum, NED University of Engineering and Technology (Pakistan).

MIIUM28-26: Direct Air Carbon Capture Using Metal-Organic Frameworks: Techno-Economic Performance of Temperature Vacuum Swing Adsorption Systems.

Dr. Haider Ali, NED University of Engineering and Technology (Pakistan).
Dr. Duraid Uddin, NED University of Engineering and Technology (Pakistan).
Dr. Asad A. Naqvi, NED University of Engineering and Technology (Pakistan).
Umair Naeem, NED University of Engineering and Technology (Pakistan).
Nomaan Akhtar, NED University of Engineering and Technology (Pakistan).
Saqib Shams, NED University of Engineering and Technology (Pakistan).
Ali Karim, NED University of Engineering and Technology (Pakistan).

MIIUM28-31: On-Time Delivery Improvement in an Injection Molding Process Applying a Problem-Solving Approach Based on Lean-Sigma and the MSA Effect.

Dr. (c) Omar Celis-Gracia, Universidad Autónoma de Ciudad Juárez (México).
Prof. Jorge Luis García-Alcaraz, Universidad Autónoma de Ciudad Juárez (México).
Dr. (c) Fabiola Hermosillo-Villalobos, Universidad Autónoma de Ciudad Juárez (México).

MIIUM28-33: Evaluación de los factores de riesgos psicosociales y la incidencia en el desempeño laboral de los trabajadores de la Municipalidad Distrital de Yuracyacu.

Abner Jesús García Castillo, Universidad Peruana Unión (Perú).
Emérida Noemí Meza Pérez, Universidad Peruana Unión (Perú).
MSc Betsabeth Teresa Padilla Macedo, Universidad Peruana Unión (Perú).

MIIUM28-42: Evolución de la Metrología Eléctrica en Uruguay Parte I: Desde sus inicios hasta la primera mitad del siglo XX.

Dr. Prof. Daniel Slomovitz, Universidad de la República (Uruguay).

Lista de Revisores – Memoria Investigaciones en Ingeniería (Número 28).

List of Reviewers – Memoria Investigaciones en Ingenieria (Volume 28).

Dr. Ricardo Oviedo Sarmiento, Universidad Nacional Federico Villarreal (Peru).
Dr. Waldo Hasperué, Universidad Nacional de La Plata (Argentina).
Dr. Ghazanfar Mehdi, University of Salento (Italy).
Dr. Asad Ali Zaidi, Islamic University of Madinah (Saudi Arabia).
MSc Jordy Joseph Sosa Rodas, Universidad de San Carlos de Guatemala (Guatemala).
Dr. Fidel Germán Sagástegui Plasencia, Universidad Privada Antenor Orrego (Peru)
Dr. Víctor Manuel Morales Rocha, Universidad Politécnica de Cataluña (Spain).
Dr. Alfonso Fernandez, Instituto Politécnico Nacional, Escuela Superior de Cómputo (Mexico).
Dr. Augusto Villa Monte, Facultad de Informática, Universidad Nacional de La Plata (Argentina).
Dr. Juan Gabriel Avina-Cervantes, Universidad de Guanajuato, (Mexico).
Dr. Johan Andrés Avendaño Arias, Universidad Distrital Francisco José de Caldas, (Colombia).
Mag. Keller Sánchez Dávila, Universidad Nacional de San Martín (Peru).
Mag. Harvey Charles Dávila Lavi, Universidad Nacional de San Martín (Peru).
Prof. Gustavo Emilio Ramírez Caballero, Universidad Industrial de Santander (Colombia).
Dr. Carlos Francisco Javierre Lardies, Universidad de Zaragoza (Spain).
Dr. Jorge Limón Romero, Universidad Autónoma de Baja California (Mexico).
Dr. Mahdi Hassan, Quaid e Awam University of Engineering Science and Technology (Pakistan).
Dr. Ahsanullah Soomro, Quaid e Awam University of Engineering Science and Technology.
Dr. Ahsan Ahmed, NED University of Engineering and Technology (Pakistan)
Dr. Muhammad Asif, National University of Science and Technology (Pakistan)